



# **Probing Structure and Dynamics of Amorphous Ice with Small-Molecule Nanoprobes**

**Sukhpreet Kaur Talewar**

Thesis submitted in partial fulfilment of the  
requirements for the degree of Doctor of  
Philosophy

Department of Chemistry  
University College London  
July 2021

I, Sukhpreet Kaur Talewar, confirm that the work presented in this thesis is my own.  
Where information has been derived from other sources, I confirm that this has been  
indicated in the thesis.

Signature:.....

Date:.....

## Abstract

Water ( $\text{H}_2\text{O}$ ) is omnipresent on the surface of the Earth, the atmosphere, in nature, and on various celestial bodies.<sup>1</sup> The phase diagram of ice exhibits enormous complexity with a plethora of structures and at least two amorphous ices.<sup>2, 3</sup> One of these, low-density amorphous ice, is the most abundant solid in the Universe. Despite  $\text{H}_2\text{O}$ 's significance, a full understanding of its role in physical processes remains elusive.<sup>4</sup>

$\text{H}_2\text{O}$  is capable of building complex hydrogen-bonded networks, and solvates hydrophobic/hydrophilic species.<sup>2</sup> Carbon and  $\text{H}_2\text{O}$  often coexist, forming interfaces in highly diverse environments.<sup>5, 6</sup> This thesis focuses on the structure of  $\text{H}_2\text{O}$  in the hydration shells of hydrophobes, tracking the structure and dynamics of vapour deposited amorphous ice with finely dispersed small-molecule nanoprobos.

Detailed insights into the morphology of amorphous solid water (ASW)<sup>7</sup> and evidence for the presence of three discernible desorption processes present in macroscopic films of amorphous ice have been demonstrated. They are attributed to gas desorption from open cracks, from the collapse of internal voids, and from matrix-isolated gas induced by the irreversible crystallisation of  $\text{H}_2\text{O}$  to stacking disordered ice.<sup>7</sup>

Due to adamantane ( $\text{C}_{10}\text{H}_{16}$ ) being expelled from the amorphous ice matrix upon heating, a number of important insights were gained – the uncharted regime of small hydrophobes surrounded by a  $\text{H}_2\text{O}$  network were detected. Neutron diffraction studies of  $\text{C}_{10}\text{H}_{16}$ /ASW employing structure refinement modelling identified a new type of cage structure, with 28  $\text{H}_2\text{O}$  molecules constructed from distorted five- and six-membered rings, named the  $5^66^4$  polyhedron. Beyond this phenomenon, unusual, yet strong orientation correlations of the  $\text{H}_2\text{O}$  molecules were detected. Intriguingly, the closest O–H bonds were found to point towards the centre of mass of  $\text{C}_{10}\text{H}_{16}$  – it is quite striking that such a non-polar solute induces intense orientation correlations in its hydration shells.

$\text{H}_2\text{O}$  has been at the forefront of many breakthroughs and will continue to push boundaries, probing the chemistry and physics of ice research.<sup>3</sup>

## References

1. L. del Rosso, M. Celli, F. Grazzi, M. Catti, T. C. Hansen, A. D. Fortes and L. Ulivi, *Nat. Mater.*, 2020, **19**, 663-668.
2. C. G. Salzmann, P. G. Radaelli, B. Slater and J. L. Finney, *Phys. Chem. Chem. Phys.*, 2011, **13**, 18468-18480.
3. C. G. Salzmann, *J. Chem. Phys.*, 2019, **150**, 060901.

4. T. Loerting, K. Winkel, M. Seidl, M. Bauer, C. Mitterdorfer, P. H. Handle, C. G. Salzmann, E. Mayer, J. L. Finney and D. T. Bowron, *Phys. Chem. Chem. Phys.*, 2011, **13**, 8783-8794.
5. M. C. De Sanctis, F. Capaccioni, M. Ciarniello, G. Filacchione, M. Formisano, S. Mottola, A. Raponi, F. Tosi, D. Bockelée-Morvan, S. Erard, C. Leyrat, B. Schmitt, E. Ammannito, G. Arnold, M. A. Barucci, M. Combi, M. T. Capria, P. Cerroni, W. H. Ip, E. Kuehrt, T. B. McCord, E. Palomba, P. Beck, E. Quirico, V. T. The, G. Piccioni, G. Bellucci, M. Fulchignoni, R. Jaumann, K. Stephan, A. Longobardo, V. Mennella, A. Migliorini, J. Benkhoff, J. P. Bibring, A. Blanco, M. Blecka, R. Carlson, U. Carsenty, L. Colangeli, M. Combes, J. Crovisier, P. Drossart, T. Encrenaz, C. Federico, U. Fink, S. Fonti, P. Irwin, Y. Langevin, G. Magni, L. Moroz, V. Orofino, U. Schade, F. Taylor, D. Tiphene, G. P. Tozzi, N. Biver, L. Bonal, J. P. Combe, D. Despan, E. Flamini, S. Fornasier, A. Frigeri, D. Grassi, M. S. Gudipati, F. Mancarella, K. Markus, F. Merlin, R. Orosei, G. Rinaldi, M. Cartacci, A. Cicchetti, S. Giuppi, Y. Hello, F. Henry, S. Jacquino, J. M. Reess, R. Noschese, R. Politi and G. Peter, *Nature*, 2015, **525**, 500.
6. B. A. Buffett, *Annu. Rev. Earth Planet Sci.*, 2000, **28**, 477-507.
7. S. K. Talewar, S. O. Halukeerthi, R. Riedlaicher, J. J. Shephard, A. E. Clout, A. Rosu-Finsen, G. R. Williams, A. Langhoff, D. Johannsmann and C. G. Salzmann, *J. Chem. Phys.*, 2019, **151**, 134505.



## Impact Statement

This thesis explored the influence of small-molecule nanoprobe, tracking the structure and dynamics of vapour deposited amorphous ice, as well as draw out observations regarding how H<sub>2</sub>O hydrates the hydrophobic species, adamantane (C<sub>10</sub>H<sub>16</sub>) in the context of hydrophobic interactions.

The H<sub>2</sub>O-ice system is a pioneering area of research and ice is a highly unusual material<sup>1</sup> in many aspects – for instance, ice exhibits polyamorphism, the occurrence of different amorphous states.<sup>2</sup> Fundamentally, the study of ice has rendered it a benchmark, prototypical material for topics such as stacking disorder in layered materials,<sup>3,4</sup> pressure-induced amorphisation<sup>5</sup> and open framework structures.<sup>6</sup>

Remarkably, research has proceeded to tend towards the study of ice with other chemical species in an attempt to gather unprecedented insights into the chemical dimension<sup>7</sup> and complicated hydrogen-bonded network structures. This, in turn, delivers a more practical study of ice which is relevant to several fields that observe mixed-ice species: fields include, astronomical,<sup>8</sup> meteorological<sup>9</sup> and general chemical relations.<sup>10</sup>

Interestingly, both H<sub>2</sub>O and carbon have been found to coexist and form interfaces in a range of diverse settings and environments. The opportunity to employ various guest species in ice matrices include advances in the hydration shells of hydrophobic moieties in biomolecules and caged-ice structures. The latter, termed clathrate hydrates, is where H<sub>2</sub>O molecules arrange themselves into special cages around hydrophobic molecules and can be tailored in many ways.

Initially, as exhibited by the results presented in this thesis, understanding the properties and behaviour of bulk H<sub>2</sub>O with the incorporation of gaseous nanoprobe has provided a unique and innovative opportunity responsible for driving a vast range of processes across the universe. Further insights into the properties of amorphous ice have led to an improved understanding of its role, not limited to cosmological processes<sup>11</sup> but also, cryogenic physical vapour deposition of other materials.

Turning to the results presented in this thesis, the versatility of the experimental approach has allowed C<sub>10</sub>H<sub>16</sub> to be confined within cavities of a well-structured, water-ice cage structure – polyhedron of 5<sup>6</sup>6<sup>4</sup> type. The interesting and uncharted hydration of C<sub>10</sub>H<sub>16</sub> has successfully been probed and C<sub>10</sub>H<sub>16</sub> has not been encapsulated in such a way before –

remarkably demonstrating a stable polyhedron which would not have been achievable without successful hydration. A significant hurdle in the research community lies with the difficulty in preparing mixtures of amorphous ice and carbonaceous species with low volatilities and very little is known about the structure and dynamics of such unusual mixtures.

The small-molecule nanoprobe employed in this study can be observed to contribute towards potential energy and materials-related applications.<sup>12</sup> In addition, the topic of hydrophobic hydration is of paramount importance in terms of the hydrophobic interactions and the poorly understood hydrophobic effect,<sup>13</sup> as they are deemed responsible for fundamental processes such as protein folding, surfactant aggregation and enzyme-substrate interactions.<sup>13</sup> Many of the findings presented here not only underpin and point us in a new direction yielding exciting new structures, but also develops a highly versatile methodology that can be used as a standard and applied to many other non-polar and polar species.

## References

1. V. F. Petrenko and R. W. Whitworth, *Physics of Ice*, OUP Oxford, 1999.
2. T. Loerting, K. Winkel, M. Seidl, M. Bauer, C. Mitterdorfer, P. H. Handle, C. G. Salzmann, E. Mayer, J. L. Finney and D. T. Bowron, *Phys. Chem. Chem. Phys.*, 2011, **13**, 8783-8794.
3. W. F. Kuhs, C. Sippel, A. Falenty and T. C. Hansen, *Proc. Natl. Acad. Sci. U. S. A.*, 2012, **109**, 21259-21264.
4. T. L. Malkin, B. J. Murray, C. G. Salzmann, V. Molinero, S. J. Pickering and T. F. Whale, *Phys. Chem. Chem. Phys.*, 2015, **17**, 60-76.
5. O. Mishima, L. D. Calvert and E. Whalley, *Nature*, 1984, **310**, 393-395.
6. A. Falenty, T. C. Hansen and W. F. Kuhs, *Nature*, 2014, **516**, 231-233.
7. C. G. Salzmann, *J. Chem. Phys.*, 2019, **150**, 060901.
8. M. C. De Sanctis, F. Capaccioni, M. Ciarniello, G. Filacchione, M. Formisano, S. Mottola, A. Raponi, F. Tosi, D. Bockelée-Morvan, S. Erard, C. Leyrat, B. Schmitt, E. Ammannito, G. Arnold, M. A. Barucci, M. Combi, M. T. Capria, P. Cerroni, W. H. Ip, E. Kuehrt, T. B. McCord, E. Palomba, P. Beck, E. Quirico, V. T. The, G. Piccioni, G. Bellucci, M. Fulchignoni, R. Jaumann, K. Stephan, A. Longobardo, V. Mennella, A. Migliorini, J. Benkhoff, J. P. Bibring, A. Blanco, M. Blecka, R. Carlson, U. Carsenty, L. Colangeli, M. Combes, J. Crovisier, P. Drossart, T. Encrenaz, C. Federico, U. Fink, S. Fonti, P. Irwin, Y. Langevin, G. Magni, L. Moroz, V. Orofino, U. Schade, F. Taylor, D. Tiphene, G. P. Tozzi, N. Biver, L. Bonal, J. P. Combe, D. Despan, E. Flamini, S. Fornasier, A. Frigeri, D. Grassi, M. S. Gudipati, F. Mancarella, K. Markus, F. Merlin, R. Orosei, G. Rinaldi, M. Cartacci, A. Cicchetti, S. Giuppi, Y. Hello, F. Henry, S. Jacquino, J. M. Reess, R. Noschese, R. Politi and G. Peter, *Nature*, 2015, **525**, 500.
9. B. J. Murray, T. L. Malkin and C. G. Salzmann, *J. Atmos. Sol.-Terr. Phys.*, 2015, **127**, 78-82.

10. S. Klotz, L. E. Bove, T. Strässle, T. C. Hansen and A. M. Saitta, *Nat. Mater.*, 2009, **8**, 405-409.
11. S. Kwok, *Physics and Chemistry of the Interstellar Medium*, University Science Books, Sausalito, USA, 2007.
12. A. Sum, C. Koh and E. Sloan, *Ind. Eng. Chem. Res.*, 2009, **48**, 7457-7465.
13. W. Blokzijl and J. B. F. N. Engberts, *Angew. Chem., Int. Ed. Engl.*, 1993, **32**, 1545-1579.

### Acknowledgements

The work presented herein for the scope of this thesis would not have been possible without the help and guidance of a vast number of people. I take this opportunity to express my appreciation towards those who helped me throughout my years at UCL Chemistry.

Most importantly, a huge thank you to Professor Christoph G. Salzmann, my supervisor, advisor, and my great mentor. I am particularly thankful for the time he has spent in helping me mature as a scientist and will forever be grateful that I was given the opportunity to learn under his supervision. Christoph, I am indebted to your excellent leadership and guidance. Your positive outlook, unrivalled knowledge, and confidence in the field of all things ice has greatly inspired me. I have benefitted enormously from your contagious enthusiasm and motivation throughout the course of this PhD. The testing times at ISIS and the trips to McDonald's during beamtime will be sorely missed. You truly are the ultimate Professor of Ice!

Dr. Alexander Rosu-Finsen, thank you for the experimental training you provided at the start of this journey upon which this thesis was reliant. You were always there in the toughest, difficult, and panicked times – I am grateful for your unwavering support and belief in me. Thank you for always being the first point of call when needed. I will always remember the fun, entertaining times and laughs of learning Danish with my excellent annunciation. I hope you enjoyed reading the synonyms during the proofread of this thesis.

Siriney O. Halukeerthi, I am glad we were both given the opportunity to start our journeys together. We have had some great times, but we have also had some really tough times and I am grateful that we had each other to get us past these obstacles. You were there for me during the late nights and early starts but your companionship during our times at ISIS has provided me with some of the fondest and funniest memories of my PhD, and I will always look back at these moments with joy.

I wish to extend a special thank you to Rachael L. Smith. Rachael, your willingness to always assist me in any way you could, will never be forgotten. You have been a sense of calm amongst my chaos and a confidant that I could always rely upon, I hope my ranting has not permanently damaged your eardrums. You have been

## Acknowledgments

unwavering in your professional and personal support during this PhD, for this, I am forever indebted to you, and I am honoured to call you my friend.

Dr. Zainab Sharif, since the start of this PhD you were the perfect example of what a PhD student should be. Your willingness to always help and teach me in the lab regardless of how busy you were will always be appreciated. I hope my introducing you to my unique musical tastes has provided you with as many laughs as it has me.

Divya Amin, your friendly, supportive, and kind nature has not gone unnoticed. You have been the person who I turned to in any situation, and you have my endless gratitude. Thank you for always listening to me and being the shoulder that I could always depend on. I feel so lucky we became friends on this journey and will continue to do so. I value our friendship and thank you for always giving me a big reality check, candid advice and also a socially distanced slap (due to the current climate) when I needed it. You truly are a real friend.

To the various members of the Salzmänn group who have provided me with support, encouragement, and advice, I thank you. Dr. Alfred Amon, your enthusiasm to teach even when I asked silly questions will be eternally appreciated. Bharvi Chikani, your arrival in the group and your constant willingness to help in the lab is greatly valued. And finally, Dr. Martin Hart, although you are no longer with the group, your dry wit and humour as well as your ability to explain difficult concepts understandingly is greatly missed.

A huge thank you to Martin Vickers for training me on the XRD instrument. Your patience and expertise within the field are appreciated immensely, and I am lucky to have been taught by you. A further thanks to Dr. Jeremy Cockcroft for instructing me on how to collect overnight low-temperature XRD measurements, your grasp of all things crystallography allowed me to learn a lot. The Department of Chemistry at UCL are truly privileged to have you both.

I would also like to thank the beamline instrument scientist Dr. Tom Headen on the NIMROD beamline at ISIS for his assistance – facilitating successful data collection in line with his expertise in EPSR analysis. I owe Tom a debt of gratitude especially during a pandemic for willingly providing me his time, patience, and intuition. Additionally, thanks must go to Dr. Luis Carlos Pardo, whom I met early this year. Thank you for your highly driven and proactive nature in acquiring such valuable analysis at

## Acknowledgments

short notice. Luis ran extensive analysis with the ANGULA software on the data obtained from the EPSR analysis. Without this type of analysis, such wonderful figures and conclusions may not have been possible! To ERC, thank you for funding my research and providing me access to facilities which without, would have made my project impossible.

Finally, I extend my unconditional thanks to my family.

Sandeep, it is a privilege to have you in my life. Thank you for your endless encouragement, reassurance, and patience. You have never failed to provide me with joy. Your continuous belief in me, especially when I doubted myself has allowed me to get this far, and I cannot thank you enough for this. You truly are a kind, caring and amazing person; one who has enriched my life. I am grateful that you are in my life and continue to stand by me during the most difficult of times. Your enormous generosity overwhelms me and amazes me every single day.

To my dear siblings, how could I have done this without you? Thank you for your sense of humour and insightful suggestions. I am blessed with the unending support you all have provided me and thank you for listening to all my complaints when things were going wrong. I honestly appreciate everything you have done for me and want you all to know how much I value and love you. I would like to express how grateful I am for you all always being there for me. The most invaluable asset I have is all of you.

To my parents: Mum, Dad, I love you more than words can ever describe. I am indebted to your constant love, guidance, and thoughtful prayers. You both have done anything and everything for me – I would not be the person I am today if it were not for you. The respect I have for you is unmatched. You really are the definition of incredible parents, and I am extremely blessed to have you. I am forever indebted to you both. I am extremely humbled by your confidence in my abilities and being your daughter will forever be my proudest achievement. This thesis stands as a testament to your unconditional love, encouragement, and support.

## Table of Contents

<b>Abstract.....</b>	<b>3</b>
<b>Impact Statement.....</b>	<b>5</b>
<b>Acknowledgements.....</b>	<b>8</b>
<b>List of Symbols.....</b>	<b>17</b>
<b>List of Abbreviations.....</b>	<b>18</b>
<b>1 Introduction.....</b>	<b>20</b>
<b>1.1 Water and Ice.....</b>	<b>20</b>
<b>1.2 Crystalline Ices.....</b>	<b>23</b>
1.2.1 The Crystal Structures of the Ice 1 Polytypes.....	23
1.2.2 Bernal-Fowler Rules.....	27
1.2.3 Defining Ice.....	27
1.2.4 High-Pressure Phase Diagram of Ice.....	29
1.2.5 Pauling Entropy.....	33
<b>1.3 Amorphous Ices.....</b>	<b>34</b>
1.3.1 The Highly Debatable Glass Transition ( $T_g$ ).....	39
1.3.2 H <sub>2</sub> O: One Liquid or a Tale of Two Liquids?.....	43
1.3.3 Amorphous Solid Water (ASW).....	46
1.3.3.1 Morphology of ASW.....	47
1.3.3.2 Crystallisation-Induced Crack Formation.....	50
1.3.3.3 Trapping of Gas Mixtures in ASW.....	52
<b>1.4 Clathrate Hydrate Inclusions Compounds.....</b>	<b>55</b>
1.4.1 Crystal Structures of Clathrate Hydrates.....	56
1.4.2 Clathrate Hydrates from Amorphous Solid Water (ASW).....	62
<b>1.5 Hydration of Hydrophobic Species.....</b>	<b>68</b>
<b>1.6 Aims of this Thesis.....</b>	<b>70</b>
<b>1.7 References.....</b>	<b>71</b>
<b>2 Experimental Procedures and Characterisation Techniques.....</b>	<b>80</b>
<b>2.1 Introduction.....</b>	<b>80</b>
<b>2.2 Materials.....</b>	<b>80</b>
<b>2.3 Instrumentation.....</b>	<b>81</b>
2.3.1 The High-Vacuum Chamber.....	81
2.3.2 Pressure Evacuation of the High-Vacuum Chamber.....	84
2.3.3 Cooled Deposition Stage for Gaseous Nanoprobe Studies.....	85
2.3.4 Cooled Deposition Stage for Adamantane (C <sub>10</sub> H <sub>16</sub> ) Studies.....	87
2.3.4.1 Thermoelectric Phenomena – Seebeck and Peltier Effects.....	89
2.3.4.2 Calibration of the Peltier Element.....	89
<b>2.4 Experimental Procedures.....</b>	<b>91</b>
2.4.1 Typical Cryogenic Deposition Experiment.....	91
2.4.2 Collection and Storage of the Deposited Material.....	93
<b>2.5 Details of Sample Characterisation Techniques.....</b>	<b>95</b>

2.5.1	Temperature-Programmed Desorption (TPD).....	95
2.5.2	Quartz-Crystal Microbalance (QCM).....	100
2.5.3	Residual Gas Analyser-Mass Spectrometry (RGA-MS).....	102
2.5.4	Differential Scanning Calorimetry (DSC).....	104
2.5.4.1	Low-Temperature DSC.....	105
2.5.5	Raman Spectroscopy.....	107
2.5.5.1	Low-Temperature Raman Spectroscopy.....	109
2.5.6	Fourier Transform Infrared Spectroscopy (FTIR).....	111
2.5.6.1	Low-Temperature FTIR.....	112
2.5.7	Diffraction (Elastic Scattering).....	114
2.5.7.1	Characterising Crystal Structures.....	114
2.5.7.2	General Diffraction.....	116
2.5.7.3	Braggs Law.....	116
2.5.7.4	Atomic Structure Factor and Scattering Lengths.....	117
2.5.7.5	Characterising Diffraction Patterns of Crystalline Materials.....	120
2.5.7.6	Diffraction Patterns of Liquid and Amorphous Materials.....	120
2.5.8	X-ray Diffraction (XRD).....	121
2.5.8.1	Low-Temperature XRD.....	121
2.5.9	Neutron Diffraction.....	124
2.5.9.1	Time-of-Flight (TOF).....	126
2.5.9.2	Scattering Vector.....	127
2.5.9.3	Self and Distinct Scattering.....	127
2.5.9.4	Coherent and Incoherent Scattering.....	128
2.5.9.5	Scattering Geometry – The Differential Cross Section (DCS).....	129
2.5.9.6	Method of Total Scattering and Correlation Functions.....	130
2.5.9.6.1	Pair Correlation Function and Structure Factors.....	131
2.5.9.6.2	Derivation of the Scattering Theory.....	134
2.5.9.7	Isotopic Substitution.....	137
2.5.9.8	Low-Temperature Neutron Diffraction.....	138
2.5.10	Spallation Source and Instrumentation.....	139
2.5.10.1	Instrumentation.....	139
2.5.10.2	Instrumentation Components.....	141
2.5.10.3	Neutron Source.....	141
2.5.10.4	Incident Neutron Flight Path.....	141
2.5.10.5	Sample and Secondary Flight Path Vacuum Path.....	142
2.5.10.6	Detector Array.....	142
2.5.10.7	Blockhouse.....	143
2.5.10.8	Transmission Monitor and Beamstop.....	143
2.5.10.9	Calibration and Correction of Raw Data.....	143



<b>2.6</b>	<b>Software.....</b>	<b>145</b>
2.6.1	MCDIFFaX.....	146
2.6.2	General Structure Analysis System (GSAS).....	148
2.6.3	Gudrun <i>N</i> Software.....	148
2.6.3.1	Sample Background.....	149
2.6.3.2	Purging Bad Detectors – Time-of-Flight (TOF) Diffraction.....	149
2.6.3.3	Multiple Scattering Factors.....	149
2.6.3.4	Deadtime Correction.....	150
2.6.3.5	Data Calibration for Neutrons.....	150
2.6.3.6	Converting the Structure Factor to the Pair Distribution Function (PDF).....	151
2.6.3.7	Running Gudrun <i>N</i> .....	151
2.6.3.8	Gudrun <i>N</i> Analysis.....	152
2.6.4	Introduction to Empirical Potential Structure Refinement (EPSR).....	153
2.6.4.1	Overview of Computer Simulations and Modelling.....	153
2.6.4.2	Construction of an EPSR Simulation Box.....	155
2.6.4.3	Fundamentals of EPSR.....	156
2.6.4.4	Interatomic Potentials – Defining the Reference Potential.....	159
2.6.4.5	Running the Simulation.....	162
2.6.4.6	The Empirical Potential.....	164
2.6.4.7	Spherical Harmonic Representation.....	166
2.6.4.8	Reverse Monte Carlo (RMC) and Metropolis Monte Carlo (MMC) EPSR.....	168
<b>2.7</b>	<b>References.....</b>	<b>170</b>
<b>3</b>	<b>Gaseous ‘Nanoprobes’ for Detecting Gas-Trapping Environments in Thick Layers of Amorphous Solid Water.....</b>	<b>174</b>
<b>3.1</b>	<b>Introduction.....</b>	<b>174</b>
<b>3.2</b>	<b>Experimental Methods.....</b>	<b>175</b>
3.2.1	Calibration Approach for Determining Desorption Rates.....	175
3.2.2	Cryogenic Deposition Experiments.....	177
3.2.3	Quartz-Crystal Microbalance (QCM) Measurements.....	180
3.2.4	Temperature-Programmed Desorption (TPD) Experiments.....	180
3.2.5	<i>Ex Situ</i> X-ray Diffraction (XRD).....	181
<b>3.3</b>	<b>Results and Discussion.....</b>	<b>182</b>
3.3.1	Shape of the H <sub>2</sub> O beam Entering the High-Vacuum Chamber.....	182
3.3.2	Preparation, Structure and Thermal Characteristics of Pure ASW Films.....	186
3.3.3	MCDIFFaX Analysis of ice <i>Isd</i> from ASW.....	189
3.3.4	Detailed Analysis and Discussion of the QCM Measurements.....	191

3.3.5	Desorption of Gaseous ‘Nanoprobes’ from ASW.....	195
3.3.6	Effect of the Desorption Rate and Film Thickness on Desorption Features.....	205
3.3.7	Increasing the Amount of Argon.....	208
3.3.8	Baffling the Gas-Flow.....	209
3.3.9	Pumping Efficiency.....	211
3.4	<b>Quantitative Analysis of the TPD Data.....</b>	<b>213</b>
3.5	<b>Conclusions.....</b>	<b>217</b>
3.6	<b>References.....</b>	<b>218</b>
4	<b>Matrix-Isolated Adamantane in Amorphous Ice.....</b>	<b>221</b>
4.1	<b>Adamantane (C<sub>10</sub>H<sub>16</sub>).....</b>	<b>221</b>
4.1.1	C <sub>10</sub> H <sub>16</sub> as a Guest Species.....	226
4.2	<b>Aims.....</b>	<b>228</b>
4.3	<b>Experimental Procedures.....</b>	<b>229</b>
4.3.1	Initial Calibration of the Deposition Rates of C <sub>10</sub> H <sub>16</sub> .....	229
4.3.2	Pellet Preparation.....	231
4.3.2.1	C <sub>10</sub> H <sub>16</sub> to H <sub>2</sub> O Molar Ratios.....	233
4.3.2.2	Molecular Volume Percentages of C <sub>10</sub> H <sub>16</sub> in C <sub>10</sub> H <sub>16</sub> /H <sub>2</sub> O Mixtures.....	237
4.3.3	Varying the QCM Locations on the Deposition Plate with Different Flow Rates of H <sub>2</sub> O.....	237
4.3.4	Varying the QCM Locations on the Deposition Plate with the Calibration of the Deposition Rates of C <sub>10</sub> H <sub>16</sub> Prepared as a Pellet.....	239
4.3.5	Calibrating the Deposition Rates of C <sub>10</sub> H <sub>16</sub> in a Round-Bottom Flask.....	239
4.3.6	Cryogenic Codeposition of C <sub>10</sub> H <sub>16</sub> and H <sub>2</sub> O Vapour.....	241
4.4	<b>Details of Sample Characterisation Techniques.....</b>	<b>243</b>
4.4.1	<i>Ex situ</i> X-ray Diffraction (XRD).....	243
4.4.2	Differential Scanning Calorimetry (DSC).....	243
4.4.2.1	Calorimetric Calibration Approach for Determining the Mole Fraction of C <sub>10</sub> H <sub>16</sub> .....	243
4.4.3	Raman Spectroscopy.....	244
4.5	<b>Results and Discussion.....</b>	<b>245</b>
4.5.1	Formation of Nitrogen (N <sub>2</sub> ) Clathrate Hydrates.....	245
4.5.2	Comparison with the XRD Pattern of bulk C <sub>10</sub> H <sub>16</sub> .....	252
4.5.3	Codeposition of the Vacuum-Annealed Samples.....	252
4.5.3.1	XRD Patterns of C <sub>10</sub> H <sub>16</sub> /H <sub>2</sub> O Mixtures Heated from 95 K to 260/270 K.....	256
4.5.4	Distribution of C <sub>10</sub> H <sub>16</sub> and H <sub>2</sub> O Across the Deposition Plate....	263
4.5.5	Thermal Annealing in the DSC.....	269
4.5.6	Thermal Annealing inside the Vacuum Chamber to 180 K.....	271
4.5.7	Effect of Fully Baffling the Flow of H <sub>2</sub> O.....	273
4.5.8	C <sub>10</sub> H <sub>16</sub> in H <sub>2</sub> O Matrices with the Addition of Argon Gas.....	275

4.5.9	Thermal Annealing in the Vacuum Chamber at 240 K.....	278
4.5.10	Thermal Annealing in the Vacuum Chamber at 200 K.....	279
4.5.11	C <sub>10</sub> H <sub>16</sub> in H <sub>2</sub> O Matrices at Very High Concentration.....	281
4.5.12	Codeposition from a Round-Bottom Flask.....	284
4.5.13	Vibrational Spectroscopy Characteristics of C <sub>10</sub> H <sub>16</sub> .....	288
4.5.13.1	Raman Spectra upon Heating.....	295
4.5.13.2	Spatial Distribution Across the Deposition Plate.....	297
4.5.13.3	Peak Ratios with Raman Spectroscopy.....	301
4.6	Conclusions.....	303
4.7	References.....	306
5	<b>Total Neutron Scattering of Amorphous Solid Water with Embedded Adamantane.....</b>	<b>309</b>
5.1	Introduction.....	309
5.2	Aims.....	310
5.3	Experimental Details.....	310
5.3.1	Materials.....	310
5.3.2	Binary Mixtures.....	310
5.3.3	Calibrating the Deposition Rate of C <sub>10</sub> D <sub>16</sub> .....	311
5.3.4	Molar Ratios of C <sub>10</sub> D <sub>16</sub> and H <sub>2</sub> O.....	312
5.3.5	Preparation of the Deposition Plate.....	313
5.3.6	Sample Container for NIMROD.....	313
5.3.7	Cryogenic Deposition Experiments.....	314
5.3.8	Fourier Transform Infrared Spectroscopy (FTIR).....	315
5.4	ISIS Experiments on NIMROD.....	316
5.4.1	Details of Experiments at ISIS.....	316
5.5	Results and Discussion.....	318
5.5.1	Merged Differential Cross Section (DCS) Data.....	318
5.5.2	Small Angle Scattering Data (SANS).....	322
5.6	Details of Structural Reconstruction by the EPSR Method.....	330
5.6.1	Data Fitting.....	333
5.6.2	Total Structure Factors ( $F(Q)$ ).....	335
5.6.3	Pair Distribution Functions (PDFs).....	338
5.6.4	Centre of Mass (COM) Pair Distribution Functions (PDFs).....	343
5.6.5	Additional Simulations.....	344
5.6.6	Structural Ordering.....	345
5.6.7	Spatial Density Functions (SDFs) from EPSR.....	346
5.6.8	Orientalional Correlation Functions (OCFs) from EPSR.....	351
5.7	ANGULA Analysis.....	352
5.7.1	Centre of Mass (COM) Pair Distribution Functions (PDFs).....	352
5.7.2	Oxygen Positional Ordering in the First Hydration Shell.....	354
5.7.3	Orientalional Correlation Functions (OCFs): SHARM and ANGULA.....	358
5.7.4	Hydrogen Positional Ordering in the First Hydration Shell.....	365
5.7.5	Orientalional Ordering in the First Hydration Shell.....	366

5.8	Fourier Transform Infrared Spectroscopy (FTIR).....	380
5.9	Discussion of Hydrophobic Hydration.....	384
5.10	Conclusions.....	391
5.11	References.....	393
6	Final Conclusions and Outlook.....	396
6.1	References.....	403
	Appendix.....	405
	Appendix 1. Formation of Nitrogen (N <sub>2</sub> ) Clathrate Hydrates.....	405
	References.....	407
	Appendix 2. NIMROD Proposal Submitted 17 <sup>th</sup> October 2018.....	408

## List of Symbols

		Units
$\text{\AA}$	Angstrom	$\text{\AA}$ or $10^{-10}$ m
$\theta$	Angle, theta	°
$^{\circ}\text{C}$	Celsius	$^{\circ}\text{C}$
$\Phi_{\text{c}}$	Cubicity	-
$\mu$	Decoupled wavenumber shift	$\text{cm}^{-1}$
$\rho$	Density	$\text{g cm}^{-3}$
$H$	Enthalpy	$\text{J mol}^{-1}$
$T_{\text{g}}$	Glass transition temperature	K
K	Kelvin	K
M	Molar concentration	$\text{mol dm}^{-3}$
$\alpha$	Ordering parameter $\alpha$	-
$\beta$	Ordering parameter $\beta$	-
$\pi$	Pi	-
$\delta^{+}/\delta^{-}$	Positive/negative partial charge	-
$\nu$	Wavenumber shift	$\text{cm}^{-1}$
$\lambda$	Wavelength	nm

## List of Abbreviations

ASW	Amorphous solid water
COM	Centre of mass
CCR	Closed cycle refrigerator
CN	Coordination number
I <sub>c</sub>	Cubic ice
CS-I	Cubic structure I
CS-II	Cubic structure II
sIII	Cubic structure III
DAE	Data acquisition electronics
DCS	Differential cross section
DSC	Differential Scanning Calorimetry
EPSR	Empirical Potential Structure Refinement
eHDA	Expanded high-density amorphous ice
FT	Fourier transform
FTIR	Fourier Transform Infrared Spectroscopy
FSL	Fractional isosurface level
GUI	Graphical user interface
I <sub>h</sub>	Hexagonal ice
sH	Hexagonal structure H
HDA	High-density amorphous ice
HDL	High-density liquid
IR	Infrared
LJ	Lennard-Jones
LJ+C	Lennard-Jones plus Coulomb
LN <sub>2</sub>	Liquid nitrogen
LDA	Low-density amorphous ice
LDL	Low-density liquid
<i>Q</i>	Magnitude of the momentum transfer vector
MS	Mass Spectrometry
<i>m/z</i>	Mass-to-charge ratio
MMC	Metropolis Monte Carlo

MD	Molecular dynamics
ML	Monolayers
MC	Monte Carlo
OCF	Orientational correlation function
PDF	Pair distribution function / pair correlation function
PAH	Polycyclic aromatic hydrocarbon
$g_{ij}(r)$	Partial pair correlation function
PBC	Periodic boundary conditions
PIA	Pressure-induced amorphisation
$p$ - $T$	Pressure-temperature
QCM	Quartz Crystal Microbalance
RDF	Radial distribution function
$F(Q)$	Reduced structure function
RAIRS	Reflection Absorption Infrared Spectroscopy
RGA	Residual Gas Analyser
RMC	Reverse Monte Carlo
S/N	Signal-to-noise ratio
SDF	Spatial density function
$I_{sd}$	Stacking disordered ice I
TS2	Target station 2 (ISIS)
TPD	Temperature-Programmed Desorption
sK	Tetragonal structure K
sT	Tetragonal structure T
NIMROD	The Near InterMediate Range Order Diffractometer
$G(r)$	Total pair correlation function
$S(Q)$	Total scattering structure function
UHV	Ultra-high vacuum
uHDA	Unannealed high density amorphous ice
VNA	Vector network analyser
vHDA	Very-high density amorphous ice
w%	Weight percent
XRD	X-ray Diffraction

# 1 Introduction

This introductory chapter initially examines the significance of water ( $\text{H}_2\text{O}$ ) before exploring the picture of ice I and the large family of crystalline and amorphous phases of ice. Following this, the final emphasis of this chapter will surround the coexistence of ice with other species.

## 1.1 Water and Ice

Liquid water is often described as the ‘matrix of life’, and  $\text{H}_2\text{O}$  in its solid form constitutes a large proportion of our Universe as the third most abundant molecular species following carbon monoxide and dihydrogen.<sup>1</sup> Liquid water is of fundamental importance to our planet as it is intrinsically linked to, and an essential ingredient for, the support of life and evolution on Earth.<sup>2</sup> It is indispensable for many processes of chemical, physical and biological nature, and its high abundance on Earth differentiates it from all other planets in the Solar System.<sup>3</sup> Water is referred to as a ‘universal solvent’.<sup>4</sup>

The  $\text{H}_2\text{O}$  molecule consists of two hydrogens and one oxygen atom. For the oxygen atom in  $\text{H}_2\text{O}$ , only two electrons from the six outer-shell electrons are used, leaving four pairs of electrons around the central oxygen atom organised as non-bonding pairs. These remaining electron pairs arrange themselves as far away from one another, reducing repulsions between negative charge clouds. Ordinarily, the coordination geometry around the oxygen atom results in a tetrahedral arrangement where the bond angle between the oxygen and hydrogen atoms ( $\text{H}-\text{O}-\text{H}$ ) is  $109^\circ$ . However, as two non-bonding pairs lie closer to the oxygen atom, stronger repulsion is exerted against the two covalent bonding pairs, forcing the hydrogen atoms to push closer to one another. Water therefore adopts and results in a distorted tetrahedral arrangement whereby the  $\text{H}-\text{O}-\text{H}$  bond angle is now  $104.5^\circ$  as shown in Figure 1.1(a). This ‘bent’ conformation is essentially a balance between repulsion and attraction.



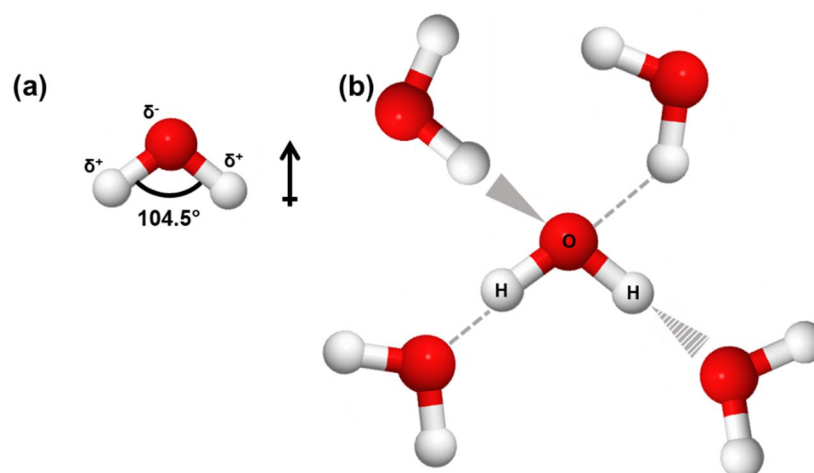


Figure 1.1. Illustrations of (a) a  $\text{H}_2\text{O}$  molecule, oxygen (red) and two hydrogen atoms (white/grey) and (b) a collection of  $\text{H}_2\text{O}$  molecules interacting with each other via hydrogen bonding (grey dotted lines) in a tetrahedral environment – formed when  $\text{H}_2\text{O}$  is frozen to produce ice.

Oxygen is more electronegative than hydrogen, with values of electronegativity of 3.5 and 2.1, respectively. Thus, the oxygen atom attracts an electron or negative charge towards itself that exists along the O–H bond, making oxygen more negative and therefore creating partial charges which are denoted  $\delta^+$  (positive partial charge) and  $\delta^-$  (negative partial charge) on the hydrogen atoms and oxygen atom, respectively, as shown in Figure 1.1(a). The  $\text{H}_2\text{O}$  molecule thus, assumes an asymmetric charge distribution creating a permanent dipole moment across the molecule. As  $\text{H}_2\text{O}$  molecules interact with one another [Figure 1.1(b)], they do so by dipole-dipole interactions and *via* hydrogen bonding. The central oxygen atom comprises four regions of electron density due to the orientation of positive and negative charges along the  $\text{H}_2\text{O}$  molecule organised in a tetrahedral arrangement.

Although the covalent bond between each oxygen and hydrogen atom in  $\text{H}_2\text{O}$  is polar, overall, the  $\text{H}_2\text{O}$  molecule is electrically neutral. This is because there are 10 protons and 10 electrons in each  $\text{H}_2\text{O}$  molecule, which adopt a net charge of 0.

Despite the scope of extensive research and scrutiny regarding water's structure and dynamics, to this current date, laboratory measurements of  $\text{H}_2\text{O}$  have been incapable of categorically explaining its 'anomalous' and 'abnormal' properties.<sup>5</sup> Water's unusual properties can somewhat be explained by hydrogen bonding as shown in Figure 1.2 within a  $\text{H}_2\text{O}$  pentamer. For instance, the boiling point of  $\text{H}_2\text{O}$  is much greater than expected for the trends that exist with other group 6 dihydrides.<sup>6</sup> A property unique to  $\text{H}_2\text{O}$  is its well-

known maximum density at 4°C and has been established for many centuries.<sup>7</sup> More striking anomalies of H<sub>2</sub>O can be observed in its ability to exhibit thermal expansion upon freezing, high isobaric heat capacity and isothermal compressibility.<sup>8</sup> Fahrenheit states how H<sub>2</sub>O remains a liquid below 0°C<sup>9</sup> and unlike dihydrogen chalcogenides, H<sub>2</sub>O is capable of forming four hydrogen bonds with neighbouring H<sub>2</sub>O molecules, impacting the melting and boiling temperature of its condensed phase.<sup>10</sup> Water remains a baffling molecule owing its highly anomalous behaviour and plays an imperative role in supporting countless areas of research including astrochemistry, geology, materials and atmospheric sciences. However, without these anomalous properties, Earth would not be as it exists to this day.

Upon cooling H<sub>2</sub>O at 0°C and ambient pressure, the formation of an equally fascinating species – ice, is produced. To date, the polymorphism of ice is a major research moiety to many scientists and the principal forefront of contemporary materials research.<sup>11</sup> When ice is formed, it assumes the tetrahedral conformation as mentioned previously and shown in Figure 1.1(b). Most of the ice on Earth is located near the Antarctic, a glacial continent, and is covered by approximately ten petatons of ice and snow. Ice, akin to H<sub>2</sub>O, covers large swathes of distant planets, comets, icy moons and poles of inner planets,<sup>2</sup> in the form of e.g. icebergs and thus, ice does not sink in H<sub>2</sub>O. This is due to ice constituting a lower density than liquid H<sub>2</sub>O (0.91668 Mg m<sup>-3</sup> and 0.9998 Mg m<sup>-3</sup>, respectively at 0°C).<sup>6</sup> This density difference is due to the open-channel structure of ice.<sup>10</sup>

## 1.2 Crystalline Ices

### 1.2.1 The Crystal Structures of the Ice I Polytypes

Several polytypes of ice arise due to layers of ice molecules being arranged in terms of stacking differences. Figure 1.2 illustrates the polytypes of ice I with respect to the stacking of the oxygen layers that make up the framework. Ice I is followed by an italicised initialisation to denote the type of stacking present within the network and some scientists may use an italicised subscript.

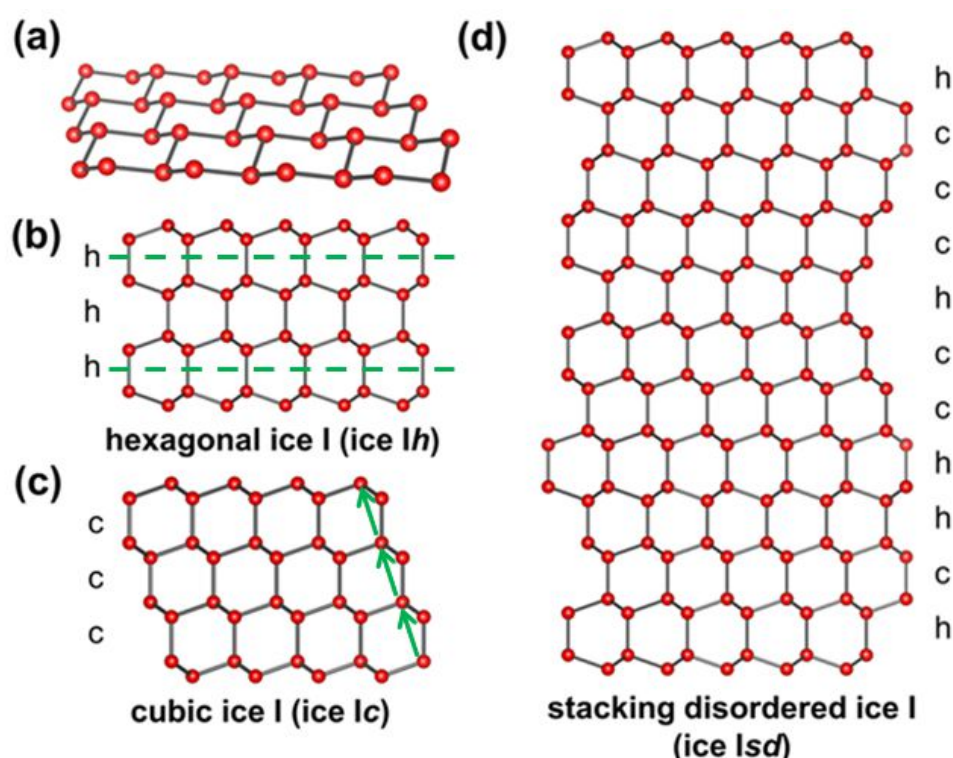


Figure 1.2. Representation of the hydrogen-bonded network in ice I, (a) structure of the layer in ice Ih, (b) stacking of layers in ice Ih, (c) stacking of layer in cubic ice, ice Ic and (d) evidence for the representation of an array of random stacking defects giving rise to stacking disordered ice, ice Isd. Only oxygen atoms which are connected by hydrogen bonds are shown for visual clarity and the hydrogen atoms have been omitted. This figure has been adapted and reprinted from reference 12 with the permission of The Royal Society of Chemistry Publishing.

The specific polymorph of ice that we encounter daily is termed hexagonal ice, ice Ih, the ‘ordinary ice’, indicating hexagonal symmetry of its crystal structure as shown in Figure 1.2(a) and Figure 1.2(b). Its six-fold rotational symmetry is reflected in snowflakes, and it is the most ubiquitous and observed phase of ice on Earth. X-ray diffraction (XRD) studies have established the tetrahedral environment of the arrangement of oxygen atoms in ice Ih.<sup>13-15</sup> Until neutron diffraction studies were

employed, the position of hydrogen atoms remained unresolved and highly controversial.<sup>16</sup> Four models of H<sub>2</sub>O were proposed and debated, and a brief account is provided here.

The Bernal-Fowler model of H<sub>2</sub>O comprised orientationally and intact H<sub>2</sub>O molecules.<sup>17</sup> Barnes<sup>15</sup> suggested a model wherein ice, H<sub>2</sub>O lost its molecular character when the hydrogen atoms were located halfway between the atoms of oxygen. A plastic phase of ice was also anticipated where rotating H<sub>2</sub>O molecules were considered.<sup>16</sup> Neutron diffraction data of deuterated ice *Ih* revealed that this model was in line and best matched the intensities as observed in the Bragg peaks. Ice *Ih* became known as a hydrogen-disordered phase of ice when Pauling proposed a model where along each hydrogen bond were two half-occupied hydrogen sites.<sup>18</sup> The orientation of the hydrogen-bonded H<sub>2</sub>O molecules is random and is reflected by the hydrogen sites that are half-occupied. Such a structure of ice is thereby described as, hydrogen disordered.

In many aspects, ice *Ih* is a highly unusual material.<sup>4,10</sup> Its complexity is governed by some of the following factors: negative thermal expansion below 70 K, increase in density when heated, pressure-induced amorphisation (PIA) and an extremely rich and complicated phase diagram.<sup>19</sup> The crystal structure of ice *Ih* assumes the space group *P6<sub>3</sub>/mmc*, consisting of six-membered puckered rings formed from tetrahedrally coordinated H<sub>2</sub>O molecules [Figure 1.2(a)] in the chair and boat conformation. Alternative ways in which neighbouring layers are stacked is characteristic of the layered structure of ice I. The layered structure of the thermodynamically stable ice *Ih* stretch is where the layers extend in the *a-b* plane of the unit cell and are stacked along the *c*-axis where each successive layer is a mirror image of the previous layer<sup>20</sup> and the hexagonal stacking is denoted by the ‘*h*’ as in Figure 1.2(b).

Similarly, another form of stacking known is referred to as cubic stacking as displayed in Figure 1.2(c) and denoted by ‘*c*’. In cubic ice, ice *Ic*, the layers are subsequently arranged by a three-fold rotational axis, displaced and shifted half the diameter diagonally across the previous layer of a six-membered ring.<sup>12</sup> In the structural arrangement of ice *Ic*, with space group, *Fd $\bar{3}m$* , the oxygen atoms are arranged identically to the cubic diamond structure. The overall structure of ice *Ic* comprises only six-membered rings and the cubic unit cell consists of eight H<sub>2</sub>O molecules with only one type of hydrogen bond and one distinct oxygen site.

With both ice *Ih* and ice *Ic* crystals, H<sub>2</sub>O is tetrahedral in its first coordination shell and the density of the two polymorphs is essentially equal. To summarise, the various polytypes of ice I are formed of chair or boat- conformation of interconnected layers of oxygen atoms. The H<sub>2</sub>O molecules in both polymorphs belong to annulated six-membered rings while the rings in ice *Ih* are composed of a 50:50 mixture of both chair and boat confirmation and in ice *Ic*, the stacking is assigned to the ‘chair’ conformation. Since structural differences between ice *Ih/Ic* lie in their stacking differences, these ices are not considered discrete polymorphs, but instead are dissimilar polytypes of ice I.

Undeterred by a copious number of studies, pure ice *Ic* [Figure 1.2(c)] was not recognised experimentally with unprecedented levels of structural purity and analysis until early 2020. Two independent techniques were employed to produce structurally pure ice *Ic* from ice XVII and thus, prepared concurrently by del Rosso<sup>21</sup> and Komatsu *et al.*<sup>22, 23</sup> In the first instance, structurally pure ice *Ic* was prepared by the transformation of powdered deuterated water (D<sub>2</sub>O) ice XVII under a dynamic vacuum and by means of increasing the temperature.<sup>21</sup> Ice XVII was recovered from annealing a pristine C<sub>0</sub> hydrate.<sup>21</sup> Secondly, hydrogen was degassed from the hydrogen hydrate, C<sub>2</sub> (high-pressure hydrate), to obtain remarkable thermal stability and was found to be free of stacking disorder, displaying pure ice *Ic*. The host framework of the C<sub>2</sub> hydrate is isostructural with ice *Ic*<sup>22</sup> which may have posed a highly templating effect for the formation of ice *Ic*.<sup>23</sup> The recent discovery of ice *Ic* has paved the way for detailed investigations into the differences of physical properties of ice *Ic* compared to ice *Ih*. Ice *Ic* is believed to be found in the upper atmosphere at high altitudes due to sightings of Scheiner’s halo<sup>4, 12, 24, 25</sup> from the occurrence of octahedral ice *Ic* crystals. Nevertheless, the discovery of ice *Ic* can allow for future work exploring its hydrogen-ordered counterpart for which studies have proposed many different structures.<sup>26</sup> The hydrogen-ordered counterpart could potentially be revealed to have aligned dipole moments (ferroelectric) and be the most polar state of condensed H<sub>2</sub>O.

Prior to this recent discovery of ice *Ic*, it became increasingly evident that ice I did not solely exist as these defined structures. Instead, ice I typically exists in a form consisting of interlaced hexagonal and cubic stacking, which together do not possess definitive cubic nor hexagonal symmetry.<sup>27</sup> To emphasise the difference of metastable ice I, the term for this finding was named, stacking disordered ice, ice *Isd* and a possible stacking sequence is shown in Figure 1.2(d).<sup>28</sup> Kuhs *et al.*<sup>27, 29</sup> and Malkin *et al.*<sup>12</sup> are

proponents of naming this polytype. The term ice *Isd* accounts for the tendency and ubiquity of the material to adopt a structure with varying fractions of cubic and hexagonal stacking sequences between pure ice *Ih* and pure ice *Ic*.

Ice *Isd* is a metastable intermediate form between polymorphs ice *Ih* and ice *Ic*, interlaced in a highly complex system within the trigonal space group,  $P3m1$ , which may help to describe the rare occurrence of snowflakes with three-fold symmetry.<sup>30</sup> In diffraction, the introduction of stacking disorder in ice is found to manifest as asymmetric peak broadening and peak absence in some cases,<sup>31, 32</sup> which results from interrupted long-range translational order from the structure influencing the diffraction pattern.<sup>12</sup> By computationally modelling diffuse features in diffraction data of ice *Isd*, it is possible to quantitatively<sup>4</sup> determine the percentage of cubic stacking within ice *Isd* and is termed as cubicity ( $\Phi_c$ ).<sup>33</sup> Furthermore, it is possible to gather information on memory effects (describing stacking disorder in materials) from within the sequence of stacking and can be visualised quite usefully in a ‘stackogram’ plot.<sup>12, 33, 34</sup> The cubicity can be obtained using MCDIFFaX, a computer program, developed by the Salzmänn group.<sup>33, 35</sup> MCDIFFaX is a diffraction fitting software that can be applied to XRD patterns to allow the calculation of stacking probabilities in stacking disordered materials.<sup>33</sup>

It has been shown that the cubicity of stacking disorder in ice *Isd* can also be determined from pair distribution functions (PDFs).<sup>36</sup> PDFs represent the pair correlations in real space and it is an appropriate method to analyse short-range effects on the structure. The cubicity is zero for pure ice *Ih* and thus, no occurrence of stacking disorder is present. As the cubicity increases, the stacking disorder increases and so does the number of possible arrangements of stacking. When the cubicity increases over 50%, the stacking disorder starts to decrease as ice *Ic* starts to become more prevalent.

Besides fitting XRD data or in some cases neutron data, ice *Isd* can be detected from its Raman spectrum<sup>35</sup> and in general, Raman spectroscopy can be used to gain insights into the spectroscopic properties of ice. Ice *Isd* spectra show the detection of stacking disorder when compared to the ‘ordinary’ ice *Ih*, this spectral signature from stacking disorder arises from structural diversity exhibiting strength in covalent bonds and vibrational modes that arise due to lower symmetry environments. The Raman spectra of ice *Ih* indicates two features in the coupled  $\nu(\text{O-H})$  spectral region. The main feature is seen at  $3100\text{ cm}^{-1}$  and  $\nu(\text{O-H})$  can couple with O-H bonds of  $\text{H}_2\text{O}$  to give anti- and symmetric vibrations and also give ‘out of phase’ and ‘in phase’ vibrations. The main

feature arising from the symmetric stretching mode in the spectra from ice I is due to the  $\text{H}_2\text{O}$  molecules vibrating ‘in phase’.<sup>35</sup>

### 1.2.2 Bernal-Fowler Rules

During its early days, ice research led to a sequence of speculations in explaining the bonding present within ice. As first described in 1933, by Bernal and Fowler,<sup>17</sup> a set of rules were rationalised to govern the arrangement of the atoms present in water-ice. These rules, termed the Bernal-Fowler rules state the following:-

- (i) one hydrogen atom is found to lie along with each hydrogen bond and
- (ii) the stoichiometry of  $\text{H}_2\text{O}$  is preserved as two hydrogen atoms are covalently bonded to each oxygen atom.<sup>17</sup>

In particular, every oxygen atom is bonded to four hydrogens, of these bonds, two bonds remain weak, and two bonds remain strong. Every hydrogen atom is then bonded to two oxygen atoms of which one strong covalent bond and one weak hydrogen bond exists. This, in turn, results in a periodic lattice.

### 1.2.3 Defining Ice

The orientation of  $\text{H}_2\text{O}$  molecules in ice are not fully defined and adhering to the limitation proposed by the Bernal-Fowler rules, fully hydrogen-bonded  $\text{H}_2\text{O}$  can adopt six different orientations as shown in Figure 1.3.<sup>4</sup> As ice freezes, it can be seen as  $\text{H}_4\text{O}$  tetrahedra linking together. Unlike liquid  $\text{H}_2\text{O}$ , effectively all crystalline ices, therefore, have four coordinate nearest neighbour environments that comprise structures consisting of tetrahedra with interlinked vertices. Figure 1.3 displays pentameric fragments of the structure of ubiquitous ice *Ih* with  $\text{H}_2\text{O}$  fully hydrogen-bonded in the centre.

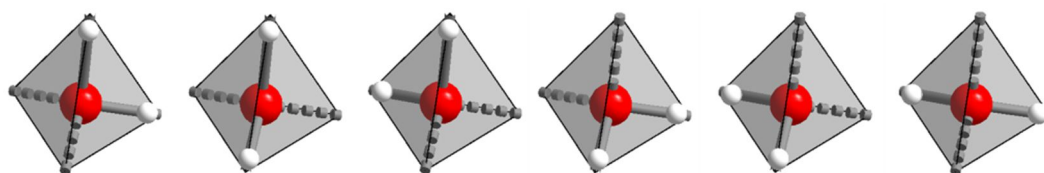


*Figure 1.3. Six orientations of the  $\text{H}_2\text{O}$  molecule in ice *Ih* in pentameric fragments. Each polyhedral shown in this figure defines one  $\text{H}_2\text{O}$  molecule. Solid lines depict covalent bonds and dashed lines indicate hydrogen bonding. The polyhedral corners are defined by the centre/midpoint of two hydrogen-bonded oxygen atoms. This figure has been reprinted from reference 4 with the permission from The Royal Society of Chemistry Publishing.*

The terms, hydrogen-ordered and hydrogen-disordered are indicated by the orientation of the hydrogens bound to the oxygen atoms in a crystal, such that when all the hydrogens are bound to the oxygen atoms in one orientation, the ice is said to be hydrogen-ordered. Comparatively, with defining a hydrogen-disordered ice, the hydrogens adopt more than one position with respect to their orientation.

Both hydrogen-ordered and hydrogen-disordered ices can be crystallographically described as is shown in the two-dimensional model ('square ice') in Figure 1.4, displaying the H<sub>2</sub>O tetrahedron. In terms of crystallography, hydrogen-disordered phases cannot be treated this way due to the long-range disorder of the hydrogen atoms. These structures are explained in terms of hydrogen atom sites with an average occupancy of 0.5. In comparison, hydrogen-ordered phases can assume a hydrogen site occupancy of 0 or 1<sup>4</sup> and exhibit long-range order of hydrogen and oxygen atoms.

With the help of a base dopant such as potassium hydroxide (KOH),<sup>37, 38</sup> ice XI forms below 72 K and is the hydrogen-ordered counterpart of ice Ih. Ice XI is classed as ferroelectric,<sup>4</sup> however, all other hydrogen-ordered phases of ice are antiferroelectric and thus, have no net dipole moment. The classification of ice XI as ferroelectric has been a topic in question and is yet disputed.<sup>39, 40</sup>

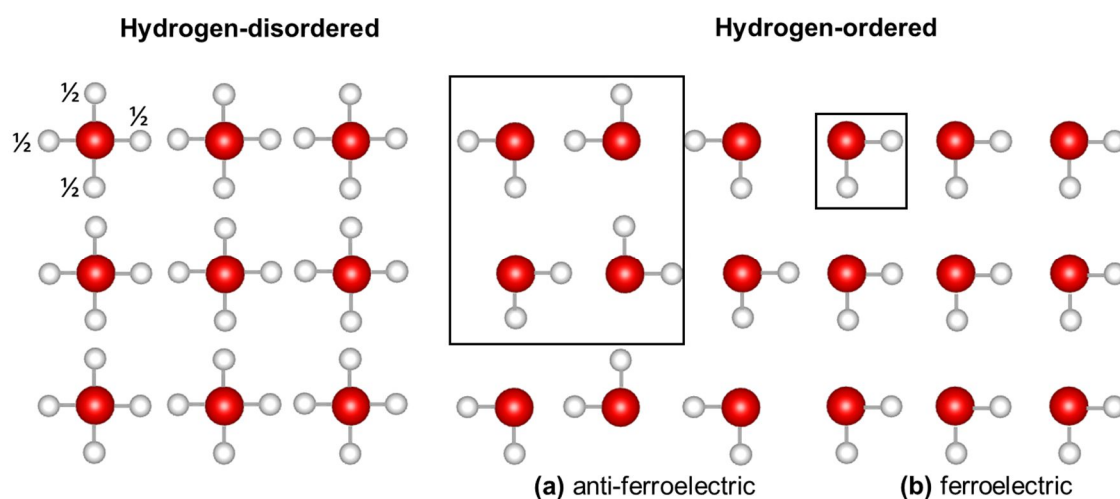


Figure 1.4. The hydrogen-disordered and hydrogen-ordered phases of ice displayed crystallographically. The white atoms as indicated in the hydrogen-disordered phase of ice show half occupied hydrogen sites and the white atoms in hydrogen-ordered ice show full occupied hydrogens with the respective unit cells indicated in the figure. The red atoms show the oxygen atoms. The hydrogen-ordered ice can be described in terms of anti- or ferroelectric.



Hydrogen site occupancies can be obtained from neutron diffraction data and isotopic substitution is used in the form of deuterated analogues due to negligible incoherent scattering properties compared to the protiated hydrogens.<sup>41</sup>

### 1.2.4 High-Pressure Phase Diagram of Ice

A plethora of physical properties, phase relationships and complex structural diversity are characteristic of H<sub>2</sub>O. This section provides a brief introduction to the high-pressure phases of ice. It must be noted that this thesis focuses primarily on the low-pressure phases of ice, which is provided later in this chapter.

In combination with ice *Ih*, an extensive study of the polymorphism of ice can be dated back to the revolutionary and pioneering work of Tammann and Bridgman in the early 1900s.<sup>42, 43</sup> Much effort has been dedicated and devoted to the discovery of new ice forms where the convention in the field consists of labelling a newly discovered ice phase with the next available Roman numeral in chronological order.

There are a total of 19 experimentally known phases of ice modifications<sup>19</sup> occupying specific regions over a large  $p$ - $T$  (pressure-temperature) range in the phase diagram of H<sub>2</sub>O.<sup>19</sup> Successive discoveries of new ices are confirmed by, and based upon crystallographic or spectroscopic data.<sup>10</sup> Figure 1.5 depicts the most up-to-date phase diagram with well-established stability conditions in the pressure range up to 100 GPa. With each protiated phase, deuterated analogues can be obtained and are known to be similar in structure to their counterpart only differing slightly with melting temperature.<sup>10</sup>

In addition, the most recently discovered ice, ice XIX, first reported by Komatsu and co-workers<sup>44</sup> was structurally characterised by *in situ* neutron diffraction and dielectric measurements. Gasser and co-workers also then structurally characterised ice XIX with neutron diffraction and *ex situ* calorimetry.<sup>45</sup> A dopant such as hydrochloric acid (HCl) was necessary to introduce here to produce ionic H<sub>3</sub>O<sup>+</sup> point defects which, in turn, speed up molecular reorientation dynamics enabling hydrogen ordering phase transitions to occur at low temperatures.<sup>45</sup> Ice XIX, was argued to be partially anti-ferroelectrically ordered,<sup>45</sup> however was contradicted by Salzmann *et al.*<sup>46</sup> who argued that the major structural feature of ice XIX are hexameric distortions.<sup>47-49</sup> In addition, the connection between the low-temperature endotherm and ice XIX is being debated.<sup>44-46</sup>

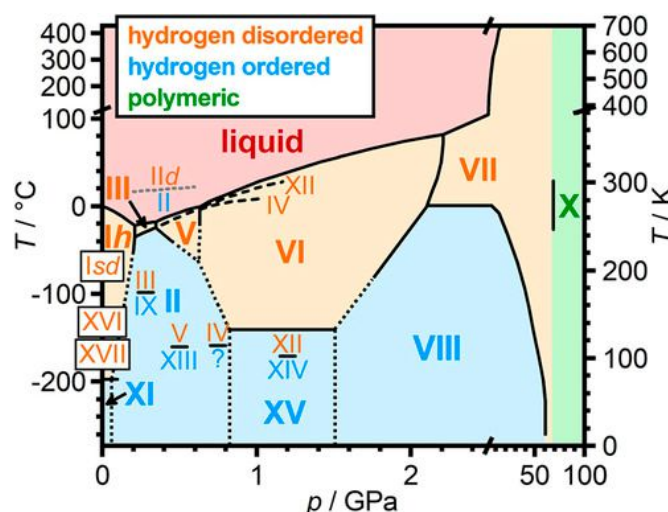


Figure 1.5. Water's rich and complicated phase diagram including regions of thermodynamic stability of the hydrogen-disordered (orange), hydrogen-ordered (blue), liquid  $\text{H}_2\text{O}$  (red) phases of ice and also the polymeric ice X (green). The stability of ices are highlighted such that: stable ices are depicted in larger bold Roman numerals and metastable phases of ice are indicated by significantly smaller font sizes. Extrapolated phase boundaries are portrayed by black dotted lines and dashed lines show the metastability lines of ices IV and XII. The small grey dotted line, a metastable phase boundary between ice II and IId has been computationally predicted.<sup>50</sup> Ice XVIII is excluded from this phase diagram due to its high pressure and temperature. Ice XIX is also excluded from this phase diagram due to its recent discovery. This figure has been reprinted from reference 11 with the permission from AIP Publishing.

These crystalline phases of ice can be categorised as hydrogen-disordered and hydrogen-ordered. Ice Ih displays orientational disorder with respect to its hydrogen atoms. The orientational order of  $\text{H}_2\text{O}$  molecules can be detected when the hydrogen-disordered ices which exist at high temperatures are cooled as phase transitions to the hydrogen-ordered counterparts are observed and thus, topologically related as illustrated in upcoming Figure 1.6. They are related in terms of their oxygen network but differ in their hydrogen positioning as discussed earlier.

The different ice phases display immense structural uniqueness and the hydrogen-bonded networks of the ices discovered have been illustrated in Figure 1.6. The density is greater for phases at higher pressure as expected and are ascribed to increases in hydrogen-bond bending and thus, the interpenetration of networks.<sup>4</sup> Open channel structures are associated with ice Ih/XI, II and XVII: ice II consists of single nanotubes hydrogen-bonded with one another and ices Ih/XI alongside ice XVII remain next to each other. The chirality of ice XVII is reflected in the spiral configuration of the crystal structure,<sup>51, 52</sup> and the ice III/IX network possesses chirality in its four-fold spirals. The flat six-membered interpenetrated rings (interpenetrated by a hydrogen bond) of the ice

IV network is a structural hallmark feature.<sup>53</sup> In any case, the structural features that exist in each phase of ice clearly defines the need to realise denser network structures. The most structurally complex ice is the ice V/XIII network, comprising several chains and ring sizes (four to twelve) along the crystallographic axes.<sup>4, 54</sup> Ices VI/XV/XIX and ices VII/VIII/X have interpenetration of two individual networks where the latter ices are the densest ice structures. With the absence of interpenetrating elements,<sup>55</sup> ices XII/XIV are considered as the densest network topology showing ‘zig-zag’ like chains. Ice XVI comprises the structure of an empty cubic structure II clathrate hydrate (CS-II). Further detail on ices XVI and XVII will be provided later in section 1.4. Ice XVIII, has been documented as the novel face-centred cubic, superionic phase, obtained by subjecting ice VII to a nanosecond, *in situ*, XRD of sophisticated laser-driven shock compressed superionic water-ice.<sup>19, 56</sup> Ice XVIII has been heated and compressed concurrently to 3000 K and 400 GPa.<sup>19</sup>

Upon cooling, ices III and VII will undergo hydrogen ordering, however, ices XI, XIII, XIV and XV require a variety of acid/base dopants.<sup>39, 57-59</sup> For a given network topology, the hydrogen-bonded networks remain unchanged when they undergo hydrogen ordering and thus, can be labelled in principle, pairs to each other. An important note is that not all ice phases have a hydrogen-ordered or hydrogen-disordered part. For ice *Isd*, IV, XVI, XVII and XVIII, the hydrogen-ordered counterparts have not yet been discovered. Ice II brings about some uniqueness due to not possessing a hydrogen-disordered counterpart as it disappears in a selective fashion from the phase diagram when doped with ammonium fluoride (NH<sub>4</sub>F).<sup>60</sup> However, computational studies have predicted the phase boundary at which ice II and its hydrogen-disordered counterpart, ice *IId*, exist in a stable region of liquid H<sub>2</sub>O (Figure 1.5).<sup>60</sup> As ice VII is compressed, H<sub>2</sub>O molecules lose molecular character due to symmetric hydrogen bonds in ice X and the phenomena of order-disorder is, therefore disregarded.<sup>11</sup>

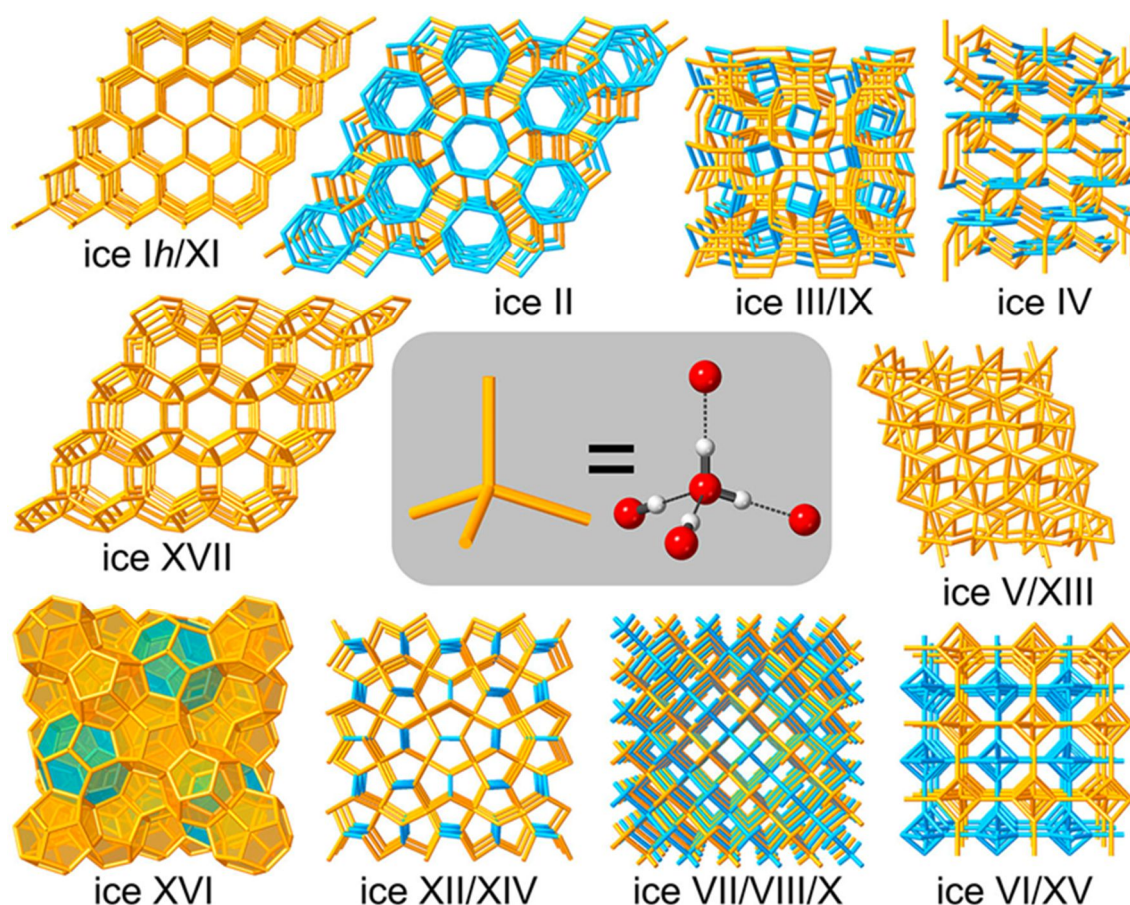


Figure 1.6. Ice polymorphs depicting a variety of hydrogen-bonded networks. The main inset displays the tetrahedral bonding environment of the  $\text{H}_2\text{O}$  molecule in stick notation (left) and ball and stick notation (right) showing a local hydrogen-bonded environment. The network topology is shared between hydrogen-disordered and hydrogen-ordered counterpart phases. The cyan highlighted features are noteworthy of their respective phase of ice. Such highlights include chiral four-fold spirals in ices III/IX, ice VI's densely knit interpenetrated six-membered rings, independent hydrogen-bonded networks that are secondary in ice VI/XV and ice VII/VIII/X. The cages in ice XVI of  $5^{12}$  and  $5^{12}6^4$  are illustrated in both, orange and cyan coloured polyhedra, respectively. It is possible to visualise the six-membered rings from the nanotubes in ice II, zig-zag like chains in ice XII/XIV. This figure has been reprinted from reference 11 with the permission from AIP Publishing.

Amid the complex array of ice phases and despite tremendous research, the complete picture of the 'ice family' is thought to be incomplete. Potential polymorphs of ice will be discovered in the near future with accompanying computationally predicted network topologies. Approximately, 75,000 new potential ice structures have been predicted on the basis of zeolite, however, it is unclear as to whether they can be prepared experimentally.<sup>11</sup>

### 1.2.5 Pauling Entropy

To establish the expected molar entropy change between hydrogen-ordered and hydrogen-disordered phases, the entropies of these fully ordered and disordered states need to be considered. This is termed the Pauling entropy.<sup>4</sup>

The molar entropy,  $S$ , as stated by Boltzmann's principle can be calculated from the gas constant,  $R$ , and the number of configurations,  $W$ , in the form of:

$$S = R \ln W \quad \text{Equation 1.1}$$

For a hydrogen-disordered state, suppose there are  $2N$  hydrogens per  $N$  oxygen atoms and that they are positioned on the two different sites along the hydrogen bonds. In one oxygen position, there are four hydrogen bonds, and thus, the possible arrangements of oxygen are 16. Only 6 of these arrangements are allowed and  $W$  at each oxygen site can be written as:

$$\begin{aligned} W &= 2^{2N} \left(\frac{6}{16}\right)^N = 4^N \left(\frac{3}{8}\right)^N \\ &= \frac{3}{2} \text{ microstates} \end{aligned} \quad \text{Equation 1.2}$$

And thus, a completely hydrogen-disordered phase would have an estimated configurational entropy of  $R \ln \frac{3}{2}$ . For complete hydrogen order, the configurational entropy of this phase will be equivalent to zero,<sup>4</sup> ( $W = 1$ , so  $S = 0$ ) and expected for a perfectly ordered crystal with respect to the third law of thermodynamics. The molar configurational entropy,  $\Delta S$ , is determined by: the entropy of hydrogen-disordered ice minus the entropy of hydrogen-ordered ice ( $R \ln \frac{3}{2} - R \ln 1$ ) which is  $3.37 \text{ J mol}^{-1} \text{ K}^{-1}$  as determined by Linus C. Pauling<sup>18</sup> and confirmed for ice *Ih*.<sup>61</sup> Although, since the Pauling entropy is only valid for a hypothetical dendritic ice structure with no rings, in reality, the configurational entropies of hydrogen-disordered ices are a few percent smaller as determined by Rosu-Finsen *et al.*<sup>39</sup>

Neutron diffraction can allow the calculation of configurational entropy of any disordered or partially ordered phase of ice by observing the hydrogen atom sites and their fractional occupancies. A detailed account is provided elsewhere.<sup>4</sup> Nevertheless, the ordering process is highly complicated as the reorientation dynamics of  $\text{H}_2\text{O}$  molecules needs to be taken into account.

### 1.3 Amorphous Ices

Alongside the cornucopia of crystalline phases of liquid H<sub>2</sub>O as indicated in the complex phase diagram in Figure 1.5, exists an array of amorphous ices and thus, ice exhibits polyamorphism, the occurrence of different amorphous states.<sup>62, 63</sup> Amorphous ice lacks long-range order due to its molecular arrangement and is understood as collapsed crystals or disordered.

Amorphous ice was initially discovered and reported in 1935<sup>64, 65</sup> when it was prepared by physical vapour deposition as H<sub>2</sub>O-vapour impinges on a cold surface cooled to below <130 K.<sup>64, 66</sup> This low-density form of H<sub>2</sub>O was termed amorphous solid water<sup>67, 68</sup> (ASW, section 1.3.3) which is the most abundant type of H<sub>2</sub>O in the universe.<sup>62</sup>

The low-pressure phase diagram of non-crystalline H<sub>2</sub>O is shown in Figure 1.7<sup>62</sup> and is an adapted classical phase diagram as first produced by Mishima<sup>69</sup> summarising the temperature and pressures at which these amorphous ices can exist.

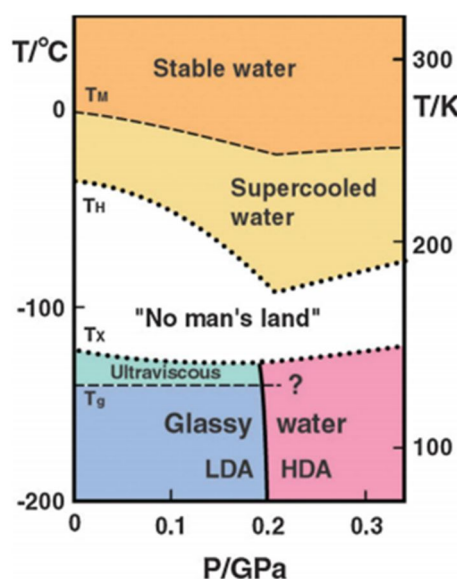


Figure 1.7. Phase diagram of non-crystalline H<sub>2</sub>O illustrating the regions where  $T_M$  is the melting temperature between the liquid and crystalline modification,  $T_H$  is defined as the homogenous nucleation temperature,  $T_x$  is the temperature for crystallisation where above this H<sub>2</sub>O rapidly crystallises and  $T_g$  is the glass-transition temperature (136 K).<sup>70, 71</sup> Proposed ultraviscous domains can be found below  $T_x$ . "No man's land" is enclosed by  $T_H$  and  $T_x$  from the top and from the bottom, respectively. This figure has been reprinted from reference 62 with the permission of The Royal Society of Chemistry Publishing.

The melting temperature,  $T_M$ , is the point at which liquid H<sub>2</sub>O is stable above (273 K). Provided that, and contingent upon the care taken to avoid ice formation or contamination

at the surface, liquid H<sub>2</sub>O can take values below  $T_M$ . Thus, heterogeneous nucleation must be avoided.

Supercooled H<sub>2</sub>O as shown in Figure 1.7 occupies a section of this phase diagram where it is metastable and can exist down to 231 K at ambient pressure<sup>72, 73</sup> and also down to 181 K at 0.2 GPa.<sup>74</sup>

Regardless of the absence and avoiding heterogeneous nucleation, ice can form below the homogenous nucleation temperature,  $T_H$ . The existence of amorphous ices, renders the extension of the phase diagram below the  $T_H$ , as it would end at this temperature if the presence of these ices ceased to exist.<sup>62</sup>

Amorphous ices form under appropriate conditions below the line of the temperature at which crystallisation occurs,  $T_X$ . As illustrated in Figure 1.7 above  $T_X$ , the phase diagram is termed, “No man’s land” indicating a region where the rapid crystallisation of amorphous ices and supercooled H<sub>2</sub>O occurs and therefore this term has been devised for this specific temperature and pressure region.<sup>62</sup> In the time-scale of milliseconds, crystalline ice can be observed experimentally or no longer exist in the “No man’s land” region, thus, the inevitable crystallisation of H<sub>2</sub>O is severely hampered in its efforts to cross into this region. No amorphous forms can be or have been, found in this region.

There is tremendous confusion in proving an explanation surrounding the glass transition temperature ( $T_g$ ) in H<sub>2</sub>O (section 1.3.1). The horizontal line in Figure 1.7 depicts the  $T_g$  where above this line lies an ‘ultraviscous liquid’ state of amorphous ice. Below this line, calorimetric and volumetric data observe that the  $T_g$  of low-density amorphous ice (LDA) is higher when compared to high-density amorphous ice (HDA).<sup>62</sup> The pressure of HDA is seen to increase when the  $T_g$  occurs.<sup>62</sup>

The known forms of amorphous ices can be grouped into two classes with differences reflected in their relative densities, such that they are: (i) LDA and (ii) HDA including unannealed high-density amorphous ice, expanded high-density amorphous ice and very-high density amorphous ice (uHDA, eHDA and vHDA, respectively).<sup>62</sup> There are debates and controversies<sup>4, 62, 75</sup> as to whether HDA and vHDA are distinct from one another. Depending on their densities, these amorphous forms of ice can exist in low- or high-pressure ranges as can be seen in Figure 1.7. Since the formation of ASW, a large family of amorphous forms of ice have been explored: these are categorised and

## 1. Introduction

summarized in Table 1.1 and are given by their respective pathways of preparation and densities.

*Table 1.1. Summary of the bulk amorphous ices with respect to their density measurements and preparation methods encountered in the literature. Adapted from reference 62.*

	The sub-types of amorphous ice	Preparation method	Density / $\text{g cm}^{-3}$
LDA	Amorphous solid water (ASW)	$\text{H}_2\text{O}$ vapour deposition <sup>64, 65</sup>	$0.94^{76}$
	Hyperquenched glassy water (HW)	Cooling of liquid droplets at a rate of $10^7 \text{ K s}^{-1}$ <sup>77</sup>	$0.94^{76}$
	Low-density amorphous ice I (LDA-I)	Heating of uHDA at $<0.1 \text{ GPa}$ to $130 \text{ K}$ <sup>78, 79</sup>	$0.94^{76}$
	Low-density amorphous ice II (LDA-II)	Decompression of vHDA at $140 \text{ K}$ to $\leq 0.05 \text{ GPa}$ <sup>79-81</sup>	$0.94^{79}$
	Low-density amorphous ice from ice VII [LDA(ice VII)]	Heating of ice VII at ambient pressure to $125 \text{ K}$ <sup>82</sup> forming ice XI	-
HDA	Unannealed high-density amorphous ice (uHDA)	Compression of ice <i>Ih</i> at $77 \text{ K}$ to $>1.2 \text{ GPa}$ <sup>83</sup>	$1.15^{84}$
	Expanded high-density amorphous ice (eHDA)	Annealing uHDA at $0.18\text{--}0.30 \text{ GPa}$ to $130 \text{ K}$ <sup>85</sup>	-
		Decompression of vHDA at $140 \text{ K}$ at $0.07 \text{ GPa}$ <sup>80, 81</sup>	$1.13^{62}$
		Compression of LDA at $130\text{--}140 \text{ K}$ to $>0.4 \text{ GPa}$ <sup>86</sup>	
	Relaxed high-density amorphous ice (rHDA)	Annealing uHDA at $0.3\text{--}1.9 \text{ GPa}$ <sup>87</sup>	Fig 5. in ref. 62
	Very-high density amorphous ice (vHDA)	Annealing uHDA at $\geq 0.8 \text{ GPa}$ to $>160 \text{ K}$ <sup>84</sup>	$1.26^{84}$
		Compression of LDA at $\geq 125 \text{ K}$ to $\geq 1.2 \text{ GPa}$ <sup>87</sup>	-
		Compression of ice <i>Ih</i> at $\geq 130 \text{ K}$ to $\geq 1.2 \text{ GPa}$ <sup>88</sup>	-

Depending on their method of preparation, amorphous ices can be further classed. LDA can be prepared *via* several routes and it must be noted that Table 1.1 is not fully comprehensive, and one should realise there may be more types of ice that can be formed by different pathways.<sup>62</sup> With increasing the temperature from  $<10 \text{ K}$  to  $>200 \text{ K}$ , the morphology of the deposited ice phase changes from porous and compact ASW to ice *Ih* and ice *Isd* or ice *Ic*.<sup>89</sup>



Neutron diffraction studies<sup>76, 90, 91</sup> have enabled the average local structures of the amorphous ices to be explored and has shown that these amorphous forms of ice are structurally dissimilar with respect to the number of interstitial H<sub>2</sub>O molecules in the first coordination shell.<sup>90, 91</sup> Radial distribution functions (RDF) can be used to validate the amorphous ice density data despite their inherent lack of long-range order. In fact, the RDF of amorphous ice resembles liquid H<sub>2</sub>O more than the RDF of crystalline forms.<sup>62</sup> By integrating the first O–O RDF function,  $g_{OO}(r)$ , the nearest neighbour coordination numbers can be obtained. On inspecting this, it has been shown that there are four-, five- and six-nearest neighbours for LDA, HDA and vHDA, respectively.<sup>62</sup> Judging from the RDFs obtained from neutron scattering experiments, this nearest neighbour value for LDA applies to LDA-I, LDA-II, hyperquenched glassy water (HGW) and ASW which are structurally similar.<sup>62</sup>

Additionally, neutron diffraction studies carried out using isotopic substitution revealed that ASW and HGW are indistinguishable from LDA and so, are structurally identical.<sup>76</sup> The subtle differences arising from LDA prepared from HDA in relation to annealing were found to be two discrete states, namely, LDA-I and LDA-II.<sup>79</sup> Based on experimental data carried out by Shephard *et al.*,<sup>82</sup> the existence of states of LDA-I and LDA-II could not be differentiated, established or defined using Raman Spectroscopy<sup>82</sup> and these states were only found to be structurally different using neutron diffraction.<sup>79</sup> An explanation for the discrepancy as discovered in neutron diffraction studies<sup>79</sup> may be that LDA-II is suggested to be more relaxed as it was kept at 140 K for a longer time than the LDA-I sample and so, the time dependency has to be taken into account. Shephard *et al.*<sup>82</sup> were able to investigate the formation of LDA at ambient pressure by heating ice VIII, in its state of relaxation. It was demonstrated that LDA recovered from ice VIII was in fact, structurally different from LDA-I and LDA-II, which were considered to be structurally identical.<sup>82</sup>

The density of ice will stay the same or change with time depending upon the degree of relaxation.<sup>62</sup> It will stay the same if the sample is a well-relaxed glass and the closer the sample is to its  $T_g$ , the closer the sample will be to such a well-relaxed state.<sup>62</sup> Depending on the degree of relaxation, there will be a continuum of states for the three polyamorphic states of ice and so, Winkel *et al.*<sup>62</sup> stated that the amorphous ices should not be viewed as structurally relaxed variants of each other but instead should be considered as part of a large energy mega-basin.<sup>62</sup>

Some liquids display strong tendencies to crystallise including H<sub>2</sub>O, and some liquids may be vitrified by rapid cooling or slow cooling. Water is difficult to vitrify as a high cooling rate is required. Liquid H<sub>2</sub>O has a cooling rate of  $10^6$ – $10^7$  K s<sup>-1</sup><sup>62, 77</sup> and this rate is needed to avoid the transformation and crystallisation to ice I. High cooling rates for H<sub>2</sub>O allow for novel techniques such as ‘splat cooling’ and ‘hyperquenching’. An amorphous form of ice was produced by Mayer and Bruggeller<sup>92, 93</sup> from projecting H<sub>2</sub>O into a liquid cryomedium and later, Mayer<sup>77</sup> improved the technique by discovering the easiest way to vitrify H<sub>2</sub>O is by the cooling of liquid droplets of micrometre size on a solid cryoplate (77 K). This further became the preparation route for preparing, non-crystalline, HGW.<sup>77, 94</sup> In an excess of  $10^5$  K s<sup>-1</sup>, and when H<sub>2</sub>O is cooled rapidly, is when the formation of HGW occurs.<sup>70</sup>

Pivotal work by Mishima *et al.*<sup>83</sup> demonstrated that ice *Ih* experiences PIA upon compression at liquid nitrogen (LN<sub>2</sub>) temperature (77 K) and 1.2 GPa, forming so-called, HDA. HDA can also be prepared by the compression of LDA at different temperatures as given in Table 1.1.<sup>78, 83</sup> The structural nature of HDA is highly debated. This is due to the rationalisation in a first instance where the PIA of ice *Ih* assumed that HDA was a glassy state of high-pressure liquid H<sub>2</sub>O.<sup>78, 83, 86, 88, 95, 96</sup> This combination and the transformation of HDA to LDA once compressed or heated at ambient pressure led to a scenario of a two-liquid model of H<sub>2</sub>O and a second critical point of liquid H<sub>2</sub>O (section 1.3.2).<sup>97, 98</sup> Further to this, HDA was thought to be mechanically unstable lacking a connection with the liquid phase of H<sub>2</sub>O.<sup>99, 100</sup> Although, more recently, Shephard *et al.*<sup>53</sup> compressed ice *Isd* and NH<sub>4</sub>F doped ice *Ih* at 77 K to discover that NH<sub>4</sub>F samples undergo collapse and were found to be crystalline NH<sub>4</sub>F-II (isostructural with ice IV) and not amorphous. This is due to the hydrogen-disordered nature of ice *Ih* which leads to a deviation from an effective mechanism named the Engelhardt-Kamb collapse<sup>53</sup> (described elsewhere) and thus, HDA is classed as a ‘derailed’ state along the ice I to ice IV transformation.<sup>53</sup> Nevertheless, a deeper insight and understanding of the mechanism of PIA of ice I is of principal importance.

The various amorphous ices are discussed in terms of their thermodynamic stability and structural differences by Johari *et al.*<sup>101-103</sup> and Loerting *et al.*<sup>62</sup> Nevertheless, after extensive research with a number of amorphous ices, distinguishable from their preparation and metastable character, the challenging issue of defining how many amorphous ices there are, still remains.

## 1.3.1 The Highly Debatable Glass Transition ( $T_g$ )

This section aims to provide an overview of the speculation and debates surrounding LDAs  $T_g$ .<sup>104-110</sup> There are many conjectures surrounding the long, convoluted history of how and if H<sub>2</sub>O forms a glass at significantly low temperatures.<sup>107, 108, 111</sup> A comprehensive understanding of structural diversity encompassing the LDA state and processes occurring upon heating, remains highly elusive and intangible.

The postulated  $T_g$  of LDA is demonstrated by a weak endothermic step based on basic calorimetry and known to take place prior to crystallisation to a supercooled liquid at  $136 \pm 2$  K<sup>70, 112-115</sup> upon heating at 30 K min<sup>-1</sup> and also at 124 K heated at 0.17 K min<sup>-1</sup>.<sup>70, 113, 114, 116</sup> To disentangle the enthalpy of relaxation causing an exotherm, the amorphous ices have been subjected to annealing and this feature is only detectable once annealed LDA is heated at 30 K min<sup>-1</sup> at ambient pressure. It is seen at lower heating rates and so, the annealing step is highly important. There are also arguments that this exothermic phase change to ice I is terminated before the endpoint of the  $T_g$  and thus, the whole breadth of the  $T_g$  cannot be considered.<sup>70, 71, 114</sup> There are also many debates as to whether waters true  $T_g$  should be at a higher temperature. To complicate this matter further, studies point towards LDA possessing a more ‘crystal-like’ nature.<sup>117-119</sup> Three scenarios considering the debate towards the  $T_g$  are given as:

- (i) the ultraviscous liquid theory
- (ii) reorientation dynamics governing the  $T_g$ <sup>107</sup>
- (iii) shadow  $T_g$ <sup>120</sup>

The fundamental obstacle, as mentioned previously, is that H<sub>2</sub>O has a strong tendency to crystallise below its melting point.<sup>107</sup> Prevention of crystallisation requires cooling rates  $>10^7$  K s<sup>-1</sup> and the resulting material at low temperatures is defined as LDA. A question of paramount significance is whether LDA and HDA as glassy materials experience a glass to supercooled liquid transition when heated and thus, linked to the liquid state.<sup>107</sup>

To conclude, in this present day, there is no accepted structure of LDA and the processes upon heating LDA. Structural relaxation processes for the different types of LDA were compared by Salzmann *et al.*<sup>104</sup> and could not be reconciled with the traditional postulated  $T_g$  prior to crystallisation.<sup>70, 113</sup> Dielectric measurements of LDA have shown to exhibit identical relaxation processes to confined H<sub>2</sub>O at approximately 180 K.<sup>121</sup> Many open-ended questions remain as to how the properties of LDA depend on its preparation.

It is already known that glasses are amorphous materials, but not all amorphous materials are glasses. As a liquid is cooled slowly below its  $T_g$ , it incessantly experiences structural relaxation with a lower enthalpy and while cooling, slows down due to a marked change/increase in viscosity. The  $T_g$  temperature is well-defined as the temperature at which the relaxation is approximately 100 seconds.<sup>108</sup> It is thought to be the temperature at which translational and rotational modes activate upon heating to allow the transition from a solid to a liquid state. The  $T_g$  suggests that amorphous ices are trapped kinetically at LN<sub>2</sub> temperature, exhibiting slow relaxation and if heated or given the time, they would eventually form stable crystalline phases.<sup>112</sup> However, this transformation is heavily influenced by the cooling rates at which it is prepared. The topic of  $T_g$  of amorphous ice is more complex in reality and recent studies by Shephard *et al.*<sup>107</sup> demonstrated that the  $T_g$  of amorphous ices is governed by reorientation dynamics only.<sup>107</sup>

The calorimetric response for ice VI, LDA and eHDA were recorded and XRD patterns were measured to assist the analysis with the same heating rate as for the calorimetric data.<sup>107</sup> Hydrogen-disordered phases of ice, ices I, IV, V, VI and XII exhibit  $T_g$ s at low temperatures,<sup>107</sup> and although they are crystalline, they possess some sort of disorder in relation to the orientation of hydrogen-bonded molecules. It must be noted that these ices are associated with the unfreezing of reorientation dynamics whilst heating. The calorimetric response from H<sub>2</sub>O to H<sub>2</sub><sup>18</sup>O or D<sub>2</sub>O ice VI with increasing molecular weight from 18 to 20 g mol<sup>-1</sup> was measured by Shephard and Salzmänn.<sup>107</sup> If the  $T_g$  involved translation motion, it was expected that H<sub>2</sub><sup>18</sup>O and D<sub>2</sub>O ice VI would exhibit significantly different behaviour than compared to H<sub>2</sub>O ice VI. For reorientation processes, only the D<sub>2</sub>O material is expected to display a delay of the onset of  $T_g$  compared to the H<sub>2</sub>O and H<sub>2</sub><sup>18</sup>O which behave similarly as expected and shown in Figure 1.8.<sup>107</sup>

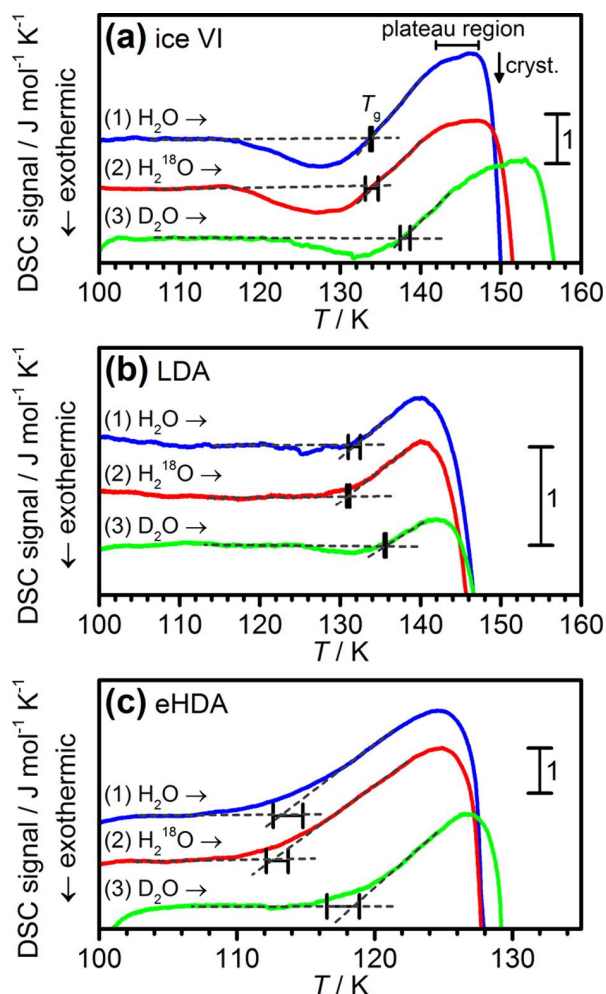


Figure 1.8. Calorimetric scans of  $\text{H}_2\text{O}$ ,  $\text{H}_2^{18}\text{O}$  and  $\text{D}_2\text{O}$ , where (a) ice VI, (b) LDA and (c) eHDA were recorded at a heating rate of  $10 \text{ K min}^{-1}$ . Prior to recording the scans for LDA, LDA was annealed at 130 K for 90 minutes. This figure has been reprinted from reference 107 with the permission of ACS Publications.

The  $T_g$  of  $\text{D}_2\text{O}$  ice VI,  $138.1 \pm 0.6 \text{ K}$  was found to significantly differ in comparison to  $\text{H}_2\text{O}$  and  $\text{H}_2^{18}\text{O}$  ice VI  $T_g$  at  $133.8 \pm 0.1 \text{ K}$  and  $133.9 \pm 0.8 \text{ K}$ , respectively.<sup>107</sup> Ice VI is shown to have no translation diffusion elements associated with the  $T_g$  concerning the kinetic unfreezing of molecules but does show molecular reorientation dynamics when the isotopic substitution technique is considered. If translational diffusion were present, the crystalline framework in ice VI of the oxygen atoms would be destroyed and XRD analysis supports this theory as the oxygen atoms are fixed into position until the transition to ice *Isd* occurs. Figure 1.9 denotes the ratios of the  $T_g$  of  $\text{D}_2\text{O}$  and  $\text{H}_2^{18}\text{O}$  ice VI, LDA and eHDA with respect to the  $T_g$  of the corresponding  $\text{H}_2\text{O}$  materials. The investigations carried out in this study reveal that the  $T_g$  is heavily influenced and governed by the unfreezing of the hydrogen atoms and thus, related to the orientational

change in the H<sub>2</sub>O molecules.<sup>107</sup> This study may be associated with the ‘shadow  $T_g$ ’,<sup>120</sup> consistent with the scenario of reorientation.

Nevertheless, the study unveils the much-appreciated controversy surrounding the  $T_g$ . A remaining question in interpretation is if translational diffusion appears above the  $T_g$  if crystallisation can be suppressed.<sup>107</sup> Well-relaxed LDA and HDA display equivalent isotopic responses in calorimetry of ice VI and thus, the  $T_g$  is governed by molecular reorientation processes.

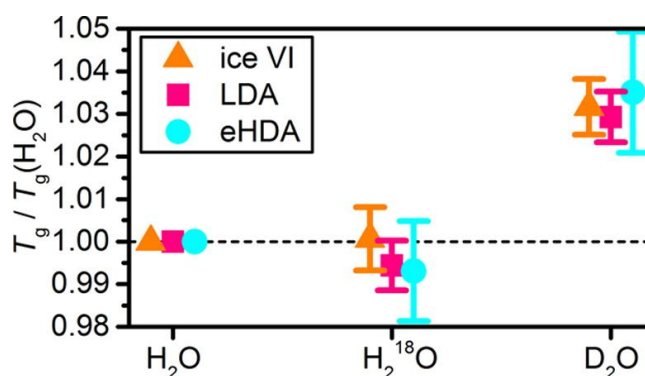


Figure 1.9. Respective ratios of the  $T_g$  of H<sub>2</sub>O and D<sub>2</sub>O ice VI, LDA and eHDA corresponding to the H<sub>2</sub>O materials. This figure has been reprinted from reference 107 with the permission of ACS Publications.

In addition, rotational diffusion of H<sub>2</sub>O molecules has been considered as thermally active at 115 K, resulting in a full micropore collapse at 121 K as determined by total scattering neutron diffraction.<sup>106</sup> This literature study compromises a non-equilibrium sample where the irreversible relaxation starts at low temperature (<121 K). Since the relaxation process is irreversible, no insights into the mechanism of the  $T_g$  can be determined from the study.<sup>106</sup> Thus, post-annealing in a vacuum, ASW exhibits a reversible thermally weak endothermic  $T_g$  caused by translation motion like other forms of LDA at ~136 K with a heat capacity increase of  $1.9 \pm 0.2 \text{ J K}^{-1} \text{ mol}^{-1}$  in calorimetric studies.<sup>113, 122</sup> However, it must be noted that only endothermic features are realised from the as-made deposited samples upon annealing, indicating the remarkably vast unrelaxed nature of vapour deposited samples.<sup>123</sup> After prolonged annealing of the deposit at 130 K, a small stepwise increase is seen in the  $T_g$  heat capacity: suggesting that the collapse of pores once heated is intrinsically related directly to the underlying process, which results in an endothermic increase of the heat capacity. The translational component of the sintering process is not considered as firm evidence for the transition thought to be related to supercooled liquid as it merely echoes the unrelaxed state of the initial material.<sup>108</sup> Additionally, the motion

of translational components may be induced by the increased vapour pressure of the ASW resonating around the temperature at which the  $T_g$  occurs.<sup>124</sup> Therefore, this notion of translation motion was later disputed showing only reorientation dynamics governing the  $T_g$  of the amorphous ice.<sup>107</sup> ASW is quite complex in line with its dynamical and structural perspective.

At higher temperatures, 150 K, long-range ordering of H<sub>2</sub>O begins as crystallisation to ice *Isd* starts: the initiation of translation diffusion of H<sub>2</sub>O molecules occurs. During the process of crystallisation and temperature increase, cracks and fissures form in the film and subsequently grow which lead to channels running throughout the H<sub>2</sub>O structure. Succeeding on from the irreversible crystallisation transition, the structure of H<sub>2</sub>O now exists in a random and disordered state of hexagonal and cubic ice I stacking event, ice *Isd*.<sup>12</sup> Temperature-programmed desorption (TPD) has been used to study such events of the behaviour of H<sub>2</sub>O on surfaces as well as study the morphological changes of ASW.<sup>125-127</sup>

There remains some ambiguity and an incomplete understanding of the structural diversity encompassed with LDA and the mechanism of the elusive  $T_g$  of LDA remains highly debatable.<sup>104-108</sup> Elucidating the mechanism of the  $T_g$  of amorphous ices may be of significant importance in understanding waters' anomalous<sup>5</sup> properties but also to understand the spectacles of polyamorphism in general. LDA is seen as a complex material than previously appreciated.

HDA's onset  $T_g$  temperature is  $116 \pm 2$  K and has been named waters' second  $T_g$ .<sup>128</sup> This second  $T_g$  may be related to the coexistence of waters' proposed two liquid phases (section 1.3.2). This scenario is seen as a prerequisite for the hypothetical probability of two different liquid phases of H<sub>2</sub>O that are supercooled liquids and the possibility of a liquid-liquid transition – presumably holding the key to eliminate the anomalous properties of H<sub>2</sub>O.

### 1.3.2 H<sub>2</sub>O: One Liquid or a Tale of Two Liquids?

There are several scenarios and conjectures that have been proposed to explain the origin of water's anomalies and briefly defined in the preceding section.<sup>129</sup>

The first scenario is called 'Speedy stability limit conjecture' whereby suggesting that thermodynamic anomalies arise from a spinodal line that originates at the critical point for liquid-gas, determining the boundary of supercooling and superheating and low

and high temperatures, respectively. This first scenario was followed by a ‘second critical-point’ hypothesis by Poole and proponents: Sciortino, Essmann and Stanley,<sup>97</sup> based on molecular dynamic (MD) simulations. This hypothesis has been the most influential and has been contested, supported and explained by many authors: Anisimov,<sup>130, 131</sup> Tanaka,<sup>132, 133</sup> Stanley *et al.*,<sup>8, 134-136</sup> Nilsson and Petterson<sup>137</sup> and Limmer and Chandler<sup>138</sup> to name a few. Thus, amongst these two scenarios which are intrinsically distinct from one another, there is a third scenario, the ‘critical-point-free’ scenario which was first presented by Poole *et al.*<sup>139</sup> as a case within a van der Waals bond-modified model of the liquid state in tetrahedral form. Further to this, a ‘singularity-free’ scenario based upon lattice model calculations was proposed by Sastry *et al.*<sup>140</sup> The key differences between these four scenarios are not shown here and are illustrated in a series of phase diagrams elsewhere.<sup>129</sup>

The ‘second critical-point’ scenario shows that a second critical-point exists at a positive pressure and terminates at a liquid-liquid critical point with respective fluctuations and is thus, deemed as a source of the anomalous properties of H<sub>2</sub>O.<sup>5</sup> Hence, this has been extensively investigated in deeply supercooled H<sub>2</sub>O and amorphous glassy H<sub>2</sub>O.<sup>83, 141-143</sup> However, many authors believe that the critical zone is where H<sub>2</sub>O lies at positive pressure as in the second scenario and believe this is the description of water’s behaviour. This belief has not been yet settled. A caveat in this belief also arises from an argument proposed by Binder<sup>144</sup> who suggests that a truly critical point within a metastable system cannot exist as the time scale needed for an ergodic manifestation would be imposed by crystallisation kinetics.

The detailed mechanisms that account for the processes involved in the PIA have eluded researchers for many years due to much controversy.<sup>53, 119, 145</sup> HDA prepared by Mishima *et al.*<sup>83</sup> motivated the hypothesis that through the crossover of the melting line of ice *Ih* and during the stage the ice was prepared, the amorphous ice formed and was represented by ‘melting’ a solid that preceded to have a structural link to liquid H<sub>2</sub>O.<sup>83</sup> These concepts have suggested the hypothesis that a two-liquid theory of H<sub>2</sub>O exists, relating the amorphous phases of ice to two states of H<sub>2</sub>O below 228 K (deeply supercooled region), speculating distinct structures and densities.<sup>8</sup> The ‘second critical-point’ of H<sub>2</sub>O is believed to exist in the “No man’s land” regime of the phase diagram. However, explicit experimental evidence has not yet been presented for the existence of high-density liquid (HDL) and low-density liquid (LDL) which are postulated analogues



of HDA and LDA, respectively,<sup>109</sup> with a demarcated transformation between both. Both phases are difficult to isolate due to fast crystallisation<sup>88, 107, 146</sup> if two phases were to be seen, only a few milliseconds or less would be permissible. The conditions to see the HDL-LDL states assuming they exist can only be seen in computer simulations,<sup>147</sup> but once again, are difficult to see due to experimental inaccessibility as the liquid would have to be probed rapidly.

This transition hypothesis is controversially claimed to be the misinterpreted transition in all explored models of H<sub>2</sub>O and most evidence does not support or indicate the two-liquid theory of H<sub>2</sub>O.<sup>53, 119, 148, 149</sup> There is a significant lack of data in the  $p$ - $T$  region of where these states are thought to reside, and a further understanding seems limited. From the work conducted by Soper,<sup>149</sup> it has become clear that the use of the pair correlation functions plays an essential role in determining the properties of H<sub>2</sub>O, particularly macroscopic properties predominantly in the supercooled region. Pending experimental data and information regarding the correlation function are required as it is difficult to see the progress towards understanding H<sub>2</sub>O. A heavily explored account in combination with Empirical Potential Structure Refinement (EPSR) of H<sub>2</sub>O has been confirmed by Soper<sup>149</sup> and not described in this thesis. Results presented by Soper also do not provide any evidence to suggest the ideas of a ‘second critical-point’ of H<sub>2</sub>O.<sup>8, 149</sup> The discussion in Soper’s work of possible inhomogeneity in H<sub>2</sub>O, is thus, disregarded.

Nevertheless, HDA from PIA has also been recognised to possess mechanical instability which causes structural collapse and is associated with slow kinetics for recrystallisation to take place. A combination of mechanical instabilities and thermodynamic ‘melting’ occurring during the PIA process have been proposed.<sup>53, 119</sup> Quasi-harmonic lattice dynamics carried out by Tse *et al.*<sup>119</sup> highlight a number of processes. Such that, the ‘melting’ only occurs at above 160 K and below 162 K, the processes taking place here are a result of mechanical instabilities.<sup>119</sup> Mechanical instability ensues when a Born condition is violated.<sup>119</sup> The onset of the latter has been found to always occur above the temperature of thermodynamic ‘melting’.<sup>119</sup> Thus, the possibility of the two-liquid theory is also invalidated when other materials undergo PIA.<sup>53, 119, 145</sup> Despite considerable attention, the theoretical interpretation of H<sub>2</sub>O is quite rudimentary. This topic is highly contentious and debatable, inferring that H<sub>2</sub>O is two liquids and not one.<sup>129, 150</sup>

### 1.3.3 Amorphous Solid Water (ASW)

Water, as we know, is a molecule of polymorphic nature with high abundance and has been located and discussed as a major component of interstellar dust grains, icy mantles, comets and larger bodies such as planetary rings and moons.<sup>1, 151-153</sup> Kinetic Monte-Carlo simulations investigating the porosity of water-ice have been conducted.<sup>154</sup> Water mantles on grains in the dark molecular clouds of the interstellar medium are predominantly created as the temperature approaches as low as 10 K in molecular cloud cores by reactive deposits and accretion of hydrogen and oxygen atoms.<sup>1, 151, 155</sup> As mentioned previously, in the laboratory, interstellar ice analogues are made by physical vapour deposition when H<sub>2</sub>O impinges directly onto a cold substrate <130 K in a vacuum.<sup>64-66</sup> Between approximately 15–30 K, physically vapour deposited H<sub>2</sub>O forms HDA (strictly not Mishima's HDA<sup>83</sup>) which can be converted to LDA upon heating to 80 K.<sup>66, 156, 157</sup> ASW is a disordered version of amorphous ice and has higher free energy and hence, a higher vapour pressure than crystalline ice. ASW is structurally identical to LDA,<sup>113</sup> differing in its method of preparation. ASW is highly porous and hence low- $Q$  ( $Q$  is the magnitude of momentum transfer vector) scattering is observed.<sup>89</sup>

ASW emanates a highly complex and multifaceted nature. Due to ASWs highly ubiquitous nature, it has been the core of many investigations,<sup>89, 106, 158-168</sup> as a prototypical material for studying vapour deposition processes. Mayer and Pletzer<sup>168</sup> investigated the absorption of nitrogen gas (N<sub>2</sub>) on ASW to discover it is a highly microporous material capable of adsorbing gases. Its absorption properties act as a major trailblazer in astrophysical studies. The most defining and significant feature that separates ASW from other LDA structures is its strong tendency to form porous structures<sup>168-170</sup> in combination with its complex  $T_g$  at 136 K,<sup>70, 71, 122</sup> desorption behaviour and relaxation. Its microporosity reflects a high surface area possessing the ability to trap/adsorb and release foreign gases.<sup>160, 168, 171, 172</sup> As a consequence, at low temperatures, molecules can remain inside these pores and may thermally be expelled at a later stage.<sup>173</sup> The mechanisms accountable for these morphological changes are poorly understood and obscure at low temperatures.<sup>158</sup>

### 1.3.3.1 Morphology of ASW

The precise detail of the experimental conditions for cryogenic physical vapour deposition may have pronounced effects on the morphology of the deposit.<sup>169</sup> A comprehensive range of factors and parameters are important in determining aspects of gas-ice, including the baffling of the H<sub>2</sub>O-vapour beam,<sup>67, 169, 174, 175</sup> angles of deposition,<sup>126, 176, 177</sup> temperature of the substrate, deposition rate, film thickness,<sup>123</sup> overall flux and collision energy.<sup>66, 169, 175-178</sup> Despite these understandings of ASW, discrepancies still lie beneath the discovery of the physical and chemical properties of ASW.

Physical properties of vapour deposited ASW depend on the vapour prior to depositing onto a cryoplate, which had not been investigated previously until Mayer and Pletzer<sup>169</sup> discovered this parameter is significantly affected. It was discovered that a supersonic flow of H<sub>2</sub>O vapour gave deposits of rough and rugged nature whereas the interrupted flow of H<sub>2</sub>O vapour using a baffle between the nozzle of the H<sub>2</sub>O-vapour tube and cryoplate gave transparent, glass-like deposits.<sup>169</sup> Both types of deposits crystallise once in the presence of adsorbed gas: (i) ASW prepared by baffling and interrupting the supersonic flow gives only one exothermic peak in differential thermal analysis upon heating, whereas, (ii) condensed H<sub>2</sub>O with the supersonic flow on the cryoplate devitrifies H<sub>2</sub>O at temperatures of 160, 164 and 177 K.<sup>169</sup> Supersonic flow conditions were determined to cause the presence H<sub>2</sub>O clusters in the gas phase, giving a highly porous solid with a network of voids and pores deposited on the cryoplate, in contrast to baffled flow, where a non-porous solid was discovered. The control of ASW morphology using molecular beams is very much explored in many literature studies.<sup>175, 177</sup> Collimated molecular beams have been employed to essentially control specific deposition conditions at low temperatures to create compositionally tailored ASW nanoscale films.<sup>174, 175</sup>

The morphology of ASW grown *via* physical vapour deposition is known to be dependent upon the growth angle of the H<sub>2</sub>O molecules.<sup>177</sup> Systematically varying the angle of deposition from  $\theta = 20\text{--}70^\circ$  was found to significantly affect the morphology of ASW.<sup>177</sup> The increase of the angle of incidence of the impinging molecule renders the structure of ASW, non-porous to highly porous.<sup>177</sup> Results obtained for N<sub>2</sub>, oxygen (O<sub>2</sub>) and argon (Ar) were similar when adsorbed on ASW, indicating that ASW adsorbs large quantities of gas dependent upon the morphology of ASW. The growth and annealing temperature influence the porosity and ability of ASW to trap volatile gases<sup>164, 168, 179</sup> and

ASW is thus, also strongly dependent upon the distribution of incident H<sub>2</sub>O molecules. A ballistic deposition described elsewhere can be used to describe ASW films for a finding of dependence of angle growth and morphology.<sup>68</sup> The results from ballistic simulations for the growth of thin films deduce that film density decreases as the incidence angle increases which is in line with experimental observations.<sup>174, 175, 177</sup> As the angle increases, the formation of a porous film leads to an increase in the surface area and thus, more area is available for gas adsorption.<sup>174, 175</sup>

In addition, the incident collision energy was also varied with the angle and the porosity of ASW films as vapour deposited were studied using infrared spectroscopy (IR) and N<sub>2</sub> physisorption.<sup>178</sup> That latter showed that there is a decrease in N<sub>2</sub> in large pores when the incident angle is high, whereas, the former, showed that the surface area increased with the incident angle. Thus, incident collision energy was found to have a pronounced effect on the morphology of ASW.<sup>178</sup>

Structural changes of vapour deposited H<sub>2</sub>O has been investigated in the temperature region of 15–188 K.<sup>66</sup> At 15 K, a range of 38–68 K and at 131 K, a progression of amorphous water-ice is found.<sup>66</sup> The transitions of these well-defined forms are deemed as accountable for many anomalous properties of astrophysical ices and allow the structural properties of the ice matrix to be interpreted. For example, the occurrence of ice after 131 K can explain the gas release from water-ice above 150 K.<sup>66</sup>

Spontaneous cracks in ASW grow when the film thickness exceeds a specific critical value.<sup>180</sup> This critical value has been determined during the growth of ASW films using a quartz crystal microbalance (QCM), IR, and an optical interferometer as a function of deposition angle and temperature.<sup>180</sup> The critical value of 1–5  $\mu\text{m}$  has been seen to change with growth temperature and angle, indicating the porosity of the film. It was suggested that ASW films experience tensile stress due to the difference between contracting forces and substrate adhesion originating from only partially coordinated molecules on the pore surface.<sup>180</sup>

A large extent of how ice traps and retains gases may influence the determination of chemical compositions of a variety of astrophysical bodies. The low-temperature physics of ASWs micropore collapse network upon heating is far from understood. While heating ASW deposits in a vacuum between the 120–140 K range, its pores experience a sudden collapse.<sup>89</sup> The onset temperature corresponding to this collapse depends on the

type of flow conditions employed in the preparation of as-made ASW and the surface area of the deposit initially. Direct experimental measurements regarding the nature, connectivity and shape of pores have remained elusive, particularly at 77 K: a spherical or cylindrical nature of the pores is a fair assumption. Cracks in ASW reported in the literature are attributed to ice phase transformation.<sup>126, 142, 181</sup> Abrupt desorption occurs *via* connected pathways open to vacuum in the H<sub>2</sub>O layer during growth of crystalline ice from ASW: as crystallisation proceeds, the number of pathways connected increases and releases the species incorporated within the amorphous ice observed experimentally. The episodic release of gases trapped in ASW films as seen in the literature and described later in this thesis, exhibits an abrupt desorption feature due to the formation of fissures, cracks or grain boundaries that accompany crystallisation and form connected pathways. Structural changes are facilitated by the formation of these connected pathways and prior to the formation of these pathways, the desorption of a species is not possible. Reflection Absorption Infrared Spectroscopy (RAIRS) and TPD studies of ASW indicate the multitude of these cracks propagate downwards from the surface of the ASW.

The reduction in surface area and thus, sintering of ASW at 113 K has been explored in the presence of N<sub>2</sub>,<sup>170</sup> confirming the microporosity of ASW.<sup>168, 172</sup> A long continuous deposition time of one week with deposition at 113 K drastically decreased the surface area by an order of magnitude and after warming ASW to 143 K, further reduction in the area was observed. The reinvestigation of N<sub>2</sub> on ASW reidentified the evidence of a microporous solid if prepared at 77 K and secondly, the reduction in surface area of ASW occurred at higher temperatures.<sup>168, 170</sup> These findings proved that amorphous ice is a microporous solid and the influence of micropores have significant effects on interstellar dust and the adsorption of volatile gases in comets. The formation of clathrate hydrates can be observed if these pores are filled with gases before subsequent collapse which is thought to be unexpectedly stable N<sub>2</sub> or O<sub>2</sub> clathrate hydrates.<sup>182</sup>

Morphological changes and surface structure of ASW during the sintering process have been studied as the dangling O–H bonds from H<sub>2</sub>O molecules on the surface of the pores are subsequently removed, according to Raman spectroscopy<sup>183</sup> and dielectric spectroscopy.<sup>31</sup> The existence of these dangling bonds are present on the walls of pores, external surfaces of the film and established to be sensitive to adsorption of gases at the micropore surface. The films are used as ideal probes for the changes occurring in porous ASW films.<sup>183</sup> Gases adsorbed in the pores and surface of ASW causes a shift in the IR

frequency of the dangling O–H bonds. Employing this result, Devlin *et al.*<sup>183</sup> demonstrated that N<sub>2</sub> does not diffuse into the pores of ASW at low temperatures of 10 K but readily diffused into porous ASW at 23 K. A steady structural relaxation process has been detected by means of Raman and Fourier Transform Infrared Spectroscopy (FTIR) upon heating the ASW deposit from 95 K to the irreversible crystallisation to ice *Isd* transition at ~150 K.<sup>104</sup> This relaxation process must not be confused with the crystallisation as these are two separate processes and relaxation does not reach completion before the onset of crystallisation. A guest species such as carbon tetrachloride (CCl<sub>4</sub>) incorporated within amorphous ice is most likely released *via* grain boundaries, generated from the impingement of crystalline grains that grow out of the amorphous phase and is described in the following section.

### 1.3.3.2 Crystallisation-Induced Crack Formation

The desorption kinetics of molecular beam experiments from codeposited CCl<sub>4</sub> and ASW produced compositionally tailored ultrathin films and were first examined by Smith *et al.*<sup>184</sup> The experimental conditions are described elsewhere,<sup>184</sup> however, in brief, an effusive molecular beam of H<sub>2</sub>O, D<sub>2</sub>O or CCl<sub>4</sub> was used to dose onto a gold Au(111) or ruthenium Ru(111) substrate at 85 K.<sup>185</sup> Overlayers of ASW were demonstrated to significantly impede the desorption of CCl<sub>4</sub> until the onset of crystallisation began, where CCl<sub>4</sub> was found to readily desorb. Abrupt desorption was observed and occurred *via* connected pathways in vacuum that form in the H<sub>2</sub>O layer when crystalline ice grows from the ASW. The irreversible phase transition of ASW to crystalline ice was seen for both H<sub>2</sub>O and D<sub>2</sub>O at 156 K and 161 K, respectively. The CCl<sub>4</sub> desorption was seen to shift to higher temperature once isotopic substitution was introduced yet still was impeded by the ASW, reflecting the dependence of isotopic substitution on crystallisation. A large desorption peak as observed in the TPD spectrum (Figure 1.10) is the hallmark for the well-known crystallisation of ASW.<sup>184, 186, 187</sup>

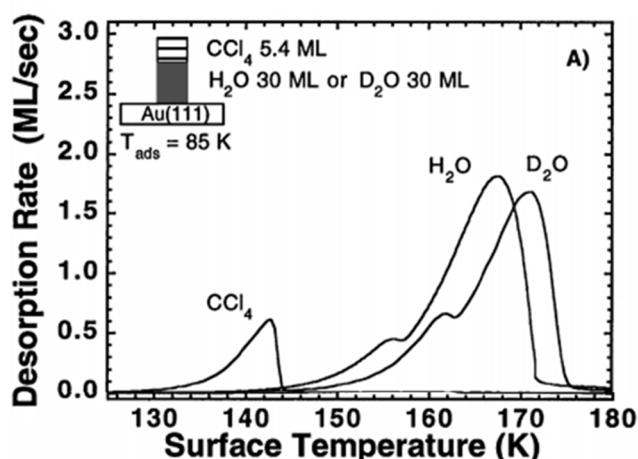


Figure 1.10. TPD spectra of a nanoscale film of 5.4 monolayers (ML) of  $\text{CCl}_4$  grown on top of either  $\text{D}_2\text{O}$  or  $\text{H}_2\text{O}$  ASW of 30 ML. The bump in  $\text{H}_2\text{O}$  (156 K) or  $\text{D}_2\text{O}$  (161 K) arises from the irreversible phase transition of ASW to crystalline ice. This figure has been adapted and reprinted from Figure 1 in reference 184 with permission from The American Physical Society.

The low-temperature desorption of  $\text{CCl}_4$  arises from the presence of connected pathways that form during ASW deposition from 85 K.<sup>184</sup> The structural changes that occur during crystallisation facilitates the formation of these pathways, arising from grain boundaries, fissures or cracks in the ASW film. As the temperature increases and crystallisation proceeds, the number of connected pathways increases and  $\text{CCl}_4$  is abruptly released, driven by the crystallisation of ASW. This dramatic effect is termed the ‘molecular volcano’.<sup>184</sup>

Further to the discovery of the phenomena of the ‘molecular volcano’, Smith and collaborators<sup>125, 126</sup> aimed to characterise the formation of crystallisation-induced cracks by using the desorption peak in their companion papers.<sup>125, 126</sup> In their preceding papers, they find that the distribution of crack length is independent of the trapped gas. Low coverage regime was probed with the ‘molecular volcano’ to realise that the mechanism of release is controlled by these crystallisation-induced cracks in the overlayer of ASW, especially near the top of the film.<sup>125</sup> More recently, they allowed for probing selective placement from beneath the films of ASW focusing on a high coverage regime, where prior to crystallisation, desorption pathways became accessible and were highly reliant on multilayer thickness and composition between the various gases used.<sup>126</sup> Two principal desorption pathways were observed in temperature ranges of (i) 100–150 K and (ii) <100 K. The latter pathway is depicted by broad desorption peaks attributed to diffusion through the pores of deposited ASW and the former manifests itself as sharp and narrower

peaks due to the structural failure of ASW overlayer caused by pressure increases.<sup>126</sup> The TPD is followed to prove that these desorption bursts are in fact, due to the structural failure of the ASW layer as seen coinciding with pressure increases. The shape of the low-temperature desorption peak and extent of desorption depends on the substrate where the deposited gas is deposited. The pre-crystallisation behaviour could be reconciled with accounting for a gas pressure of Ar, krypton (Kr) and xenon (Xe), contrary to the behaviour of methane (CH<sub>4</sub>), N<sub>2</sub>, O<sub>2</sub> and carbon monoxide (CO) which all exhibit broad, low-temperature peaks, seen to increase with the thickness of the underlayer. The differences between the gases are thought to be due to changes in surface roughness, and it was plausible to suggest that atomic gases form a smoother outer surface when compared to molecular gases. These dramatic differences are in line with the angle ballistic deposition of ASW, where the porosity can be increased and thus, the morphology of ASW changes. Nonetheless, it is likely that small changes in ASW such as porosity and density give rise to distinct features and kinetics gathered from the TPD.

Further to this assignment, the ‘molecular volcano’ was later revisited by May *et al.*<sup>186</sup> to determine and investigate how ASW thickness alters the changes of desorption with O<sub>2</sub>. ASW was found to prevent O<sub>2</sub> desorbing.<sup>186</sup> However, during the crystallisation process, cracks form in the structure of ASW, allowing an open pathway to vacuum, and thus, the rapid episodic release of O<sub>2</sub> was observed.<sup>186</sup> Thicker layers of ASW further trapped O<sub>2</sub>, resulting in the formation of a desorption peak at higher temperatures.<sup>186</sup> The thickness and evolution of the trapping peak may form the basis of determining the distribution of crystallisation-induced cracks in ASW. The use of TPD and RAIRS measurements in multicomponent parfait structures of ASW allows for the detection that cracks originate and propagate at the ASW/vacuum interface.<sup>186</sup>

### 1.3.3.3 Trapping of Gas Mixtures in ASW

The efficiency of noble gas-trapping within planetesimals and the presence of gases in these terrestrial planet atmospheres have been proposed to arise from the accretion of comets.<sup>161</sup> Noble gases have very low condensation temperatures, typically that of <50 K, signifying that these elements cannot be contained within solids that are present where planets form. Water could essentially serve as a carrier for these elements by trapping them within an icy matrix at low temperatures and would only be lost once heated to higher temperatures. Amorphous ice has long remained a means for the trapping of volatile species into solids – trapping and releasing foreign gases by vapour deposited



water-ice. Implications for icy bodies and laboratory studies would be characteristic of water-ice with trapped species. Typical laboratory experiments employ ultra-high vacuum (UHV) or high vacuum with temperatures ranging from 10–300 K. The use of TPD has been a growing avalanche in studying codeposited systems. It is yet still debated how water-ice incorporates guest species or noble gases into its structure, with two well-established methods. Gases can be trapped in ice *via* simple condensation on the surface of the ice at low temperatures at a given pressure and below the gas freezing temperature. Trapped molecules may escape during the ASW phase transition and the remaining molecules desorb after crystallisation of ASW. A small number of trapped molecules that remain after crystallisation >185 K, that do not get released, is a question of importance and a highly dubious topic. It may be due to trapped gas in a simple pore, covered by H<sub>2</sub>O layers or may, in turn, be trapped as a clathrate hydrate.<sup>160, 163</sup> The gases trapped inside a cage of water-ice as clathrate hydrates (section 1.4) are predicted to form at fairly high temperatures.<sup>188, 189</sup>

ASW is revealed to experimentally trap and integrate chemical components into its structure such as e.g., carbon dioxide (CO<sub>2</sub>), ammonia (NH<sub>3</sub>), methanol (CH<sub>3</sub>OH) and CO<sup>190</sup> and more complex organic molecules may also be trapped.<sup>191</sup> The adsorption and desorption behaviour of CO from ASW was studied using TPD and RAIRS and found to be highly complex when compared to what astrochemical models have predicted.<sup>173</sup> CO was retained and trapped in the porous structure of ASW at low temperatures of 15 K and upon heating, an irreversible phase transition of ASW occurred from a highly porous to non-porous amorphous ice structure in the temperature range of 30–70 K. This change causes a collapse of pores and CO is thus, entrapped within the icy matrix. This change fashions a closure in pores on the surface and CO that was adsorbed earlier within these pores cannot escape into the gas phase.<sup>173, 190, 192</sup> Several other gases of astrophysical relevance, have been shown to exhibit similar behaviour to CO with respect to trapping.<sup>160, 163</sup> As porous ASW crystallises, trapped molecules are episodically released in the desorption process – ‘molecular volcano’.<sup>184</sup> Trapped molecules are retained until the crystalline H<sub>2</sub>O film itself desorbs and the thickness of the film determines the intensity of this codesorption peak.<sup>173, 190, 192</sup>

The interactions between the surface of ASW and gas-phase molecules are important to determine the history, composition, and outgassing kinetics of such multicomponent ices. The desorption of species from comets facilitates the determination

of the relative composition and estimates the astral conditions at the time of formation.<sup>160</sup> ASWs morphology severely affects the interactions with volatile gases. As mentioned, porous ASW grown by vapour deposition is affected by the incident growth angle<sup>177</sup> but also, impingement flux and substrate temperature (77 K).<sup>168, 171</sup> Ayotte *et al.*<sup>160</sup> discovered for the film thickness used in their study, porous ASW absorbed 20 to 50 times more gaseous species than denser films. The temperature of desorption of the adsorbed gas influences the porosity of the ASW films. Akin to previous studies of trapped gases, abrupt desorption of the gases in this study occurs concomitantly with ASW crystallisation and are independent of the gas studied. Nevertheless, whether gas is adsorbed and trapped or not, is dominated by the porosity of ASW. For a gaseous species to remain trapped, pores must collapse before the escape of the gaseous molecules since the mentioned pathways that are connected, must have pre-existed when the gas was adsorbed.<sup>160</sup> Studies into the codeposition of ASW and CO<sub>2</sub> has highlighted the complexity of mixed films: illustrating that the trapping efficiency of ASW is related to film thickness, the ratio of both species and the nature of the trapped species.<sup>162, 163, 193-195</sup>

To summarise, ASW has been the central subject of intense investigations designed to reveal underlying, highly complex and anomalous properties from a structural and dynamic perspective. Further comprehensive insights into ASW properties will result in a more extensive understanding of its role in cosmological processes and also for laboratory studies of physical vapour deposition of various materials.<sup>196</sup>

## 1.4 Clathrate Hydrate Inclusion Compounds

The astounding plethora of structural diversity surrounding  $\text{H}_2\text{O}$  does not merely terminate with the pure phases of ice. Clathrate hydrates are ubiquitous and defined as non-stoichiometric inclusion compounds that serve to occupy open interlinked cage-like voids formed by a network of  $\text{H}_2\text{O}$  molecules.  $\text{H}_2\text{O}$  molecules are capable of forming a loosely bonded framework of hydrogen atoms rendering internal cavities unoccupied and stabilised by the presence and encapsulation of ‘guest’ species.

The ‘guest’ species whether it is a gaseous or hydrophobic molecule does not form chemical bonds with the ‘host’ ice cage as it is not truly bonded to the lattice. The cage of  $\text{H}_2\text{O}$  is unstable without the entrapment of ‘guest’ species and without them, the lattice structure of the clathrate hydrates would experience collapse into the conventional crystal ice structure or liquid  $\text{H}_2\text{O}$ . Figure 1.11 displays the delicate balance of the hydrogen-bonded network of these structures.

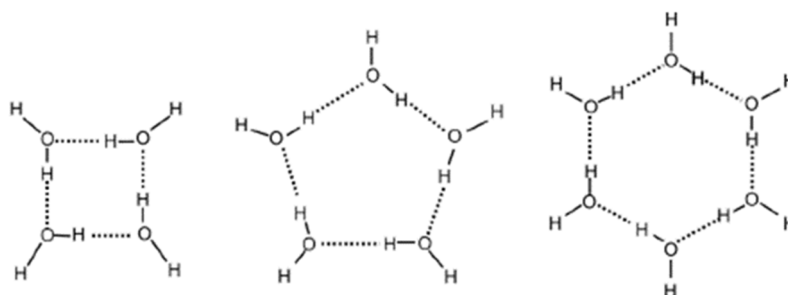


*Figure 1.11. Hydrogen-bonded framework required to form interlinked cages, resulting in clathrate hydrates. This figure has been reprinted from reference 197.*

The first gas hydrate discovered and documented by Davy in 1811,<sup>198</sup> was the chlorine hydrate, which revealed that  $\text{H}_2\text{O}$  was the primary component of hitherto assumed solidified chlorine.<sup>198</sup> After discovering that clathrate hydrates of natural gases were responsible for blocking pipelines, widespread exertions were aimed at reducing costs of decreasing this problem. Further attention towards gas hydrates was initiated due to their occurrence on Earth in natural environments (ice sheets, deep-sea sediments) and thus, raised questions surrounding their putative role in the storage and release of volatile species.

### 1.4.1 Crystal Structures of Clathrate Hydrates

The two types of bonds stabilising the structure of clathrate hydrates are: (1) van der Waals forces and (2) hydrogen bonds. The latter type of bonding maintains the icy skeleton, the former type are the repulsive interactions that are trapped between the icy skeleton and the gas molecule(s) which are required to withstand the cage structure. The stability of these compounds is determined by the interplay of (i) repulsion of hydrophobic interaction between the host and guest species and (ii) attraction of the cage and H<sub>2</sub>O molecules.

Gas-water clathrate hydrate compounds exhibit a spectacle of large structural variability with different shapes and sizes<sup>199</sup> and are specific to the pressure range they occur in. To date, several distinct ice clathrates have been experimentally discovered<sup>200-202</sup> and catalogued.<sup>203</sup> The network in Figure 1.11 link together to form cavities and cages within the water-host framework by sharing common faces. The notation of clathrate hydrates is A<sup>B</sup>, where A characterises the number of edges of the faces and B, characterises the number of faces of A. These hydrates are a combination of small and large-sized cages. For example, the unit cell may contain a pentagonal dodecahedron (5<sup>12</sup>) cage formed of twelve pentagons, combined with other types of polyhedra as shown in Figure 1.12, such as a tetrakaidekahedron (5<sup>12</sup>6<sup>2</sup>), hexakaidekahedron (5<sup>12</sup>6<sup>4</sup>), the irregular dodecahedron (4<sup>3</sup>5<sup>6</sup>6<sup>3</sup>) and an icosahedron (5<sup>12</sup>6<sup>8</sup>).<sup>204</sup> Table 1.2 aims to deliver an up-to-date summary of all clathrate hydrates with relevant properties and parameters. Best efforts have been employed in order to identify these parameters within the literature, however, it should be noted that Table 1.2 is unlikely to be entirely comprehensive.

The most common and recognised structural motifs adopted with the 5<sup>12</sup>-building block are molecular structures: cubic structure I (CS-I), cubic structure II (CS-II) and the hexagonal structure (sH). These clathrate hydrates exist at near-ambient conditions. Other structures are the tetragonal structure T (sT),<sup>205</sup> tetragonal structure K (sK),<sup>203</sup> cubic structure III (sIII)<sup>206</sup> and cubic structure L (sL).<sup>207</sup> Structure sT has been found experimentally and structures sK, sIII and sL have only ever been predicted computationally.

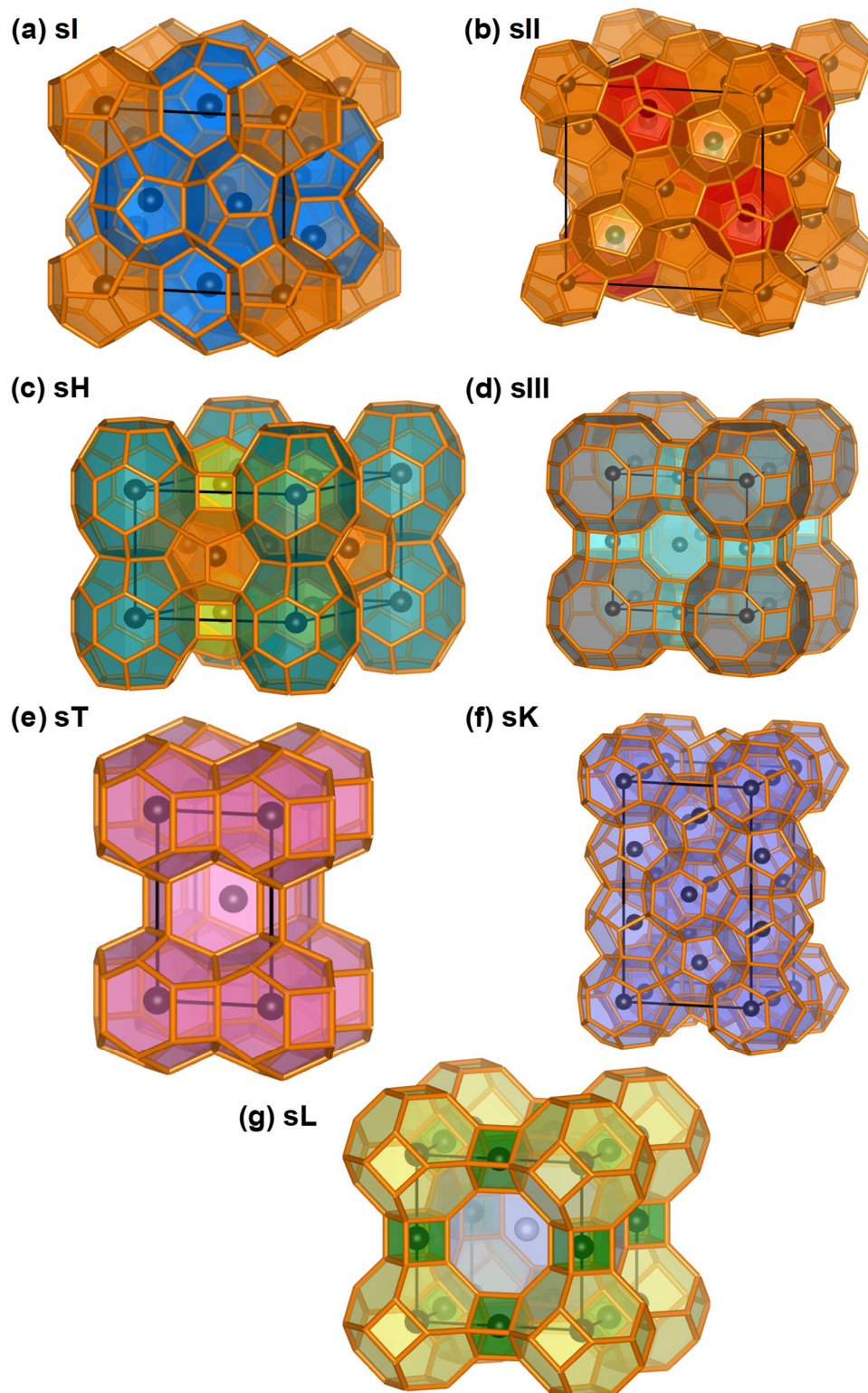


Figure 1.12. A three-dimensional illustration of the gallery of clathrate hydrate structures created in the Vesta software, as cage polyhedra where (a) sI (CS-I), (b) sII (CS-II) (c) sH, (d) sIII (e) sT, (f) sK and (g) sL clathrate structures. Structures (d), (f) and (g) are predicted computationally and the remaining clathrate hydrates have been prepared experimentally. Structure (a) and (c) have been reprinted from reference 208 with the permission of the nonexclusive License to Publish from PNAS-post-2018.

Clathrate hydrates, CS-I, CS-II and sH have been detected at pressures below 500 MPa.<sup>204</sup> Pressure poses a dramatic effect on the structural network of clathrate hydrates. When a structure experiences compression, the radius of the cage will decrease rendering the structure unstable and thus, a transition to a different clathrate hydrate may be seen. Figure 1.13 illustrates structural transitions that can take place when clathrate hydrates are compressed.

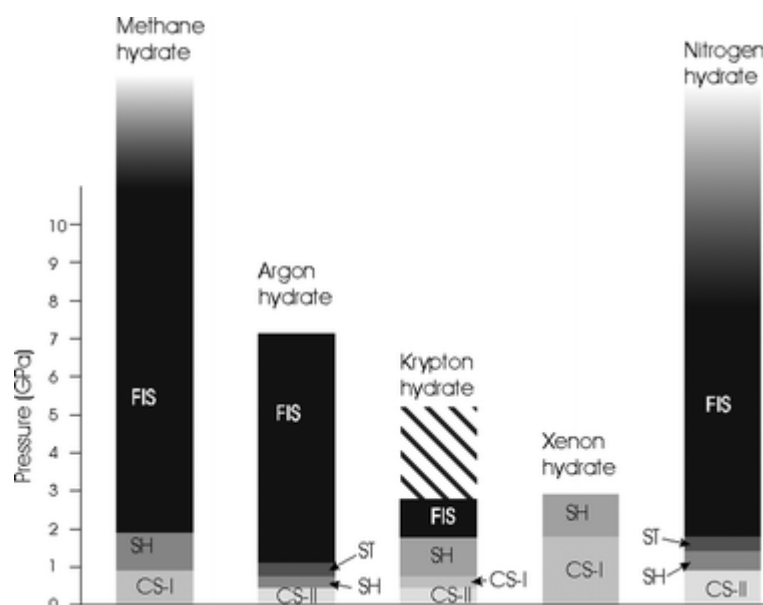


Figure 1.13. Structural phase transition sequence adopted by caged gas hydrates. The methane hydrate and nitrogen hydrate fade out in this figure as these structures have not yet been observed to decompose to their respective temperature. For the krypton hydrate (dashed), there are disagreements for the decomposition pressure which are not discussed in this thesis. This figure has been reprinted from reference 199 with the permission of The Royal Society of Chemistry Publishing.

For example, the lowest pressure hydrate for methane found on the seafloor is, MH-I.<sup>208</sup> As MH-I is compressed, it transforms to a structure similar to that of the sH unit cell at 0.9 GPa and when further compressed to above 2 GPa to a structure known as a ‘filled ice’ is observed and shown in Figure 1.14.<sup>208</sup> The definition of a filled ice is when a caged structure breaks down and forms ice networks where guest species can be present. In the structure of filled ices, H<sub>2</sub>O molecules are arranged similar to as they are found in ice Ih and methane in this structure occupies the open channels and voids in MH-III and MH-IV.<sup>208</sup>

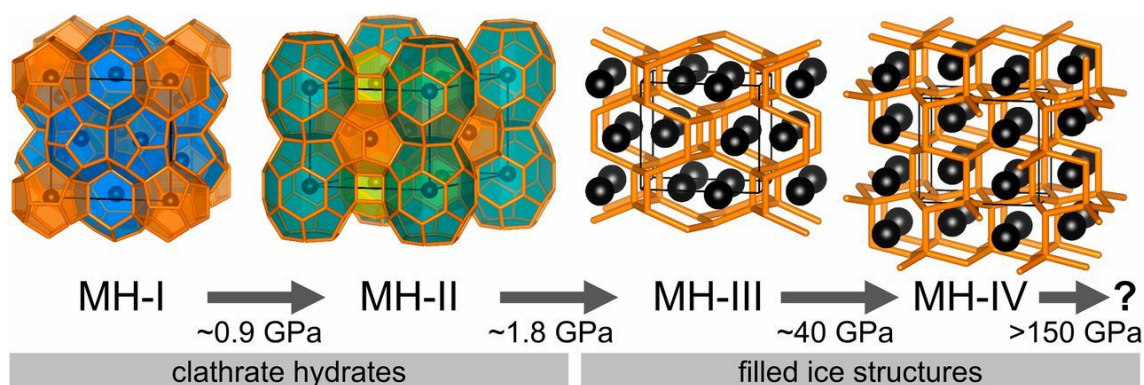


Figure 1.14. Phase transition sequence of the methane hydrate when compressed at ambient temperature. At low pressures, the hydrates are caged up to 1.8 GPa until they adopt a filled ice structure after this pressure. The orange lines in MH-III and MH-IV similar to that of ice Ih indicates the hydrogen-bonded network. This figure is reproduced under the nonexclusive License to Publish from PNAS post-2018, taken with permission from reference 208.

The formation of newly filled ice clathrates denoted, clathrate one ( $C_1$ ) and clathrate two ( $C_2$ ) were observed by Vos *et al.*<sup>209</sup> at high pressures. The hydrogen-water mixture crystallises to  $C_1$  at 0.7 GPa and 300 K.<sup>210, 211</sup> The  $H_2O$  sublattice of  $C_1$  is akin to, and based on the framework of ice II, with similar resemblance and isostructural to the small cage with encapsulation of the helium clathrate hydrate.<sup>212</sup>  $C_1$  structure favours guest species of small molecules and this  $C_1$ -type structure is essentially filled ice II.

With further compression to higher pressures and at ambient temperature of the hydrogen  $C_1$  structure, the phase becomes highly unstable and a different novel filled ice clathrate is produced at 2.3 GPa, the cubic  $C_2$  clathrate.<sup>209, 211</sup> The  $H_2O$  sublattice of this clathrate is diamond-like, which is similar to the metastable ice I phase at ambient pressures. The hydrogen molecules in this clathrate can occupy voids in the open framework of  $H_2O$ , meaning two interpenetrating diamond lattices represented a fully filled form of ice Ic and a high stoichiometric ratio of hydrogen and  $H_2O$  is formed with an ideal ratio of 1:1. The  $C_2$  structure is related to ice VII, where one  $H_2O$  is replaced by hydrogen<sup>209</sup> and can accommodate small or medium-sized molecules at high pressures. At ambient temperature,  $C_2$  is stable up to 40 GPa. The transition from  $C_1$  to  $C_2$  could be seen as a cornerstone in investigating a similar transition in small molecules such as neon and helium. Since both these clathrates have high melting temperatures at the same pressure as their pure ice phases, they are expected to be of substantial importance and relevance for planetary layers of hydrogen-helium and ice where these high temperature and pressure conditions exist.<sup>209</sup>

A new hydrate, named  $C_0$  was discovered within the hydrogen-water binary system by Efimchenko *et al.*<sup>213</sup> and the structure was further solved with *in situ* Raman spectroscopy and XRD by Strobel *et al.*<sup>210</sup> This phase is created at 280 K at 0.4 GPa with the composition of  $(H_2O)_2H_2$ .<sup>210</sup> A study that coalesced both low temperature with high pressures specified that the three phases were stable, however, the new phase, as now called  $C_0$  appeared and exists between the stability region of CS-II and  $C_1$ .<sup>211</sup> The structure of  $C_0$  is of hexagonal crystal symmetry and exhibits no analogue to any high-pressure ices or gas hydrates studied so far.<sup>210</sup> Its chiral nature consists of hydrogen-bonded  $H_2O$  molecules of interpenetrating spiral chains and disordered hydrogen molecules. The hydrogen-filled structure displays some topological similarities to the silicate mineral quartz found on Earth. Thus,  $C_0$  may be related to  $H_2O$ -based minerals which exist on planetary icy bodies. To summarise, these compounds highlight how structural diversity is influenced by the presence of guest species within the water-ice structure.

Several hypothetical structures have been examined by computational methods in the search for new modifications of ice however hitherto, only two have been found experimentally.<sup>52, 200</sup> This exciting discovery of two new ultralow density ice polymorphs have been successfully prepared and are accessed from corresponding clathrate hydrates. They have raised substantial interest as they are stable at negative pressures. These ultralow density ice polymorphs are less dense than ice *Ih*. The two new empty clathrate hydrates discovered are known as, ices XVI and XVII.

Ice XVI, an empty clathrate hydrate has been obtained by leaching neon atoms from the corresponding sII filled neon hydrate. Firstly, the neon sII clathrate<sup>200</sup> can be obtained from pressuring ice *Ih* to 0.35 GPa at 244 K. Continuous vacuum pumping on this clathrate at 142 K leached neon atoms, allowing the escape of small particles from the filled structure resulting in an empty clathrate hydrate structure, named ice XVI.<sup>200</sup> Comparing ice XVI, the guest free sII structure to the neon filled clathrate hydrate, ice XVI displays negative thermal expansion below <55 K and is less dense than known crystalline phases of ice with a density of  $0.81 \text{ g cm}^{-3}$ . Hydrogen disordered ice XVI is made up of two cages comprising one  $5^{12}$  and one  $5^{12}6^4$  cage, consisting of 126  $H_2O$  molecules in its unit cell as shown in Figure 1.6. Moreover, it has been realised and confirmed that refilling ice XVI with helium has led to the formation of the long-sought



helium clathrate hydrate.<sup>214</sup> This method has opened up new routes of synthesis for many forms of clathrate hydrates and can be used for removing guest species from sI and sH hydrates, however, guest species must be larger than neon which may, in turn, be difficult to remove by continuous pumping.<sup>11</sup> Similarly, as mentioned previously, the hydrogen-filled, C<sub>0</sub>-type structure forms at 0.4 GPa and 280 K.<sup>210</sup> The emptying of this dihydrogen C<sub>0</sub> hydrate with continuous pumping at 120 K for one to two hours allows for the reversible removal of hydrogen as monitored by Raman spectroscopy, leaving behind an empty clathrate hydrate named, ice XVII.<sup>52</sup> Ice XVII is formed from the C<sub>0</sub>-type hydrate of a dihydrogen-water binary compound once quenched at 77 K and ambient pressures after allowing the hydrogen to leach out of the crystal. Metastable ice XVII is chiral and thus, a porous material with interconnected spiral chains of open, spacious hexagonal channels (Figure 1.6) which allow easy leaching of gaseous species.<sup>52</sup> In addition, the dihydrogen dynamics were followed by high-resolution inelastic neutron scattering.<sup>215</sup> The C<sub>0</sub>-type hydrate was also found for CO<sub>2</sub> and also displayed a chiral ice XVII structure.<sup>216</sup>

Another guest-free clathrate hydrate structure with cubic symmetry has been identified and named sIII.<sup>206</sup> Employing extensive Monte Carlo (MC) algorithm and density functional theory (DFT) optimisation, sIII has a predicted structure typical of a clathrate hydrate. The structure is composed of two icosihexahedral cavities  $8^6 6^8 4^{12}$  and six  $8^2 4^8$  cages (small) per unit cell with 48 H<sub>2</sub>O molecules and the structure is dynamically stable without a guest and can be stabilised with an appropriately sized guest species.<sup>206</sup> Guest species such as dodecahedrane can be encapsulated into the model of the sIII structure. Based on MD simulations, and calculations with the monatomic H<sub>2</sub>O potential, the stable nature of the empty sII structure was predicted. Stability was found at low temperature and pressure: ~1300 bar and <275 K.<sup>217</sup> More computational methods using a TIP4P/2005 H<sub>2</sub>O potential revealed that both empty sII and the sH phases were found in the negative pressure region of H<sub>2</sub>O's phase diagram.<sup>218</sup> However, the sIII hydrate was found to have ultralow density and thus, replaced the low density of the sII and sH phases in the pressure region of the phase diagram below -5834 bar and below -3411 bar at 0 and 300 K, respectively.

So far, the phase of ice experimentally confirmed to be stable at negative pressures is the clathrate ice, sII. In addition to the computationally predicted clathrate hydrate structure, sIII, a second ultralow density phase of ice is reported, called the clathrate ice,

sL.<sup>207</sup> This sL clathrate ice is guest-free due to being obtained from pumping off guest atoms and molecules from the gas hydrate. The sL clathrate has been predicted as stable at lower pressures than the sII clathrate using computational methods.<sup>207</sup> The largest storage capacity in hydrogen hydrates known for sII is 5.3 w% and for the filled C<sub>2</sub> phase, 11.2 w%.<sup>207</sup> With theoretical predictions, for the sL clathrate, the hydrogen mass storage density is 7.7 w%.<sup>207</sup> The discovery of the sL clathrate proposes a type of ice that is stable in negative pressures and explores the application of phases that are ultralow in density while extending and enriching waters phase diagram.<sup>207</sup>

In addition, as ice *Ih* is compressed at 135 K, above 0.2 GPa, and further warmed, it transformed into a metastable state that had lower free energy than ice *Ih* but greater than C<sub>0</sub>, and thus, termed C<sub>-1</sub>.<sup>219</sup> The sample was further heated to obtain enough energy overcoming the C<sub>0</sub> energy barrier and upon more heating, the energy barrier to form the sII clathrate hydrate was overcome at 0.3 GPa. The comparison of the general sequence gives a transition of sequence at 0.2 and 0.3 GPa upon heating of, ice *Ih* → C<sub>-1</sub> → C<sub>0</sub> → sII. The ice *Ih* samples are less stable than the C<sub>0</sub> hydrate and thus, as the transition proceeds, the stability increases. This cascade of transitions *via* metastable phases from the original unstable ice *Ih*, resulting in the formation of stable sII clathrate hydrate, is known as, Ostwald's Rule of Stages.<sup>219, 220</sup>

### 1.4.2 Clathrate Hydrates from Amorphous Solid Water (ASW)

Experimentally, the formation of clathrate hydrates *in situ* UHV or interstellar cryogenic conditions has not been widely explored. Clathrate hydrate formation in the solar system has been believed to occur from vapour deposited ASW with species such as N<sub>2</sub>, O<sub>2</sub>, CO and Ar at low temperatures and pressures.<sup>182, 221, 222</sup> At low pressures, clathrate hydrates may also be grown epitaxially by annealing condensed water-gas mixtures.<sup>223</sup>

A common procedure for producing clathrate hydrates is the exposure of ice powder to pressurised gas of a guest species and a second route of unusual nature to crystallise clathrate hydrates is by heating LDA in the presence of a guest species.<sup>182</sup> The formation of clathrate hydrates from ASW has been reported in pioneering work by Devlin *et al.*<sup>224-227</sup> and is applied to a range of organic guest species using cocondensation techniques. From ASWs microporous nature, a model for clathrate hydrate formation was proposed where unusual adsorption, gas enclosure and sintering were observed.<sup>168</sup> Once ASW was prepared and the apparatus was pressurised with N<sub>2</sub> at 1 bar external guest

pressure, the deposit was warmed to 113 K which caused the sample to sinter and thus, trap the N<sub>2</sub> guest species. The trapped species cannot be pumped away *in vacuo*.<sup>182</sup> Using XRD, the N<sub>2</sub> and O<sub>2</sub> hydrate of CS-II displayed such reflections that it was inferred that the guest forms onto the pore walls where sintering does not allow any guest species that are enclosed or adsorbed, to escape. Thus, with increasing temperature, the pressure increases which is needed for the formation of clathrate hydrates to occur at  $\leq 193$ .<sup>182, 221</sup> For a heating rate of 10 K min<sup>-1</sup>, the formation of clathrate hydrates with ASW in the pores was found to occur at temperatures of: 208 K (N<sub>2</sub> and CO), 206 K (Ar) and 201 K (O<sub>2</sub>). The formation of clathrate hydrates is observed in XRD between 170 and 210 K. Figure 1.15 from the literature<sup>221</sup> displays the XRD patterns of equally prepared ASW deposits heated with O<sub>2</sub>, Ar, CO and N<sub>2</sub>.

In addition to the reflections present for ice *Ih* and ice *Isd* in the XRD patterns, additional Bragg reflections for CS-II [Figure 1.14(a), (b) and (d)] and also CS-I [Figure 1.16(c)] are indicated. The corresponding DSC thermograms to the XRD patterns as shown in Figure 1.15 are illustrated in Figure 1.16. An estimate for the amount of clathrate hydrate was observed, correlating the crystalline ice and clathrate hydrate peaks. The yield indicated a rough estimate that coincided with the boiling point of the guest species where O<sub>2</sub> was recorded to provide the highest yield when compared to N<sub>2</sub>.<sup>221</sup>

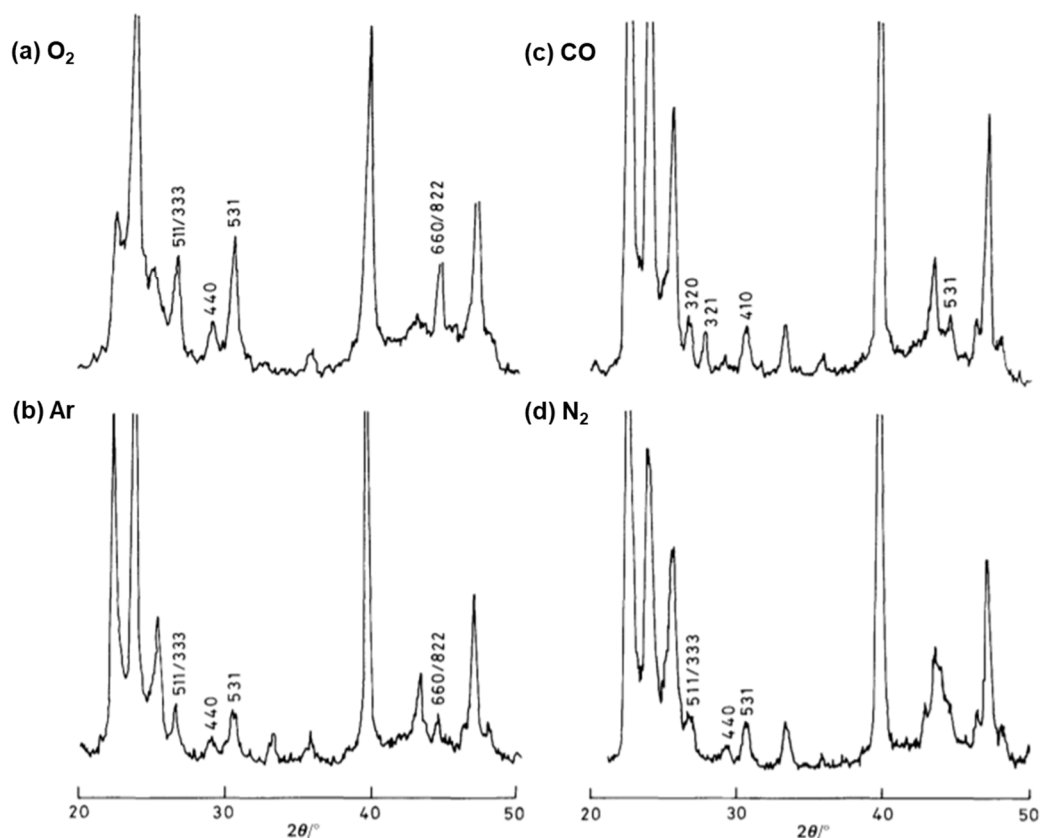


Figure 1.15. XRD diffractograms ( $\text{Cu K}\alpha$ ,  $\lambda = 1.54 \text{ \AA}$ ) of identically prepared ASW deposits incorporating (a)  $\text{O}_2$ , (b) Ar, (c) CO and (d)  $\text{N}_2$  gaseous species where (a) recorded at 100 K after heating to 193 K and (b)–(d) were recorded at 100 K after heating to 220 K. The reflections from CS-II for (a), (b) and (d) are indicated and CS-I for (c) is also indicated. Other reflections not indicated are contributions from ice Ih and ice Isd. This figure has been reprinted from reference 221 with the permission of The Royal Society of Chemistry Publishing.

Figure 1.16 depicts DSC thermograms for ASW samples treated with different species. The broad exotherm at 160 K is the reduction in surface area of ASW and the crystallisation of ASW to ice Isd. In Figure 1.16(a), at 253 K, for the deposit with the  $\text{O}_2$  guest species, the clathrate hydrate is seen to fully decompose, close to that of the melting point of ice (273 K) due to stabilisation by enclosing layers of ASW.<sup>221</sup> The onset of decomposition reflects the disappearance of Bragg peaks in the diffractogram and the subsequent endotherm starting at 246 K in Figure 1.16(a). A similar trend can be seen with the deposit when treated with helium.

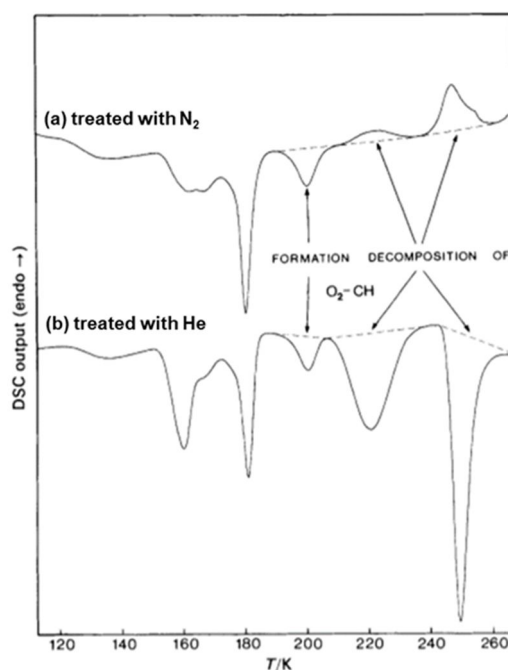


Figure 1.16. DSC thermograms of two ASW samples heated at  $10 \text{ K min}^{-1}$ , treated with  $\text{O}_2$ , (a) using  $\text{N}_2$  and (b) using helium,  $\text{He}$ . The DSC thermograms have been normalised with respect to the amount of  $\text{H}_2\text{O}$  in the sample and the dashed lines indicate integration limits. This figure has been reprinted from reference 221 with the permission of The Royal Society of Chemistry Publishing.

The gas that is enclosed in ASW allows this build-up of pressure to form clathrate hydrates at temperatures that are above the equilibrium temperature for 1 bar guest pressure, and they are stabilised by identical layers of crystalline ice. This process is equivalent to how air-clathrate hydrates in deep ice cores are stabilised.<sup>182</sup> It is believed that the large presence of micropores in ASW and the peculiar sintering processes it may undergo is quite essential for the formation of clathrate hydrates and their stability.<sup>222</sup>

Nevertheless, clathrate hydrates are of pivotal interest which arises from their vast capacity to store a large volume of gases. Clathrate hydrates involve the trapping of volatile gases into icy solids and may be formed in the solid nebula.<sup>228</sup> The existence of clathrate hydrates in comets is yet debated and remains ambiguous,<sup>229</sup> although, there are robust indications of these compounds influencing their role in atmospheres and satellites.<sup>230</sup> This section only outlines a fraction of the literature for clathrate hydrates as the exploration of these compounds have received a vast amount of attention in previous decades and many more to come. In any case, it will be of great importance to experimentally produce clathrate hydrates of all remaining structures and despite many years of active research, it is clear that water-ice exhibits many mysteries yet to be solved.

## 1. Introduction

Table 1.2. Summary of clathrate hydrate (CH) parameters including the number of H<sub>2</sub>O molecules per unit cell ( $n$ ), the ratio of H<sub>2</sub>O to guest molecules, mass density ( $\rho$  / g cm<sup>-3</sup>), lattice energy per H<sub>2</sub>O molecule ( $E_{latt}$ ), average oxygen-oxygen distance (O–O / Å) and many other parameters are provided. A few parameters have not been defined or found due to incomplete data in the literature.

CH	Unit cell cages	$n$	Crystal structure	Space group	Unit cell lattice parameters / Å	Volume of unit cell / $V_{cell}$ (Å <sup>3</sup> )	$\rho$ (g cm <sup>-3</sup> )	$E_{latt}$	O–O / Å	Characteristics	Guest species
sI	2 x 5 <sup>12</sup> 6 x 5 <sup>12</sup> 6 <sup>2</sup>	46	cubic	$Pm\bar{3}n$	$a = 12.03$	1692 <sup>206</sup>	0.813 <sup>206</sup>	61.38 <sup>206</sup>	2.765 <sup>206</sup>	Topologically related to SiO <sub>2</sub>	CO <sub>2</sub> , CH <sub>4</sub>
sII	16 x 5 <sup>12</sup> 8 x 5 <sup>12</sup> 6 <sup>4</sup>	136	cubic	$Fd\bar{3}m$	$a = 17.31$	5059 <sup>206</sup>	0.804 <sup>206</sup>	61.37 <sup>206</sup>	2.765 <sup>206</sup> 2.77– 2.79 <sup>52</sup>	Topologically related to SiO <sub>2</sub>	Ar, Kr, O <sub>2</sub> , N <sub>2</sub>
sH <sup>231</sup>	3 x 5 <sup>12</sup> 2 x 4 <sup>3</sup> 5 <sup>6</sup> 6 <sup>3</sup> 1 x 5 <sup>12</sup> 6 <sup>8</sup>	34	hexagonal	$P6_3/m\bar{m}$	$a = 12.3$ $c = 10.2$	1325 <sup>206</sup>	0.768 <sup>206</sup>	60.79 <sup>206</sup>	2.785 <sup>206</sup>	Large barrel shaped cage	C <sub>4</sub> H <sub>10</sub> , C <sub>6</sub> H <sub>12</sub> C <sub>10</sub> H <sub>16</sub>
sIII <sup>206</sup>	2 x 8 <sup>6</sup> 6 <sup>8</sup> 4 <sup>12</sup> 6 x 8 <sup>2</sup> 4 <sup>8</sup>	48 <sup>2</sup> <sub>06</sub>	cubic	$P\bar{4}3n$	$a = 13.131$ <sub>6</sub> <sup>20</sup>	2423 <sup>206</sup>	0.593 <sup>206</sup>	55.77 <sup>206</sup>	2.765 <sup>206</sup>	Ultralow density <sup>206</sup>	C <sub>20</sub> H <sub>20</sub> <sup>20</sup> <sub>6</sub>
XVI <sup>200</sup>	16 x 5 <sup>12</sup> 8 x 5 <sup>12</sup> 6 <sup>4</sup>	136	cubic	$Fd\bar{3}m$	$a = 17.125$ <sub>0</sub> <sup>20</sup>	-	0.81 <sup>200</sup>	-	-	Empty sII hydrate, stable LT phase of H <sub>2</sub> O under tension. same as sII	He <sup>214</sup>
XVII <sup>52</sup>	-	-	hexagonal	$P6_322$	$a = 6.3305$ $c = 6.0580$	210.249	0.9491 <sup>21</sup>	-	2.83– 2.85 <sup>52</sup>	Empty hydrate and was H <sub>2</sub> filled ice. spiralling channels of a diameter of 6.10 Å, porous, chiral	Ne, O <sub>2</sub> , CO <sub>2</sub> <sup>51</sup>
C <sub>I</sub> <sup>209</sup>	-	6 <sup>209</sup>	hexagonal	-	$a = 12.736$	-	-	-	-	Filled form of ice II	H <sub>2</sub> <sup>209</sup>

## 1. Introduction

					$c = 5.968$						
$C_2^{209}$	-	$8^{209}$	cubic	$Fd\bar{3}m_{209}^{199}$	$a = 6.434_{206, 209}$		-	-	-	Two interpenetrating diamond lattices, stable to 30 GPa	$H_2^{209}$
$C_0^{210}$	-		-	$P6_122^{210}$	$a = 6.285$ $c = 6.213^{210}$	$26.45^{210}$	-	-	$2.76-2.78^{210}$	Hydrogen-stuffed, topologically similar to mineral quartz	-
$C_{-1}^{219}$	-	-	-	$P6_3/mmc^{219}$	$a = 4.5160$ $c = 7.2691^{21}_9$	$128.39^{21}_9$	-	-	$2.7299-2.8256^{219}$	Samples needs to be approached in sequence to obtain $C_{-1}$ . $Ih \rightarrow C_{-1} \rightarrow C_0 \rightarrow sII$ following Ostwalds Rule of Stages. <sup>219</sup>	-
$sT_{232}^{205, 232}$	$2 \times 4^2 5^8 6^4$	$12^2_{06}$	tetragonal	$P4_2/mnm^{199}$	$a = 11.987$ $c = 12.15$	$453^{206}$	$0.792^{206}$	$60.23^{206}$	$2.795^{206}$		$Br_2^{205}$ $Ar^{199}$ $C_6H_{14}O_2^{233}$
$sK^{203}$	$6 \times 5^{12}$ $4 \times 5^{12} 6^2$ $4 \times 5^{12} 6^3$	$80^2_{06}$	tetragonal	-	$a = 12.116$ $b = 12.116$ $c = 20.824$	$2962^{206}$	$0.808^{206}$	$60.76^{206}$	$2.765^{206}$	Guest-free	$CH_4$
$sL^{207}$	$3 \times 4^6$ $1 \times 4^6 6^8$ $1 \times 4^{12} 6^8 8^6$	24	cubic	-	$a = 10.7117$	1229	0.584	-56.90	2.797	Named clathrate ice due to being guest-free, forms of sL_I and sL_II	-

### 1.5 Hydration of Hydrophobic Species

The complementary nature and coexistence of H<sub>2</sub>O with carbon species span a wide range of diverse settings and environments. Both species are highly dissimilar with respect to their chemical and physical properties. Elemental carbon, a highly diverse building block and hydrophobic material, coexists with H<sub>2</sub>O unveiling a series of the critical processes that occur at the interface. Such processes include, (i) the hydration shells of hydrophobic moieties in biomolecules, (ii) influencing ice phase transitions, (iii) search for new clathrate hydrates and (iv) desorption of H<sub>2</sub>O from carbonaceous species. In one particular instance, the presence of icy comets appears black in colour due to carbon on their surfaces. The carbon situated on these comets is thought to regulate complex ‘weather’ cycles by acting as a ‘blanket’ on top of the amorphous ice.<sup>152, 153</sup> However, experimental difficulties come into play during the preparation of mixtures of amorphous ice and carbonaceous species and so, only sparse amounts of information are known about the structure and dynamics of such complex and unusual mixtures.

Elucidating the structure of H<sub>2</sub>O in the hydration shells of hydrophobes gives access to unprecedented insights into how H<sub>2</sub>O hydrates hydrophobic species. This concept is responsible for a large number of fundamental processes such as surfactant aggregation, protein folding and enzyme-substrate interactions.<sup>234</sup> Previous experimental studies were only strictly limited to amphiphilic molecules.<sup>235, 236</sup> It was proposed that H<sub>2</sub>O molecules in hydrations shells of hydrophobic species were ‘ice-like’ and the ‘iceberg’ term was coined.<sup>237</sup> It was then suggested that H<sub>2</sub>O is capable of forming pentagonal rings in the hydration shells of hydrophobic species, small in nature, as have been found for clathrate hydrates.<sup>238</sup> However, this structural view has been challenged from a theoretical, computational,<sup>239</sup> and experimental side.<sup>240</sup> Simulations<sup>241</sup> and experimental evidence<sup>237</sup> have shown to suggest that the ‘iceberg’ around hydrophobes should be viewed from the perspective of slow dynamics. On the other hand, slower dynamics have been shown to give rise to ordered structures, not to the extent as proposed with the ‘iceberg’ model.

From a structural perspective, it is clear that the arrangement of the H<sub>2</sub>O molecules that hydrate hydrophobic species undergo changes that depend on the shape of the species. For instance, the cages that makeup clathrate hydrates and ‘square ice’ which was discovered ‘sandwiched’ between graphene sheets.<sup>242</sup>



## 1. Introduction

It has been insinuated that there are two different distinct regimes in regards to hydrophobic hydration: a large hydrophobic particle or small hydrophobic solute. Water molecules have been observed to adjust to the curvature of hydrophobic species as a result of mechanisms caused by surface drying effects as well as O–H bonds vaguely to the solute surface.<sup>238</sup>

As mentioned previously, clathrate hydrates are seen as standard systems to investigate hydrophobic hydration. This study prepares mixtures of amorphous ice and hydrophobic carbon species which can be deemed highly supersaturated at very low temperatures. The approach to answer and contribute to many open-ended questions surrounding the dynamics and structure of the iconic H<sub>2</sub>O molecule will be presented in this thesis and the specific aims are detailed herein.

### 1.6 Aims of this Thesis

This thesis aims to uncover and probe the structure and dynamics of poorly understood ASW using small-molecule nanoprobes. Gaseous species will initially be used to understand the gas-trapping environments in ASW. This research aligns with the emerging trend to explore insights into how H<sub>2</sub>O hydrates hydrophobic species, elucidating the structure of H<sub>2</sub>O in the hydration shells of true hydrophobes. The current limit in terms of what is possible with respect to the size and shape of the hydrophobic guest species in water-ice will be explored. This will enable insights into how flexible a building block of H<sub>2</sub>O is for building an entire network structure and also benefit the understanding of hydrophobic hydration.

The specific aims of this thesis to explore are to:

- (a) The thermal desorption characteristics of ASW with gaseous ‘nanoprobes’ to detect pore collapses, sintering of amorphous ice and follow the crystallisation process of ASW upon heating. This aim extends to consider any gas-trapping environments in macroscopic films of a mixture of vapour deposited amorphous ice and various gases.
- (b) Explore the influence of carbonaceous species, such as adamantane (C<sub>10</sub>H<sub>16</sub>), on ASW to determine how C<sub>10</sub>H<sub>16</sub> affects the amorphous matrix with a particular focus on the crystallisation and potential clathrate hydrate formation.
- (c) Following on from point (b), investigations will be carried out from the viewpoint of C<sub>10</sub>H<sub>16</sub> guest species with the total neutron scattering of C<sub>10</sub>H<sub>16</sub> in amorphous ice: a nanoprobe for detecting sintering and potential clathrate hydrate formation. C<sub>10</sub>H<sub>16</sub> finely dispersed within the amorphous ice matrix at two different temperatures, as-made at 80 K and after annealing at 140 K will be investigated in detail. Several questions as provided below will be addressed:
  - (i) how hydrated C<sub>10</sub>H<sub>16</sub> is.
  - (ii) coordination number of C<sub>10</sub>H<sub>16</sub>.
  - (iii) PDFs of atom pairs in the matrix.
  - (iv) positional and orientational ordering of H<sub>2</sub>O molecules in the first coordination shell around hydrophobic C<sub>10</sub>H<sub>16</sub> in amorphous ice.

## 1.7 References

1. A. G. G. M. Tielens, *Rev. Mod. Phys.*, 2013, **85**, 1021-1081.
2. P. Ball, *H<sub>2</sub>O: A Biography of Water*, Hachette UK, London, 2015.
3. E. A. Zheligovskaya and G. G. Malenkov, *Russ. Chem. Rev.*, 2006, **75**, 57-76.
4. C. G. Salzmann, P. G. Radaelli, B. Slater and J. L. Finney, *Phys. Chem. Chem. Phys.*, 2011, **13**, 18468-18480.
5. P. G. Debenedetti, *J. Phys.: Condens. Matter*, 2003, **15**, R1669-R1726.
6. P. W. Atkins and J. de Paula, *Atkins' Physical Chemistry*, OUP Oxford, 2010.
7. G. Wypych, in *Handbook of Solvents, Volume 1: Properties*, ChemTec Publishing, Canada, 3 edn., 2014.
8. O. Mishima and H. E. Stanley, *Nature*, 1998, **396**, 329-335.
9. K. Amann-Winkel, R. Böhmer, F. Fujara, C. Gainaru, B. Geil and T. Loerting, *Rev. Mod. Phys.*, 2016, **88**, 011002.
10. V. F. Petrenko and R. W. Whitworth, *Physics of Ice*, OUP Oxford, 1999.
11. C. G. Salzmann, *J. Chem. Phys.*, 2019, **150**, 060901.
12. T. L. Malkin, B. J. Murray, C. G. Salzmann, V. Molinero, S. J. Pickering and T. F. Whale, *Phys. Chem. Chem. Phys.*, 2015, **17**, 60-76.
13. D. M. Dennison, *Phys. Rev.*, 1921, **17**, 20-22.
14. S. W. H. Bragg, *Proc. Phys. Soc.*, 1921, **34**, 98-103.
15. W. H. Barnes and W. H. Bragg, *Proc. Roy. Soc.*, 1929, **A125**, 670-693.
16. E. O. Wollan, W. L. Davidson and C. G. Shull, *Phys. Rev.*, 1949, **75**, 1348-1352.
17. J. D. Bernal and R. H. Fowler, *J. Chem. Phys.*, 1933, **1**, 515-548.
18. L. Pauling, *J. Am. Chem. Soc.*, 1935, **57**, 2680-2684.
19. M. Millot, F. Coppari, J. R. Rygg, A. Correa Barrios, S. Hamel, D. C. Swift and J. H. Eggert, *Nature*, 2019, **569**, 251-255.
20. C. Frondel and U. B. Marvin, *Nature*, 1967, **214**, 587.
21. L. del Rosso, M. Celli, F. Grazzi, M. Catti, T. C. Hansen, A. D. Fortes and L. Ulivi, *Nat. Mater.*, 2020, **19**, 663-668.
22. K. Komatsu, S. Machida, F. Noritake, T. Hattori, A. Sano-Furukawa, R. Yamane, K. Yamashita and H. Kagi, *Nat. Commun.*, 2020, **11**, 464.
23. C. G. Salzmann and B. J. Murray, *Nat. Mater.*, 2020, **19**, 586-587.
24. E. Whalley, *Science*, 1981, **211**, 389.
25. J. E. Shilling, M. A. Tolbert, O. B. Toon, E. J. Jensen, B. J. Murray and A. K. Bertram, *Geophys. Res. Lett.*, 2006, **33**, L17801.
26. Z. Raza, D. Alfe, C. G. Salzmann, J. Klimes, A. Michaelides and B. Slater, *Phys. Chem. Chem. Phys.*, 2011, **13**, 19788-19795.
27. W. F. Kuhs, C. Sippel, A. Falenty and T. C. Hansen, *Proc. Natl. Acad. Sci. U. S. A.*, 2012, **109**, 21259-21264.
28. T. L. Malkin, B. J. Murray, A. V. Brukhno, J. Anwar and C. G. Salzmann, *Proc. Natl. Acad. Sci. U. S. A.*, 2012, **109**, 1041-1045.
29. W. F. Kuhs, D. V. Bliss and J. L. Finney, *J. Phys. Colloques*, 1987, **48**, C1-631-C631-636.
30. B. J. Murray, C. G. Salzmann, A. J. Heymsfield, S. Dobbie, R. R. Neely and C. J. Cox, *Bull. Am. Meteorol. Soc.*, 2015, **96**, 1519-1531.
31. S. Lele, T. R. Anantharaman and C. A. Johnson, *Phys. Status Solidi (b)*, 1967, **20**, 59-68.
32. B. Prasad and S. Lele, *Acta. Cryst.*, 1971, **27**, 54-64.
33. C. G. Salzmann, B. J. Murray and J. J. Shephard, *Diamond Relat. Mater.*, 2015, **59**, 69-72.

34. T. C. Hansen, M. M. Koza and W. F. Kuhs, *J. Phys.: Condens. Matter*, 2008, **20**, 285104.
35. T. H. Carr, J. J. Shephard and C. G. Salzmann, *J. Phys. Chem. Lett.*, 2014, **5**, 2469-2473.
36. H. Y. Playford, T. F. Whale, B. J. Murray, M. G. Tucker and C. G. Salzmann, *J. Appl. Cryst.*, 2018, **51**, 1211-1220.
37. Y. Tajima, T. Matsuo and H. Suga, *J. Phys. Chem. Solids*, 1984, **45**, 1135-1144.
38. T. Matsuo and H. Suga, *J. Phys. Colloques*, 1987, **48**, C1-477-C471-483.
39. A. Rosu-Finsen and C. G. Salzmann, *J. Chem. Phys.*, 2018, **148**, 244507.
40. P. Parkkinen, S. Riikonen and L. Halonen, *J. Phys. Chem. C*, 2014, **118**, 26264-26275.
41. C. Lobban, PhD thesis, University College London, 1998.
42. G. Tammann, *Ann. Phys.*, 1900, **307**, 1-31.
43. P. W. Bridgman, *Proc. Am. Acad.*, 1912, **47**, 441-558.
44. R. Yamane, K. Komatsu, J. Gouchi, Y. Uwatoko, S. Machida, T. Hattori, H. Ito and H. Kagi, *Nat. Commun.*, 2021, **12**, 1129.
45. T. M. Gasser, A. V. Thoeny, A. D. Fortes and T. Loerting, *Nat. Commun.*, 2021, **12**, 1128.
46. C. G. Salzmann, J. S. Loveday, A. Rosu-Finsen and C. L. Bull, *Nat. Commun.*, 2021, **12**, 3162.
47. A. Rosu-Finsen and C. G. Salzmann, *Chem. Sci.*, 2019, **10**, 515-523.
48. Tobias M. Gasser, A. V. Thoeny, L. J. Plaga, K. W. Köster, M. Etter, R. Böhmer and T. Loerting, *Chem. Sci.*, 2018, **9**, 4224-4234.
49. A. Rosu-Finsen, A. Amon, J. Armstrong, F. Fernandez-Alonso and C. G. Salzmann, *J. Phys. Chem. Lett.*, 2020, **11**, 1106-1111.
50. T. Nakamura, M. Matsumoto, T. Yagasaki and H. Tanaka, *J. Phys. Chem. B*, 2016, **120**, 1843-1848.
51. L. del Rosso, F. Grazzi, M. Celli, D. Colognesi, V. Garcia-Sakai and L. Ulivi, *J. Phys. Chem. C*, 2016, **120**, 26955-26959.
52. L. del Rosso, M. Celli and L. Ulivi, *Nat. Commun.*, 2016, **7**, 13394.
53. J. J. Shephard, S. Ling, G. C. Sosso, A. Michaelides, B. Slater and C. G. Salzmann, *J. Phys. Chem. Lett.*, 2017, **8**, 1645-1650.
54. C. G. Salzmann, A. Rosu-Finsen, Z. Sharif, P. G. Radaelli and J. L. Finney, *J. Chem. Phys.*, 2021, **154**, 134504.
55. C. G. Salzmann, I. Kohl, T. Loerting, E. Mayer and A. Hallbrucker, *J. Phys. Chem. B*, 2003, **107**, 2802-2807.
56. M. Millot, S. Hamel, J. R. Rygg, P. M. Celliers, G. W. Collins, F. Coppari, D. E. Fratanduono, R. Jeanloz, D. C. Swift and J. H. Eggert, *Nat. Phys.*, 2018, **14**, 297-302.
57. Y. Tajima, T. Matsuo and H. Suga, *Nature*, 1982, **299**, 810-812.
58. C. G. Salzmann, P. G. Radaelli, E. Mayer and J. L. Finney, *Phys. Rev. Lett.*, 2009, **103**, 105701.
59. C. G. Salzmann, P. G. Radaelli, A. Hallbrucker, E. Mayer and J. L. Finney, *Science*, 2006, **311**, 1758.
60. J. J. Shephard, B. Slater, P. Harvey, M. Hart, C. L. Bull, S. T. Bramwell and C. G. Salzmann, *Nat. Phys.*, 2018, **14**, 569-572.
61. W. F. Giauque and J. W. Stout, *J. Am. Chem. Soc.*, 1936, **58**, 1144-1150.
62. T. Loerting, K. Winkel, M. Seidl, M. Bauer, C. Mitterdorfer, P. H. Handle, C. G. Salzmann, E. Mayer, J. L. Finney and D. T. Bowron, *Phys. Chem. Chem. Phys.*, 2011, **13**, 8783-8794.

63. O. Mishima, *Proc. Jpn. Acad. Ser. B. Phys. Biol. Sci.*, 2010, **86**, 165-175.
64. E. F. Burton, W. F. Oliver and J. C. McLennan, *Proc. R. Soc. Lond. A*, 1935, **153**, 166-172.
65. E. F. Burton and W. F. Oliver, *Nature*, 1935, **135**, 505-506.
66. P. Jenniskens and D. F. Blake, *Science*, 1994, **265**, 753.
67. D. S. Olander and S. A. Rice, *Proc. Natl. Acad. Sci. U. S. A.*, 1972, **69**, 98.
68. R. S. Smith, N. G. Petrik, G. A. Kimmel and B. D. Kay, *Acc. Chem. Res.*, 2012, **45**, 33-42.
69. H. E. Stanley, S. V. Buldyrev, M. Canpolat, O. Mishima, M. R. Sadr-Lahijany, A. Scala and F. W. Starr, *Phys. Chem. Chem. Phys.*, 2000, **2**, 1551-1558.
70. G. P. Johari, A. Hallbrucker and E. Mayer, *Nature*, 1987, **330**, 552.
71. M. S. Elsaesser, K. Winkel, E. Mayer and T. Loerting, *Phys. Chem. Chem. Phys.*, 2010, **12**, 708-712.
72. S. C. Mossop, *Proc. Phys. Soc. B*, 1955, **68**, 193-208.
73. C. A. Angell, J. Shuppert and J. C. Tucker, *J. Phys. Chem.*, 1973, **77**, 3092-3099.
74. H. Kanno, R. J. Speedy and C. A. Angell, *Science*, 1975, **189**, 880.
75. A. Parmentier, J. J. Shephard, G. Romanelli, R. Senesi, C. G. Salzmann and C. Andreani, *J. Phys. Chem. Lett.*, 2015, **6**, 2038-2042.
76. D. T. Bowron, J. L. Finney, A. Hallbrucker, I. Kohl, T. Loerting, E. Mayer and A. K. Soper, *J. Chem. Phys.*, 2006, **125**, 194502.
77. E. Mayer, *J. Appl. Phys.*, 1985, **58**, 663-667.
78. O. Mishima, L. D. Calvert and E. Whalley, *Nature*, 1985, **314**, 76-78.
79. K. Winkel, D. T. Bowron, T. Loerting, E. Mayer and J. L. Finney, *J. Chem. Phys.*, 2009, **130**, 204502.
80. K. Winkel, M. S. Elsaesser, E. Mayer and T. Loerting, *J. Chem. Phys.*, 2008, **128**, 044510.
81. K. Winkel, M. Bauer, E. Mayer, M. Seidl, M. S. Elsaesser and T. Loerting, *J. Phys.: Condens. Matter*, 2008, **20**, 494212.
82. J. J. Shephard, S. Klotz, M. Vickers and C. G. Salzmann, *J. Chem. Phys.*, 2016, **144**, 204502.
83. O. Mishima, L. D. Calvert and E. Whalley, *Nature*, 1984, **310**, 393-395.
84. T. Loerting, C. Salzmann, I. Kohl, E. Mayer and A. Hallbrucker, *Phys. Chem. Chem. Phys.*, 2001, **3**, 5355-5357.
85. R. J. Nelmes, J. S. Loveday, T. Strässle, C. L. Bull, M. Guthrie, G. Hamel and S. Klotz, *Nat. Phys.*, 2006, **2**, 414-418.
86. O. Mishima, *J. Chem. Phys.*, 1994, **100**, 5910-5912.
87. T. Loerting, W. Schustereder, K. Winkel, C. G. Salzmann, I. Kohl and E. Mayer, *Phys. Rev. Lett.*, 2006, **96**, 025702.
88. O. Mishima, *Nature*, 1996, **384**, 546-549.
89. C. Mitterdorfer, M. Bauer, T. G. Youngs, D. T. Bowron, C. R. Hill, H. J. Fraser, J. L. Finney and T. Loerting, *Phys. Chem. Chem. Phys.*, 2014, **16**, 16013-16020.
90. J. L. Finney, D. T. Bowron, A. K. Soper, T. Loerting, E. Mayer and A. Hallbrucker, *Phys. Rev. Lett.*, 2002, **89**, 205503.
91. J. L. Finney, A. Hallbrucker, I. Kohl, A. K. Soper and D. T. Bowron, *Phys. Rev. Lett.*, 2002, **88**, 225503.
92. P. Brüggeller and E. Mayer, *Nature*, 1980, **288**, 569-571.
93. E. Mayer and P. Brüggeller, *Nature*, 1982, **298**, 715-718.
94. E. Mayer, *J. Phys. Chem.*, 1985, **89**, 3474-3477.
95. M. A. Floriano, Y. P. Handa, D. D. Klug and E. Whalley, *J. Chem. Phys.*, 1989, **91**, 7187-7192.

96. E. Whalley, D. D. Klug and Y. P. Handa, *Nature*, 1989, **342**, 782-783.
97. P. Poole, F. Sciortino, U. Essmann and H. Stanley, *Nature*, 1992, **360**, 324-328.
98. H. Stanley, C. Angell, U. Essmann, M. Hemmati, P. Poole and F. Sciortino, *Phys. A Statist. Mech. Appl.*, 1994, **205**, 122-139.
99. D. T. Limmer and D. Chandler, *Proc. Natl. Acad. Sci. U. S. A.*, 2014, **111**, 9413-9418.
100. G. P. Johari and J. Teixeira, *J. Phys. Chem. B*, 2015, **119**, 14210-14220.
101. G. P. Johari, *J. Chem. Phys.*, 1995, **102**, 6224-6229.
102. G. P. Johari, *J. Chem. Phys.*, 2000, **112**, 8573-8580.
103. G. P. Johari and O. Andersson, *Thermochim. Acta.*, 2007, **461**, 14-43.
104. J. J. Shephard, J. S. O. Evans and C. G. Salzmann, *J. Phys. Chem. Lett.*, 2013, **4**, 3672-3676.
105. M. Fisher and J. P. Devlin, *J. Phys. Chem. A*, 1995, **99**, 11584-11590.
106. C. R. Hill, C. Mitterdorfer, T. G. Youngs, D. T. Bowron, H. J. Fraser and T. Loerting, *Phys. Rev. Lett.*, 2016, **116**, 215501.
107. J. J. Shephard and C. G. Salzmann, *J. Phys. Chem. Lett.*, 2016, **7**, 2281-2285.
108. J. Swenson, *Phys. Chem. Chem. Phys.*, 2018, **20**, 30095-30103.
109. F. Perakis, K. Amann-Winkel, F. Lehmkuhler, M. Sprung, D. Mariedahl, J. A. Sellberg, H. Pathak, A. Spah, F. Cavalca, D. Schlesinger, A. Ricci, A. Jain, B. Massani, F. Aubree, C. J. Benmore, T. Loerting, G. Grubel, L. G. M. Pettersson and A. Nilsson, *Proc. Natl. Acad. Sci. U. S. A.*, 2017, **114**, 8193-8198.
110. Y. Xu, N. G. Petrik, R. S. Smith, B. D. Kay and G. A. Kimmel, *Proc. Natl. Acad. Sci. U. S. A.*, 2016, **113**, 14921-14925.
111. Y. Yue and C. A. Angell, *Nature*, 2004, **427**, 717-720.
112. O. Andersson, *Proc. Natl. Acad. Sci. U. S. A.*, 2011, **108**, 11013-11016.
113. A. Hallbrucker, E. Mayer and G. P. Johari, *J. Phys. Chem.*, 1989, **93**, 4986-4990.
114. A. Hallbrucker, E. Mayer and G. P. Johari, *Philos. Mag. B*, 1989, **60**, 179-187.
115. G. P. Johari, *J. Phys. Chem. B*, 1998, **102**, 4711-4714.
116. Y. P. Handa and D. D. Klug, *J. Phys. Chem.*, 1988, **92**, 3323-3325.
117. O. Andersson and A. Inaba, *Phys. Chem. Chem. Phys.*, 2005, **7**, 1441-1449.
118. J. C. Li and P. Jenniskens, *Planet. Space Sci.*, 1997, **45**, 469-473.
119. J. S. Tse, D. D. Klug, C. A. Tulk, I. Swainson, E. C. Svensson, C. K. Loong, V. Shpakov, V. R. Belosludov, R. V. Belosludov and Y. Kawazoe, *Nature*, 1999, **400**, 647-649.
120. V. Velikov, S. Borick and C. A. Angell, *Science*, 2001, **294**, 2335-2338.
121. O. Andersson, *Phys. Rev. Lett.*, 2007, **98**, 057602.
122. J. A. McMillan and S. C. Los, *Nature*, 1965, **206**, 806-807.
123. S. K. Talewar, S. O. Halukeerthi, R. Riedlaicher, J. J. Shephard, A. E. Clout, A. Rosu-Finsen, G. R. Williams, A. Langhoff, D. Johannsmann and C. G. Salzmann, *J. Chem. Phys.*, 2019, **151**, 134505.
124. S. M. McClure, D. J. Safarik, T. M. Truskett and C. B. Mullins, *J. Phys. Chem. B*, 2006, **110**, 11033-11036.
125. R. A. May, R. S. Smith and B. D. Kay, *J. Chem. Phys.*, 2013, **138**, 104501.
126. R. A. May, R. S. Smith and B. D. Kay, *J. Chem. Phys.*, 2013, **138**, 104502.
127. R. S. Smith, R. A. May and B. D. Kay, *J. Phys. Chem. B*, 2016, **120**, 1979-1987.
128. K. Amann-Winkel, C. Gainaru, P. H. Handle, M. Seidl, H. Nelson, R. Bohmer and T. Loerting, *Proc. Natl. Acad. Sci. U. S. A.*, 2013, **110**, 17720-17725.
129. P. Gallo, K. Amann-Winkel, C. A. Angell, M. A. Anisimov, F. Caupin, C. Chakravarty, E. Lascaris, T. Loerting, A. Z. Panagiotopoulos, J. Russo, J. A.

- Sellberg, H. E. Stanley, H. Tanaka, C. Vega, L. Xu and L. G. Pettersson, *Chem. Rev.*, 2016, **116**, 7463-7500.
130. D. A. Fuentevilla and M. A. Anisimov, *Phys. Rev. Lett.*, 2006, **97**, 195702.
  131. C. E. Bertrand and M. A. Anisimov, *J. Phys. Chem. B*, 2011, **115**, 14099-14111.
  132. H. Tanaka, *J. Chem. Phys.*, 1999, **112**, 799-809.
  133. H. Tanaka, *Eur. Phys. J. E*, 2012, **35**, 113.
  134. F. Sciortino, P. H. Poole, U. Essmann and H. E. Stanley, *Phys. Rev. E*, 1997, **55**, 727-737.
  135. H. Stanley, P. Kumar, G. Franzese, L. Xu, Z. Yan, M. G. Mazza, S. Buldyrev, S.-H. Chen and F. Mallamace, *Eur. Phys. J. Special Topics*, 2008, **161**, 1-17.
  136. L. Xu, P. Kumar, S. V. Buldyrev, S.-H. Chen, P. H. Poole, F. Sciortino and H. E. Stanley, *Proc. Natl. Acad. Sci. U. S. A.*, 2005, **102**, 16558-16562.
  137. A. Nilsson and L. G. M. Pettersson, *Nat. Commun.*, 2015, **6**, 8998.
  138. D. T. Limmer and D. Chandler, *J. Chem. Phys.*, 2011, **135**, 134503.
  139. P. H. Poole, F. Sciortino, T. Grande, H. E. Stanley and C. A. Angell, *Phys. Rev. Lett.*, 1994, **73**, 1632.
  140. S. Sastry, P. G. Debenedetti, F. Sciortino and H. E. Stanley, *Phys. Rev. E*, 1996, **53**, 6144.
  141. F. Sciortino, E. La Nave and P. Tartaglia, *Phys. Rev. Lett.*, 2003, **91**, 155701.
  142. T. C. Sivakumar, S. A. Rice and M. G. Sceats, *J. Chem. Phys.*, 1978, **69**, 3468-3476.
  143. S. Maruyama, K. Wakabayashi and M. Oguni, *AIP Conference Proceedings*, 2004, **708**, 675-676.
  144. K. Binder, *Proc. Natl. Acad. Sci. U. S. A.*, 2014, **111**, 9374.
  145. N. Binggeli, N. R. Keskar and J. R. Chelikowsky, *Phys. Rev. B Condens. Matter*, 1994, **49**, 3075-3081.
  146. D. Mariedahl, F. Perakis, A. Späh, H. Pathak, K. H. Kim, C. Benmore, A. Nilsson and K. Amann-Winkel, *Philos. Trans. A Math. Phys. Eng. Sci.*, 2019, **377**, 20180164.
  147. J. C. Palmer, P. H. Poole, F. Sciortino and P. G. Debenedetti, *Chem. Rev.*, 2018, **118**, 9129-9151.
  148. C. A. Tulk, J. J. Molaison, A. R. Makhlof, C. E. Manning and D. D. Klug, *Nature*, 2019, **569**, 542-545.
  149. A. K. Soper, *J. Chem. Phys.*, 2019, **150**, 234503.
  150. L. Kringle, W. A. Thornley, B. D. Kay and G. A. Kimmel, *Science*, 2020, **369**, 1490.
  151. H. J. Fraser, M. R. McCoustra and D. A. Williams, *Astron. Geophys.*, 2002, **43**, 2.10-2.18.
  152. G. Filacchione, M. C. De Sanctis, F. Capaccioni, A. Raponi, F. Tosi, M. Ciarniello, P. Cerroni, G. Piccioni, M. T. Capria, E. Palomba, G. Bellucci, S. Erard, D. Bockelee-Morvan, C. Leyrat, G. Arnold, M. A. Barucci, M. Fulchignoni, B. Schmitt, E. Quirico, R. Jaumann, K. Stephan, A. Longobardo, V. Mennella, A. Migliorini, E. Ammannito, J. Benkhoff, J. P. Bibring, A. Blanco, M. I. Blecka, R. Carlson, U. Carsenty, L. Colangeli, M. Combes, M. Combi, J. Crovisier, P. Drossart, T. Encrenaz, C. Federico, U. Fink, S. Fonti, W. H. Ip, P. Irwin, E. Kuehrt, Y. Langevin, G. Magni, T. McCord, L. Moroz, S. Mottola, V. Orofino, U. Schade, F. Taylor, D. Tiphene, G. P. Tozzi, P. Beck, N. Biver, L. Bonal, J. P. Combe, D. Despan, E. Flamini, M. Formisano, S. Fornasier, A. Frigeri, D. Grassi, M. S. Gudipati, D. Kappel, F. Mancarella, K. Markus, F. Merlin, R. Orosei, G. Rinaldi, M. Cartacci, A. Cicchetti, S. Giuppi, Y. Hello, F.

- Henry, S. Jacquino, J. M. Reess, R. Noschese, R. Politi and G. Peter, *Nature*, 2016, **529**, 368-372.
153. M. C. De Sanctis, F. Capaccioni, M. Ciarniello, G. Filacchione, M. Formisano, S. Mottola, A. Raponi, F. Tosi, D. Bockelée-Morvan, S. Erard, C. Leyrat, B. Schmitt, E. Ammannito, G. Arnold, M. A. Barucci, M. Combi, M. T. Capria, P. Cerroni, W. H. Ip, E. Kuehrt, T. B. McCord, E. Palomba, P. Beck, E. Quirico, V. T. The, G. Piccioni, G. Bellucci, M. Fulchignoni, R. Jaumann, K. Stephan, A. Longobardo, V. Mennella, A. Migliorini, J. Benkhoff, J. P. Bibring, A. Blanco, M. Blecka, R. Carlson, U. Carsenty, L. Colangeli, M. Combes, J. Crovisier, P. Drossart, T. Encrenaz, C. Federico, U. Fink, S. Fonti, P. Irwin, Y. Langevin, G. Magni, L. Moroz, V. Orofino, U. Schade, F. Taylor, D. Tiphene, G. P. Tozzi, N. Biver, L. Bonal, J. P. Combe, D. Despan, E. Flamini, S. Fornasier, A. Frigeri, D. Grassi, M. S. Gudipati, F. Mancarella, K. Markus, F. Merlin, R. Orosei, G. Rinaldi, M. Cartacci, A. Cicchetti, S. Giuppi, Y. Hello, F. Henry, S. Jacquino, J. M. Reess, R. Noschese, R. Politi and G. Peter, *Nature*, 2015, **525**, 500.
  154. A. R. Clements, B. Berk, I. R. Cooke and R. T. Garrod, *Phys. Chem. Chem. Phys.*, 2018, **20**, 5553-5568.
  155. Y. Oba, N. Miyauchi, H. Hidaka, T. Chigai, N. Watanabe and A. Kouchi, *Astrophys. J.*, 2009, **701**, 464-470.
  156. A. H. Narten, C. G. Venkatesh and S. A. Rice, *J. Chem. Phys.*, 1976, **64**, 1106-1121.
  157. P. Jenniskens, D. F. Blake, M. A. Wilson and A. Pohorille, *Astrophys. J.*, 1995, **455**, 389.
  158. J. B. Bossa, K. Isokoski, M. S. de Valois and H. Linnartz, *Astron. Astrophys.*, 2012, **545**, A82.
  159. T. Zubkov, R. S. Smith, T. R. Engstrom and B. D. Kay, *J. Chem. Phys.*, 2007, **127**, 184708.
  160. P. Ayotte, R. S. Smith, K. P. Stevenson, Z. Dohnálek, G. A. Kimmel and B. D. Kay, *J. Geophys. Res. Planets*, 2001, **106**, 33387-33392.
  161. G. Notesco, A. Bar-Nun and T. Owen, *Icarus*, 2003, **162**, 183-189.
  162. J. L. Edridge, K. Freimann, D. J. Burke and W. A. Brown, *Philos. Trans. R. Soc., A*, 2013, **371**, 20110578.
  163. S. Malyk, G. Kumi, H. Reisler and C. Wittig, *J. Phys. Chem. A*, 2007, **111**, 13365-13370.
  164. A. Bar-Nun, I. Kleinfeld and E. Kochavi, *Phys. Rev. B*, 1988, **38**, 7749-7754.
  165. A. Bar-Nun, G. Notesco and T. Owen, *Icarus*, 2007, **190**, 655-659.
  166. U. Raut, M. Fama, B. D. Teolis and R. A. Baragiola, *J. Chem. Phys.*, 2007, **127**, 204713.
  167. C. Bu, J. Shi, U. Raut, E. H. Mitchell and R. A. Baragiola, *J. Chem. Phys.*, 2015, **142**, 134702.
  168. E. Mayer and R. Pletzer, *Nature*, 1986, **319**, 298-301.
  169. E. Mayer and R. Pletzer, *J. Chem. Phys.*, 1984, **80**, 2939-2952.
  170. E. Mayer and R. Pletzer, *J. Phys. Colloq.*, 1987, **48**, C1-581-C581-586.
  171. R. Pletzer and E. Mayer, *J. Chem. Phys.*, 1989, **90**, 5207-5208.
  172. J. Ghormley, *J. Chem. Phys.*, 1967, **46**, 1321-1325.
  173. M. P. Collings, J. W. Dever, H. J. Fraser, M. R. McCoustra and D. A. Williams, *Astrophys. J.*, 2003, **583**, 1058.
  174. G. A. Kimmel, Z. Dohnálek, K. P. Stevenson, R. S. Smith and B. D. Kay, *J. Chem. Phys.*, 2001, **114**, 5295-5303.



175. G. A. Kimmel, K. P. Stevenson, Z. Dohnálek, R. S. Smith and B. D. Kay, *J. Chem. Phys.*, 2001, **114**, 5284-5294.
176. Z. Dohnálek, G. A. Kimmel, P. Ayotte, R. S. Smith and B. D. Kay, *J. Chem. Phys.*, 2003, **118**, 364-372.
177. K. P. Stevenson, G. A. Kimmel, Z. Dohnalek, R. S. Smith and B. D. Kay, *Science*, 1999, **283**, 1505-1507.
178. R. S. Smith, T. Zubkov, Z. Dohnálek and B. D. Kay, *J. Phys. Chem. B*, 2009, **113**, 4000-4007.
179. A. Bar-Nun, J. Dror, E. Kochavi and D. Laufer, *Phys. Rev. B*, 1987, **35**, 2427-2435.
180. C. Bu, C. A. Dukes and R. A. Baragiola, *Appl. Phys. Lett.*, 2016, **109**, 201902.
181. J. A. Ghormley and C. J. Hochanadel, *Science*, 1971, **171**, 62.
182. E. Mayer and A. Hallbrucker, *J. Chem. Soc., Chem. Commun.*, 1989, **12**, 749-751.
183. B. Rowland, M. Fisher and J. P. Devlin, *J. Chem. Phys.*, 1991, **95**, 1378-1384.
184. R. S. Smith, C. Huang, E. K. L. Wong and B. D. Kay, *Phys. Rev. Lett.*, 1997, **79**, 909-912.
185. R. A. May, R. S. Smith and B. D. Kay, *Phys. Chem. Chem. Phys.*, 2011, **13**, 19848-19855.
186. R. A. May, R. S. Smith and B. D. Kay, *J. Phys. Chem. Lett.*, 2012, **3**, 327-331.
187. R. J. Speedy, P. G. Debenedetti, R. S. Smith, C. Huang and B. D. Kay, *J. Chem. Phys.*, 1996, **105**, 240-244.
188. A. Bar-Nun, G. Herman, D. Laufer and M. Rappaport, *Icarus*, 1985, **63**, 317-332.
189. F. J. Ciesla, S. Krijt, R. Yokochi and S. Sandford, *Astrophys. J*, 2018, **867**, 146.
190. M. P. Collings, M. A. Anderson, R. Chen, J. W. Dever, S. Viti, D. A. Williams and M. R. S. McCoustra, *Mon. Not. R. Astron. Soc.*, 2004, **354**, 1133-1140.
191. A. Fresneau, G. Danger, A. Rimola, P. Theule, F. Duvernay and T. Chiavassa, *Mon. Not. R. Astron. Soc.*, 2014, **443**, 2991-3000.
192. M. P. Collings, J. W. Dever, H. J. Fraser and M. R. S. McCoustra, *Astron. and Space Sci.*, 2003, **285**, 633-659.
193. E. C. Fayolle, K. I. Öberg, H. M. Cuppen, R. Visser and H. Linnartz, *Astron. Astrophys.*, 2011, **529**, A74.
194. Ó. Gálvez, B. Maté, V. J. Herrero and R. Escribano, *Icarus*, 2008, **197**, 599-605.
195. T. P. Mangan, V. L. Frankland and J. M. C. Plane, *J. Atmos. Sol.-Terr. Phys.*, 2015, **127**, 92-96.
196. M. D. Ediger, *J. Chem. Phys.*, 2017, **147**, 210901.
197. J. W. Steed and J. L. Atwood, *Supramolecular Chemistry*, John Wiley & Sons, Chichester, 2000.
198. H. Davy, *Phil. Trans. Roy. Soc.*, 1811, **101**, 1-35.
199. J. S. Loveday and R. J. Nelmes, *Phys. Chem. Chem. Phys.*, 2008, **10**, 937-950.
200. A. Falenty, T. C. Hansen and W. F. Kuhs, *Nature*, 2014, **516**, 231-233.
201. A. Kurnosov, A. Y. Manakov, V. Y. Komarov, V. Voronin, A. Teplykh and Y. A. Dyadin, *Doklady Physical Chemistry*, 2001, **381**, 303-305.
202. M. T. Kirchner, R. Boese, W. E. Billups and L. R. Norman, *J. Am. Chem. Soc.*, 2004, **126**, 9407-9412.
203. J. Vatamanu and P. G. Kusalik, *J. Am. Chem. Soc.*, 2006, **128**, 15588-15589.
204. M. Choukroun, S. W. Kieffer, X. Lu and G. Tobie, *Clathrate Hydrates: Implications for Exchange Processes in the Outer Solar System*, Springer, New York, 2013.
205. I. U. Goldschleger, G. Kerenskaya, K. C. Janda and V. A. Apkarian, *J. Phys. Chem. A*, 2008, **112**, 787-789.

206. Y. Huang, C. Zhu, L. Wang, X. Cao, Y. Su, X. Jiang, S. Meng, J. Zhao and X. C. Zeng, *Sci. Adv.*, 2016, **2**, e1501010.
207. Y. Liu and L. Ojamäe, *Phys. Chem. Chem. Phys.*, 2018, **20**, 8333-8340.
208. C. G. Salzmann, *Proc. Natl. Acad. Sci. U. S. A.*, 2019, **116**, 16164.
209. W. L. Vos, L. W. Finger, R. J. Hemley and H.-k. Mao, *Phys. Rev. Lett.*, 1993, **71**, 3150-3153.
210. T. A. Strobel, M. Somayazulu, S. V. Sinogeikin, P. Dera and R. J. Hemley, *J. Am. Chem. Soc.*, 2016, **138**, 13786-13789.
211. T. A. Strobel, M. Somayazulu and R. J. Hemley, *J. Phys. Chem. C*, 2011, **115**, 4898-4903.
212. D. Londono, W. F. Kuhs and J. L. Finney, *Nature*, 1988, **332**, 141-142.
213. V. S. Efimchenko, M. A. Kuzovnikov, V. K. Fedotov, M. K. Sakharov, S. V. Simonov and M. Tkacz, *J. Alloys Comp.*, 2011, **509**, S860-S863.
214. W. F. Kuhs, T. C. Hansen and A. Falenty, *J. Phys. Chem. Lett.*, 2018, **9**, 3194-3198.
215. L. del Rosso, M. Celli, D. Colognesi, S. Rudić, N. J. English, C. J. Burnham and L. Ulivi, *Phys. Rev. Materials*, 2017, **1**, 065602.
216. D. M. Amos, M. E. Donnelly, P. Teeratchanan, C. L. Bull, A. Falenty, W. F. Kuhs, A. Hermann and J. S. Loveday, *J. Phys. Chem. Lett.*, 2017, **8**, 4295-4299.
217. L. C. Jacobson, W. Hujo and V. Molinero, *J. Phys. Chem. B*, 2009, **113**, 10298-10307.
218. M. M. Conde, C. Vega, G. A. Tribello and B. Slater, *J. Chem. Phys.*, 2009, **131**, 034510.
219. M. E. Donnelly, P. Teeratchanan, C. L. Bull, A. Hermann and J. S. Loveday, *Phys. Chem. Chem. Phys.*, 2018, **20**, 26853-26858.
220. W. Ostwald, *Z. Phys. Chem.*, 1897, **22U**, 289-330.
221. A. Hallbrucker and E. Mayer, *J. Chem. Soc., Faraday Trans.*, 1990, **86**, 3785.
222. A. Hallbrucker and E. Mayer, *Icarus*, 1991, **90**, 176-180.
223. J. Ghosh, R. R. J. Methikkalam, R. G. Bhui, G. Ragupathy, N. Choudhary, R. Kumar and T. Pradeep, *Proc. Natl. Acad. Sci. U. S. A.*, 2019, **116**, 1526-1531.
224. P. J. Wooldridge, H. H. Richardson and J. P. Devlin, *J. Chem. Phys.*, 1987, **87**, 4126-4131.
225. J. E. Bertie and J. P. Devlin, *J. Chem. Phys.*, 1983, **78**, 6340-6341.
226. H. H. Richardson, P. J. Wooldridge and J. P. Devlin, *J. Chem. Phys.*, 1985, **83**, 4387-4394.
227. F. Fleyfel and J. P. Devlin, *J. Phys. Chem.*, 1988, **92**, 631-635.
228. B. A. Buffett, *Annu. Rev. Earth Planet Sci.*, 2000, **28**, 477-507.
229. J. Klinger, *Physical Properties of Frozen Volatiles—Their Relevance to the Study of Comet Nuclei*, Cambridge University Press, Cambridge, 1989.
230. J. I. Lunine and D. J. Stevenson, *Icarus*, 1987, **70**, 61-77.
231. J. A. Ripmeester, S. T. John, C. I. Ratcliffe and B. M. Powell, *Nature*, 1987, **325**, 135-136.
232. K. A. Udachin, C. I. Ratcliffe and J. A. Ripmeester, *Angew. Chem. Int. Ed.*, 2001, **40**, 1303-1305.
233. H. Kim and G. Jeffrey, *J. Chem. Phys.*, 1970, **53**, 3610-3615.
234. W. Blokzijl and J. B. F. N. Engberts, *Angew. Chem., Int. Ed. Engl.*, 1993, **32**, 1545-1579.
235. D. T. Bowron and J. L. Finney, *J. Phys. Chem. B*, 2007, **111**, 9838-9852.
236. D. T. Bowron, A. K. Soper and J. L. Finney, *J. Chem. Phys.*, 2001, **114**, 6203-6219.

- 237. H. S. Frank and M. W. Evans, *J. Chem. Phys.*, 1945, **13**, 507-532.
- 238. P. Ball, *Chem. Rev.*, 2008, **108**, 74-108.
- 239. T. Head-Gordon, *Proc. Natl. Acad. Sci. U. S. A.*, 1995, **92**, 8308-8312.
- 240. P. Buchanan, N. Aldiwan, A. K. Soper, J. L. Creek and C. A. Koh, *Chem. Phys. Lett.*, 2005, **415**, 89-93.
- 241. S. Matysiak, P. G. Debenedetti and P. J. Rossky, *J. Phys. Chem. B*, 2011, **115**, 14859-14865.
- 242. G. Algara-Siller, O. Lehtinen, F. C. Wang, R. R. Nair, U. Kaiser, H. A. Wu, A. K. Geim and I. V. Grigorieva, *Nature*, 2015, **519**, 443-445.

## 2 Experimental Procedures and Characterisation Techniques

### 2.1 Introduction

Physical vapour deposition is the main vacuum deposition method employed in this thesis. This chapter sets out to describe the basic experimental principles and characterisation techniques used to complete the course of this research. Initially, the main apparatus will be described in detail and typical deposition experiments will be described hereafter. The remainder of the chapter will touch on the techniques used to characterise the samples prepared in this research. Samples prepared in the study comprise thick films of amorphous solid water (ASW) with the incorporation of various guest species within the amorphous ice structure.

### 2.2 Materials

Ultrapure water ( $\text{H}_2\text{O}$ , Milli-Q®, Millipore) was continually used throughout this research. Heavy water ( $\text{D}_2\text{O}$ ) (D/H isotope purity >99.8%, 435767-25G) was purchased from Sigma Aldrich. Both  $\text{H}_2\text{O}$  and  $\text{D}_2\text{O}$  were used to prepare ASW and degassed through several freeze-pump-thaw (FPT) cycles. During these cycles,  $\text{H}_2\text{O}$  is flash frozen and evacuated to  $1 \times 10^{-2}$  mbar. Contaminants and impurities from guest species such as oxygen, carbon dioxide ( $\text{CO}_2$ ) and nitrogen gases are expelled due to their insoluble nature. Several FPT cycles are performed due to the difficulty to completely remove unwanted gases.

Argon (99.998%), methane (99.995%,  $\text{CH}_4$ ), helium (99.995%),  $\text{CO}_2$  (99.8%) gases and liquid nitrogen ( $\text{LN}_2$ ) were used as received and provided by BOC Ltd. Adamantane ( $\text{C}_{10}\text{H}_{16}$ ) and deuterated adamantane ( $\text{C}_{10}\text{D}_{16}$ ) with purities of  $\geq 99\%$  and 98 atom%, respectively, were purchased from Sigma Aldrich and used without further purification. Indium metal (99.99%) was used to line the copper cryostat body for Raman spectroscopy measurements and purchased from Alfa Aesar.

## 2. Experimental Procedures and Characterisation Techniques

### 2.3 Instrumentation

Typically, in surface science, the requirements for a high vacuum system are, (i) a chamber attached with pumps, needed to create a vacuum and (ii) a substrate is essential to deposit molecules onto to allow for investigations and also analyse processes occurring at the surface through any desired technique.<sup>1</sup>

#### 2.3.1 The High-Vacuum Chamber

A simplified and schematic illustration of the high vacuum chamber (Kurt Lesker Ltd., internal dimensions of the main body of the apparatus = 12" × 12" × 24")<sup>2</sup> is depicted in Figure 2.1. A photograph image of the vacuum chamber is also represented in Figure 2.2. The chamber is equipped with three KF-40 and six ISO-K 100 ports and flanges, and access to the chamber is gained *via* a large aluminium door. It is possible to visually view the inside of the chamber at all times through a glass viewing window. The total internal surface area of the chamber is  $\sim 1 \text{ m}^2$ . A double-stage, rotary-vane pump (model 12, BOC Edwards) is used to achieve a rough vacuum and thereafter, to back a diffusion pump (Diffstak 63/150M, BOC Edwards) containing polyphenol ether oil, (Santovac 5, BOC Edwards) capable of pumping the chamber down to a high vacuum ( $10^{-6}$  mbar). A liquid-nitrogen ( $\text{LN}_2$ ) trap is situated directly above the diffusion pump, separated by an isolation butterfly valve, trapping contaminants such as ice and oil residues. The body of the diffusion pump is  $\text{H}_2\text{O}$ -cooled and is made of stainless-steel and a steel nickel-plated base. This pressure is measured by a dual Pirani gauge (PenningVac PTR 90, Oerlikon Leybold Vacuum, Cologne, Germany) and recorded on a LabView VI program using RS232 connections to a computer. The active- and cryo-pumping leads to a routinely attainable pressure of  $2 \times 10^{-6}$  mbar. The total pressure of the chamber and the procedure for evacuating the chamber will be provided in the next section (Figure 2.3) with a labelled plot showing the stages involved in the pump down of the vacuum chamber.

Within the vacuum chamber, a  $\text{LN}_2$  cryostat is fitted to a linear  $z$ -positioner (Standard Travel (LSM and HLSM) Linear Shift Mechanical Series, Kurt J. Lesker, Hastings, UK) with a 25 cm travel distance, used to adjust the distance between the deposition stage and aperture,<sup>2</sup> and actively cools a 20.3 cm diameter two-component copper deposition plate. The copper deposition plate is mounted in the chamber at a distance of 15 cm, in line of sight with a  $\text{H}_2\text{O}$ -inlet tube (situated below the chamber, see detail below). There are two parts to the deposition stage/plate: (1) the first part of the plate is permanently attached inside the chamber for good thermal contact to the cryostat

## 2. Experimental Procedures and Characterisation Techniques

and, (2) the bottom part is the sample plate that is attached with six screws and can be removed from the chamber after deposition. The deposition plate has been designed with one bevelled hole, with an equal diameter distance corresponding to tailor-made aluminium storage vessels with a length of 30 mm and, a width of 28 mm, frequently used for the storage of samples and shown later in this chapter [Figure 2.8(b)]. This ensures efficient recovery of the sample from the entirety of the surface of the deposition plate. The deposition plate also compromises a series of small holes in the centre, the edge and midpoint of the radius of the deposition plate, which allow the attachment of a quartz-crystal microbalance (QCM) sensor head (QCM, 710-SH Sensor Head, Alleclra). Coaxial cables are used to connect the QCM sensor head to a reflection bridge and N2PK myVNA (0.5–60 MHz) network analyser software.<sup>3</sup> Specific details of the QCM are provided in the characterisation section of this chapter.

A five-way inlet system consisting of two high-accuracy needle valves (EV 016 DOS AB, Oerlikon Leybold Vacuum), controlling gas flow and H<sub>2</sub>O-inlet, and a Pirani pressure sensor (Thermovac TTR91, Oerlikon Leybold Vacuum) is situated below the vacuum chamber. Also positioned below the chamber is a 32 cm long and 2.6 cm wide stainless-steel tube, enabling the inlet of H<sub>2</sub>O-vapour and gases into the vacuum chamber. A round-bottom flask with a Young's tap is attached to the needle valve containing ultrapure H<sub>2</sub>O or D<sub>2</sub>O and fitted *via* Radley's joints. The round-bottom flask can be dismounted from the needle valve before and after an experiment to weigh the amount of liquid dosed into the chamber. The second needle valve employs a gas reservoir to flush through gases from commercial gas cylinders. Here, the pressure inlet difference is approximately 1 bar; hence precise amounts of gas can be leaked into the vacuum chamber and conversion from typical surface science units of (torr s<sup>-1</sup>) into dosing rates of units of mmol s<sup>-1</sup> can be determined. The calibrated air flow charts provided by the manufacturer for the needle valves are utilised to calculate defined gas flow rates (Chapter 3). A standard computer and monitor (Dell, Optiplex 380) is used to display the incoming measurements of the vacuum chamber with RS232 connections or a universal serial bus (USB) such as sample temperature, pressure from the various needle valves, and the pumps used to pump LN<sub>2</sub> vapour through to the deposition stage. The total chamber volume alongside the connections is estimated at, ~0.080 m<sup>3</sup>.

The H<sub>2</sub>O-inlet tube can directly be baffled with an iron mesh with dimensions of 0.5 mm thick spaced wires, approximately 1 mm apart. Disruption of the gas flow can be

## 2. Experimental Procedures and Characterisation Techniques

enhanced by raising the mesh by 1 cm and using a two-pence coin to block the flow, matching the diameter of the H<sub>2</sub>O-inlet tube. Baffling the flow of gas into the vacuum chamber has been anticipated to alter the morphology of the deposit (Chapter 3). In Figure 2.1, a 5 L LN<sub>2</sub> dewar displayed, is used to cool the deposition stage inside the vacuum chamber. The apparatus used for the cooling of the deposition stage is discussed in detail in a separate section to follow.

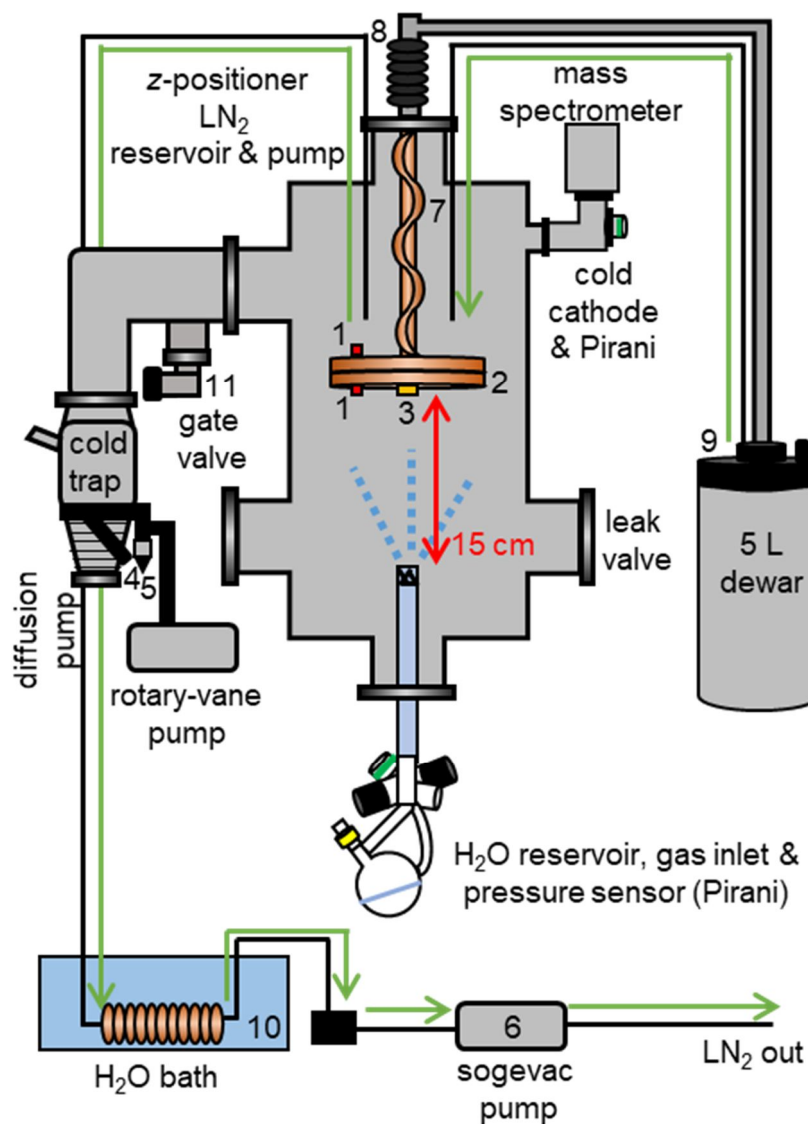


*Figure 2.1. Simplified schematic diagram of the main chamber viewed front-facing, without the large aluminium door. The labels illustrate the (1) K-type thermocouples for temperature readings, (2) the deposition plate, (3) QCM, (4) high-vacuum isolation butterfly valve situated on the diffusion pump (5) bypass allowing isolation of chamber or diffusion pump, (6) sogevac pump for cooling the deposition plate, (7) copper tubing, (8) linear z-positioner, (9) 5 L dewar for LN<sub>2</sub> storage, (10) H<sub>2</sub>O bath and (11) the gate valve (as described later). The green arrow shows the direction of cooling from the 5 L dewar.*

## 2. Experimental Procedures and Characterisation Techniques

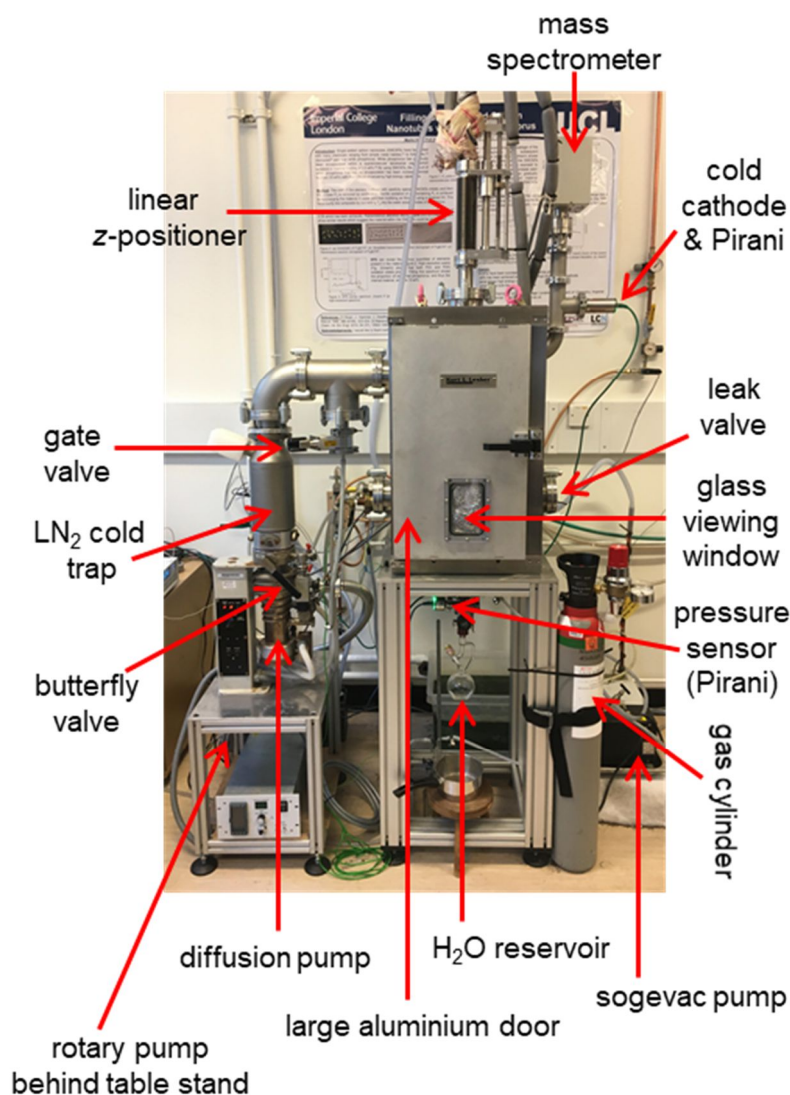


Figure 2.2. Photographic image of the high-vacuum chamber corresponding to labelled parts as depicted in schematic Figure 2.1.

### 2.3.2 Pressure Evacuation of the High-Vacuum Chamber

The pressure inside the vacuum chamber is reduced in several stages as described herein. Initially, the chamber was evacuated to  $2 \times 10^{-3}$  mbar using the rotary-vane pump (model 12, BOC Edwards). A two-way bypass was adjusted to isolate the chamber and start evacuating the diffusion pump. The LN<sub>2</sub> cold trap was filled with approximately 1.5 L of LN<sub>2</sub> to significantly reduce the chamber pressure to approximately  $5 \times 10^{-4}$  mbar. The high-vacuum butterfly valve above the diffusion pump is opened after one-hour of heating of the diffusion pump. This further reduces the chamber pressure to approximately,  $2 \times 10^{-6}$  mbar. A general cleanse/purge of the system is completed daily before deposition with the guest species to be used for experiments by exposing the gas handling line with a small volume of that gas before pumping it out. This is to eliminate and minimise N<sub>2</sub>



## 2. Experimental Procedures and Characterisation Techniques

gas and any other gases that may be present in the system.<sup>2</sup> The cryo-cooling of the deposition stage is described in the detail in the next section.

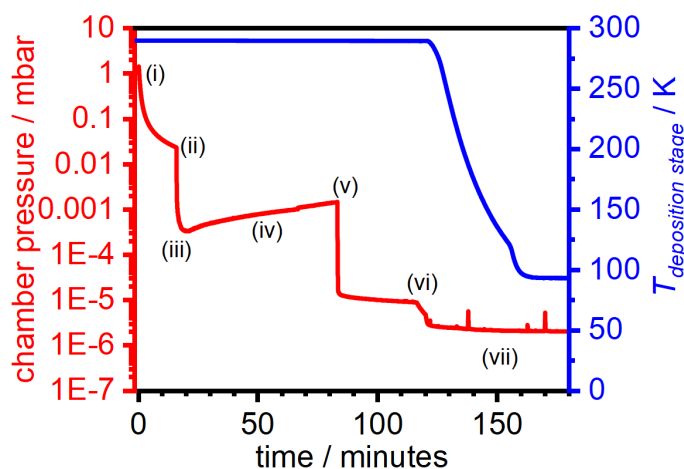


Figure 2.3. Total pressure from the evacuation and cooling of the deposition apparatus for the preparation of ASW films. Variation in the chamber pressure (red line) and the temperature of the deposition stage (blue line). Each stage of the total pressure pump-down is described later in this chapter. For a brief account, (i) the chamber is evacuated with the rotary-vane pump to a pressure of  $2 \times 10^{-3}$  mbar, (ii) the LN<sub>2</sub> cold-trap is filled with approximately, 1.5 L of LN<sub>2</sub>, reducing the pressure significantly, (iii) the diffusion pump is evacuated for one-hour, (iv) diffusion pump is switched on for one-hour to heat up, (v) the butterfly valve is opened and the chamber is evacuated, (vi) the deposition stage can then be cooled to base temperature and this is reflected in the blue line depicting the actual temperature of the deposition stage, (vii) deposition.

### 2.3.3 Cooled Deposition Stage for Gaseous Nanoprobe Studies

Figure 2.1 shows the deposition stage through the open door as the chamber is vented. The deposition plate and deposition stage are labelled as (2). This arrangement allows easy removal from the chamber under LN<sub>2</sub>. The cooled deposition stage (2) comprises a two-component, circular eight-inch diameter copper plate (mentioned earlier) suspended with two feedthrough tubes connected to the LN<sub>2</sub> reservoir on one side and to a rotary-vane pump (6) (Sogevac SV16, Oerlikon Leybold Vacuum) on the other side. In order to achieve maximum cooling of the plate, embedded copper spiral tubing (7) ( $\frac{1}{4}$  inch diameter and a stainless-steel feedthrough ( $\frac{1}{4}$  inch diameter) (Kurt J. Leskar, Hastings, UK)) is soldered (Silverflow 55, Johnson Matthey) around the tubing onto the copper plate allowing it to be cooled with LN<sub>2</sub> vapour. The deposition stage can be altered using the linear z-positioner (8) from a range of 5–25 cm distance from the H<sub>2</sub>O-inlet aperture. The flow of nitrogen (N<sub>2</sub>) is achieved by connecting the feedthrough to the 5 L dewar (9) using insulated tubing (approximately 2 metres) connected to the rotary-vane pump (6), again with tubing (5 metres). The N<sub>2</sub> vapour was warmed by a H<sub>2</sub>O bath (10) which is

## 2. Experimental Procedures and Characterisation Techniques

situated between the feedthrough and the rotary-vane pump; the vapour is circulated out from the system and out through exhaust tubing. The temperature variation of both plates was measured using K-type thermocouples linked to an IJ-6 software-based temperature controller (IJ Instruments Ltd), linked to LabView VI software (version six, National Instruments). A second temperature recording station was employed using a K-type thermocouple attached to a self-built device, containing two Adafruit MAX31856 universal thermocouple amplifiers that are controlled with an Adafruit Feather 32u4 Basic Proto microcontroller. A K-type thermocouple (1) is made up of two wires, chromel-alumel (chromel: 90% nickel and 10% chromium and alumel: 95% nickel, 2% manganese, 2% aluminium and 1% silicon) where the connecting junction measures the temperature. The K-type thermocouple feedthrough was used to attach both external and internal parts of the thermocouple wire, one K-type thermocouple is attached to the upside of the deposition stage and the second thermocouple is directly located on the copper plate. This is to monitor the temperature when the sample and stage have reached approximately 95 K and to monitor when the sample is heated during temperature-programmed desorption (TPD) experiments, which may interfere with the species when desorbing from the sample.<sup>1</sup> The sample and deposition stage regularly achieve a temperature of 95 K with maximal suction with the single-stage rotary-vane pump and further information is provided below. Thermal/heat-conducting paste is regularly used to ensure good thermal contact between the deposition stage and thermocouples.

The flow of cold LN<sub>2</sub> vapour was adjusted through to the deposition stage using a tap located between the H<sub>2</sub>O bath and rotary-vane pump to allow the temperature to be controlled. To achieve a base temperature of 95 K, the tap was fully opened with a LN<sub>2</sub> evaporation rate of 5 L h<sup>-1</sup>, and to maintain this temperature during deposition, the LN<sub>2</sub> evaporation rate required, was approximately 1 L h<sup>-1</sup>. These rates are necessary to counteract any heating processes occurring during the experiment including (i) energy transfer during deposition, (ii) heat transfer through the metal tubes, (iii) convective mass transfer from the movement of gas, and (iv) heat from radiative sources such as the room temperature and walls of the vacuum chamber.

Once the temperature reaches base temperature and deposition for a specific desired amount of time is acquired, the LN<sub>2</sub> cooling is stopped by switching off the rotary-vane pump and thus, interrupting the cooling. The heating resulting from this process is shown in Figure 2.4 which is the rate at which the deposition stage and surface is heated.

## 2. Experimental Procedures and Characterisation Techniques

In this case, the heating rate from 95 K to 185 K changes from  $1.7 \text{ K min}^{-1}$  to  $0.8 \text{ K min}^{-1}$  at 100 K and 185 K, respectively.

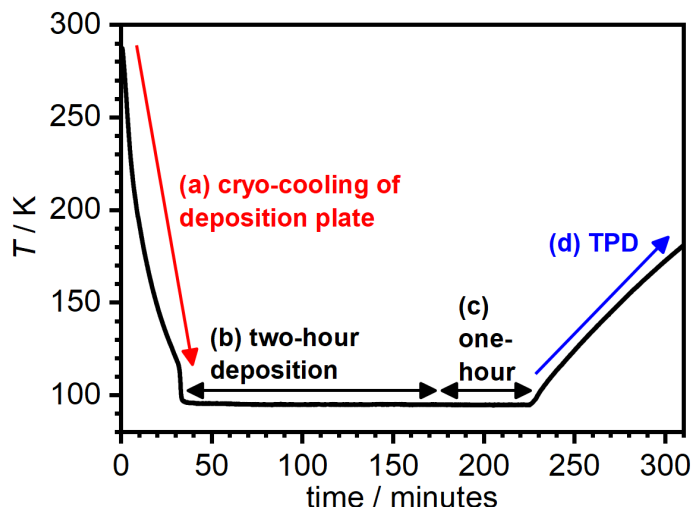


Figure 2.4. The variations in temperature during a typical deposition experiment in sequential stages, of (a) cooling of the deposition stage, (b) two-hour deposition, (c) one-hour time to allow for the system to reach base pressure and (d) TPD, heating from 95 K to 180 K. A more detailed account of this figure is provided in Chapter 3.

### 2.3.4 Cooled Deposition Stage for Adamantane ( $\text{C}_{10}\text{H}_{16}$ ) Studies

In a second chamber (Figure 2.5), almost identical to the chamber described above (Figure 2.1 and 2.2),  $\text{C}_{10}\text{H}_{16}$  and amorphous ice mixtures were prepared. The major difference between the two chambers is the cooled deposition stage and the additional attachment of a Peltier element (active area =  $30 \times 30 \text{ mm}$ , max voltage = 15.7 V, max current = 3.9 A, maximum cooling capacity = 37.9 W, RS Components, Part No. ET-127-10-13-RS) within the second chamber *via* a feedthrough, and thus, connected to a power supply (80 W Constant Power Switching Mode Power Supply). With the former component, the cooled deposition stage is simply a cylindrical copper cryostat that can be manually filled with  $\text{LN}_2$  until a base temperature of 82 K is achieved. For the latter component and on the top of the chamber, surrounding the area of the cryostat inlet for  $\text{LN}_2$ , there is an additional  $\text{H}_2\text{O}$ -cooling holder/element, tailor-made for this second chamber. This surrounding holder is a large flat-circular copper piece, akin to the size of an ISO-100 flange. On the topside of this copper piece, there is embedded copper tubing which allows  $\text{H}_2\text{O}$  cooling to take place through the tubes to cool the cryostat. In addition, the  $\text{H}_2\text{O}$  supply for the Peltier element is shared through these tubes constantly, ensuring a stable pressure inside the vacuum chamber is achieved. This element was not in place in the initial experiments which rendered the pressure of the chamber extremely high ( $1 \times 10^{-2} \text{ mbar}$ ). After this installation, it was possible to stabilise the pressure inside the chamber

## 2. Experimental Procedures and Characterisation Techniques

to  $2 \times 10^{-6}$  mbar due to the H<sub>2</sub>O cooling. The Peltier element is fitted next to the end of the H<sub>2</sub>O-inlet tube with copper tubing, where the hot underside can be cooled with room temperature H<sub>2</sub>O. The H<sub>2</sub>O flows through copper pipes to help support and cool the Peltier inside the chamber (Figure 2.5). The cold upper side is used to cool a copper crucible (30 × 30 mm) with a circular cavity for a K-type thermocouple, to a base temperature of ~240 K holding a 1 g pellet of C<sub>10</sub>H<sub>16</sub> or C<sub>10</sub>D<sub>16</sub>. The preparation for C<sub>10</sub>H<sub>16</sub> pellets is described in Chapter 4. In addition, to remove LN<sub>2</sub> from the cryostat within the chamber during annealing stages after deposition, a single-stage twin-cylinder pump (Gast 87 series compressor oil-free rocking piston single-stage twin-cylinder pump, Order Number: 87R642–103R–N470X, Thorite Direct, UK) is used to draw out the LN<sub>2</sub>.

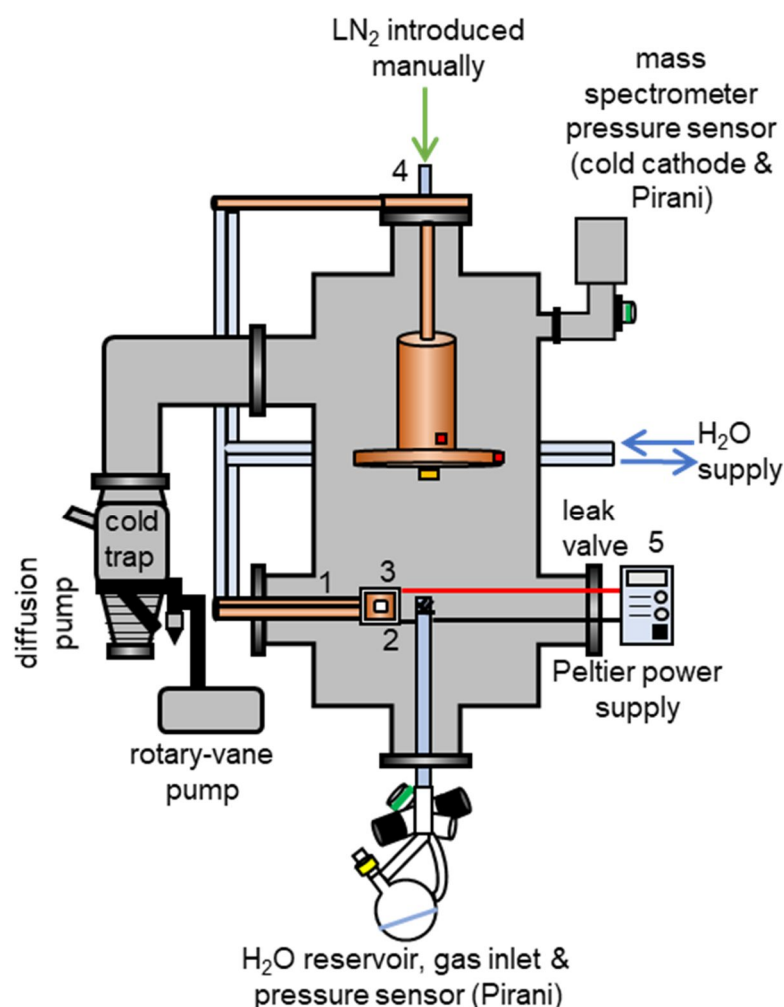


Figure 2.5. Simple schematic depicting the cooled deposition stage difference from Figure 2.1 with a few additions. Labels indicate, (1) Peltier element, (2) copper crucible, (3) C<sub>10</sub>H<sub>16</sub> pellet, (4) copper element for stabilising pressure with H<sub>2</sub>O supply and (5) the Peltier power supply situated externally from the chamber. All other components of this chamber have been illustrated in Figure 2.1 and described in the earlier text.

## 2. Experimental Procedures and Characterisation Techniques

### 2.3.4.1 Thermoelectric Phenomena – Seebeck and Peltier Effects

Thermoelectric cooling operates through the Seebeck effect (thermoelectric effect).<sup>4, 5</sup> Seebeck,<sup>6</sup> in the early 1800s, discovered the fundamental phenomena that a temperature difference is created between the junction of two dissimilar materials where a voltage difference is created and is proportional to the temperature difference. A similarly related effect (Peltier effect) was discovered by Peltier<sup>7</sup> in the early 1800s, observing that when an electrical current passes or flows through dissimilar materials, cooling can occur as heat is removed at one junction. Heat is therefore deposited at the other junction. Heat can either be absorbed or rejected depending on the direction of the movement of the current, consuming electrical energy. An electric current is created by applying a voltage across joined conductors. Both the Seebeck and Peltier effects are related to each other.

A thermoelectric cooling device features an arrangement of alternating p- and n-type semiconductors. The array of elements are thermally parallel with each other and electrically in series, ensuring the absorption of heat (cold side) and release of heat (hot side). Figure 2.6 depicts a schematic of a typical thermoelectric device illustrating both the Seebeck and Peltier effect. Section 2.3.4.2 sets out to describe the calibration of the Peltier element.

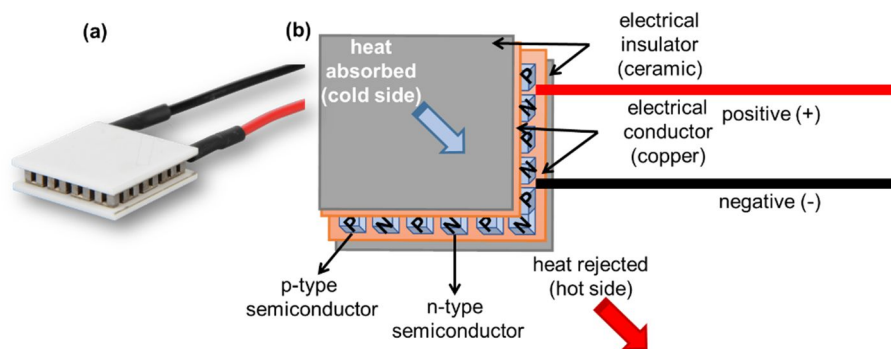


*Figure 2.6. Demonstration of (a) a typical Peltier element used for cooling, heating, and temperature stabilisation and (b) a simple schematic of the components inside a Peltier element, illustrating the segregation of the hot and cold side.*

### 2.3.4.2 Calibration of the Peltier Element

The evaporation source response was tested several times to allow for some approximation of voltage with its corresponding temperature. The vacuum chamber is pumped down in sequential stages to base pressure as described earlier in section 2.3.2 before the voltage was altered to test the temperature. Figure 2.7 displays (a) a simple total pressure graph of the calibration experiment, (b) the measured temperature against

## 2. Experimental Procedures and Characterisation Techniques

time and (c) an average plot of different calibrations of voltage against temperature. As the temperature was varied in 5 K steps, starting from 240 K, a plateau was achieved to check for stability of the evaporation source. At this specific temperature, the voltage and current were noted down. In any case, the response of the evaporation source was found to be reproducible, Figure 2.7(c).

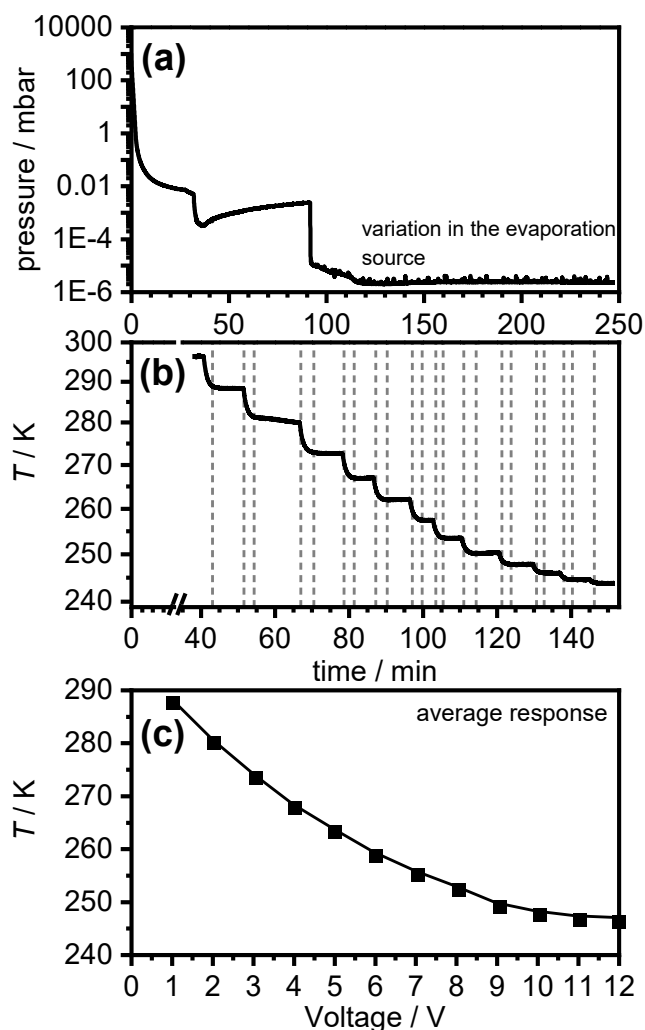


Figure 2.7. Calibration experiment depicting changes in the temperature in relation to the evaporation source response and voltage where (a) total pressure graph indicative of the recording of the changes where the pressure remains stable, (b) measured temperature changes and plateau regions to validate the stability of the response, the dashed grey lines indicate when and where the temperature is recorded and changed, (c) a final plot of the measured voltage vs. temperature reading.

Nevertheless, this approximation is used later in this study (Chapter 4 and Chapter 5) to achieve a desired temperature, altering the ratio of  $C_{10}H_{16}$  or  $C_{10}D_{16}$  to  $H_2O$  molecules. The preparation for the pellets and the calibration experiments for each  $C_{10}H_{16}$  and  $C_{10}D_{16}$  are provided in their respective chapters, Chapter 4, and Chapter 5.

## 2. Experimental Procedures and Characterisation Techniques

### 2.4 Experimental Procedures

#### 2.4.1 Typical Cryogenic Deposition Experiment

This section will set out to describe a typical deposition experiment employed in this study to prepare the amorphous ice mixtures. Specific details will be provided in respective results chapters. Several parameters can be varied throughout deposition experiments which include deposition times, dosing rates of guest species and H<sub>2</sub>O-inlet pressure. In each experiment, the H<sub>2</sub>O-inlet tube was capped with an iron mesh unless stated otherwise.

Prior to any deposition experiment, the copper deposition plate was cleaned with H<sub>2</sub>O, sandpaper, and ethanol to remove a copper oxide layer off of the surface and fastened to the deposition stage. In the first chamber, the deposition stage is fastened and attached inside the chamber with six bolts as depicted in Figure 2.1 and Figure 2.3 and to visibly check the connections between the stage and plate, the deposition stage has been designed with six protruding copper pieces. The second chamber only requires three bolts for fastening the plate to the deposition stage.

The procedure to prepare ASW has been described previously.<sup>8,9</sup> In this study, the addition of a guest species within the amorphous ice is introduced using the apparatus described in section 2.3. The H<sub>2</sub>O-inlet flask is weighed on a balance (Sartorius, Balance Technology) with 0.001 g precision. Initially, the QCM was placed in the centre of the deposition plate, in line of sight with the H<sub>2</sub>O-inlet tube to ensure uniform deposition of ASW and guest species. The pressure inside the chamber is reduced in several sequential stages (Figure 2.3).

Once the base pressure ( $2 \times 10^{-6}$  mbar) was achieved, the deposition rate was measured using the QCM configured at 5.98 MHz (gold-plated AT-cut 6 MHz planoconvex quartz crystals, Sycon Instruments, USA) before the cooling of the deposition plate. The QCM oscillates from this frequency. The coaxial cables connected to the QCM sensor and a reflection bridge allows data collection *via* the N2PK myVNA (0.5–60 MHz) network analyser software.<sup>3</sup> The configuration including the impedance factor of ice and density of ice were pre-set before the cooling of the system and so, deposition can be started. The cooling of the deposition stage is initiated by either, (i) a second rotary-vane pump (Sogevac SV16, Oerlikon Leybold Vacuum) for gaseous species studies or (ii) manually filling the cryostat for C<sub>10</sub>H<sub>16</sub> studies. Once the tap of the Sogevac pump is fully opened to its maximum capacity, the temperature of both

## 2. Experimental Procedures and Characterisation Techniques

deposition plates decreases to 95 K in one-hour. For the second chamber, the base temperature is maintained at 82 K.

Once the system is evacuated to the low-pressure and low-temperature environment, deposition can begin by introducing H<sub>2</sub>O from the reservoir held at room temperature below the chamber. To introduce desired gaseous species into the chamber, the graduated needle valves are utilised: both H<sub>2</sub>O and gas are held in the handling lines under a rough vacuum. To deposit C<sub>10</sub>H<sub>16</sub>, the Peltier element voltage and current are adjusted to reach a temperature required for a desired ratio of C<sub>10</sub>H<sub>16</sub> to H<sub>2</sub>O molecules. Dosing times can be altered, and the temperature is constantly maintained at 95 K or 82 K throughout this time. For a two-hour deposition, approximately 1.500 g of H<sub>2</sub>O is deposited at  $1 \times 10^{-1}$  mbar inlet pressure onto the copper substrate precooled to low temperature. The pressure of H<sub>2</sub>O is kept constant at  $1 \times 10^{-1}$  mbar throughout all experiments conducted in this study unless stated otherwise. This pressure is chosen for the preparation of all samples to ensure a small amount of H<sub>2</sub>O is dosed in with a corresponding low enough deposition rate. This, in turn, helps avoid the formation and transformation to crystalline ice and avoids overheating the amorphous condensed phase on the copper substrate.

For gaseous studies, once the deposition is complete, the sample is further kept cold at 95 K for one-hour to allow for the vacuum system to reach base pressure and remove excess gas. During this time, the residual gas analyser mass spectrometer (RGA-MS, Hiden Analytical, HALO 201 – single filter mass spectrometer equipped with a Faraday cup) is set to record a mass range of 1–100  $m/z$  (mass-to-charge ratio). After this time, TPD experiments begin from 100 K as the sample is left to gradually heat up to ~185 K from a rate of 1.7–0.8 K min<sup>-1</sup>, respectively, monitored by the K-type thermocouple. This is to monitor gas release from layers of amorphous ice mixtures. Samples heated to 180 K show H<sub>2</sub>O beginning to fully desorb.

For C<sub>10</sub>H<sub>16</sub> studies, post-deposition, the sample is annealed at 125 K, closing pores of ASW,<sup>10</sup> avoiding the formation of N<sub>2</sub> clathrate hydrates and cooled back down to 82 K before removal from the chamber. Once the sample is removed from the chamber, analysis by various means of characterisation techniques is carried out as described in upcoming section 2.5.



## 2. Experimental Procedures and Characterisation Techniques

### 2.4.2 Collection and Storage of the Deposited Material

In order to recover material from the vacuum chamber following deposition, samples are cooled back down to 95 K (temperature of the vacuum chamber for gaseous nanoprobe studies) or 82 K (temperature of the vacuum chamber for  $C_{10}H_{16}$  studies) after they have been annealed at 125 K and the deposition plate is detached and removed under  $LN_2$ . This setup and arrangement can be seen in Figure 2.8. In specific detail, the chamber is vented in an inert atmosphere with  $LN_2$  to atmospheric pressure *via* a gate valve (series 012 mini gate valve, VAT valve, Haag, Switzerland) (Figure 2.1, labelled 11) attached to a  $LN_2$  dewar, keeping the copper substrate cold. The copper deposition plate and the QCM are quickly submerged in  $LN_2$  to minimise heat and air exposure and unscrewed, detached from the cryostat, and then removed from the chamber. Once detached and removed, the deposition plate is flipped onto a copper trivet in an open polystyrene container, pre-cooled with  $LN_2$ . The deposited material on the deposition plate can be scraped using a scraper tool from the surface of the plate and transferred into an aluminium storage vessel, filled with  $LN_2$ . This container comprises internal dimensions of  $28 \times 30$  mm. The cylindrical aluminium storage vessel, as depicted in Figure 2.8(b), is pre-cooled (77 K) and fastened directly on the underside of the plate and in line with the bevelled hole of the deposition plate using a small screw. A metal tin, with a spring on its side, can then be fastened, securing the deposition plate on the copper trivet and in turn, isolating the sample from the  $LN_2$  filled container. A small amount of  $LN_2$  always covered the surface of the plate to keep the deposition plate cold. Once the sample has been recovered from the surface and carefully collected into the storage vessel by scraping, the vessel can quickly be sealed with a lid and screw and transported to a  $LN_2$  storage dewar. A small piece of wire surrounds the circumference of the vessel to allow easy access and extraction from the  $LN_2$  dewar. Samples are handled under  $LN_2$  to avoid the possible transformation that may occur upon heating; such transformations are highly unlikely to take place in such a low-temperature environment (77 K). Stored samples are held at 77 K in this storage dewar which is frequently topped up with  $LN_2$ .

As ASW is slightly denser than  $LN_2$ , it was possible to successfully scrape the surface of the plate and collect enough sample to carefully place into the aluminium vessel positioned beneath the bevelled hole. This approach approximately yields most of the samples, however, it is possible some sample is lost during the flipping of the plate transfer or even the floating of some sample, away from the storage vessel and into the

## 2. Experimental Procedures and Characterisation Techniques

large polystyrene container. The apparatus and actual procedure are depicted below in Figure 2.8(a). To carry out analytical techniques characterising such deposits, the aluminium vessel can be easily removed from the storage dewar. The sample can be carefully extracted out of the vessel with pre-cooled tools and placed into the desired sample holder for analysis.

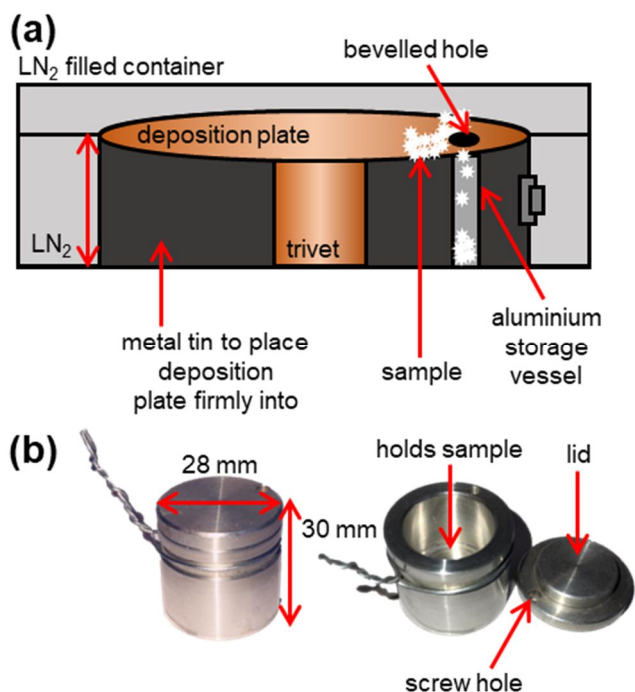


Figure 2.8. (a) Schematic procedure showing the collection and storage of samples from the deposition plate in a container of LN<sub>2</sub> and pre-cooled equipment. The copper trivet and aluminium storage vessel are situated below the deposition plate. Aluminium storage vessel in (a) is not drawn to scale but drawn for visual clarity. The deposition plate is firmly fastened into place with the metal tin. (b) Images of the aluminium vessel used with a total length of 30 mm and diameter of 28 mm. The left-hand side shows the vessel closed and the right-hand side shows the vessel itself and the underside of the lid. All components in this figure (a) and (b) are pre-cooled and submerged in LN<sub>2</sub>. Note: the sample covers the entire diameter of the plate and the figure only shows the sample scraped in close proximity to the bevelled hole.

## 2. Experimental Procedures and Characterisation Techniques

### 2.5 Details of Sample Characterisation Techniques

#### 2.5.1 Temperature-Programmed Desorption (TPD)

Temperature-programmed desorption (TPD) is a destructive analytical method used to observe desorbed molecules from a surface as the temperature is increased.<sup>1, 11, 12</sup> Desorption of adsorbed molecules and atoms is a fundamental tool in surface kinetics and provides information regarding the interactions between adsorbed species and the surface.<sup>11, 12</sup>

In a typical TPD experiment, a temperature ramp is applied to the surface and the amount of adsorbate that is desorbed into the gas phase in the vacuum chamber is monitored as a function of temperature to obtain a specific initial coverage. The surface is then heated in a controlled manner to allow the desorption of gas and pressure is monitored as the surface heats up. To obtain meaningful data from a TPD experiment, experimental requirements must be implemented to interpret data:

- (i) The surface must be heated in a controlled manner and the method to implement this is to apply a linear heating rate ( $\beta$ ) to the sample. This heating rate must obey the relationship:

$$T(t) = T_0 + \beta t$$

where  $T(t)$ , is the sample temperature,  $T_0$ , is the initial sample temperature and  $\beta$  is the heating rate which can be determined experimentally.

- (ii) A method to monitor the sample temperature should be implemented. In this study, as mentioned before, a K-type thermocouple junction is spot-welded and placed on the sample plate and deposition stage with heat-conducting paste.
- (iii) A detector to monitor desorbed species/desorption is needed. This is usually a quadrupole MS, where the ratio of species can be monitored and detected as they are removed from the surface. The pressure sensor was used to also observe desorption species.

As the surface temperature increases, thermal energy available from the chemical species becomes sufficiently enough, so adsorption energies are overcome and thus, desorption can be observed. The active competition of molecules entering the gas phase *via* desorption and leaving *via* the pumping of the experimental vacuum chamber, creates a

## 2. Experimental Procedures and Characterisation Techniques

characteristic peak shape measured by the pressure or MS data. For a very simple case of the adsorbate, a single desorption peak is determined if activation energy for an adsorbate where desorption is constant, as a function of surface coverage.<sup>12</sup> There are more complex cases where broad peaks are observed with more than one component.<sup>13</sup> In a vacuum chamber that is pumped on continually; the maximum desorption rate corresponds to the temperature at which the maximum desorption occurs,  $T_p$ . The desorption of molecules or atoms from a surface under heating obeys the Arrhenius law and the rate constant,  $k_d$ , increases exponentially with temperature:

$$k_d = A \exp\left(-E_d/RT\right) \quad \text{Equation 2.1}$$

where  $A$ , is the pre-exponential factor,  $E_d$ , is the desorption energy,  $R$ , is the ideal gas constant and  $T$ , is the temperature of the surface.<sup>1</sup> Surface coverage decreases as  $k_d$  exponentially increases with an increase in temperature and so a maximum will be observed. Figure 2.9 illustrates a prototypical TPD trace of the changes in surface coverage and rate of desorption.

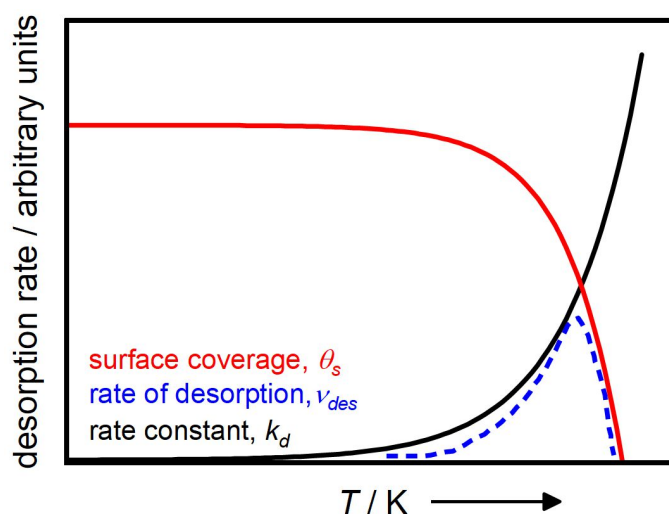


Figure 2.9. Typical TPD trace of the rate of desorption (dotted line). Molecules are initially deposited onto a surface before the sample is heated. As the sample heats, the surface coverage,  $\theta_s$ , decreases and the rate constant,  $k_d$  increases. These points then intersect with each other, and this is the peak of desorption. The subsequent area under this curve,  $v_{des}$ , can be viewed as proportional to the number of species deposited in the gas phase. This figure has been readapted from reference 12.

When the maximum desorption rate is obtained, it is possible to analyse and calculate the desorption energy. Using the rate constant, an equation can be set up such that:

$$-\frac{dN}{dt} = k_d N^m \quad \text{Equation 2.2}$$

## 2. Experimental Procedures and Characterisation Techniques

where  $N$ , is the number of adsorbed molecules,  $m$ , is the order of reaction and as mentioned earlier,  $k_d$ , is the rate constant. Equation 2.2 shows how molecules will desorb with respect to time<sup>1</sup> and so a substitution such as Equation 2.3 can be introduced:

$$\frac{dN}{dt} = \frac{dN}{dT} \times \frac{dT}{dt} = \frac{dN}{dT} \beta \quad \text{Equation 2.3}$$

where  $\beta$ , is equal to  $\frac{dT}{dt}$ , known as the heating ramp/rate which one can apply to experimental procedures such as in this study. Combining Equation 2.2 and 2.3 to obtain Equation 2.4, it is now rewritten as:

$$\frac{-dN}{dT} = \frac{k_d}{\beta} N^m \quad \text{Equation 2.4}$$

and further substituting  $k_d$  from Equation 2.1:

$$\frac{-dN}{dT} = N^m \frac{A}{\beta} \exp \left( -E_d / RT \right) \quad \text{Equation 2.5}$$

when  $T = T_p$ , where  $T_p$ , is the maximum thermal desorption peak,

$$\frac{d^2N}{dT^2} = 0 \quad \text{Equation 2.6}$$

the rate of desorption reaches a maximum.

In order to obtain the temperature at which maximum desorption is reached, one can differentiate Equation 2.5 with respect to  $T$ , and setting  $m$  to 0, leads to the expression:

$$\frac{E_d}{RT_p^2} = \frac{A}{\beta} m N^{m-1} \exp \left( -E_d / RT_p \right) \quad \text{Equation 2.7}$$

As a heating rate is set experimentally, the desorption energy can be determined as the ideal gas constant,  $R$ , is known ( $8.314 \text{ J mol}^{-1} \text{ K}^{-1}$ ) and the  $T_p$  (K) is monitored constantly. The pre-exponential factor,  $A$ , can be assumed to be the magnitude of molecular vibrational frequencies<sup>1</sup> such that it is approximately  $10^{13} \text{ s}^{-1}$  if  $m = 1$ , first-order desorption.<sup>12</sup>

Desorption families are such that they can be of zeroth, first and second-order reactions. In order to determine the order of desorption, several experiments have to be conducted on the same species with different initial surface coverages.<sup>1</sup> When enough data has been collected, trends will be visible. Such trends are shown in Figure 2.10. As seen in Figure 2.10(a), the ideal desorption behaviour of films deposited onto a surface

## 2. Experimental Procedures and Characterisation Techniques

for zero-order kinetics, would depict alignment of leading edges and thus, desorption of bulk material with large coverage. This is typical for multilayer desorption and is due to adsorbate-adsorbate interactions where  $m$  is zero in Equation 2.7. The temperature for desorption changes slightly with coverage due to the desorption rate increasing exponentially as in Figure 2.9.<sup>1</sup> For first-order kinetics, in Figure 2.10(b) all peaks line up to the same temperature peak for desorption which is expected for monolayers or sub-monolayer desorption at low coverages as seen in Equation 2.7. The interactions are mainly surface-adsorbate and are the same for molecules adsorbed onto a flat and pristine surface.<sup>1</sup> As one goes from a monolayer to multilayer, the desorption kinetics change between the surface and adsorbate.<sup>1</sup> Depending on the surface temperature and when low coverages are dosed, molecules may diffuse and find optimal binding sites leading to larger amounts of energy needed to break the interaction and allow the molecules to desorb. As the number of molecules dosed, increases, the interaction between adsorbate-adsorbate interactions become more prominent for desorption kinetics when compared to a lower number of molecules associated with adsorbate-surface interactions.<sup>1</sup> For second-order kinetics, the coincident trailing edges will align and indicate recombination of molecules during desorption on the surface, Figure 2.10(c).

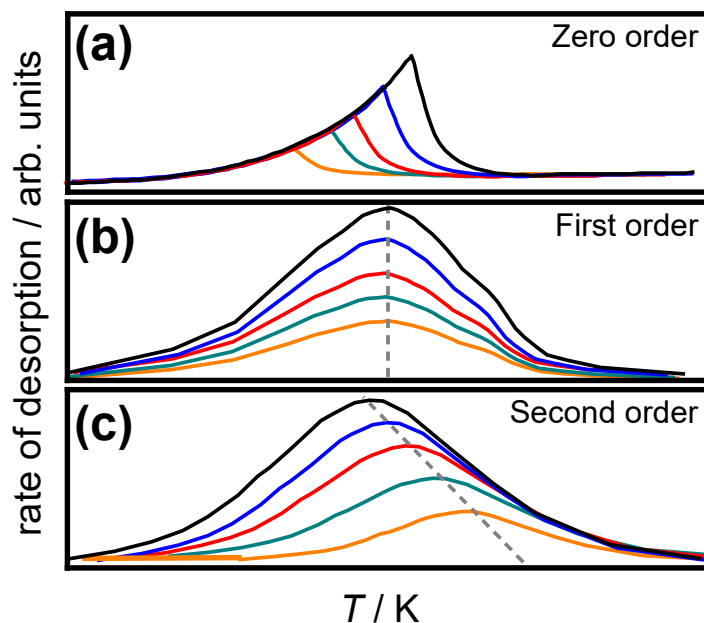


Figure 2.10. The traces in (a), (b) and (c) indicate ideal desorption behaviours for zero, first and second-order kinetics deposited onto a surface, respectively. In (a) the leading edges align with one another as the material desorbs, (b) the peaks line up at the same temperature of desorption which is expected for this order for sub-monolayer desorption and (c) the trailing edges of the traces align at the end indicating recombination of the molecules on the surface. This figure has been readapted from reference 1.

## 2. Experimental Procedures and Characterisation Techniques

These are typical behaviours for desorbing layers, however, more complex interactions such as pseudo desorption exists. Pseudo desorption is described in terms of the surface. If a rough surface is present, multiple binding sites will be available for sub-monolayer coverages of molecules and a collection of TPD traces can appear to look like a second-order desorption process, when compared to first-order desorption, despite that it would be physically highly unlikely. Such desorption kinetics are closer to pseudo-first-order and thus, do not recombine on a surface and so second-order desorption kinetics can be disregarded.

Figure 2.10 can be seen as visual and therefore very subjective. In order to determine the desorption order through maths using such data, several calculations must be carried out and thus, the data from these calculations must be fitted. This gives a gradient between the different TPD measurements which in turn determines the order. The procedure for determining the kinetic order of desorption has been described thoroughly elsewhere.<sup>14</sup> However, the leading edge analysis is based on the natural logarithm applied to the Polanyi-Wigner equation as rearranged in Equation 2.8.<sup>15</sup> The Polanyi-Wigner equation interprets the desorption rate defined as  $r_{des}$  as a function of the surface concentration of the adsorbed species,  $N(t)$ , where  $t$ , is time. This equation shows a linear relationship for a given  $T$ , the surface temperature between the  $\ln(r_{des})$  and  $\ln(N)$ . The gradient here equals  $n$ .

$$r_{des} = -\frac{dN}{dt} = vN(t)^n \exp\left[\frac{-E_{des}}{k_B T}\right] \quad \text{Equation 2.8}$$

where  $v$ , is the pre-exponential factor,  $n$ , is the desorption order,  $E_{des}$ , is the desorption energy and  $k_B$ , is the Boltzmann constant. And in order to govern what  $N(t)$  is, the initial surface concentration which is defined as  $N_{tot}$ , can be assumed to be equal to the bombardment rate, defined as  $Z_w$ , which is further multiplied by the dose time,  $\tau$ , according to Equation 2.9.<sup>15</sup>

$$N_{tot} = Z_w \tau = \frac{PS\tau}{\sqrt{2\pi mk_B T}} \quad \text{Equation 2.9}$$

where  $P$ , is the pressure in Pascal units,  $S$ , is defined as the sticking coefficient and  $m$ , is the mass of one molecule.<sup>15</sup> All molecules are presumed to stick to the surface if  $S$  is unity. These measurements have not been carried out in this study and this description is for theoretical purposes only.

## 2. Experimental Procedures and Characterisation Techniques

### 2.5.2 Quartz-Crystal Microbalance (QCM)

The thickness of films, named the Sauerbrey thickness, as deposited in this study were measured using a quartz-crystal microbalance (QCM). Besides being a piezoelectric resonator, quartz crystals can be fabricated, where wafers are cut from a bulk of quartz crystals at precise orientations with respect to the crystallographic axes. With the QCM utilised in this study, the ‘AT’-cut piezoelectric quartz planoconvex crystals (mentioned earlier, section 2.4.1) are designed to provide shear mode oscillation, this is where the crystal surface move in such a fashion, anti-parallel to each other. After the cuts are made, the metallic electrodes are evaporated directly onto the top and bottom of the surfaces of the quartz disc as shown in Figure 2.11(a). AT-cut crystals are established to have fairly good stability at room temperature with a corresponding small frequency change of 1–3 Hz / °C.<sup>16</sup> The quartz is designed to oscillate at a defined frequency once a voltage has been applied through the electrodes. The change in frequency in QCMs can be detected and measured with a resolution of 0.1 Hz with a fundamental resonance frequency in the range of MHz and are converted to changes in mass on the QCM crystal.

The quartz application has become more well-known following the pioneering work established by Sauerbrey.<sup>17</sup> QCMs are mainly operated in vacuum or gas, coinciding with thin and rigid deposited films and the Sauerbrey equation (Equation 2.10) is used for monitoring this film thickness (Sauerbrey thickness). Viscoelastic effects contribute and affect the half-width properties of the crystal as the thickness of the film increases. These effects are described in detail where the QCM is more profoundly employed in Chapter 3 of this thesis.



## 2. Experimental Procedures and Characterisation Techniques

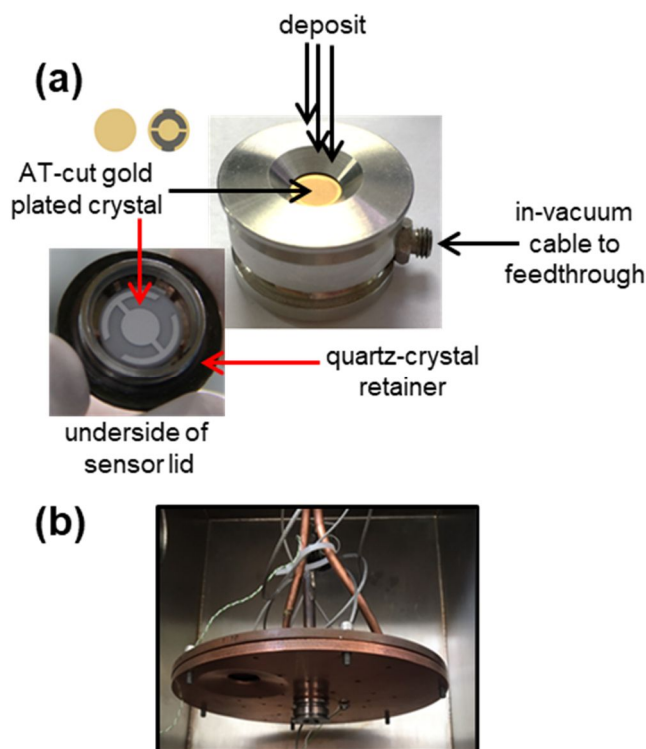


Figure 2.11. (a) Detailed view of the QCM and (b) view of the QCM positioned in the centre of the deposition plate inside the vacuum chamber.

Due to some uncertainty, the crystal deviates slightly from 6 MHz with respect to the change in mass during deposition. For example, when mass is accumulated onto the crystal, the frequency will decrease in a repeatable manner. It is understood that deposition of mass onto the surface is highly sensitive and therefore, molecular monolayers can be detected. The QCM is a suitable instrument to exploit this effect.<sup>3, 17</sup> The change in frequency due to the addition of mass can be converted to mass change and thus, defined by the Sauerbrey equation, Equation 2.10. The limitation of the Sauerbrey equation is that the deposited film is rigid and uniform when  $\Delta f/f < 2\%$ .<sup>18</sup> And so, the equation is only valid for small changes of frequency, such that  $\Delta f/f < 0.05$ .<sup>19</sup>

$$\Delta f = -\frac{2f_0^2}{A\sqrt{\rho_q\mu_q}}\Delta m \quad \text{Equation 2.10}$$

where  $\Delta f$  = change in QCM frequency (Hz) resulting from mass changes per unit area  $\Delta m / A$  ( $\text{g cm}^{-2}$ ),  $f_0$  = resonant frequency of QCM (Hz) which is 6 MHz,  $\mu_q$  = shear modulus quartz ( $2.947 \times 10^{11} \text{ g cm}^{-1} \text{ s}^{-2}$ ),  $\rho_q$  = density of quartz ( $\rho_q = 2.648 \text{ g cm}^{-3}$ )  $A$  = area of electrode ( $\text{cm}^2$ ) and  $\Delta m$  = mass change. It is assumed that the change in mass is uniform over the entirety of the crystal.<sup>19</sup>

## 2. Experimental Procedures and Characterisation Techniques

The QCM is located between two electrodes and is used to determine mass changes through the dependence of the QCM resonance frequency. The QCM measures the frequency change of a thin disc made cut from gold-plated AT-cut 6 MHz crystals, these crystals are firmly held and secure in place by the sensor head. The gold electrode is calibrated at approximately 5.98 MHz. In this study, the QCM, as displayed in Figure 2.11(b) within the chamber, consists of the piezoelectric quartz-crystal (described earlier) with metallic electrodes and a sensor head. The vacuum QCM sensor head with crystals can be firmly attached to the bottom of the deposition plate with two screws and can easily be detached and positioned at various locations on the plate. The holes for the screws are located at the centre, edge, and the midpoint of the radius of the deposition plate. The QCM employs an in-vacuum cable connected to a feedthrough *via* an ISO-100 flange where micro-coaxial cables further connect through into the chamber *via* the vacuum feedthrough in order to conduct electrical signals. Data was acquired using RS232 based programs.

Outside the chamber, as mentioned earlier, the QCM is further connected to a reflection bridge and data is measured using a vector network analyser (N2PK Vector Network Analyser (VNA), 0.05–60 MHz, Makarov.ca) together with myVNA, marakov.ca graphical user interface (GUI) and analysed with QTZ software (Institute of Physical Chemistry, Clausthal University of Technology).<sup>3</sup> The deposition rate of a material being deposited can be calculated from these QCM measurements by plotting mass adsorbed with respect to time and ensuring the differential of the curve is considered. The QTZ software allows the user to change between different parameters, for example, the Sauerbrey thickness, frequency shift, frequency and many more. This measurement technique is widely used for monitoring the deposition of thin films and microbalance applications; this detail is described elsewhere.<sup>19-22</sup>

### 2.5.3 Residual Gas Analyser-Mass Spectrometry (RGA-MS)

Residual gas analysis (RGA, where A is analyser) is the generic term for measuring gas and vapour species in vacuum chambers. RGA measures the chemical composition of a gas within a high-vacuum environment. A quadrupole MS for RGA (RGA-MS, Hiden Analytical, HALO 201 – single filter mass spectrometer) provides a unique window to monitor minute traces of impurities and monitor the quality of vacuum systems in a low-pressure gaseous environment. Impurities can be measured down to the  $10^{-14}$  torr range. An analytical technique such as MS can quantify and identify unknown compounds

## 2. Experimental Procedures and Characterisation Techniques

contained within a sample and elucidate the chemical and structural properties of various molecules. The RGA ionises the components of a gas creating ions and detects them based on their  $m/z$  ratios. The importance of an RGA allows one to, (i) monitor changes in a gas environment, (ii) analyse gas-phase reactions, (iii) detect and check for vacuum leaks and (iv) mass flow controllers can be checked. The main components of a RGA include, (i) ioniser (neutral gas or molecules are converted to positive ions), (ii) mass analyser and filter (quadrupole), (iii) detector and (iv) a MS (depicts peaks from ions with their  $m/z$  ratio in amu [atomic mass unit] units).

In particular, the sample is converted into multiple gaseous ions, produced by bombarding the material with electrons by means of electron ionisation. This causes the sample's molecules to break up into charged fragments and converge onto the MS. At the MS, alternating and direct current voltages are applied to quadrupoles (four cylindrical electrodes), further separating, and characterising the ions by their  $m/z$  ratios and detecting their relative abundances. The separated ions are detected by an electron multiplier as electric current by a Faraday cup and results are displayed as a mass spectrum showing the signal intensity of detected ions as a function of  $m/z$ . Ions provide the information that concerns the structure and nature of its precursor molecule.

A dual Faraday cup and electron multiplier detector allow the identification of particles or species in a vacuum with a partial pressure range of  $10^{-4}$  and  $10^{-13}$  mbar. In particular, the RGA-MS utilised in this study can operate at a minimum detecting partial pressure of  $5 \times 10^{-14}$  mbar and the maximum pressure reached is  $1 \times 10^{-4}$  mbar. In this study,  $\text{H}_2\text{O}$  ( $m/z = 18$ ), argon ( $m/z = 40$ ),  $\text{CH}_4$  ( $m/z = 16$ ),  $\text{CO}_2$  ( $m/z = 44$ ) and helium ( $m/z = 4$ ) were monitored. In addition, the levels of  $\text{N}_2$  gas ( $m/z = 28$ ) within the chamber were kept low, so as to prevent any contamination in the ASW matrices.

## 2. Experimental Procedures and Characterisation Techniques

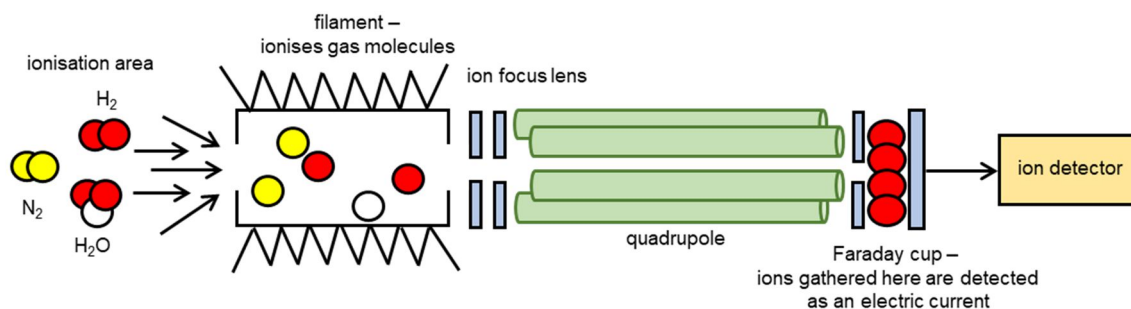


Figure 2.12. Simple schematic diagram of the components of a MS displaying the main components needed: ioniser, quadrupole, and detector.

### 2.5.4 Differential Scanning Calorimetry (DSC)

The main objective of calorimetry is to measure heat.<sup>23, 24</sup> DSC is a thermal analytical technique used to determine how a material's heat capacity ( $C_p$ ) changes with temperature. Phase transitions upon heating and cooling of a sample are monitored based upon heat flow changes, leading to endotherm and exotherm effects.<sup>24</sup> Samples of known mass are heated or cooled and the change in specific heat capacity is tracked with respect to heat flow. This thus allows the detection of transitions such as glass transitions ( $T_g$ ), phase transitions, decompositions, chemical reactions and absorption/desorption.<sup>23, 24</sup>

There are two types of DSC, (i) power-compensated DSC (heat flow) and (ii) heat-flux DSC, where the power supply to both cells remain constant and the heat flux remains constant, respectively.<sup>23</sup>

With a power compensation DSC, the sample and reference pan are held in separate microfurnaces as can be seen in Figure 2.13(a). When an exo/endothermic process occurs, the distinct furnace will accommodate to increase or decrease the heating power to maintain a linear temperature program which is defined by the user.<sup>23, 24</sup> In the case of a power compensation DSC, power is measured directly which is provided by the compensation process. The temperature difference is the measurement signal and the input signal of a second circuit which will always try to compensate for the heat flow; the resulting power difference here is proportional to the heat flow. The quantity measured here is the energy flow given as a function of time or temperature. The heat measured is almost compensated with electrical energy with increasing or decreasing adjustable Joule's heat. To determine the heat capacity per mg or mol, and as provided below, the sample mass needs to be input into the program.

## 2. Experimental Procedures and Characterisation Techniques

$$\text{DSC signal (W g}^{-1}\text{)} = \text{scanning rate (K s}^{-1}\text{)} \times \text{heat capacity (J K}^{-1}\text{ g}^{-1}\text{)}$$

$$\frac{dH}{dt} = \frac{dH}{dT} \times \frac{dT}{dt} \quad \text{Equation 2.11}$$

In a heat-flux DSC, Figure 2.13(b), the sample, and reference pan are maintained at the same temperature throughout the experiment in a single furnace only. The temperature program requires the sample temperature to increase linearly as a function of time and therefore, the reference pan should have a well-defined heat capacity over the temperatures being scanned. The reference pan is heated the same as the sample pan, so energy differences can be monitored to provide calorimetric data. The primary signal measured here is the temperature difference between the sample pan and the reference pan, and from this difference, the heat flow can be calculated.

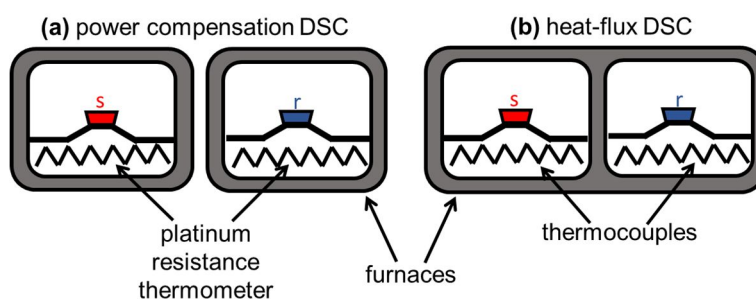


Figure 2.13. Schematic diagrams of (a) double furnace power compensation DSC and (b) single furnace heat-flux DSC with both instruments showing the sample (s) and reference (r) pans, respectively.

Heat transfer is a ubiquitous parameter that does not provide structural or molecular information; further events such as sintering, or decomposition may show heat changes that are not due to a phase transition in the sample. DSC analysis may be informative when used in isolation, however, any other information needed is impossible with ancillary data, hence, a DSC is most commonly used together with X-ray diffraction (XRD).<sup>25</sup>

### 2.5.4.1 Low-Temperature DSC

In this study, the sample is transferred into a stainless-steel capsule with a screwable lid in a LN<sub>2</sub> environment before subsequent transfer into a precooled (93 K) calorimeter (Perkin Elmer, DSC 8000, advanced Double-Furnace DSC). Helium gas is used as a heat exchange gas with a flow rate of 40 mL min<sup>-1</sup>. The stainless-steel pans are precooled in LN<sub>2</sub> and once the sample is placed into the pan, the lid of the capsule was only loosely closed so as to avoid a build-up of pressure and allow any released gas to escape. The

## 2. Experimental Procedures and Characterisation Techniques

sample pan is then quickly transferred into the furnace. An empty stainless-steel reference pan is situated inside the calorimeter undergoing the corresponding heating program set for the sample under investigation. In the current work, (unless stated otherwise) the deposits are heated from 93 K to 263 K at  $10 \text{ K min}^{-1}$  before cooling back to 93 K at  $50 \text{ K min}^{-1}$ . This heating rate provides a good signal-to-noise (S/N) ratio. During this stage, the sample in the capsule undergoes a phase transition from ASW to stacking disordered ice, ice *Isd* to hexagonal ice, ice *Ih*, which is then reheated at  $10 \text{ K min}^{-1}$ , creating a background correction factor. After this, the sample is melted by further heating. The issue here is the fact that when filling the sample into the pan, one cannot measure the mass of the sample at that moment in time and hence, the number of moles cannot be measured under  $\text{LN}_2$  conditions. Thus, to address this issue, the area under the curve of the melting endotherm can be integrated to give an area in Joules and using  $6012 \text{ J mol}^{-1}$  as the enthalpy of melting of  $\text{H}_2\text{O}$  ice *Ih*, the number of moles of ice can be determined, allowing for direct comparison between different samples. The resulting DSC thermogram (mW) (background corrected) is then divided by the moles of  $\text{H}_2\text{O}$  (mol) in the sample and considering the heating rate ( $\text{K s}^{-1}$ ) of the program, a quantity yielding the unit of  $\text{J mol}^{-1} \text{ K}^{-1}$  is obtained. This step is necessary to scale the DSC thermograms in order to compare them to one another. Data from the DSC instrument is converted using the Pyris software.

To prove that a purely amorphous ASW deposit is prepared in this study, the thermal annealing during a calorimetric study was carried out on the sample as seen in Figure 2.14. After annealing the sample in the DSC, ASW is seen to display a reversible glass transition with an onset temperature of 136 K.<sup>26-28</sup> The exotherm peak at 160 K shows the transformation of ASW to ice *Isd*. The enthalpy of the phase transition was calculated as  $1260 \pm 35 \text{ J mol}^{-1}$  and the result presented here is in good agreement with the literature values of approximately,  $1285 \pm 93 \text{ J mol}^{-1}$ .<sup>29-34</sup> It can be difficult to choose integration values for the exothermic peak and contributions from background signal may be an issue. However, it is concluded that the as-made sample prepared was pure ASW. There is a slight broad feature before the crystallisation of ASW, starting at 125 K which can be assigned to pore sintering and structural relaxation of the amorphous solid which is described in more detail in Chapter 3 and Chapter 4.

## 2. Experimental Procedures and Characterisation Techniques

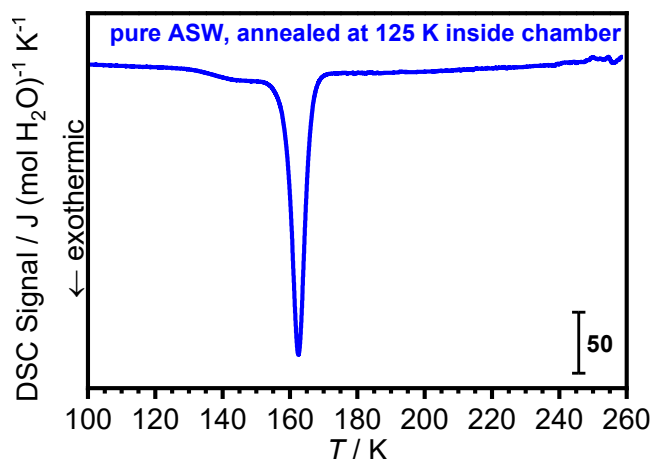


Figure 2.14. DSC thermogram for vapour deposited ASW annealed at 125 K in the high-vacuum chamber and cooled back down to 95 K before removal. The curve is normalised with respect to the area of its melting endotherm. The heating rate during this scan was  $10 \text{ K min}^{-1}$  and the DSC signals are normalised per mole of  $\text{H}_2\text{O}$ .

### 2.5.5 Raman Spectroscopy

The inelastic scattering of light phenomena is known as Raman spectroscopy. When light interacts with matter, the photons from the light may be scattered or adsorbed or may not interact with material and will pass through it. When the energy of an incident photon resembles the energy gap between the excited state and ground state of a molecule, the photon will be absorbed, and the molecule will reach a higher energy excited state. This is the change that is measured in absorption spectroscopy by detecting the loss of this energy of radiation from the light. The photon could interact with the material and therefore, scatter. Raman spectroscopy comprises a selection rule in which the sample must experience a change in its polarizability ( $\alpha$ ) when subject to an electric field.

When monochromatic light interacts with the sample, radiation is scattered during the point at which the incident radiation strikes the sample's molecules. Three potential scattering events arise due to this process and are depicted in Figure 2.15.

The Rayleigh scattering event is when the incident photon's energy is the same and equal to the scattered energy and thus, no energy change is involved. Raman scattering from the ground vibrational state, 0, leads to absorption of energy by the molecule and thus, is promoted to excited higher energy vibration states. This is where the scattered energy is less than that from the incident photon and thus, is termed, Stokes scattering. The frequency scattered from the photon in Stokes scattering will be small. However, some molecules may be already present in a vibrationally excited state due to

## 2. Experimental Procedures and Characterisation Techniques

thermal energy such as shown in Figure 2.15. Scattering from higher energy states back to the ground state is referred to as anti-Stokes scattering. This is where the scattered photon has more energy than the incident photon.

The intensities of both processes depend on the population of the various states of matter. At room temperature, there are only a small number of molecules expected to be present in an excited state compared to a low-energy state. Raman spectroscopy records the intensity of the net absorption of the scattered radiation as a function of wavenumber shift ( $\text{cm}^{-1}$ ).

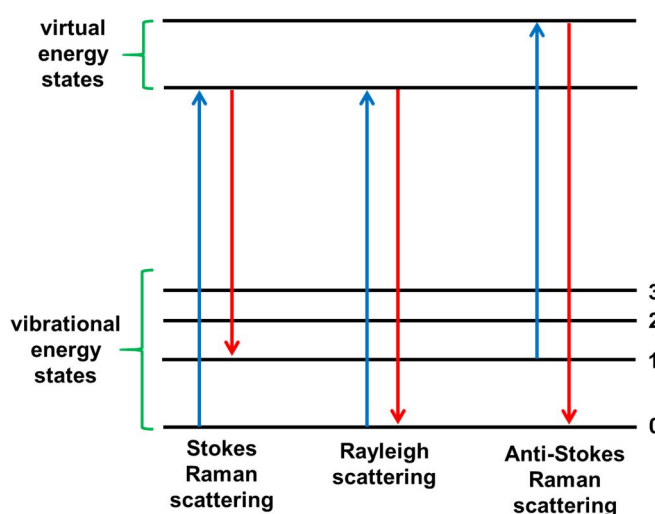


Figure 2.15. Energy level diagram of three transitions upon inelastic and elastic scattering; Stokes Raman scattering, Rayleigh scattering and anti-Stokes scattering, respectively. The lowest energy level is 0 shown at the foot of the figure with increasing energy levels above it. This figure has been reproduced from reference 35 in this thesis and was originally illustrated by Jablonski.<sup>35</sup>

As we know, Raman scattering occurs from vibrations which causes a change in polarisation in the cloud of electrons. The largest changes and greatest scattering are measured from the cause of symmetric vibrations. This is different when compared to infrared spectroscopy (IR) where the most intense absorption is instigated by changes in the dipole moment and thus, asymmetric vibrations are the most pronounced. Both techniques are complementary and used together to understand and obtain an improved view of the structure of a molecule. Centrosymmetric molecules ensure that there are active bands in both techniques; this is a selection rule termed the mutual exclusion rule. In centrosymmetric molecules, the reflection of a point through the centre will reach the other side of the molecule on the same point. This is useful as it is possible to determine and differentiate between *cis* and *trans*-forms of molecules.



## 2. Experimental Procedures and Characterisation Techniques

### 2.5.5.1 Low-Temperature Raman Spectroscopy

For this study, a Renishaw Ramascope spectrometer equipped with a 632.8 nm (He-Ne) laser, was used to record low-temperature Raman spectra. Ice samples were recorded in a low-pressure ( $10^{-2}$  mbar) and low-temperature environment achieved by using a modified Oxford Instruments Microstat<sup>N</sup> cryostat. The temperature of the samples was controlled using temperature control units, Oxford Instruments Nitrogen Gas Flow Controller and Oxford Instruments Temperature Controller. Raman shifts of all spectra were obtained by calibration of the sharp emission lines from a neon-discharge lamp.<sup>36</sup> Continuous Raman spectra were recorded over a range of 3550 to 100  $\text{cm}^{-1}$  and spectra were accumulated four times to reduce the S/N ratio by half and for a collection time of 100 seconds. For the thermal annealing steps, the cryostat was attached to a temperature control unit and the sample was heated at 5  $\text{K min}^{-1}$  from 78 K to any given temperature in sequential steps. Once a temperature was approached, the sample was always cooled back down to 78 K and at this point, spectra were recorded.

A Frimo Hypress 30 tonne hydraulic press was used to prepare the cryostat body of the sample holder by pressing an indium plate into the copper cryostat body. Only the cryostat with the indium plate was pressed using the hydraulic press applying a small amount of force, less than five tonne. This was to ensure good thermal contact between the cryostat body and the sample. Small pieces of the sample were loaded into the pre-cooled cryostat at 78 K under  $\text{LN}_2$  and ground up into the indium-pressed cryostat stage, covered with  $\text{LN}_2$  with a precooled hand-held steel piston.

Consistent with an earlier study as conducted by Shephard *et al.*<sup>37, 38</sup> with Raman spectroscopy, the annealing of as-made pure ASW through to the transformation to ice *Isd* can be seen here. The Raman spectrum of ASW as a function of temperature was recorded and shown in Figure 2.16, illustrating the spectral changes occurring due to heating and structural differences are observed, described as relaxation. For ice, there are many areas of spectral interest (Figure 2.16).

## 2. Experimental Procedures and Characterisation Techniques

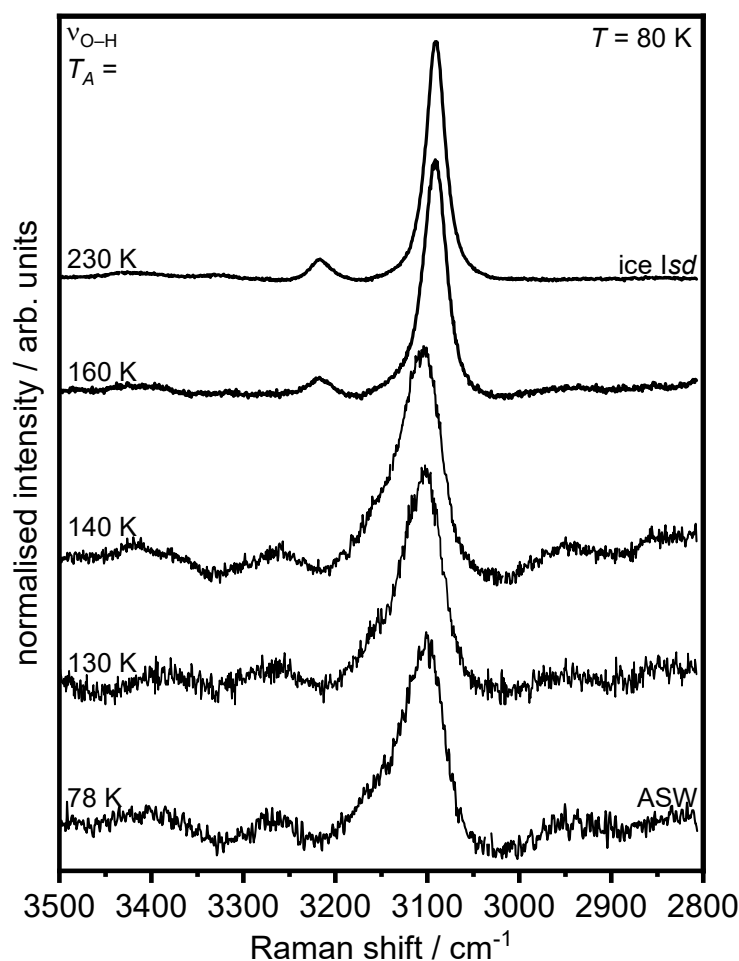


Figure 2.16. Raman spectra of the starting material, pure ASW, at 78 K and  $10^{-2}$  mbar, showing the gradual irreversible phase transition of amorphous ice (ASW) to ice Icd upon thermal annealing in the coupled  $\nu(\text{O-H})$  stretching region. All Raman spectra have been recorded at 78 K after annealing to 130, 140, 160 and 230 K. Spectra are normalised with respect to the most intense feature and vertically translated for visual clarity. Spectroscopic features characteristic of ASW and ice Icd are illustrated.

Annealing pure ASW to  $\sim 160$  K led to the formation of ice Icd, and in line with XRD and DSC measurements, the process of annealing results in a peak shift. This shift is detected with the broad peak centred at  $3116 \text{ cm}^{-1}$  (ASW) to a sharper, stronger peak at  $3080 \text{ cm}^{-1}$  stretching ( $\nu$ ) of coupled O-H, that of ice Icd. In analogy to the shifts in peaks and changes in spectral features observed during heating, the main feature at  $3080 \text{ cm}^{-1}$  at 78 K, is more pronounced towards higher frequencies / lower wavenumbers and a decrease in the intensities of the broad shoulders at  $3400$  and  $3250 \text{ cm}^{-1}$  is seen.

The primary feature of coupled  $\nu(\text{O-H})$  sharpens upon thermal annealing and can be interpreted as an increase in structural order when observed on an intermediate-range length scale.<sup>37, 38</sup> This proposal originates from the fact that O-H oscillators in ice are able to couple with each other in-phase, beyond the locally direct environment of a  $\text{H}_2\text{O}$

## 2. Experimental Procedures and Characterisation Techniques

molecule.<sup>39</sup> Nevertheless, the spectrum at 78 K, shows the absence of any crystalline contaminants and impurities due to the broad amorphous peak centred at  $3116\text{ cm}^{-1}$ .

### 2.5.6 Fourier Transform Infrared Spectroscopy (FTIR)

The aim of absorption spectroscopy techniques such as Fourier Transform Infrared Spectroscopy (FTIR) is to measure how much light a material will absorb at each wavelength. The principal way to measure this is by shining monochromatic light at the material and measuring how much light is absorbed, repeating this process for every wavelength.

In the case of Fourier transform (FT), a beam consisting of many frequencies of light is shone all at once at the material. The beam is further modified to consist of a combination of frequencies providing a second data point. Over a short time span, this process is repeated rapidly and thus, the computer will infer what the absorption is at every wavelength.

Light is then shone into an interferometer (Michelson) which contains specific configurations of mirrors. As the mirror moves, wave interference is present and different wavelengths are then modulated so the beam coming out of the interferometer will have a different spectrum. Computer processing is necessary to convert raw data to the desired result where the latter is light absorption for each wavelength, this process is measured using the FT algorithm. The FT converts a domain to its inverse domain which is wavenumbers /  $\text{cm}^{-1}$  and this data is referred to as an interferogram.

As IR radiation passes through a sample or material, some radiation is absorbed by specific wavelengths, which in turn causes the dipole moment change of the molecules and the remaining radiation passes through to be transmitted. As mentioned, FT comes into play here by converting the output from the detector to an interpretable spectrum. The resulting FTIR spectrum from the signal in the detector represents a molecular 'fingerprint' from the sample. FTIR combined uses interferometry to record the information from a material that is placed into the IR beam. The FT outcome provides the spectra which one can use to quantify or identify the material in use since molecules exhibit explicit IR fingerprints. A spectrum obtained from FTIR arises due to the decoding of interferograms into spectra that is recognisable. Background measurements are important as they measure the contribution of the instrument and environment to the corresponding spectrum. A background can thus, be subtracted from the sample signal.

## 2. Experimental Procedures and Characterisation Techniques

### 2.5.6.1 Low-Temperature FTIR

The FTIR employed for this study is a Bruker Invenio-R spectrometer equipped with a cryostat (Optistat DN-V, Oxford Instruments) fitted with four optical radial windows and one blank axial window (42 mm diameter). The program for recording the IR spectra was the OPUS-TOUCH R&D Software (Bruker, Spectroscopy Software). The temperature of the cryostat can be measured using a NanoScience Mercury iTc cryogenic environment controller (Oxford Instruments) box connected to the housing of the cryostat. The main electrical supply to the iTC controller consists of an IEC C14 connector. The iTC is connected to the cryostat *via* a standard RS232 connector. The Michelson interferometer employed in the instrument is a RockSolid™ interferometer unique to Bruker technology.

To prepare the FTIR spectrometer for measurements, the detector was first cooled with ~0.5 L of LN<sub>2</sub>. The apparatus used to reduce the temperature and pressure of the cryostat includes a rotary pump (Model Code. RV5, Serial No. 076009466, BOC Edwards, BOC Ltd) attached to the cryostat and a turbomolecular pump (Model Code. B722-01-000, Serial No. 006564732, BOC Edwards, BOC Ltd). At first, the rotary pump was switched on to achieve a rough vacuum pressure of  $2 \times 10^{-2}$  mbar measured with a Pirani pressure gauge (Thermovac TTR91, Oerlikon Leybold Vacuum). Once this pressure was achieved, the cryostat was cooled to 78 K with the flow of LN<sub>2</sub>. At this point, once the cryostat is cold, the pressure achieved is  $5 \times 10^{-4}$  mbar. Since only the temperature is important in these cases, this pressure is low enough to conduct all measurements. Once the base pressure and temperature are obtained and depending on the measurements the user wishes to carry out, background scans can be recorded with or without the sample deposition window.

Contamination of samples with H<sub>2</sub>O is created due to moisture in the air and is difficult to prevent, thus, 5 w% D<sub>2</sub>O was incorporated into the H<sub>2</sub>O round-bottom flask. The round-bottom flask was degassed with seven FPT cycles to remove gases such as CO<sub>2</sub> from the solution. To calibrate H<sub>2</sub>O *in situ*, the round-bottom flask containing H<sub>2</sub>O and 5 w% D<sub>2</sub>O was attached to the front housing of the cryostat. A circular CaF<sub>2</sub> sample deposition window (UQG Optics, item number: WCF-152 CaF<sub>2</sub> Window – Mono) with a diameter of 15 mm and a thickness of 2 mm was assembled inside the cryostat housing under LN<sub>2</sub> and the cryostat was then closed up, evacuated, and the system reached a

## 2. Experimental Procedures and Characterisation Techniques

temperature of 78 K. The turbopump is also switched on at this point to decrease the pressure further.

All linear absorption spectra were recorded in transmission geometry with a spectral resolution of  $4\text{ cm}^{-1}$ . The source setting was mid-IR with an aperture setting of 1 mm and a scanner velocity of 20 kHz. A background spectrum was always recorded at 78 K with an empty sample holder in line with the beam or with a sample deposition window for *in situ* studies. Water is introduced through the graduated needle valve at 0.05 mbar measured with the pressure sensor, for a deposition time of 5 minutes onto the sample deposition window. Once the deposition is stopped, spectra were recorded. The spectra were set to produce 512 scans ( $\sim 2$  minutes) and were recorded from  $4000\text{ cm}^{-1}$  to  $500\text{ cm}^{-1}$ . The optimum alignment conditions were achieved by trial and error, and the corresponding spectra with the best alignments are shown below in Figure 2.17.

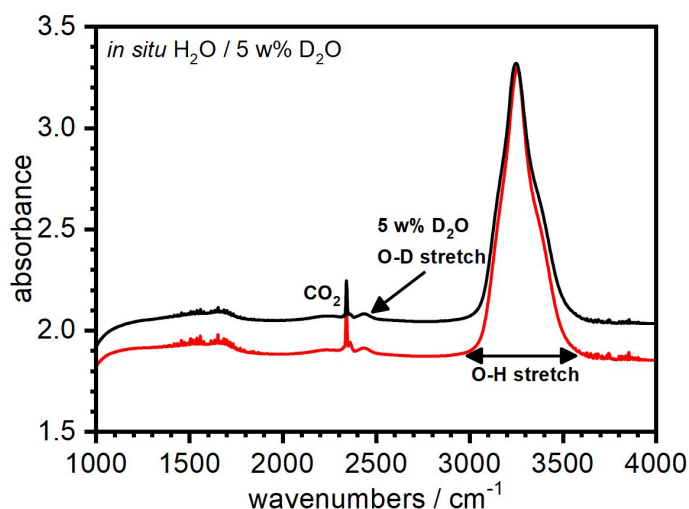


Figure 2.17. The experimental absorption spectra of pure  $\text{H}_2\text{O}$  with 5 w%  $\text{D}_2\text{O}$  at 80 K is shown in red and black where the best alignment is shown in red with a higher transmittance value. Gaseous  $\text{CO}_2$  is indicated in the figure which was present in the spectrometer housing and could not be eliminated.

The spectrum shows a large peak for the O–H stretching and a smaller O–D stretch at approximately  $3242\text{ cm}^{-1}$  and  $2440\text{ cm}^{-1}$ , respectively. The S/N ratio and the background of the red spectrum is better when compared to the black spectrum. This data is in good agreement for verifying the reliability and alignment of the detector with the sample.

To collect FTIR spectra of vapour-deposited samples, thin films of ASW were deposited or codeposited with  $\text{C}_{10}\text{H}_{16}$  in the vacuum chamber onto the circular  $\text{CaF}_2$  sample deposition windows. Initially, these windows were placed firmly inside a circular

## 2. Experimental Procedures and Characterisation Techniques

copper ring, separated by a Teflon ring, and attached to the deposition plate with three screws. A dosing time of 2.5 minutes was deposited directly onto the window for all samples, in line of sight with the H<sub>2</sub>O-inlet tube. After deposition, the deposition plate was removed from the chamber under LN<sub>2</sub> as mentioned in section 2.4.2, three screws attaching the copper ring to the plate were unscrewed and the window was carefully removed out of the copper housing. The window was transferred into an aluminium storage can and stored in the LN<sub>2</sub> reservoir for analysis once the FTIR was prepared to a low-temperature and pressure environment. During the sample transfer to the FTIR, small amounts of H<sub>2</sub>O may condense onto the surface of the window for a short period of time, approximately three seconds, where the sample window is exposed to open air. This is minimised as much as possible by keeping each component used and transferred, submerged in LN<sub>2</sub>.

Once the sample was transferred into the cryostat at 78 K, measurements were initiated. To anneal the samples from 78 K, the cryostat was set to auto heating for a linear heating rate of 1 K min<sup>-1</sup> to a specific temperature using the internal heating element and regulated by the Mercury iTc cryogenic environment controller. At this time, the LN<sub>2</sub> cooling was stopped, and the temperature of the cryostat was increased. Once the temperature was reached, the cryostat was cooled back down to 78 K for data collection.

### 2.5.7 Diffraction (Elastic Scattering)

The following sections aim to describe the basis of diffraction as an important characterisation technique and the two diffraction techniques used extensively for this thesis were XRD and neutron diffraction.

The seven most important components of any diffraction experiment must include: (i) radiation source, (ii) incident beam monochromator and collimator, (iii) sample under investigation, (iv) scattered beam collimator, (v) radiation detector, (vi) data acquisition electronics (DAE) and (vii) data analysis software, converting raw data to differential cross sections (DCS).

#### 2.5.7.1 Characterising Crystal Structures

The feature that provides crystalline materials with long-range order and the central property of this material is its inherently repetitive nature. The discrete nature resonating from scattering from crystals provides a link with the atomic structure. The characterisation of crystalline materials (and lesser extent, amorphous materials), which have a regular array of atoms, requires determination of their atomic planes.

## 2. Experimental Procedures and Characterisation Techniques

A unit cell is a building block of a small volume of atoms from which gives rise to an entire lattice with an overall symmetry of a crystal and in three dimensions in a repetitive manner, a unit cell is defined using six parameters such that they are, lengths of  $a$ ,  $b$ ,  $c$ , and angles  $\alpha$ ,  $\beta$  and  $\gamma$ . Figure 2.18 depicts a simple unit cell defined by a parallelepiped lengths and angles. Lattice constants ( $a$ ,  $b$ ,  $c$ ) are the physical dimensions of the unit cell in a crystal system describing the lengths of a unit cell along different axes. For a lattice, each infinite array of point has identical surroundings. A crystal structure can be built up using the unit cell.

There are four distinct types of unit cells: primitive, body-centred, face-centred, and centred. There are thus, seven different possible unit cell shapes, which when combined with these four distinct lattices, give rise to 14 Bravais lattices.<sup>40</sup> These Bravais lattices define the translation symmetry of the crystal and thus more detailed descriptions of the structure can be provided by belonging to, one of 230 space groups. A range of symmetry operations can be applied to the asymmetric unit cell to describe the crystal structure. Miller indices as shown in Figure 2.18 form a notation system and describe planes within crystal structures by  $h$ ,  $k$ ,  $l$ . These three integers define the number on the divisions of the  $a$ ,  $b$ ,  $c$  lattice parameters, respectively. The spacing between planes is defined as  $d_{hkl}$  and the plane ( $h$ ,  $k$ ,  $l$ ) intercepts the  $a$ ,  $b$  and  $c$  axis at  $a/h$ ,  $b/k$  and  $c/l$ .

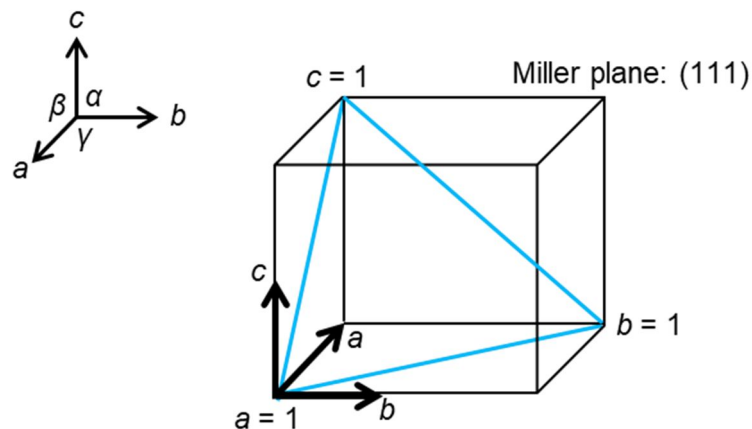


Figure 2.18. A simple unit cell showing the parameters as mentioned in the earlier text, illustration of the lengths and angles along the unit cell and a visualisation of a (111) Miller plane going through a unit cell.

## 2. Experimental Procedures and Characterisation Techniques

### 2.5.7.2 General Diffraction

Powder diffraction data lacks three-dimensionality, however, represents a one-dimensional snapshot of the reciprocal lattice of a crystal.

During the process of scattering, the electron starts to oscillate, and a spherical wave is created. If the energy and wavelength of the scattered wave does not change, this is termed ‘elastic scattering’. Spherical waves created by more than one atom can interact with each other producing negative and positive interferences. When waves interact, they can cancel each other out by destructive interference being out-of-phase or remain in-phase with each other by means of constructive interference. X-rays scatter via the electron cloud surrounding each atom and are suited for shallow depths.<sup>41, 42</sup> Light atoms are not scattered well in comparison to electron-rich and heavier elements which scatter X-rays more strongly.<sup>43</sup> In contrary to X-rays, neutrons eminently scatter *via* atomic nuclei and enable a high penetration depth (low absorption) mainly suited for probing properties of bulk materials.

### 2.5.7.3 Braggs Law

Diffraction is an important tool and can conceptually be understood with Braggs law, demonstrating both constructive and destructive interference:

$$n\lambda = 2d_{hkl}\sin\theta \quad \text{Equation 2.12}$$

where  $n$  is an integer and non-integer for constructive and destructive interference, respectively,  $\lambda$ , is the wavelength of the incident beam,  $d$ , is the interplanar spacing between atoms and  $\theta$ , is the incident angle (Figure 2.19) of the incoming beam. Constructive interference can only occur in specific directions, so when  $n$  is an integer, any difference in path length planes must equal an integer number of wavelengths so the diffracted waves remain in-phase with each other. Figure 2.19 illustrates a schematic description of how Braggs law was derived.



## 2. Experimental Procedures and Characterisation Techniques

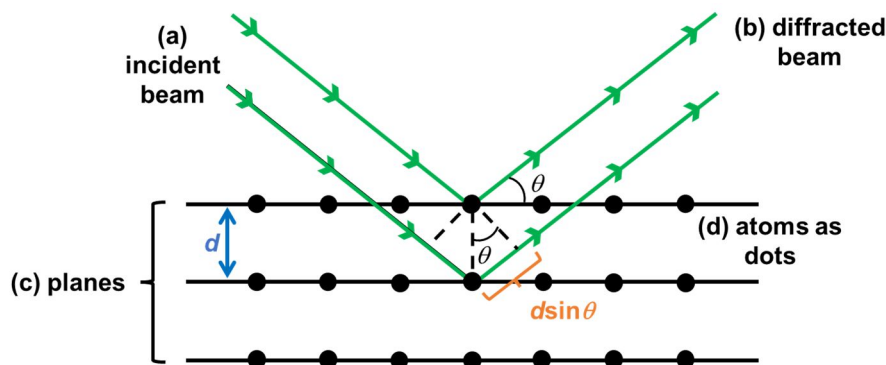


Figure 2.19. Illustration of how Bragg's law was first derived – the setup of uniformly spaced layers (a) the incoming beam, (b) diffracted beam, (c) planes in a crystal lattice and (d) atoms seen as black dots.

When atoms are symmetrically arranged, they are separated by  $d$  and with constructive interference, their path length,  $2d_{hkl}\sin\theta$ , is equal to an integer of wavelength  $\lambda$ . Therefore, the incoming beam is deflected by  $2\theta$ , producing a reflection spot in the pattern. Once a diffraction pattern is obtained, it is simple to calculate the  $d$ -spacing using the Bragg equation, resulting in information that allows one to find unit cell parameters and the crystal structure.

### 2.5.7.4 Atomic Structure Factor and Scattering Lengths

There are two mathematical expressions both named the 'structure factor'. One is written as  $S(Q)$  which is used mostly for disordered systems and considers the diffraction intensity per atom formed by a single scattering. Systems with long-range order can be defined by the atomic structure factor,  $F_{hkl}$ , considering the number of atoms scattering radiation. This expression is defined as:

$$\text{Structure factor, } F_{hkl} = \frac{\text{amplitude scattered by atoms in the unit cell}}{\text{amplitude scattered by single electron}} \quad \text{Equation 2.13}$$

$F_{hkl}$  can be defined by other quantities such as the atomic scattering factor,  $f$ , and Miller indices. The atomic scattering factors can be defined by Equation 2.14, and it describes a single atoms scattering power. This factor depends on the atoms element in question, the angle of scattered radiation and the type of radiation.<sup>40</sup>

$$\text{Atomic scattering factor, } f = \frac{\text{amplitude scattered by atom}}{\text{amplitude scattered by a single electron}} \quad \text{Equation 2.14}$$

When the scattering angle is zero, the scattered amplitude is the contribution from all  $Z$  electrons where  $f = Z$ . When the scattering angle increases,  $f$  drops below  $Z$  due to destructive interference between the electrons scattered waves, and so they are out-of-

## 2. Experimental Procedures and Characterisation Techniques

phase, Figure 2.20. A fall in intensity can be seen in the case of XRD for species with larger radii due to more opportunities for destructive interference to take place.

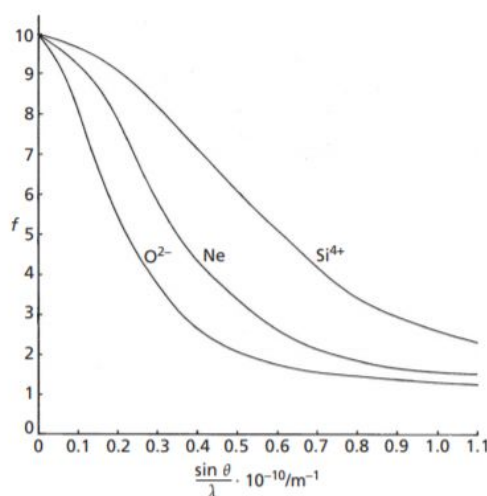


Figure 2.20. Atomic scattering factors,  $f$ , plotted as a function of scattering angle expressed in terms of  $\sin \theta/\lambda$ . Atoms with a higher  $Z$  (such as silicon, Si) have higher scattering factors at given angles and all the scattering factor of all atoms taper off with the increase in scattering angle. This figure has been adapted from Figure 9.1 in reference 40.

On the other hand, in neutron diffraction, electrons do not experience a fall in the scattering factors. This is due to neutrons having a larger wavelength than compared to electrons which render them indifferent to electronic distribution. Thus, the nucleus leads to no drop off in the relative intensity of  $f$ , with increased angles. The sensitivity difference in electronic contribution from both techniques can be used to describe that in X-rays, the atomic scattering factor aligns well with a consistent trend of increasing scattering angle than when compared to neutrons. The corresponding analogous quantity used for neutron diffraction in this respect, is the neutron scattering length,  $b$ .

Scattering length is a measure of the strength of the interaction between the neutron and nucleus. Scattering lengths for neutrons are isotope specific and do not vary with atomic number, e.g. hydrogen ( $^1H$ ) and deuterium (D) have different scattering lengths and so, contribute differently.<sup>40</sup> Scattering lengths can be positive or negative, the opposite signs of each isotope allow the technique to distinguish between them as seen in the case of protium  $^1H$  and D where there is a large difference of  $-3.74$  fm and  $6.67$  fm, respectively.<sup>41</sup> The X-ray structure factors,  $f(\theta = 0)$  are 1 for both  $^1H$  and D.

Figure 2.21 describes the difference in the relationship of both techniques with respect to atomic number. For XRD where the X-ray is scattered by electrons, the atomic

## 2. Experimental Procedures and Characterisation Techniques

scattering factors increase monotonously with increasing atomic numbers. A linear dependence of scattering factors with increasing atomic numbers is established and for neutron diffraction, neutrons eminently scatter by the nucleus and no systematic trend with atomic number is seen – the scattering length does not change monotonously. No atomic form factor is needed to describe the shape of the cloud of electrons for neutrons as the scattering power is not comparable to X-rays where in this case, the scattering power falls off with the scattering angle.

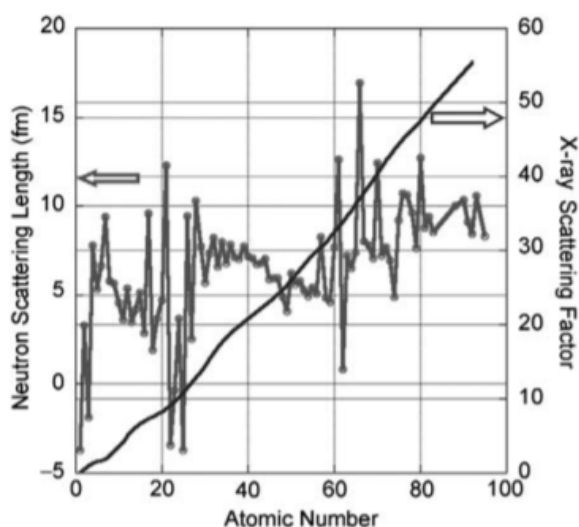


Figure 2.21. The difference in dependence of scattering factor ( $\sin \theta/\lambda = 0.5 \text{ \AA}^{-1}$ ) with respect to the atomic number in XRD compared to the lack of systematic trend on the atomic number for the scattering lengths in neutron diffraction. This figure has been reprinted from reference 44 with the permission from Elsevier.

It is possible for a material to be composed of both a positive and negative scattering length with the advantage of using these materials as sample containers. The net scattering factor is null and such a material is the titanium-zirconium (TiZr) alloy. TiZr is used as sample containers due to a neutron scattering length of 0.00 fm.

In the case of neutron diffraction for ice, a great deal of information is required for the hydrogen atoms, and so, the greater neutron scattering length for deuterium is employed more frequently in neutron diffraction than hydrogen to obtain good quality data.

## 2. Experimental Procedures and Characterisation Techniques

### 2.5.7.5 Characterising Diffraction Patterns of Crystalline Materials

In order to appreciate and understand how the structural information of a material is confined and encoded in a powder diffraction pattern,<sup>45</sup> discrete peaks from the pattern are known to be superimposed over a continuous background.<sup>41</sup> Discounting the background, the structure from a powder pattern can be described by determining the following parameters: intensities, shapes and positions of Bragg reflections:-

- The position of Bragg peaks provides information for the crystal structure in terms of the unit cell parameters ( $a$ ,  $b$ ,  $c$ ,  $\alpha$ ,  $\beta$ ,  $\gamma$ ) and symmetry. Porosity and absorption may influence the pattern and instrumental parameters such as radiation (wavelength), sample alignment and axial divergence of the beam may significantly contribute to the pattern.
- The peak intensity provides the atomic parameters ( $x$ ,  $y$ ,  $z$ ) of the crystal structure and the space group. Again, porosity and absorption may affect the pattern. Preferred orientation may be considered to influence the peak intensity. Peak intensities can be calculated for each individual Bragg reflection from the structural model. The intensities require the knowledge of the coordinates in the unit cell from the atoms together with geometrical and atomic parameters. The intensity of reflections may be used to calculate the positions of atoms and molecules.
- The peak shape determines disorder, defects, and crystallinity in the powder diffraction pattern. Grain size, strain and stress are properties that influence the shape of the peak.

The resultant powder diffraction pattern is the sum of the peak shape functions and a background function. The entire diffraction pattern is thus, used to refine peak-shape functions and all crystallographic data.<sup>41, 45</sup>

### 2.5.7.6 Diffraction Patterns of Liquid and Amorphous Materials

Diffraction can also be observed from amorphous (characteristic of a few atomic or molecular dimensions) and low crystallinity solids, where the final pattern will result in a broad hump or halo in a wide-angle and/or range ( $2\theta$ ) rather than show high intensity, sharp peak maxima as seen for crystalline materials. Thus, the absence of peaks shows a clear lack of structure and no defined shape or form. Limited information can be gathered from the pattern produced from an amorphous solid. Regardless of the peak broadness,

## 2. Experimental Procedures and Characterisation Techniques

the pattern may resemble that of the original crystalline material, where the humps will coincide with the strongest Bragg peak location from the crystalline phase. It can be said that order and lattice are present, but the presence of significant disorder remains.<sup>41</sup>

More recently, total scattering techniques have been introduced for structural studies of amorphous materials which are based on pair distribution function (PDF) analysis. The name itself, ‘total scattering’ echoes that, all of the diffraction pattern is analysed. The name ‘pair distribution’ emphasizes atom pairs or interatomic distances which can be calculated directly from the continuous pattern and are compared with the pattern simulated from a structural model.

### 2.5.8 X-ray Diffraction (XRD)

X-rays can be performed on powdered or single-crystal samples and can be produced *via* two methods. The first, as used in this study to generate X-rays is from a conventional, laboratory-based X-ray tube, where electromagnetic waves are produced from the impact of high energy electrons with a metal target, such as the monochromatic incident beam of copper, Cu ( $K\alpha$ ,  $\lambda = 1.54 \text{ \AA}$ ) or molybdenum, Mo ( $K\alpha$ ,  $\lambda = 0.71 \text{ \AA}$ ) radiation. The second is a more innovative, advanced source of X-ray radiation, known as a synchrotron, where the high-energy electrons are specifically confined in a large storage ring.<sup>45</sup> As the electrons move in a circular motion/orbit they are accelerated towards the centre of the storage ring, hence, emitting radiation of electromagnetic nature. There is no prime difference between the phenomena of using conventional or synchrotron X-ray sources, except for the absence of a continuous photon energy distribution using a synchrotron and the presence of highly intense peaks with a fixed wavelength with a conventional X-ray source.<sup>45</sup>

#### 2.5.8.1 Low-Temperature XRD

Low-temperature XRD was performed for structural characterisation and phase identification. Diffraction patterns were collected using a Mythen 1K linear detector on a Stoe Stadi P diffractometer with Cu  $K\alpha 1$  radiation at 40 kV, 30 mA and monochromated by a Ge 111 crystal. The temperature was maintained using a CryojetHT provided by Oxford Instruments.

Samples prepared in the high-vacuum chamber were transferred into a purpose-built brass holder, equipped with two thin sheets of Kapton® in a LN<sub>2</sub> environment. Kapton® has the ability to withstand temperatures from  $-269$  to  $400^\circ\text{C}$ <sup>46</sup> and was thus,

## 2. Experimental Procedures and Characterisation Techniques

used to ensure data from the diffraction patterns was unaffected. Kapton® can be identified in XRD patterns at  $2\theta = 5.5^\circ$ . Once filled, the sample holder was quickly transferred and mounted into a pre-cooled, LN<sub>2</sub> stream flowing from a cryojet (CryojetHT, Oxford Instruments) combined with the diffractometer. The cryojet here allows the sample temperature to be kept at 95 K, which is well below the threshold temperature for a phase transition of ASW to ice *Isd*.

Diffraction patterns were measured from 95 K over a  $2\theta$  range of 2–60°. Many samples were heated to 160 K or 270 K in steps of 5 K and 10 K depending on the nature of the sample. A computer program, OxCom, was used to control the temperature of the samples when heated.

For the purpose of this study, the main bulk of the XRD results presented here will primarily be amorphous deposits exhibiting no discernible sharp peaks, however, the broad features will see a transformation to ice *Isd* and further crystalline ice *Ih* upon heating. A typical XRD pattern is displayed in Figure 2.22 which illustrates an as-made pure ASW deposit upon thermal annealing. Both Figure 2.22 and Figure 2.23 show features of amorphous H<sub>2</sub>O that are highly discernible in the diffraction patterns from 95 K up to 140 K confirming the amorphous nature of the deposit. Due to difficulty transferring the sample holder into the stream, the formation of ice *Ih* externally was common. This can be seen by the strong characteristic ‘trident’ peaks. This issue arises due to the condensation of H<sub>2</sub>O in the atmosphere which surrounds the sample and any gas residue from N<sub>2</sub> that is not moisture-free.

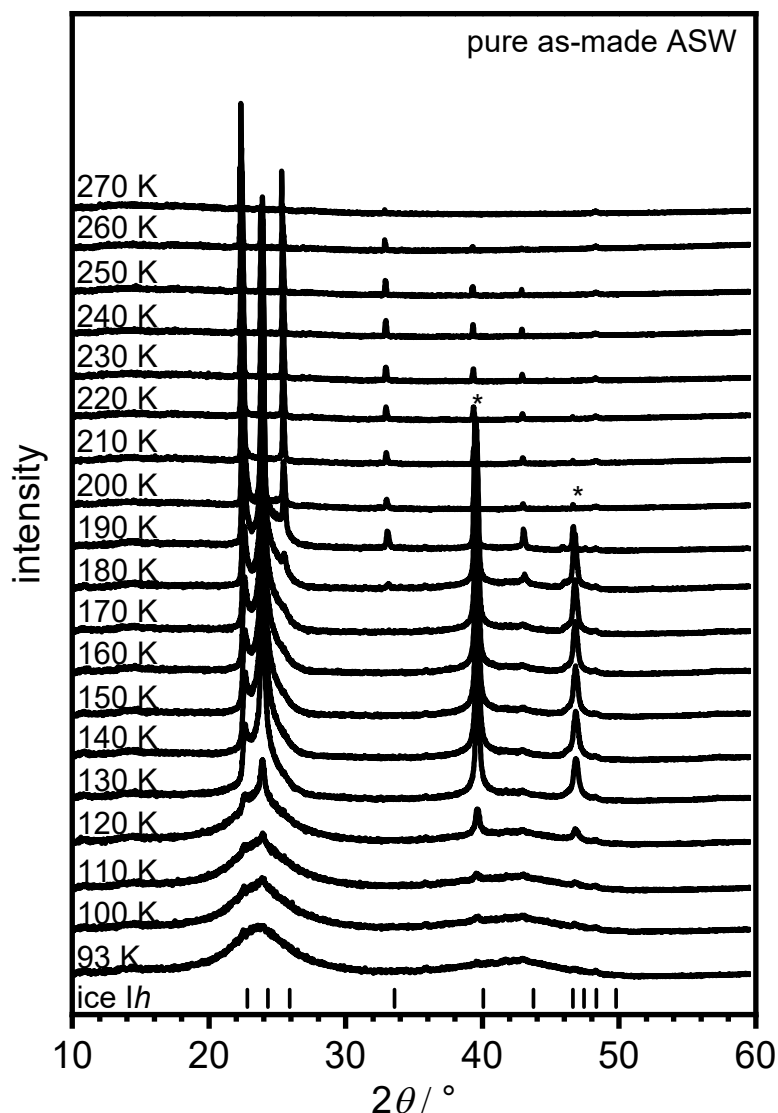


Figure 2.22. XRD patterns ( $\text{Cu K}\alpha$ ,  $\lambda = 1.54 \text{ \AA}$ ) of a fully thermally annealed ASW sample from 95 K to 270 K, this sample was deposited for two-hours and further annealed in the chamber at 125 K and cooled back down to 90 K for sample removal. The entire transition from a purely amorphous deposit is followed through gradually to 270 K, where between this temperature range, ice Isd is approached and further crystallised to ice Ih. Figure 2.23 below depicts these transformations in more detail. Tickmarks indicate the position of Bragg peaks expected for ice Ih.

## 2. Experimental Procedures and Characterisation Techniques

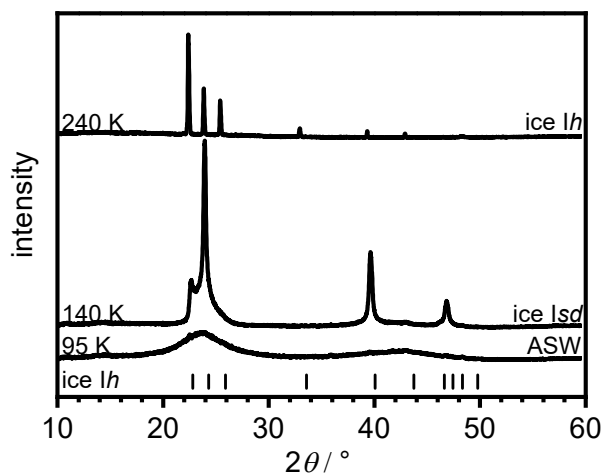


Figure 2.23. XRD patterns ( $\text{Cu K}\alpha$ ,  $\lambda = 1.54 \text{ \AA}$ ) upon heating pure as-made ASW after a two-hour deposition after its recovery under  $\text{LN}_2$  and then transferred into the cryojel at 95 K. The smooth pattern at 95 K indicates a fully amorphous deposit. Tickmarks indicate the position of Bragg peaks expected for ice Ih,  $2\theta = 22.8, 24.3, 25.9, 33.6, 40.1$  and  $46.6^\circ$ . These reflections are absent from the 95 K data but are visible in patterns recorded at higher temperatures. The starting of the transformation of the as-made ASW deposit to ice Isd starts at 140 K. The transition from ice Isd to ice Ih at 240 K is indicated by additional reflections at  $2\theta = 25.9^\circ$  and  $33.6^\circ$ .

Phase identification and quantitative Rietveld analysis can be carried out with the aid of special programs: General Structure Analysis System (GSAS)<sup>47</sup> and PowderCell 2.3.<sup>48</sup> Both software's allow the comparison of calculated diffraction patterns and refinement of crystal structure.<sup>47, 48</sup> In addition, the cubicity of materials can be obtained from analysing an XRD pattern with a computer program, MCDIFFaX, developed in the Salzmann group.<sup>49, 50</sup> Section 2.6 describes GSAS and MCDIFFaX in detail.

### 2.5.9 Neutron Diffraction

Unlike XRD, generating neutrons is a more complex process as neutron diffraction is not so readily available. Neutrons can be generated by two different sources, such that they are generated at a spallation source or a reactor. Neutrons are inherently powerful as they can penetrate matter more greatly than charged particles.

Neutrons can be produced by fission of Uranium-235 by the bombardment of beryllium by  $\alpha$ -particles. The neutrons produced this way are of 2 MeV. A well-renowned neutron source reactor is located in Grenoble, France, named the Institute Laue-Langevin (ILL).<sup>51</sup> This reactor source helps to bring the energy of the neutrons to a lower order, tens of meV and thus, one can use them more efficiently. Moderators are used here to cool the neutrons to lower orders.



## 2. Experimental Procedures and Characterisation Techniques

In a spallation source, protons collide with a heavy metal target and once collided, short potent pulses of high energetic spallation neutrons are created. Neutrons originating from the spallation source thus, arrive in ‘pulses’ rather than continually when in a reactor. In this case, as mentioned, moderators are used to lower the energies of the neutrons to be used directly. Synchrotrons/neutron sources are equipped with liquid helium systems that allow data collection to extremely low temperatures of 4.2 K. The measurements reported in this study, were carried out on The Near and InterMediate Range Order Diffractometer (NIMROD) at the pulsed spallation source at ISIS (Didcot, Oxford, UK). A comprehensive account of the beamline instrument will be provided later (section 2.5.10).

In a typical neutron scattering experiment, (Figure 2.24) a sample is placed in a beam of high energy neutrons to obtain a diffraction intensity pattern. Structures can be studied with a neutron diffractometer where total scattering intensity is measured as a function of the scattering angle. The basic quantity originating from a scattering experiment is to measure the incident particles that appear in several directions and can be defined by a set of spherical polar coordinates,  $\theta$  and  $\phi$ , as described later.

A high-intensity beam of incoming monochromatic radiation with wavelength,  $\lambda$ , impinges on the sample and is scattered by the sample at scattering angles of  $2\theta$  and further detected by the detector.<sup>52</sup> The wavelength of the scattered neutrons is measured with the variable of the magnitude of the momentum transfer vector,  $Q$ , calculated from the wavelength of the incident neutrons, according to:

$$Q = \frac{4\pi}{\lambda} \sin \theta \quad \text{Equation 2.15}$$

$Q$  determines the length scale probed by the diffraction experiments where smaller  $Q$  corresponds to longer distances and larger  $Q$  values correspond to shorter distances. An underlying diffraction signal from an amorphous material will be intrinsically weak and will consist of diffuse scattering features unless the sample is crystalline. Inevitably, some radiation will be present in the diffraction data present from background scattering and not from the sample itself.

## 2. Experimental Procedures and Characterisation Techniques

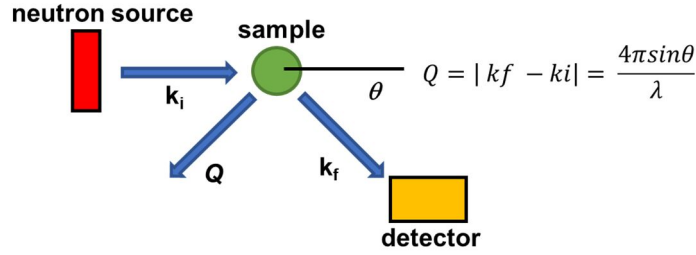


Figure 2.24. Schematic of a typical diffraction set-up. Neutron scattering measures the total structure factor as a function of  $Q$ , where  $Q$  is the magnitude of the momentum transfer vector /  $\text{\AA}^{-1}$  and  $\lambda$  = wavelength.

Samples for neutron diffraction are significantly larger than they are for XRD.<sup>41</sup> A large incoherent scattering from hydrogen is problematic for neutron diffraction studies, thus substituting hydrogen for deuterium can help to clear this problem. Vanadium is the most commonly used background for sample containers in neutron diffraction, as its nuclei scarcely scatter neutrons. No significant Bragg scattering can be detected with the walls of a vanadium container and only a minuscule amount of incoherent scattering is present. In addition, as mentioned earlier, TiZr sample cells are used due to their low coherent, null-scattering properties and relatively high strength. The specific cells used for the neutron diffraction studies in this research are described in detail in Chapter 5.

### 2.5.9.1 Time-of-Flight (TOF)

The spallation source, ISIS, uses the time-of-flight (TOF) diffraction technique. The theory of TOF diffraction is well established in history and the full theory is provided elsewhere.<sup>53, 54</sup> The final and incident wavevectors can be determined as the neutrons arrive at the detector at a given time and all have the same TOF from the source.<sup>52</sup> This is given by:

$$\frac{1+R}{k_e} = \frac{1}{k_i} + \frac{R}{k_f} \quad \text{Equation 2.16}$$

where,  $R$ , is the ratio of scattered to incident flight,  $k_i$ , is the incident wavevector,  $k_f$ , is the scattered neutron wavevector and thus  $k_e$ , is the wavevector when the energy transfer is zero ( $k_i = k_f$ ).<sup>52</sup> Thus,  $k_e$  is determined from the TOF of a specific channel and the elastic momentum transfer is defined as:

$$Q_e = 2k_e \sin\left(\frac{\theta}{2}\right) \quad \text{Equation 2.17}$$

It must be noted that diffraction from glasses or liquids is reported as this  $Q$  value, but they contain contributions from a range of energy transfers and  $Q$  values. When  $R = 0$ , a

## 2. Experimental Procedures and Characterisation Techniques

zero scattered flight path, it takes zero time for the neutrons to reach the detector and the TOF fixes the incident wavelength so that  $k_i = k_e$ .<sup>52</sup>

### 2.5.9.2 Scattering Vector

The data in reciprocal space is what is measured in a diffraction experiment, this is often referred to as  $Q$ -space. On the other hand, radiation from the atoms' nuclei is scattered in real space and thus, these two spaces are related by a FT.

The scattering vector in reciprocal space,  $Q$  can be expressed in terms of wave-vectors, such that,  $k_i$  and  $k_f$  are the incoming and final wave-vectors, respectively, as illustrated in Figure 2.25.  $Q$  can be described in terms of  $Q = k_i - k_f$ , the difference between both the incident and scattered wave-vectors. In this case, both the wave-vectors are equal, and the process is thus, elastic.

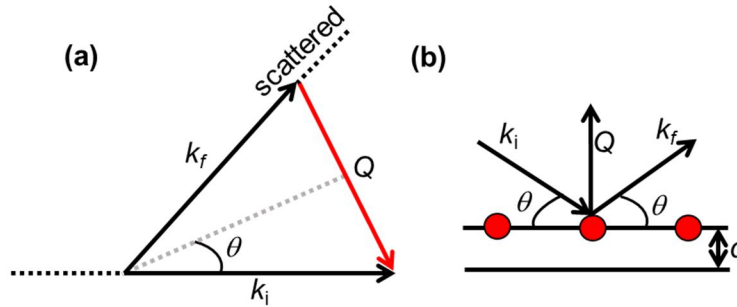


Figure 2.25. Schematics of (a) an expanded scattering triangle and (b) the scattering triangle shown with respect to diffraction conditions where 'd' is the interplanar d-spacing and  $Q$  is drawn perpendicular to these planes.

The incident waves and scattered waves have equal kinetic energy, and the scattering atom is fixed into position. The magnitude of  $Q$  when combined with Bragg's law, can be defined as  $Q = \frac{4\pi \sin \theta}{\lambda}$ , where  $\lambda$  is the incident neutron wavelength impinging on the sample as mentioned previously.

### 2.5.9.3 Self and Distinct Scattering

Neutron diffraction techniques measure the differential cross section (DCS) that is proportional to the structure factor of monoatomic systems or the weighted sum of partial structure factors for a polyatomic system.<sup>52</sup> The DCS for total diffraction can be expressed as two contributions of self and distinct scattering as given by Equation 2.18:<sup>52</sup>

$$DCS = \left( \frac{d\sigma}{d\Omega} \right)_{total} = I(Q) + \langle \bar{b}^2 \rangle - i(Q) \quad \text{Equation 2.18}$$

## 2. Experimental Procedures and Characterisation Techniques

where  $I(Q)$  is the intensity in a neutron scattering experiment,  $\langle \bar{b}^2 \rangle$  is the self-scattering term and  $i(Q)$  is the distinct scattering term. Self-scattering is a  $Q$ -dependent constant, and the self-scattering term arises from correlations between an atom and itself. On the other hand, the distinct scattering term arises from the correlation or interference between two distinct and different atoms.<sup>52</sup> Information about the interatomic distances, and thus, the structure can be determined from the distinct scattering term.<sup>52, 55</sup>

### 2.5.9.4 Coherent and Incoherent Scattering

Each and every element and every isotope of each element consists of coherent and incoherent scattering lengths, defined as  $b_{coh}$  and  $b_{inc}$ , respectively.<sup>52</sup> They are expressed as:

$$b_{coh} = \langle b \rangle \quad \text{Equation 2.19}$$

$$b_{inc} = (\langle b^2 \rangle - \langle b \rangle^2)^{\frac{1}{2}} \quad \text{Equation 2.20}$$

The coherent term (Equation 2.19) involves the correlations between the positions of the nucleus,  $i$ , at time =  $t$  and nuclei,  $j$ , at time = 0. The terms,  $i$  and  $j$  are the same nucleus, however, for large nuclei, occasionally they are not the same. Therefore, the coherent scattering of a sample gives rise to interference, which in turn, provides structural information. Incoherent scattering is dependent upon correlations arising from the same nucleus at different times and thus, no interference effects are produced.

During diffraction measurements, incoherent scattering provides a structureless background to the signal and coherent scattering is the most useful measurement. Coherent scattering lengths of zero can be achieved for example, by using mixed alloy sample cells made from niobium (Nb), titanium (Ti), and zirconium (Zr). They are known as null-scatterers and the signal arising from these alloys are heavily dominated by incoherent scattering. Their specific composition ensures no contribution to the measured signal is provided by coherent scattering. They are most commonly used to produce sample cans for neutron diffraction. In addition, hydrogen ( $^1\text{H}$ ) and deuterium (D) have a negative and positive neutron scattering length ( $-3.74$  fm and  $+6.67$  fm), respectively, and deuterium is used more frequently due to its low incoherent cross-section, rendering it a prime material for use in neutron diffraction.

## 2. Experimental Procedures and Characterisation Techniques

### 2.5.9.5 Scattering Geometry – The Differential Cross Section (DCS)

During a scattering experiment, incident neutrons are scattered by the sample and their rate of arrival occurs in different directions, defined by the spherical polar coordinates,  $2\theta$  and  $\phi$  into the detector, subtending a small angle,  $\Delta\Omega$ , in steradians (sr).<sup>41</sup> This is illustrated in Figure 2.26. The ratio between the number of particles deflected per unit solid angle divided by the number of incident particles per unit area of the beam is known as the differential cross section (DCS),  $d\sigma/d\Omega$ , with SI units of  $\text{m}^2 \text{sr}^{-1}$ .<sup>41</sup> Figure 2.26 depicts how the DCS is calculated.

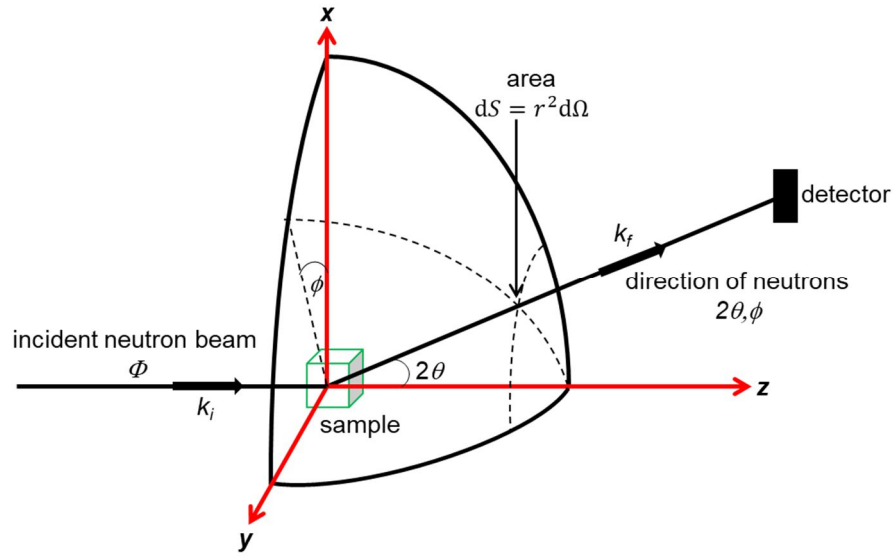


Figure 2.26. Scattering experiment geometry illustrating the incident neutron beam ( $k_i$ ) hitting the sample (represented by the green cube) and further, the neutrons are scattered into a small solid angle of  $d\Omega$  in the direction of polar coordinates,  $\theta$  and  $\phi$ .

The neutrons scattered in the direction of  $\theta$  and  $\phi$  into the solid angle,  $d\Omega$ , given by the DCS can be written as:

$$\left(\frac{d\sigma}{d\Omega}\right)_{tot} = \frac{R_{total}}{\Phi d\Omega} \quad \text{Equation 2.21}$$

where  $R_{total}$ , is the number of scattered neutron per second into the solid angle,  $d\Omega$ , and direction,  $\theta$  and  $\phi$ . The incident flux,  $\Phi$ , from an incoming stream of particles from neutrons, is defined by their number per unit time and per unit area which is perpendicular to the flow in SI units of  $\text{m}^{-2} \text{s}^{-1}$ .

The total DCS,  $\left(\frac{d\sigma}{d\Omega}\right)_{tot}$  can be represented as the partial DCS,  $\frac{d^2\sigma}{d\Omega dE'}$  as:

$$\frac{d\sigma}{d\Omega} = \int_0^\infty \frac{d^2\sigma}{d\Omega dE'} dE' \quad \text{Equation 2.22}$$

## 2. Experimental Procedures and Characterisation Techniques

And akin to this, the total scattering cross-section,  $\sigma$ , in terms of the DCS,  $\left(\frac{d\sigma}{d\Omega}\right)$  can be written as:

$$\sigma_{total} = \int_{all\ directions} \frac{d\sigma}{d\Omega} 2\pi \sin\theta d\theta \quad \text{Equation 2.23}$$

The DCS designates the cross-section (barns,  $b$ ) that is normalised by the solid angle ( $1/4\pi$ , steradian<sup>-1</sup>) and number of atoms in the beam (atom<sup>-1</sup>).<sup>41, 52</sup> The average DCS level is obtained and given by,  $\langle b^2 \rangle$ , which can subsequently be separated into incoherent and coherent scattering contributions as shown above. These are normalisation factors. Both factors  $\langle b^2 \rangle$  and  $\langle b \rangle^2$ , can be calculated easily due to the nature of the average scattering lengths of the atoms present in the sample. The DCS can also be defined with respect to the structure factor,  $S(Q)$ :

$$\text{DCS} = \left(\frac{d\sigma}{d\Omega}\right) = \langle b \rangle^2 [S(Q) - 1] + \langle b \rangle^2 \quad \text{Equation 2.24}$$

The scattering cross-section is the factor that defines how much or how little a sample scatters neutrons or X-rays compared to a reference value.<sup>52</sup> Once formulated as a cross-section, the cross-section describes the probability of a scattering event. In Equation 2.24,  $\sigma$  is the cross-section and  $\Omega$  is defined as the solid angle in the scattering. Not all scattered neutrons are measured as they are only measured at a small angle and so they must be normalised and said to be per an angle ( $\Omega$ ).<sup>41</sup>

### 2.5.9.6 Method of Total Scattering and Correlation Functions

A more thorough treatment for the analysis of correlation functions and total scattering methods has been provided elsewhere.<sup>56, 57</sup> As mentioned earlier, in general, crystallographic analysis, diffuse scattering intensity and Bragg peaks are treated separately, whereby, the structure can be determined from the position and intensity of the Bragg peaks. Additional information can be obtained by investigating the diffuse scattering contributions. This approach is appropriate when small deviations from long-range order are present, however, when amorphous materials are analysed, this approach is not sufficient.

In the upcoming section, an alternative approach of treating the full diffraction pattern including the Bragg and diffuse components will be presented. This approach is called the total scattering technique.<sup>56, 57</sup>

## 2. Experimental Procedures and Characterisation Techniques

### 2.5.9.6.1 Pair Correlation Function and Structure Factors

The site-site pair distribution function (PDF) is construed from the pair correlation function,  $g_{ij}(r)$ , describing how density varies as a function of radial distance,  $r$ , from a reference point and reflecting the probability of finding atoms,  $j$ , from atom  $i$ , as a function of  $r$ . Simply, the  $g_{ij}(r)$  represents correlations between atom pairs in real space as a function of the radial separation,  $r$ . A system with atomic number density is defined as,  $\rho$  and the ideal distribution of atoms can be expressed as Equation 2.25. Thus, the PDF,  $g_{ij}(r)$ , as shown in Figure 2.27, can be defined as the measured distribution divided by the ideal distribution. The PDF is defined as the product of  $\rho(r)$  and the area of a sphere with radius,  $r$ , and therefore proportional to the number of atoms at distance  $r$ , surrounding an atom at the origin.

$$\text{Ideal Distribution} = \frac{4}{3}\pi\rho(r_{\max}^3 - r_{\min}^3) \quad \text{Equation 2.25}$$

where the PDF,  $g_{ij}(r)$ , as shown in Figure 2.27 can be determined by the following:

$$g(r) = \frac{\text{measured distribution}}{\text{ideal distribution}} \quad \text{Equation 2.26}$$

The normalisation of  $g_{ij}(r)$  has two very important characteristics, such that, (i) at low  $r$  distances,  $g_{ij}(r)$  is equal to zero [ $g_{ij}(r) = 0$  as  $r \rightarrow 0$ ], indicating the repulsive natures of atoms within that region and (ii)  $g_{ij}(r)$  tends to 1 as  $r$  increases [ $r \rightarrow \infty$ ,  $g_{ij}(r) = 1$ ].<sup>57</sup> This is where atoms are fully randomised and so the measured distribution starts to converge more towards the ideal distribution of atoms. A representative  $g_{ij}(r)$ , illustrating several peaks and maxima are shown in Figure 2.27 which can be associated with neighbouring coordination shells of atoms. The upper limit of each coordination shell is represented by the trough of each peak at  $r$ .

## 2. Experimental Procedures and Characterisation Techniques

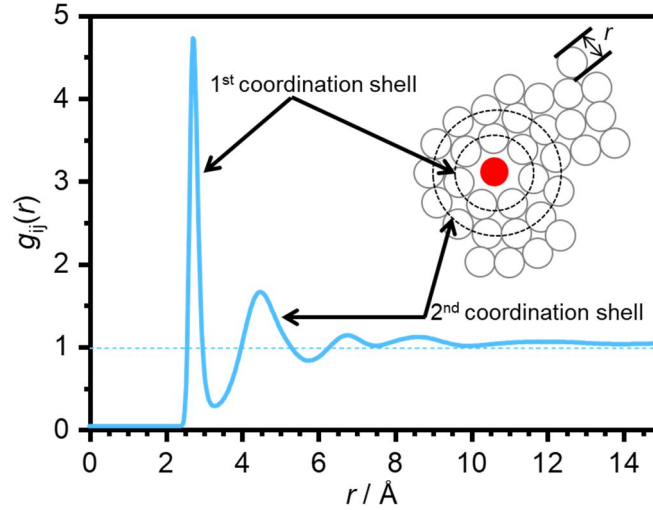


Figure 2.27. Schematic illustration showing the PDF,  $g_{ij}(r)$ , representing how correlations between atom pairs are quantified with dependence on the radial distance and coordination shells.

With liquids, the specific interactions occurring between neighbouring atoms will govern the local structure. The structure can be determined by looking at sharp features in the PDFs, where the total pair distribution function,  $G(r)$ , is the weighted sum of the partials,  $g_{ij}(r)$ . To obtain a set of  $g_{ij}(r)$ , simulations can be run.

When looking out in real space, it is useful to use  $g_{ij}(r)$ . The  $g_{ij}(r)$  is expressed in terms of the real space density function, as defined by the local density of atoms,<sup>58</sup>  $\rho(r)$  as follows:

$$g_{ij}(r) = \frac{\rho(r)}{\rho_0} \quad \text{Equation 2.27}$$

where  $\rho_0$  is defined as the number density of the sample<sup>59</sup> in question. The  $G(r)$  and correlation function,  $T(r)$  are correlated, such that:

$$G(r) = \frac{T(r)}{4\pi r} \quad \text{Equation 2.28}$$

Through Fourier transformation from a structural model, radially averaged pair correlation functions can be obtained and are related to the Faber-Ziman partial structure factors,  $S_{ij}(Q)$ .<sup>41</sup> In real space, these  $S_{ij}(Q)$  are related to the atomic distances,  $g_{ij}(r)$ , via the FT as follows:<sup>41</sup>

$$S_{ij}(Q) = 1 + \frac{4\pi\rho_0}{Q} \int_0^\infty r [g_{ij}(r) - 1] \sin(Qr) dr \quad \text{Equation 2.29}$$

where the total structure factor,  $F(Q)$ , can be determined from the weighted sum of the  $S_{ij}(Q)$  and atomic fractions,<sup>41, 60, 61</sup> expressed as:



## 2. Experimental Procedures and Characterisation Techniques

$$F(Q) = \sum_{i \leq j} (2 - \delta_{ij}) w_{ij} (S_{ij}(Q) - 1) \quad \text{Equation 2.30}$$

The term, ' $\delta_{ij}$ ' is called the Kronecker delta and accounts for 'like' terms where  $i=j$  are not double-counted,  $w_{ij}$  are the weighted factors by which the partial structure factors contribute to  $F(Q)$ <sup>41, 60, 61</sup> such that:

$$w_{ij} = c_i c_j b_i b_j \quad \text{Equation 2.31}$$

where ' $c$ ' is the atomic fraction of a different atom,  $i$  or  $j$  and ' $b$ ' is the neutron scattering lengths.

$F(Q)$  is closely correlated to  $G(r)$  by Fourier sine transform, which can be given by Equation 2.32, where  $F(Q) = Q[S(Q)-1]$ <sup>62</sup> in reciprocal space:

$$G(r) = \frac{1}{(2\pi)^3} \int_0^\infty 4\pi Q^2 [F(Q)] \frac{\sin(Qr)}{Qr} dQ \quad \text{Equation 2.32}$$

The following equation displays how  $G(r)$  includes  $g_{ij}(r)$ . The closely related FT relationship from Equation 2.32 above can be used to interconvert partial structure factors,  $S_{ij}(Q)-1$  and the partial pair distribution functions,  $g_{ij}(r)-1$ .

$$G(r) = \sum_{i,j}^n c_i c_j b_i b_j [g_{ij}(r) - 1] \quad \text{Equation 2.33}$$

Thus,  $S_{ij}(Q)$  and then  $g_{ij}(r)$ , can be extracted for different atom pairs.<sup>61</sup>

Peaks found in  $g_{ij}(r)$ , as shown in Figure 2.27, represent atoms present in coordination shells, and is expected to be zero for a distance,  $r <$  particle diameter where ripples are caused by truncation artefacts from the FT of  $S_{ij}(Q)$ .<sup>52</sup>

The main aim for structural studies is to extract a real space function representing the correlations between atom pairs,  $g_{ij}(r)$  as a function of  $r$ , between atom pairs under investigation within a given volume. The EPSR method is used to obtain a structural model best fitted and aligned to the experimental data. Thus, from the model,  $G(r)$  is obtained which is the Fourier transformation of  $F(Q)$  and fitted to the experimental  $F(Q)$  enabling this type of structural analysis. The derivation for these equations is provided below.

## 2. Experimental Procedures and Characterisation Techniques

### 2.5.9.6.2 Derivation of the Scattering Theory

The foundation of the total scattering method is described by the total scattering structure-function,  $S(Q)$ , which can be obtained after normalisation and correction of the scattering intensity originating from the sample. The total scattering structure factor,  $S(Q)$  contains both the Bragg and diffuse intensity and thus, the intensity distribution from a sample is a continuous function of the scattering vector,  $Q$ . There are many conflicting names in different communities and a good overview has been presented by Keen.<sup>56</sup> Thorough comparisons of the nomenclature of total scattering with respect to different correlation functions have been given by Keen.<sup>56</sup>

The  $Q$ -dependent scattering amplitude,  $\Psi(Q)$ , from a set of  $i$  atoms located at  $r_i$  can be described by:<sup>59, 62</sup>

$$\Psi(Q) = \sum_i f_i(Q) \exp(iQ \cdot r_i) = \sum_i \Psi_i \quad \text{Equation 2.34}$$

where  $f_i$  is the scattering amplitude of atom  $i$ ,  $r_i$  is the position of the  $i^{\text{th}}$  atom.<sup>59</sup> In the case of neutron scattering,  $f_i$  equals the  $Q$ -independent coherent neutron scattering length and in the case of X-ray scattering,  $f_i$ , corresponds to the  $Q$ -dependent atomic form factor.

Incoherent scattering from these atoms is described by the total sum of intensities defined as:

$$\begin{aligned} I_{inc} &= \sum_i \Psi_i^* \Psi_i = \sum_i f_i^*(Q) f_i(Q) \\ &= \sum_{\alpha} N_{\alpha} f_{\alpha}^*(Q) f_{\alpha}(Q) = N \sum_{\alpha} c_{\alpha} f_{\alpha}^*(Q) f_{\alpha}(Q) \\ &= N \langle f^2 \rangle \end{aligned} \quad \text{Equation 2.35}$$

where  $N$  is the total number of atoms and  $N_{\alpha}$  is the number of atoms of type  $\alpha$  and the concentration of species of  $\alpha$  is given by  $c_{\alpha} = N_{\alpha}/N$ . The sum over  $\alpha$  is over the different species of atoms in the sample. Asterisks in the equation derivation denote the complex conjugate. The average of the scattering power is given by:-

$$\langle f \rangle = \sum_{\alpha} c_{\alpha} f_{\alpha}$$

and

## 2. Experimental Procedures and Characterisation Techniques

$$\begin{aligned}\langle f \rangle^2 &= \frac{1}{N^2} \sum_{ij} f_j^* f_i \\ &= \sum_{\alpha\beta} c_\alpha c_\beta f_\alpha^* f_\beta\end{aligned}\quad \text{Equation 2.36}$$

The coherent scattering is given by,  $\Psi^* \Psi$  and thus, defined as:

$$I_c = \sum_{i,j} f_j^* f_i \exp(i\mathbf{Q} \cdot \mathbf{r}_{ij}) \quad \text{Equation 3.37}$$

Where  $r_{ij}$  is the distance between two scattering atoms. The self-scattering contribution, for the case,  $i=j$ , contains no structural information and can be separated:

$$\begin{aligned}I_c &= \sum_i f_i^* f_i + \sum_{i \neq j} f_j^* f_i \exp(i\mathbf{Q} \cdot \mathbf{r}_{ij}) \\ &= N\langle f^2 \rangle + \sum_{i \neq j} f_j^* f_i \exp(i\mathbf{Q} \cdot \mathbf{r}_{ij})\end{aligned}\quad \text{Equation 2.38}$$

where Equation 2.35 is used and an expression for the discrete scattering intensity,  $I_d$ , for atoms  $i \neq j$  is given by:

$$\begin{aligned}I_d &= I_c - N\langle f^2 \rangle \\ &= \sum_{i \neq j} f_j^* f_i \exp(i\mathbf{Q} \cdot \mathbf{r}_{ij})\end{aligned}\quad \text{Equation 2.39}$$

An expression for  $S(\mathbf{Q})$  is required which is now defined as:  $I_c/(N\langle f \rangle^2) - \langle (f - \langle f \rangle)^2 \rangle / \langle f \rangle^2$ .

To obtain  $S(\mathbf{Q})$  from Equation 2.38, the intensity must be normalised by the number of scatterers,  $N$ :

$$\frac{I_c}{N} = \langle f^2 \rangle + \left(\frac{1}{N}\right) \sum_{i \neq j} f_j^* f_i \exp(i\mathbf{Q} \cdot \mathbf{r}_{ij}) \quad \text{Equation 2.40}$$

Subtracting the self-scattering yields:

$$\frac{I_c}{N} - \langle f^2 \rangle = \left(\frac{1}{N}\right) \sum_{i \neq j} f_j^* f_i \exp(i\mathbf{Q} \cdot \mathbf{r}_{ij}) \quad \text{Equation 2.41}$$

And thus, by normalising by  $\langle f \rangle^2$ , the following expression is obtained, defining the structure factor,  $S(\mathbf{Q})$ :

$$I_c/(N\langle f \rangle^2) - \frac{\langle f^2 \rangle}{\langle f \rangle^2} = [1/(N\langle f \rangle^2)] \sum_{i \neq j} f_j^* f_i \exp(i\mathbf{Q} \cdot \mathbf{r}_{ij}) \quad \text{Equation 2.42}$$

## 2. Experimental Procedures and Characterisation Techniques

$$\begin{aligned}
 S(Q) - 1 &= I_c / (N\langle f \rangle^2) - \frac{\langle f^2 \rangle}{\langle f \rangle^2} \\
 &= \frac{I_d}{N\langle f \rangle^2} = 1 / (N\langle f \rangle^2) \sum_{i \neq j} f_j^* f_i \exp(i\mathbf{Q} \cdot \mathbf{r}_{ij}) \quad \text{Equation 2.43}
 \end{aligned}$$

$S(Q)$  defined in this way is direction-dependent and if the scattering is isotropic as in amorphous materials, then  $S(Q)$  will depend only on the magnitude of  $Q$  and not the direction. Consequently, we can define the reduced structure factor as a scalar quantity,  $F(Q) = Q[S(Q) - 1]$ . The inverse FT of  $F(Q)$  yields the pair correlation function,  $G(r)$ , and due to  $F(Q)$  being an odd function, the Fourier sine transform can be used as previously mentioned.

For  $G(r)$  as defined in Equation 2.32, it is clear that this function oscillates about 0 with the limits of large  $r$  and so as to  $r \rightarrow 0$ , this function behaves as  $-4\pi\rho_0 r$ . A benefit of the correlation function is that  $G(r)$  is the direct FT of the structure factor and the random uncertainties in the data will be constant in  $r$ . If fluctuations decrease with increasing  $r$ , it suggests that the simulated model and fit are getting better at long distances.

The PDF has well-defined atom pairs that are a reflection of the exact shape of the pair correlation function.<sup>62</sup> The partial radial distribution function,  $t_{ij}(r)$ , is calculated from  $g_{ij}(r)$  according to  $t_{ij}(r) = 4\pi r^2 \rho g_{ij}(r)$  which means that the area under  $t_{ij}(r)$  yields coordination numbers (CN).

The disadvantage of  $t_{ij}(r)$  is its divergence with increasing  $r$ . Structural studies using the PDF can be orientationally averaged over angular coordinates however, the PDF can only provide a limited amount of information of the local structure in the system. Due to contributions from high/low probability in different parts of the structure, some structural information is lost.<sup>63</sup> PDFs only provide structural pictures of liquids of spherical particles, however, these limitations can be overcome by determining the spatial density functions (SDFs).<sup>63, 64</sup>

The PDF was used to study amorphous ices such as low-density amorphous ice (LDA), very-high density amorphous ice (vHDA) and high-density amorphous ice (HDA).<sup>61</sup> The PDF of amorphous ices, not unexpectedly, resembles the PDF of liquid H<sub>2</sub>O more than crystalline polymorphs. One extreme difficulty with amorphous ices is their non-equilibrium nature and they possess a slow relaxation time.<sup>65</sup> The structure of amorphous ices cannot be defined with space groups or long-range ordering. Thus, the  $S_{ij}(Q)$  or  $t_{ij}(r)$  are used to define and analyse short and intermediate-range ordering for

## 2. Experimental Procedures and Characterisation Techniques

amorphous ices. These parameters are obtained by neutron scattering analysis analysed by means of the EPSR method.<sup>65-68</sup> A summary of notations and definitions for the correlation functions are provided in Table 2.1 below.

*Table 2.1. Brief summary of the correlation functions as presented in this thesis, displaying the notation, definition, and corresponding equation.*

Notation	Definition	Equation
$S_{ij}(Q)$	partial structure factor	$S_{ij}(Q) = 1 + \frac{4\pi\rho_0}{Q} \int_0^\infty r[g_{ij}(r) - 1] \sin(Qr) dr$
$F(Q)$	reduced structure function	$F(Q) = Q[(S(Q)-1)]$
$G(r)$	total pair correlation function	$G(r) = \frac{1}{(2\pi)^3} \int_0^\infty 4\pi Q^2 [F(Q)] \frac{\sin(Qr)}{Qr} dQ$

Atoms in a monatomic system are chemically identical and it is assumed that the scattering length and atomic position do not correlate in the sample. In the case of a polyatomic system, a given chemical species will have different isotopes and thus, different scattering length distributions. Different chemical species will have different chemical bonding (interatomic interactions) and do not occupy each other's sites.<sup>55</sup> In a monatomic system, single dimensionless structure factors are obtained whereas, in a polyatomic system, several partial structure factors are considered.

Thus, in this thesis, using the technique of isotopic substitution offers this additional information when gathering data from different atom pairs. It is assumed that substituted atoms in a material with isotopes of different scattering lengths do not affect the structure.<sup>62</sup> Any interference to the data is perturbed by substitution and thus, several datasets where atom types contribute to the interference can be subtracted and interference can be reduced. With different scattering lengths,  $S_{ij}(Q)$  and  $g_{ij}(r)$  for the various atom pairs may be extracted.

### 2.5.9.7 Isotopic Substitution

Techniques such as isotopic substitution offers the possibility of obtaining a set of partial structure factors from total diffraction data, allowing in-depth analysis for the correlations between specific atom types in the material.

In more detail, isotopic substitution is a unique technique in which a standard procedure is used to elucidate structural information contained within multicomponent

## 2. Experimental Procedures and Characterisation Techniques

disordered materials.<sup>69</sup> Atoms within a material are substituted with different isotopes with different scattering lengths. It is assumed that the isotopic composition has no effect or impact upon the structure and so, measurements of different materials with different scattering lengths give rise to a sequence of diffraction patterns. Several datasets may be subtracted to reduce the amount of interference and with different scattering lengths, associated PDFs from site-site correlations can be extracted.

As previously mentioned, a simple fact is implemented: the measured scattering structure factor can be represented as the weighted sum of partial structure factors where the weights are determined by the scattering length and atomic fraction from each component. In simpler terms, it is possible to convert total diffraction patterns from disordered or liquid materials into a set of partial structure factors which, in turn, define the correlations between any given specific atoms in the material.<sup>68</sup>

A comparable and analogous process to isotope substitution as used in neutron diffraction studies is accessible for X-rays which uses the inconsistent change of the form factor near an absorption edge.<sup>68, 70</sup> It is possible to combine neutron and X-ray diffraction (XRD) data.

The isotopic substitution technique is very powerful for structural characterisation of disordered materials and the increased number of experimental data sets will significantly decrease the S/N ratio. For this work, full advantage of the differences in scattering lengths of  $^1\text{H}$  ( $-3.74$  fm) and  $\text{D}$  ( $+6.67$  fm) were employed. ASW was substituted by means of using water ( $\text{H}_2\text{O}$ ), heavy water ( $\text{D}_2\text{O}$ ) and a 50/50 mix of  $\text{H}_2\text{O}$  and  $\text{D}_2\text{O}$  as HDO.  $\text{C}_{10}\text{H}_{16}$  and deuterated  $\text{C}_{10}\text{H}_{16}$  ( $\text{C}_{10}\text{D}_{16}$ ) were also used which were necessary to obtain low S/N ratio neutron data and investigate the kinetic formation of clathrate hydrates.

### 2.5.9.8 Low-Temperature Neutron Diffraction

ASW samples codeposited with  $\text{C}_{10}\text{H}_{16}$  were prepared for use in  $\text{Ti}_{0.68}\text{Zr}_{0.32}$  alloy cells as mentioned in upcoming Chapter 5. The sample temperature was regulated by a closed cycle refrigerator (CCR). The raw diffraction data from the NIMROD beamline were run through the Gudrun $N$  software<sup>52, 54, 71</sup> (Gudrun-2017-10) to allow for routine reduction of total scattering data and is the principal software used for disordered materials instruments. Refinement of the data was carried out by the Empirical Potential Structure Refinement (EPSR) method.<sup>67, 68</sup>

## 2. Experimental Procedures and Characterisation Techniques

### 2.5.10 Spallation Source and Instrumentation

The ISIS neutron and muon source is a spallation source. This type of neutron source makes use of protons being accelerated in a synchrotron to sufficiently very high energies ( $\sim 800$  MeV at ISIS) where they collide with a heavy metal target producing excited nuclear states. These highly excited states may decay immediately or after delay. The maximum energy of neutrons, in this case, corresponds to the energy on the proton impinging onto the beam, rendering the spallation source neutrons more highly energetic when compared to neutrons at a reactor source. The prime benefit of a spallation source is its safety. At the touch of a button, no nuclear fuel is produced and the energy can be measured from the time-of-flight (TOF) to the detector when the proton beam is pulsed into shorter pulses.<sup>72</sup>

TS2, at ISIS, is a 10 Hz neutron spallation source capable of delivering an exceedingly optimised neutron target and a moderator configuration. TS2 distributes and delivers neutrons at a 100 ms time frame between pulses of neutrons over a wide spectral range with wavelengths typically in the range of 0.04 to  $>12$  Å. TS2 has a significantly heightened long-wavelength flux compared to the 50 Hz target station supplied from the facility. The expansion and development of ISIS has provided novel, innovative instrumentation, providing advantages of many orders of magnitude in terms of performance investigating nanoscale phenomena and dynamics of structures.

#### 2.5.10.1 Instrumentation

Under current operating conditions, NIMROD, (Figure 2.28) a total scattering instrument is designed to allow length scale access from interatomic ( $<1$  Å), i.e., the quantum world of atoms through access to mesoscopic ( $>300$  Å) i.e., classical world ranges. It is ingeniously optimised for structural studies of liquids and disordered materials in this continuous scale in a single measurement while supporting subatomic distances.<sup>73</sup> This aptitude is achieved by equally, low, and wide-angle arrays of high-efficiency neutron scintillation, in particular, zinc sulfide (ZnS) based detectors ranging and covering wide angles from  $2\theta = 0.5$ – $40^\circ$ . In combination with longer wavelengths, routine instantaneous  $Q$  can be collected from a critical range of 0.02 to  $50 \text{ Å}^{-1}$ . This is delivered by the combination of a hybrid hydrogen and a  $\text{H}_2\text{O}$  moderator which gives rise to higher and improved fluxes during the collection of shorter wavelengths.<sup>73</sup> This TOF spectrometer has detectors over low scattering angles which has been designed to reduce the influence of inelastic perturbations.

## 2. Experimental Procedures and Characterisation Techniques

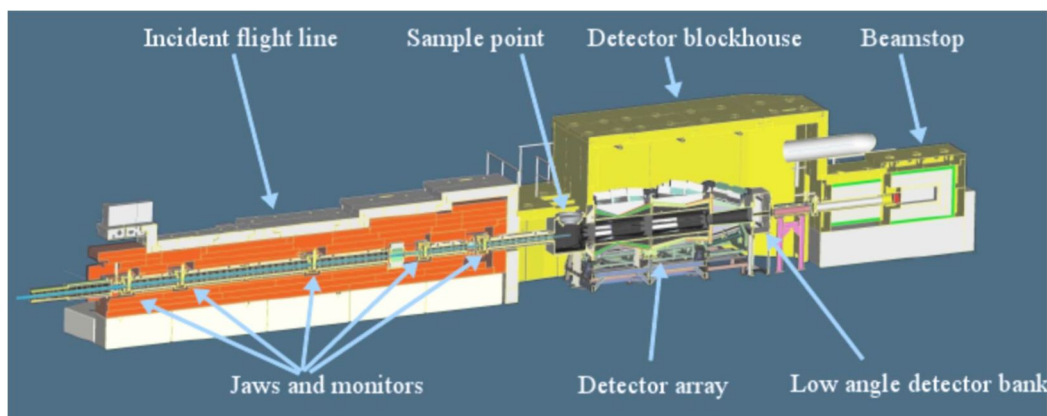


Figure 2.28. NIMROD instrument displaying the main components from which it has been designed.<sup>73</sup> This figure has been reprinted from reference 73 with the permission of AIP Publishing.

The complex capability of the NIMROD instrument bridges the gap between traditional Small-Angle Neutron Scattering (SANS) and wide-angle neutron scattering *via* the use of a standard calibration procedure for the full length of the  $Q$  scale. To maximise the utility of NIMROD, forward scattering geometry is used to reduce inelasticity effects<sup>54</sup> (for light elements), using high energy and shorter wavelengths to obtain high structure resolution and full use of the longer wavelengths (increasing limits of accessible correlation lengths). The shorter wavelengths are ideal for isotopic substitution experiments mainly for hydrogen/deuterium (H/D) which is a strength of this instrument and thus neutron scattering methods.<sup>73</sup>

NIMROD is somewhat similar to the SANDALS instrument (The Small-Angle Neutron Diffractometer for Amorphous and Liquid Samples) where both scattered, and incident flight paths are under vacuum. However, NIMROD provides accurate control of the beam footprint on the samples as it involves an incident collimator with a sequence of adjustable beam defining apertures. There are a staggering number of 2,268 detectors contained in a humidity and large temperature-controlled blockhouse. Out of these detectors, 756 remain in the low-angle range banks with scattering angles of  $2\theta = 0.5$ – $2.2^\circ$ . The other 1,512 detectors remain in seven banks with scattering angles of  $2\theta = 3.5$ – $40^\circ$ , all arranged in Debye-Scherrer cones. Compared to SANDALS, NIMROD has higher neutron fluxes and is amenable for time-dependant investigations with a large amount of data being acquired in a short amount of time and beam.<sup>73</sup>

To conclude, an essential design advantage of NIMROD is to permit simultaneous measurements from atomistic and mesoscale correlations within any given system;



## 2. Experimental Procedures and Characterisation Techniques

scientific areas such as two-dimensional nanomaterials, micellar and confined systems and crystallisation of polymers can be studied. NIMROD's capability has allowed unprecedented *in situ* analysis of dynamical systems such as heterogeneous catalysis, setting of dental cements and most importantly for this thesis, the structural evolution of amorphous ice upon heating.

### 2.5.10.2 Instrumentation Components

This section will aim to provide a brief, simple, yet wide-ranging dissection of the NIMROD instrument. A more heavily detailed overview is provided by Bowron *et al.*<sup>73</sup>

### 2.5.10.3 Neutron Source

The moderator of the instrument is a combination of two compartments, (i) solid methane (CH<sub>4</sub>) filled moderator and (ii) liquid hydrogen filled at ~17 K moderator.<sup>73</sup> The CH<sub>4</sub> filled part backs up against the second compartment. A H<sub>2</sub>O filled pre-moderator surrounds the hydrogen moderator to improve neutron coupling to the target. A total neutron size of 19.5 cm (width) and 11.5 cm (length) can be viewed by the sample so that a larger flux can be obtained in a short wavelength region. The combination of the moderator and pre-moderator allows neutrons to be delivered from ranges of 0.04 to 10 Å when combined with the 10 Hz operation of the target station.<sup>73</sup>

### 2.5.10.4 Incident Neutron Flight Path

To obtain epithermal, thermal, and cold neutrons in every neutron pulse and stringent incident beam control, a collimated neutron flight path is utilised. Control of beam characteristics is achieved by employing a set of six collimating jaws that are carefully positioned along the flight path. The final set is positioned so that it acts to clean up the residual beam before it approaches the sample. The material that these motorised jaws are produced from need to be able to withhold and deal with the full range of neutron energy. Nimonic alloy and sintered boron carbide are used. The latter absorbs cold and thermal neutrons while the former scatters the high energy neutrons and reduces their energy. For data normalisation, neutron beam monitors are placed after five sets of jaws in the flight path. These monitors contain vanadium scattering foil which can intercept the beam profile and most importantly, the full cross-section is captured.<sup>73</sup>

## 2. Experimental Procedures and Characterisation Techniques

### 2.5.10.5 Sample and Secondary Flight Path Vacuum Tank

A large vacuum tank/vessel resides at the heart of the instrument [Figure 2.29(a)]. The vacuum serves to remove parasitic scattering from the air from secondary neutron flight path and from around the sample. The vacuum is critical to minimise background scattering that may contaminate the diffraction pattern and it renders the correction in data analysis virtually impossible. Neutron windows are implemented, providing a wide-angle coverage in the forward scattering geometry with  $2\theta = 0.5$  to  $40^\circ$ . Figure 2.29(b) also illustrates the windows from the samples view and depicts how scattered radiation can be minimised. In addition, collimating vanes are utilised to decrease the risk of increasing levels of background scattering signals.

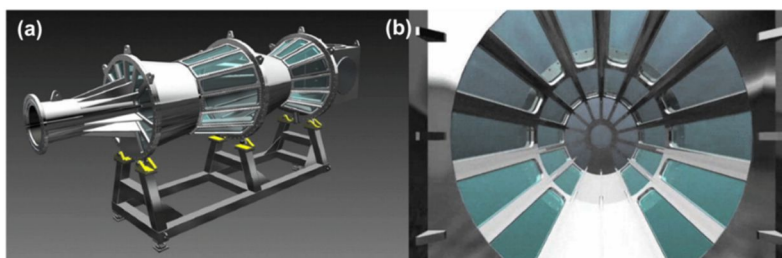


*Figure 2.29. (a) Three-dimensional illustration of the vacuum that is situated at the heart of the instrument providing a clean path for the scattering of neutrons and (b) the forward view of the positioned sample within the large solid angle detector. This figure has been reprinted from reference 73 with the permission of AIP Publishing.*

A circular opening of 40 cm in diameter for experiments allows the sample to be accessed. This benefits many areas of studies which can implement cryostats between the temperature range of 4–300 K, CCR between 10–320 K, and furnaces between 473–1373 K. In turn, NIMROD offers a range of compatible sample cells operating from atmospheric to high and low pressures.<sup>73</sup>

### 2.5.10.6 Detector Array

The detector array and data acquisition electronics (DAE) are vital for the capabilities and performance of the instrument. The different detector modules and elements for wide-angle scattering angles can be found elsewhere<sup>73</sup> and the design for the array of detector modules is shown in Figure 2.30. Nevertheless, each element operates as a neutron detector and are viewed by two photomultiplier tubes. In comparison, the low-angle detector bank is based on ZnS (Ag) scintillation technology. In total, 756 elements are fibre coupled to 120 photomultipliers, allows them to be located in the sample and secondary flight path vacuum tank. Exposure is minimised from these elements to the low-angle scattering background that originates from the neutron windows and vacuum.<sup>73</sup>

## 2. Experimental Procedures and Characterisation Techniques

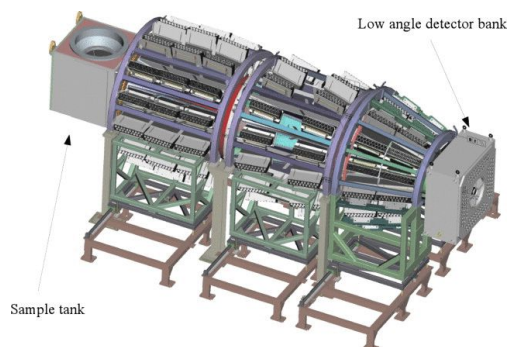


*Figure 2.30. Distribution of detector modules mounted onto NIMROD, with the sample tank and low-angle banks labelled. This figure has been reprinted from reference 73 with the permission of AIP Publishing.*

### 2.5.10.7 Blockhouse

The blockhouse contains the sample, vacuum tank, and array of detector modules. It is constructed from wax-filled steel tanks and has a thickness of 30 cm to shield from background radiation that does not arise from within the instrument and to protect scientists around the instrument itself. The blockhouse has vacuum interlock systems to prevent human radiation exposure. The blockhouse is humidity controlled to  $50 \pm 5\%$  (to ensure performance regardless of weather conditions) and temperature-controlled to a stable  $\pm 1^\circ\text{C}$ .<sup>73</sup>

### 2.5.10.8 Transmission Monitor and Beamstop

The final components of the NIMROD beamline are the transmission monitor and the beam stopper of neutrons. The transmission monitor resides at the exit of the beam in the blockhouse and is based on a thin vanadium foil angled to scatter a small amount of the beam into a ZnS scintillator and thus, viewed by a photomultiplier. The construct of the neutron beamstop is formed of large steel and concrete, wax blocks.<sup>73</sup>

### 2.5.10.9 Calibration and Correction of Raw Data

As shown in Figure 2.31, only a small number of incident neutrons are scattered during an experiment. The remaining are transmitted through the sample and may undergo multiple scattering events or attenuation. The latter involves the sample absorbing the neutron and the former, multiple scattering, involves events where radiation is scattered more than once before it is able to leave the sample. In the case of the work presented in this thesis, the sample is fairly porous and loosely packed and so, the raw diffraction data was corrected for these contributions before the structure factor was yielded. Whereas, in

## 2. Experimental Procedures and Characterisation Techniques

solid samples, the contributions from attenuation, inelastic scattering and multiple scattering are proposed to be insignificant due to a constant atomic structure.

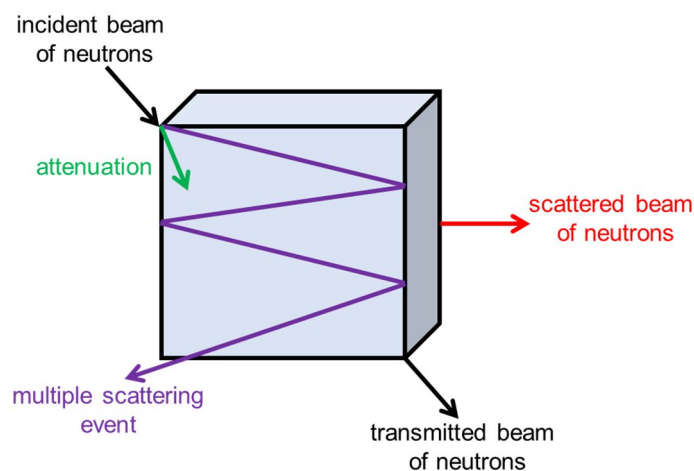


*Figure 2.31. Possible events that may occur during a neutron scattering experiment.*

To ensure that these events are corrected for in the raw data, several diffraction measurements are taken from the instrument: standard cells, and sample holders. The correction and calibration to the diffraction data have been carried out by software Gudrun $N$  (Gudrun-2017-10).<sup>52, 54, 71</sup> Detailed information on Gudrun $N$ <sup>52</sup> and the routines performed on the samples is provided in section 2.6.3.

## 2. Experimental Procedures and Characterisation Techniques

### 2.6 Software

Herein, listed in Table 2.2 below, are key software platforms employed as part of data analysis for this thesis. The MCDIFFaX and GSAS software are described initially and detailed information on Gudrun $N$ ,<sup>52, 54, 71</sup> the EPSR method,<sup>58, 67</sup> and the ANGULA<sup>74-77</sup> software are provided hereafter.

*Table 2.2. Significance of all the software used for data analysis and figures produced in this thesis.*

Software	Significance
OriginPro-2018	Graphing and data analysis software.
PowderCell 2.3	Calculates powder pattern from XRD data and carries out simple refinements.
MCDIFFaX <sup>50</sup>	Diffraction fitting software to refine unknown parameters such as stacking probability, peak profile parameters and zero shift.
GSAS <sup>47</sup>	GSAS was used to model XRD data for phase identification and calculate lattice parameters values in combination with its GUI, EXPGUI. <sup>78</sup>
Jmol	Computer software for molecular modelling of chemical structures in three dimensions.
Spectragryph	Optical spectragryph software used to normalise and subtract baselines of raw Raman spectra data.
Vesta (Visualisation for Electronic and Structural Analysis)	Visualisation of three-dimensional structural models, volumetric data, and crystal morphologies.
CrystalMaker X (version 10.3.2)	Visualise structures with rotatable animations and energy modelling tools.
Gudrun $N$ <sup>52, 54, 71</sup>	Correction of raw neutron total scattering measurements to the DCS.
EPSR <sup>67, 68</sup>	Construction of one, two or three-dimensional structures exploiting information contained in total scattering data.
ANGULA <sup>74-77</sup>	ANGULA software offers a set of tools to calculate from and convert pair distribution functions (PDF) to spatial density functions (SDFs) / maps, where the PDF is in a specific direction.

## 2. Experimental Procedures and Characterisation Techniques

### 2.6.1 MCDIFFaX

MCDIFFaX is a diffraction fitting software that can be applied to XRD patterns to allow the calculation of stacking probabilities in stacking disordered materials.<sup>49, 50</sup> MCDIFFaX is composed of DIFFaX software that calculates neutron and XRD patterns of materials with stacking faults but is furthered by the implementation of the Monte Carlo (MC) refinement method. DIFFaX can generate diffraction patterns with various parameters such as lattice constants, thermal parameters, stacking probabilities, fractional coordinates, zero shift and the peak profile parameters ( $u$ ,  $v$ ,  $w$  [Cagliotti terms] and Gaussian/Lorentzian ratios) can be refined. The parameters,  $u$ ,  $v$ , and  $w$  are related to the full width half maximum peak broadening,  $\Gamma(\theta)$ , and defined as Equation 2.44. The Gaussian/Lorentzian ratios are profile functions that bring in experimental peak broadening. The equation for  $\Gamma(\theta)$ :

$$\Gamma(\theta) = \sqrt{u \tan^2\left(\frac{\theta}{2}\right) + v \tan\left(\frac{\theta}{2}\right) + w} \quad \text{Equation 2.44}$$

The software DIFFaX itself cannot refine these parameters and so MCDIFFaX is embedded with a least-square environment and includes MC procedures to determine the best values and fits for these parameters. Such parameters are altered until a low chi,  $\chi^2$  value is observed between the MCDIFFaX-simulated XRD pattern and experimental XRD data. The use of a MC approach enables the possibility of allowing a certain percentage of unfavourable changes or refinements to avoid becoming trapped in a local  $\chi^2$  minima.

The presence of so-called memory effects can be used to describe stacking disorder in materials. During the initial stages of the refinement, it is assumed that there are zero memory effects present and thus, the stacking of a specific layer is not influenced by the stacking of the previous layer. When a good fit has been obtained, the first or second-order memory effects can be ‘switched on’ in the software to allow fits to be optimised. First-order memory effects define how the stacking of a specific layer is dependent upon the stacking in the previous layer.

The probability of stacking can be defined by  $\Phi$ , with subscripts ‘ $h$ ’ or ‘ $c$ ’ for hexagonal or cubic stacking, respectively. Cubicity in a material is denoted with  $\Phi_c$  to describe the amount of cubic stacking present in a sample.<sup>49</sup> The probability of a cubic stacking event occurring after a hexagonal stacking event is given by  $\Phi_{hc}$  and the

## 2. Experimental Procedures and Characterisation Techniques

probability of a cubic stacking event occurring after a cubic stacking event is given by  $\Phi_{cc}$ . Provided that only either cubic or hexagonal stacking can occur, the stacking probabilities of  $\Phi_{hc}$  and  $\Phi_{cc}$  can be defined as,  $\Phi_{ch} = 1 - \Phi_{cc}$  and  $\Phi_{hh} = 1 - \Phi_{hc}$ , respectively. These first-order memory effects can be viewed in terms of a ‘stackogram’ plot as depicted in Figure 2.32.

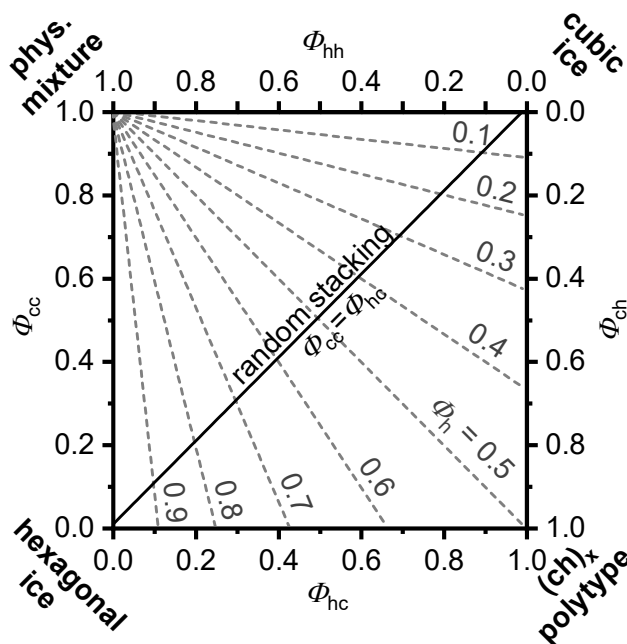


Figure 2.32. The ‘stackogram’ used to describe the structure of stacking disorder in ice. The solid black lines define structures with the stacking of random layers and the dashed lines from the top left-hand corner describe structures with constant hexagonality nature.<sup>49</sup>

The four corners in this ‘stackogram’ denote possible end-member states as it indicates and provides information with regards to the type of stacking present within a material. The states at the corners indicate physical mixtures, cubic ice, (ch)<sub>x</sub> polytype and also hexagonal ice. Alternating stacking sequences of cubic and hexagonal stacking can be described by polytype (ch)<sub>x</sub> end-member state. The black solid line labelled ‘random stacking’ denotes the position where no memory effects are found.

Cubicity,  $\Phi_c$ , can be described by, and calculated by first-order stacking probabilities conferring to:

$$\Phi_c = \frac{\Phi_{hc}}{\Phi_{hc} + \Phi_{ch}} \quad \text{Equation 2.45}$$

Hexagonality,  $\Phi_h$ , can be defined by  $1 - \Phi_c$ .

## 2. Experimental Procedures and Characterisation Techniques

MCDIFFaX was used to analyse the XRD pattern for the extent of stacking in pure ASW when heated from 95 K to 270 K at 10 K min<sup>-1</sup>. This pattern covered a  $2\theta$  range of 10 to 60°. In particular, the patterns recorded at 160–190 K were refined to show the extent of cubicity for ice *Isd*. The data and simulated fits can be found in Chapter 3.

### 2.6.2 General Structure Analysis System (GSAS)

General Structure Analysis System (GSAS)<sup>47</sup> is used to model and determine crystal structures from X-ray and neutron diffraction data enabling identification of phases, calculate weight fractions of mixed-phase samples and determine lattice parameters. GSAS is used in combination with its GUI, EXPGUI.<sup>78</sup> GSAS allows the inclusion of the Bernal-Fowler ice rules and is used to implement a Rietveld refinement. In the former, hydrogens that are meant to have an occupancy of 1 can be controlled by implementing atom constraints. In the latter, a Rietveld refinement creates a model of the experimental data collected, based on the inclusion of parameters such as lattice parameters, space group symmetry and instrumental parameters.<sup>78</sup> The remaining quantity left between the experimental data and model,  $S$ , can be further minimised in a least squares environment.

$$S = \sum_i w_i (y_i - y_{ic})^2 \quad \text{Equation 2.46}$$

The weighting factor is represented by  $w_i = 1/y_i$ ,  $y_i$  and  $y_{ic}$  are the observed and calculated intensity at the  $i$ th step, respectively. As the remaining,  $S$ , converges with a good fit, the refinement can be completed.

### 2.6.3 GudrunN Software

To understand the steps and processes in data analysis and to assist in diagnosing problems, GudrunN will, when requested, output different results from every stage of analysis with various file extensions. GudrunN was employed here to correct multiple scattering such as removing incoherent scattering, input correct parameters specific for the experiments carried out in this thesis and subtract perturbation which were caused by inelastic collisions to the raw data. The GudrunN algorithm is a lengthy, iterative process and is described in the GudrunN manual.<sup>52</sup> Correction procedures performed using GudrunN are based upon the analysis of time-of-flight diffraction data from liquid and amorphous samples (ATLAS) package.<sup>71</sup> The components, factors, and parameters needed in the analysis and how the total scattering data was refined in this software are briefly explained below before producing models of C<sub>10</sub>H<sub>16</sub> in amorphous ice with the EPSR method.



## 2. Experimental Procedures and Characterisation Techniques

### 2.6.3.1 Sample Background

Before each measurement, a sample background must be made in every case as it is not possible to run Gudrun*N* without this data. The sample background is measured with a radiated beam and with nothing in line with the scattering position. This measurement is conducted to eliminate any background that may arise from the sample that scatters into the surroundings and any scattered radiation that may be deflected back into the detector. This, in turn, may not eliminate all the background but it will decrease significantly. The background that is sample dependent is difficult to remove in the data and will cause issues when analysing the data. When collecting data at low scattering angles, background from the incident beam collimator may arise which is transmitted through the sample and thus, affects the sample transmittance. Measurements recorded in this study for sample background include the empty instrument, empty CCR and the empty vanadium candlestick.

### 2.6.3.2 Purging Bad Detectors – Time-of-Flight (TOF) Diffraction

TOF diffractometers are equipped with a large array of detectors, and it is highly doubtful that every detector will be working seamlessly. Therefore, an automated method to remove bad detectors from the data analysis has been introduced. This method is termed, ‘purge’ and must be performed prior to any data processing. ‘Purge’ produces a list of the bad detectors which is read into Gudrun*N* and thus, does not use the detectors to formulate the final files required from this software.

### 2.6.3.3 Multiple Scattering Factors

To calculate multiple scattering factors and attenuation, it is necessary to have a total cross-section for all samples and their containers. The neutron scattering cross-section, which is the energy employed to measure the structure is independent of wavelength. This rule is omitted when there are significant amounts of inelasticity effects with hydrogen and deuterium containing materials and when samples have strong Bragg scattering. It is necessary to avoid nuclear resonance to avoid non-analysable data. More detail into this theory is provided in the Gudrun*N* manual.<sup>52</sup>

It was necessary to input into Gudrun*N* the beam size, geometry, and composition of the  $\text{Ti}_{0.68}\text{Zr}_{0.32}$  flat plate container. The multiple scattering is calculated based on the scattering cross-section of averages of the sample, container, CCR and vanadium

## 2. Experimental Procedures and Characterisation Techniques

candlestick for a wavelength. This is based on the assumption that atoms in those components will scatter isotopically in the same direction.

### 2.6.3.4 Deadtime Correction

Most detectors will have an intrinsic deadtime, this is the minimum time required between events needed for the detector to resolve these two separate events. Any events that come closer together than this time will get counted as one event rather than two separate events. Deadtime correction details depend on how the detectors have been attached to the DAE system. ISIS detectors have been placed in such a way into groups that will be singly inputted into the DAE. If the input presents its own deadtime correction for any reason, this deadtime will in turn affect every detector that is input into the DAE. The DAE inputs are faster than the deadtime of each individual detector elements. The individual detector elements produce a more substantial deadtime correction. Once detectors are grouped, standard deviations are compared: those that yield noisy data have large standard deviations and those with weak counting detectors have low standard deviation are removed from the analysis. After this has been followed for all samples, the data can be normalised, and the background can be subtracted directly.

### 2.6.3.5 Data Calibration for Neutrons

As mentioned earlier, the most ideal material used to place the diffraction data on an absolute scale is vanadium. Neutrons tend to have a very small coherent scattering length which in turn indicates, distinct scattering is intrinsically very weak from Bragg reflections. Vanadium has a precisely known density ( $6.11 \text{ g cm}^{-3}$ ) and is a stable solid metal that does not require a container and may be formed into a solid flat plate or cylinder when required. The mass of a vanadium atom ( $50.9415 \text{ g mol}^{-1}$ ) allows for very small inelasticity effects and can be estimated using e.g., the Placzek-type model for approximating inelasticity. The Placzek model is not suitable for light atoms. Using vanadium as the calibration material, allows the user to run parallel experiments that correspond to the sample using the exact same beamline conditions, such as detector positions and apertures. The DCS is flat due to vanadium existing as dominated by single atom scattering and with a few known and weak Bragg peak positions. Vanadium is also ideal as it has recognised attenuation properties and so, multiple scattering factors are readily anticipated and calculable.

## 2. Experimental Procedures and Characterisation Techniques

### 2.6.3.6 Converting the Structure Factor to the Pair Distribution Function (PDF)

In most cases, the user will want to view their data in  $r$ -space. Gudrun $N$  provides the option to perform a FT on the structure factors,  $F(Q)$ , extracted from the software. The  $F(Q)$  can be converted to real space pair correlation functions. The method required for a FT involves the top-hat convolution. In brief, it can be assumed that data analysis has not progressed perfectly, and the  $F(Q)$  relies on some  $Q$ -dependent background. Prior to performing a FT on the data, this background needs to be removed, which was created by the top-hat function by convoluting the data.

The correction for self-scattering must also be removed. The background associated with self-scattering is complicated due to the presence of truncation ripples that are caused after FT and thus, due to  $Q_{\max}$  finite nature. The former can be corrected with the Placzek model as mentioned earlier.

### 2.6.3.7 Running Gudrun $N$

The graphical user interface (GUI) for Gudrun $N$  runs with Java. A standard start-up file for Gudrun $N$  is opened once the GUI is started and includes separate tabs/sections for inputting (i) instrument data, (ii) beam data, (iii) normalisation data and (iv) sample background. If the start-up file is set up correctly, these four start-up tabs are precise and used in every data analysis in the software. The file should correspond to the instrument specific to the data the user measured their data on. Only one tab for each of these are present and cannot be removed from the file with the exception of, (iv) sample background. If different instruments, beam, or normalisation is used or required, a separate input file will need to be generated for each configuration. Additional tabs are available for 'sample' and 'container': the container tab is to be inserted always after the sample tab and must be consecutively ordered in which they occur in the experiment. Sample background (empty instrument data file), sample and container can be added as many times as required.

Specifically, in the beam tab, the sample geometry is crucial. Since a  $\text{Ti}_{0.68}\text{Zr}_{0.32}$  flat plate was employed, the standard incident beam edges relative to the centre of the sample are specific to the instrument used. The normalisation tab will require the vanadium plate data file and the empty instrument data file for the normalisation background. In addition, the atomic composition for vanadium is required and the thickness and density of the plate were also included.

## 2. Experimental Procedures and Characterisation Techniques

The sample tab consists of many parameters that must be accurate for when data will be input into EPSR. The minimum radius for FT should be the shortest distance expected to see in the samples, e.g., 0.7 is an appropriate number for a hydrocarbon like  $C_{10}H_{16}$ . To look at larger structural features producing small-angle scattering in  $Q$ , data needs to be collected to a small enough  $Q$  value to see large features such that  $r_{\max} = 2\pi / Q_{\min}$ .

The sample tweak factor is a significant contributor to data analysis here. This factor is employed for powdered samples and is the reciprocal of the packing fraction, e.g., for a 50% packing fraction, the tweak factor will be 2. It was not possible to fill the sample container with powdered samples perfectly and so the need for GudrunN to be iterated with suggested tweak factors was carried out.

Since  $Ti_{0.68}Zr_{0.32}$  containers used in this study were of 1 mm and 2 mm thicknesses, their upstream and downstream thicknesses were different to the wall thickness in front of, and behind the sample. Once all tabs and parameters are edited and input correctly, a purge, as aforementioned was run. When hydrogen atoms are present, as in the samples prepared for this study, the incoherent scattering may be seen as a rise in the scattering for low- $Q$  values and needed to be removed from the sample in order for  $G(r)$  in EPSR to be calculated correctly. Subtracting wavelength binned data and iterating this several times increased the chances of removing incoherent scattering.

To summarise, data correction is a highly iterative process and so it is unlikely that data will be corrected in the first instance. In any case, the structure factors were required to input into EPSR. The \*.mint01 files give the merged DCS after processing using the top-hat function and deconvoluting the functions in  $r$ -space. Scattering was removed which tends to give high levels of spurious data below  $r = r_{\min}$ .

### 2.6.3.8 GudrunN Analysis

Inelasticity features from inelastic collisions<sup>54</sup> were removed using a subroutine ‘*Iterate Gudrun*’ function in the software to provide the total structure factors,  $F(Q)$ , of the various samples. The ‘*Iterate Gudrun*’ subroutine comprises a minimum intermolecular spacing / separation of 0.70 Å for each sample. Each sample was iterated 10 times to ensure the tweak factor was refined correctly.

A vanadium calibration was conducted to enable the calculation of the absolute DCS levels. This was adjusted for microporosity factors and the incomplete packing

## 2. Experimental Procedures and Characterisation Techniques

fraction of the samples in the containers while assuming the atom number density of ASW was unchanged, that of  $0.094067 \text{ atom } \text{\AA}^{-3}$ .

After normalising the data to a vanadium standard, and following the corrections for sample absorption, multiple scattering, inelastic scattering, background scattering and the atomic self-scattering, the main function that is observed in neutron diffraction patterns is the DCS.<sup>61</sup> As mentioned previously, the DCS is the factor that tells us how much or little a sample scatters neutrons/X-rays compared to some reference value. This function is measured on an absolute scale with units of  $\text{b sr}^{-1} \text{ atom}^{-1}$  and thus, is calibrated against a known amount of scattered vanadium standard. The absolute measurement of the DCS nature permits the isotopic compositions and chemical composition to be checked if the sample density is known. Each sample in this study that was measured had the same composition with differing isotopic nature. While assuming these isotopic analogues are identical structurally, partial structure factors can be deduced for the system and thus, specific pairwise atomic correlations were obtained.

### 2.6.4 Introduction to Empirical Potential Structure Refinement (EPSR)

#### 2.6.4.1 Overview of Computer Simulations and Modelling

Computer simulations generate models of real-world systems and can present theoretical data. Their advantage relies on the fact that in order to simulate an adequate macroscopic system, only a few hundred or thousand atoms are required. To study liquids, there are two main algorithms used which are known as: (i) stochastic MC and (ii) deterministic Molecular Dynamics (MD). In the latter, time-dependent processes are studied where trajectories of particles are tracked with time to allow for access to dynamic information. In the former algorithm, a set of configurations is ensembled by probability in order to employ static property calculations.

The Empirical Potential Structure Refinement (EPSR) method developed by Soper<sup>67, 68</sup> is based upon the standard Metropolis Monte Carlo (MMC) simulation of the system being studied which allows the correction of pair interaction potentials by comparing with various diffraction data sets. The EPSR method was designed specifically for studying molecular liquids and used for solvent investigations. EPSR allows the construction of three-dimensional atomistic molecular models of structurally disordered systems and attempts to find the distribution of atoms in a structure consistent with diffraction data.

## 2. Experimental Procedures and Characterisation Techniques

EPSR has previously been used to prepare models of liquid H<sub>2</sub>O,<sup>79, 80</sup> methanol<sup>81</sup>, tetrahydrofuran<sup>82</sup>, acetone<sup>83</sup> and study the crystallisation of benzoic acid.<sup>84</sup> Other studies include the determination of polar stacking in chloroform<sup>60</sup> and the orientational ordering in liquid bromoform.<sup>85</sup>

Briefly, EPSR builds upon diffraction data by building a simulation box representing the system and refines atom positions to give the best possible fit with the diffraction data. Once a suitable agreement is achieved with the simulated model and the diffraction data, the box is interrogated and information concerning the positions and orientations of atoms can be extracted. A detailed discussion of the theory behind EPSR analysis is provided by Soper<sup>67</sup> and explained herein.

There are typically four types of constituents required for a model to be produced in EPSR.

- (i) A set of coordinates is needed to represent a box of molecules and atoms.
- (ii) A set of established potential energy functions that will model the intra- and intermolecular interactions between all molecules and atoms in the box.
- (iii) Typically, four types of atom moves with a set of rules are needed; (a) atomic and (b) molecular translations, (c) molecule functional group rotations and (d) molecule rotations. A move consists of mainly a small random change in their coordinates ( $x, y, z$ ).
- (iv) Some tools to cross-examine developments of intermolecular and interatomic structures that the simulated model produces.

Predominantly, the difference between the experimental data and the simulated data from a MC simulation which includes the reference potentials, allows EPSR to derive a perturbation to the force field. Empirical potentials can be introduced into the system which drives the MC simulation towards structural convergence with the experimental data. There are many inaccuracies associated with the classical MC simulation, which are corrected with the empirical potentials introduced with EPSR and for systems that lack scattering length contrasts. The aptitude for isolating partial structure factors from total structure factors is improved significantly using EPSR so-called ‘empirical potentials’.

## 2. Experimental Procedures and Characterisation Techniques

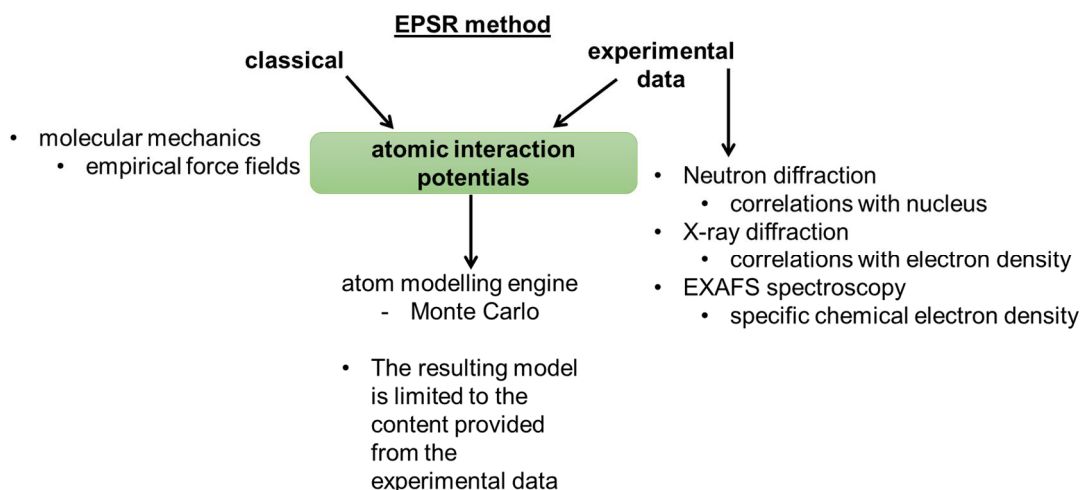


Figure 2.33. Simple map of the methods combined to derive a model from the EPSR method.

The empirical potentials produced by EPSR deliver a good representation of the intermolecular potentials from the structure, whilst the artefacts and statistical noise of the measurements are smoothed, may potentially be transferred to the final structure model. The empirical potentials can be positive or negative and can vary quite quickly with distance,  $r$ , which allows for the insufficiencies of the reference force fields to be overcome, thus, the model structure can fit with the experimental measurements better than for a classical MC simulation. Herein, the theory behind the reference and empirical potentials will be described in more detail.

### 2.6.4.2 Construction of an EPSR Simulation Box

A simulation box containing  $N$  number of atoms or molecules is set up so that the arrangement of atoms or molecules is random with predefined box lengths. The simulation box essentially represents a repeatable unit cell of the structure of a liquid. The total size of the box will govern the range with which the structure will be modelled with and  $r_{\max}$  is half the box edge. The temperature and number composition are input into the initial setup of the simulation so that the atomic number density of the simulation model is constrained.<sup>58</sup>

When the box is repeated, every molecule or atom is placed in a way that is repeated periodically so that every repeat behaves identically and has the same number of particles also behaving identically. EPSR implements periodic boundary conditions (PBC) whereby, if a particle were to leave one side of the simulation box, it would simply re-enter the box on the opposite side as shown in Figure 2.34. The PBC used here will

## 2. Experimental Procedures and Characterisation Techniques

ensure boundary effects are overcome and a constant number of particles throughout the simulation are maintained.

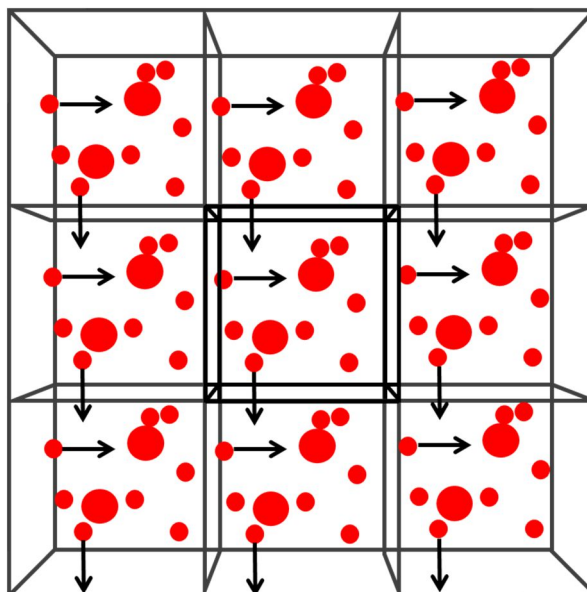


*Figure 2.34. Schematic illustration of the idea of PBC, where the atoms or particles (red circles) may leave a simulation box in the direction of the arrow by one side and its periodic image in the adjacent box is reintroduced into the box on the opposite side in three-dimensional space.*

When defining molecules in EPSR, there are restrictions on the first and second neighbouring atom distances. Bond angles are constrained between the first and third atoms. Between the first and fourth atoms, bonds are created, and thus, bond dihedrals are preserved.

### 2.6.4.3 Fundamentals of EPSR

When setting up EPSR, the user initially defines a set of starting parameters including the reference potential, effective charges on the atoms, assumed molecular shapes and minimum distances approaches. These can initially be read into EPSR to allow the computer to sift through various possibilities of arrangements of atoms and molecules which coincide with the experimental and starting prejudice data.<sup>58</sup> Molecules input into EPSR are well-defined by their harmonic force constants between atom pairs which are required to define the molecules themselves as well as looking at dihedral angles. In addition, intra- and intermolecular distances not consisting of harmonic forces are defined and are subsequently controlled by the Lennard-Jones (LJ) potentials, representing the repulsive short-range and dispersive long-range attraction forces. The combination of



## 2. Experimental Procedures and Characterisation Techniques

these forces is defined as the ‘reference potential’ in EPSR. The scattering data is introduced by another potential termed the ‘empirical potential’, empirical, as it is essentially developed to fit the data. The empirical potential is obtained from the difference between the simulated and diffracted data. Once the reference potentials are input and reach an equilibrium, the empirical potential is used to guide the molecular and atomic moves in directions that give the best fit and closest representation of scattering data. These terms are described herein.

With the standard MC approach, molecules must be randomly arranged in a simulation box as the first starting condition. There are four atom movement types in EPSR<sup>58</sup> as described earlier which involve the following:

- i) whole molecule rotation
- ii) whole molecule translations
- iii) the specific rotation of molecular sidechains (where suitable)
- iv) individual atomic movements

A ‘move’ involves small random changes in the  $x,y,z$  coordinates of an atom or molecule or a rotation about an axis. Molecules are then further simulated in individual successive steps which can be disregarded or accepted conferring to the Metropolis condition. In this condition, if a move of a molecule or atom decreases the total potential energy ( $U$ ) of a system, defined as  $U$ ,  $\Delta U < 0$ , then the move is always accepted. Moves that contribute to increasing  $U$ ,  $\Delta U > 0$ , are accepted with an acceptance probability given by Equation 2.47:

$$\exp \left[ -\frac{\Delta U}{kT} \right] \quad \text{Equation 2.47}$$

where  $k$  is the Boltzmann constant and  $T$  is the temperature. The dependence upon temperature and potential energy ensures the system proceeds to reproduce MC simulations of intermolecular interactions. The Metropolis condition ensures that the system follows a Markov chain over some time while visiting a large volume of phase space that is available.<sup>58</sup>

In EPSR, the potential energy consists of two terms such that they are the reference potential energy,  $U_{(Ref)}$  and the empirical potential energy,  $U_{(Ep)}$ .  $U_{(Ref)}$  is a benchmark form where the parameters of atoms can be easily found in the literature (see later). This potential is utilised throughout and independently in EPSR simulations to obtain a simulation box with an approximation of the region in phase space the system is

## 2. Experimental Procedures and Characterisation Techniques

likely to adopt, e.g., no atomic overlaps, sensible geometries etc. On the other hand,  $U_{(Ep)}$  is unlike  $U_{(Ref)}$  and does not take any standard form, so once the simulation and this potential come to converge or equilibrate, the ‘moves’ are guided in directions that correspond closely to best represent the diffraction data.<sup>58</sup>

The total potential energy of the system is given by the expression:  $U = U_{(Ref)} + U_{(Ep)}$  and can be used to separate different terms of atoms with different types of interaction potentials such that the potential energy for given atoms of a type  $\alpha$  and type  $\beta$  separated by a distance,  $r$  is given by Equation 2.48:

$$U_{\alpha\beta} = U_{\alpha\beta}^{(Ref)}(r) + U_{\alpha\beta}^{(Ep)}(r) \quad \text{Equation 2.48}$$

And the total potential energy of the system is specified by Equation 2.49:

$$U = \frac{1}{2} \sum_i \sum_{j \neq i} U_{\alpha(i)\alpha(j)}(r_{ij}) \quad \text{Equation 2.49}$$

where the separation of atoms  $(i, j)$  is  $r_{ij}$  and  $\alpha_{ij}$  is the type of atom  $i$ . The factor of  $\frac{1}{2}$  is required to consider the double-counting of atom pairs.<sup>58</sup>

Within EPSR, there are no considerations for the correction of long-range effects on the potential energy of the system, this is mainly due to time-consuming corrections without providing a suitable benefit with respect to modifying the atom arrangement. The pressure and energy in EPSR are calculated and can be viewed at any time as a guide to view whether the simulation is sensible. In the latter, the energy should be negative for a sensible box to ensure no overlapping atoms. The former, once extremely positive values are seen, is indicative that there is some significant overlap of atoms and thus, parameters have not been implemented correctly. If the pressure is firmly negative on the other hand, the system is attempting to collapse on itself, and the structure presents voids which are indicated by the rise in low- $Q$  scattering.

Regardless of an accurate method for long-range correction, the non-Coulomb terms from the reference potentials, thus, the LJ terms can be smoothly truncated by a function as defined by Equation 2.50:

$$T(r) = \frac{1}{0.5} \begin{cases} r < r_{minpt} \\ 1 \\ r > r_{maxpt} \end{cases} + \cos\pi \left( \frac{r - r_{minpt}}{r_{maxpt} - r_{minpt}} \right) \quad r_{minpt} < r < r_{maxpt} \quad \text{Equation 2.50}$$

## 2. Experimental Procedures and Characterisation Techniques

where,  $r_{maxpt}$  and  $r_{minpt}$  are the points where the truncation function drops to 0 and below 1, respectively and  $r_{minpt}$  and  $r_{maxpt}$  are typically 9 and 12 Å, respectively.

The Coulomb terms are truncated differently with the function derived from charged clouds interaction<sup>86</sup> (details in this reference) and expressed as Equation 2.51:

$$T_c(r) = \operatorname{erfc}\left(\frac{r}{\sigma_c}\right) \quad \text{Equation 2.51}$$

where  $\sigma_c$  is set by the user in EPSR as a width parameter and would likely be the diameter of the largest molecule in the box.<sup>58</sup>

In this study, both the LJ and Coulomb potentials are truncated smoothly. All refinements carried out and reported in this study make use of effective charges and reduced well-depths for the reference potentials. The values for the reference potentials used in this study are provided later in Chapter 5, Table 5.3.

### 2.6.4.4 Interatomic Potentials – Defining the Reference Potential

The initial starting point of the EPSR simulation in an attempt to analyse data is to derive the reference potential. The reference potential is defined as Equation 2.52:

$$U_{ref} = U_{intra} + U_{inter} \quad \text{Equation 2.52}$$

which is calculated from the pairwise addition of both intramolecular ( $U_{intra}$ ) and intermolecular ( $U_{inter}$ ) reference potential contributions over all the atom pairs within the system.

Essentially the potential energy function that will be utilized as the starting point for structure refinement allows an ensemble of molecules to be built where the internal structure is reproduced from the diffraction data. These potentials can be obtained from the literature or if possible, derived by inspection of the data. The Optimized Potentials for Liquid Simulations of all-atom (OPLS-AA) force field was developed by the Jorgenson<sup>87</sup> group and is world-renowned as the most accurate and successful empirical generic all-atom force field which is quite pertinent to a wide range of chemical species.

In particular,  $U_{inter}$  is based on a 12–6 LJ potential plus the addition of a Coulomb potential (LJ+C) when required; this is a simple mathematical model used to approximate the various interaction between pairs of atoms and molecules. Between atom pairs,  $U_{inter}$  is built from this combination of LJ and Coulomb potentials with a total potential energy of the system expressed as shown in Equation 2.53:

## 2. Experimental Procedures and Characterisation Techniques

$$U_{inter} = U_{LJ} + U_{Coulomb}$$

$$U_{\alpha\beta}(r_{ij}) = 4\varepsilon_{\alpha\beta} \left[ \left( \frac{\sigma_{\alpha\beta}}{r_{ij}} \right)^{12} - \left( \frac{\sigma_{\alpha\beta}}{r_{ij}} \right)^6 \right] + \frac{1}{4\pi\varepsilon_0} \frac{q_{\alpha}q_{\beta}}{r_{ij}} \quad \text{Equation 2.53}$$

where  $\varepsilon$  (epsilon) is the depth of the potential well (permittivity of the vacuum/free space) ( $\text{kJ mol}^{-1}$ ),  $\sigma$  (sigma) is the limited distance at which the interparticle potential is zero and  $r_{ij}$  is the separation between atoms,  $i$  and  $j$ .  $\alpha$  and  $\beta$  represent  $i$  and  $j$  and there will be  $N(N+1)/2$  pairs of interaction when there are  $N$  different types of atoms. The LJ distance is defined as  $\sigma_{\alpha\beta}$  ( $\text{\AA}$ ) and the energy parameters  $\varepsilon_{\alpha\beta}$  ( $\text{kJ mol}^{-1}$ ) both describe the potential energy well depth and separation,  $r$ , where the repulsive potential is equal to zero.

Lorentz-Berthelot rules are used to calculate the individual atoms which are given by:  $\varepsilon_{\alpha\beta} = \sqrt{\varepsilon_{\alpha}\varepsilon_{\beta}}$ ,  $\sigma_{\alpha\beta} = 0.5(\sigma_{\alpha} + \sigma_{\beta})$ . The latter part of the equation is the Coulomb interaction.

The basic shaped curve as shown in Figure 2.35 is common to most empirical potentials and helps describe the interatomic, non-bonding forces. The LJ forces fall off with increasing  $r$  and represent short-range forces, whereas the Coulombic forces fall off with  $r^{-2}$  and represent long-range forces. The ‘6’ term in the LJ forces represent van der Waals attractions arising due to London dispersion forces and the ‘12’ term signifies short-range repulsive interactions between atoms due to the Pauli Exclusion Principle. This reproduces repulsions between molecules with overlapping electron clouds.

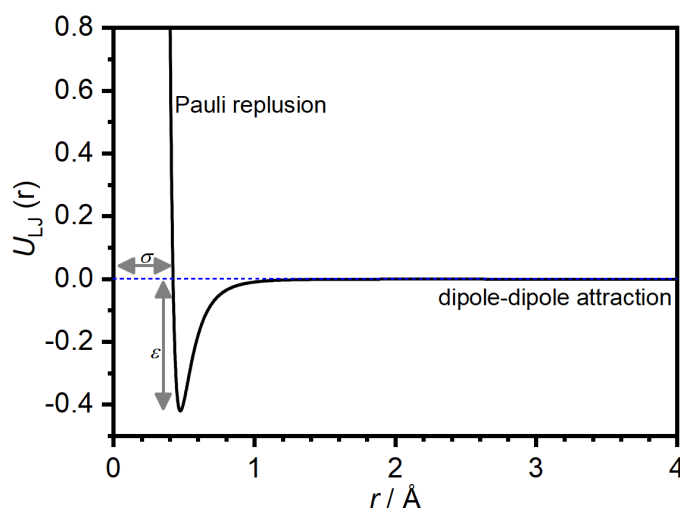


Figure 2.35. Standard energy vs. distance curve for the 12–6 LJ potential,  $U_{LJ}$ , as a function of the radial distance,  $r$ . The diameter,  $\sigma$ , is the radial distance where the potential energy,  $U$ , is equal to 0 and the potential minimum is given by  $\varepsilon$ .

## 2. Experimental Procedures and Characterisation Techniques

At small  $r$  values, the potential energy is positive, large, and rather unfavourable concerning the arrangement of atoms, indicating that any two atoms will be strongly overlapping with one another. At larger  $r$  values, the potential energy is negative and small, indicating a stable influence of atom pairs. This resembles the London dispersion energy which is caused by instantaneous dipole-dipole interaction. When the separation of atoms is greater than  $\sigma$ , the energy reaches a minimum rendering atom pairs stable unless another external influence disrupts them. Repulsive and attractive interactions are also present in regions of negative and positive charges, represented by Coulomb charge interactions. As mentioned earlier, truncation terms can be used to reduce potentials to zero in EPSR for distances greater than half the dimensions of the box, as specified by Soper.<sup>68</sup>

As well as defining the intermolecular potential,  $U_{\text{inter}}$ , the intramolecular potential,  $U_{\text{intra}}$  can be defined as:

$$U_{\text{intra}} = C \sum_i \sum_{\alpha\beta > \alpha} \frac{(r_{\alpha(i)\beta(i)} - d_{\alpha\beta})^2}{2w_{\alpha\beta}^2} \quad \text{Equation 2.54}$$

where  $d_{\alpha\beta}$  and  $w_{\alpha\beta}$  are the average distances (equilibrium bond distance) and widths, respectively. Each intramolecular distance is characterised by an average distance and width and interact via a harmonic potential.  $r_{\alpha(i)\beta(i)}$  is the actual separation of  $i$  and  $j$  atoms and  $C$  is a constant defined by the user where the intramolecular disorder can be fine-tuned. A broadening function is employed to avoid the need to refine and specify individual Debye-Waller factors for every intramolecular distance. The broadening function is defined as,  $w_{\alpha\beta}^2 = d_{\alpha\beta} / \sqrt{U_{\alpha\beta}}$ .<sup>58</sup>

## 2. Experimental Procedures and Characterisation Techniques

### 2.6.4.5 Running the Simulation

As mentioned earlier, EPSR simulations consist of four different types of atom movements. The initial guess of the reference potential is simulated with random moves in an iterative process, altering the system configuration until the system has equilibrated, i.e., the calculated structure factors and distribution functions become stationary and do not change further as the simulation proceeds, the so-called ‘empirical potential’ is introduced. The iterative process for the EPSR method is depicted in Figure 2.36. The difference in  $Q$  space is calculated between the diffraction data,  $D(Q)$ , and the simulated structure factor,  $F(Q)$ , thus, a set of coefficients are obtained that are further used to generate the empirical potential. Modifying the potentials between atoms drives the model towards experimental data and a flow chart of the processes that occur are described in upcoming Figure 2.37.

## 2. Experimental Procedures and Characterisation Techniques

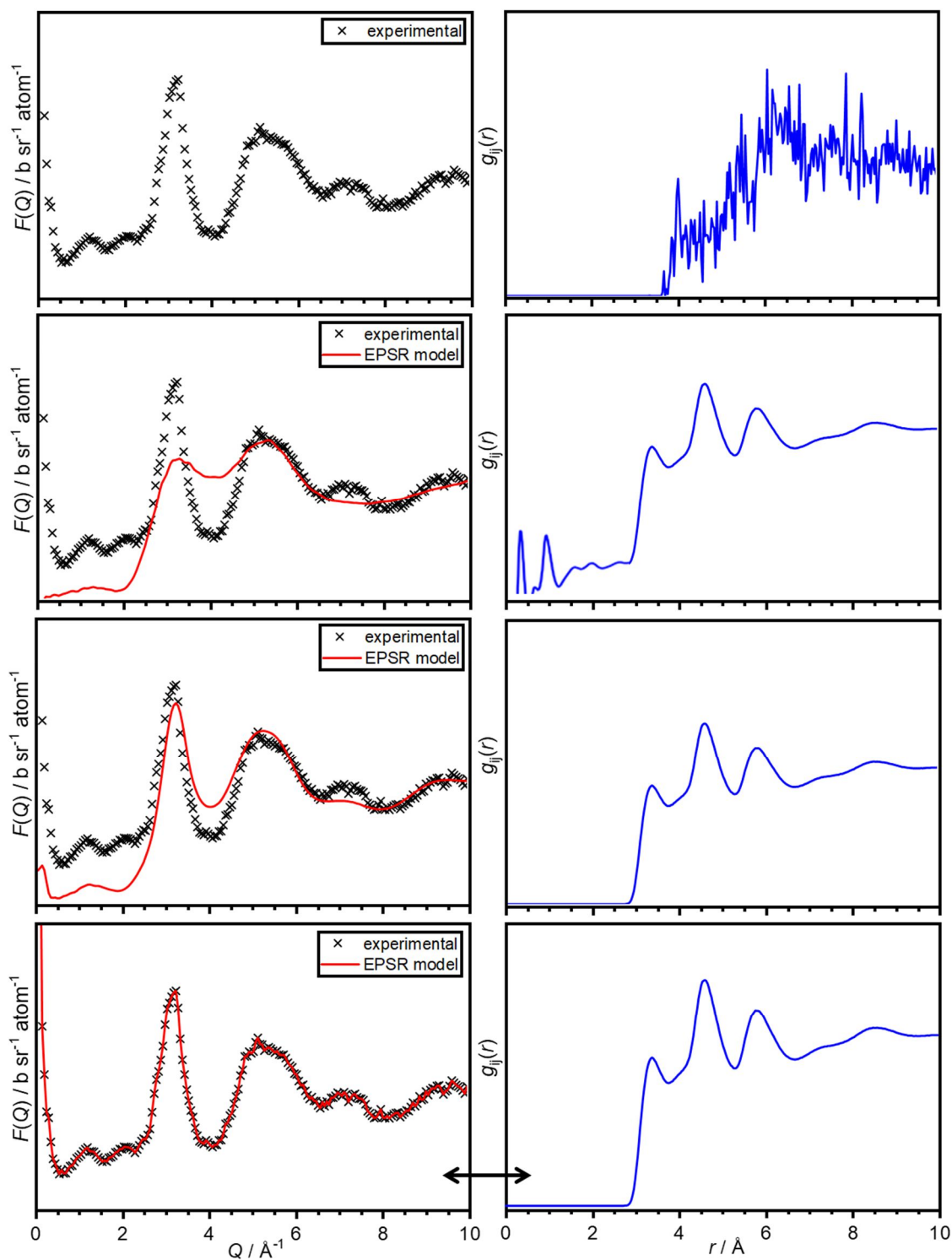


Figure 2.36. Illustration of the EPSR modelling of a system, showing column 1 as the experimental diffraction data and EPSR simulation fits, and column 2 is the progress in the system configuration for  $g_{ij}(r)$ . This experimental data is of an as-made  $C_{10}H_{16}$  in amorphous ice sample and extracted for the  $gc2-o1$  atom pair.

## 2. Experimental Procedures and Characterisation Techniques

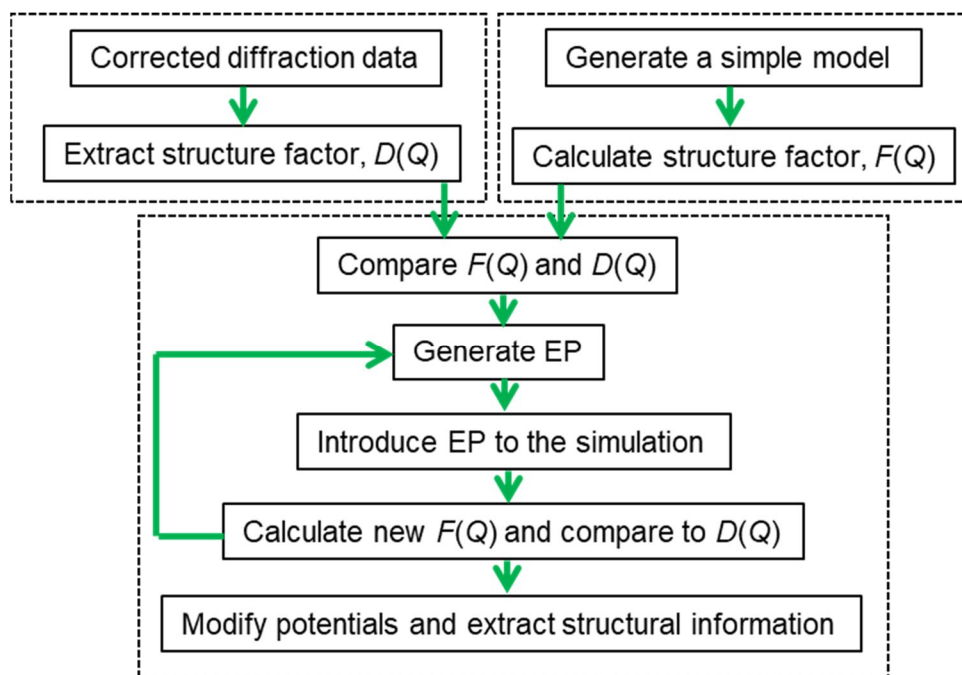


Figure 2.37. Simple flow chart diagram displaying the steps in the data correction and the iterative EPSR simulation process. The abbreviation ‘EP’ = empirical potential. By extracting  $D(Q)$  and calculating the  $F(Q)$  from EPSR, potentials can be modified between atoms and the model can be driven towards the experimental data. When the user is satisfied with the fits of the model with the experimental data, a wealth of structural information can be extracted.

### 2.6.4.6 The Empirical Potential

In principle, attempts to refine charges and the LJ parameters could be carried out, however, there is a lack of guarantee of success. This is where the empirical potentials are introduced and need to be perturbed in a way to make the simulated data fit the diffraction data.<sup>68</sup> When setting up the empirical potential, one must consider that it must represent true differences between the scattered diffraction data and simulated data; ideally no artefacts should be reflected associated with truncation errors, statistical noise, or systematic errors of the diffraction data.<sup>68</sup> If such artefacts were present then they would be carried over into the distribution functions in the system.<sup>58</sup>

The empirical potential is switched on to acquire and improve the fit. Each simulation requires different values and once the absolute energy of the simulation is reached or exceeds the value of the empirical potential, the simulation does not improve further. The value of the empirical potential can be increased until the quality of the fit significantly improves. Once all changes are complete and the simulation has reached a stable equilibrium where the energy is stable, accumulators and other parameters can be switched on to start forming ensemble-averaged distribution functions. This, in principle,



## 2. Experimental Procedures and Characterisation Techniques

is very difficult to achieve and various methods for generating the empirical potential have been tested. The most successful exists in the form of a set of Poisson functions and the derivation is provided by Soper.<sup>68</sup> This function represents the interatomic potential and varies significantly at short and long  $r$  distances as mentioned earlier. The use of this function helps to avoid or reduce truncation effects being transferred to the empirical potential.

Through the isotopic substitution technique, EPSR has the ability to isolate partial structure factors and estimate those that are unavailable from the diffraction data, therefore, estimating all the partial structure factors in the system. Accordingly, while iterating, the accuracy in the structure improves, considering the estimates of the partial structure factors.

The weighted sums of partial structure factors are determined from the neutron scattering lengths, e.g., if there are  $J$  number of distinct atomic components in the system being investigated, the number of functions to be determined is given by:  $N = J(J+1)/2$ , where empirical potentials are generated and thus, PDFs and partial structure factors are determined. Therefore, in order to extract  $N$  terms from the data,  $N$  number of experiments will be needed with independent weight which is possible with isotopic substitution.<sup>88</sup> In this thesis, isotopic substitution is performed, and so several data sets are input into the model to generate an empirical potential for every site-site distribution in the system.

Estimated partial structure factors are obtained from the simulation which can undergo FT to real space and give the estimates for the site-site PDFs. The empirical potential is cumulative in EPSR and retains information as well. Once the empirical potential shows no change and the energy of the system reaches a limit, the simulation can be used to extract structural information.

Referring back to Figure 2.36 and Figure 2.37, whilst iterating the model under Metropolis conditions, the structure accuracy and the estimates of partial structure factors gradually improves until the differences of the coefficients reach close to zero. This indicates that the simulation approaches and converges with the experimental data, i.e., structural reconstruction is reached. The empirical potential provides a good picture of intermolecular potentials as well as smoothing the artefacts and noise from the data that may be transferred into the structural model.

## 2. Experimental Procedures and Characterisation Techniques

Defining the amplitude of empirical potential is important, e.g., EPSR26 has been designed to reflect the ability of the empirical potential accurately as it modifies the atomic distribution functions, whilst aiming to prohibit the possibility of the potential becoming very large causing the atoms to refuse to diffuse and thus, they become stuck. The empirical potential will take larger values to overcome the reference potential defects.

For the EPSR simulations of  $C_{10}H_{16}$  and  $C_{10}D_{16}$  in amorphous ice carried out in this study, H/D isotopic substitution has been employed. EPSR has been used to produce three-dimensional structural models of finely dispersed vapour deposited  $C_{10}H_{16}$  and  $C_{10}D_{16}$  in amorphous ice.

### 2.6.4.7 Spherical Harmonic Representation

PDFs are not direction-dependent and thus they carry no information on any angle-dependent distribution probabilities. In principle, as mentioned earlier, PDFs can be obtained from just the FT of the  $S(Q)$  without the need for EPSR analysis and the partial PDFs can be obtained from smart analysis of several diffraction datasets. However, EPSR is one way to analyse the data where several molecules are placed into a simulation box and refined until the  $S(Q)$  matches the experimental  $S(Q)$ . This results in a real atomistic model of atoms that are located at  $x$ ,  $y$ ,  $z$  coordinates in the simulation box. Thus, assuming the model is correct and accurate enough, a small part of the actual material is viewed, and the PDFs can be easily calculated by counting the atoms at a distance,  $r$ . At this point, nothing more is known other than what is obtained from the FT of  $S(Q)$ , but now, the atoms are a function of angular distribution and not solely the distance can be calculated. This is because in the diffraction data, we ‘formally’ only have information on the distances. For angular information, it is important that one is dealing with molecules and that the axis is defined within the molecule. The atoms that contribute to the distances have an angular distribution that is not isotropic unless there is e.g., liquid argon and so now, once an EPSR atomistic model is achieved, the assumption is that this box represents the distribution of atoms in the real material itself and thus, it is possible to obtain the SDFs.

Once the PDFs are established from EPSR, two underlying issues become apparent. These issues are such:

- (i) storage: the storage of a large number of pixels from defining functions of different dimensions is significantly important.

## 2. Experimental Procedures and Characterisation Techniques

- (ii) the process of visualising the output from EPSR needs to be implemented so as to avoid a large array of numbers.<sup>58</sup>

Therefore, the spherical harmonic representation is the benchmark method to store a large array of numbers of many-body correlation functions. The advantageous addition to these harmonics includes calculated coefficients which can be returned to at any time without the need to recalculate the positions of atoms. SDFs span angular and radial coordinates of interatomic separation and describe the three-dimensional density distribution of molecules, making use of fractional isosurface levels (FSL).<sup>60</sup>

The SDF<sup>64</sup> involves an entity of a molecule/s or atom/s at the origin. The entities must be well-defined in a sense that coordinate axes can be distinctly relative to them, thus, at least a minimum of two atoms are required. Figure 2.38 displays how H<sub>2</sub>O molecules are located with respect to the central entity such as, C<sub>10</sub>H<sub>16</sub>.<sup>58</sup>

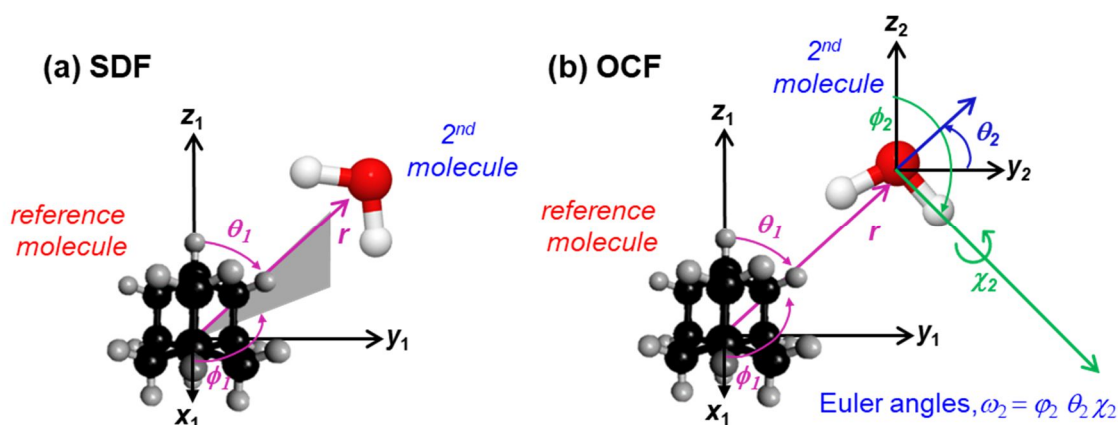


Figure 2.38. Spherical harmonic representations of site-site partial structure factors. Illustration of spherical coordinates of a second molecule (H<sub>2</sub>O) with respect to a reference molecule (C<sub>10</sub>H<sub>16</sub>) at (a) fixed orientation – defining positions of atoms of the H<sub>2</sub>O molecule in the first coordination shell and (b) representation of the Euler angles that define clockwise rotations about the  $z_2$ ,  $y_2$  axes of the second molecule indicating orientation with respect to the reference molecule.

Regarding Figure 2.38, the centre of mass (COM) of C<sub>10</sub>H<sub>16</sub> is located at the origin of the coordinate system. The question of the density of the second entity with respect to  $r$  can be calculated and is called the SDF. The orientation of the second entity as a function of  $r$  for a given  $\theta_1\phi_1$  can be calculated and named the orientational correlation function (OCF). The spherical harmonics of the SDF and OCF functions can be expressed using the Clebsch-Gordan coefficients ( $l_1, l_2, l; m_1, m_2, m$ ).<sup>58</sup> The OCF is indicated by three

## 2. Experimental Procedures and Characterisation Techniques

Euler angles ( $\omega_2 = \varphi_2\theta_2\chi_2$ ) about the  $zyz$  rotation as displayed in Figure 2.38. The description of Euler angles are written and found by Gubbins.<sup>89</sup>

The order of rotations is important to understand the final orientation. In the first instance, the entity is rotated by  $\varphi_2$  about the  $z$ -axis and then rotated by  $\theta_2$  about a new  $y$ -axis and finally by  $\chi_2$  about a revised  $z$ -axis which has been generated by a second rotation.<sup>58</sup>

The calculations of these coefficients are carried out by auxiliary routines in EPSR named, SHARM and SDF. The routine SHARM requires the user to define two cartesian axes as the third can be calculated from the first two. The SHARM routine in EPSR26 only estimates the real coefficients and so, the molecule in question must have a mirror plane and it must coincide with the  $z$ - $x$  plane.

### 2.6.4.8 Reverse Monte Carlo (RMC) and Metropolis Monte Carlo (MMC) EPSR

EPSR evolved and progressed from many efforts to use the reverse Monte Carlo (RMC) algorithm.<sup>90</sup> A few key difference between both approaches is outlined here.

EPSR indicates that pairwise forces can be obtained and within the reference potential, extra non-pair terms can be included. However, RMC is only a pairwise method. In RMC, the data is truncated and will consist of systematic and statistical errors in  $Q$ -space, which in turn, causes truncation and noise oscillations in the simulation and then, render bias to accept or reject a move of the molecules or atoms. The effects of this caveat on the outcome from RMC have not been explored, and nevertheless, the outcome is determined by pairwise interactions. This is fairly similar and analogous to the form used in EPSR with respect to reference and empirical potentials. In principle, truncation and noise artefacts will be present in the empirical potential in EPSR as in RMC, however, a Poisson function is used to minimise such effects.<sup>68</sup>

In EPSR, as a fit is acquired, and differences between the simulated and diffraction data are reduced and significantly small, the empirical potential holds information on the perturbation of the pair potential needed to obtain a fit. For instance, if the diffraction data were removed and the simulation was to be run itself, both potentials would retain information such as the partial structure factors and PDFs as if they were present. In comparison, in RMC with small differences, the simulation holds no record of obtained atomic configurations and thus, the configuration collapses into a different random array of atoms. Besides such difficulties, both EPSR and RMC are analogous and comparable

## 2. Experimental Procedures and Characterisation Techniques

methods.<sup>88, 90</sup> EPSR differences are in the reference and empirical potentials where the latter represents perturbation to the reference potential which is required to fit the data. The former assumes how atoms interact. RMC only makes use of the reference potential where it is limited to a repulsive term employed for the prevention of atomic overlap and a few coordination restrictions once geometries are available. No interatomic potential is employed in RMC. Thus, RMC is limited, yet minimises assumed knowledge on the outcome.<sup>91</sup>

### 2.7 References

1. A. Rosu-Finsen, PhD thesis, Heriot-Watt University, 2016.
2. J. J. Shephard, PhD thesis, Durham University, 2014.
3. D. Johannsmann, *Phys. Chem. Chem. Phys.*, 2008, **10**, 4516-4534.
4. D. T. Morelli, in *Thermoelectric Devices*, eds. G. L. Trigg and E. H. Immergut, Encyclopedia of Applied Physics, Wiley-VCH, New York, 1997, vol. 21, pp. 339-354.
5. T. M. Tritt, *Encycl. Mater. Sci. Technol.*, 2002, 1-11.
6. T. J. Seebeck, *Magnetic Polarization of Metals and Ores by Temperature Differences*, Berlin, 1822.
7. J. C. A. Peltier, *Ann. Chim. Phys.*, 1834, **56**, 371-386.
8. S. K. Talewar, S. O. Halukeerthi, R. Riedlaicher, J. J. Shephard, A. E. Clout, A. Rosu-Finsen, G. R. Williams, A. Langhoff, D. Johannsmann and C. G. Salzmann, *J. Chem. Phys.*, 2019, **151**, 134505.
9. E. Mayer and R. Pletzer, *J. Chem. Phys.*, 1984, **80**, 2939-2952.
10. A. Hallbrucker and E. Mayer, *Icarus*, 1991, **90**, 176-180.
11. J. T. Yates, *Experimental Innovations in Surface Science*, Springer, New York, 1998.
12. G. Attard and C. Barnes, *Surfaces*, OUP Oxford, 1998.
13. R. S. Smith, R. A. May and B. D. Kay, *J. Phys. Chem. B*, 2016, **120**, 1979-1987.
14. S. D. Green, A. S. Bolina, R. Chen, M. P. Collings, W. A. Brown and M. R. McCoustra, *Mon. Not. R. Astron. Soc.*, 2009, **398**, 357-367.
15. M. P. Collings, V. L. Frankland, J. Lasne, D. Marchione, A. Rosu-Finsen and M. R. S. McCoustra, *Mon. Not. R. Astron. Soc.*, 2015, **449**, 1826-1833.
16. L. Bradshaw, *RF Design*, 2000, **23**, 50-59.
17. G. Sauerbrey, *Z. Phys.*, 1959, **155**, 206-222.
18. D. A. Buttry and M. D. Ward, *Chem. Rev.*, 1992, **92**, 1355-1379.
19. A. K. Srivastava and P. Sakthivel, *J. Vac. Sci. Technol. A*, 2001, **19**, 97-100.
20. V. Matijasevic, E. L. Garwin and R. H. Hammond, *Rev. Sci. Instrum.*, 1990, **61**, 1747.
21. V. Tsionsky and E. Gileadi, *Langmuir*, 1994, **10**, 2830-2835.
22. A. W. Czanderna, *J. Phys. Chem.*, 1964, **68**, 2765.
23. G. Höhne, W. F. Hemminger and H.-J. Flammersheim, *Differential Scanning Calorimetry*, Springer Berlin Heidelberg, 2013.
24. W. M. Groenewoud, *Characterisation of Polymers by Thermal Analysis*, Elsevier Science B.V., Amsterdam, 2001.
25. P. W. Atkins and J. de Paula, *Physical Chemistry Thermodynamics, Structure, and Change*, ed. W. H. Freeman, OUP Oxford, 2014.
26. G. P. Johari, A. Hallbrucker and E. Mayer, *Nature*, 1987, **330**, 552.
27. J. A. McMillan and S. C. Los, *Nature*, 1965, **206**, 806-807.
28. M. S. Elsaesser, K. Winkel, E. Mayer and T. Loerting, *Phys. Chem. Chem. Phys.*, 2010, **12**, 708-712.
29. A. Hallbrucker, E. Mayer and G. P. Johari, *J. Phys. Chem.*, 1989, **93**, 4986-4990.
30. J. A. Ghormley, *J. Chem. Phys.*, 1968, **48**, 503-508.
31. M. A. Floriano, Y. P. Handa, D. D. Klug and E. Whalley, *J. Chem. Phys.*, 1989, **91**, 7187-7192.
32. A. Hallbrucker and E. Mayer, *J. Phys. Chem.*, 1987, **91**, 503-505.
33. G. P. Johari, G. Fleissner, A. Hallbrucker and E. Mayer, *J. Phys. Chem.*, 1994, **98**, 4719-4725.

## 2. Experimental Procedures and Characterisation Techniques

34. D. MacFarlane and C. Angell, *J. Phys. Chem.*, 1984, **88**, 759-762.
35. A. Jablonski, *Nature*, 1933, **131**, 839-840.
36. K. Burns, K. B. Adams and J. Longwell, *J. Opt. Soc. Am.*, 1950, **40**, 339-344.
37. J. J. Shephard, S. Klotz, M. Vickers and C. G. Salzmann, *J. Chem. Phys.*, 2016, **144**, 204502.
38. J. J. Shephard, J. S. O. Evans and C. G. Salzmann, *J. Phys. Chem. Lett.*, 2013, **4**, 3672-3676.
39. E. Whalley, *Can. J. Chem.*, 1977, **55**, 3429-3441.
40. C. Hammond, *The Basics of Crystallography and Diffraction*, OUP Oxford, 4 edn., 2015.
41. D. S. Sivia, *Elementary Scattering Theory For X-ray and Neutron Users*, OUP Oxford, 2011.
42. R. Pynn, *Los Alamos Science*, 1990, **19**, 1-31.
43. W. Massa, *Crystal Structure Determination*, Springer Berlin Heidelberg, 2000.
44. T. Yokoyama, *Nanoparticle Technology Handbook (Second Edition)*, Elsevier, 2012.
45. V. Pecharsky and P. Zavalij, *Fundamentals of Powder Diffraction and Structural Characterization of Materials*, Springer Science & Business Media, New York, 2008.
46. A. Leone, A. Forleo, L. Francioso, S. Capone, P. Siciliano and C. Di Natale, *Sensors and Microsystems: Proceedings of the 19th AISEM 2017 National Conference*, Springer International Publishing, 2017.
47. A. C. Larson, R. B. Dreele and B. Toby, "General Structure Analysis System (GSAS)", Los Alamos National Laboratory Report LAUR 86-748 2000.
48. W. Kraus and G. Nolze, *J. Appl. Cryst.*, 1996, **29**, 301-303.
49. C. G. Salzmann, B. J. Murray and J. J. Shephard, *Diamond Relat. Mater.*, 2015, **59**, 69-72.
50. T. L. Malkin, B. J. Murray, C. G. Salzmann, V. Molinero, S. J. Pickering and T. F. Whale, *Phys. Chem. Chem. Phys.*, 2015, **17**, 60-76.
51. C. Lobban, PhD thesis, University College London, 1998.
52. A. K. Soper, *GudrunN and GudrunX: Programs for correcting raw neutron and x-ray total scattering data to differential cross section*, Science & Technology Facilities Council, Swindon, UK, 2011.
53. J. R. D. Copley and T. J. Udovic, *J. Res. Natl. Inst. Stand Technol.*, 1993, **98**, 71-87.
54. A. K. Soper, *Mol. Phys.*, 2009, **107**, 1667-1684.
55. H. E. Fischer, A. C. Barnes and P. S. Salmon, *Rep. Prog. Phys.*, 2005, **69**, 233-299.
56. D. Keen, *J. Appl. Cryst.*, 2001, **34**, 172-177.
57. E. Takeshi and S. J. L. Billinge, in *The Method of Total Scattering and Atomic Pair Distribution Function Analysis*, eds. E. Takeshi and S. J. L. Billinge, Pergamon Materials Series, 2 edn., 2012, vol. 16, ch. 3, pp. 55-111.
58. A. K. Soper, Empirical Potential Structure Refinement EPSRshell User Manual Version 26, (accessed 16th March, 2020).
59. C. L. Farrow and S. J. L. Billinge, *Acta. Cryst.*, 2009, **65**, 232-239.
60. J. J. Shephard, A. K. Soper, S. K. Callear, S. Imberti, J. S. O. Evans and C. G. Salzmann, *Chem. Commun.*, 2015, **51**, 4770-4773.
61. D. T. Bowron, J. L. Finney, A. Hallbrucker, I. Kohl, T. Loerting, E. Mayer and A. K. Soper, *J. Chem. Phys.*, 2006, **125**, 194502.

## 2. Experimental Procedures and Characterisation Techniques

62. T. Egami and S. J. Billinge, *Underneath the Bragg Peaks: Structural Analysis of Complex Materials*, Elsevier, Oxford: Pergamon, 2003.
63. A. Laaksonen, P. Kusalik and I. Svishchev, *J. Phys. Chem. A*, 1997, **101**, 5910-5918.
64. P. G. Kusalik and I. M. Svishchev, *Science*, 1994, **265**, 1219.
65. T. Loerting, K. Winkel, M. Seidl, M. Bauer, C. Mitterdorfer, P. H. Handle, C. G. Salzmann, E. Mayer, J. L. Finney and D. T. Bowron, *Phys. Chem. Chem. Phys.*, 2011, **13**, 8783-8794.
66. A. K. Soper, *J. Phys.: Condens. Matter*, 2007, **19**, 335206.
67. A. K. Soper, *Chem. Phys.*, 1996, **202**, 295-306.
68. A. K. Soper, *Phys. Rev. B*, 2005, **72**, 104204.
69. J. E. Enderby, D. M. North and P. A. Egelstaff, *Philos. Mag.*, 1966, **14**, 961-970.
70. A. Le Bail, L. M. Cranswick, I. Madsen, A. Fitch, R. Allmann, C. Giacobozzo, A. Altomare, J. K. Cockcroft, R. Caliendo and P. Norby, *Powder Diffraction: Theory and Practice*, The Royal Society of Chemistry, Cambridge, 2008.
71. A. Soper, W. Howells and A. Hannon, *Analysis of Time-of-Flight Diffraction Data from Liquid and Amorphous Samples*, ISIS Facility, RAL, Oxon, UK, RAL-89-046, 1989.
72. J. W. G. Thomason, *Nucl. Instrum. Methods Phys. Res., Sect. A*, 2019, **917**, 61-67.
73. D. T. Bowron, A. K. Soper, K. Jones, S. Ansell, S. Birch, J. Norris, L. Perrott, D. Riedel, N. J. Rhodes, S. R. Wakefield, A. Botti, M. A. Ricci, F. Grazzi and M. Zoppi, *Rev. Sci. Instrum.*, 2010, **81**, 033905.
74. L. C. Pardo, ANGULA Software Download, <https://gcm.upc.edu/en/members/luis-carlos/angula/ANGULA>, (accessed 5th January, 2021).
75. L. C. Pardo, A. Henao and A. Vispa, *J. Non-Cryst. Solids*, 2015, **407**, 220-227.
76. L. C. Pardo, A. Henao, S. Busch, E. Guàrdia and J. L. Tamarit, *Phys. Chem. Chem. Phys.*, 2014, **16**, 24479-24483.
77. A. J. Johnston, S. Busch, L. C. Pardo, S. K. Callear, P. C. Biggin and S. E. McLain, *Phys. Chem. Chem. Phys.*, 2016, **18**, 991-999.
78. B. H. Toby, *J. Appl. Crystallogr.*, 2001, **34**, 210-213.
79. A. K. Soper, *Int. Scholarly Res. Not.*, 2013, 279463.
80. A. K. Soper, *J. Chem. Phys.*, 1994, **101**, 6888-6901.
81. T. Yamaguchi, K. Hidaka and A. K. Soper, *Mol. Phys.*, 1999, **96**, 1159-1168.
82. D. T. Bowron, J. L. Finney and A. K. Soper, *J. Am. Chem. Soc.*, 2006, **128**, 5119-5126.
83. S. E. McLain, A. K. Soper and A. Luzar, *J. Chem. Phys.*, 2006, **124**, 074502.
84. R. C. Burton, E. S. Ferrari, R. J. Davey, J. L. Finney and D. T. Bowron, *J. Phys. Chem. B*, 2010, **114**, 8807-8816.
85. J. J. Shephard, J. S. O. Evans and C. G. Salzmann, *Mol. Phys.*, 2019, **117**, 3337-3344.
86. G. Hummer, D. M. Soumpasis and M. Neumann, *J. Phys.: Condens. Matter*, 1994, **6**, A141-A144.
87. W. L. Jorgensen, D. S. Maxwell and J. Tirado-Rives, *J. Am. Chem. Soc.*, 1996, **118**, 11225-11236.
88. A. K. Soper, *Mol. Simul.*, 2012, **38**, 1171-1185.
89. C. Gray and K. Gubbins, *Theory of Molecular Fluids: Fundamentals*, Clarendon Press, Oxford, 1984.
90. R. McGreevy and L. Pusztai, *Mol. Sim.*, 1988, **1**, 359-367.



## 2. Experimental Procedures and Characterisation Techniques

91. R. McGreevy and M. Howe, *Phys. Chem. Liq.*, 1991, **24**, 1-12.

### **3 Gaseous ‘Nanoprobes’ for Detecting Gas-Trapping Environments in Thick Layers of Amorphous Solid Water**

I declare that this chapter has been adapted from reference 1.

#### **3.1 Introduction**

Codeposited films of amorphous ice and gaseous species have been investigated to a much lesser extent when compared to the layered films as mentioned in Chapter 1. This thesis distinguishes the poorly understood mechanisms of amorphous solid water (ASW) from the scope in the literature due to the preparation of thick films, whereas the literature mainly extends to exploring only several hundred monolayers (ML) of ASW films. The aim to further explore the behaviour of poorly understood ASW is tackled in this chapter by incorporating gaseous ‘nanoprobes’ into the amorphous ice structure.

In the present chapter, a detailed evaluation of ASW using small amounts of gaseous ‘nanoprobes’ incorporated into the ASW matrix during codeposition, is extensively explored for the existence of gas ‘trapping’ environments and hence, ASW’s morphology in the 25–100  $\mu\text{m}$  thickness range.<sup>1</sup> Such gaseous ‘nanoprobes’ with differing physical properties include, argon (Ar), methane ( $\text{CH}_4$ ), carbon dioxide ( $\text{CO}_2$ ) and helium. Argon is used more specifically as a ‘nanoprobe’ due to its small, inert nature and simply because it does not stick to surfaces. This ‘nanoprobe’ approach is aimed at characterising the argon-water system as a model system used to elucidate the changes of ASW upon heating and report for the first time, an additional feature observed during the thermal desorption of the matrix. This approach is probed by monitoring the desorption processes of ASW deposits, followed by using mass spectrometry (MS) upon heating in the 95–185 K temperature range.<sup>1</sup> Macroscopic films are prepared on a large substrate on the gram scale in comparison to previous studies of nanoscale ASW films.<sup>2–6</sup> Deposition on the cryoplate is suggested here with evidence to create a highly porous solid network of pores and voids within the amorphous ice matrix. The trapping of gases is not only determined by the structure and dynamics of ice, but also inclined by the gas itself.

Moreover, the effects of film thickness, deposition rate of argon, and the baffling of the  $\text{H}_2\text{O}$ -vapour beam towards the deposition plate are investigated. The deposition distance and the angle of incidence have been fixed throughout this thesis. As previously

### 3. Gaseous ‘Nanoprobes’ for Detecting Gas-Trapping Environments in Thick Layers of Amorphous Solid Water

stated, the experimental conditions for deposition are critical and precise and so, a quartz-crystal microbalance (QCM) was employed to essentially ‘map’ the shape of the H<sub>2</sub>O-vapour beam inflowing into the vacuum chamber. QCM measurements were used to detect perhaps potential changes in the viscoelastic properties or readsorption effects that may exist in the deposit upon heating.<sup>1</sup>

## 3.2 Experimental Methods

### 3.2.1 Calibration Approach for Determining Desorption Rates

A schematic illustration and labelled parts of the vacuum chamber have previously been provided and explained in Chapter 2 and also depicted later in Figure 3.4(a). High-accuracy graduated needle valves were used to leak gases and H<sub>2</sub>O-vapour into the vacuum chamber, supplied with a manufacturer calibrated flow chart of air flow / mmol s<sup>-1</sup>. As displayed in Figure 3.1, a defined gas flow rate can be determined, and desired rates can be adjusted in mmol s<sup>-1</sup> if the pressure difference across the needle valve is approximately 1 bar.

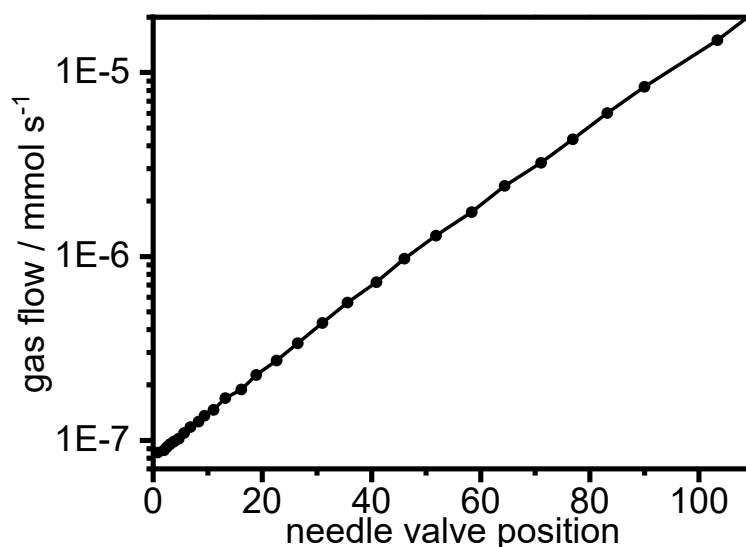


*Figure 3.1. Manufacturer flow-rate chart supplied by Oerlikon Leybold Vacuum for the high-accuracy graduated needle valves (EV 016 DOS AB) in the required range used throughout this study. This figure has been reprinted from reference 1 with the permission of AIP Publishing.*

The experimental set-up and needle valves employed in this study allows defined amounts of gaseous ‘nanoprobes’ to be leaked into the vacuum chamber, however, H<sub>2</sub>O-vapour cannot be precisely defined as the pressure in the H<sub>2</sub>O reservoir is equal to the vapour pressure of H<sub>2</sub>O which is approximately 20 mbar at ambient temperature.<sup>1</sup>

### 3. Gaseous ‘Nanoprobes’ for Detecting Gas-Trapping Environments in Thick Layers of Amorphous Solid Water

The variations in the rate of pumping in line with the chamber pressure were estimated using the high-accuracy graduated needle valves by measuring the response of the chamber pressure. Once the chamber pressure was reduced in sequential stages (Chapter 2) and reached a pressure of  $2 \times 10^{-6}$  mbar, gases were precisely leaked into the chamber. In particular, a range of different leak rates for argon, CH<sub>4</sub>, CO<sub>2</sub> and helium (Figure 3.2 and Figure 3.3) were realised by gradually increasing the needle valve position in increments of 10. Partial pressure responses corresponding to these positions were measured with the MS and recorded to slightly larger partial pressures observed in the temperature-programmed desorption (TPD) experiments.

As argon was the main focus of this study, the partial pressures recorded while the needle valve was fully closed off was used as a background correction and therefore, subtracted from all recorded partial pressures. Figure 3.2 shows the calibration data quantifying the correlation of partial pressure / torr with gas flow / mmol s<sup>-1</sup>.

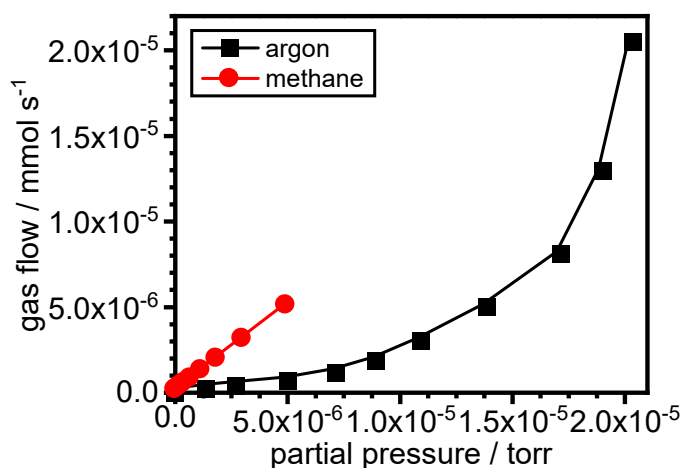


Figure 3.2. The correlation of partial pressures of argon (black squares) and methane, CH<sub>4</sub> (red circles) with gas flow. The correlating needle valve positions and chamber pressures were recorded together with the MS and interpolated with the manufacture flow-rate chart to obtain partial pressures and gas flows used for this study, taken from Figure 3.1. Details on the interpolation are provided later in this chapter (section 3.4). This figure has been reprinted from reference 1 with the permission of AIP Publishing.

### 3. Gaseous ‘Nanoprobes’ for Detecting Gas-Trapping Environments in Thick Layers of Amorphous Solid Water

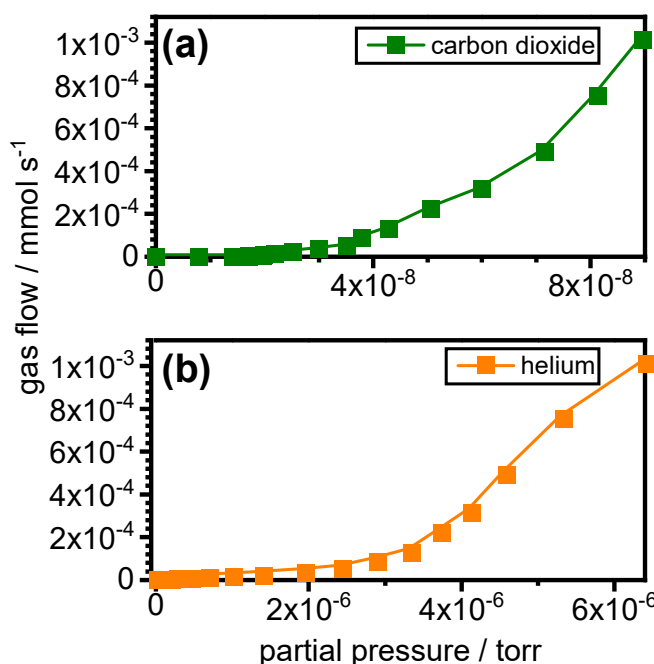


Figure 3.3. Partial pressure correlation of (a) carbon dioxide, CO<sub>2</sub> and (b) helium with gas flow / mmol s<sup>-1</sup>. As with the argon and CH<sub>4</sub> calibration, the corresponding needle valve positions and chamber pressures were recorded together with the MS partial pressures and interpolated with the manufacturer flow-rate chart to obtain gas flows and partial pressures. Detail on the interpolation is given later in this chapter (section 3.4).

The calculation of desorption rates from the TPD data then included the conversion of partial pressures / torr into desorption rate / mmol s<sup>-1</sup>. A controlled leak rate is used for calibration to simulate desorption. The needle valve position obtained from the MS of the calibration was interpolated with the airflow / mmol s<sup>-1</sup> provided by the manufacturer. More detail is provided in section 3.4 of this chapter.

A LabView VI program, version six (National Instruments) is used to record real-time data which records the temperature or chamber pressures with respect to time. The axes of these data sets can be swapped from temperatures, partial pressures or desorption rates using the Interpolate/Extrapolate Y from X function in OriginPro 2018.

#### 3.2.2 Cryogenic Deposition Experiments

A simple schematic of the apparatus is presented in Figure 3.4(a) and Figure 3.4(b) which illustrates the heating and cooling rates during a typical deposition experiment. In this study, as mentioned, deposits in a temperature window of 95–185 K are measured to investigate the interaction of gas-water ice systems. Cryogenic deposition experiments were carried out at a base pressure of  $<2 \times 10^{-6}$  mbar and a base deposition plate

### 3. Gaseous ‘Nanoprobes’ for Detecting Gas-Trapping Environments in Thick Layers of Amorphous Solid Water

temperature of approximately 95 K. Once these conditions were approached, H<sub>2</sub>O-vapour was leaked in the vacuum chamber at an inlet pressure of  $1 \times 10^{-1}$  mbar; the leak rate was adjusted using the graduated needle valve attached to the bottom of the chamber. The deposition rate obtained from the QCM with the inlet pressure of H<sub>2</sub>O at  $1 \times 10^{-1}$  mbar was determined to be  $\sim 0.96 \mu\text{g cm}^{-2} \text{s}^{-1}$ , calculated by performing a linear fit to the data as shown in upcoming Figure 3.5 where the gradient of the slope is equivalent to the mass deposition rate. The deposition rate is then divided by the molar mass of H<sub>2</sub>O, 18.02 g mol<sup>-1</sup> to obtain a value for a molar deposition rate of  $5.33 \times 10^{-2} \mu\text{mol cm}^{-2} \text{s}^{-1}$ .

A pressure of  $1 \times 10^{-1}$  mbar of H<sub>2</sub>O led to a small increase in pressure at the backside of the deposition plate towards  $1 \times 10^{-5}$  mbar, demonstrating the effective cryogenic action from the deposition plate. For codeposition, before the cooling of the substrate to 95 K, the system is purged with the guest species to eliminate and minimise nitrogen (N<sub>2</sub>) gas and any other gases that may be present in the system. As mentioned, the system is evacuated to its base pressure and temperature of  $< 2 \times 10^{-6}$  mbar and 95 K, respectively. Gaseous species were then introduced into the vacuum chamber and mixed with the flow of H<sub>2</sub>O-vapour by selecting desired leak rates on the second graduated needle valve. During a typical deposition experiment, approximately 1.5 g of H<sub>2</sub>O was deposited in the vacuum chamber and the weight of the round-bottom flask was measured before and after deposition to determine the amount deposited. The temperature of the deposition plate remained constant at 95 K during this time. Unless stated otherwise, the deposition time was two-hours, equating to 7200 seconds and the leak rate for the gaseous species was set to be  $1.35 \times 10^{-5} \text{mmol s}^{-1}$  (Table 3.1).

A typical deposition experiment displayed pronounced increases in cooling rates that were below 120 K, Figure 3.4(b). This effect is due to the Leidenfrost effect in which, liquid nitrogen (LN<sub>2</sub>), close to the copper surface, is significantly higher in temperature than the liquid’s boiling point, creating an insulating layer of vapour keeping the liquid from boiling off. The cold LN<sub>2</sub> gas begins to wet the surfaces inside of the cooling system below the Leidenfrost temperature and is thus, named the Leidenfrost effect.

### 3. Gaseous ‘Nanoprobes’ for Detecting Gas-Trapping Environments in Thick Layers of Amorphous Solid Water

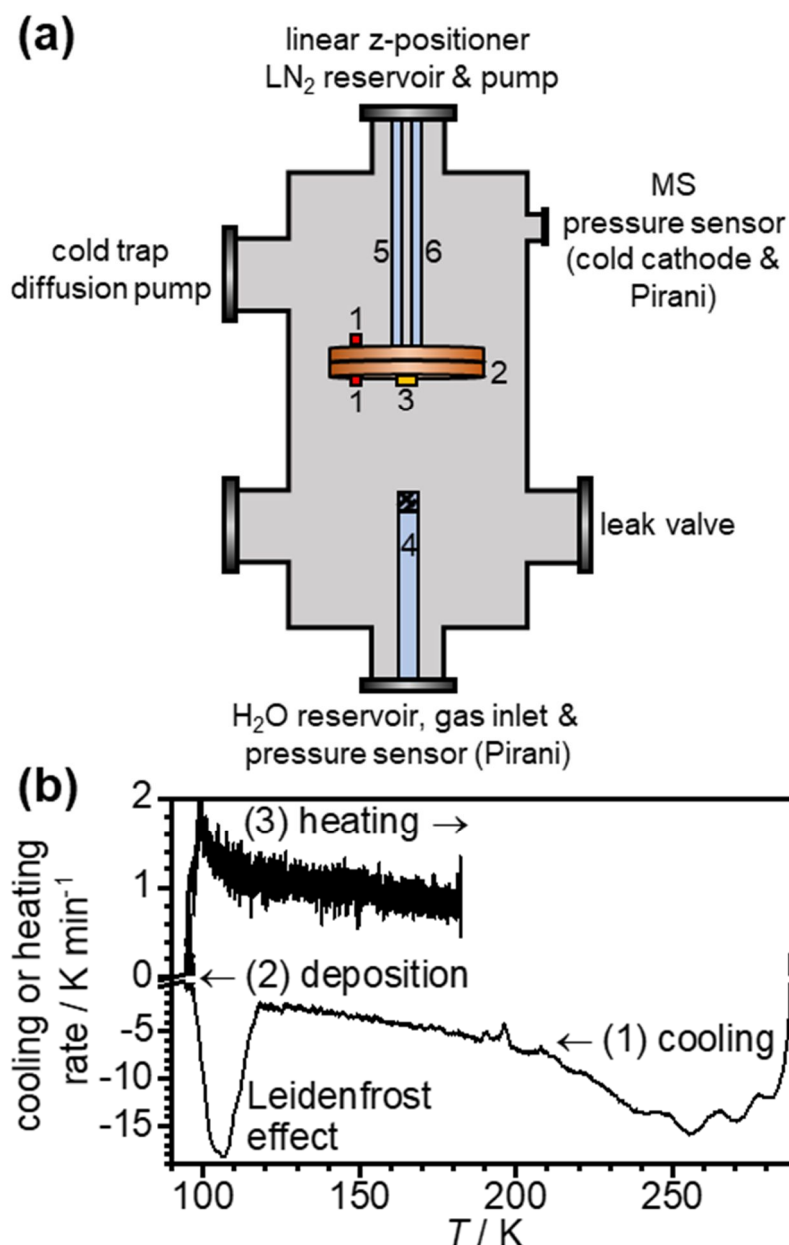


Figure 3.4. (a) Illustration of the set-up for cryogenic deposition experiments. Several ports are available on the vacuum chamber for the attachment of many accessories. The numbered components within the vacuum system consist of (1) K-type thermocouples, (2) detachable cryogenic plate, (3) QCM sensor head, (4) H<sub>2</sub>O-vapour inlet tube equipped with a metal (iron) mesh, (5) LN<sub>2</sub> feedthrough and (6) rotary-vane pump feedthrough and (b) heating and cooling rates for a typical deposition experiment. This figure has been reprinted from reference 1 with the permission of AIP Publishing.

### 3. Gaseous ‘Nanoprobes’ for Detecting Gas-Trapping Environments in Thick Layers of Amorphous Solid Water

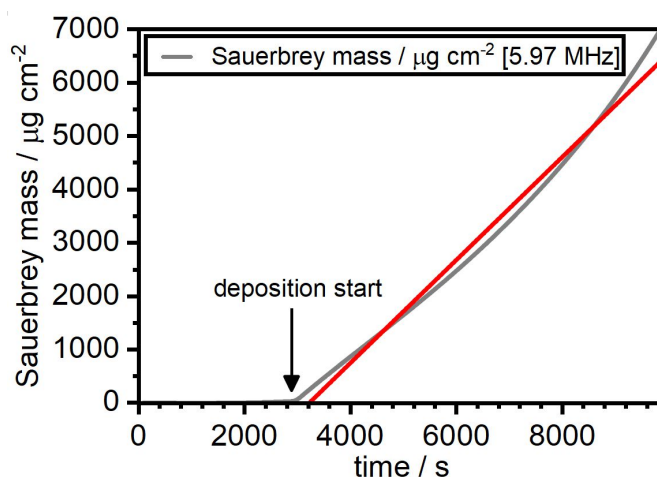


Figure 3.5. QCM response depicting the Sauerbrey mass recorded during a two-hour deposition (grey line depicts pure  $\text{H}_2\text{O}$  at a  $\text{H}_2\text{O}$  inlet pressure of  $1 \times 10^{-1}$  mbar with a mesh covering the  $\text{H}_2\text{O}$ -vapour inlet tube). The red line shows a linear fit measured from the beginning of the deposition through to the end of the deposition.

#### 3.2.3 Quartz-Crystal Microbalance (QCM) Measurements

Gold-plated, AT-cut, 6 MHz quartz planoconvex crystals were placed firmly inside the QCM sensor head and attached to the deposition plate [Figure 3.4(a), (3)]. Coaxial cables were used to connect the QCM sensor to a reflection bridge and N2PK myVNA (0.5–60 MHz) network analyser software. Deposition rates during experiments were monitored by recording the fundamental frequency changes in electrical conductance with respect to time, using the QTZ and myVNA software.<sup>7,8</sup> The shape of the  $\text{H}_2\text{O}$ -vapour beam was determined by placing the QCM sensor head at different locations across the plate and altering the vertical position of the deposition plate using the linear z-positioner. Details for the position of the deposition plate is provided in section 3.3.1. Derivatives of the fundamental frequency changes were calculated and deposition rates from these values were obtained with respect to time.  $\text{H}_2\text{O}$ -vapour enters the vacuum chamber through the fine needle valves and travels a long distance in the vacuum before it hits the QCM [Figure 3.4(a), (4)].

#### 3.2.4 Temperature-Programmed Desorption (TPD) Experiments

Following the completion of the two-hour deposition, the deposit is kept cold at 95 K for a further one-hour to allow for the vacuum system to reach base pressure and remove any excess gas. During this time, the residual gas analyser MS equipped with a Faraday cup is set to record a mass range of 1–100  $m/z$  partial pressures. After this time, TPD experiments began as the deposit is left to gradually heat up to 185 K at a constant rate of



### 3. Gaseous ‘Nanoprobes’ for Detecting Gas-Trapping Environments in Thick Layers of Amorphous Solid Water

0.01–0.02 K min<sup>-1</sup>, monitored by the K-type thermocouple. This is to monitor gas release from layers of amorphous ice mixtures and observe the desorption of H<sub>2</sub>O. At this temperature, the pressure reaches the maximum working capacity of the Faraday cup:  $1 \times 10^{-4}$  mbar. The heating rate from 95 to 185 K is found to be 1.7 K min<sup>-1</sup> at 100 K and decreases to 0.8 K min<sup>-1</sup>, when it approaches 185 K as displayed in Figure 3.4(b).

#### 3.2.5 *Ex situ* X-ray Diffraction (XRD)

This procedure is also described in Chapter 2. Following deposition, ASW is annealed at 125 K under vacuum and cooled back down to base temperature. This is to avoid the formation of the N<sub>2</sub> clathrate hydrate of cubic structure II (CS-II), prone to form as the highly porous as-made ASW is exposed to LN<sub>2</sub>.<sup>9-11</sup> Clathrate hydrate formation is prevented when the pore walls block further trapping of N<sub>2</sub> gas with the amorphous ice, or when closed pores are depleted of N<sub>2</sub> gas and the pressure of the gas reaches its dissociation pressure of the clathrate hydrate.<sup>10</sup> The chamber was vented to atmospheric pressure under LN<sub>2</sub> *via* a gate valve and the deposition plate was submerged and detached from the cryostat in LN<sub>2</sub> and further removed from the chamber. Full detail on sample removal is provided in Chapter 2. The deposited materials are transferred under LN<sub>2</sub> to purpose-built Kapton sample holders for XRD measurements. The measurements for XRD were collected from 95 K to 270 K in 10 K steps.

### 3. Gaseous ‘Nanoprobes’ for Detecting Gas-Trapping Environments in Thick Layers of Amorphous Solid Water

#### 3.3 Results and Discussion

In the first instance, to optimise the conditions of the vacuum chamber, pure ASW was deposited onto the cryoplate and quantitative QCM analysis was carried out (section 3.3.1). Further to this, to corroborate the highly porous amorphous nature of the deposits in this study after a two-hour deposition experiment, a pure ASW deposit was carefully recovered from the deposition plate under LN<sub>2</sub> (section 3.3.2).

##### 3.3.1 Shape of the H<sub>2</sub>O Beam Entering the High-Vacuum Chamber

The precise experimental details of cryogenic physical vapour deposition have been known to have pronounced effects on deposit morphology.<sup>12, 13, 14, 15-17</sup> In particular, the size and number of pores of highly microporous ASW highly depend upon deposition conditions for its preparation, such as baffled flow-conditions<sup>13</sup>, deposition angle,<sup>14</sup> temperature<sup>12</sup> and deposition rate.<sup>18</sup> The experimental set-up used in this study, which, compared to other studies, consists of a large deposition plate made from copper with an area of 324 cm<sup>2</sup>. This cryogenic deposition plate allows gram-scale production of ASW deposits, however, acts as a drawback as deposition rates may, unavoidably be non-uniform across the entirety of the plate.

To allow the precise determination of deposition rates inside the vacuum chamber, a QCM sensor was attached to the deposition plate at different locations across the plate and the vertical position of the plate was changed using the linear z-positioner. The positions of the QCM were located at (i) central, (ii) edge and the (iii) midpoint of the radius of the deposition plate, all equidistance to one another. The adsorption process for H<sub>2</sub>O is assumed to have a high sticking probability of unity at 77 K which allows the effective ‘mapping’ of the shape of the H<sub>2</sub>O-vapour beam entering the chamber. This sticking coefficient of unity infers that each molecule striking the surface will adsorb onto it.<sup>19</sup>

Referring to the Sauerbrey equation (Chapter 2, Equation 2.10), the resonance frequency of the piezoelectric crystal decreases during deposition experiments.<sup>8, 20</sup> This is due to the linear relationship with a negative proportionality between the resonance frequency and deposited mass. Using this data, the deposition rate can be determined for each position on the plate (Figure 3.6, raw data) and estimated with respect to time from the derivative of the quartz frequency.

### 3. Gaseous ‘Nanoprobes’ for Detecting Gas-Trapping Environments in Thick Layers of Amorphous Solid Water

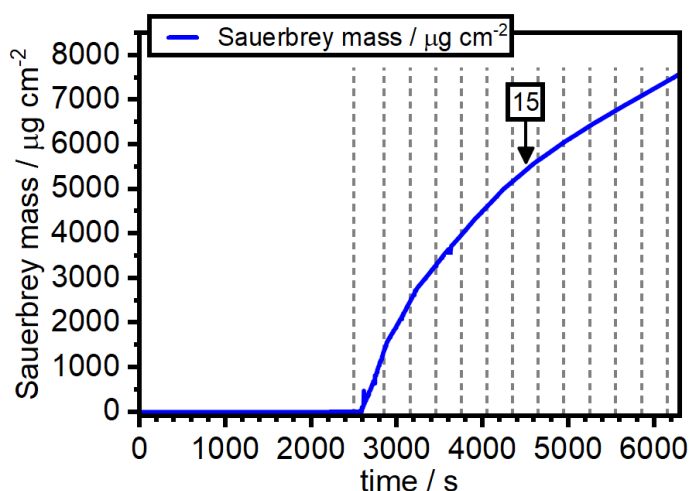


Figure 3.6. Raw data measurements from a central QCM position whilst changing the linear z-positioner, initially from 5 cm to 22 cm at every five-minute intervals. Experimental conditions for this data include a mesh placed on top of the H<sub>2</sub>O-vapour beam. An indication of a 15 cm position is shown with its respective QCM measurement of five minutes. The grey lines denote the interval times at which the QCM measurements were recorded from the central position from the deposition plate and 15 cm above the H<sub>2</sub>O-inlet tube (black arrow indicating 15 cm).

Raw data obtained from the QCM measurements of the H<sub>2</sub>O-vapour beam as shown in Figure 3.6 were measured several times for validity and reproducibility at different deposition stage distances (5, 7, 9, 10, 11, 13, 15, 17, 19, 20, 21 and 22 cm) for pure ASW. The QCM response recorded the frequency and calculated the mass changes during the experiment and the response was recorded at each distance for the same amount of time (five minutes) while pure ASW was deposited. At each distance, as indicated by the grey dashed lines in Figure 3.6, a linear fit was performed to obtain a deposition rate for each distance in units of  $\mu\text{g cm}^{-2} \text{ s}^{-1}$ .

The deposition rates determined from the vacuum chamber are presented in Figure 3.7, where the three panels, (a), (b) and (c) correspond to the various locations and vertical positions of the plate depict the shape of the H<sub>2</sub>O-vapour beam. The panels correspond to the flow of H<sub>2</sub>O-vapour in the chamber remaining unperturbed, baffled with an iron mesh, and fully blocked above the H<sub>2</sub>O-inlet tube, respectively. For the purpose of ‘mapping’ the shape of the beam, the Sauerbrey mass was accounted for in this case. In addition, several experiments for the deposition of pure ASW were conducted where the QCM sensor head was positioned in the centre, edge, and the midpoint of the radius of the deposition plate for unbaffled, mesh and full blockage of the H<sub>2</sub>O-vapour beam. After several measurements of placing the QCM at different locations on the plate, it was

### 3. Gaseous ‘Nanoprobes’ for Detecting Gas-Trapping Environments in Thick Layers of Amorphous Solid Water

possible to construct a contour plot, depicting the shape of the beam as can be seen in Figure 3.7 below.

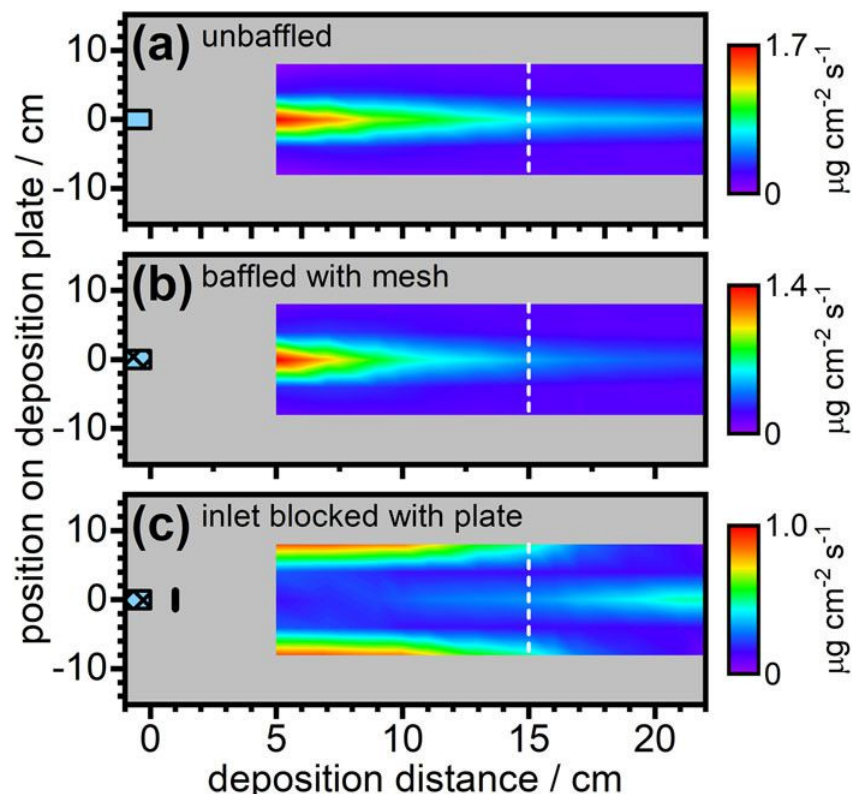


Figure 3.7. The ‘mapping’ of the shape of the H<sub>2</sub>O-vapour beam within the chamber using the QCM sensor for (a) unbaffled flow, (b) baffled flow using an iron mesh and (c) blocked flow using a two-pence coin. Local deposition rates are displayed as contour plots, showing deposition distances and positions on the deposition plate. This figure also displays grey colour in all panels corresponding to the vacuum chamber where deposition distances could not be determined [Figure 3.4(a)]. Each panel displays a white line, indicating a 15 cm chosen distance for optimum deposition experiments. This figure has been reprinted from reference 1 with the permission of AIP Publishing.

Figure 3.7(a) illustrates that the H<sub>2</sub>O-vapour beam displays a strong directionality towards the centre of the plate without the use of an iron mesh baffling the H<sub>2</sub>O-inlet tube. Moving further away from the H<sub>2</sub>O-inlet tube, the flow became more diffuse. Yet, at a vertical distance of 22 cm, the plate is quite far away from the H<sub>2</sub>O-inlet tube and the deposition profile is extremely more non-uniform at 5 cm when compared to 22 cm across the plate. At larger deposition distances, the iron mesh renders the flow of H<sub>2</sub>O-vapour showing a more diffuse nature, [Figure 3.7(b)] indicating a few degrees of perturbation. A two-pence coin was placed on top of the mesh on the H<sub>2</sub>O-inlet tube with a small gap on the side. The vertical direction of the flow of vapour was blocked, leading to a drastic change in the beam profile shape [Figure 3.7(c)]. As seen in Figure 3.7(c), at smaller distances, between the deposition plate and H<sub>2</sub>O-inlet tube, large deposition rates are found towards

### 3. Gaseous ‘Nanoprobes’ for Detecting Gas-Trapping Environments in Thick Layers of Amorphous Solid Water

the edges of the plate which can be assumed to be from the ‘reflection’ of the beam from the inside walls of the vacuum chamber. In comparison, larger distances show that the centre of the plate displays the fastest deposition rates. It is speculated that this arises due to a second ‘bounce’ originating from the beam of the inside walls of the vacuum chamber. At the centre of the deposition plate, the optimum position of the vertical position of the plate was found to be 15 cm, where the deposition rate was found to decrease from 0.724 to 0.472 and 0.316  $\mu\text{g cm}^{-2} \text{s}^{-1}$  respectively, for unbaffled flow, baffled and blocked flow.<sup>1</sup> Quantitative QCM deposition rates are depicted in Figure 3.8 below.

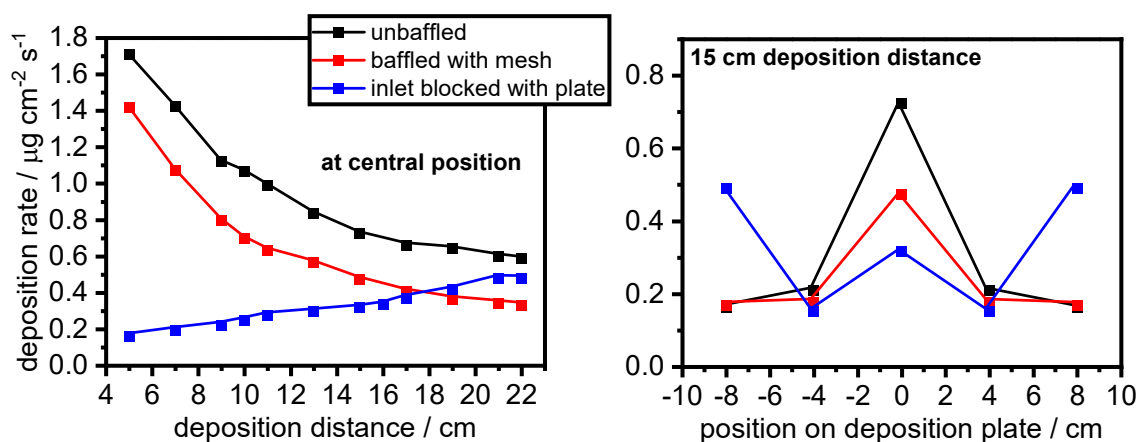


Figure 3.8. Influence of QCM deposition rates illustrated as a function of (a) deposition distance at the central position of the deposition plate and (b) position of QCM on the deposition plate at optimum deposition distance position of 15 cm. This figure has been reprinted from reference 1 with the permission of AIP Publishing.

Hence, on the basis of these experiments, it was determined that the mesh was to be employed in order to baffle the flow of  $\text{H}_2\text{O}$ -vapour with the deposition plate suspended from the chamber at 15 cm, in line of sight with the  $\text{H}_2\text{O}$ -inlet tube. The baffle is utilised in these experiments herein as it should essentially disrupt the  $\text{H}_2\text{O}$ -vapour beam by diffusing and dispersing  $\text{H}_2\text{O}$  molecules randomly across the deposition plate and also, to induce pore formation in ASW.

These optimum conditions are reasonable for achieving a relatively uniform film thickness across the plate while not compromising the overall deposition yield. Some small pressure increases arise from the backside of the deposition plate while the flow is baffled (see the experimental section of this chapter) and the profile of the beam at 15 cm, so it can be assumed  $\text{H}_2\text{O}$ -vapour that is leaked in the chamber is almost ‘quantitatively’ deposited onto the plate. In line with this, no ice deposit appeared on the  $\text{LN}_2$ -cooled parts on the down-stream of the deposition plate after deposition experiments, while visibly

### 3. Gaseous ‘Nanoprobes’ for Detecting Gas-Trapping Environments in Thick Layers of Amorphous Solid Water

‘milky’ ice deposits formed on the deposition plate, which was extracted for *ex situ* XRD analysis.

#### 3.3.2 Preparation, Structure and Thermal Characteristics of Pure ASW Films

In this study, to confirm the amorphous nature of the deposit after a two-hour deposition experiment, pure ASW deposit was carefully recovered from the deposition plate in the chamber under LN<sub>2</sub> and *ex situ* analysis of the deposit was carried out using XRD. *Ex situ* analysis of pure ASW displayed the absence of Bragg peaks and thus, confirmed a fully amorphous deposit. At 95 K, the as-made pure ASW displayed well-known characteristic broad features, centred at (i)  $2\theta = 24^\circ$  and (ii)  $2\theta = 42^\circ$ ,<sup>21-23</sup> Figure 3.9(a). Upon heating as-made ASW from 95 K to 270 K, the transition from an amorphous deposit to stacking-disordered ice, ice *Isd*, is observed, and upon further heating, fully hexagonal ice, ice *Ih*, is observed. The transformation to ice *Isd* begins at approximately 140 K.<sup>23-26</sup> Section 3.3.3 makes use of the MCDIFFaX program analysing the crystallisation of the pure ASW sample from 160 K to 190 K, confirming the stacking probability.

Using the QCM, the changes in the fundamental quartz-oscillator frequency during a typical two-hour deposition experiment were monitored, followed by heating in the vacuum. Figure 3.9(b) depicts these changes and as expected, the frequency is seen to decrease during deposition by 500 kHz, which renders this change quite exceptional. In many other cases, films made of similar thickness are known to overdamp the resonance.<sup>27</sup> The Sauerbrey equation represents the relative resonance frequency, illustrating accurate responses originating from thin and rigid films, assuming the deposited mass acts as an extension to the crystal thickness. Due to the large frequency changes encountered here, common artefacts may arise which are caused by i.e., temperature and can thus, be disregarded in this instance. A more detailed, comprehensive evaluation of the changes occurring within the film monitored by QCM is described in section 3.3.4.

Before the deposition is initiated, the quartz crystal resonates at 5.972 MHz and is seen to decrease to 5.454 MHz after a two-hour deposition [Figure 3.10(b)]. The Sauerbrey equation in this instance can only be seen as an approximation due to the large frequency change as it is used to derive a mass per unit area from a frequency shift.<sup>28</sup> This is due to limitations of the Sauerbrey relationship where only small changes in frequency are valid ( $\Delta f/f < 0.05$ ). Nevertheless, this approximation is considered due to the large

### 3. Gaseous ‘Nanoprobes’ for Detecting Gas-Trapping Environments in Thick Layers of Amorphous Solid Water

frequency shift itself, but also, another influence may arise from viscoelastic effects which should be considered when the film thickness is a substantial fraction of the wavelength of the shear sound.<sup>1</sup> The limitations of the Sauerbrey equation are acknowledged earlier and an estimate of the mass per unit area can be calculated. Using the known constants of the Sauerbrey equation ( $\sim 5.7 \text{ Hz nm}^{-1}$  at a density,  $\rho = 1 \text{ g cm}^{-3}$ ), the frequency change,  $\Delta f$ , was measured as  $-518 \text{ kHz}$ , corresponding to a total mass per unit area of  $9050 \text{ } \mu\text{g cm}^{-2}$ . A film thickness can only be calculated in this case if the density of the deposit is assumed, however, the density of the samples prepared in this study is poorly known due to the high porosity of ASW. If one assumes that  $\rho$  is approximately  $0.93 \text{ g cm}^{-3}$  as a bulk density number of low-density amorphous ice (LDA),<sup>29</sup> a  $100 \text{ } \mu\text{m}$  film thickness is obtained. Due to the porosity of as-made ASW,<sup>16, 30, 31</sup> the actual thickness of the films prepared in this study will most likely be greater.

When the ASW film is heated, the QCM detects a frequency increase beginning at  $130 \text{ K}$ . During this time, the vapour pressure increases as visible in Figure 3.9(c), which indicates a mass decrease as the frequency increases. However, the release of bending stress and viscoelastic effects may possibly be a contributing factor here where these effects may be responsible for the unusual decrease in frequency above  $150 \text{ K}$ . A further detailed analysis and account of the QCM data is provided in the next section. The frequency is seen to rise once again at  $170 \text{ K}$ , which is likely to be due to the desorption of ice *Isd*, where its vapour pressure increases significantly with respect to temperature.

### 3. Gaseous ‘Nanoprobes’ for Detecting Gas-Trapping Environments in Thick Layers of Amorphous Solid Water

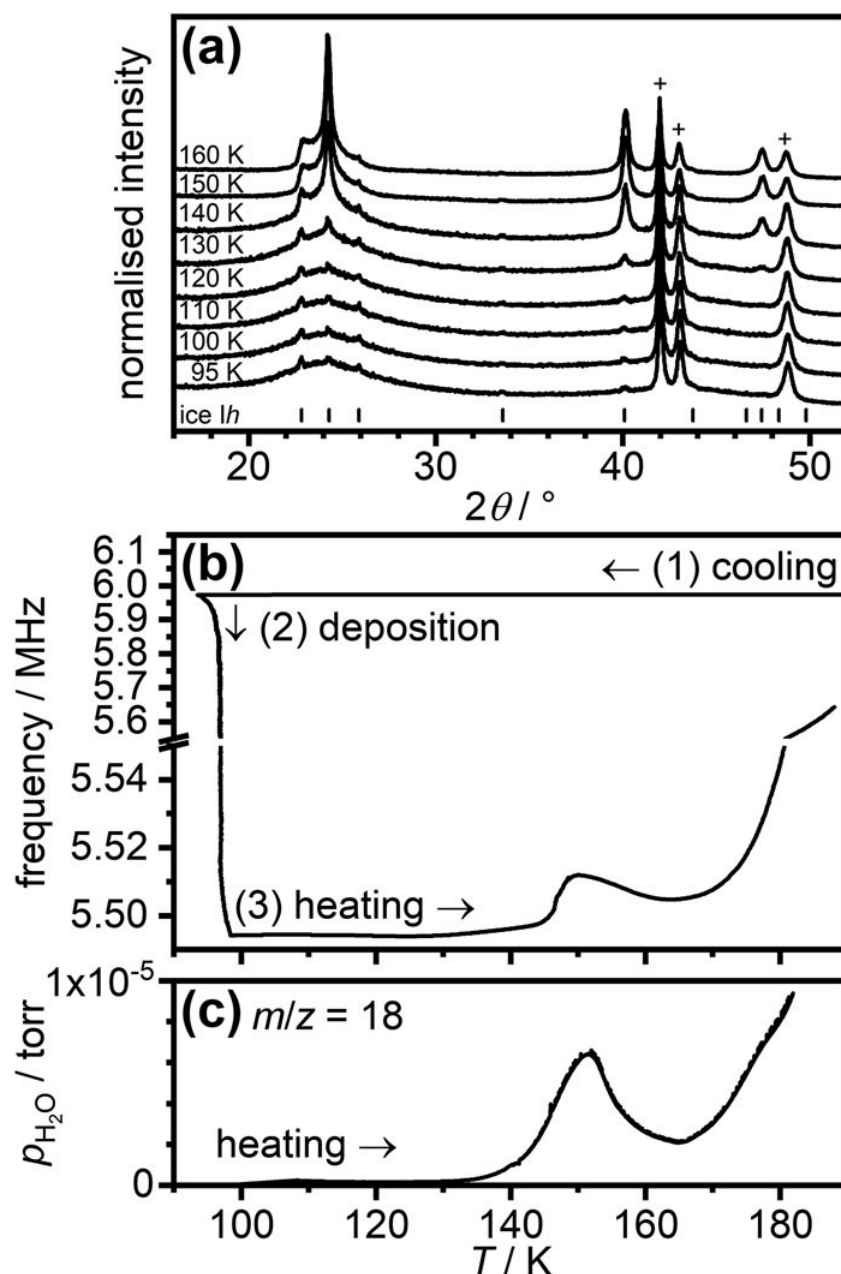


Figure 3.9. Preparation and thermal characteristics of pure as-made ASW. (a) XRD patterns ( $\text{Cu K}\alpha$ ,  $\lambda = 1.54 \text{ \AA}$ ) carried out ex situ of recovered ASW upon heating from 95 K to 160 K. Black crosses indicate Bragg peaks arising from the brass sample holder and tickmarks indicate the expected Bragg positions of ice Ih. Small peaks from the presence of ice Ih during the initial sample are due to vapour condensation during sample transfer into the holder. (b) Fundamental frequency changes from the QCM showing (1) cooling, (2) deposition at 95 K and (3) heating the deposit with the QCM sensor in the centre of the deposition plate and at 15 cm away from the  $\text{H}_2\text{O}$ -inlet tube. (c) TPD trace showing partial pressure of  $\text{H}_2\text{O}$  upon heating ASW. This figure has been reprinted from reference 1 with the permission of AIP Publishing.



### 3. Gaseous ‘Nanoprobes’ for Detecting Gas-Trapping Environments in Thick Layers of Amorphous Solid Water

These sequential phase changes observed from the corresponding partial pressures of H<sub>2</sub>O upon heating were recorded using the MS as shown in Figure 3.9(c). At 150 K, a sharp feature is observed as a first maximum, where there is an increase in vapour pressure, followed by a decrease in pressure as the sample undergoes an irreversible transformation from ASW to ice *Isd*. It is expected that ASW displays a higher vapour pressure than ice *Isd* as ASW is higher in free energy.<sup>32-34</sup> The vapour pressure of ASW is approximately two orders of magnitude higher than that of ice *Isd* since ASW is energetically unfavourable when compared to ice *Isd*.<sup>33</sup> Metastable ASW also has a higher desorption rate and thus, concomitant free energy when compared with crystalline ice. The vapour pressure of ice *Isd* continues to rise after 170 K due to the increase in temperature and in corroboration to the QCM data presented in Figure 3.9(b), approximately half of the film evaporates at ~190 K. Such trends of vapour pressure as observed in this research has been noted in the heating of pure nanoscale ASW films.<sup>32, 33</sup> However, in thinner films, the TPD experiment ends with the full desorption of species. The desorption peak in this study is seen to change with inlet pressures and deposition rates and is discussed later in this chapter.

#### 3.3.3 MCDIFFaX Analysis of ice *Isd* from ASW

The MCDIFFaX software was employed for analysing the XRD patterns of vapour deposited ice *Isd* from ASW. The effects of the amount of hexagonal stacking on the XRD data were investigated and found to be distinct from trends previously presented by Werner *et al.*<sup>25</sup>

MCDIFFaX fits of ice *Isd* obtained from crystallising ASW heated from 160 K to 180 K are displayed in Figure 3.10. Information regarding the memory effects of the stacking events in the sample was determined and mapped onto a stackogram, Figure 3.11. The MCDIFFaX fit and XRD pattern for 190 K is not depicted in Figure 3.10 due to the difficulty in fitting the model to the experimental data caused by ice evaporation and recondensation.

### 3. Gaseous ‘Nanoprobes’ for Detecting Gas-Trapping Environments in Thick Layers of Amorphous Solid Water

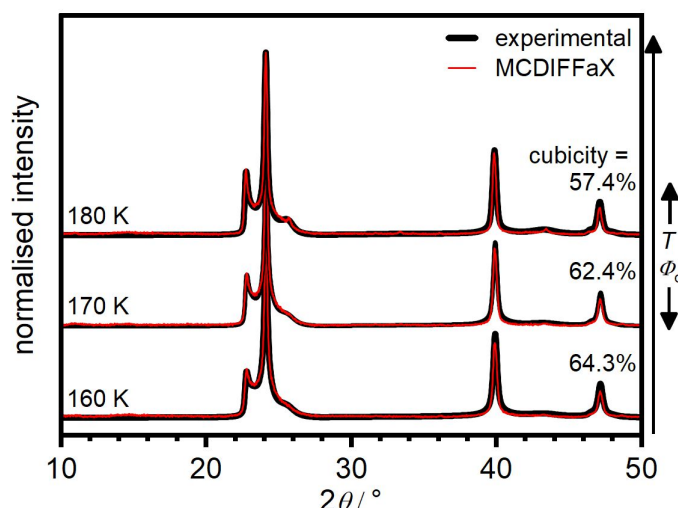


Figure 3.10. MCDIFFaX fits of the XRD patterns (Cu K $\alpha$ ,  $\lambda = 1.54 \text{ \AA}$ ) of ice Icd obtained after crystallisation of pure ASW, heated from 160 K to 180 K. The experimental data are shown as thick black lines and MCDIFFaX fits are shown as thin red lines, respectively. The determined cubicities,  $\Phi_c$ , are indicated for all diffraction patterns. The XRD pattern of the 190 K data is not present as it proved difficult to fit the pattern with the MCDIFFaX model.

As mentioned in Chapter 2, a stackogram illustrates how one stacking event depends on the previous stacking and is defined by four corners, referring to physical mixtures of cubic ice (ice Ic), hexagonal and cubic stacking and lastly, ice Ih. In essence, a stackogram maps  $\Phi_{cc}$  against  $\Phi_{hc}$ , where  $\Phi_{cc}$  describes the probability of a cubic stacking event followed by a cubic stacking event and similarly,  $\Phi_{hc}$ , describes the probability of a hexagonal stacking event followed by a cubic stacking event.<sup>35</sup> A major feature in the stackogram is the diagonal black line, which is termed the random stacking line and does not represent any memory effects.<sup>35</sup>

As seen in Figure 3.10, MCDIFFaX was carried out at a low temperature of 160 K where the sample is no longer amorphous up to 190 K, and akin to these XRD patterns, no substantial changes occurred with respect to the stacking probabilities seen in Figure 3.11. Although, as the temperature increases from 160 K to 180 K, they tend to change slightly in values and experience higher tendencies to follow a decrease in cubicity. From 160 K to 180 K, the cubicity values are similar yet remain to hover near the random stacking line with both, a mixture of ice Ic and ice Ih, respectively. There was a large difference in cubicity observed from 180 K to 190 K where the sample abruptly begins to resemble ice Ih. The cubicity of the 190 K MCDIFFaX fit hovers quite close to the random stacking line and hexagonal corner of the stackogram. Upon further heating, the

### 3. Gaseous ‘Nanoprobes’ for Detecting Gas-Trapping Environments in Thick Layers of Amorphous Solid Water

cubicity decreases and reaches out to an entirely hexagonal character. Since ice *Ih* is formed from the sample, stacking probabilities would lie towards the bottom left-hand corner of the stackogram. It must be noted that a full transformation to pure *Ih* would not be observed as a substantial fraction, or a few percent of cubic stacking would remain. Only at higher temperatures, it transforms completely.

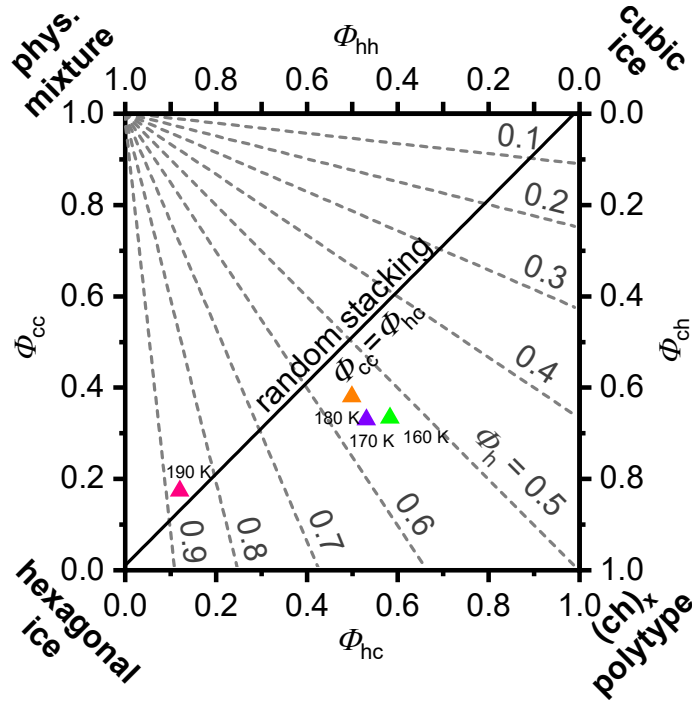


Figure 3.11. Stackogram plot<sup>35</sup> displaying the stacking probabilities of vapour deposited ice upon heating ASW from 160 K to 190 K from this study. Upon heating, stacking probabilities are seen to tend towards more hexagonal stacking in line with a decrease in cubicity.

Ice samples do not tend to veer towards the bottom right-hand side given the (ch)<sub>x</sub> polytype term of the stackogram as they remain in a specific stacking sequence.<sup>36</sup> Remarkably, as also seen in this section, depending on how ice *Isd* is prepared, a range of cubicities values are obtained.<sup>25, 26, 37</sup> To the present date, it is rather doubtful which factors determine the cubicity of an ice *Isd* material.

#### 3.3.4 Detailed Analysis and Discussion of the QCM Measurements

As mentioned earlier in this chapter, frequency changes upon heating can be observed and it is best to assume and attribute these variations to desorption processes and readsorption effects that have not yet been uncovered. This section follows on to describe, in detail, an additional heating experiment of ASW as employed and presented in Figure 3.9(b). In this experiment, the data for the bandwidth was recorded of the fundamental in

### 3. Gaseous ‘Nanoprobes’ for Detecting Gas-Trapping Environments in Thick Layers of Amorphous Solid Water

addition to recording the peak positions (Figure 3.12, and Figure 3.13). Panel (a), (b) and (c) from Figure 3.12 have been enlarged and are shown in Figure 3.13.

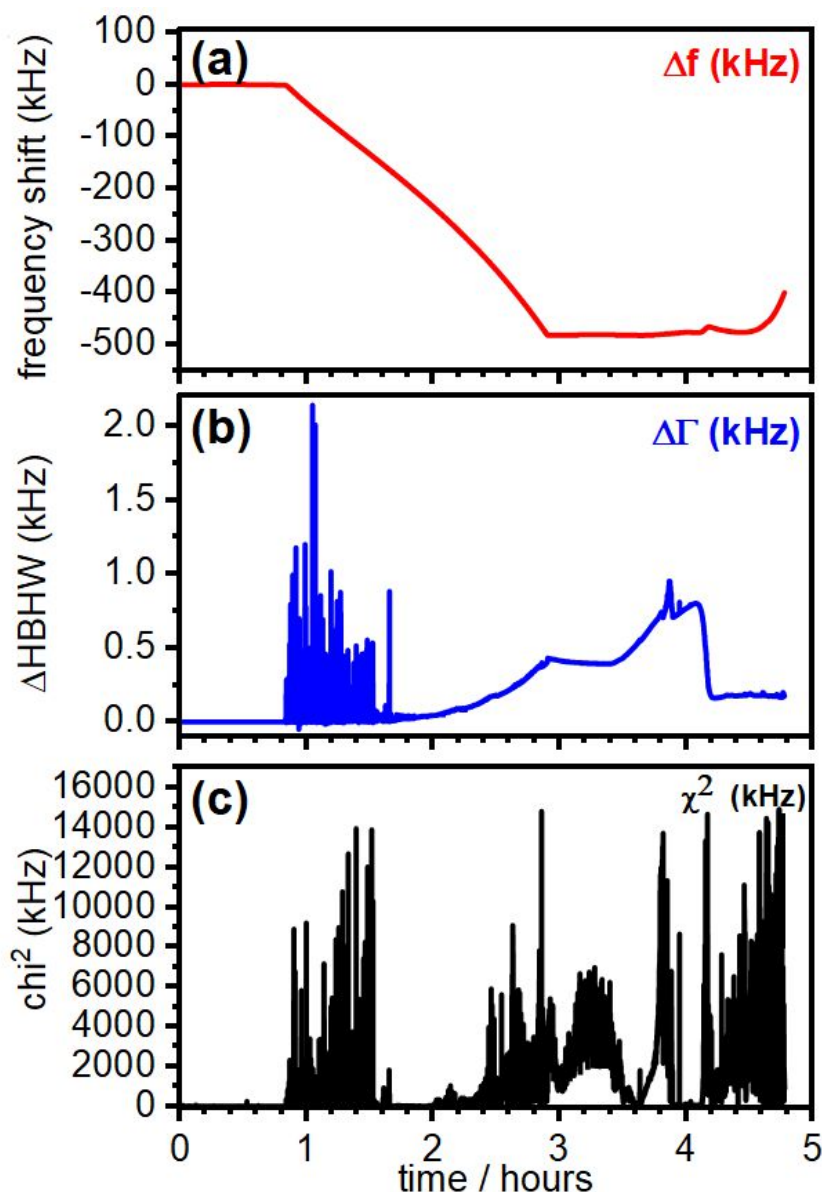


Figure 3.12. Additional QCM measurements for a typical deposition experiment as shown in Figure 3.9(b), where (a) frequency shift, (b) bandwidth shift and (c) fit for this experiment with respect to time is presented. The change in Lorentzian ( $\Delta \Gamma$ ) is much smaller than compared to  $-\Delta f$ . The sharp peaks in (b) are due to sudden peak movement/shift and these peaks are therefore, regarded as artefacts. These artefacts may be due to the possible formation of cracks and (c) the fit of the data. This figure has been reprinted from reference 1 with the permission of AIP Publishing.

Interestingly, in Figure 3.12(a), a large frequency shift to  $-500$  kHz upon deposition is observed which corresponds to a 10% decrease in the frequency which is exceedingly unusual. The frequency shift increases to  $\sim -400$  kHz upon heating. Many repeats of this

### 3. Gaseous ‘Nanoprobes’ for Detecting Gas-Trapping Environments in Thick Layers of Amorphous Solid Water

experiment were carried out and the same result was observed. The samples prepared in this study are of large thickness and they dampen the vibration to a degree where the admittance trace cannot be fitted reliably with a Lorentzian function. The large thickness of samples shows low damping, and their thickness does not cause an issue in the analysis and so they can be dealt with mathematically/statistically.

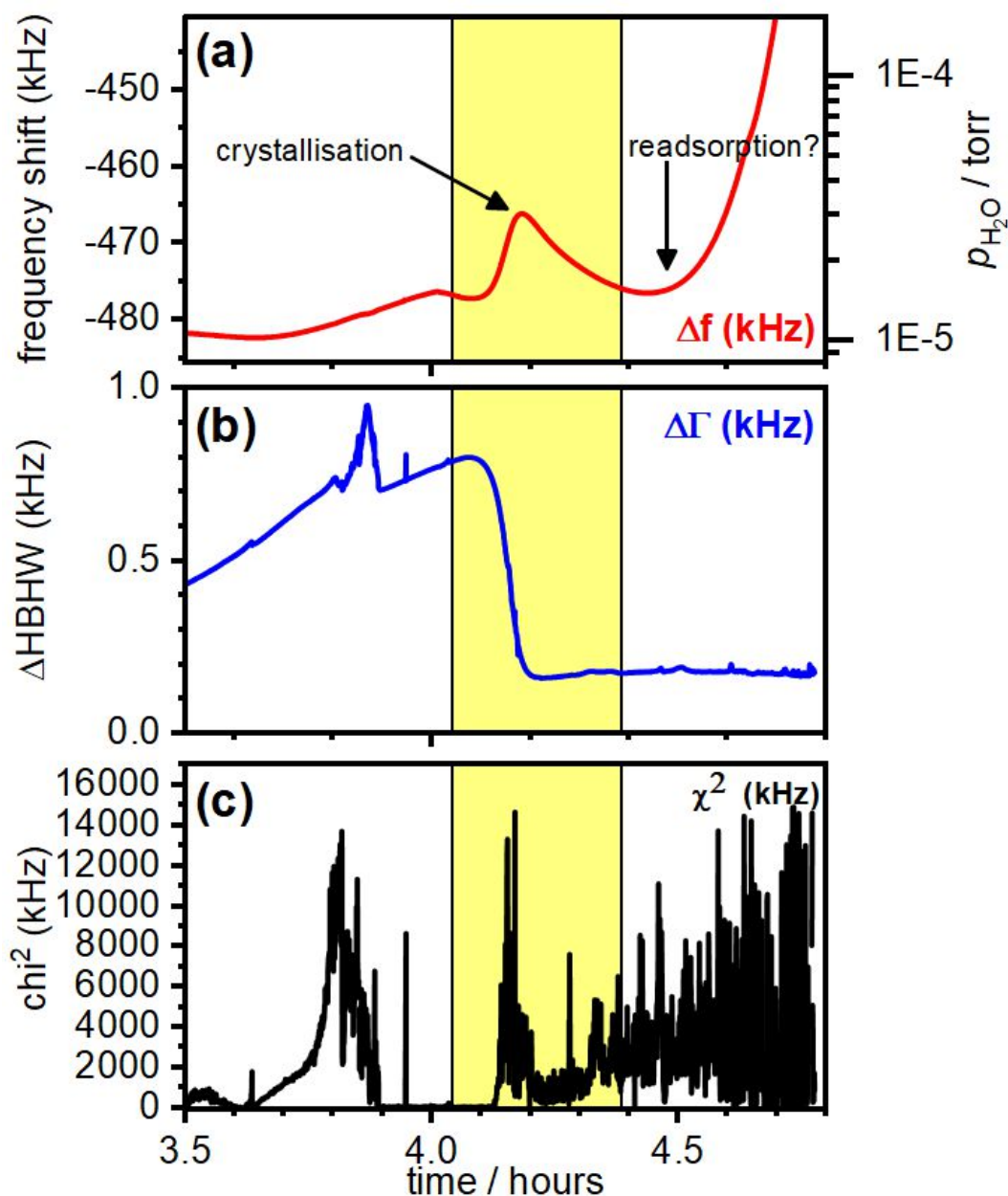


Figure 3.13. Enlarged and detailed plot of Figure 3.12. The right-hand side of panel (a) includes the comparison with the pressure of  $H_2O$ . The significant drop in bandwidth in (b) can be ascribed to the crystallisation of ASW and (c) the fit of the data. The drop in the frequency is not as easily interpreted due to no equivalent change in  $\Delta\Gamma$ . This figure has been reprinted from reference 1 with the permission of AIP Publishing.

### 3. Gaseous ‘Nanoprobes’ for Detecting Gas-Trapping Environments in Thick Layers of Amorphous Solid Water

It can be assumed that the deposition rate is constant, so the frequency and bandwidth imply an apparent shear modulus of the ASW film.<sup>1</sup> It is named apparent since some caveats should be noted. Such caveats include:

- It is possible that the film spontaneously cracks since spikes in the bandwidth data as shown in Figure 3.12(b) are observed.<sup>38</sup> The spikes visible in  $\Delta\Gamma$  correspond quite well with the spikes seen in Figure 3.12(c),  $\chi^2$ , in this case,  $\chi^2$  depicts the fit and a large  $\chi^2$  indicates a poor fit. Bu *et al.*<sup>38</sup> describe the spontaneous cracking of ASW films and dependence on the microporous structure and thus, here, it can be suggested that cracking is at the basis of the differences in  $\Delta\Gamma$ . These cracking events occur quite rapidly and cause disturbance to the resonance, therefore, prohibiting a good fit to a Lorentzian function. A rapid acquisition time of resonance is approximately one second, and so, once the resonance properties undergo a change during a sweep of frequency, the raw data will be ruined. Thus, these outliers related to sudden, sporadic events, are attributed to cracking in ASW.
- Thick films as prepared in this study may cause tensile stress and result in the bending of the crystal. The bending effects may also result in changes in the resonance.
- If a peripheral or indirect motion of the resonator surface is assumed, then the shear modulus can be derived. Flexural stress contributions to pattern vibrations can be overlooked and they produce compression waves when compared to shear waves.
- It is not possible to determine parameters of density ( $\rho$ ), and thickness ( $d_f$ ) within a planar sample with QCM. The product of  $\rho$  and  $d_f$ , i.e., mass per unit area ( $m_f = \rho \times d_f$ ) enter the model. This is a constant problem due to the porosity of ASW and it is difficult to determine the porosity. When  $\rho$  is assumed, it is possible to determine a value of thickness by the conversion from  $d_f$ . The uncertainty in porosity can be related to shear modulus where the shear angle is defined as  $dx/dz$ , where  $x$  and  $z$  are the tangential and normal coordinates, respectively. Seeing as QCM only determines the mass, ‘ $dz$ ’ becomes uncertain under laboratory conditions. Comparing laboratory and materials-based coordinates, and the conversion between both results in the determination of  $\rho$ , it is also possible to look at wave propagation on a mathematical level. Two parameters govern wave propagation,  $Z_f$  and  $c$ : the films shear-wave impedance and wave velocity, respectively.  $Z_f$  can be seen as  $(\rho G)^{1/2}$ , ( $G$  is the shear modulus) and if viscoelastic effects are present then the QCM has the ability to

### 3. Gaseous ‘Nanoprobes’ for Detecting Gas-Trapping Environments in Thick Layers of Amorphous Solid Water

determine  $Z_f$  and not  $G$ . Intricate detail is provided elsewhere<sup>27</sup> and not discussed further. However, in brief, viscous softness increase the bandwidth and the elastic softness lowers the frequency. If a contribution of softness to the overall frequency shift is accepted as more than 10%, frequency increases alongside a drop in the bandwidth can be explained naturally with crystallisation, Figure 3.13. Crystallisation may not be the only case for this. As seen in Figure 3.9(c), the maximum vapour pressure suggests a contribution from evaporation but also, softness can influence this. Figure 3.9(c) and Figure 3.13(a) display a frequency decrease above the crystallisation temperature and a detailed analysis of the QCM data for these results is not possible. Nevertheless, the contact between ice and H<sub>2</sub>O should not be viewed as homogenous, flat, and simple. Rather so, they should be viewed as spots, where the normal pressure is higher than average, and the shear stress is transported here. However, this is quite tentative, and the findings portrayed in Figure 3.12 and Figure 3.13 are maximally exciting.

- Bending stress may be a caveat also in this case. Quartz resonators will respond disagreeably with substantial bending stress, provided the thickness of layers and cracking evidence. Frequency decreases that do not correspond to any signature unseen in bandwidth may be caused by bending stress release.<sup>1,27</sup>

As mentioned earlier, a decrease in the vapour pressure at the crystallisation temperature is observed, yet a reasonable explanation for this change based on QCM data is not yet possible. It can be assumed that viscoelastic effects are a strong contributor or influencer to this change. It can also be proposed from looking at the enlarged Figure 3.13(a) that the decrease upon heating may be due to readsorption effects and in order to study this, an additional turbomolecular pump needs to be implemented below the deposition plate and placed horizontally in line with the H<sub>2</sub>O-vapour tube. This would eliminate readsorption. If trends in the data are seen repeatedly, it would eliminate the possibility that this is due to readsorption effects.

#### 3.3.5 Desorption of Gaseous ‘Nanoprobes’ from ASW

After having recognised the optimum vacuum conditions for deposition studies, alongside the TPD behaviour of ASW films in this particular set-up, H<sub>2</sub>O-vapour was codeposited with argon for two-hours. The flow of H<sub>2</sub>O-vapour into the vacuum chamber (0.0116 mmol s<sup>-1</sup>) and argon gas at a flow rate of  $1.34 \times 10^{-5}$  mmol s<sup>-1</sup> was mixed into the H<sub>2</sub>O-vapour beam. This flow of argon compared to the flow of H<sub>2</sub>O gives a ratio of 1:860,

### 3. Gaseous ‘Nanoprobes’ for Detecting Gas-Trapping Environments in Thick Layers of Amorphous Solid Water

argon to H<sub>2</sub>O molecules. As argon is more volatile than H<sub>2</sub>O, it is likely that the actual amount of argon present in the ASW film will be smaller – full quantification is provided in Table 3.1. Systematic trends were not detected in the QCM data to suggest the incorporation of argon in the deposits as can be seen in Figure 3.14, wherein, a typical two-hour deposition experiment, the frequency change of both, argon and H<sub>2</sub>O were measured. Both H<sub>2</sub>O and argon were followed by the TPD. It is observed that H<sub>2</sub>O depicts a large frequency change (~489 kHz) as illustrated in Figure 3.14, and in comparison, argon could not be detected in the measurements.

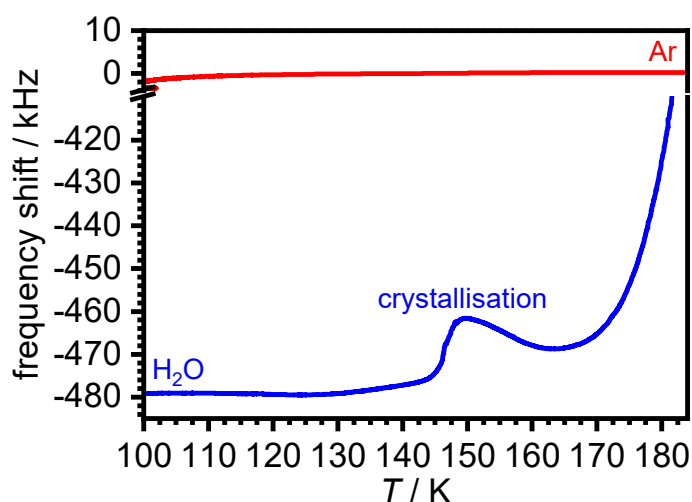


Figure 3.14. Frequency shift (kHz) for H<sub>2</sub>O and argon from a two-hour deposition during the TPD measurement. Insignificant amounts of argon are detected in comparison to the shift in frequency for H<sub>2</sub>O.

Due to the small amount of argon, it can be justified that argon is the perfect candidate to incorporate into the amorphous ice as a ‘nanoprobe’ in this study, to detect various gas-trapping environments in macroscopic films without having to alter the properties of ASW itself. Herein, a detailed analysis of quantitative data will be provided later.

The measured TPD data of argon in ASW is displayed in Figure 3.15(a). Previously, the transformation of ASW to ice *Isd*, is seen in the TPD data of H<sub>2</sub>O only. In Figure 3.15(a), the abrupt peak at ~150–160 K indicates the approximate temperature at which ASW crystallises and the TPD data in this thesis also illustrates the hallmark peak of ASW crystallisation to ice *Isd*. This desorption peak arises as ASW transforms to a thermodynamically stable crystalline ice.<sup>39</sup> In addition to the trend from the pressure trace previously observed for H<sub>2</sub>O-vapour pressure [Figure 3.9(c)] as detected in the MS, three additional distinct features originating from argon desorption processes were



### 3. Gaseous ‘Nanoprobes’ for Detecting Gas-Trapping Environments in Thick Layers of Amorphous Solid Water

recorded by the MS. Feature (1) in the TPD data [Figure 3.15(a)] starts at around 100 K and is a small, broad feature which is followed by desorption feature (2), slightly slimmer and sharper in shape at ~125 K. The final desorption feature (3) is the most prominent and intense peak which is the H<sub>2</sub>O desorption feature associated with ASW crystallisation. As observed beforehand (Figure 3.14), there are tremendously low levels of argon present in the deposit which were not detected in the QCM measurements, and three desorption events were identified in the MS. The presence of argon in the deposit did not modify any desorption properties of H<sub>2</sub>O and once again, justifies its use as an effective ‘nanoprobe’.

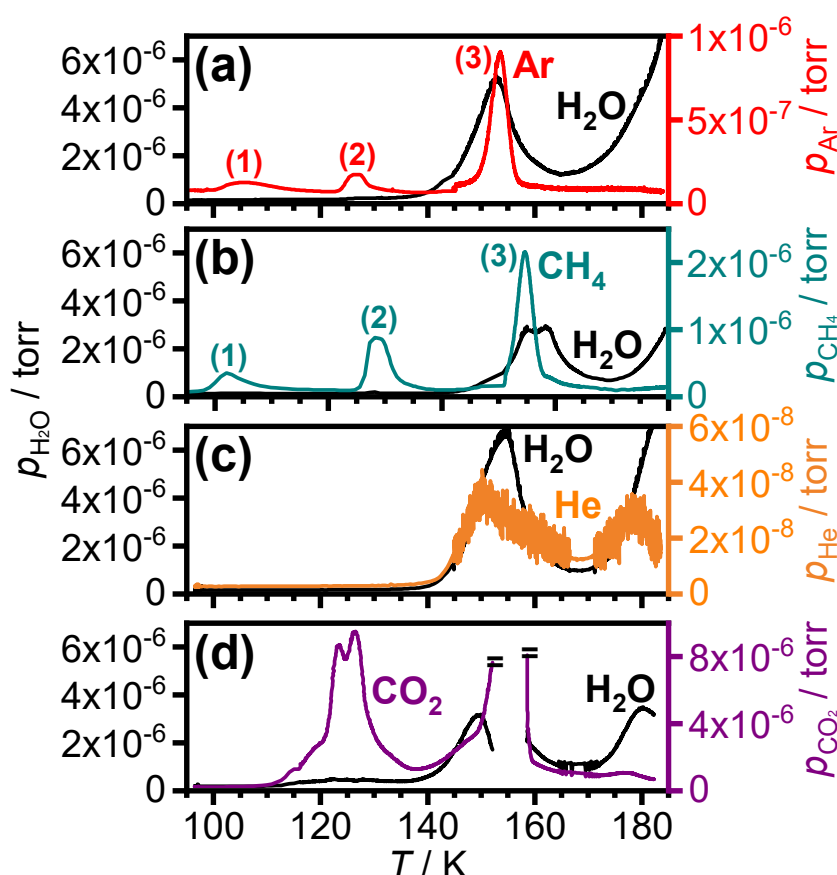


Figure 3.15. TPD data illustrating the partial pressures of H<sub>2</sub>O ( $m/z = 18$ ) and various gaseous ‘nanoprobes’ recorded upon thermal annealing of codeposited films. The ‘nanoprobes’ are such that (a) argon ( $m/z = 40$ ), (b) CH<sub>4</sub> ( $m/z = 16$ ), (c) helium ( $m/z = 4$ ) and (d) CO<sub>2</sub> ( $m/z = 44$ ). Panels (a) and (b) illustrate the three desorption features detected and labelled with (1), (2) and (3). Panel (d) shows a cut off in the TPD due to the MS limits – the instrument had to be switched off in the 150–160 K range due to partial pressure exceeding the limits of the upper working limit of the Faraday cup. \*Note: panel (b), (c) and (d) are discussed later. This figure has been reprinted from reference 1 with the permission of AIP Publishing.

### 3. Gaseous ‘Nanoprobes’ for Detecting Gas-Trapping Environments in Thick Layers of Amorphous Solid Water

The three distinct features in the 95–185 K temperature region are in fact, highly significant. When a surface is exposed to an adsorbent in surface science, the quantity is measured in Langmuir, L. For a period of one second, the definition of 1 L is equal to a pressure of  $1.33 \times 10^{-6}$  mbar or  $10^{-6}$  Torr. When experimental measurements are carried out, the exposure in units of L can be reported in terms of ML. In previous studies and the literature, many hundred MLs of ASW were deposited onto only 1 ML of argon<sup>2,3</sup> in comparison with thick film deposition in this study. Smith and Kay<sup>3</sup> deposited 1 ML of argon, covered by 300 ML of ASW and they also observed the TPD spectra of 1 ML of argon covered by an ASW thickness of 25 to 800 ML.

The abrupt desorption at ~160 K in this study and literature is consistent with argon evaporation, somewhat impeded by ASW until the onset of crystallisation is reached. Comparable to this study and in the literature, such deposits detect one intense crystallisation feature at ~160 K and further a weak feature after crystallisation at higher temperatures (~180 K) as the entirety of the film evaporated.<sup>3,4</sup> Figure 3.16 depicts TPD spectra from the literature,<sup>3</sup> indicating the weak feature observed after crystallisation at 180 K.

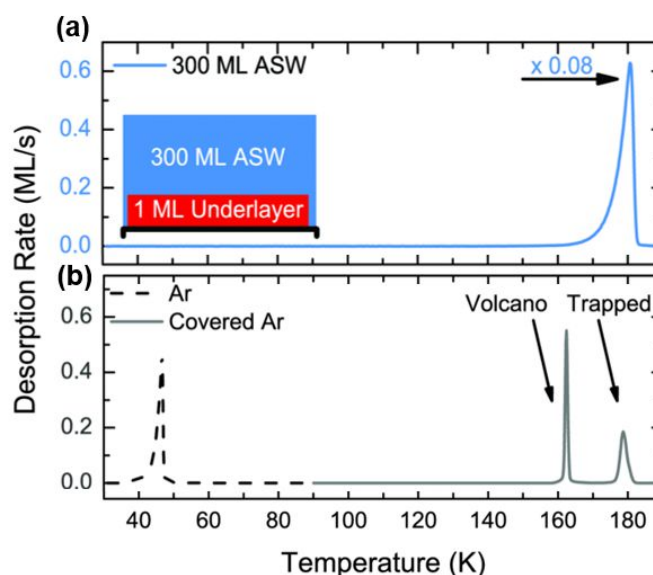


Figure 3.16. TPD spectra of (a) 300 ML of ASW overlayer and (b) TPD spectra of a 1 ML of argon that is desorbed directly from graphene (dashed line), covered by 300 ML of ASW (solid line) with a heating rate of  $1 \text{ K s}^{-1}$ . This figure has been adapted and reprinted from reference 3 with the permission of AIP Publishing.

### 3. Gaseous ‘Nanoprobes’ for Detecting Gas-Trapping Environments in Thick Layers of Amorphous Solid Water

In addition, and parallel to earlier studies with carbon tetrachloride ( $\text{CCl}_4$ ) films, the abrupt desorption in line with crystallisation ( $\sim 163$  K) was described as a ‘molecular volcano’.<sup>3, 39</sup> This is where gases are trapped subsequently by an ASW overlayer and further released by an abrupt desorption peak coinciding with crystallisation of ASW.<sup>2, 39-41</sup> Figure 3.16 compares the TPD spectra of argon and ASW heated at  $1 \text{ K s}^{-1}$  from graphene, displaying a peak at approximately 46.7 K for argon where it desorbs. In comparison, argon was deposited on top of ASW and found to already desorb at  $< 50$  K, however, due to our experimental set-up and certain constraints, it was not possible to reach a temperature as low as 50 K.<sup>2, 42</sup> When argon is covered by 300 ML of ASW, no desorption of argon is observed until a sharp peak emerges at approximately 163 K, followed by another small peak at approximately 180 K (Figure 3.16, solid line).

The second peak at  $\sim 180$  K [Figure 3.16(b)], is known to commensurate with the remaining MLs of ASW where desorption from this region corresponds to trapped ASW where gas was not able to escape during the formation of cracks in ASW. As observed in Figure 3.16, a volatile ML beneath and an ASW overlayer can desorb from either of two pathways: (i) ‘molecular volcano’ desorption due to crystallisation-induced cracks forming in ASW to allow an open path to vacuum or (ii) ‘trapped’ desorption in the region where gas does not escape during the ‘molecular volcano’ and only desorbs once the ASW experiences desorption itself.

In addition, for a thick, 100 nm ASW film codeposited with argon, one desorption feature due to crystallisation-induced desorption could be observed,<sup>5</sup> regardless of the extreme deposition ratio of 1:1 Ar:H<sub>2</sub>O in the literature.<sup>43</sup> Whilst heating argon-rich mixtures at 20 K, seven different overlapping features were observed which were combined with desorption rates differing in several orders of magnitude.<sup>44</sup> Solid argon may likely have formed in these experiments, influencing the morphology of ASW. This study uses extremely small amounts of argon compared to the literature and therefore, it is stressed that this study achieved a baseline separation from the three distinct desorption features.

Desorption features (1) and (2) as observed in Figure 3.15(a) have not been reported in the literature and are absent for nanoscale Ar@ASW,<sup>2, 3, 5, 43</sup> and so, they must originate from different trapping environments that are only present in macroscopic ASW films from the desorption processes. As displayed schematically in Figure 3.17, the

### 3. Gaseous ‘Nanoprobes’ for Detecting Gas-Trapping Environments in Thick Layers of Amorphous Solid Water

origins of desorbing gas molecules are attributed to the local environments of argon in ASW films. Process (1) is proposed to be due to trapped argon in narrow cracks in which pathways are open to the vacuum. In line with this, a study using scanning electron microscopy discovered that ASW presents a ‘cauliflower’-like morphology where the observation with internal void-separated tapered columns was observed.<sup>45, 46</sup> It is to be noted that ASW arguably also shows cracks once a thickness maximum is reached in the macroscopic film.<sup>38</sup>

Desorption feature (2) is proposed to demonstrate the collapse of internal voids driven by the onset of the orientational glass transition and thus, sintering occurs, reducing the surface area as temperature increases. Previously, it has been shown that pure as-made ASW is highly microporous and substantial sintering occurs with the loss of porosity upon thermal annealing.<sup>30, 47</sup> The pore collapse from the micropore network due to heating is yet poorly understood, however, this process is consistent with low-angle neutron scattering analysis changes.<sup>48</sup> As the deposit sinters, some degrees of movement such as translation and diffusion due to the highly out-of-equilibrium nature of the deposit can be observed.<sup>49</sup> For gas to remain trapped within the film, the collapse of pores must take place prior to any gas escape since pathways must have had to exist while gas was being adsorbed.

The final desorption process (3), occurs concurrently with the crystallisation of ASW to ice *Isd* and therefore, fully embedded matrix-isolated argon is liberated as is observed for nanoscale Ar@ASW.<sup>2, 5</sup> Cracks formed in this study originate from ASW and propagate downwards towards the substrate. It may be the case that not all argon is released after observing crystallisation and argon may be trapped inside cages in ASW similar to those found in clathrate hydrates. Thus, the most probable source of enhanced trapping is, argon travelling into the crack propagation only to be trapped before cracks are fully opened. In addition, due to the experimental set-up in this study, it was not possible to determine whether the trapped gas is in a simple pore, or just covered by a layer of H<sub>2</sub>O.

### 3. Gaseous ‘Nanoprobes’ for Detecting Gas-Trapping Environments in Thick Layers of Amorphous Solid Water

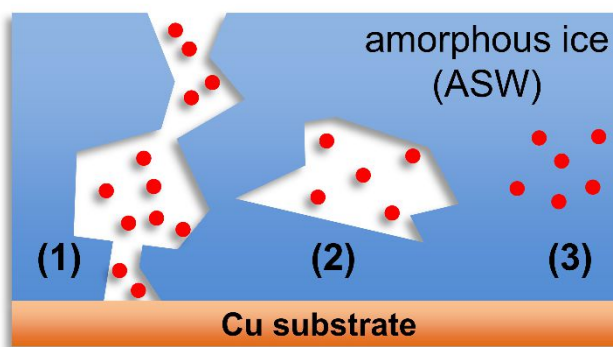


*Figure 3.17. Schematic illustration of different possibilities of the origins of gas-trapping environments for argon incorporation in ASW films including (1) opening of cracks, (2) collapse of internal voids and (3) fully matrix-isolated argon liberated into the gas phase. This figure has been reprinted from reference 1 with the permission of AIP Publishing.*

To investigate whether the open cracks in ASW can be filled after deposition of only H<sub>2</sub>O, the pure ASW film was ‘bombarded’ for two-hours with argon gas at the ‘standard’ flow rate of  $1.34 \times 10^{-5} \text{ mmol s}^{-1}$ , and after deposition, the film was heated straight away. The TPD was recorded and is shown in Figure 3.18(a). In comparison to a typical codeposition experiment, and quantitatively speaking, this trace indicates the amount of argon released during feature (1) was in fact doubly larger, proving that after deposition, cracks can be easily accessed and filled with argon (Table 3.1). There is the presence of a small additional weak feature, pre-crystallisation, which is just below 140 K and together with desorption at higher temperatures, only 15% of argon is released comparable to a codeposition experiment. Initially, small fractions of argon may be located in open cracks which become trapped in different environments and thus, weak features are thought to originate from this as the sample is heated. In the literature, N<sub>2</sub> gas on porous ASW films was investigated,<sup>50, 51</sup> at 23 K, with thicknesses of  $\sim 9 \text{ }\mu\text{m}$ . The experimental results showed that fixed doses of N<sub>2</sub> gas shifted to higher temperatures with thicknesses of ASW films. The desorption feature was seen to deviate from a sole peak above 3000 MLs and beyond 75 K, became a highly complex tail. With the first desorption process in this study, it may be possible to relate both processes, however, shifts to higher temperatures due to the thickness of films produced and analysed in this study. In this context, and along these lines, the first feature is seen much more later and delayed in this study’s TPD data and speculate it is due to thickness differences from enhanced confinement of argon molecules within narrow, tortuous, and convoluted cracks. Bombarding a pure H<sub>2</sub>O film leads to negligible trapped argon molecules compared to codeposited films and it is

### **3. Gaseous ‘Nanoprobes’ for Detecting Gas-Trapping Environments in Thick Layers of Amorphous Solid Water**

difficult to fill the microscopic cracks after depositing. An additional experiment was carried out to determine whether the pores of ASW can be refilled. In detail, H<sub>2</sub>O-vapour was dosed into the high-vacuum chamber for two-hours, the sample was further annealed at 125 K, cooled back down to base temperature, 95 K, and then the surface was bombarded with argon for a further two-hours. After deposition, the sample was kept cold at 95 K for one-hour to allow for the vacuum to reach base pressure. Subsequently, a TPD was followed with the MS and shown in Figure 3.18(b). In comparison to a normal codeposition experiment, it is realised that the pores could not be refilled after annealing the pure ASW film at 125 K, this is due to pore closure at 125 K and layers to vacuum fully cease to open for the trapping of argon gas. During pore opening as mentioned in an earlier section, structural changes occur and facilitate the formation of desorption pathways of gaseous species in the ASW layer. Such pathways arise from the crack formation during the heating process and the growth of crystalline ice originating from ASW. In this case, the pores are opened and thus closed upon annealing at 125 K and desorption is prohibited so that argon can then not escape. The amount of argon released is next to nothing compared to the pressure of H<sub>2</sub>O as seen in the TPD trace. Desorption features (1), (2) and (3) could not be seen in this TPD. To reiterate, bombarding a pure ASW film after closing the pores and exposing it to argon leads to insignificant trapping of argon compared to codeposited films. It is therefore proven difficult to fill and open the microscopic cracks after depositing and annealing the deposit.

### 3. Gaseous ‘Nanoprobes’ for Detecting Gas-Trapping Environments in Thick Layers of Amorphous Solid Water

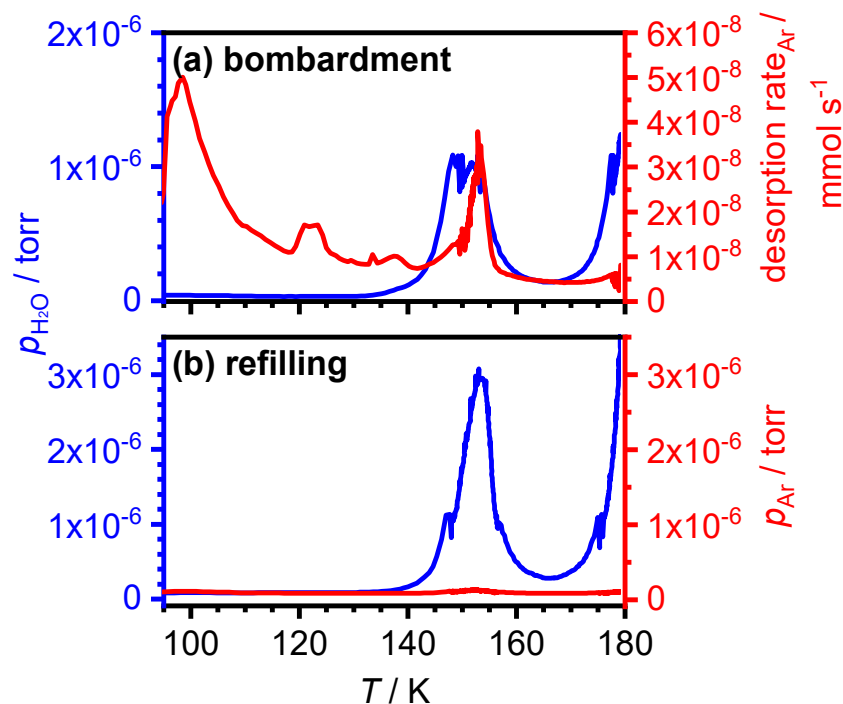


Figure 3.18. (a) TPD after ‘bombarding’ the film of ASW with argon, illustrating the desorption rates of argon recorded during the heating process after a film of pure ASW (two-hour deposition) was exposed to a ‘bombardment’ of argon ( $2.4 \times 10^{-3} \text{ mmol s}^{-1}$ ) for a further two-hours at 95 K. The TPD trace of  $H_2O$  is also shown in blue on the left-hand side of the figure in partial pressure / torr and (b) TPD trace after refilling the ‘pores’ of ASW after annealing at 125 K. A typical deposition experiment of pure ASW, annealed at 125 K, and then ‘bombarded’ with argon to see the effects of refilling pores.

Looking back at Figure 3.15, to probe and further test the assignments of these desorption features in line with gas-trapping environments, a few more gaseous ‘nanoprobes’ such as  $CH_4$ , helium and  $CO_2$  were finely dispersed and incorporated into ASW films. These gases were leaked into the chamber *via* the  $H_2O$ -vapour beam at the same leak rate as argon, in order to maintain the equivalent 1:860 ratio as mentioned earlier, into the vacuum chamber. The results from Figure 3.15 confirm that all ‘nanoprobes’ are somewhat correlated with the crystallisation of ASW at  $\sim 160$  K. The TPD recorded for  $CH_4@ASW$  [Figure 3.15(b)] similarly displays three desorption features as seen for  $Ar@ASW$ , verifying that  $CH_4$  can also be trapped in environments in the ASW film, as shown in schematic Figure 3.17. Analogous to  $Ar@ASW$ , desorption features (2) and (3) are delayed, and thus, shifted towards higher temperatures for a  $CH_4@ASW$  film.  $CH_4$  similarly exhibits the ‘molecular volcano’ peak at high temperatures and the temperature shift suggests van der Waals forces are stronger than argon while interacting with ASW. Table 3.1 and upcoming Figure 3.23(b) quantitatively confirm the stronger interactions and

### 3. Gaseous ‘Nanoprobes’ for Detecting Gas-Trapping Environments in Thick Layers of Amorphous Solid Water

amount of CH<sub>4</sub> released during deposition. Upon changing the ‘nanoprobe’ from argon to CH<sub>4</sub>, while keeping deposition conditions identical, the gas captured in ASW increased from 0.07% to 0.75% resulting in the conclusion that CH<sub>4</sub> is captured 10 times more greatly than argon. A possible explanation as to why CH<sub>4</sub> is captured more than argon is that, since CH<sub>4</sub> is a molecule rather than a small atom compared to argon, and in terms of van der Waals interactions, more fluctuations in the electron cloud in CH<sub>4</sub> exist compared to argon, and thus, a stronger interaction with H<sub>2</sub>O can be observed.

Contrary to argon and CH<sub>4</sub>, helium does not appear to exhibit any desorption features and it is too mobile to be trapped within ASW<sup>52</sup> above 95 K, as depicted in Figure 3.15(c). Macroscopic entrapment is not seen in this case and weak increases in the partial pressure of helium in the temperature range of where H<sub>2</sub>O desorbs can be speculated and linked to the desorption of H<sub>2</sub>O. The pumping efficiency of the pumps on the chamber allows the removal of increasing levels of H<sub>2</sub>O gas and so, the minute rises in helium partial pressures is instigated by an increase in the total pressure. Insignificant amounts of helium are trapped in ASW films and the cracks of ASW cannot trap helium gas: helium is known to have a very low desorption temperature.<sup>53, 54</sup> In the event of CO<sub>2</sub>@ASW, due to its low volatility compared to other gases,<sup>55</sup> the first desorption feature is not clearly observed. In this case, provided the broadness of the feature at a higher temperature, the onset of desorption feature (1) is delayed and overlaps with feature (2). Nanoscale CO<sub>2</sub>@ASW depicts and coincides with ASW crystallisation, where most of the CO<sub>2</sub> escapes during the ASW-to-ice *Isd* phase transition at ~160 K.<sup>56</sup> In CO<sub>2</sub>-rich mixtures, CO<sub>2</sub> has been shown to be fairly mobile resulting in low-temperature features<sup>57, 58</sup> and the isolation of CO<sub>2</sub>.<sup>59</sup> Such changes are speculated here and these effects may occur in the TPD data as shown in this study. CO<sub>2</sub> would interact a lot more strongly than argon and CH<sub>4</sub> as it is a polar molecule: a positive and negative charge exists within the CO<sub>2</sub>, which provides strong van der Waals forces.

In detail, as codeposited films have been studied to a lesser extent than layered films in literature, an investigation of ASW codeposited with CO<sub>2</sub> was carried out to show the trapping efficiency of ASW – related to the thickness of both species, and the nature of the trapped species. Two desorption features were observed: the first feature at 75 K was observed due to the CO<sub>2</sub> desorption from ASW while the second desorption event occurred during H<sub>2</sub>O crystallisation.<sup>60</sup> The first desorption event was assigned to molecular diffusion of CO<sub>2</sub> from top layers of ASW through open cracks and pores



### 3. Gaseous ‘Nanoprobes’ for Detecting Gas-Trapping Environments in Thick Layers of Amorphous Solid Water

towards the ice mantle surfaces that CO<sub>2</sub> was free to desorb from. CO<sub>2</sub> firmly embedded in ASW was released upon crystallisation.<sup>60</sup> Another study of codeposited systems of these species were complemented with infrared spectroscopy (IR) and observed the same findings of desorption events of mixed films being the same as codeposited films.<sup>57</sup>

This study reports data for very thick films (100 µm) and in upcoming section 3.3.6, analogous studies for a variety of film thicknesses have been performed, overlapping data with prior studies carried out in the literature of thinner films.

#### 3.3.6 Effect of the Deposition Rate and Film Thickness on Desorption Features

In the following section, due to the very weak interaction of argon with ASW, further investigations will exclusively be probed by altering deposition conditions on the desorption features. Different thicknesses were studied in order to learn how the desorption spectra evolve with film thickness where data is presented as quantitative desorption fluxes for argon. Two new processes are present for these 100 µm ASW films that are not observed in nanoscale ASW films. Molecules trapped in several films with different thicknesses of ASW following codeposition conditions are seen to be ejected at distinct temperatures.

Film thickness was reduced by altering the deposition times of codeposition experiments. The effect of reducing the deposition time on the three desorption features was studied, keeping the H<sub>2</sub>O leak rate constant and amounts of argon unchanged. Specifically, deposition times were changed from two hours, one hour and finally, 30 minutes. In this case, the films display thicknesses of 100 µm, 50 µm and 25 µm, respectively. The TPD data and quantitative analysis for these experiments were recorded and displayed in Figure 3.19(a) and Figure 3.19(c), respectively. The latter presents data of the amounts of argon released during the three desorption progressions, linearly showing the scale with respect to the deposition time. The former displays the three desorption processes observed upon heating, independent of film thickness. The effect of film thickness does not influence or change the morphology and therefore, the structural characteristics of the trapping environments of gas within the ASW films remain the same as the thickness is reduced from 100 µm to 25 µm. Macroscopic cracks have been studied by Bu *et al.*<sup>38</sup> and are realised to form in the critical thickness of 1–5 µm of ASW. In theory, the low-temperature feature should not be present in the absence of macroscopic cracks. Nevertheless, our experimental set-up has limitations, and these experimental

### 3. Gaseous ‘Nanoprobes’ for Detecting Gas-Trapping Environments in Thick Layers of Amorphous Solid Water

constraints render a lower thickness range inaccessible. Such constraints may include the heating rate, H<sub>2</sub>O to argon ratio and the overall base pressure of the vacuum system.

In the next step, the leak rates of both H<sub>2</sub>O and argon were reduced and the deposition times thereby were kept constant. The leak rates were reduced from 100% to 50% and 25% with respect to the original rates of  $1.157 \times 10^{-2} \text{ mmol s}^{-1}$  and  $1.345 \times 10^{-5} \text{ mmol s}^{-1}$  of H<sub>2</sub>O and argon, respectively, maintaining the ratio of both species. Once more, the TPD data and quantitative analysis were recorded and are shown in Figure 3.19(b) and Figure 3.19(d). In contrary to the effect of film thickness, the reduction of deposition rate presented an exponential decrease for all three desorption features from the amount of argon trapped. Thus, this finding indicates that deposition rate does in fact influence the morphology of the deposit in accordance with earlier studies.<sup>12-15, 17, 57</sup> In the extent of these experiments, kinetic effects of the H<sub>2</sub>O molecules may play an important role in the trapping of argon. The question arises: how quickly do gas-trapping environments form by the H<sub>2</sub>O molecules? It is evident from the quantitative data and TPD data, using lower H<sub>2</sub>O deposition rates while argon leak rates are reduced proportionally, leads to fewer and fewer H<sub>2</sub>O molecules available to trap any given atom of argon gas. Thus, when the deposition rates are reduced by 50% and 25%, the H<sub>2</sub>O to argon ratios in the deposit mixtures increases significantly from, 1,169,000:1 to 2,517,000:1 and 3,595,000:1. This data is provided in Table 3.1.

On the whole, it appears that reducing the deposition time has more effect on the gas-trapping environment efficiency rather than the morphology. Supporting evidence for this conclusion is the fact that the relative amounts of argon released upon heating and observed in the deposition features, do not significantly change whilst altering the deposition rates (Table 3.1). Nevertheless, it can be concluded that these three desorption features and gas-trapping environments are present and robust throughout the experimental setup across a wide range of deposition rates and film thicknesses.<sup>1</sup>

### 3. Gaseous ‘Nanoprobes’ for Detecting Gas-Trapping Environments in Thick Layers of Amorphous Solid Water

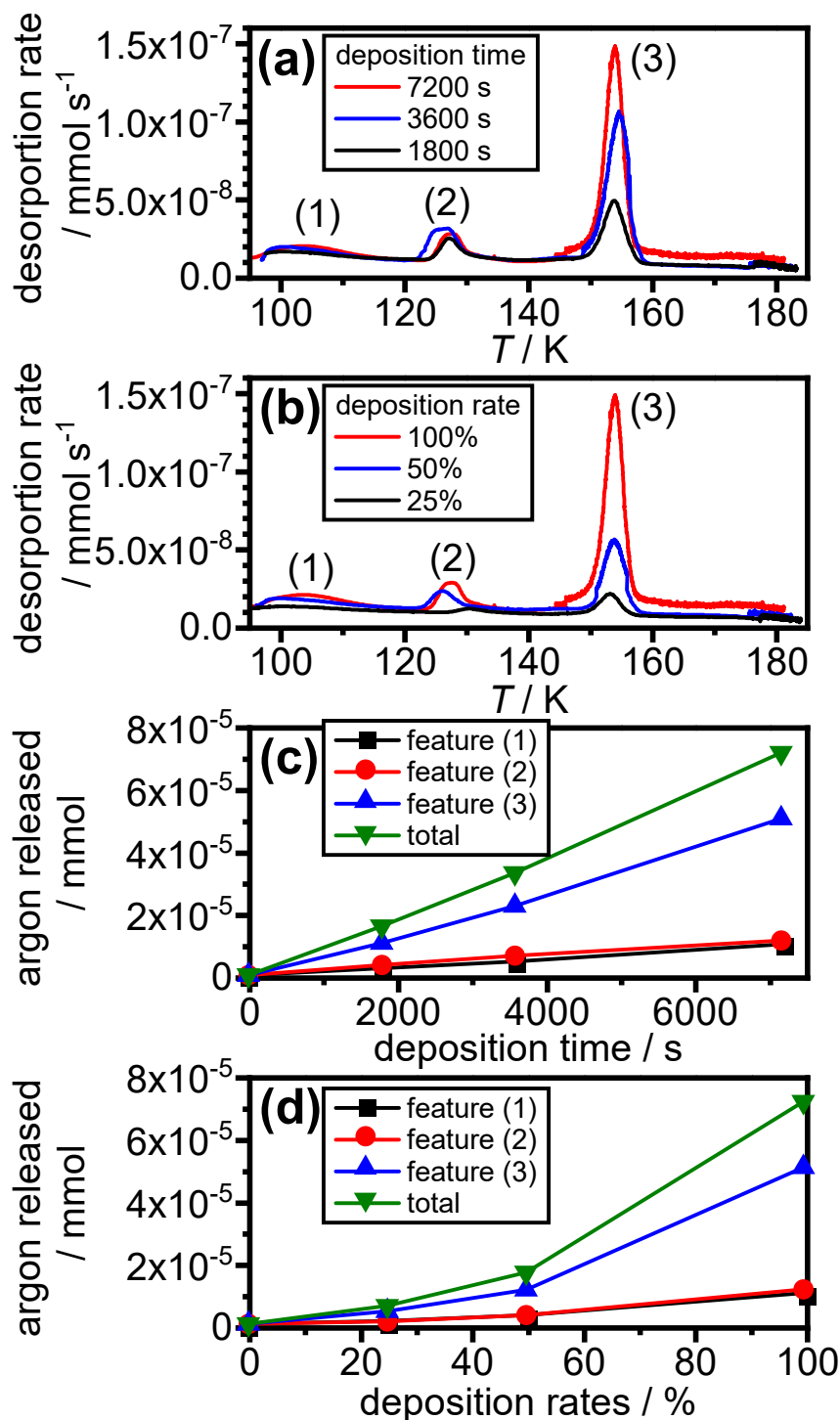


Figure 3.19. Desorption rates of argon for several different film thicknesses and deposition rates where (a) TPD data for various deposition times using  $1.157 \times 10^{-2} \text{ mmol s}^{-1}$  and  $1.345 \times 10^{-5} \text{ mmol s}^{-1}$  of  $\text{H}_2\text{O}$  and argon, respectively. (b) TPD data for various deposition rates with a two-hour deposition time indicated with percentages of the deposition rates. Panel (c) and (d) show the quantitative analysis of the amount of argon released from panel (a) and (b) desorption processes. This figure has been reprinted from reference 1 with the permission of AIP Publishing. Data in this figure was collected by S. O. Halukeerthi.

### 3. Gaseous ‘Nanoprobes’ for Detecting Gas-Trapping Environments in Thick Layers of Amorphous Solid Water

#### 3.3.7 Increasing the Amount of Argon

Films made in this study are of  $\sim 100$   $\mu\text{m}$  thickness and to investigate the amount of argon that can be immobilised in these films, the argon to  $\text{H}_2\text{O}$  ratios were increased while keeping the leak rate of  $\text{H}_2\text{O}$  constant,  $1.157 \times 10^{-2} \text{ mmol s}^{-1}$ . Argon to  $\text{H}_2\text{O}$  ratios was such that, they increased from 1:2460 to 1:1860 and 1:5. The partial pressures of these ratios were recorded and the corresponding TPD data are shown in Figure 3.20(a). While the flow rates of argon were increased, it is fascinating to note that in the 1:5 ratio, the onset temperature of the first (1) and second (2) desorption features is shifted towards lower temperatures: it is speculated that this change is due to locally increased pressures of argon that now influence desorption temperatures. The third (3) feature in the TPD data does not show any influence with respect to the onset temperature and argon concentration. This finding is consistent with the desorption of argon, matrix-isolated upon crystallisation.

Quantitative analysis was conducted on the desorption features with respect to partial pressures as displayed in Figure 3.20(b) (Table 3.1). This analysis shows that the typical argon experiments carried out earlier were far away from the maximal solubility that argon could be incorporated into ASW. Due to the MS restrictions, in particular, the limit of the Faraday cup, the pressure exceeded the limit for the 1:5 ratio and so, it was not possible to record above a temperature of  $\sim 155$  K. The ratio for the areas of the two other experiments, in line with the third (3) feature, with respect to the first (1) and second (2) features, are consistent with each other. One can assume this is the case for the higher ratio, 1:5, and estimate that the ratio of  $\text{H}_2\text{O}$  molecules to gas ratio is 74,120:1 compared to 1,169,000:1 in the typical codeposition experiment (Table 3.1).

### 3. Gaseous ‘Nanoprobes’ for Detecting Gas-Trapping Environments in Thick Layers of Amorphous Solid Water

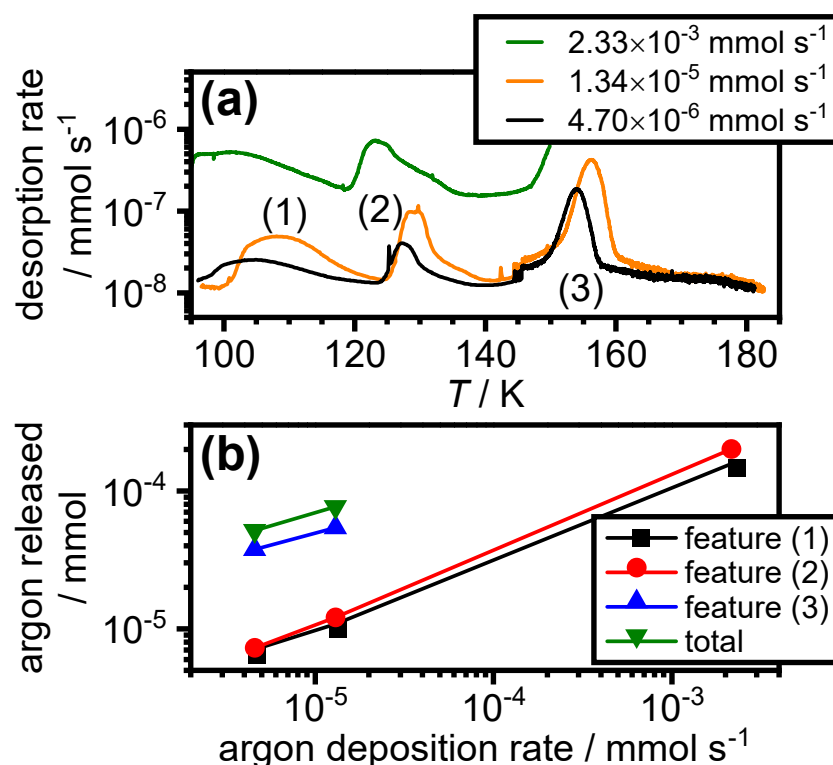


Figure 3.20. Influence of increasing the amount of argon where (a) desorption rates of argon after increasing the flow rates of argon from  $4.70 \times 10^{-6} \text{ mmol s}^{-1}$  to  $1.34 \times 10^{-5} \text{ mmol s}^{-1}$  and  $2.33 \times 10^{-3} \text{ mmol s}^{-1}$ , (b) corresponding quantitative data for panel (a). This figure has been reprinted from reference 1 with the permission of AIP Publishing.

#### 3.3.8 Baffling the Gas-Flow

Further to this study, the effect of baffling the  $\text{H}_2\text{O}$  beam on the three different desorption features was investigated. Baffling the flow of  $\text{H}_2\text{O}$ -vapour beam has been shown to generally lead to a decrease in the porosity of ASW.<sup>13, 30, 31, 61</sup> In the literature, ASW films made by baffling the  $\text{H}_2\text{O}$ -vapour beam show pore collapse initiating around 120 K, while non-baffled samples were observed to exhibit more stable pores that decomposed at higher temperatures of 140 K: neutron diffraction studies support this finding.<sup>61</sup>

Two different types of baffling were used: (i) an iron mesh to baffle the beam and (ii) full block of the  $\text{H}_2\text{O}$ -vapour beam using a solid metal plate was implemented. Figure 3.7(b) has shown that using an iron mesh results in some degree of baffling. To investigate the baffling effect in more detail and the degree of disruption of gas flow into the chamber, a ‘typical codeposition’ experiment of a 1:860 Ar: $\text{H}_2\text{O}$  ratio was conducted, a metal plate was placed on top of the mesh with a gap on the side on the  $\text{H}_2\text{O}$ -inlet tube. QCM measurements as displayed in Figure 3.7(c) demonstrate severe disruption of the gas flow. Figure 3.21(a) displays a comparison of the partial pressures recorded for  $\text{H}_2\text{O}$  upon

### 3. Gaseous ‘Nanoprobes’ for Detecting Gas-Trapping Environments in Thick Layers of Amorphous Solid Water

heating the Ar@ASW deposit, where both TPD traces for baffled with a mesh and blocked with a two-pence metal coin, respectively, are shown for H<sub>2</sub>O and argon. The latter illustrates that a smaller amount of deposit is deposited onto the plate which was consistent with the QCM measurements as previously shown in Figure 3.9(c).

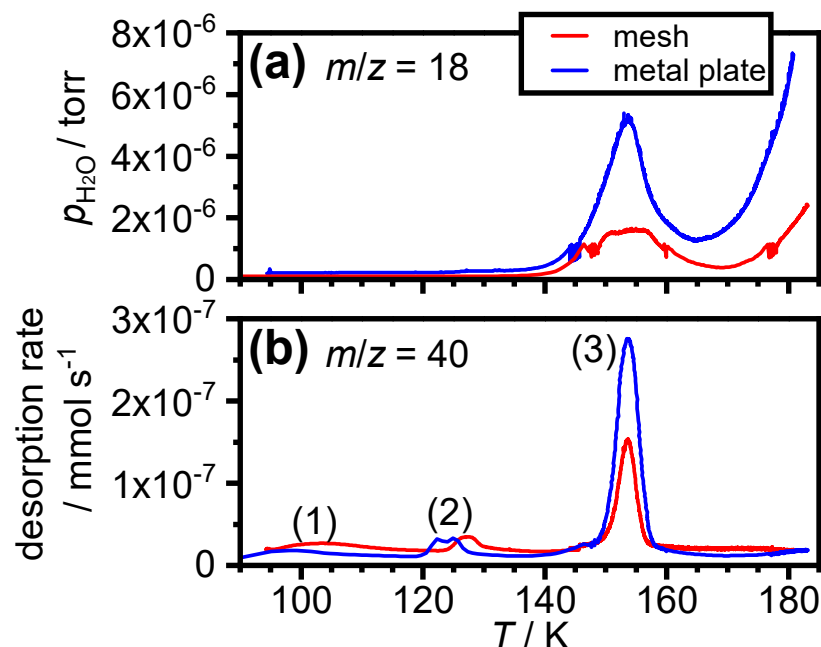


Figure 3.21. Influence of the degree of baffling the gas-flow into the chamber where (a) H<sub>2</sub>O partial pressures recorded upon heating and (b) desorption rates from argon during codeposition under baffling conditions using a mesh or metal plate. This figure has been reprinted from reference 1 with the permission of AIP Publishing.

The desorption data analysed in Figure 3.21(b) indicates substantial differences. The low-temperature desorption feature at approximately 100 K, (1), is weaker for the experiment with a ‘metal plate’ and quantitative data is provided in Table 3.1. The weaker desorption feature indicates that background deposition conditions lead to a reduced number of open cracks existing in the ASW film. Additionally, a greater amount of matrix-isolated argon is observed which is caused by the background deposition as specified and shown by the intense third desorption feature which is significantly larger when compared to the corresponding desorption feature for the ‘mesh’ experiment. Despite the overall amount of ASW being lower, there are still large amounts of matrix-isolated argon present which is an exceptional finding. It is not possible to assume all the H<sub>2</sub>O is deposited onto the deposition plate during the ‘metal plate’ experiment and therefore, further quantifications of this remain difficult and will continue to remain difficult as it is not possible to know where 100% of the deposit is. Nonetheless, it is evident that baffling the flow of H<sub>2</sub>O-

### **3. Gaseous ‘Nanoprobes’ for Detecting Gas-Trapping Environments in Thick Layers of Amorphous Solid Water**

vapour compared to all other investigated parameters had the most distinct and pronounced effect on the morphology of the deposit. To review, random fluxes of unavoidable background deposition are seen to decrease the number of open cracks in the ASW deposit in line with increasing the amounts of matrix-isolated argon.

#### **3.3.9 Pumping Efficiency**

An additional experiment was carried out to test the pumping efficiency of the pump. Once the base pressure was achieved, the pressure of H<sub>2</sub>O was increased gradually to illustrate the effect on the general pressure. At the same time, a background gas which does not stick, such as argon, was also introduced into the chamber. In Figure 3.22(a), increases in the general background pressure of argon were detected when the partial pressure of H<sub>2</sub>O was increased. Figure 3.22(b) shows similar trends such that, when the amount of argon is increased, and when it is assumed that the partial pressure of H<sub>2</sub>O acts as the background gas, a significant decrease in pressure is observed. It can be inferred that any increases in H<sub>2</sub>O or gas, renders the partial pressure in the chamber slightly higher too. Desorption of argon therefore may seem or look greater as deposition proceeds. It was not possible to quantify this properly and in turn, the calibration data as shown in Figure 3.2 was used in all experiments as the partial pressure is not fully reliable in the presence of two different species. In any case, there is always a slight increase in the background pressure when a species is introduced into the system.

### 3. Gaseous ‘Nanoprobes’ for Detecting Gas-Trapping Environments in Thick Layers of Amorphous Solid Water

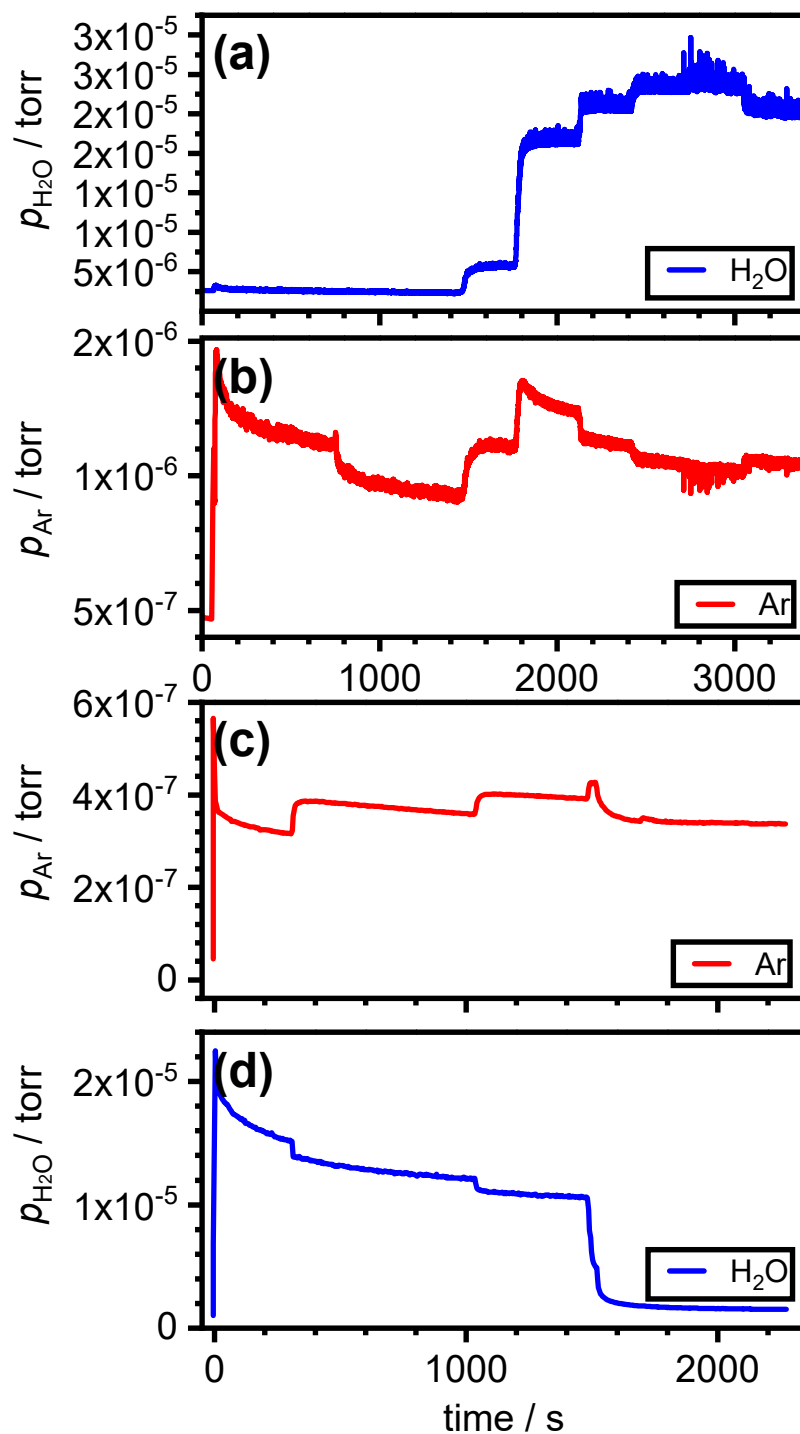


Figure 3.22. Partial pressures recorded from the MS when a background gas is dosed into the chamber and the effect of pumping efficiency is monitored where (a) increase of  $\text{H}_2\text{O}$  gradually with corresponding (b) increase of argon, (c) partial pressure of argon when leaked into the chamber and gradually increased with corresponding (d)  $\text{H}_2\text{O}$  acting as background pressure.



### 3. Gaseous ‘Nanoprobes’ for Detecting Gas-Trapping Environments in Thick Layers of Amorphous Solid Water

#### 3.4 Quantitative Analysis of the TPD Data

TPD experiments monitoring the desorption of species can be regarded as a ‘virtual’ gas leak that is indistinguishable from any gas that may be leaked into the vacuum chamber through the needle valves. High-accuracy graduated needle valves as mentioned in section 3.2.1 were used for calibration measures to allow the argon partial pressures from the MS to be converted to desorption rates in units of  $\text{mmol s}^{-1}$ . The calibration curve as shown in Figure 3.2, alongside the partial pressures from the TPD data in Figure 3.15 were converted to desorption rates. The total release of argon can be confirmed by integration of the TPD spectra, and once the desorption rates are plotted with respect to time, the amount of argon released from each desorption feature is obtained. The area of each desorption feature is integrated with respect to time and summed to obtain a total value. This value is converted to  $\text{mmol s}^{-1}$  by interpolation of Figure 3.1 and Figure 3.2 as described herein.

In particular, and to begin with, as argon is introduced into the chamber, the chamber pressure is recorded in units of mbar and the manufacturer factory values for the needle valve are provided in Figure 3.1. Using the same needle valve positions, it is possible to see that the value of the chamber pressure increases each time the needle valve position is altered for increases in argon. Both these data (Figure 3.1 and Figure 3.2) can be interpolated to obtain a value in  $\text{mmol s}^{-1}$ . This is due to the fact that in these experiments, the chamber pressure is essentially a reflection of the  $\text{H}_2\text{O}$  desorption rate as the monitored pressure depends on the balance of outwards and negative transfer due to effective pumping, and inwards and positive transfer caused by  $\text{H}_2\text{O}$  desorption. The chamber is purged consistently before deposition experiments with  $\text{H}_2\text{O}$  and the desired gas to detect and avoid chamber leaks which may affect the desorption rate or gas composition and to also ensure any  $\text{N}_2$  in the chamber, is eliminated. The chamber pressure,  $p$ , pumping rate,  $pmp$ , desorption rate,  $des$ , and re-adsorption rate,  $ads$ , are related by a simple equation as given below (Equation 3.1):

$$des = pmp(p) + ads \quad \text{Equation 3.1}$$

Once a value for mbar has been converted by interpolation to  $\text{mmol s}^{-1}$ , this value can be multiplied by the deposition time, typically 7200 seconds to obtain a value for the total amount of gas or  $\text{H}_2\text{O}$  dosed into the chamber in units of, mmol. The ratio of  $\text{H}_2\text{O}$  to gas in the deposit can be obtained by dividing the total dosed  $\text{H}_2\text{O}$  / mmol with the total gas

### 3. Gaseous ‘Nanoprobes’ for Detecting Gas-Trapping Environments in Thick Layers of Amorphous Solid Water

desorption / mmol to determine the fraction of gas captured. Quantitative analyses of every TPD trace are provided in Table 3.1 at the end of this chapter, where a systematic order of analysis corresponding to the description above, is provided.

It is realised that after summing over all three desorption features as shown in Figure 3.23(a), the total amount of argon released is  $7.127 \times 10^{-5} \text{ mmol s}^{-1}$ . This value, in turn, indicates that only 0.07% of the gas leaked into the chamber is integrated within the ASW film and corresponds with a H<sub>2</sub>O to argon ratio of 1,169,000:1 within the deposit. After quantitative analysis, it is evident there are more than one million H<sub>2</sub>O molecules present for every argon atom and this clearly defines argon as an ideal gaseous ‘nanoprobe’ towards the approach used in this study.

It must be highlighted that the link with leak rate and partial pressure is valid and effective, assuming the pumping efficiency is constant and only one gaseous ‘nanoprobe’ is leaked directly into the vacuum chamber. If a second species is introduced into the chamber, the pumping efficiency would decrease, and the pump would need to work harder to efficiently remove two gaseous species. Thus, the partial pressure recorded from the initial species will be higher for any given leak rate than what is expected from leaking only one species into the vacuum chamber. This has been shown previously in Figure 3.18.

Figure 3.23 below illustrates the TPD data of argon and CH<sub>4</sub> in amorphous ice once partial pressures were converted into desorption rates. Once partial pressures are converted to desorption rates, they can be plotted with respect to time and the gas released from each feature seen in the TPD can be obtained by integration of each desorption peak. The resulting quantity is expressed in mmol and indicated for the three desorption features in Figure 3.23.

### 3. Gaseous ‘Nanoprobes’ for Detecting Gas-Trapping Environments in Thick Layers of Amorphous Solid Water

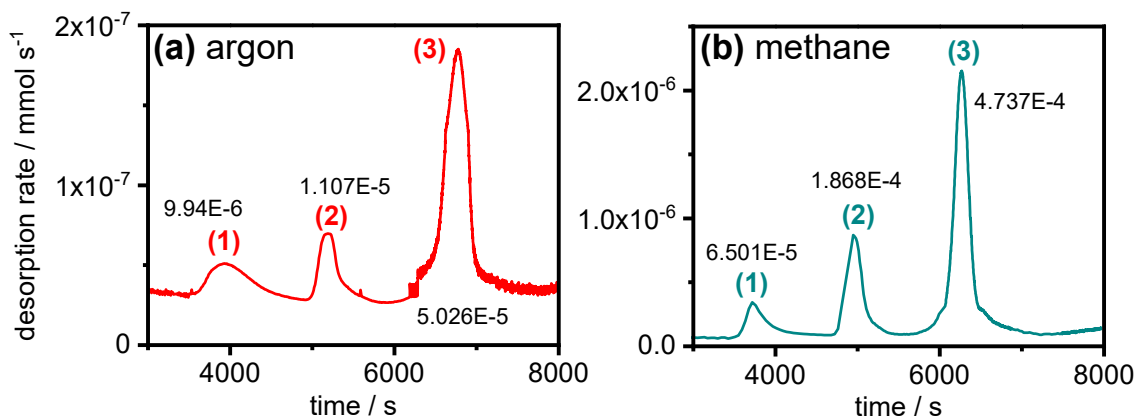


Figure 3.23. Typical desorption of (a) argon and (b) CH<sub>4</sub> followed during TPD measurements. The deposition time was typically two-hours and samples were kept cold for one-hour to allow for the chamber to reach base pressure before the TPD was initialised. The data is displayed with respect to time to allow integration of the specific desorption peaks giving the amount of gas desorbed in units, mmol. Each figure lists the amount of desorbed gas for each feature. The crystallisation is omitted from this figure for the clarity of a single species. This figure has been reprinted from reference 1 with the permission of AIP Publishing.

### 3. Gaseous ‘Nanoprobes’ for Detecting Gas-Trapping Environments in Thick Layers of Amorphous Solid Water

The table below presents the full quantitative analysis of the TPD data as displayed in this chapter.

*Table 3.1. Complete list of experimental detail for codeposition experiments and analysis of various desorption features. This table has been adapted and reprinted from reference 1 with the permission of AIP Publishing.*

H <sub>2</sub> O flow into the chamber / mmol s <sup>-1</sup>	gas	gas flow into the chamber / mmol s <sup>-1</sup>	baffle conditions	deposition time / s	total dosed H <sub>2</sub> O / mmol	total dosed gas / mmol	H <sub>2</sub> O to gas ratio in beam	desorption feature (1) / mmol	desorption feature (2) / mmol	desorption feature (3) / mmol	total gas desorption / mmol	fraction of gas captured	H <sub>2</sub> O to gas ratio in deposit	Figure
1.157E-02	Ar	1.345E-05	mesh	7200	8.328E+01	9.684E-02	8.600E+02	9.940E-06	1.107E-05	5.026E-05	7.127E-05	7.359E-04	1.169E+06	3.15(a)
1.157E-02	CH <sub>4</sub>	1.345E-05	mesh	7200	8.328E+01	9.684E-02	8.600E+02	6.501E-05	1.868E-04	4.737E-04	7.255E-04	7.492E-03	1.148E+05	3.15(b)
1.157E-02	Ar	1.345E-05	mesh	3600	4.164E+01	4.842E-02	8.600E+02	4.308E-06	6.221E-06	2.226E-05	3.279E-05	6.771E-04	1.270E+06	3.19(a)
1.157E-02	Ar	1.345E-05	mesh	1800	2.082E+01	2.421E-02	8.600E+02	2.117E-06	3.254E-06	1.035E-05	1.572E-05	6.492E-04	1.325E+06	3.19(a)
5.784E-03	Ar	6.725E-06	mesh	7200	4.164E+01	4.842E-02	8.600E+02	2.860E-06	2.779E-06	1.090E-05	1.654E-05	3.416E-04	2.517E+06	3.19(b)
2.892E-03	Ar	3.363E-06	mesh	7200	2.082E+01	2.421E-02	8.600E+02	8.972E-07	8.415E-07	4.052E-06	5.791E-06	2.392E-04	3.595E+06	3.19(b)
1.157E-02	Ar	4.700E-06	mesh	7200	8.328E+01	3.384E-02	2.461E+03	6.456E-06	6.660E-06	3.471E-05	4.783E-05	1.413E-03	1.741E+06	3.20(a)
1.157E-02	Ar	2.330E-03	mesh	7200	8.328E+01	1.678E+01	4.964E+00	1.471E-04	1.883E-04	-	-	-	-	3.20(a)
1.157E-02	Ar	1.345E-05	plate	7200	8.328E+01	9.684E-02	8.600E+02	3.342E-06	6.209E-06	6.760E-05	7.716E-05	-	-	3.21(b)
1.157E-02	Ar	1.345E-05	mesh	7200	8.328E+01	9.684E-02	8.600E+02	2.014E-05	1.885E-06	7.834E-06	2.986E-05	3.083E-04	2.790E+06	3.18(a)

### 3. Gaseous ‘Nanoprobes’ for Detecting Gas-Trapping Environments in Thick Layers of Amorphous Solid Water

#### 3.5 Conclusions

This study reinforces the highly complex and multifaceted nature of ASW which arises from its heterogeneity, ranging across numerous length scales, in combination with the dynamic behaviour of intricate H<sub>2</sub>O molecules. Since employing argon as a gaseous ‘nanoprobe’ in the 95–185 K temperature range, it was concluded that two trapping environments, absent in nanoscale films were identified and only present in macroscopic ASW films. Foremost, argon gas is released at ~100 K in cracks which is further removed upon heating above this temperature. When ASW forms *via* background deposition, these particular cracks appear to be reduced. Disregarding deposition geometry and independent of this, argon is released *via* a second desorption process which is attributed to the collapse of internal voids at ~125 K. This process arises from the underlying orientational glass transition of LDA/ASW,<sup>62, 63</sup> facilitating void collapse. The third desorption process as seen in nanoscale Ar@ASW,<sup>2, 5</sup> agrees with matrix-isolated argon that is fully liberated as ASW crystallises at ~160 K. Effective matrix-isolation is observed as background deposition occurs.

The desorption features assigned to local environments are supported by means of using additional ‘nanoprobes’: CH<sub>4</sub>, helium and CO<sub>2</sub>. Inclusive of this study, it is evident that the morphology of the deposits become more complex as the films become more thickness-dependent from nanoscale to macroscopic. The focus of future studies will in fact follow the crossover between nanoscale and thick films and also delve deeper into the low-temperature deposition features as discovered in this study. Additionally, probing the use of argon as a ‘nanoprobe’ resulted in determining how baffling the flow of the H<sub>2</sub>O-vapour beam altered the morphology of the deposit.

In addition to the structural complexity and somewhat unsolved mysteries of ASW, ice *Isd*, formed from the crystallisation of ASW has proven to be quite a complex material. A range of different fractions of cubic and hexagonal stacking has been discovered for ice *Isd*, and long-range memory effects within stacking are probable.<sup>25, 26, 35, 37, 64</sup> The precise details of stacking disorder present in ice *Isd* from ASW has been shown to significantly affect its chemical and physical properties.<sup>65-68</sup> The literature remains limited in regards to how, and if, the structural variances in ASW may influence the stacking disorder in ice *Isd*, thus, further investigations will need to be conducted through QCM measurements around the temperature ranges where crystallisation occurs.

### 3. Gaseous ‘Nanoprobes’ for Detecting Gas-Trapping Environments in Thick Layers of Amorphous Solid Water

#### 3.6 References

1. S. K. Talewar, S. O. Halukeerthi, R. Riedlaicher, J. J. Shephard, A. E. Clout, A. Rosu-Finsen, G. R. Williams, A. Langhoff, D. Johannsmann and C. G. Salzmann, *J. Chem. Phys.*, 2019, **151**, 134505.
2. P. Ayotte, R. S. Smith, K. P. Stevenson, Z. Dohnálek, G. A. Kimmel and B. D. Kay, *J. Geophys. Res. Planets*, 2001, **106**, 33387-33392.
3. R. A. May, R. S. Smith and B. D. Kay, *J. Chem. Phys.*, 2013, **138**, 104501.
4. R. A. May, R. S. Smith and B. D. Kay, *J. Chem. Phys.*, 2013, **138**, 104502.
5. A. Bar-Nun, G. Notesco and T. Owen, *Icarus*, 2007, **190**, 655-659.
6. G. Notesco, A. Bar-Nun and T. Owen, *Icarus*, 2003, **162**, 183-189.
7. A. Peschel, A. Böttcher, A. Langhoff and D. Johannsmann, *Rev. Sci. Instrum.*, 2016, **87**, 115002.
8. D. Johannsmann, *Phys. Chem. Chem. Phys.*, 2008, **10**, 4516-4534.
9. A. Hallbrucker and E. Mayer, *Icarus*, 1991, **90**, 176-180.
10. E. Mayer and A. Hallbrucker, *J. Chem. Soc., Chem. Commun.*, 1989, **12**, 749-751.
11. A. Hallbrucker and E. Mayer, *J. Chem. Soc., Faraday Trans.*, 1990, **86**, 3785.
12. P. Jenniskens and D. F. Blake, *Science*, 1994, **265**, 753.
13. E. Mayer and R. Pletzer, *J. Chem. Phys.*, 1984, **80**, 2939-2952.
14. K. P. Stevenson, G. A. Kimmel, Z. Dohnalek, R. S. Smith and B. D. Kay, *Science*, 1999, **283**, 1505-1507.
15. G. A. Kimmel, K. P. Stevenson, Z. Dohnálek, R. S. Smith and B. D. Kay, *J. Chem. Phys.*, 2001, **114**, 5284-5294.
16. Z. Dohnálek, G. A. Kimmel, P. Ayotte, R. S. Smith and B. D. Kay, *J. Chem. Phys.*, 2003, **118**, 364-372.
17. R. S. Smith, T. Zubkov, Z. Dohnálek and B. D. Kay, *J. Phys. Chem. B*, 2009, **113**, 4000-4007.
18. M. T. Suter, K. Bolton, P. U. Andersson and J. B. C. Pettersson, *Chem. Phys.*, 2006, **326**, 281-288.
19. D. A. King and M. G. Wells, *Surf. Sci.*, 1972, **29**, 454-482.
20. G. Sauerbrey, *Z. Phys.*, 1959, **155**, 206-222.
21. E. F. Burton and W. F. Oliver, *Nature*, 1935, **135**, 505-506.
22. A. Hallbrucker, E. Mayer and G. Johari, *J. Phys. Chem.*, 1989, **93**, 4986-4990.
23. L. G. Dowell and A. P. Rinfret, *Nature*, 1960, **188**, 1144-1148.
24. J. A. McMillan and S. C. Los, *Nature*, 1965, **206**, 806-807.
25. W. F. Kuhs, C. Sippel, A. Falenty and T. C. Hansen, *Proc. Natl. Acad. Sci. U. S. A.*, 2012, **109**, 21259-21264.
26. T. L. Malkin, B. J. Murray, C. G. Salzmann, V. Molinero, S. J. Pickering and T. F. Whale, *Phys. Chem. Chem. Phys.*, 2015, **17**, 60-76.
27. D. Johannsman, *The Quartz Crystal Microbalance in Soft Matter Research*, Springer International Publishing, 2015.
28. A. K. Srivastava and P. Sakthivel, *J. Vac. Sci. Technol. A*, 2001, **19**, 97-100.
29. T. Loerting, K. Winkel, M. Seidl, M. Bauer, C. Mitterdorfer, P. H. Handle, C. G. Salzmann, E. Mayer, J. L. Finney and D. T. Bowron, *Phys. Chem. Chem. Phys.*, 2011, **13**, 8783-8794.
30. E. Mayer and R. Pletzer, *Nature*, 1986, **319**, 298-301.
31. E. Mayer and R. Pletzer, *J. Phys. Colloq.*, 1987, **48**, C1-581-C581-586.
32. R. S. Smith, N. G. Petrik, G. A. Kimmel and B. D. Kay, *Acc. Chem. Res.*, 2012, **45**, 33-42.
33. A. Kouchi, *Nature*, 1987, **330**, 550-552.

### 3. Gaseous ‘Nanoprobes’ for Detecting Gas-Trapping Environments in Thick Layers of Amorphous Solid Water

34. M. Nachbar, D. Duft and T. Leisner, *J. Phys. Chem. B*, 2018, **122**, 10044-10050.
35. C. G. Salzmann, B. J. Murray and J. J. Shephard, *Diamond Relat. Mater.*, 2015, **59**, 69-72.
36. C. G. Salzmann, *J. Chem. Phys.*, 2019, **150**, 060901.
37. T. L. Malkin, B. J. Murray, A. V. Brukhno, J. Anwar and C. G. Salzmann, *Proc. Natl. Acad. Sci. U. S. A.*, 2012, **109**, 1041-1045.
38. C. Bu, C. A. Dukes and R. A. Baragiola, *Appl. Phys. Lett.*, 2016, **109**, 201902.
39. R. S. Smith, C. Huang, E. K. L. Wong and B. D. Kay, *Phys. Rev. Lett.*, 1997, **79**, 909-912.
40. R. A. May, R. S. Smith and B. D. Kay, *Phys. Chem. Chem. Phys.*, 2011, **13**, 19848-19855.
41. R. A. May, R. S. Smith and B. D. Kay, *J. Phys. Chem. Lett.*, 2012, **3**, 327-331.
42. R. S. Smith, R. A. May and B. D. Kay, *J. Phys. Chem. B*, 2016, **120**, 1979-1987.
43. G. Natesco, *Icarus*, 2003, **162**, 183-189.
44. A. Bar-Nun, I. Kleinfeld and E. Kochavi, *Phys. Rev. B*, 1988, **38**, 7749-7754.
45. J. H. E. Cartwright, B. Escribano and C. I. Sainz-Díaz, *Thin Solid Films*, 2010, **518**, 3422-3427.
46. E. Lisitsin-Baranovsky, S. Delage, O. Sucre, O. Ofer, P. Ayotte and G. Alexandrowicz, *J. Phys. Chem. C*, 2016, **120**, 25445-25450.
47. A. Hallbrucker, E. Mayer and G. P. Johari, *J. Phys. Chem.*, 1989, **93**, 4986-4990.
48. C. R. Hill, C. Mitterdorfer, T. G. Youngs, D. T. Bowron, H. J. Fraser and T. Loerting, *Phys. Rev. Lett.*, 2016, **116**, 215501.
49. J. Swenson and S. Cervený, *J. Phys.: Condens. Matter*, 2014, **27**, 033102.
50. T. Zubkov, R. S. Smith, T. R. Engstrom and B. D. Kay, *J. Chem. Phys.*, 2007, **127**, 184707.
51. T. Zubkov, R. S. Smith, T. R. Engstrom and B. D. Kay, *J. Chem. Phys.*, 2007, **127**, 184708.
52. M. Minissale, E. Congiu and F. Dulieu, *Astron. Astrophys.*, 2016, **585**, A146.
53. A. Van Itterbeek and W. Van Dingenen, *Physica*, 1938, **5**, 529-540.
54. P. Taborek and L. J. Senator, *Phys. Rev. Lett.*, 1986, **56**, 628-631.
55. M. P. Collings, M. A. Anderson, R. Chen, J. W. Dever, S. Viti, D. A. Williams and M. R. S. McCoustra, *Mon. Not. R. Astron. Soc.*, 2004, **354**, 1133-1140.
56. S. Malyk, G. Kumi, H. Reisler and C. Wittig, *J. Phys. Chem. A*, 2007, **111**, 13365-13370.
57. J. L. Edridge, K. Freimann, D. J. Burke and W. A. Brown, *Philos. Trans. R. Soc., A*, 2013, **371**, 20110578.
58. J. He, S. M. Emtiaz, A. Boogert and G. Vidali, *Astrophys. J.*, 2018, **869**, 41.
59. K. Isokoski, J. B. Bossa, T. Triemstra and H. Linnartz, *Phys. Chem. Chem. Phys.*, 2014, **16**, 3456-3465.
60. E. C. Fayolle, K. I. Öberg, H. M. Cuppen, R. Visser and H. Linnartz, *Astron. Astrophys.*, 2011, **529**, A74.
61. C. Mitterdorfer, M. Bauer, T. G. Youngs, D. T. Bowron, C. R. Hill, H. J. Fraser, J. L. Finney and T. Loerting, *Phys. Chem. Chem. Phys.*, 2014, **16**, 16013-16020.
62. M. Fisher and J. P. Devlin, *J. Phys. Chem. A*, 1995, **99**, 11584-11590.
63. J. J. Shephard and C. G. Salzmann, *J. Phys. Chem. Lett.*, 2016, **7**, 2281-2285.
64. T. C. Hansen, M. M. Koza and W. F. Kuhs, *J. Phys.: Condens. Matter*, 2008, **20**, 285104.
65. J. E. Shilling, M. A. Tolbert, O. B. Toon, E. J. Jensen, B. J. Murray and A. K. Bertram, *Geophys. Res. Lett.*, 2006, **33**, L17801.

### 3. Gaseous ‘Nanoprobes’ for Detecting Gas-Trapping Environments in Thick Layers of Amorphous Solid Water

- 66. T. H. Carr, J. J. Shephard and C. G. Salzmann, *J. Phys. Chem. Lett.*, 2014, **5**, 2469-2473.
- 67. B. J. Murray, C. G. Salzmann, A. J. Heymsfield, S. Dobbie, R. R. Neely and C. J. Cox, *Bull. Am. Meteorol. Soc.*, 2015, **96**, 1519-1531.
- 68. P. Behr, A. Terziyski and R. Zellner, *J. Phys. Chem. A*, 2006, **110**, 8098-8107.



### 4 Matrix-Isolated Adamantane in Amorphous Ice

So far, the vast majority of amorphous solid water (ASW) mixture studies that have been conducted, have primarily focused on gas-laden amorphous ices<sup>1-4</sup> with small amounts of gas and there is sparse literature surrounding the nature of micrometre-thick ASW films codeposited with solid guest species. Low volatile guest species have included polyaromatic hydrocarbons (PAHs) and a range of studies have explored the photochemical and spectrochemical properties of PAHs/ASW mixtures.<sup>5-11</sup> Benzene has been used as a PAH analogue amongst studies.<sup>12, 13</sup> The mechanism of the glass transition of ASW<sup>14</sup> was investigated from the viewpoint of matrix-isolated 2-naphthol as a spectroscopic probe and similarly, as a consequence of the crystallisation of ASW, the aggregation of pyrene was examined spectroscopically.<sup>15</sup> Here, the hydrocarbon adamantane ( $C_{10}H_{16}$ ) has been codeposited with amorphous ice by physical vapour deposition for the first time in this study.

This approach will aim to open up new spyholes in understanding how water ( $H_2O$ ) behaves in terms of hydrophobic effects and the hydration of hydrophobic materials. Hitherto, experimental studies in this area were limited to amphiphilic molecules and hydrophobic surfaces.<sup>16-18</sup> The use of this carbon-ice composite will also help facilitate the discovery of new types of hydrates with large cages and investigate the effect of  $C_{10}H_{16}$  on the properties of ASW. The exploration into hydrate formation will provide unprecedented insights into how flexible a building block of  $H_2O$  is for producing open framework architectures.

#### 4.1 Adamantane ( $C_{10}H_{16}$ )

Adamantane, [ $C_{10}H_{16}$ , Figure 4.1(a)], is the most basic building block of diamond, the parent molecule of all diamondoids. Diamondoid molecules have recently been established as an essential class of hydrocarbons.<sup>19</sup> Diamondoid molecules are ultra-stable, saturated, stress-free cycloalkanes and have rigid cage-like structures.<sup>20, 21</sup> They are nanometre-sized, with well-defined structures, hydrogen-terminated diamond-like alkanes.<sup>19</sup> They are named ‘diamondoid’ as their carbon-carbon framework ( $sp^3$ – $sp^3$  hybridised) is largely superimposable on the bulk diamond cubic lattice structure, consisting of interlocked, fused cyclohexane rings and dangling carbon bonds are terminated with hydrogen.<sup>20</sup>

#### 4. Matrix-Isolated Adamantane in Amorphous Ice

As of more recently, diamondoids have received much attention due to their unique structure, chemical and physical properties, rendering them captivating molecules for building blocks in a wide number of applications, e.g., pharmaceuticals and synthesis of high-temperature polymers.<sup>21-24</sup> Diamondoids are also used as functional additive materials in nanotechnology<sup>25</sup> in a widespread range of applications, including polymer science, chemical synthesis and biomedical sciences.<sup>19</sup> Additionally, due to the high stability of nanodiamondoids, their presence throughout interstellar environments has been suggested.<sup>19</sup>

On Earth, these class of compounds occur naturally and are found to be isolatable from natural gas reservoirs and volatile oils,<sup>26</sup> such as petroleum deposits or distilled by-products from the oil. The first diamondoid to be isolated from petroleum by fractional distillation and thus synthesized, was C<sub>10</sub>H<sub>16</sub>.<sup>24</sup> C<sub>10</sub>H<sub>16</sub> is studied widely as a result of its many applications in the synthesis and design of drug delivery systems and in surface recognition studies.<sup>27</sup> Diamondoids of higher carbon numbers have been accessible from crude oil<sup>28</sup> and at low pressures and temperatures. C<sub>10</sub>H<sub>16</sub> and its stable derivatives have well-defined structures in line with no proven toxicity.

All diamondoids are variants of small and pristine, C<sub>10</sub>H<sub>16</sub> molecule [Figure 4.1(a)], (tricyclo[3.3.1.1]decane, molecular weight: 136.24 g mol<sup>-1</sup>) which more explicitly, comprises a ten-carbon tetracyclic cage system<sup>20</sup> surrounded by 16 hydrogen atoms and a *T<sub>d</sub>* point group symmetry. This sub-unit of diamond is further followed by a series of structures displaying a plethora of polymantane/adamantolog homologues: diamantane, tria-, tetra- and penta-, etc. Higher caged hydrocarbons of this series also display the same structure as the diamond lattice possessing strain-free highly symmetrical nature, allowing the carbon structure to be superimposable onto the diamond lattice as mentioned earlier. The use of these structures arises from their conformational rigidity, availability, and ease of functionalisation. These diamondoids, being hydrogen-terminated nanosized fragments of diamond, occur in a variety of shapes and sizes as shown in Figure 4.1, which are of nanometre size and contain more than tens of carbon atoms.

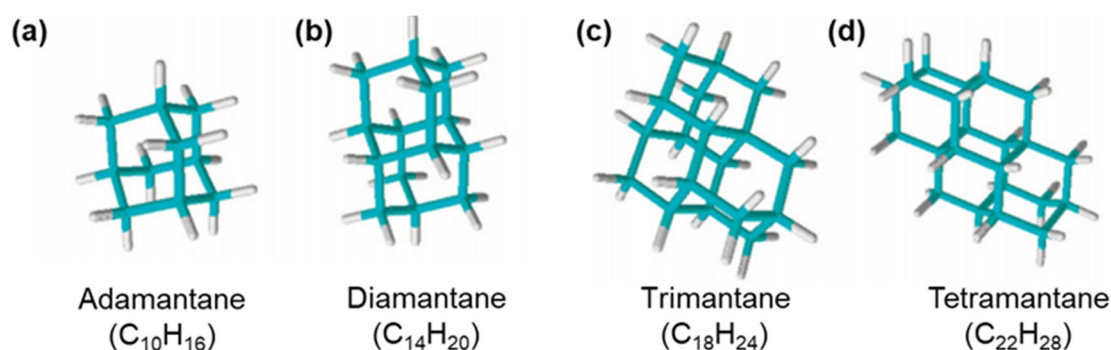


Figure 4.1. The molecular structures of  $C_{10}H_{16}$  and lower diamondoids including (a)  $C_{10}H_{16}$ , (b) diamantane ( $C_{14}H_{20}$ ), (c) trimantane ( $C_{18}H_{24}$ ) and (d) tetramantane ( $C_{22}H_{28}$ ). The hydrogen atoms that terminate the carbon skeleton on each structure are provided by the white sticks. This figure has been reprinted and adapted from reference 29 with the permission of ACS Publications. Copyright (2008) American Chemical Society.

At room temperature,  $C_{10}H_{16}$  is a colourless crystal with a camphor-like smell.  $C_{10}H_{16}$  is almost spherical, possesses the ability to rotate without steric hindrance in the crystal (ideal tetrahedral environment, thus, stable) and torsional strain (C–C bonds are staggered in a perfect manner), in three-dimensional space.<sup>26</sup> Cyclohexane rings composing the structure of  $C_{10}H_{16}$  exists in ‘chair’ conformation and these fused rings maintain the tetrahedral coordination of diamond. The C–C bond length in  $C_{10}H_{16}$  (1.53 Å) is almost identical to that in diamond at 1.54 Å. Weak intermolecular interactions bind the molecules together into the crystal whilst strong bonds for C–C atoms hold the molecule together.  $C_{10}H_{16}$  has four methine (CH) groups that are situated on its three-fold axes and also six methylene ( $CH_2$ ) groups that are located on the two-fold axes. The almost uniform distribution of 16 hydrogen atoms on the surface and the almost spherical nature of the molecule makes it clear why rotational motion barriers can be overcome so easily.<sup>30</sup>

Despite the rigid skeleton of  $C_{10}H_{16}$ , a series of solid-solid thermally induced phase transitions are exhibited before melting. This is the consequence of the ability to obtain rotational degrees of freedom while  $C_{10}H_{16}$  is in its crystalline state.<sup>21</sup> The crystal structure of  $C_{10}H_{16}$ <sup>31, 32</sup> displays orientationally disordered molecules, with a space group of face-centred cubic (*fcc*) structure,  $Fm\bar{3}m$  ( $a = 9.426$  Å,  $\alpha$ -phase) at room temperature with four molecules in the unit cell.

The  $\alpha$ -phase shows a phase transition upon cooling at 208.62 K/–65°C.<sup>33, 34</sup> At these low temperatures, the crystal exhibits mechanical properties that are in line with organic crystals, i.e., brittle with limited plasticity. During this phase transition,  $C_{10}H_{16}$  transforms from the *fcc* structure to a body-centred tetragonal (*bct*) phase, with space group,  $P\bar{4}2_1c$  ( $a = 6.641$  Å,  $c = 8.875$  Å,  $\beta$ -phase) and two molecules per unit cell with

#### 4. Matrix-Isolated Adamantane in Amorphous Ice

symmetry of  $D_{2d}^4$ . The transition from the tetragonal phase to the cubic phase results in a density change from  $1.18 \text{ g cm}^{-3}$  to  $1.08 \text{ g cm}^{-3}$ ,<sup>30</sup> accompanied by an entropy change of  $1594 \text{ J mol}^{-1} \text{ K}^{-1}$ .<sup>30</sup> The cubic phase of  $\text{C}_{10}\text{H}_{16}$  indicates that there is a random distribution of molecules amongst two different orientations, related to one another by a  $90^\circ$  rotation of a  $\text{C}_{10}\text{H}_{16}$  molecule about a line that joins two opposite methylene groups.<sup>32</sup> The  $\alpha$ -phase of  $\text{C}_{10}\text{H}_{16}$  is the best-known example of a dynamical orientationally disordered prototypical plastic phase<sup>30</sup> and the origin of the plastic phase lies in the symmetrical, compact cage-like structure. This structure is characterised and demonstrates molecular reorientation, giving rise to this cubic  $Fm\bar{3}m$  space group.<sup>35</sup> Thus, as the  $\alpha$ -phase of  $\text{C}_{10}\text{H}_{16}$  is cooled, it transforms into an ordered state where the molecules are frozen and so, cannot rotate.<sup>26</sup> Similar phase transitions (disorder-order) are seen for many  $\text{C}_{10}\text{H}_{16}$  derivatives.<sup>26, 36-39</sup> The phase diagram of  $\text{C}_{10}\text{H}_{16}$  is far less complex and diverse than that compared to ice (Chapter 1) and is shown in Figure 4.2 and Figure 4.3.

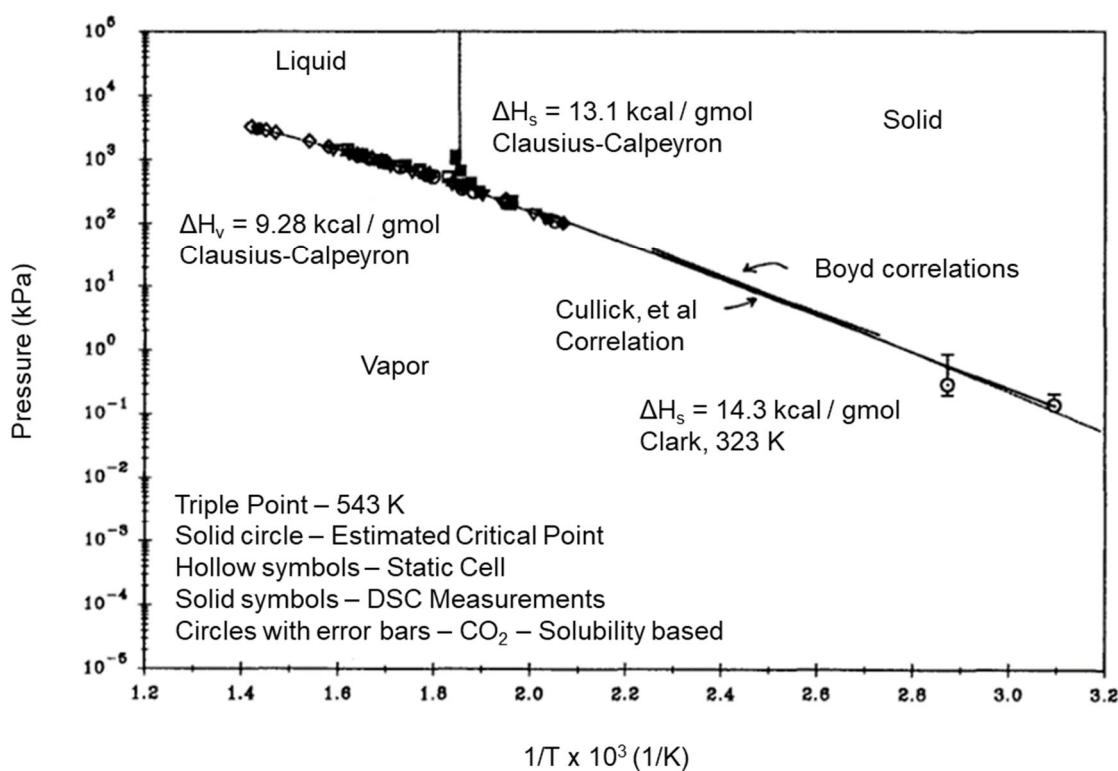


Figure 4.2. The phase diagram of  $\text{C}_{10}\text{H}_{16}$  up to  $10^6 \text{ kPa}$ . This figure has been adapted reprinted from reference 40 with the permission of Elsevier.

The transition points of the *fcc* to the tetragonal phase are shown in Figure 4.3(a) and the tetragonal phase of  $\text{C}_{10}\text{H}_{16}$  is shown in Figure 4.3(b). No high-pressure phase transitions were detected up to 40 kilobar and the pressures given in this phase diagram are correct

#### 4. Matrix-Isolated Adamantane in Amorphous Ice

to  $\pm 1$  kilobar.<sup>41</sup> Beyond 25 kilobar, the melting curve was not recorded as the material graphitizes at pressures of 10 kilobar to 45 kilobar at 480°C.<sup>41</sup>

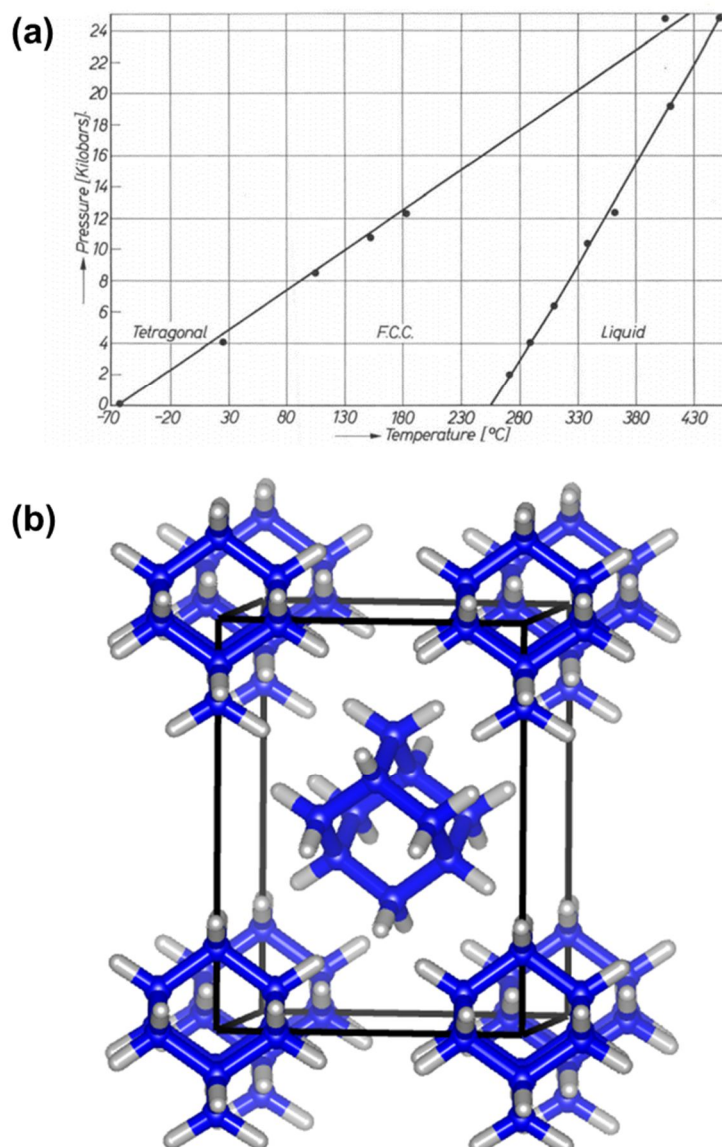


Figure 4.3. (a) Phase diagram of  $C_{10}H_{16}$  in the region of  $-70^{\circ}\text{C}$  to  $480^{\circ}\text{C}$  up to a pressure of 30 kilobar. This figure has been reprinted from reference 41 and (b) the crystal structure of the tetragonal phase of  $C_{10}H_{16}$  showing order which was created in the Vesta software. The molecule is not symmetry dependent.

The slope of the phase boundary of the  $\alpha$ -phase of  $C_{10}H_{16}$  is  $\frac{dP}{dT} = 51 \pm 4$  bar and the triple point of  $fcc$ -tetragonal-liquid is located at approximately 27 kilobar and a temperature of  $470^{\circ}\text{C}$ .<sup>41</sup>

The chemistry of  $C_{10}H_{16}$  has attracted the attention and interest of the scientific community for some time and remarkably, the thermodynamic properties of  $C_{10}H_{16}$  are significantly sparse in the literature and yet not well-established.<sup>34</sup> Data for the enthalpy of combustion, vapour pressure, and enthalpy of sublimation have been measured and on

## 4. Matrix-Isolated Adamantane in Amorphous Ice

the basis of spectroscopic data, the gas properties for  $C_{10}H_{16}$  have been calculated by statistical thermodynamic methods.<sup>34</sup> However, the sublimation, vaporisation enthalpies, ( $\Delta_{\text{sub(vap)}}H_m^\circ$ ) and the vapour pressure ( $p_{\text{sat}}$ ) are under important evaluation due to several significant discrepancies of up to approximately  $10 \text{ kJ mol}^{-1}$  in the  $\Delta_{\text{sub(vap)}}H_m^\circ$  and 30% in the  $p_{\text{sat}}$ .<sup>34</sup> In this study, the  $p_{\text{sat}}$  of  $C_{10}H_{16}$  is important to note in order to avoid contamination before the codeposition of  $H_2O$  and  $C_{10}H_{16}$ . The most recent calculated  $p_{\text{sat}}$  of  $C_{10}H_{16}$  at  $T = 298.15 \text{ K}$  is,  $p_{\text{sat}} = 18.1 \pm 0.9 \text{ Pa}$ .<sup>34</sup> The solid-solid transition enthalpy is known as  $3213 \text{ J mol}^{-1}$  at  $208 \text{ K}$ .<sup>42</sup> The thermodynamic properties are discussed elsewhere<sup>34</sup> and will not be discussed further.

While there are considerably large amounts of theoretical and experimental investigations on the behaviour and high-pressure structural changes on carbon materials such as fullerenes,<sup>43, 44</sup> the simple  $C_{10}H_{16}$  molecule remains underexplored and yet, the low-temperature phase even more underexplored. The pair distribution function (PDF) was obtained by total neutron scattering data of the high-temperature phase of  $C_{10}H_{16}$  and subsequent Reverse Monte Carlo (RMC) refinements were carried out.<sup>26</sup> It was discovered that there was very little or no correlation between the orientations of neighbouring molecules.<sup>26</sup> The intermolecular potential energy thus, results in a strong dependence on the orientation of the reference molecules and very weakly on the orientation of the neighbours.<sup>26</sup>

### 4.1.1 $C_{10}H_{16}$ as a Guest Species

Clathrate hydrates are non-stoichiometric inclusion compounds where the host  $H_2O$  molecules encapsulate guest molecules. The hexagonal clathrate hydrate, sH was first discovered by Ripmeester *et al.*<sup>45</sup> long after the discovery of the cubic clathrate hydrate structures, CS-I and CS-II.

$^{129}\text{Xe}$  nuclear magnetic resonance (NMR) studies were carried out to discover the sizes of guest species that can accommodate the sH structure.<sup>46</sup> Approximately, 25 guest molecules were assessed and identified as stable moieties for structure sH and guests with a variety of functional groups revealed that sH signifies a large family of hydrate structures. A large guest molecule with a van der Waals radius between  $7.5$  and  $8.6 \text{ \AA}$ <sup>47</sup> such as  $C_{10}H_{16}$  ( $7.8 \text{ \AA}$ ) is suitable for promoting a stable sH hydrate that can coexist with smaller help-gases such as argon (Ar), methane ( $CH_4$ ), xenon (Xe), krypton (Kr) or hydrogen (H) to support the remaining cavities.<sup>45</sup> The sH unit cell has 34  $H_2O$  molecules and is composed of three cavity types, such that, there are three-5<sup>12</sup>, two-4<sup>3</sup>5<sup>6</sup>6<sup>3</sup> and one-

#### 4. Matrix-Isolated Adamantane in Amorphous Ice

$5^{12}6^8$ .<sup>47</sup> In addition to the requirements for a large guest species, the correct shape (spheroidal) for the space-filling of a large sH cage ( $5^{12}6^8$ , ‘barrel’, Figure 4.4) should be adhered to.<sup>46</sup> The first sH hydrate was reported with  $C_{10}H_{16}$  and  $CH_4$  as a help-gas. Four phase equilibrium data for sH was obtained for  $C_{10}H_{16}$  and  $CH_4$  hydrates.<sup>47</sup> The initial equilibrium data and results presented by Ripmeester *et al.*<sup>45, 46, 48</sup> suggests that the sH clathrate hydrates occur in the petroleum and natural gas industry.<sup>47</sup> Yet, the limited characteristics of this clathrate hydrate reinforce the need for diffraction data to define the crystal structure of the clathrate hydrate.<sup>47</sup>

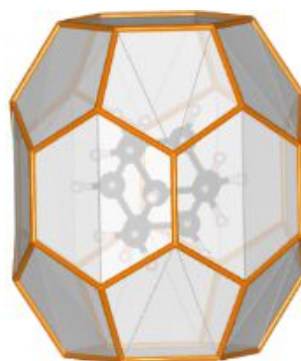


Figure 4.4. The largest cage observed so far in clathrate hydrates of  $5^{12}6^8$  cage shape, where molecules with the largest van der Waals diameters of  $8.6 \text{ \AA}$  fit. This barrel cage includes the insertion of the large guest species,  $C_{10}H_{16}$  with a van der Waals diameter of  $7.8 \text{ \AA}$ . This figure was produced by the Vesta software.

The crystal structure of the sH hydrate is quite unusual in the fact that it is isostructural with clathrasil dodecasil-1H with an accompanying host network, silicon dioxide ( $SiO_2$ ).<sup>47</sup> A variety of hypothetical structures have been proposed for clathrate hydrates with large cages of  $4^35^{12}6^{18}3$  and  $4^35^96^{27}3$ <sup>49, 50</sup> and it is indicated that a systematic and complete study of all possible networks of structures with large cages is a topologically formidable problem.<sup>49</sup> The search for these large cages and new large cages is timely as current research interests lie with inclusion compounds and their use in energy-related applications.<sup>51</sup>

$C_{10}H_{16}$  as an ideal candidate guest species has been selected in this study due to its low vapour pressure at low temperature. No diffraction data have been collected for the  $C_{10}H_{16}$  clathrate hydrate. This condition gives the idea for a seamless formation of clathrate hydrates where the organics cannot escape into the gas phase and so the  $H_2O$  molecules have to ‘deal’ with the presence of the organic molecule. The ‘nanoprobe’ aspect, in this case, is also ideal and is employed due to its small size, non-polar properties and highly symmetric nature which will help aid structural analysis.

### 4.2 Aims

The motivation of the present work is to study and probe the structure and dynamics of ASW from the perspective of the highly symmetric carbon species,  $C_{10}H_{16}$ , explored across a specific composition range ( $C_{10}H_{16}/H_2O$  molar ratios from 1:6 to 1:100). The question of spatial distribution across the entire diameter of the deposition plate will be addressed. This molecule should help to explain the poorly understood ASW in view of its sintering processes. In this chapter,  $C_{10}H_{16}$  is used at low and high concentrations, through a range of compositions to investigate the effect of  $C_{10}H_{16}$  on ASW. The study of the structure of  $H_2O$  in the hydration shell of  $C_{10}H_{16}$  will also be investigated and provided in upcoming Chapter 5. New structural insights will be highly important with respect to hydrophobic hydration and potentially in the wider context of the hydrophobic effect.<sup>52</sup>

The low-temperature conditions at which the experiments are carried out here should be ideal for preparing, but also isolating, and characterising metastable clathrate hydrates. A common procedure for preparing clathrate hydrates is to expose ice powder to a pressurised gas of the guest species, for instance,  $CH_4$ .<sup>47</sup> A more uncommon route for crystallising clathrate hydrates is to heat low-density amorphous ice (LDA) in the presence of a gaseous gas species.<sup>53</sup> Thus, in an extension to this approach, it is anticipated that crystallising a hydrophobic molecule/LDA mixtures will yield clathrate hydrates. In this case,  $C_{10}H_{16}$  will be investigated for clathrate hydrate formation to see if the route *via* amorphous ice is more effective in making the clathrate hydrate when compared with exposing ice powder to the pressurised gas of a guest species.



### 4.3 Experimental Procedures

The nature of  $C_{10}H_{16}$  and amorphous ice mixtures were investigated to determine the specific composition where the generation of clathrate hydrates may occur. The deposition rates of  $C_{10}H_{16}$  were thus, calibrated and were monitored by measuring the changes in fundamental frequency in the electrical conductance data over time by means of utilizing the myVNA and QTZ software<sup>54</sup> with the quartz-crystal microbalance (QCM).

The following section aims to describe and provide a guided tour of the use of three different deposition methods employed in order to ensure the ratios of  $C_{10}H_{16}$  and  $H_2O$  are as reproducible as possible. The following sections describe the calibration of the deposition rates of  $C_{10}H_{16}$  by using:

- (a) section 4.3.1 –  $C_{10}H_{16}$  crystals.
- (b) section 4.3.2 –  $C_{10}H_{16}$  prepared as a pellet.
- (c) section 4.3.5 –  $C_{10}H_{16}$  from a round-bottom flask.

#### 4.3.1 Initial Calibration of the Deposition Rates of $C_{10}H_{16}$

Initially,  $C_{10}H_{16}$  powder was simply weighed out to a suitable amount and placed in a copper crucible. As mentioned in Chapter 2, the copper crucible was placed onto the ‘cold’ upper side of the Peltier element with a fine layer of a non-silicone heatsink compound (Servisol, Batch Number: 313893) to ensure good thermal contact. This crucible has a small circular incision where a K-type thermocouple can be attached to monitor the temperature of the Peltier element. The Peltier element was controlled using the power supply mentioned in Chapter 2 where a voltage and a corresponding current is supplied to the element to allow for temperature control.

Prior to evacuating the chamber, the Peltier element was set to a base temperature of 240 K. This base temperature is low enough and thus important, as contaminants of  $C_{10}H_{16}$  can arise from  $C_{10}H_{16}$  possessing a very high vapour pressure reported at ambient conditions.<sup>34, 55</sup> The vapour pressure is a function of the temperature and so decreasing the pressure results in an increase in vapour pressure, however, reducing the temperature will decrease the vapour pressure. Therefore, to avoid any uncontrolled deposition of  $C_{10}H_{16}$  in the vacuum chamber while evacuating to low pressure and cooling of the

#### 4. Matrix-Isolated Adamantane in Amorphous Ice

deposition plate,  $C_{10}H_{16}$  is cooled prior to evacuating the vacuum chamber to 240 K using the Peltier element.

Before cooling and depositing  $C_{10}H_{16}$ , the QCM was firmly attached to the deposition plate in the central position and the fundamental frequency of the AT-cut gold-plated crystal was located at 6 MHz where the crystal oscillates. This was to monitor the amount of  $C_{10}H_{16}$  deposited on the plate at varying temperatures of the Peltier element. Once a low pressure and temperature environment within the chamber was achieved (Chapter 2), deposition was initiated as described earlier in this thesis for the calibration of the Peltier element.  $C_{10}H_{16}$  was deposited in a similar fashion by means of altering the temperature of the Peltier element in sequential stages. In other words, when the deposition plate reached 90 K and the Peltier element remained at a base temperature of 240 K, the voltage was decreased from 12.13 V in sequential stages in order to increase the temperature of the Peltier element in 5 K steps.

Particularly, the temperature was increased from 240 K to 290 K with the Peltier element to obtain the desired temperature, raising the vapour pressure, and therefore subliming  $C_{10}H_{16}$ . To ensure the stability of the evaporation source before changing the voltage to approach another temperature, the temperature was kept stable for five minutes and plateaued until a final temperature of 290 K. The QCM response was recorded during the deposition process in order to calculate the deposition rate for each temperature by performing a linear fit to the gradients of each temperature.

Initially, several failed attempts of calibrating  $C_{10}H_{16}$  as a function of the temperature of the evaporation source (Chapter 2, Figure 2.7) were initially observed. The deposition rates of  $C_{10}H_{16}$  recorded from the QCM response between several experiments resulted in highly inconsistent measurements and thus, not in line with the expectation of an exponential increase with temperature as depicted in Figure 4.5. Considering the number of attempts of calibrating the deposition rates of  $C_{10}H_{16}$ , the figure clearly indicates the highly unreliable method of obtaining reproducible deposition rates by simply spreading the  $C_{10}H_{16}$  powder and compacting in the copper crucible. No data sets were found to agree with each other or produce reproducible deposition rates and thus, were disregarded. Reproducible deposition rates and thus, ratios of  $C_{10}H_{16}/H_2O$  are needed to observe trends and patterns in the data. This data was not reproducible, and it is speculated this was the case due to poor thermal contact within the  $C_{10}H_{16}$  powder.

## 4. Matrix-Isolated Adamantane in Amorphous Ice

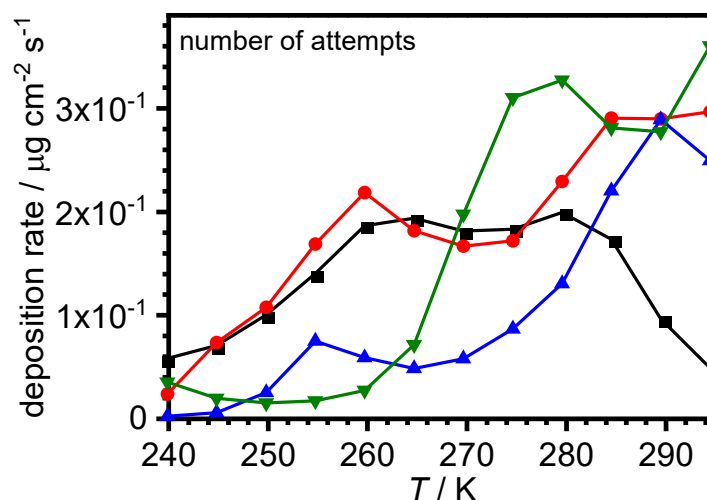


Figure 4.5. Mass deposition rate of  $C_{10}H_{16}$  against the corresponding temperature of the evaporation source, showing the number of attempts for the calibration of the deposition rates of  $C_{10}H_{16}$ .  $C_{10}H_{16}$  was simply placed into the copper crucible which led to several unsuccessful attempts of reproducing deposition rates. The deposition rates were irreproducible and not in line with expectation of an exponential increase with temperature.

### 4.3.2 Pellet Preparation

Consequently, due to the inconsistency in deposition rates found for  $C_{10}H_{16}$ ,  $C_{10}H_{16}$  was then prepared for deposition as a pellet by pressing down a 1.3 mm piston filled with the desired amount of  $C_{10}H_{16}$  (1 g) using a hydraulic press (Frimo Hypress 30 tonne press equipped with a Powerteam P59B 700 bar hydraulic pump) up to a pressure of five tonne. This force was applied to the pellet for approximately one minute dwelling time. The set-up for the pellet is shown in Figure 4.6.

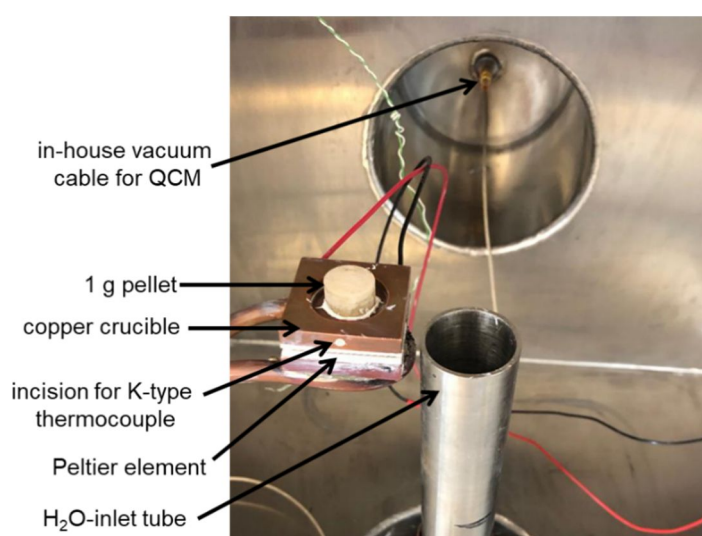


Figure 4.6. The set-up of the  $C_{10}H_{16}$  evaporation source within the chamber.

#### 4. Matrix-Isolated Adamantane in Amorphous Ice

The same temperature ramp as described in section 4.3.1 was carried out for calibrating the deposition rates of  $C_{10}H_{16}$  as a pellet. Swap axes program was used to interpolate the QCM Sauerbrey mass data and temperature data as shown in Figure 4.7(a); where the left-hand side axis represents the recorded temperature data, and the right-hand side axis displays the corresponding Sauerbrey mass data. Both data sets are associated with the same time and once the temperature was stable and plateaued, the deposition rate of this plateau region was recorded and calculated for its corresponding temperature by performing a linear fit and determining the gradients from the QCM data. Figure 4.7(b) depicts the calibration of the deposition rates of  $C_{10}H_{16}$ , showing the effect of  $C_{10}H_{16}$  deposition rate as a function of regulating the temperature of the evaporation source with respect to varying the starting amount of  $C_{10}H_{16}$ . Several calibration experiments were conducted with sample masses of 0.5 g and 1 g of  $C_{10}H_{16}$ , and all experiments were seen to have very similar deposition rates indicating good reproducibility of data.

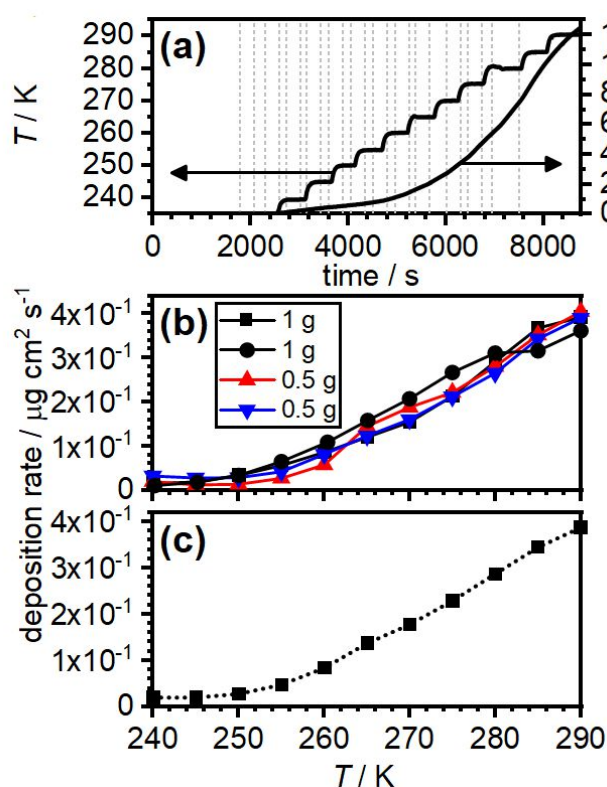


Figure 4.7. Effect of the deposition rate of  $C_{10}H_{16}$  from the evaporation source as a function of temperature, where (a) one set of raw data obtained from the deposition of  $C_{10}H_{16}$  while increasing the temperature from 240 K to 290 K in 5 K steps. Grey dashed lines show the start and finish of recorded deposition rate for each temperature, (b) the deposition rate of each temperature from different calibration experiments with differing starting pellet masses and (c) average mass deposition rate of  $C_{10}H_{16}$  of four calibrations from (b) against the corresponding Peltier temperature. The QCM sensor is located at the centre of the deposition plate for these experiments.

## 4. Matrix-Isolated Adamantane in Amorphous Ice

Each sample used for experiments from here on were prepared as a pellet using the hydraulic press, unless stated otherwise. The main bulk of this chapter describes samples prepared using this method and apparatus as deposition rates of  $C_{10}H_{16}$  were reproducible.

### 4.3.2.1 $C_{10}H_{16}$ to $H_2O$ Molar Ratios

The calibration data as displayed in Figure 4.7(b) and Figure 4.7(c) was necessary to record in order to adjust various  $C_{10}H_{16}$  to  $H_2O$  ratios. The settings used for  $H_2O$  are described in this section. This section aims to describe how the ratio of  $C_{10}H_{16}$  molecules to  $H_2O$  molecules is strongly dependent upon the temperature of the evaporation source as determined by recording the QCM response and defined by changing deposition rates in units of  $\mu g\ cm^{-2}\ s^{-1}$ . As expected, increasing the temperature of the Peltier element leads to a higher ratio of  $C_{10}H_{16}$  molecules to  $H_2O$  molecules and, therefore, it is assumed that this can enable the formation of clathrate hydrates. However, it must be stressed that a higher ratio may also be too much to form a clathrate hydrate. The unit cell of a type sH clathrate hydrate comprises 34  $H_2O$  molecules. One  $C_{10}H_{16}$  molecule is confined by 34  $H_2O$  molecules in the large barrel cage with the help of small gaseous species that occupy and support the remaining cavities.<sup>45</sup> For the codeposition of  $H_2O$  and  $C_{10}H_{16}$ , the materials were weighed by mass, before and after deposition to calculate the ratio and compare it with the QCM and differential scanning calorimetry (DSC) data.

In the first instance, the deposition of  $H_2O$  in the second vacuum chamber was recorded for a short amount of time (approximately 15 minutes) and monitored using a QCM. The  $H_2O$  inlet pressure of  $1 \times 10^{-1}$  mbar generated a deposition rate of  $0.65466\ \mu g\ cm^{-2}\ s^{-1}$  which was determined by performing a linear fit to the recorded data as shown in Figure 4.8 and the data displayed gives a gradient that is equivalent to the mass deposition rate. This value of deposition rate was determined for 15-minute deposition time and can be scaled to the desired amount of time of deposition such as three hours of deposition. The amount of mass deposited in this short time was 0.254 g. It was also possible to calculate a molar deposition rate of  $H_2O$  for 15 minutes ( $0.03630\ \mu mol\ cm^{-2}\ s^{-1}$ ) by dividing the deposition rate obtained from this data by the molar mass of  $H_2O$ ,  $18.02\ g\ mol^{-1}$  (Equation 4.1).

#### 4. Matrix-Isolated Adamantane in Amorphous Ice

$$\frac{\text{deposition rate of H}_2\text{O at } 1 \times 10^{-1} \text{ mbar } (\mu\text{g cm}^{-2}\text{s}^{-1})}{\text{molar mass of H}_2\text{O } (\text{g mol}^{-1})} = \text{molar deposition rate } (\mu\text{mol cm}^{-2} \text{ s}^{-1}) \quad \text{Equation 4.1}$$

Mixtures of amorphous ice and C<sub>10</sub>H<sub>16</sub> were deposited for three hours for sample extraction and the deposition rate of H<sub>2</sub>O (0.65466  $\mu\text{g cm}^{-2} \text{ s}^{-1}$ ) was applied for three hours for the desired ratio to obtain a three-hour deposition amount of 7.85592  $\mu\text{g cm}^{-2}$  and thus, the molar deposition amount of H<sub>2</sub>O was calculated to be 0.43590  $\mu\text{mol cm}^{-2}$ .

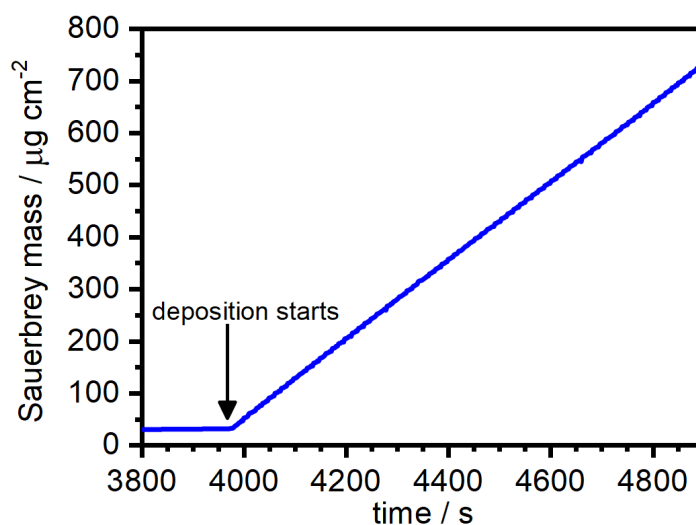


Figure 4.8. QCM response displaying the Sauerbrey mass recorded during the time of deposition of pure H<sub>2</sub>O at a H<sub>2</sub>O inlet pressure of  $1 \times 10^{-1}$  mbar.

The mass deposition rate of C<sub>10</sub>H<sub>16</sub> at different temperatures of the evaporation source was divided by the molar mass of C<sub>10</sub>H<sub>16</sub> (136.24  $\text{g mol}^{-1}$ ) to acquire molar deposition rates as shown in Table 4.1.

Table 4.1. Average deposition rates, molar deposition rates and C<sub>10</sub>H<sub>16</sub> to H<sub>2</sub>O molar ratios for specific temperatures of the evaporation source with a molar H<sub>2</sub>O deposition rate of 0.0363  $\mu\text{mol cm}^{-2} \text{ s}^{-1}$ . Note these deposition rates are recorded to the best of abilities and the approximate evaporation source temperature corresponding to the nearest ratio is used.

$T / \text{K}$	Average C <sub>10</sub> H <sub>16</sub> deposition rate / $\mu\text{g cm}^{-2} \text{ s}^{-1}$	Average C <sub>10</sub> H <sub>16</sub> molar deposition rate / $\mu\text{mol cm}^{-2} \text{ s}^{-1}$	Approximate H <sub>2</sub> O/C <sub>10</sub> H <sub>16</sub> molar ratio
255	$4.22 \times 10^{-2}$	$3.09 \times 10^{-4}$	100:1
275	$1.68 \times 10^{-1}$	$1.23 \times 10^{-3}$	34:1

#### 4. Matrix-Isolated Adamantane in Amorphous Ice

To determine the molar ratios of  $\text{H}_2\text{O}/\text{C}_{10}\text{H}_{16}$  for the specific temperatures, the molar deposition rate of  $\text{H}_2\text{O}$  was divided by the molar deposition rate of  $\text{C}_{10}\text{H}_{16}$ . The full set of ratios are depicted in Figure 4.9.

To realise ratios in line with the expected sH clathrate hydrate composition and possibly a new clathrate hydrate, molar  $\text{H}_2\text{O}/\text{C}_{10}\text{H}_{16}$  ratios were realised such that the chosen molar ratios were 34:1 ( $T = \sim 275\text{ K}$ ), and 100:1 ( $T = \sim 255\text{ K}$ ).

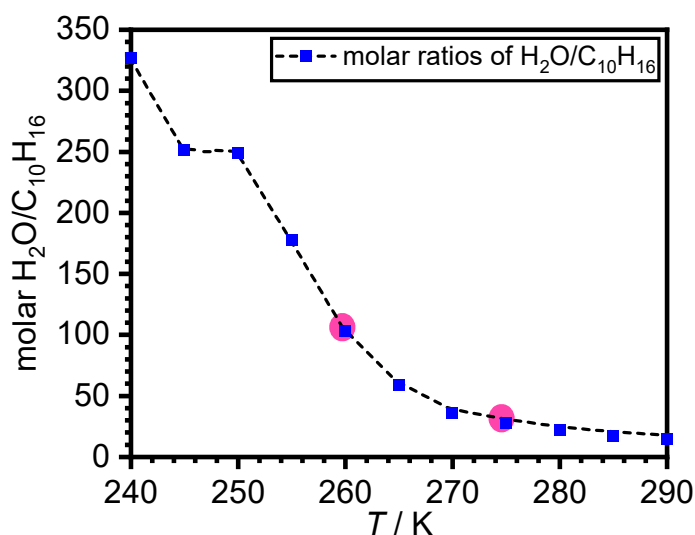


Figure 4.9. The molar ratios for  $\text{H}_2\text{O}/\text{C}_{10}\text{H}_{16}$  as a function of the evaporation source temperature with a  $\text{H}_2\text{O}$  deposition rate of  $0.0363\ \mu\text{mol cm}^{-2}\text{ s}^{-1}$ . The pink circles indicated in the figure define the molar ratios as chosen for the bulk of this chapter.

In addition, to achieve higher mixing ratios, such as 1:6 or 1:20 for  $\text{C}_{10}\text{H}_{16}$  in  $\text{H}_2\text{O}$  matrices, the evaporation source was heated to temperatures above room temperature (up to  $\sim 340\text{ K}$ ). For these calibration experiments, the evaporation source was kept at a base temperature of  $240\text{ K}$  during the pump down of the chamber and once the chamber was at high-vacuum ( $2 \times 10^{-6}\text{ mbar}$ ) and base temperature ( $78\text{ K}$ ) to start depositing  $\text{C}_{10}\text{H}_{16}$ , the power supply was switched off and the wires of the power supply were swapped over to reverse the polarity and thus, apply the voltage required for heating. The deposition rates as recorded by the QCM for the heating of the evaporation source while depositing  $\text{C}_{10}\text{H}_{16}$  are displayed below in Figure 4.10 and summarised in Table 4.2.

#### 4. Matrix-Isolated Adamantane in Amorphous Ice

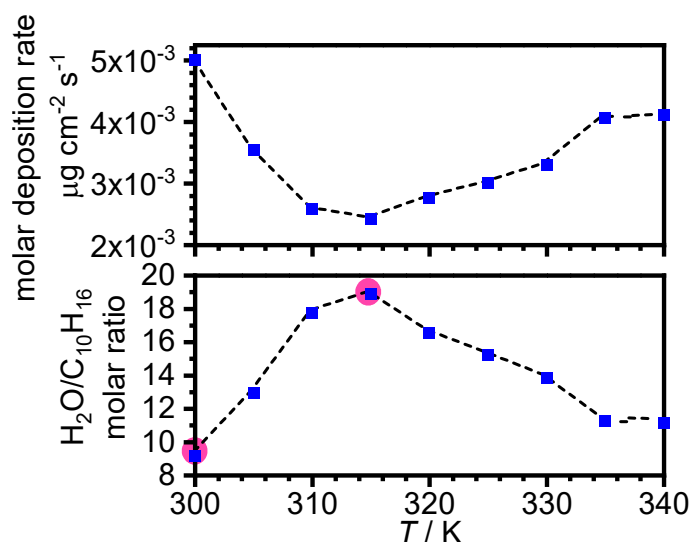


Figure 4.10. (a) Effect of the molar deposition rate of  $C_{10}H_{16}$  from the evaporation source as a function of temperature and (b) the  $H_2O/C_{10}H_{16}$  molar ratios, with pink circles indicating that the highest ratio can be achieved is, 9:1 and the next highest ratio, 19:1. The QCM sensor is located at the centre of the plate for these experiments.

The molar deposition rates do not display uniform measurements and the origin for this unusual behaviour is unclear. However, the mixing ratio required for very concentrated samples were achieved. Therefore, only these deposition rates were used for preparing the codeposited samples.

Table 4.2. Deposition rates, molar deposition rates and  $H_2O/C_{10}H_{16}$  molar ratios for specific temperatures of the evaporation source with a molar  $H_2O$  deposition rate of  $0.0457\ \mu mol\ cm^{-2}\ s^{-1}$  (Note that this molar deposition rate of  $H_2O$  is slightly higher than previously stated. A second  $H_2O$  calibration was carried out and the deposition rate was calculated to the best of ability). These deposition rates are recorded to the best of abilities and the approximate evaporation source temperature corresponding to the nearest ratio is used.

$T / K$	$C_{10}H_{16}$ deposition rate / $\mu g\ cm^{-2}\ s^{-1}$	$C_{10}H_{16}$ molar deposition rate / $\mu mol\ cm^{-2}\ s^{-1}$	Approximate $H_2O/C_{10}H_{16}$ molar ratio
300	$6.82 \times 10^{-1}$	$5.01 \times 10^{-3}$	9:1
315	$3.30 \times 10^{-1}$	$2.42 \times 10^{-3}$	19:1



## 4. Matrix-Isolated Adamantane in Amorphous Ice

### 4.3.2.2 Molecular Volume Percentages of C<sub>10</sub>H<sub>16</sub> in C<sub>10</sub>H<sub>16</sub>/H<sub>2</sub>O Mixtures

Initially, the molar volume of LDA was calculated from its density of 0.93 g cm<sup>-3</sup>.<sup>56</sup> This density can be divided by the molar mass of H<sub>2</sub>O (18.02 g mol<sup>-1</sup>) to give the molar volume of H<sub>2</sub>O as 5.16 x 10<sup>-2</sup> mol cm<sup>-3</sup>. Further to this calculation, the molecular volume was determined to be 32.18 Å<sup>3</sup> or 3.21 x 10<sup>-23</sup> cm<sup>3</sup>.

The next step was to calculate the molecular volume of C<sub>10</sub>H<sub>16</sub> at low temperatures. Upon cooling, C<sub>10</sub>H<sub>16</sub> transforms to a tetragonal structure with a density of 1.18 g cm<sup>-3</sup> at 208 K. The latter density reflects conditions that are used in this study since there is a close to 10% difference between these two values (density of LDA and density of C<sub>10</sub>H<sub>16</sub>). Using 1.18 g cm<sup>-3</sup> for the density and the molar of C<sub>10</sub>H<sub>16</sub> as 136.24 g mol<sup>-1</sup>, the molar volume was calculated as 8.66 x 10<sup>-3</sup> mol cm<sup>-3</sup>. The molecular volume of C<sub>10</sub>H<sub>16</sub> was further calculated to be 191.72 Å<sup>3</sup> or 1.9172 x 10<sup>-22</sup> cm<sup>3</sup>.

In Table 4.3, the molecular volumes of LDA and C<sub>10</sub>H<sub>16</sub> were employed to calculate the molecular volume percentage of C<sub>10</sub>H<sub>16</sub> in the various mixtures prepared. These calculations are assumed on the basis of zero excess volumes.

*Table 4.3. The C<sub>10</sub>H<sub>16</sub>/H<sub>2</sub>O molar ratios with their respective C<sub>10</sub>H<sub>16</sub> molecular-volume percentages.*

<i>T</i> / K	C <sub>10</sub> H <sub>16</sub> /H <sub>2</sub> O molar ratios	C <sub>10</sub> H <sub>16</sub> volume percent / %
255	1:100	5.6
275	1:34	14.9

### 4.3.3 Varying the QCM Locations on the Deposition Plate with Different Flow Rates of H<sub>2</sub>O

To measure how the H<sub>2</sub>O-vapour flow was distributed across the deposition plate and thus, determine local deposition rates, the QCM sensor head was placed at the centre, edge, and midpoint of the radius of the deposition plate. Inlet pressures of 1 × 10<sup>-1</sup> mbar to 8 × 10<sup>-2</sup> and 7.5 × 10<sup>-2</sup> mbar of H<sub>2</sub>O were used and to ensure the reliability of data, each pressure recording was calibrated three times. The Sauerbrey mass was recorded for each H<sub>2</sub>O pressure and position, and the deposition rates were calculated. Table 4.4 shows the average deposition rates for H<sub>2</sub>O at the different pressures and positions and Figure 4.11 displays the calibration data in terms of average deposition rates in µg cm<sup>-2</sup> s<sup>-1</sup> for H<sub>2</sub>O at the various pressures and positions on the plate.

#### 4. Matrix-Isolated Adamantane in Amorphous Ice

Table 4.4. Average mass deposition rates and molar deposition rates for H<sub>2</sub>O for each position on the deposition plate, including the centre, midpoint of the radius of the deposition plate and the edge of deposition plate.

$P_{\text{H}_2\text{O}}$ / mbar	Average mass deposition rate / $\mu\text{g cm}^{-2} \text{s}^{-1}$			Average molar deposition rate / $\mu\text{g mol cm}^{-2} \text{s}^{-1}$		
	Centre	Midpoint	Edge	Centre	Midpoint	Edge
$1 \times 10^{-1}$	$8.25 \times 10^{-1}$	$6.40 \times 10^{-1}$	$3.98 \times 10^{-1}$	$4.58 \times 10^{-2}$	$2.21 \times 10^{-2}$	$3.55 \times 10^{-2}$
$8 \times 10^{-2}$	$6.07 \times 10^{-1}$	$4.53 \times 10^{-1}$	$2.81 \times 10^{-1}$	$3.37 \times 10^{-2}$	$1.56 \times 10^{-2}$	$2.51 \times 10^{-2}$
$7.5 \times 10^{-2}$	$4.93 \times 10^{-1}$	$4.08 \times 10^{-1}$	$2.53 \times 10^{-1}$	$2.74 \times 10^{-2}$	$1.41 \times 10^{-2}$	$2.26 \times 10^{-2}$

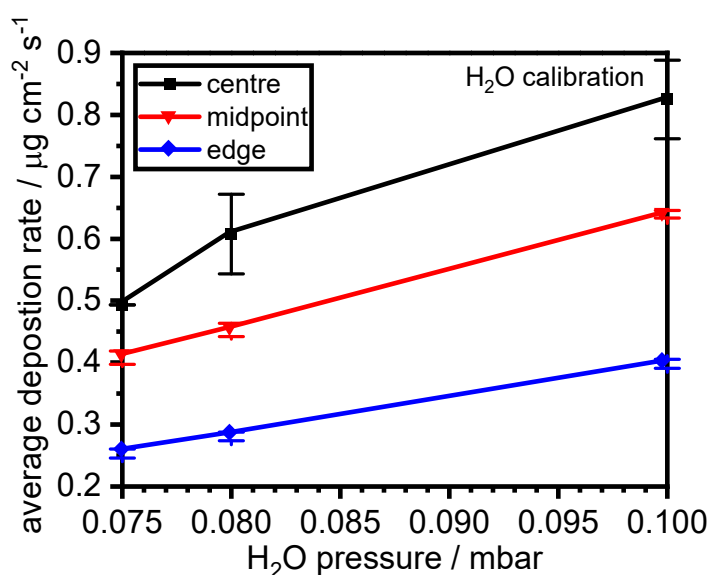


Figure 4.11. Average mass deposition rate of H<sub>2</sub>O against the corresponding H<sub>2</sub>O pressure. The coloured lines as displayed in the figure show the measured deposition rates for the QCM sensor head positioned at the centre, midpoint of the radius of the deposition plate, and edge of the deposition plate. The errors have been plotted.

The average molar deposition rates were divided by the deposition rates of C<sub>10</sub>H<sub>16</sub> at 255 K and 290 K to determine the C<sub>10</sub>H<sub>16</sub>/H<sub>2</sub>O ratios of mixtures at different H<sub>2</sub>O inlet pressures to ensure the reliability of uniform distribution across the deposition plate.

#### 4.3.4 Varying the QCM Locations on the Deposition Plate with the Calibration of the Deposition Rates of $C_{10}H_{16}$ Prepared as a Pellet

To further optimise and determine the spatial distribution across the plate with  $C_{10}H_{16}$ , an extensive range of calibrations were carried out. The QCM was placed once again, at the centre, midpoint of the radius, and edge of the deposition plate. Figure 4.12 depicts the deposition rates for each position of the QCM with each specific temperature.

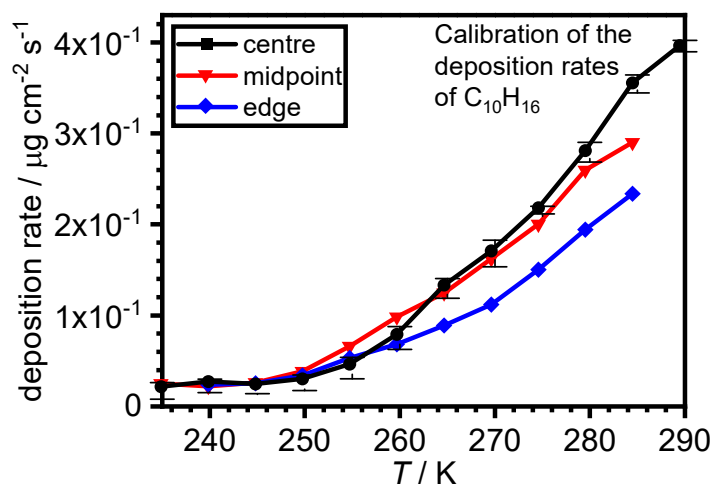


Figure 4.12. Calibration of the mass deposition rates of  $C_{10}H_{16}$  vs. the corresponding temperature of the evaporation source. The errors have been plotted for the deposition rates where the QCM was placed at the centre of the deposition plate.

The deposition rate was found to not vary significantly across the deposition plate when comparing all positions of the QCM, indicating that the ratio and spatial distribution across the plate is fairly uniform with respect of  $C_{10}H_{16}$  deposition. The overall average molar ratio of  $C_{10}H_{16}/H_2O$  will be uniform; however, the specific regional ratio will vary since  $H_2O$  shows quite a location dependence.

#### 4.3.5 Calibrating the Deposition Rates of $C_{10}H_{16}$ in a Round-Bottom Flask

In addition, approximately eight grams of solid  $C_{10}H_{16}$  was placed into a round-bottom flask and attached to the bottom of the chamber on a second graduated needle valve. This method of introducing  $C_{10}H_{16}$  into the chamber would mean both species ( $H_2O$  and  $C_{10}H_{16}$ ) would be introduced into the chamber from the same inlet tube and deposit onto the deposition plate with a constant ratio. The calibration data for solid  $C_{10}H_{16}$  in the round-bottom flask is displayed below in Figure 4.13. The deposition rates for a range of needle valve positions were measured at different QCM positions of the deposition plate. Three repeats of this data were carried out.

#### 4. Matrix-Isolated Adamantane in Amorphous Ice

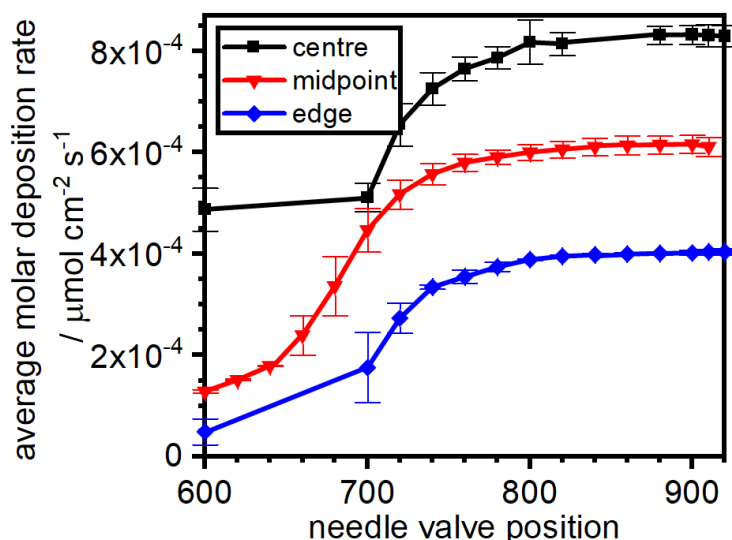


Figure 4.13. Average mass molar deposition rate of  $C_{10}H_{16}$  in the round-bottom flask against the corresponding needle valve position. The errors have been plotted for each data set.

In order to determine which needle valve needs to be utilised for codeposition with the materials in a round-bottom flask, the molar deposition rate of  $H_2O$  at  $1 \times 10^{-1}$  mbar was divided by each molar deposition rate of  $C_{10}H_{16}$  at every needle valve position. The maximum limit the needle valve can be opened to is position 930, however, for a molar deposition rate of  $H_2O$  at an inlet pressure of  $1 \times 10^{-1}$  mbar, the desired ratio of the matrix was not achievable. Thus, the inlet pressure of  $H_2O$  as shown previously in Figure 4.11 was reduced from  $1 \times 10^{-1}$  mbar to  $8 \times 10^{-2}$  and  $7.5 \times 10^{-2}$  mbar to obtain lower deposition rates and therefore, achieving a higher ratio of  $C_{10}H_{16}$  to  $H_2O$  molecules. The higher ratio targeted was a 1:6 ratio of  $C_{10}H_{16}$  to  $H_2O$  molecules. Table 4.5 summarises the molar ratios of  $C_{10}H_{16}/H_2O$  as used for the round-bottom flask experiments.

Table 4.5. Average deposition rates, molar deposition rates and  $H_2O$  to  $C_{10}H_{16}$  molar ratios for specific temperatures of the evaporation source with a molar  $H_2O$  deposition rate of  $0.0457 \mu\text{mol cm}^{-2} \text{s}^{-1}$ . Note these deposition rates are recorded to the best of abilities and the approximate evaporation source temperature corresponding to the nearest ratio is used.

Needle valve position	Average $C_{10}H_{16}$ deposition rate / $\mu\text{g cm}^{-2} \text{s}^{-1}$	Average $C_{10}H_{16}$ molar deposition rate / $\mu\text{mol cm}^{-2} \text{s}^{-1}$	Approximate $H_2O/C_{10}H_{16}$ molar ratio
600	0.065500	$4.81 \times 10^{-4}$	100:1
760	0.102820	$7.55 \times 10^{-4}$	60:1
820	0.109417	$8.03 \times 10^{-4}$	34:1

## 4. Matrix-Isolated Adamantane in Amorphous Ice

To determine the molar ratios of  $\text{H}_2\text{O}/\text{C}_{10}\text{H}_{16}$  for the specific needle valve positions, the molar deposition rate of  $\text{H}_2\text{O}$  was divided by the molar deposition rate of  $\text{C}_{10}\text{H}_{16}$ .

To realise the ratios in line with the expected sH clathrate hydrate and possibly a new clathrate hydrate, molar  $\text{H}_2\text{O}/\text{C}_{10}\text{H}_{16}$  ratios were realised, such that the chosen molar ratios were 34:1, 60:1 and 100:1. The ratio of 60:1 was chosen to bridge the gap between the wide-ratio gap of the previously achieved ratios.

### 4.3.6 Cryogenic Codeposition of $\text{C}_{10}\text{H}_{16}$ and $\text{H}_2\text{O}$ vapour

The experimental set-up for the  $\text{C}_{10}\text{H}_{16}$  mixtures with  $\text{H}_2\text{O}$  preparation is depicted in the instrumental chapter, Chapter 2 (Figure 2.5). Details for the setup are also provided in the literature.<sup>4, 57, 58</sup> For this study, the second vacuum chamber was equipped with an evaporation source as mentioned previously. For each experiment, the  $\text{H}_2\text{O}$ -inlet tube was capped with an iron mesh as it is known to influence the morphology of the deposit<sup>53</sup> by baffling the flow of  $\text{H}_2\text{O}$ , causing the collapse of pores and ensuring a more uniform distribution of  $\text{H}_2\text{O}$  molecules on the copper substrate.<sup>4</sup>

The general procedure to prepare mixtures of amorphous ice and guest species has been described in Chapter 2 and 3. The differing factor, in this case, is evidently the guest species,  $\text{C}_{10}\text{H}_{16}$ . Prior to achieving a base pressure of the vacuum chamber, a pellet of  $\text{C}_{10}\text{H}_{16}$  of precisely 1 g is prepared as described earlier. For the codeposition of  $\text{C}_{10}\text{H}_{16}$ , the copper crucible is precooled to a base temperature of  $\sim 240$  K before preparing the vacuum system to reach its base pressure. Once a base pressure of the chamber is reached and a cold environment is obtained, in order to deposit  $\text{C}_{10}\text{H}_{16}$ , the Peltier element is set to a certain voltage using the power supply to reach the temperature required for the desired ratio of  $\text{C}_{10}\text{H}_{16}$  molecules to  $\text{H}_2\text{O}$  molecules (Table 4.1). The voltage and current can easily be adjusted manually on the power supply to obtain the temperature required for deposition. Once the desired temperature is reached and the needle valve of  $\text{H}_2\text{O}$  is opened to an inlet pressure of  $1 \times 10^{-1}$  mbar, deposition can begin. After a three-hour deposition is complete, the temperature of the Peltier element is reduced back to 240 K to terminate the deposition of  $\text{C}_{10}\text{H}_{16}$ , and the needle valve of  $\text{H}_2\text{O}$  is closed at the same time, so no species enter or deposit inside the chamber.

Subsequently, after deposition, the sample is annealed at 125 K and  $\text{LN}_2$  is pumped and drawn out from the cryostat with a single-stage twin cylinder pump (Gast 87 series compressor oil-free rocking piston single stage twin cylinder pump, Order Number:

#### 4. Matrix-Isolated Adamantane in Amorphous Ice

87R642-103R-N470X, Thorite Direct, UK). When all LN<sub>2</sub> is removed from the cryostat, the cold trap and the deposition plate is left to heat up to 125 K under vacuum to essentially reduced the surface area of the sample. Thus, to close the pores of ASW, the sample is annealed at 125 K which avoids the formation of nitrogen (N<sub>2</sub>) clathrate hydrates.<sup>53</sup> The cold trap and deposition plate are rapidly cooled back down to base temperature (82 K) before removal and collection of the sample (Chapter 2).

With this set-up, it was possible to produce amorphous ice mixtures on the gram scale with C<sub>10</sub>H<sub>16</sub> finely dispersed within the amorphous matrix. Successive preparation of ASW samples was characterised by X-ray diffraction (XRD), DSC and Raman spectroscopy.

### 4.4 Details of Sample Characterisation Techniques

#### 4.4.1 *Ex situ* X-ray Diffraction (XRD)

Once the samples were extracted from the vacuum chamber, the samples were transferred to a custom-made sample holder equipped with Kapton windows under cryogenic conditions and mounted to the XRD instrument. Details for the instrument and procedure are provided in Chapter 2. Diffraction data for the  $\text{C}_{10}\text{H}_{16}$  and  $\text{H}_2\text{O}$  samples were collected from  $2\theta = 2\text{--}60^\circ$  in  $5^\circ$  steps with 100 seconds per step. A script for the control of temperature was applied to the sample collection. Samples were maintained at 95 K initially, increasing in 5 K steps until 190 K, and then increased further in 10 K steps up to 270 K. Some samples included an isothermal hold at 130 K to see if it was possible to probe the orientational glass transition and will be discussed later. The Kapton peak in each diffraction pattern occurs at approximately  $2\theta = 5^\circ$  and is absent from the figures presented in this work. This Bragg peak is used to normalise against the features observed since this is the only constant available throughout the experiment unless stated otherwise.

#### 4.4.2 Differential Scanning Calorimetry (DSC)

The recovered samples were carefully transferred into stainless-steel DSC pans under cryogenic conditions. These pans were rapidly placed inside the DSC and heated from 93 K to 263 K at  $10\text{ K min}^{-1}$ , thus forming  $\text{C}_{10}\text{H}_{16}$  and bulk ice *Ih*. A background scan for subtraction was recorded and finally, the ice mixture melted at  $0^\circ\text{C}$ . In order to see the amount of  $\text{C}_{10}\text{H}_{16}$  in the DSC thermogram, an extra step in the program was added to follow after the first melt. The DSC was taken to 183 K below the  $\text{C}_{10}\text{H}_{16}$  phase transition upon cooling to 183 K and further heated through the transition.  $\text{C}_{10}\text{H}_{16}$  is seen to go through a phase transition at 208 K.<sup>32</sup>

##### 4.4.2.1 Calorimetric Calibration Approach for Determining the Mole Fraction of $\text{C}_{10}\text{H}_{16}$

To determine the amount of  $\text{C}_{10}\text{H}_{16}$  in the mixtures, several DSC scans for bulk  $\text{C}_{10}\text{H}_{16}$  were run.  $\text{C}_{10}\text{H}_{16}$  was weighed in on a microbalance (Sartorius micro, Balance Technology) with weights of 3.152, 5.561 and 8.150 mg. The DSC sample pans were placed inside the DSC and held for four minutes at 293 K, cooled to 93 K at  $10\text{ K min}^{-1}$ , then held for a further four minutes at 93 K and finally, heated to 303 K at  $10\text{ K min}^{-1}$ . DSC thermograms for the heating and cooling of  $\text{C}_{10}\text{H}_{16}$  are provided in Figure 4.14(a) and the subsequent areas for these thermograms are provided in Figure 4.14(b).

#### 4. Matrix-Isolated Adamantane in Amorphous Ice

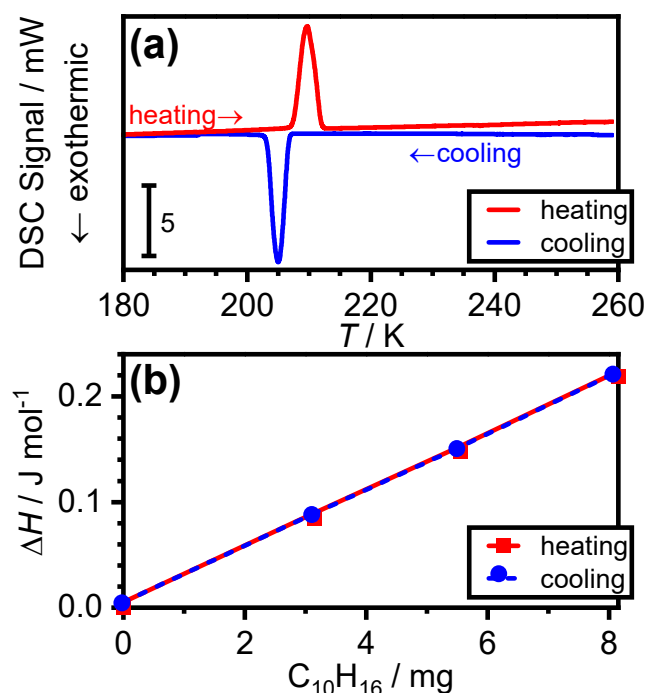


Figure 4.14. Calorimetry of the known quantities of pure  $\text{C}_{10}\text{H}_{16}$  used to quantify and determine the mole fraction of  $\text{H}_2\text{O}$  to  $\text{C}_{10}\text{H}_{16}$  in the vapour deposited ice matrix where (a) DSC thermograms of the heating and cooling steps and (b) the associated areas of the known quantities of pure  $\text{C}_{10}\text{H}_{16}$ . All thermograms were collected with a heating rate of  $10 \text{ K min}^{-1}$ .

##### 4.4.3 Raman Spectroscopy

Raman spectra of ASW,  $\text{C}_{10}\text{H}_{16}$  and  $\text{C}_{10}\text{H}_{16}$ /ASW were recorded on the Renishaw Ramascope spectrometer equipped with a 632.8 nm (He-Ne) laser using a modified Oxford MicrostatN cryostat. Once the sample was transferred, the lid of the cryostat was rapidly placed on top of the cryostat and sealed so the system could be evacuated. Spectra were recorded initially in a static position to visualise peaks and further recorded in the extended ranges of  $3550\text{--}2800 \text{ cm}^{-1}$  and  $1700\text{--}50 \text{ cm}^{-1}$ . To reduce the signal-to-noise (S/N) ratio by half, four accumulations were collected and the collection time for each scan was 100 seconds. Mixtures of samples were thermally annealed from 78 K at  $5 \text{ K min}^{-1}$  to a given temperature in gradual steps to see the transition from amorphous to stacking disordered ice (ice *Isd*) and finally, ice *Ih*. Once the desired temperature was reached, the sample temperature was reduced back to 78 K and the spectrum was recorded.



### 4.5 Results and Discussion

#### 4.5.1 Formation of Nitrogen (N<sub>2</sub>) Clathrate Hydrates

Clathrate hydrates in space are expected to be formed from vapour deposited ASW at low pressures and temperatures.<sup>53, 59, 60</sup> Clathrate hydrates that form from carefully prepared ASW are known to decompose completely upon heating between a temperature range of 240–250 K and at a rate of 10 K min<sup>-1</sup>.<sup>60</sup> These particular clathrate hydrates formed between 170 K and 210 K at high pressure: 10, 100, 200 and 1700 mbar.<sup>60</sup> The formation of clathrate hydrates occurs since ASW encloses around substantial amounts of the guest gas species during heating which cannot be further pumped off *in vacuo*.<sup>60</sup> ASW's peculiar sintering and gas enclosure properties have been proposed to play an essential part in the process of clathrate hydrate formation and stabilisation.<sup>53, 59, 60</sup>

The DSC patterns for a 1:34 and a 1:100 C<sub>10</sub>H<sub>16</sub>/H<sub>2</sub>O molar ratio are depicted in Figure 4.15 with a comparison of the pure ASW DSC thermogram. The codeposited samples are markedly distinct in their appearance of exotherms and the number of exotherms with associated areas are much smaller when compared to that of pure ASW. The disparity between the codeposited samples with respect to as-made ASW in the DSC thermograms results from the successful mixing of the two species. It must be stressed that the DSC is not the sum of the traces of the pure materials.

The thermogram for pure ASW displays a sharp exotherm at 160 K with an associated area of 1260±35 J mol<sup>-1</sup>, which corresponds to the irreversible phase transition for the crystallisation of ASW to ice *Isd*. This transition occurs at approximately 150–160 K for the codeposited samples as indicated by the shaded area in Figure 4.15. The associated area with the transition for the 1:100 and 1:34 molar ratio is 138±12 J mol<sup>-1</sup> and 133±5 J mol<sup>-1</sup>, respectively. Nevertheless, the enthalpy change ( $\Delta H$ ) associated with the ASW to ice *Isd* transition is almost ten times the value that is seen for the codeposited samples at 160 K. Beyond the crystallisation exotherm and upon heating, it must be noted that a second pronounced exothermic feature at 180 K in the codeposited DSC thermograms is seen. For the concentrated sample, 1:34 molar ratio, the associated area with respect to the feature seen at 180 K is 285±5 J mol<sup>-1</sup>. The more dilute sample of 1:100 molar ratio, indicates the same feature at 180 K with an associated area of 548±20 J mol<sup>-1</sup>, almost double the area of the concentrated sample. A summary of the peak areas and features are provided in the upcoming Table 4.6. The question now remains as to

#### 4. Matrix-Isolated Adamantane in Amorphous Ice

what the exact nature of these peculiar features results from. Comparing both molar ratios, 1:34 and 1:100  $C_{10}H_{16}$  to  $H_2O$ , the features after 180 K are slightly broader for the latter. This feature may be attributed to the formation of a clathrate hydrate as can be seen in the XRD patterns at temperatures from 200 K and evidently displayed in Figure 4.15. Hence, this exotherm cannot simply result from the transformation of ASW to ice *Isd*, however, is due to the mixing of the two species.

It is interesting to note that after the phase transition of ASW to ice *Isd* and the feature at 180 K in the DSC thermograms, broad peaks at approximately 210 K can also be seen and assigned to the start of decomposition of the clathrate hydrates. The 1:34 molar ratio shows that this feature after 200 K is rather stretched out across the rest of the thermogram, which may indicate a slow energy process is taking place.

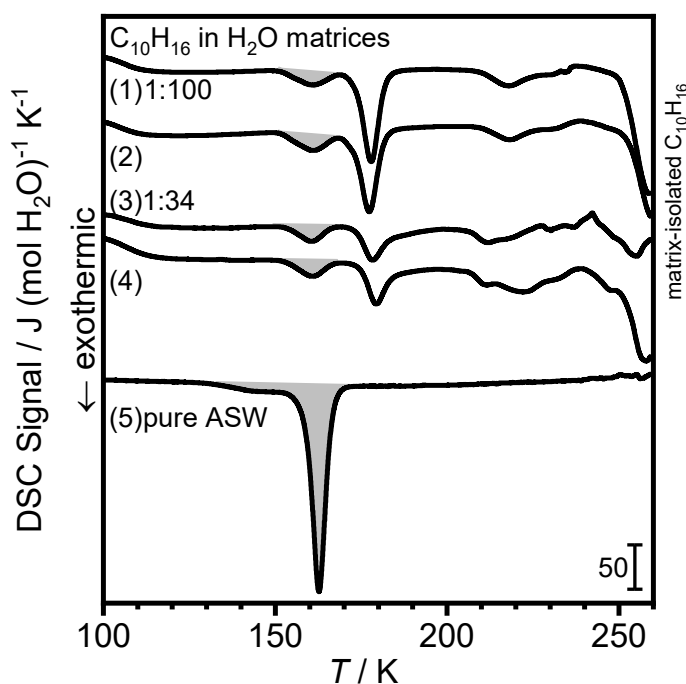


Figure 4.15. DSC thermograms of unannealed  $C_{10}H_{16}/H_2O$  and pure ASW with indicated  $C_{10}H_{16}/H_2O$  molar ratios heated at  $10\text{ K min}^{-1}$ . All scans were performed at ambient pressure. The shaded areas display the  $H_2O$  crystallisation process and the limits for integration. The DSC signals are normalised with respect to per mole of  $H_2O$ .

#### 4. Matrix-Isolated Adamantane in Amorphous Ice

Table 4.6. Spread of enthalpies relating to the pure ASW and codeposited samples from indicated molar ratios in Figure 4.15. The DSC thermograms were recorded at  $10 \text{ K min}^{-1}$  and at ambient pressure.

Sample	Scan in Figure 4.15	$\Delta H / \text{J mol}^{-1}$	
		160 K	180 K
1:100	(1)	126	569
	(2)	149	527
1:34	(3)	127	280
	(4)	138	290
Pure ASW	(5)	1260	-

Based on the findings presented here, it may be possible to assign the DSC exotherms after the transition to ice *Isd* to clathrate hydrate formation and decomposition. This finding is also reflected in the XRD patterns as shown in Figure 4.16, which indicate the appearance of Bragg peaks after the transition to ice *Isd* and at 180 K through to 220 K. These peaks grow in intensity and do not illustrate any sudden or drastic changes in their appearance from temperature steps but instead, display a slow evolution upon heating and are retained from 180 K through to 220 K. These peaks disappear suddenly at the temperature of 230 K and one can speculate that this is the decomposition of the clathrate hydrates since other clathrate hydrates behave similarly.<sup>53, 59</sup>

In detail, as seen in Figure 4.16(a) and (b), at 160 K, the Bragg peaks from  $2\theta = 23\text{--}26^\circ$  are due to ice *Isd* which are superimposed on the broad peaks of ASW. From 200 K, specifically at 220 K, there are several other additional peaks at  $2\theta = 14.47, 16.96, 17.75, 29.13, 30.43, 34.05$  and  $44.45^\circ$  which were observed in the XRD patterns and are due to neither ice *Isd* nor ice *Ih*. The powder pattern for the sII hydrate was calculated in the Vesta software and overlayed with the XRD patterns to identify peak similarities. Some of these peaks are difficult to view due to low intensities, however, these peaks are assigned to the  $\text{N}_2$  CS-II clathrate hydrate and such Bragg peaks are in good agreement with that in the literature.<sup>53, 59, 60</sup> This is not a  $\text{C}_{10}\text{H}_{16}$  clathrate hydrate since no Bragg reflections for the sH clathrate hydrate are observed and it must be stressed that these samples are not annealed in the vacuum chamber, they were removed immediately after depositing. When samples are annealed (section 4.5.3), the expected Bragg peaks for the  $\text{N}_2$  CS-II clathrate hydrate are not observed, although,  $\text{C}_{10}\text{H}_{16}$  could be making the CS-II clathrate hydrate. After 225 K, these additional peaks disappear as ice *Isd* transforms to ice *Ih* and are thus, indicative of clathrate hydrate decomposition. No Bragg peaks for the sH clathrate hydrate arising from  $\text{C}_{10}\text{H}_{16}$  as a guest species could be detected due to the

#### 4. Matrix-Isolated Adamantane in Amorphous Ice

N<sub>2</sub> clathrate hydrate dominating and superimposing any C<sub>10</sub>H<sub>16</sub> features. Peaks that could not be assigned to the characteristic ice *Isd* or ice *Ih* formed after the formation of ice *Isd* and had decomposed once 230 K was approached. These were assigned to the N<sub>2</sub> clathrate hydrate of cubic structure II (CS-II, as mentioned earlier) and are confirmed with the literature.<sup>53, 59, 60</sup> Unexpectedly, ice *Isd* was found to be the active material for making the clathrate hydrate. All XRD patterns for the codeposited samples when compared to pure ASW did not indicate any unassignable Bragg peaks, thus, suggesting that the presence of the guest species may influence the formation of a CS-II hydrate. Although, CS-II can be made solely with ASW and N<sub>2</sub>.

As mentioned in Chapter 3, when heating the sample in the vacuum, the pores of ASW collapse in the 120–140 K range. Thus, in this case, samples were unannealed and removed from the chamber straight after deposition and so the pores of ASW remain open and fill up with gases before the collapse and clathrate hydrates are formed. Such a clathrate hydrate, in this case, can be identified as the N<sub>2</sub> CS-II clathrate hydrate and further characterisation *via* XRD and General Structure Analysis System (GSAS)<sup>61</sup> analysis has been carried out to confirm the presence of this clathrate hydrate. These N<sub>2</sub> clathrate hydrates form when the ASW sample is exposed to LN<sub>2</sub> during the removal of the sample. The effects of not closing the pores can be seen in the XRD patterns herein. Figure 4.16 illustrates the formation and decomposition of the N<sub>2</sub> sII clathrate hydrate. In addition, a 1:37 molar ratio of unannealed C<sub>10</sub>H<sub>16</sub>/H<sub>2</sub>O was also prepared and the equivalent conclusion of the formation of N<sub>2</sub> clathrate hydrates was obtained. The corresponding DSC and XRD measurements are reported in the appendix along with the Rietveld refinement carried out with GSAS (Appendix 1) for the as-made sample.

#### 4. Matrix-Isolated Adamantane in Amorphous Ice

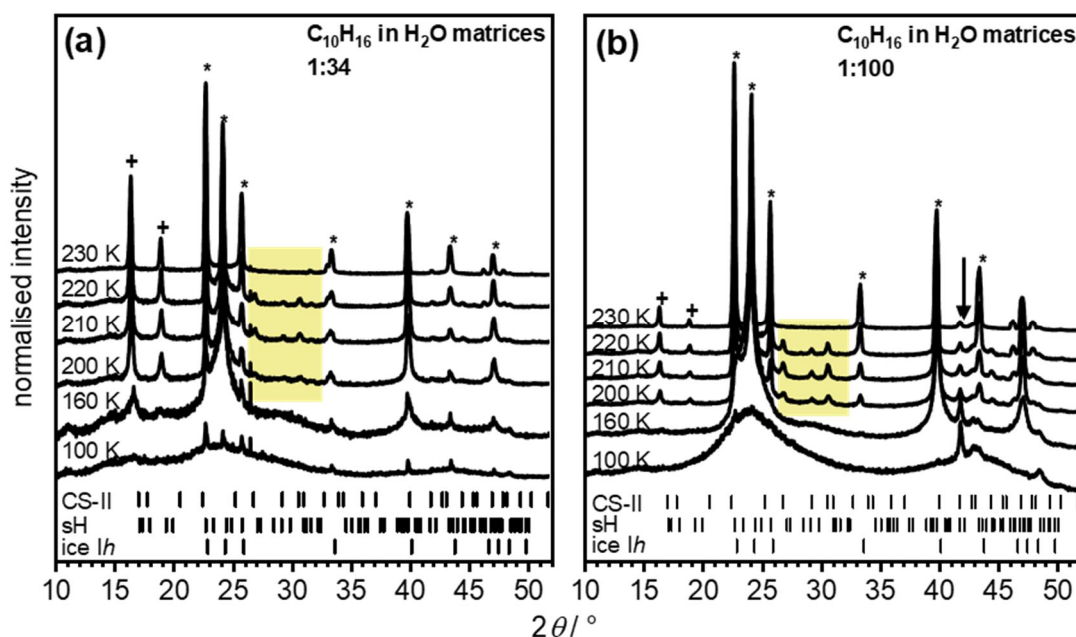


Figure 4.16. XRD diffractograms ( $\text{Cu K}\alpha$ ,  $\lambda = 1.54 \text{ \AA}$ ) of unannealed  $\text{C}_{10}\text{H}_{16}/\text{H}_2\text{O}$  mixtures at a (a) 1:34 molar ratio and (b) 1:100 molar ratio. The indicated tickmarks show the expected Bragg peaks for ice Ih, CS-II and sH clathrate hydrate. The yellow shaded area illustrates the clathrate hydrate, the asterisks are expected Bragg peaks for ice Ih and the plus signs are denoted by strong  $\text{C}_{10}\text{H}_{16}$  peaks. At 95 K, the broad peaks are characteristic of ASW as described throughout this thesis.

In XRD patterns, the peak positions are dependent upon the lattice constants of a materials unit cell and the zero shift is related to the instrument that collected the diffraction data.<sup>62</sup> The XRD instrument used here does not have a reliable zero shift to use and so, this value had to be determined. The lattice constants of ice Ih at 95 K are reported by Fortes<sup>63</sup> and are known as:  $a = 4.49703(3) \text{ \AA}$  and  $c = 7.32220(9) \text{ \AA}$ <sup>63</sup> at 95 K. These lattice constants have been collected on the High-Resolution Powder Diffractometer beamline at ISIS<sup>63</sup> with a silicon standard and these values are now the benchmark standards of ambient pressure lattice constants of  $\text{H}_2\text{O}$  and deuterated water ( $\text{D}_2\text{O}$ ).

The GSAS<sup>61</sup> software was used to confirm the presence of the  $\text{N}_2$  clathrate hydrate. The diffraction pattern of the 1:34 and 1:100 molar ratio of  $\text{C}_{10}\text{H}_{16}$  in  $\text{H}_2\text{O}$  matrices at 210 K are shown in Figure 4.17(a) and (b), respectively. The Rietveld refinements showed the presences of ice Isd,  $\text{C}_{10}\text{H}_{16}$  and the CS-II clathrate hydrate. This is the first time this mixture has been prepared and analysed.

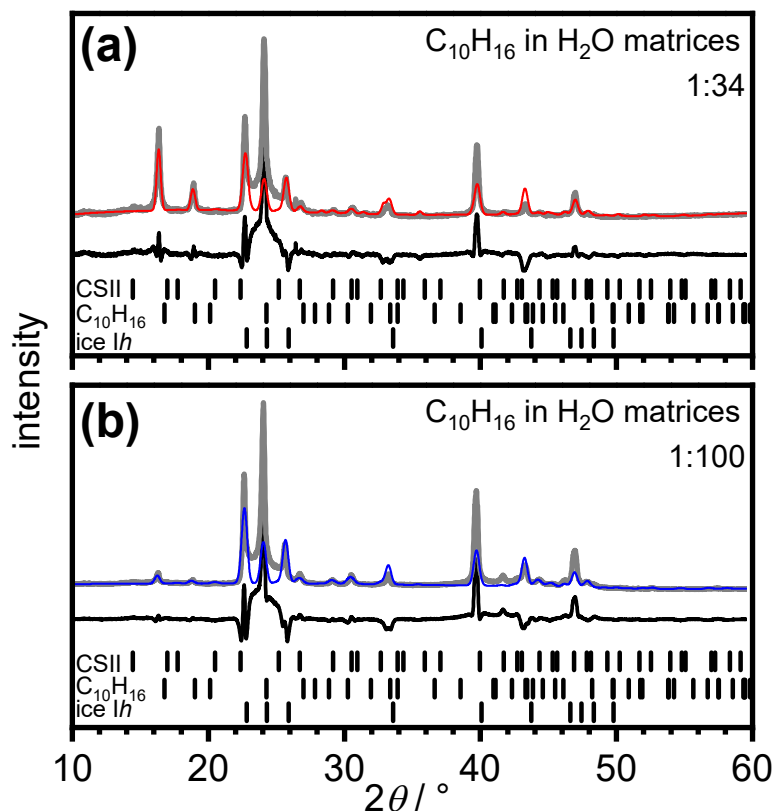


Figure 4.17. XRD patterns ( $\text{Cu K}\alpha$ ,  $\lambda = 1.54 \text{ \AA}$ ) at 210 K of  $\text{C}_{10}\text{H}_{16}$  in  $\text{H}_2\text{O}$  matrices, (a) 1:34 molar ratio and (b) 1:100 molar ratio. The experimental data is shown in this figure as thick grey lines and the thinner coloured lines are the Rietveld fits from GSAS. The thin black lines indicate the differences between the experimental and fitted data. Both panel (a) and (b) include tickmarks indicating the expected positions of Bragg peaks.

The data recorded in Figure 4.17 uses the Fortes' lattice constants in the GSAS model as fixed constants used to 'calibrate' the data and the zero shift was then refined. In this case with the mixtures, the  $\text{C}_{10}\text{H}_{16}$  phase was also added in with lattice constants of  $a/\beta = 6.684567 \text{ \AA}$  and  $c = 9.341652 \text{ \AA}$ . Additionally, the sII clathrate hydrate structure file was also added into the GSAS model with a lattice constant of  $17.263903 \text{ \AA}$ . Both phases ( $\text{C}_{10}\text{H}_{16}$  and sH) were fit to the ice Ih cell using the EXPGUI<sup>64</sup> of GSAS<sup>61</sup>. The zero shift was identified to be 13.75574 and 4.73758 centidegrees for the 1:34 and 1:100 molar ratio, respectively. This shift was used to determine the lattice parameters of the system and the refined lattice constants are provided in Table 4.7.

#### 4. Matrix-Isolated Adamantane in Amorphous Ice

Table 4.7. Refined lattice constants of ice Ih, C<sub>10</sub>H<sub>16</sub> and the CS-II structure calculated from the XRD patterns shown in Figure 4.17. It must be stressed these patterns and lattice constants are for an XRD pattern recorded at 210 K, thus, crystalline C<sub>10</sub>H<sub>16</sub> is present in both samples. The c/a ratios are also provided in this table. The values given for each phase labelled and marked with an asterisk (\*) are the literature values<sup>63</sup> used to calibrate the various phases in the measurements.

phase	molar ratio	<i>a</i> / Å	<i>c</i> / Å	<i>c</i> / <i>a</i>
Ice Ih	-	4.49703(3)*	7.32220(9)*	1.628
	1:34	4.513401	7.373542	1.634
	1:100	4.510022	7.362440	1.632
C <sub>10</sub> H <sub>16</sub>	-	6.6000	8.8100	1.335
	1:34	6.670170	9.355885	1.403
	1:100	6.684567	9.341652	1.397
CS-II	-	17.31500	-	-
	1:34	17.282342	-	-
	1:100	17.263903	-	-

After positive identification (sharp features) in the DSC thermograms and XRD patterns due to the formation of N<sub>2</sub> clathrate hydrates and consistent with studies conducted by Hallbrucker and Mayer in 1989–1991,<sup>53, 59, 60</sup> it has been demonstrated that the N<sub>2</sub> clathrate hydrate formed upon heating the codeposited samples at ambient pressure. Strictly speaking, N<sub>2</sub> clathrate hydrates form without C<sub>10</sub>H<sub>16</sub>, however, it must be stressed that these N<sub>2</sub> clathrate hydrates do not form when the sample is annealed in vacuum. It was recognised that the formation of this hydrate occurred due to open pores in the ASW matrix and the use of LN<sub>2</sub>. In addition, successfully reporting the N<sub>2</sub> clathrate hydrates after the crystallisation to ice *Isd* with C<sub>10</sub>H<sub>16</sub> is reported for the first time in this study. From this stage onwards, all samples were annealed at 125 K, preventing LN<sub>2</sub> from entering the pores of ASW during sample removal in order to avoid the formation of the N<sub>2</sub> CS-II clathrate hydrate. The sample was then cooled back down to 80 K before removal of the sample, causing sintering of ASW and enclosure of substantial amounts of gas which cannot be pumped off anymore *in vacuo*.

The composition of clathrate hydrates can be pinned down in the next step and bulk amounts of the samples can be produced for full characterisation. As an overview, this combinatorial approach of producing clathrate hydrates, avoiding the formation of an N<sub>2</sub> clathrate hydrate, can enable the exploration of hydrates in a highly efficient and high-throughput fashion.

### 4.5.2 Comparison with the XRD Pattern of bulk $C_{10}H_{16}$

The XRD patterns of bulk  $C_{10}H_{16}$  at room temperature and the most  $C_{10}H_{16}$ -rich sample (1:34) at 270 K are shown in Figure 4.18. The XRD patterns of bulk  $C_{10}H_{16}$  recorded at 95 K prepared by crushing pure  $C_{10}H_{16}$  crystals in a pestle and mortar into a fine powder and the most  $C_{10}H_{16}$ -rich sample from vapour deposition recorded at 95 K are also shown in Figure 4.18. In this figure, the pattern of vapour deposited  $C_{10}H_{16}$  at 95 K shows signs of a less ordered structure as can be seen by the slightly reduced number of peaks in the pattern and one can infer that the system is fairly complex due to the mixture of both  $C_{10}H_{16}$  and  $H_2O$ .

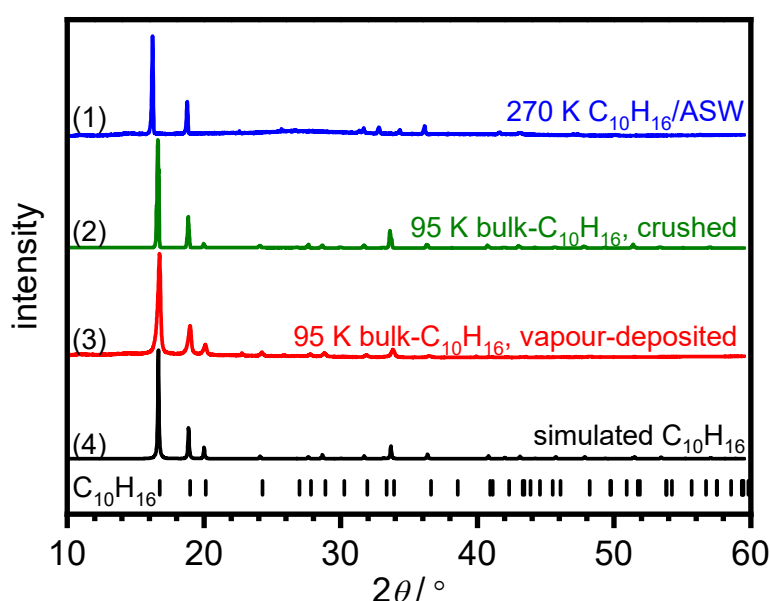


Figure 4.18. XRD patterns ( $Cu\ K\alpha$ ,  $\lambda = 1.54\ \text{\AA}$ ) of simulated  $C_{10}H_{16}$  (black line), bulk  $C_{10}H_{16}$  vapour deposited, bulk  $C_{10}H_{16}$  crushed and the most-rich sample (1:34) at 270 K. The XRD pattern in a green line depicts bulk  $C_{10}H_{16}$  crushed in a pestle and mortar vs. bulk  $C_{10}H_{16}$  vapour deposited at 95 K (red and blue lines). The tickmarks indicate the Bragg positions of bulk  $C_{10}H_{16}$ .

For the XRD pattern labelled (2) in Figure 4.18, due to  $C_{10}H_{16}$  having a viscous and crystal-like nature, it was ground up with a porcelain pestle and mortar in  $LN_2$  and carefully inserted into a 0.8 mm capillary in order to record its pattern at 95 K.

### 4.5.3 Codeposition of the Vacuum-Annealed Samples

Samples annealed at 125 K in the vacuum chamber and cooled back down to 80 K before removal were characterised herein. Low-temperature XRD patterns as shown in Figure 4.19 demonstrate the amorphous nature of the as-made pure ASW and the  $C_{10}H_{16}/H_2O$  mixtures. As mentioned in earlier chapters, pure ASW displays a highly characteristic strong diffraction peak centred at  $\sim 24^\circ$  and a weaker feature at  $\sim 43^\circ$ .<sup>65-67</sup> With increasing



#### 4. Matrix-Isolated Adamantane in Amorphous Ice

the amount of  $C_{10}H_{16}$  content, the diffraction patterns are seen to remain very similar to the pure ASW for all ratios at 95 K. The low angle peaks at  $2\theta = 16.771^\circ$  and  $19.001^\circ$  for  $C_{10}H_{16}$  are only slightly visible at 95 K. It is important to emphasize here in these patterns that at 95 K, none of the samples display strong Bragg peaks characteristic of bulk  $C_{10}H_{16}$  due to the thoroughly mixed sample forming a large network (Figure 4.19).

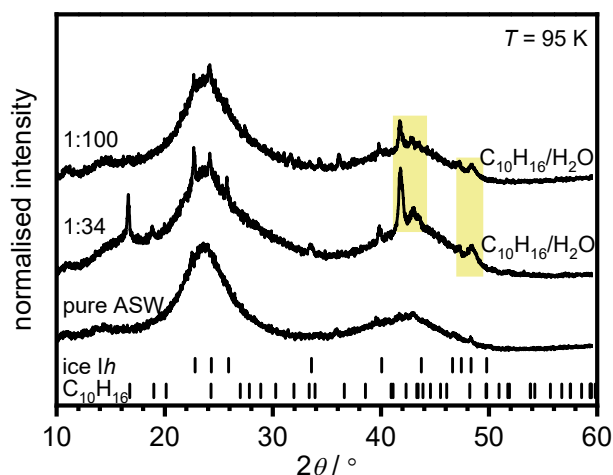


Figure 4.19. XRD patterns ( $Cu\ K\alpha$ ,  $\lambda = 1.54\ \text{\AA}$ ) at 95 K of pure ASW and  $C_{10}H_{16}/H_2O$  mixtures with the indicated  $C_{10}H_{16}/H_2O$  molar ratios. All samples as shown were annealed in the chamber at 125 K and cooled back down to base temperature, 82 K and thus, removed for characterisation. The tickmarks indicate the positions of the expected Bragg peaks for ice Ih and  $C_{10}H_{16}$ . Some minor contaminants may arise due to sample transfer in a humid environment or external ice Ih on the sample holder. The yellow-shaded area shows the Bragg peaks of the brass sample holder. All diffraction patterns have been normalised with respect to the Bragg peak at  $2\theta = \sim 24^\circ$ .

The visible appearances of the samples were dependent upon the concentration of the molar ratio. Upon changing the composition of  $C_{10}H_{16}$ , i.e., the content of  $C_{10}H_{16}$  at a 1:34 molar ratio, the visible nature of the samples was a very fine white powder. In comparison, the 1:100 sample of  $C_{10}H_{16}/H_2O$  showed a visibly denser film when compared to the  $C_{10}H_{16}$ -rich (1:34) sample. Photographic images were taken but due to the colour and visibility of the sample these photos were of low quality. Based on the visual appearance of the sample and diffraction data shown later, it can be concluded that  $C_{10}H_{16}$  and  $H_2O$  have been successfully well-mixed over a fairly large composition range using cryogenic physical vapour deposition. This mixing would be difficult to accomplish by other methods as the solubility of  $C_{10}H_{16}$  in  $H_2O$  is very poor and only  $0.0049\ \text{mg mL}^{-1}$ . For the 1:100 ratio, one would expect there to be less  $C_{10}H_{16}$  present at 95 K when compared to the 1:34 ratio due to more  $H_2O$  present in the 1:100 molar ratio,  $C_{10}H_{16}/H_2O$ .

#### 4. Matrix-Isolated Adamantane in Amorphous Ice

To further investigate the effect of  $C_{10}H_{16}$  on amorphous  $H_2O$  incorporated within the ASW matrix, the various  $C_{10}H_{16}/H_2O$  mixtures from the entirety of the plate were heated in the DSC at  $10\text{ K min}^{-1}$ . The resulting DSC scans were normalised with respect to the mole of  $H_2O$  present in each sample and are displayed in Figure 4.20. Pure ASW has also been presented here for clarity when comparing the well-mixed  $C_{10}H_{16}/H_2O$  samples. The onset temperature of the feature at 125 K is due to the thermal annealing step in the vacuum chamber. In line with the similarities in the XRD patterns, the DSC scans of the 1:34 and 1:100 ratio display similarities with those of pure ASW with the exotherm for crystallisation starting at above 150 K. The exotherm of the pure ASW as mentioned previously was found to be  $1260 \pm 35\text{ J mol}^{-1}$ , in good agreement with the literature values.<sup>67-72</sup> However, the addition of extra features in these mixed samples before and after 150 K demonstrate the complexity of this system and are discussed later. The onset temperatures for the crystallisation of  $H_2O$  were not found to change significantly with respect to pure ASW upon increasing the content of  $C_{10}H_{16}$ . The areas of the  $H_2O$  crystallisation peaks were found to differ from one another due to the introduction of a second species,  $C_{10}H_{16}$  or may be due to the formation of a clathrate hydrate and associated enthalpies are provided in Table 4.8.

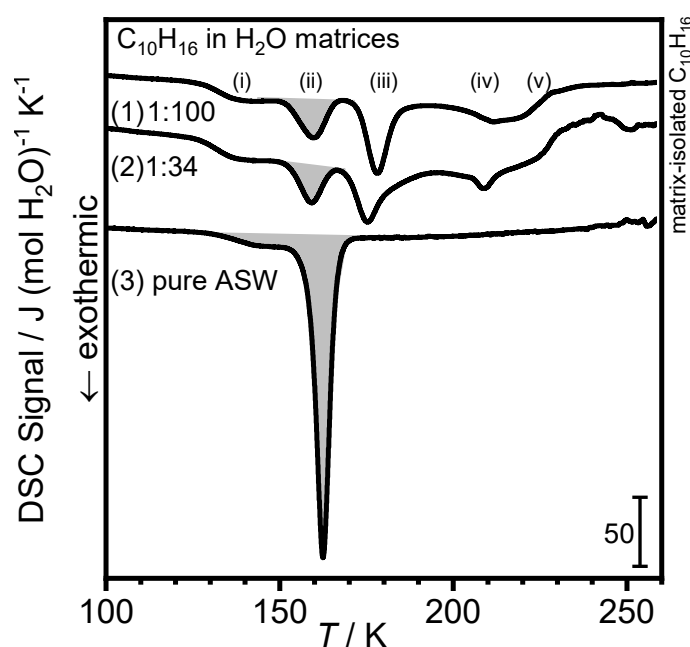


Figure 4.20. DSC thermograms of pure ASW and indicated  $C_{10}H_{16}/H_2O$  mixtures heated at  $10\text{ K min}^{-1}$ . The DSC signals have been normalised with respect to the number of mole per  $H_2O$ . The shaded areas show the crystallisation of  $H_2O$  and the limits of the integration of the feature.

#### 4. Matrix-Isolated Adamantane in Amorphous Ice

The presence of  $C_{10}H_{16}$  had a substantial effect on the enthalpy of crystallisation of  $H_2O$  in both composition ranges as can be seen in Figure 4.20 and enthalpies in Table 4.8.

*Table 4.8. Spread of enthalpies relating to pure ASW and codeposited samples from indicated molar ratios in Figure 4.20. The DSC thermograms were recorded at  $10\text{ K min}^{-1}$  and at ambient pressure. It must be noted that it was difficult to find integration limits for processes (iv) and (v), hence why only one enthalpy change is provided from 195–230 K.*

Sample	Scan in Figure 4.20	$\Delta H / \text{J mol}^{-1}$		
		160 K	175–179 K	195–230 K
1:100	(1)	223	372	342
1:34	(2)	185	363	444
Pure ASW	(3)	1260	-	-

The introduction of  $C_{10}H_{16}$  did not impact the crystallisation exotherm other than reducing the peak areas by ten times due to the other pronounced features. This is highly significant due to the possible formation of a clathrate hydrate and may suggest the presence of some bulk ASW in the samples. However, the impact of the introduction of  $C_{10}H_{16}$  within the ASW matrix can evidently be seen in the DSC scans displaying successful mixing. Exothermic peaks emerge at 175 K and  $\sim 209$  K for the 1:34 sample, which decrease in area and an insignificant shift in temperature with respect to pure ASW crystallisation is seen. Similarly, for the 1:100 sample, peaks at 179 K and 212 K are observed as the latter peak is seen as a broad feature with a 5 K shift in temperature and increase in the associated area. A proposed summary of the temperature position for the peaks for each ratio is provided below in Table 4.9.

*Table 4.9. Peak temperatures and assignments for the respective DSC scans as shown in Figure 4.20.*

Process	$T / \text{K}$	Assignment
(i)	125	sample annealed at 125 K in the vacuum chamber
(ii)	160	crystallisation to ice <i>Isd</i>
(iii)	175/179	start of clathrate hydrate formation
(iv)	209/212	clathrate hydrate formation
(v)	220/230	clathrate hydrate decomposition

In addition to the crystallisation of  $H_2O$ ,  $C_{10}H_{16}$  can be expected to form clathrate hydrates upon heating after crystallisation as it is expelled from the ASW matrix or as the amorphous  $C_{10}H_{16}$  clusters crystallise. The difference between the unannealed samples and annealed samples is that the annealing stage in the vacuum chamber at 125 K rules out the formation of  $N_2$  clathrate hydrates. The formation and decomposition of clathrate

#### 4. Matrix-Isolated Adamantane in Amorphous Ice

hydrates from this sample composition may be identified by the temperatures of the exotherm peaks. Judging by the DSC scans alone, it is not possible to identify which clathrate hydrate is formed or the processes that take place upon formation and decomposition. Although, it is tempting to assign the low- and high-temperature exotherm peaks to the crystallisation of bulk H<sub>2</sub>O and then the features of C<sub>10</sub>H<sub>16</sub>, respectively, particularly for processes (iii)–(v).

It is important to note that these exotherms observed in all scans are irreversible and thus, were not observed upon second heating. The phase transition of bulk C<sub>10</sub>H<sub>16</sub> (208.62 K, order to disorder transition)<sup>32</sup> is endothermic upon heating and is not observed in the data presented here which can be attributed to C<sub>10</sub>H<sub>16</sub> owing to a poorly crystalline nature with small domain sizes.

##### 4.5.3.1 XRD Patterns of C<sub>10</sub>H<sub>16</sub> / H<sub>2</sub>O Mixtures Heated from 95 K to 260/270 K

In line with the observed processes seen in the DSC data, the XRD data of the same samples were recorded upon heating from 95 K to 270 K and corresponding contour plots are shown in Figure 4.21. Several changes have been detected as the temperature increases as shown in Figure 4.21(b) and Figure 4.21(c) for the 1:34 and 1:100 sample, respectively. The complete set of diffraction data is shown in Figure 4.22 and Figure 4.23. The XRD data for pure ASW is shown in Figure 4.21(a) as a contour plot that displays the well-known sequence of events of the irreversible phase transition upon heating. This starts with the crystallisation of H<sub>2</sub>O to ice *Isd* starting at 140 K to 170 K, followed by the gradual conversion to ice *Ih* above this temperature.<sup>73</sup> At ~163 K, the reflections for ice *Isd* superimpose on the broad peaks of ASW which can also be detected across all mixed samples. In combination with the DSC data, with increasing the content of C<sub>10</sub>H<sub>16</sub> in the mixtures from 1:100 to 1:34, the content does not lead to many differences upon heating in the XRD data as shown in Figure 4.21(b) and Figure 4.22. Upon decreasing the concentration of the C<sub>10</sub>H<sub>16</sub>/H<sub>2</sub>O molar ratios from 1:34 to 1:100 compared to pure ASW, the 1:100 molar ratio exhibits significant differences within the XRD data and can be clearly seen in upcoming Figure 4.23. It must be noted that as the temperature increases in the mixture samples, atomic fluctuations in the sample increase, which causes *d*-spacings to increase and leads to a slight shift in peaks.

The set of XRD heat maps are depicted in Figure 4.21 of pure H<sub>2</sub>O and C<sub>10</sub>H<sub>16</sub>/H<sub>2</sub>O mixtures of 5.6 and 14.9 v% C<sub>10</sub>H<sub>16</sub>, corresponding to 1:100 and 1:34 molar

#### 4. Matrix-Isolated Adamantane in Amorphous Ice

ratios, respectively. The XRD data of the 14.9 v% of the  $C_{10}H_{16}$  sample is a fine powder and since  $C_{10}H_{16}$  is finely mixed in with  $H_2O$ , there is a larger network of  $C_{10}H_{16}$ .

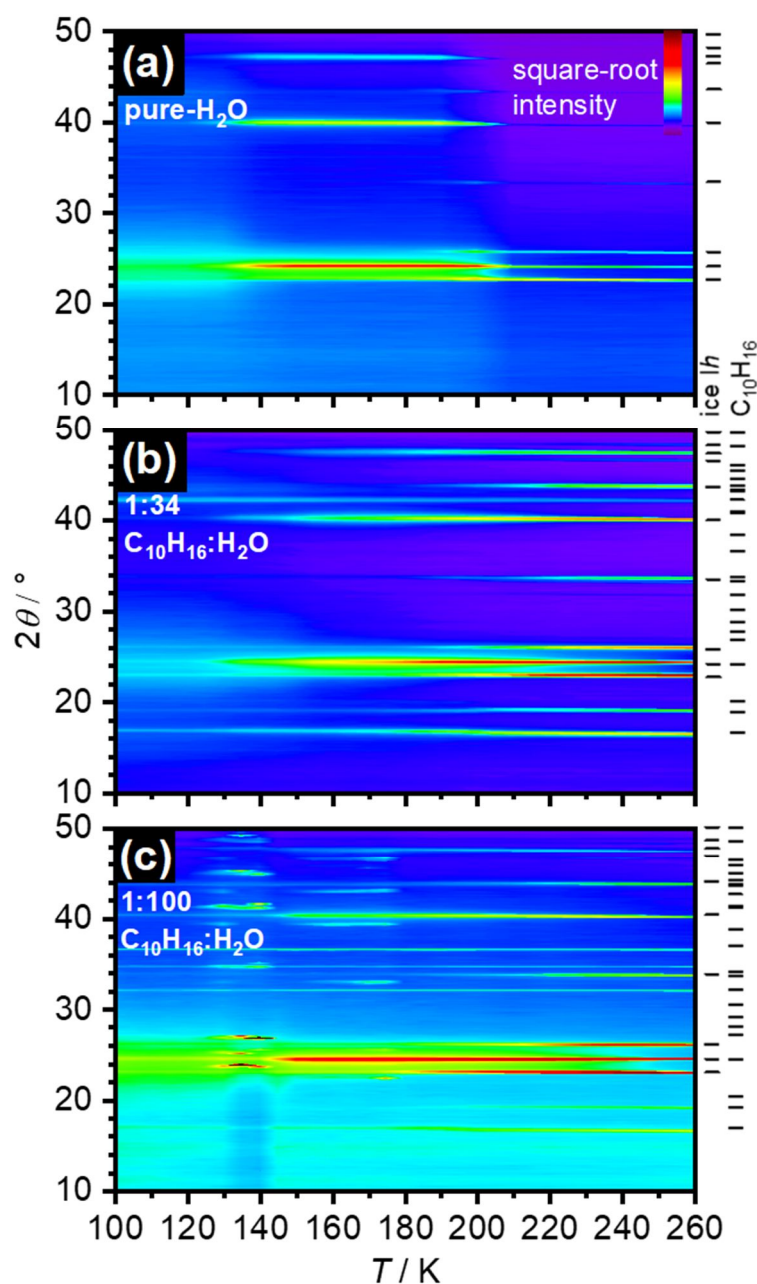


Figure 4.21. Contour plots of XRD patterns ( $Cu\ K\alpha$ ,  $\lambda = 1.54\ \text{\AA}$ ) recorded upon heating at ambient pressure of pure  $H_2O$  and the  $C_{10}H_{16}/H_2O$  mixtures with indicated molar ratios. Slightly different heating programs were run on these plots where (a) 93 K, 100–260 K in 10 K steps, (b) 95, 100 K, 110 K, 120–230 K in 5 K steps, 240–260 K in 10 K steps and (c) 95–130 K in 5 K steps, then an isothermal hold at 130 K for 5 patterns, followed by 140–190 in 5 K steps and then 200–260 K in 10 K steps. The tickmarks on the right-hand side of the contour plots show the expected Bragg positions for ice Ih and  $C_{10}H_{16}$ .

#### 4. Matrix-Isolated Adamantane in Amorphous Ice

As previously observed in the DSC data, the XRD data recorded upon heating showed additional changes with the 1:34 sample when compared to pure ASW as shown in Figure 4.21(c) and upcoming Figure 4.22. Already at 90 K, the first two peaks of C<sub>10</sub>H<sub>16</sub> at  $2\theta = 16.771^\circ$  and  $19.001^\circ$  are seen in the diffraction data throughout the temperature program and grow simultaneously with an increase in temperature. An extremely weak Bragg peak appears at 135 K at  $2\theta = 19.91^\circ$  which grows slightly in intensity until 200 K. This weak peak is attributed to a reflection from which occurs at  $2\theta = 20.14^\circ$  for the  $\alpha$ -phase of C<sub>10</sub>H<sub>16</sub>. The formation temperature of ice *Isd* shifts from 140 K to 130 K when compared to pure ASW. Reflections of the structure sH clathrate hydrate are known to appear at  $2\theta = 22.25, 25.30, 26.80, 27.90, 28.55, 29.25, 30.45$  and  $31.60^\circ$ .<sup>74</sup> However, in these samples, only a weak Bragg peak appears above 175 K at  $2\theta = 31.69^\circ$  (highlighted in yellow boxes in Figure 4.22) assigned to the sH hydrate which occurs after the transformation to ice *Isd* and the lower Bragg peaks at earlier temperatures cannot be seen in the patterns due to the amorphous ice superimposing these peaks. This may represent the suppression of the formation of the clathrate hydrate and the XRD measurements carried out here show no other peaks attributing the formation of a clathrate hydrate. This may pose the idea that there is some preferred orientation of C<sub>10</sub>H<sub>16</sub> in the sample. In this case, it proved difficult to form a clathrate hydrate with the guest species, C<sub>10</sub>H<sub>16</sub> for the annealed at 125 K (in the vacuum) samples. These measurements show that no N<sub>2</sub> clathrate hydrates were formed for this sample which was annealed at 125 K under vacuum before removal and characterisation. The corresponding DSC pattern for this 1:34 molar ratio sample shows perhaps a decomposition of a clathrate hydrate, however, the XRD data does not detect this due to possible preferred orientation.

The diffraction data recorded at 180 K, 200 K and 220 K were refined with ice *Ih*, C<sub>10</sub>H<sub>16</sub>, sH, CS-I, CS-II, sIII, sK and the sT phases (as defined in Chapter 1). In every case, all three temperatures patterns did not correspond to any known hydrate and only indicated the presence of ice *Ih* and C<sub>10</sub>H<sub>16</sub>. Nevertheless, the presence of a guest species in the entire vapour deposited system is thought to lead to great complexity and the search for a clathrate hydrate remains.

To reiterate, Figure 4.22 provides a breakdown of every XRD pattern following systematic heating of the 1:34 C<sub>10</sub>H<sub>16</sub>/H<sub>2</sub>O sample.

#### 4. Matrix-Isolated Adamantane in Amorphous Ice

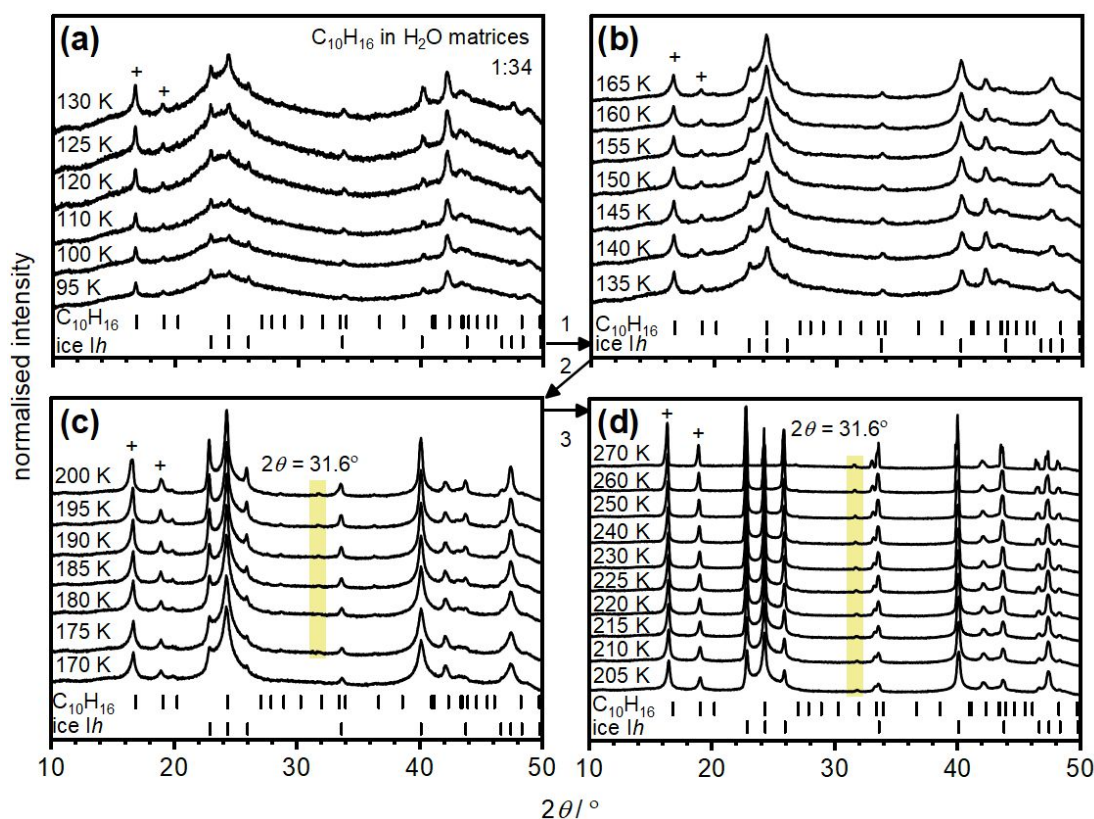


Figure 4.22. XRD patterns ( $\text{Cu K}\alpha$ ,  $\lambda = 1.54 \text{ \AA}$ ) recorded of a 1:34  $\text{C}_{10}\text{H}_{16}/\text{H}_2\text{O}$  sample where (a) 95–130 K, (b) 135–165 K, (c) 170–200 K and (d) 205–270 K. The arrows in the centre of the figure show the increase in temperature starting from (a) to (d). The tickmarks at the bottom of the plots show the expected Bragg positions for ice Ih and  $\text{C}_{10}\text{H}_{16}$  and the (+) system indicates  $\text{C}_{10}\text{H}_{16}$  Bragg peaks as mentioned in the main text.

Since the DSC data and XRD showed some assumed clathrate hydrate formation for the 1:34 molar ratio, the XRD patterns for the 1:100 molar ratio was also recorded and is depicted in Figure 4.23. Several peak changes compared to the 1:34 molar ratio was seen within this composition and the pronounced features in the figure have been highlighted in yellow.

Within the region of 95–125 K and aside from the amorphous features of ASW, Figure 4.23 indicates peaks at  $2\theta = 31.26^\circ$  and  $34.52^\circ$ . These two peaks do not correspond to any known hydrate,  $\text{C}_{10}\text{H}_{16}$  or ice Ih. During the isothermal hold at 130 K and up to 190 K, these peaks do not grow and remain in the sample. As the temperature increases from 150 K, the formation of ice Isd is detected and these features continually grow until a trident is seen at higher temperatures. The sample goes through the amorphous to crystalline transition upon a temperature increase. There is a significant amount of sharp Bragg peaks at  $2\theta = 42.12, 43.24$  and  $48.88^\circ$  which could not be eliminated as these peaks are a result of the sample holder alignment with respect to the detector. Expected  $\text{C}_{10}\text{H}_{16}$



#### 4. Matrix-Isolated Adamantane in Amorphous Ice

peaks at approximately  $2\theta = 16.771$ ,  $19.001$  and  $31.952^\circ$ , indicate the formation of small crystalline domains of  $C_{10}H_{16}$  within the sample and can be seen growing from 95 K through to 260 K. For the 1:100 sample, the  $C_{10}H_{16}$  diffraction features are less intense compared to those of the 1:34 sample. During heating and in both cases, the appearance of the  $C_{10}H_{16}$  Bragg peaks at low  $2\theta$  are accompanied by the disappearance of the broad ASW features and formation of ice *Isd*. The growth in intensity of these low-angle peaks with respect to the molar ratios could be thought to arise from local density differences between the  $C_{10}H_{16}$  and ice. The intensity may also be attributed to the fact that  $C_{10}H_{16}$  is expelled out of the amorphous matrix upon heating and its presence provides evidence for successful mixing of both species. As the sample crystallises, embedded  $C_{10}H_{16}$  molecules are expelled from the amorphous matrix and both components undergo phase separation, leading to the differences in the XRD patterns where both  $H_2O$  and growing  $C_{10}H_{16}$  peaks can be observed.

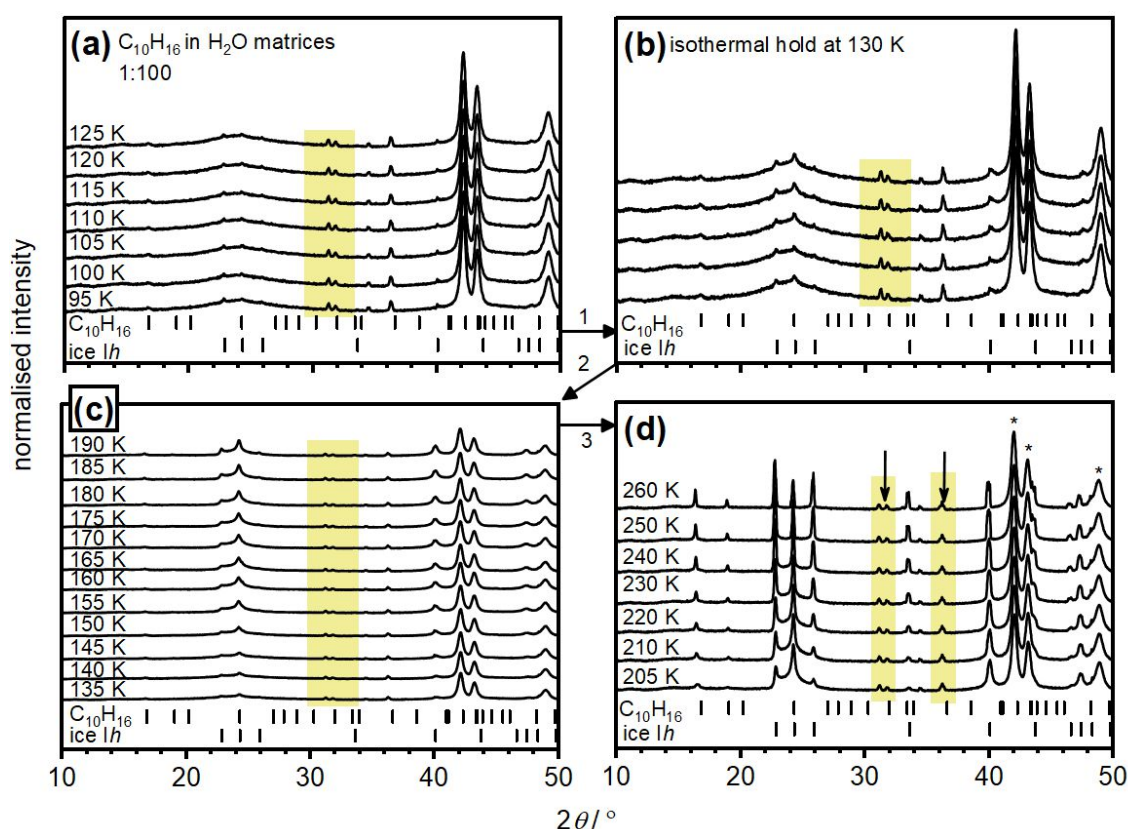


Figure 4.23. XRD patterns ( $Cu\ K\alpha$ ,  $\lambda = 1.54\ \text{\AA}$ ) recorded of a 1:100  $C_{10}H_{16}/H_2O$  sample where (a) 95–125 K, (b) five XRD patterns recorded at 130 K as an isothermal hold, (c) 135–190 K and (d) 205–260 K. The arrows in the centre of the figure show the increase in temperature starting from (a) to (d). The arrows in plot (d) show the extra peaks found in the system. The asterisks marked in the figure show the Bragg peaks arising from the sample holder which could not be omitted. The tickmarks at the bottom of the plots show the expected Bragg positions for ice *Ih* and  $C_{10}H_{16}$ .



#### 4. Matrix-Isolated Adamantane in Amorphous Ice

As this highly diluted 1:100 sample indicated the presence of several peaks which did not reconcile with known hydrates,  $C_{10}H_{16}$  or ice  $I_h$ , they could be classed as artefacts and so, the sample was prepared with identical conditions two more times repeatedly to ensure reproducibility of these features. Figure 4.24 portrays the experimental XRD patterns in the form of contour plots for three identically prepared 1:100 molar ratios of  $C_{10}H_{16}/H_2O$ .

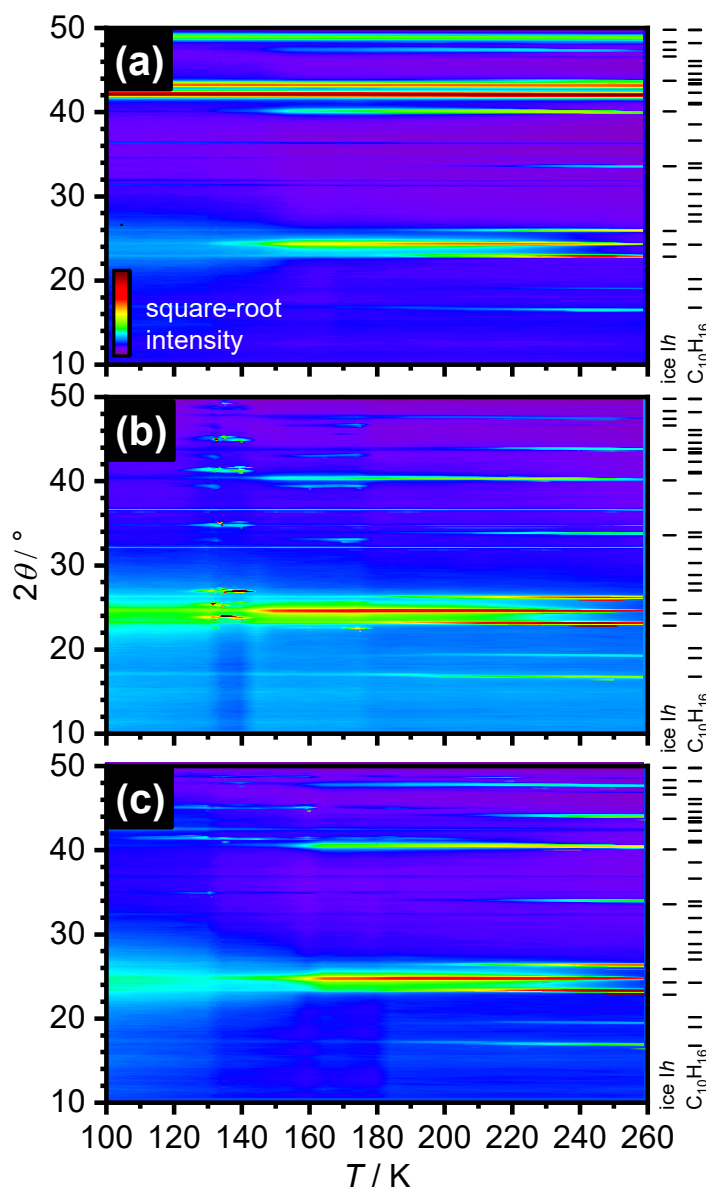


Figure 4.24. Contour plots of XRD patterns ( $Cu\ K\alpha$ ,  $\lambda = 1.54\ \text{\AA}$ ) recorded upon heating at ambient pressure of three identically prepared  $C_{10}H_{16}/H_2O$  mixtures with a molar ratio of 1:100. Heating programs are such that: 100–130 K in 5 K steps, then an isothermal hold at 130 K for 5 patterns, followed by 140–190 in 5 K steps and then 200–260 K in 10 K steps. The tickmarks on the right-hand side of the contour plots show the expected Bragg positions for ice  $I_h$  and  $C_{10}H_{16}$ .

The XRD patterns as shown in Figure 4.24 show the existence of  $H_2O$  and  $C_{10}H_{16}$ . Most tickmarks, which are the expected Bragg positions of  $C_{10}H_{16}$  align with the  $C_{10}H_{16}$  phase

#### 4. Matrix-Isolated Adamantane in Amorphous Ice

in the mixture, however most prominently for example, in Figure 4.24(b) at  $2\theta = 31.6$ ,  $34.5$  and  $36.5^\circ$ , the peaks do not seem to grow in intensity with heating. The features below  $2\theta = 20^\circ$  at  $2\theta = 16.771^\circ$  and  $19.001^\circ$  grow immensely with temperature and from the contour plot shown in Figure 4.24(b), it almost seems as if the features between  $2\theta = 31.6^\circ$  and  $36.5^\circ$  are related to one another since there are minimal intensity changes. The contour plot indicates the expected result of such a mixture where ASW is mixed with a small amount of  $C_{10}H_{16}$  and not in a three-dimensional network. In other terms, this actively demonstrates that there are more long-range interactions as more  $C_{10}H_{16}$  is expelled from the ASW matrix and thus, forced out of the amorphous ice. Larger regions of pure crystalline  $C_{10}H_{16}$  are formed with increasing temperature, hence why the peaks grow in intensity. As the sample is heated,  $H_2O$  crystallises, perhaps forming a certain cage structure as well as forcing the  $C_{10}H_{16}$  out of the  $H_2O$  matrix. It could be assumed that there are two types of cages formed at different temperatures. During crystallisation at 130 K, new Bragg features form and then disappear near 160 K and more features are formed before decomposing. After these temperatures, at 180 K, the so-called cage features disappear and more ice *Ih* is formed from ice *Isd*. Again, at this same time,  $C_{10}H_{16}$  is forced out of the  $H_2O$  matrix forming a long-range network shown by the increasing intensity of the  $C_{10}H_{16}$  features. In addition, the XRD data shows a growth of the  $C_{10}H_{16}$  features after crystallisation and decomposition of the cages which would be expected from what is known of ice. An interesting peak at  $2\theta = 34.5^\circ$  in this 1:100 ratio is observed throughout the repeats of this molar experiment; however, this peak is not present in the 1:34 molar ratio diffraction data. The peak features at  $2\theta = 31.6$ ,  $34.5$  and  $36.5^\circ$  mentioned earlier, remain persistent throughout the entire experiment, and do not disappear at any given temperature.

The aim was to see if the sample preparation with a 1:100 molar ratio repeated several times was reproducible. Unfortunately, the resulting XRD patterns did not display the same features with temperature, hence why the next section (4.5.4) will aim to eliminate this. No concrete direction was obtained in relation to uncovering a  $C_{10}H_{16}$  clathrate hydrate since peculiar Bragg peaks were observed and all XRD patterns were dissimilar from one another despite the equally prepared samples. Thus, it was necessary to understand the distribution across the deposition plate. In the next section, the 1:100 and the 1:34 molar ratio samples are investigated further in terms of their spatial distribution across the plate.

### 4.5.4 Distribution of $C_{10}H_{16}$ and $H_2O$ Across the Deposition Plate

Understanding the origin of the peculiar features seen in XRD and DSC of  $C_{10}H_{16}$  in amorphous ice has begun to unravel anomalies that are not related to any known clathrate hydrates, such as the position of the Bragg peaks in the XRD data and features in the DSC scans. These features confirm the structural complexity of this system and the need for a full analysis of a possible new clathrate hydrate. To maximise the chances of success of discovering a new clathrate hydrate and to explain the difference between three repeated experiments resulting in different results, a combinatorial approach was used. In several experiments, gradients in the mole fraction of  $C_{10}H_{16}$  across the deposition were produced. These various locations on the plate were analysed using the characterisation methods described earlier; in-house low-temperature XRD and also rapid screening with the DSC.

In detail, the diameter of the plate was sectioned into three equal circles as shown in the schematic figure, Figure 4.25. Boundary lines drawn on the deposition plate were adhered to when scraping the sample off the deposition plate. The characterisation by DSC and XRD includes sample taken and analysed from the marked diameters (1–3) of each circle.

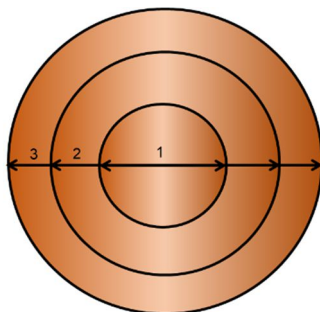


*Figure 4.25. Schematic illustration of the boundaries of where the sample was removed for characterisation where, (1) is the centre of the plate, (2) midpoint of the radius of the deposition plate and (3) the edge of the deposition plate.*

The calorimetric data from each position for the two different ratios are provided in Figure 4.26. As an overview, there are differences with respect to increasing the concentration of  $C_{10}H_{16}$  in  $H_2O$  which are discussed in the following text.

#### 4. Matrix-Isolated Adamantane in Amorphous Ice

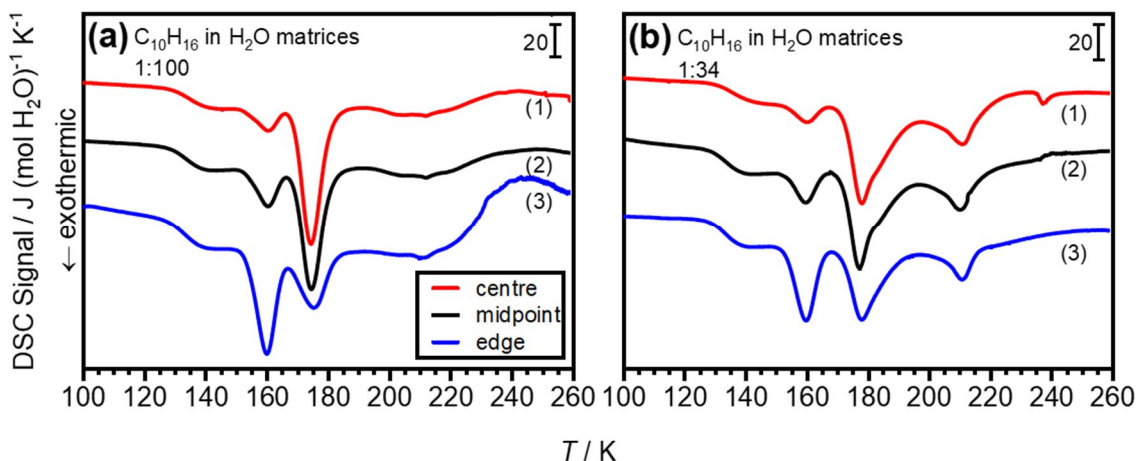


Figure 4.26. DSC thermograms of  $C_{10}H_{16}/H_2O$  with indicated  $C_{10}H_{16}/H_2O$  molar ratios heated at  $10\text{ K min}^{-1}$ , where (a) 1:100 molar ratio sample and (b) 1:34 molar ratio sample. Both (a) and (b) show the differences in the sample distribution across the plate where scan (1) (red line) is the sample collected from the centre of the plate, scan (2) (black line) is the sample collected from the midpoint of the radius and edge of the deposition plate and scan (3) (blue line) is the sample collected from the edge of the plate. All scans were performed at ambient pressure. The DSC signals are normalised with respect to per mole of  $H_2O$ .

It can already be noted that there are differences in the DSC thermograms with respect to the composition of the sample. The composition of the samples changes across the deposition plate since the areas are offset from one another and thus, angle dependence of the deposition must be different. If the angle dependence were identical there would be no changes in the composition. The problem encountered here is that the angle dependence of deposition is not known. The angle is different for each position on the plate since the centre of the deposition plate is in line with the  $H_2O$  aperture. The evaporation source is placed towards the left-hand side of the  $H_2O$ -inlet tube and not directly in the centre of the deposition plate. In this setup there are two deposition sources, (i)  $H_2O$ -inlet tube and (ii) evaporation source from where  $C_{10}H_{16}$  is deposited. The thicker deposits are found in the centre of the deposition plate with a deposition angle,  $0^\circ$ , in line with the  $H_2O$  aperture.<sup>57</sup> The angle is not  $0^\circ$  for the mixtures where the sample was deposited towards the edge and midpoint of the radius and edge of the plate. The bottom line suggesting the differences between the compositions and spatial inhomogeneity is due to angle dependence. Both molar ratios display the annealing stage at 125 K which occurs in the chamber and also the crystallisation of  $H_2O$  to ice  $Isd$ . It is important to note, the presence of  $C_{10}H_{16}$  embedded within the amorphous ice matrix does not delay the exotherm but affects the enthalpy of crystallisation of  $H_2O$  to ice  $Isd$ . At 160 K, the

#### 4. Matrix-Isolated Adamantane in Amorphous Ice

exotherms for both the dilute and concentrated samples in Figure 4.26(a) and Figure 4.26(b), respectively, have different associated areas which appear to coincide with the distribution across the plate. Table 4.10 summarises the associated enthalpies with respect to the spatial distribution across the deposition plate.

*Table 4.10. Spread of enthalpies for the crystallisation of H<sub>2</sub>O relating to the spatial distribution from the DSC thermograms in Figure 4.26. The heating rate of all DSC thermograms was 10 K min<sup>-1</sup> and carried out at ambient pressure.*

Position	$\Delta H / \text{J mol}^{-1}$	
	1:100 C <sub>10</sub> H <sub>16</sub> /H <sub>2</sub> O	1:34 C <sub>10</sub> H <sub>16</sub> /H <sub>2</sub> O
Centre	81	66
Midpoint	136	125
Edge	385	297

There is a clear disparity in relation to the spatial distribution across the plate as can be seen from the calorimetric measurements. In light of the 1:100 molar ratio, the second feature (H<sub>2</sub>O crystallisation) is approximately five times the size at the edge of the deposition plate when compared to the centre of the deposition plate. The associated area from the centre to the edge of the deposition plate increases significantly. It is possible to speculate that in a different location, there is more movement of H<sub>2</sub>O molecules in the matrix, however, in the centre of the plate, it could be proposed that the sample is more concentrated with respect to the other locations since thicker deposits were found here and so there are less H<sub>2</sub>O molecules when compared to the edge of the deposition plate where H<sub>2</sub>O molecules are more freely dispersed. In the literature, ASW grown by vapour deposition was found to strongly depend on the angular distribution of incident H<sub>2</sub>O molecules.<sup>75-78</sup> As the angle of incidence increases, the growth of a nonporous to highly porous ASW is observed.<sup>77</sup> This ratio is H<sub>2</sub>O-rich and would be expected to show a larger area with crystallisation when compared to the C<sub>10</sub>H<sub>16</sub>-rich sample. Similarly, the same trend is seen for this C<sub>10</sub>H<sub>16</sub>-rich sample where the edge of the deposition plate displays an associated area nearly five times greater when compared to the centre of the deposition plate. In this C<sub>10</sub>H<sub>16</sub>-rich sample, there are fewer H<sub>2</sub>O molecules in a fixed volume which is reflected in the decrease of associated areas when compared to the H<sub>2</sub>O-rich sample.

The third feature in Figure 4.26(a), at approximately 175 K, for the centre of the plate is significantly larger by eye when compared to the midpoint of the radius and edge of the deposition plate. The associated area for the centre is 190 J mol<sup>-1</sup> and the associated area for the edge of the plate is given by 493 J mol<sup>-1</sup>. The associated areas are about two

#### 4. Matrix-Isolated Adamantane in Amorphous Ice

and a half times bigger towards the edge of the plate. Note, it is difficult to choose the limits of where the peak starts and ends. However, yet again, it seems as though ice *Isd* is the active material for preparing the clathrate hydrate, followed by a fourth, very broad feature at 212 K which could be attributed to the decomposition of the hydrate. In the literature, for N<sub>2</sub> clathrate hydrates, the decomposition is found to be 220 K.<sup>53, 59, 60</sup> Equally, the C<sub>10</sub>H<sub>16</sub>-rich sample [Figure 4.26(b)] decreases in the associated area going from the centre of the deposition plate towards the edge of the deposition plate with respect to the third feature at 175 K. The associated areas for scans 1–3 are, 206, 190, and 159 J mol<sup>-1</sup>, respectively. If this is the formation of the clathrate hydrate at the centre of the plate of a 1:34 molar ratio, less movement of the H<sub>2</sub>O molecules is experienced in the centre of the deposition plate due to the high concentration and the H<sub>2</sub>O-inlet tube directly hitting the centre of the deposition plate first which may be attributed to the increased value in the associated area. In addition, at 212 K, a fourth fairly narrow feature, can be seen for all sections of the deposition plate. Nevertheless, it can be anticipated that there is most definitely a change of composition and non-uniformity across the deposition plate in both cases of molar ratios. The corresponding XRD patterns for the spatial distribution across the deposition plate is provided in Figure 4.27.

The aim was to address the spatial distribution across the deposition plate to see if the unassignable peaks from samples from the entirety of the plate can be solved. However, since the spatial distribution is unequal, an in-depth analysis of the XRD patterns in Figure 4.27 was carried out. Despite the differences seen in the DSC thermograms with respect to the spatial distributions, the XRD patterns yet depict very erratic or unpredictable results.

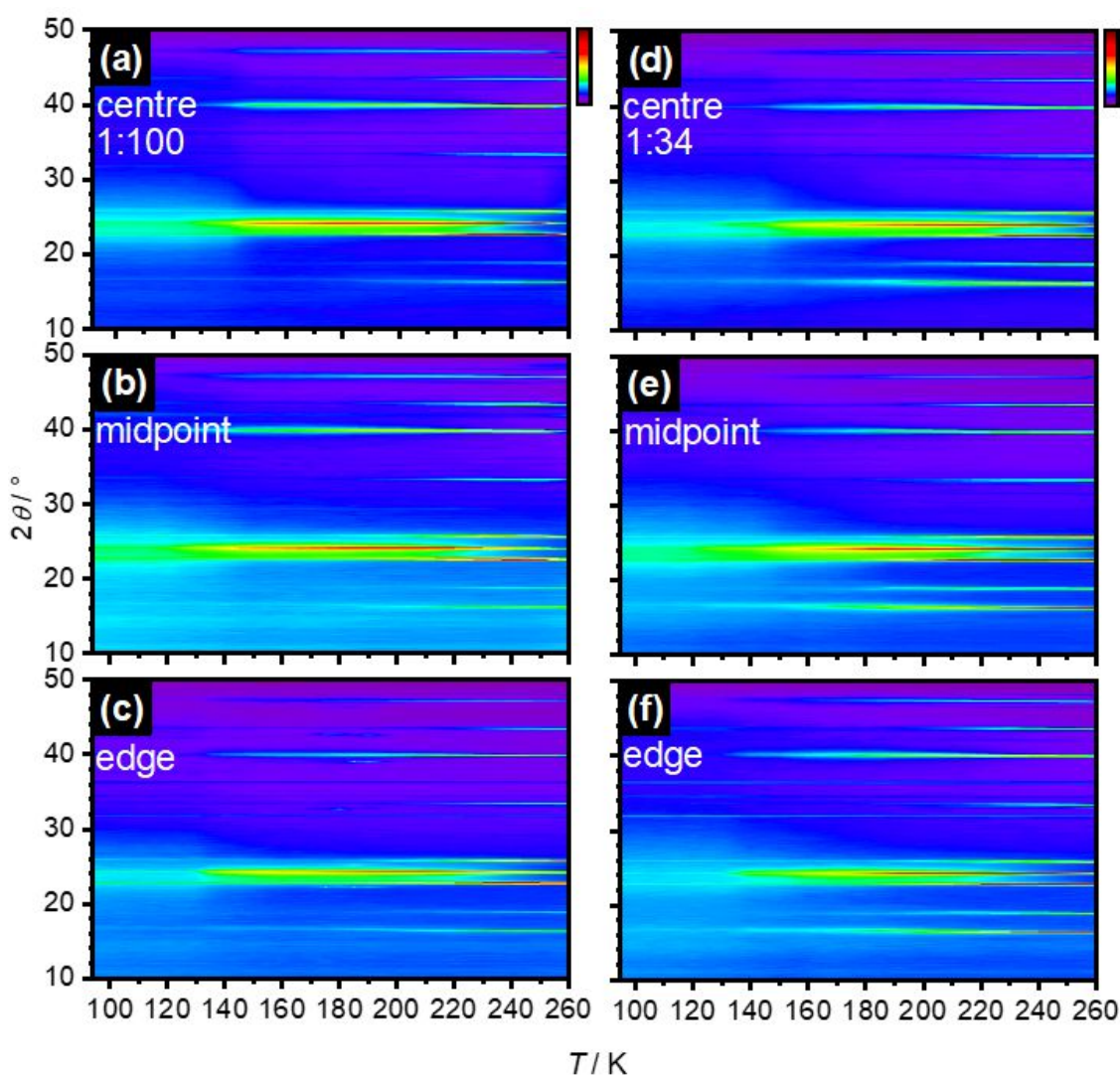


Figure 4.27. Contour plots of XRD patterns ( $\text{Cu K}\alpha$ ,  $\lambda = 1.54 \text{ \AA}$ ) recorded upon heating at ambient pressure of  $\text{C}_{10}\text{H}_{16}/\text{H}_2\text{O}$ , where (a)–(c) 1:100 molar ratio and (d)–(e) 1:34 molar ratio. The spatial distribution across the deposition plate is indicated on the figure.

Besides ASW crystallising shown in each panel of Figure 4.27 to ice  $\text{I}_{sd}$  and finally ice  $\text{I}_h$ , the main  $\text{C}_{10}\text{H}_{16}$  peaks at  $2\theta = 16.771^\circ$  and  $19.001^\circ$  grow in intensity as expected. This is due to  $\text{C}_{10}\text{H}_{16}$  being expelled or released out of the amorphous matrix upon heating.

Addressing the  $\text{H}_2\text{O}$ -rich sample from the centre of the deposition plate, a collection of several small peaks is present from 95 K and do not disappear even at 260 K. The intensities of these peaks remain constant throughout the experiment. They are found at  $2\theta = 31.7, 33.5, 34.5$  and  $36.2^\circ$ . What is interesting to note, is the reproducibility of the previously mentioned peak at  $2\theta = 34.5^\circ$ . Once again, the origin of this peak remains a mystery. The midpoint of the radius of the deposition plate intriguingly only illustrates the presence of  $\text{H}_2\text{O}$  and  $\text{C}_{10}\text{H}_{16}$ . No peculiar peaks or features were identified

#### 4. Matrix-Isolated Adamantane in Amorphous Ice

upon heating. However, at the edge of the plate, the same four peaks which do not grow in intensity as seen in the centre of the plate are present ( $2\theta =$  as above). Interestingly at 170 K, a small peak at  $2\theta = 36.61^\circ$  appears and tends to grow in intensity up to a temperature of 180 K before it decreases in intensity until 190 K. After 190 K, this peak is not present. This feature is due to  $C_{10}H_{16}$  and thus, may arise only for a short time due to the preferred orientation of  $C_{10}H_{16}$ . Between 170–190 K, the characteristic ice *Isd* trident shows many extra peaks which may be due to a clathrate hydrate, so the occurrence of the small peak at  $2\theta = 36.61^\circ$  is in line with these hydrate peaks. Nevertheless, no other features upon heating that have not already been listed for the centre of the deposition plate have been observed.

Regarding the most  $C_{10}H_{16}$ -rich sample, at all temperatures, and similar to the  $H_2O$ -rich sample, at  $2\theta = 31.7, 33.5, 34.5$  and  $36.2^\circ$ , features are present from 95 K through to 260 K. They once again, do not grow in intensity upon a temperature increase. In comparison to the intensity in the  $H_2O$ -rich sample, these features in Figure 4.27(a) are much less intense. Investigating the midpoint of the radius of the deposition plate for the  $H_2O$ -rich sample, some features are not present in any other patterns as already mentioned earlier. At 200 K, growing in intensity to 260 K, a peak at  $2\theta = 33.2^\circ$  is seen and upon heating, a shift in this peak towards lower  $d$ -spacings with a resulting peak maximum at  $2\theta = 32.7^\circ$  is observed. From 220 K to 260 K, a small peak at  $2\theta = 31.6^\circ$  is observed and grows in intensity only slightly until 260 K where the peak maximum shifts to read  $2\theta = 31.49^\circ$ . Once again, these peaks are unassignable to any known hydrate, ice or  $C_{10}H_{16}$  phase. Ultimately, much like the centre and edge of the deposition plate for the  $H_2O$ -rich sample, at the edge of the deposition plate for the  $C_{10}H_{16}$ -rich sample, peaks at  $2\theta = 31.7, 33.3, 34.4$  and  $36.2^\circ$  are observed. They are much greater in intensity when compared to the  $H_2O$ -rich sample which is expected due to a higher concentration of  $C_{10}H_{16}$ . These peculiar peaks do not align with the features seen in any DSCs as they appear from 95 K and interestingly, they decrease in intensity when approaching 260 K. However, this may be due to  $C_{10}H_{16}$  being expelled out of the amorphous matrix much more and also the irreversible transformation of ASW to ice *Isd* and finally, ice *Ih* may superimpose these peaks. Thus, they decrease in intensity.

The aim was to see if the DSC thermograms for the spatial distribution of the samples across the deposition plate aligned with the proposed theories of the formation and decomposition of clathrate hydrates. The question now would be which clathrate



#### 4. Matrix-Isolated Adamantane in Amorphous Ice

hydrate is formed? XRD analysis on these samples would confirm this. Unfortunately, the resulting XRD data did not align with the temperature of the features of the DSC thermograms, and many differences were displayed with temperature. After several attempts of trying to identify and solve the mysterious peaks, no conclusion could be made. Clathrate hydrates are seen as a model system used to study hydrophobic hydration in which this system with the  $C_{10}H_{16}$  guest species would be ideal. In the next section, a few more singular experiments were carried out in the hope of yielding clathrate hydrates from this complex mixture.

Simply, it could be proposed that a new clathrate hydrate is formed or that a new phase of  $C_{10}H_{16}$  has been identified.

##### 4.5.5 Thermal Annealing in the DSC

In a separate experiment, to test whether thermal annealing would have an effect on the exotherms as shown earlier, another sample of a 1:100  $C_{10}H_{16}/H_2O$  molar ratio was annealed at ambient pressure in the DSC at 130 K for 24 hours (Figure 4.28). Also considering the features as previously seen in the XRD patterns (Figure 4.24), it was necessary to anneal the equally prepared sample before the DSC exotherms are seen to ensure the samples are reproducible. Thus, the 130 K temperature was chosen to ensure the sample was annealed before the first exotherm and before the crystallisation of  $H_2O$  to ice *Isd*. For comparison, Figure 4.28 also includes a previous DSC scan that has not been annealed for 24 hours. The thermal annealing was successful in reproducing the same DSC scan as seen by the presence of the exotherm at 160 K on heating the sample past this temperature. The associated areas for the irreversible crystallisation of  $H_2O$  to ice *Isd* is found to be  $49 \text{ J mol}^{-1}$  for the 24 hours anneal in the DSC where this area was found to be significantly lower when compared to the sample which was not annealed in the DSC with an associated area of  $225 \text{ J mol}^{-1}$ . No shift of the 160 K exotherm was found with respect to both samples. The crystallisation is significantly suppressed in the DSC when annealed for 24 hours at 130 K due to irreversible processes taking place.

#### 4. Matrix-Isolated Adamantane in Amorphous Ice

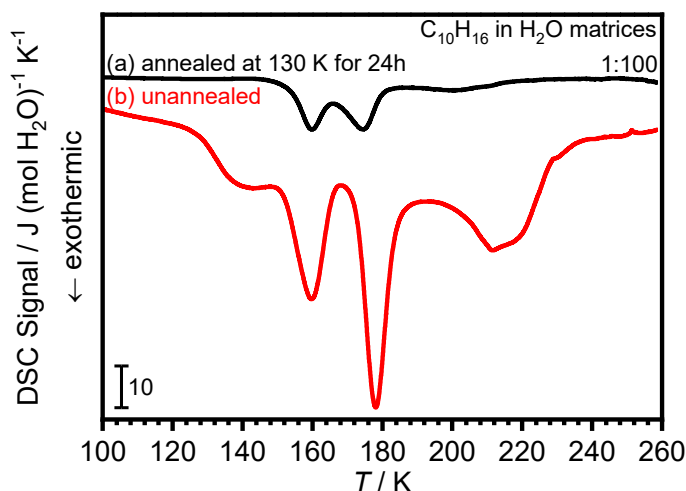


Figure 4.28. DSC thermogram of  $C_{10}H_{16}$  in  $H_2O$  matrices with the indicated  $C_{10}H_{16}/H_2O$  molar ratio heated at  $10\text{ K min}^{-1}$ , where (a) sample thermally annealed at 130 K for 24 hours in the DSC (black line) and (b) sample that was not annealed in the DSC (red line). The DSC signal is normalised per mole of  $H_2O$ .

Beyond the well-known irreversible transitions of ASW to ice *Isd*, the onset temperature of the second exotherm is found at 166 K for the sample annealed in the DSC for 24 hours, however, it is interesting to note that sample that was not annealed in the DSC has an onset temperature of 169 K. Similarly, this second feature is seen to display an exotherm at 175 and 178 K, respectively. The early onset temperature and features for the long-annealed sample may be due to the relaxation of the sample. This feature could be assumed to be the formation of a hydrate since it occurs after the formation of ice *Isd* as mentioned previously. The associated area of this sample is given by a value of  $56\text{ J mol}^{-1}$  compared to the sample unannealed in the DSC with an area of  $369\text{ J mol}^{-1}$ . Nevertheless, the  $\Delta H$  associated with the long-annealed sample is almost seven times smaller the value than seen for the sample that was unannealed in the DSC. After the second exotherm and upon further heating up to the maximum temperature, there is a broad feature where the onset of the third feature is seen at 186 K, ending at approximately 227 K, with the exotherm peak at 200 K. This feature is stretched out across the rest of the DSC thermogram and could infer that there is some decomposition of a potential clathrate hydrate taking place. Since XRD data could not be gathered for 24 hours inside the vacuum chamber to confirm the presence of a clathrate hydrate, more structural information would be needed.

## 4.5.6 Thermal Annealing inside the Vacuum Chamber to 180 K

To further probe and yield the possible ways in which a clathrate hydrate could be formed, a concentrated 1:34 sample was codeposited for three hours. After deposition, the sample was annealed within the chamber at 180 K, cooled back down to 80 K and removed for characterisation. The corresponding DSC thermograms and XRD patterns are depicted in Figure 4.29(a) and Figure 4.29(b). This sample was annealed at 180 K since this is where the proposed clathrate hydrate is observed in the previous DSC thermograms after the transition to ice *Isd*.

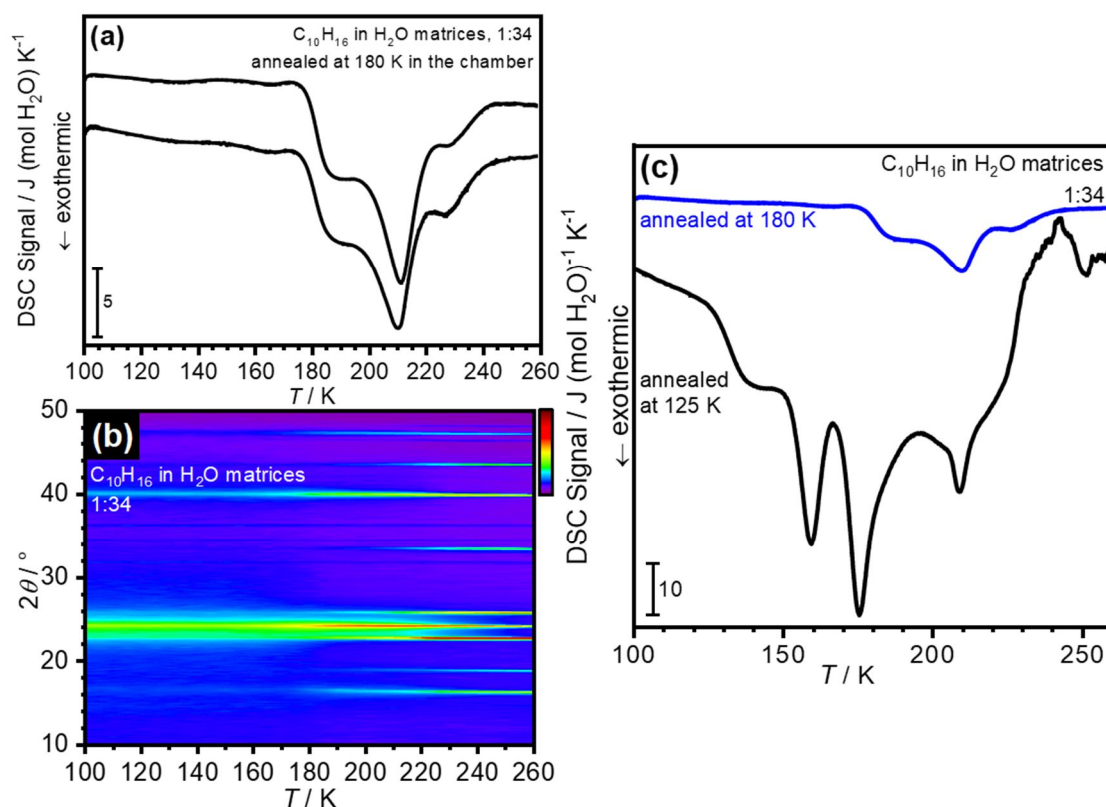


Figure 4.29. Characterisation of a sample of 1:34  $C_{10}H_{16}/H_2O$  molar ratio annealed in the vacuum chamber at 180 K where, (a) DSC thermogram of the sample with the indicated  $C_{10}H_{16}/H_2O$  molar ratio heated at  $10\text{ K min}^{-1}$  and ambient pressure, (b) corresponding XRD ( $Cu\ K\alpha$ ,  $\lambda = 1.54\text{ \AA}$ ) temperature program heated from 95 to 260 K and (c) calorimetric comparison of the sample annealed at 180 K in the chamber (blue line) and typical sample annealed at 125 K in the chamber (black line). The DSC signals for (a) and (c) have been normalised per mole of  $H_2O$ .

As the sample was annealed at 180 K in the chamber before removal, the sample already crystallised within the chamber and therefore does not display the ASW to ice *Isd* transition at 160 K [Figure 4.29(a)]. The start of first offset in the thermograms are seen at 175 K and subsequently, at 185 K, the peak is seen to drop and display an exotherm. Further to this drop, the peak plateaus from 185 K until 200 K where a further decrease

#### 4. Matrix-Isolated Adamantane in Amorphous Ice

is seen. At 212 K, a strong feature is displayed and could be attributed to the decomposition of a clathrate hydrate. It is problematic to determine the associated area in these thermograms due to the difficulty in choosing integration limits. The increase in temperature during the offset at the 175 K exotherm and further until 200 K is not consistent with the recorded XRD patterns. The XRD patterns in Figure 4.29(b) exhibited several peaks which are assigned to ice *Ih* and  $C_{10}H_{16}$ , except for a feature that was present from 95 K through to 260 K. This feature was found at  $2\theta = 34.5^\circ$ . This peculiar feature did not grow in intensity but rather stayed the same intensity and persisted throughout all temperature patterns.

In the next step in the analysis of this feature in the XRD patterns, analysis with GSAS was carried out and the XRD patterns were refined and scrutinised against all clathrate hydrate phases. Yet, no identification against any known clathrate hydrates was achieved. The possibility of the sample being contaminated was eliminated; copper oxide (CuO) and copper (Cu) were investigated as potential sources of contamination arising from the deposition plate. Cu peaks are observed only at  $2\theta = 43.62^\circ$  and  $50.81^\circ$  due to its very small unit cell and no peaks from the mixtures aligning with Cu Bragg peaks were observed. The same investigation was carried out for CuO and was also, eliminated as a potential source of contamination.

Figure 4.29(c) displays the DSC thermogram from Figure 4.26(a) compared with a sample of the same molar ratio (1:34), which was annealed at 125 K only. There are significant differences between both samples. The feature seen at 175 K for both thermograms is more pronounced in the sample that was only annealed at 125 K. The feature after 175 K, seen at 212 K as mentioned earlier could be assigned to clathrate hydrate decomposition. Only the thermogram that was annealed at 125 K, displayed  $H_2O$  crystallisation. Comparing both thermograms with one another, it can be proposed that a clathrate hydrate forms and decomposes after the transformation to ice *Isd*. In the case of the corresponding XRD pattern, no features arise after 175 K that were not previously mentioned before. The absence of Bragg peaks in XRD as seen in the DSC could be speculated to the assumption that the clathrate hydrate may form the transition of ASW to ice *Isd*. Since lots of changes occur during this transition, in this ‘chaos’, a clathrate hydrate may form. The possibility of the X-ray beam not passing through the sample can be eliminated since the XRD spot is large and thus, one is sampling most of the sample already. It is unclear as to why there are differences in the calorimetric and diffraction data seeing as the sample is from the same experiment.

#### 4. Matrix-Isolated Adamantane in Amorphous Ice

In the case of the DSC thermograms, once again, the only probable explanation for the extra features in line with the species in this system is that ice *Isd* is the active material for making the clathrate hydrate. However, since no current or known phases of clathrate hydrate could be assigned to any XRD data or DSC data, there may be a possibility that these unexplainable features are a new clathrate hydrate or a new phase of  $C_{10}H_{16}$ . It is quite strange that not much is seen in XRD when the sample was annealed in the chamber at 180 K.

To reiterate, due to the indistinguishability of the features in the XRD patterns from the same repeats of the same samples, another dependable technique was adopted in order to determine the existence of these features.

##### 4.5.7 Effect of Fully Baffling the Flow of $H_2O$

In an attempt to increase the yield of clathrate hydrates, the  $H_2O$ -inlet tube was baffled with a metal plate as described in Chapter 3. After codeposition for three hours at the ideal sH hydrate composition ratio of 1:34 for  $C_{10}H_{16}/H_2O$ , the sample was annealed at 125 K and cooled back down to 90 K for removal. The question is what would happen to this mixture with a fully obstructed  $H_2O$  flow, since  $H_2O$  should essentially adsorb from random directions which may lead to more clathrate hydrates.

The DSC thermograms show exothermic peaks as previously observed and are labelled in Figure 4.30. Once again, several features are observed which are not solely attributed to pure ASW. The feature labelled (i) is due to the annealing step in the chamber at 125 K, (ii) is the irreversible phase transition of pure ASW to ice *Isd*, (iii) may be proposed to be the formation of a new clathrate hydrate and (iv) is the possible decomposition of the clathrate hydrate. These features are very prominent and more structural analysis is needed to identify whether these features are tangible with the proposals of a clathrate hydrate. The green thermogram as depicted in Figure 4.30 is a typical trace of the same ratio that has been baffled only with an iron mesh and placed in the figure for comparison with a fully baffled with a metal plate sample.

#### 4. Matrix-Isolated Adamantane in Amorphous Ice

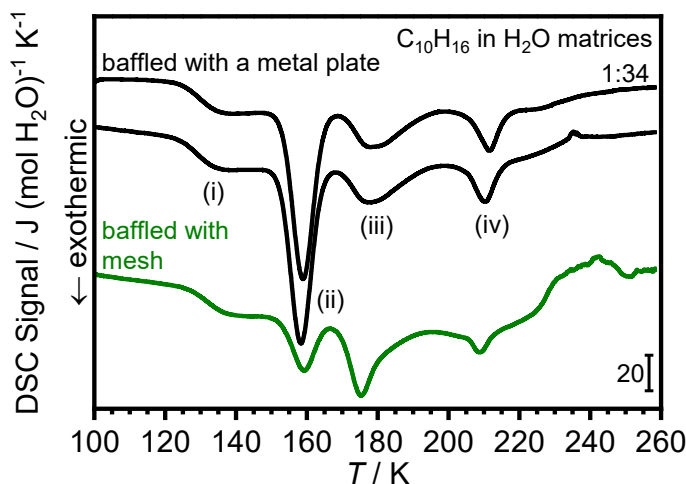


Figure 4.30. DSC thermograms from a sample of 1:34 molar ratio of  $C_{10}H_{16}/H_2O$  heated at  $10\text{ K min}^{-1}$  after deposited with a metal plate baffling the  $H_2O$ -inlet tube (black scans). The green scan has been placed at the bottom of the figure to show a comparison of not baffling with a metal plate. The DSC signals are normalised with respect to per mole of  $H_2O$ .

XRD patterns were recorded in 10 K steps from 100 K to 270 K, with an initial pattern recorded at 94 K. Figure 4.31 illustrates the large low-temperature XRD profile for every pattern recorded at each temperature for the 1:34  $C_{10}H_{16}/H_2O$  molar ratio mixture prepared by the blocked  $H_2O$ -inlet tube. The diffraction intensities have been square rooted to highlight and emphasise the weaker features. Although it is difficult to view in Figure 4.31, at 94 K, the sample is purely amorphous without the presence of any Bragg reflections for  $C_{10}H_{16}$ . This is quite interesting since these Bragg reflections were quite strong for the 1:34 sample that was not baffled with a metal plate. At 130 K, ice *Isd*, starts to form very slowly and a Bragg peak for  $C_{10}H_{16}$  starts to form at  $2\theta = 16.771^\circ$ . Similarly, the second peak for  $C_{10}H_{16}$  starts to grow at  $2\theta = 19.001^\circ$ . Upon a temperature increase, these two  $C_{10}H_{16}$  peaks grow to become sharper and more intense. This is due to embedded  $C_{10}H_{16}$  being expelled and forced out of the amorphous matrix.

Overall, the mixture experiences the transition from amorphous to ice *Isd* and thus, ice *Ih* and crystalline  $C_{10}H_{16}$ . During this temperature program, no extra peaks due to clathrate hydrates can be seen and only reflections from ice *Ih* and  $C_{10}H_{16}$  can be identified. This may be due to preferred orientation as in the corresponding DSC signals, features can be assigned to the formation and decomposition of clathrate hydrates. In this case, it was not possible to identify any structural information on the clathrate hydrate,

however, these findings and data analysis evidently display the complexity of these mixtures and systems.

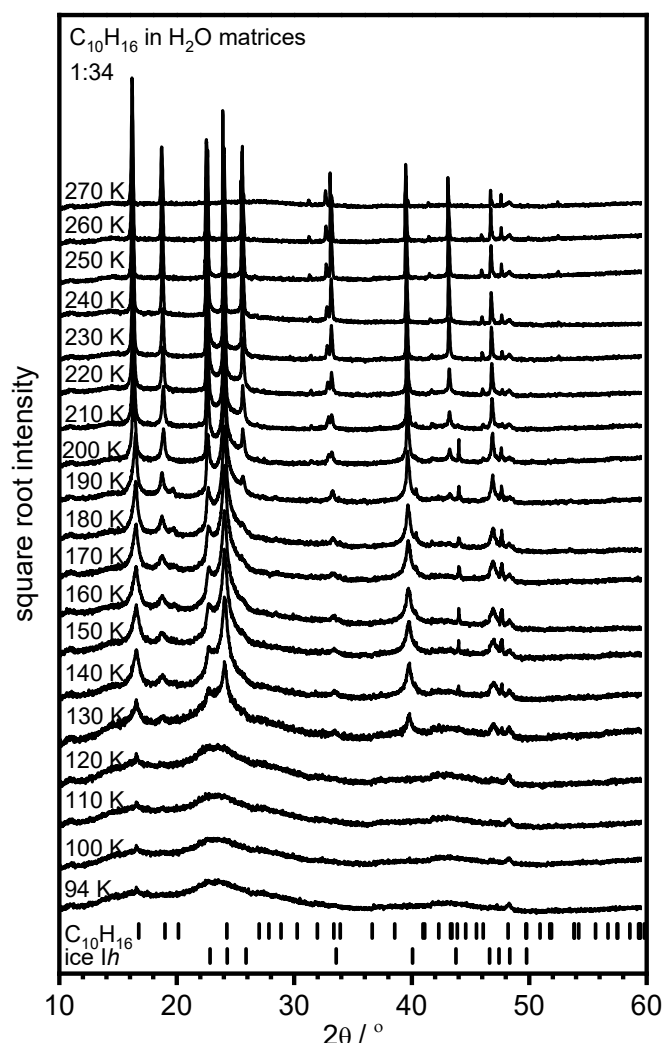


Figure 4.31. Complete set of XRD data (Cu  $K\alpha$ ,  $\lambda = 1.54 \text{ \AA}$ ) recorded from 94 to 270 K of a 1:34  $C_{10}H_{16}/H_2O$  mixture prepared by blocking the  $H_2O$ -inlet tube with a metal plate. The indicated tickmarks show the expected Bragg peaks for ice Ih and  $C_{10}H_{16}$ .

### 4.5.8 $C_{10}H_{16}$ in $H_2O$ Matrices with the Addition of Argon Gas

The additional use of a small ‘help-gas’ incorporated within the mixture of  $C_{10}H_{16}$  and  $H_2O$  may be considered beneficial for these experiments as they are thought to stabilise small cages that exist alongside larger cages. To investigate the influence of a ‘help-gas’, in this case, argon gas was used. For the formation of a clathrate hydrate with a large cage, the argon help-gas was introduced into the system at a rate of  $1.35 \times 10^{-5} \text{ mmol s}^{-1}$  (as measured in Chapter 3) into the chamber for a 1:34 molar ratio of  $C_{10}H_{16}/H_2O$  for three hours of deposition. Using the 15 cm deposition distance between the aperture and

#### 4. Matrix-Isolated Adamantane in Amorphous Ice

the H<sub>2</sub>O-inlet tube will create a concentration gradient of C<sub>10</sub>H<sub>16</sub> hydrophobes across the eight-inch diameter deposition plate.

Figure 4.32(a) displays the DSC thermograms from the argon ‘help-gas’ incorporated into the C<sub>10</sub>H<sub>16</sub>/H<sub>2</sub>O 1:34 mixture. As previously mentioned, the feature labelled (i) is due to the annealing stage at 125 K in the vacuum, (ii) crystallisation of H<sub>2</sub>O to ice *Isd*, (iii) proposed formation of clathrate hydrates and (iv) proposed decomposition of this clathrate hydrate. Nevertheless, these thermograms are significantly different from pure ASW and shown to be from a highly complex system. Using XRD measurements for the same sample, Figure 4.32(b) and Figure 4.33 depict the temperature program run on the C<sub>10</sub>H<sub>16</sub>+Ar:H<sub>2</sub>O sample. The transformation from ASW to ice *Isd* and then further to ice *Ih* can be seen as the broad feature centred at  $2\theta = 24^\circ$  transforms to a trident, characteristic of ice *Isd* and further, ice *Ih*. C<sub>10</sub>H<sub>16</sub> was seen to aggregate upon annealing and the two most intense Bragg features for C<sub>10</sub>H<sub>16</sub> are seen at  $2\theta = 16.771^\circ$  and  $19.001^\circ$ . No additional peaks can be seen other than the two species, H<sub>2</sub>O and C<sub>10</sub>H<sub>16</sub> and thus, no assignments due to argon gas to any known clathrate hydrate could be identified. In this case, it is suitable to say that the amount of argon gas deposited was significantly insufficient and so no clathrate hydrates were yielded. It can also be noted that there may be some preferred orientation in this case. This arises when there is a strong tendency for the sample as a powder to be in an orientation more than one way than compared to others. Thus, during the temperature program, the beam of X-rays did not focus on an orientation where the concentration of clathrate hydrates was greater. Nevertheless, it is probable that a clathrate hydrate has formed but the nature of the structure and type of clathrate hydrate has not yet been identified.



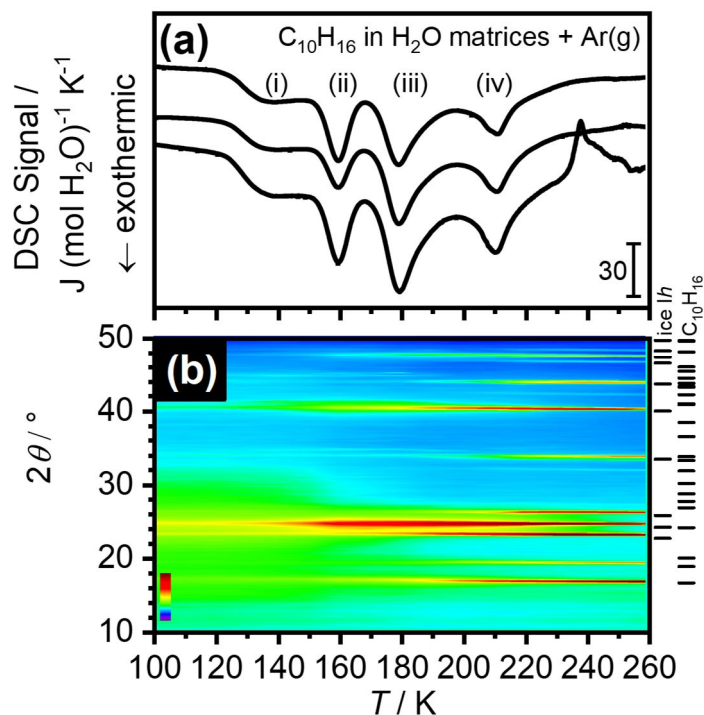


Figure 4.32. (a) DSC thermograms for a 1:34 mixture of  $C_{10}H_{16}/H_2O$  with argon gas heated at a rate of  $10\text{ K min}^{-1}$ . These DSC scans were normalised per mole of  $H_2O$ . (b) XRD data (Cu  $K\alpha$ ,  $\lambda = 1.54\text{ \AA}$ ) of a mixture  $C_{10}H_{16}/H_2O$  with argon gas upon heating shown by the contour plot of the patterns recorded upon heating from 100 K to 260 K in steps of 10 K. The intensity from the diffraction data is shown on a square-root scale to emphasize the weaker features in the patterns. The tickmarks on the side of the panel in (b) indicate the expected Bragg peak positions for ice  $I_h$  and  $C_{10}H_{16}$ . The complete set of raw diffraction data is shown in Figure 4.33 below.

The full view of the XRD patterns recorded upon annealing the sample to 260 K is depicted below in Figure 4.33. The sample is fully amorphous at 95 K with a few impurities of external ice  $I_h$  on the sample holder. A slight small shoulder at  $2\theta = 16.771^\circ$  is assigned to  $C_{10}H_{16}$ . Ice  $I_{sd}$  fully forms at 160 K and  $C_{10}H_{16}$ 's second peak at  $2\theta = 19.001^\circ$  begins to form. The two  $C_{10}H_{16}$  peaks grow as the temperature increases and become sharper and more intense. By 260 K, some  $H_2O$  is present in the sample and only  $C_{10}H_{16}$  peaks at low  $2\theta$  angles are present. Once again, no other peaks can be assigned to any existing clathrate hydrates and only  $C_{10}H_{16}$  and  $H_2O$  are present, exhibiting the well-mixed nature of both species.

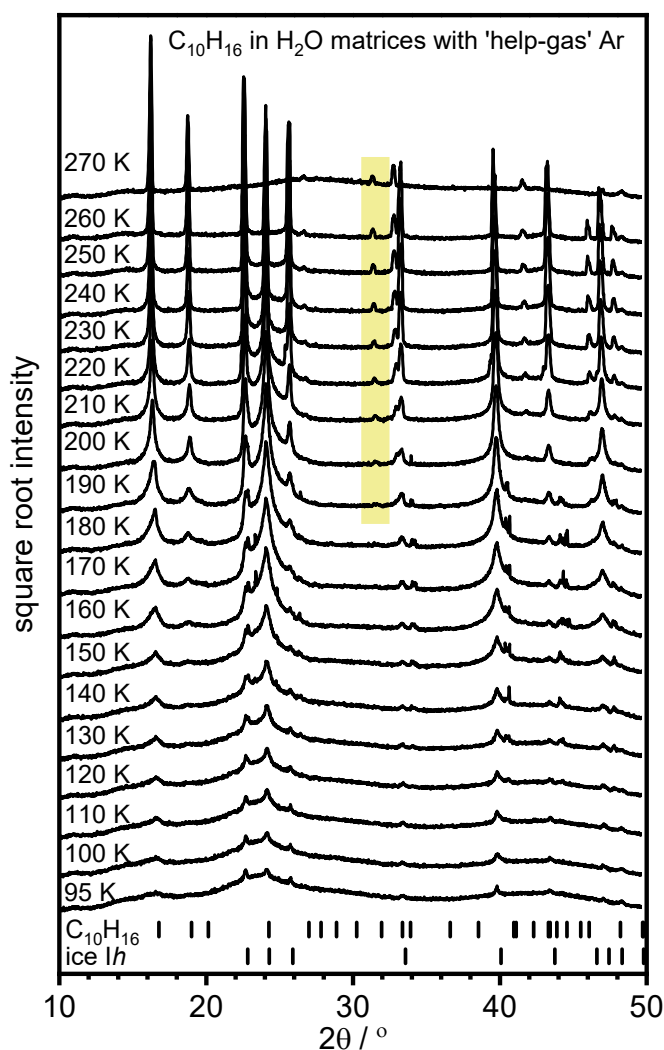


Figure 4.33. Complete set of XRD data (Cu K $\alpha$ ,  $\lambda = 1.54 \text{ \AA}$ ) following the temperature program recorded from 95 K to 270 K of a 1:34 C<sub>10</sub>H<sub>16</sub>/H<sub>2</sub>O/Ar mixture prepared by introducing argon gas through the H<sub>2</sub>O-inlet tube. The indicated tickmarks show the expected Bragg peaks for ice Ih and C<sub>10</sub>H<sub>16</sub>.

#### 4.5.9 Thermal Annealing in the Vacuum Chamber at 240 K

In this instance, the C<sub>10</sub>H<sub>16</sub>/H<sub>2</sub>O sample at a 1:34 molar ratio was annealed in the vacuum chamber after three hours of deposition past 240 K (still in the vacuum chamber) and further removed for characterisation. The sample, once removed, looked very fine and powder-like, and so it was very difficult to remove from the plate into the sample holder. This experiment was carried out to determine whether the clathrate hydrate remained and was stable, thus, extracting the pure hydrate only. It has been proposed in this study that a clathrate hydrate has already been made and therefore, producing them in the chamber should give a clathrate hydrate at 180 K in diffraction. Unfortunately, during this heating step in the chamber, all H<sub>2</sub>O desorbed, and no clathrate hydrate was prepared in the high vacuum chamber. The data has not been shown here as the data implied that no sample

#### 4. Matrix-Isolated Adamantane in Amorphous Ice

was present in the sample holder, however, since it was extremely difficult to remove the samples from the deposition plate and into the sample holder, best efforts were carried out to ensure as much sample was placed into the XRD sample holder.

##### 4.5.10 Thermal Annealing in the Vacuum Chamber at 200 K

As in section 4.5.9, the next step was to heat the sample in the chamber to only 200 K, essentially heating above the clathrate hydrate temperature yet not allowing decomposition to take place in the chamber as seen in previous XRD measurements where the clathrate hydrates have been proposed to form after ice *Isd*. In this case, the same conclusion can be extracted as previously, such that, most H<sub>2</sub>O desorbed, C<sub>10</sub>H<sub>16</sub> was expelled out of the matrix and no hydrates could be formed within the vacuum chamber. The DSC and XRD measurements support this conclusion; clathrate hydrates cannot be made within a high-vacuum with the experimental set-up used in this study. It is important to appreciate how highly complex and well-mixed this matrix is. Figure 4.34 displays the DSC and XRD data obtained from this experiment.

#### 4. Matrix-Isolated Adamantane in Amorphous Ice

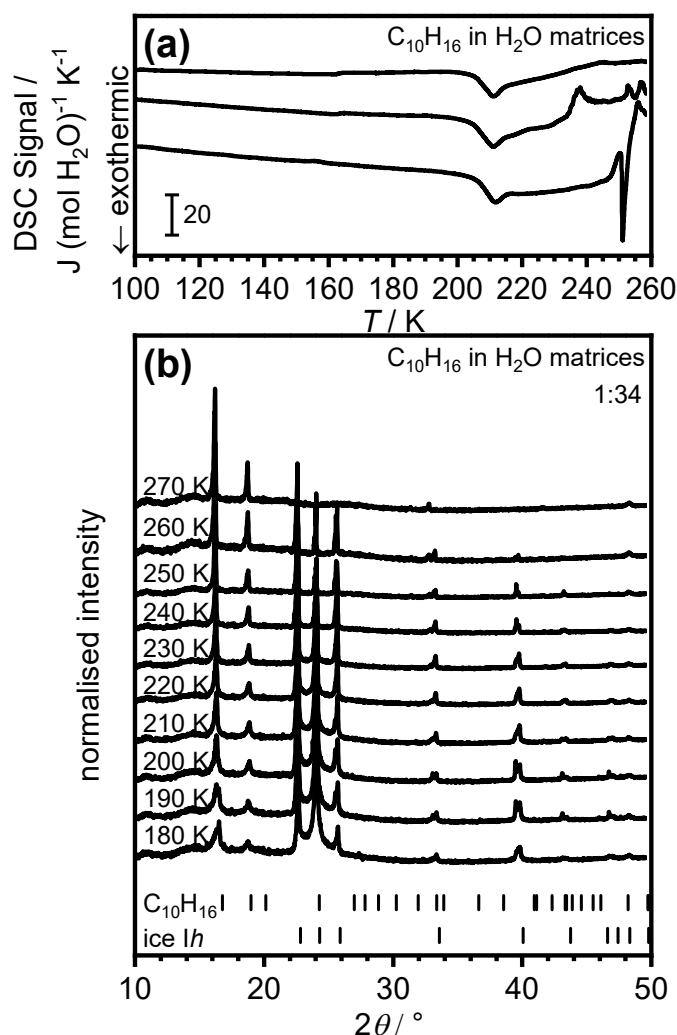


Figure 4.34.(a) DSC thermograms for a 1:34 mixture of C<sub>10</sub>H<sub>16</sub>/H<sub>2</sub>O sample heated to 200 K in the vacuum chamber and then removed after cooling to 80 K and recorded in the DSC at a rate of 10 K min<sup>-1</sup>. These DSC scans were normalised per mole of H<sub>2</sub>O, (b) the complete set of XRD data (Cu Kα, λ = 1.54 Å) following the temperature program recorded from 180 K to 260 K at 10 K min<sup>-1</sup> of a 1:34 C<sub>10</sub>H<sub>16</sub>/H<sub>2</sub>O mixture prepared by heating the sample in the vacuum chamber to 200 K. The indicated tickmarks show the expected Bragg peaks for ice Ih and C<sub>10</sub>H<sub>16</sub>.

The exotherm in Figure 4.34(a) at 212 K is interesting. If no clathrate hydrate is seen in the DSC, the question becomes, why is there an exotherm at this temperature? This is usually allocated to the decomposition of the clathrate hydrate. Since the DSC and XRD did not show any extra features that are already mentioned, no conclusion could be obtained other than ice Ih formation. Simply, C<sub>10</sub>H<sub>16</sub> was observed to expel out of the ASW matrix and the crystallisation of H<sub>2</sub>O to ice Ih had already occurred inside the vacuum chamber.

4.5.11 C<sub>10</sub>H<sub>16</sub> in H<sub>2</sub>O Matrices of Very High Concentration

To further probe the possibility of yielding a clathrate hydrate, and to examine the effect of the concentration of C<sub>10</sub>H<sub>16</sub> guest species in ASW, 1:6 and 1:19 molar ratios of C<sub>10</sub>H<sub>16</sub>/H<sub>2</sub>O mixtures were characterised with XRD and DSC (Figure 4.35).

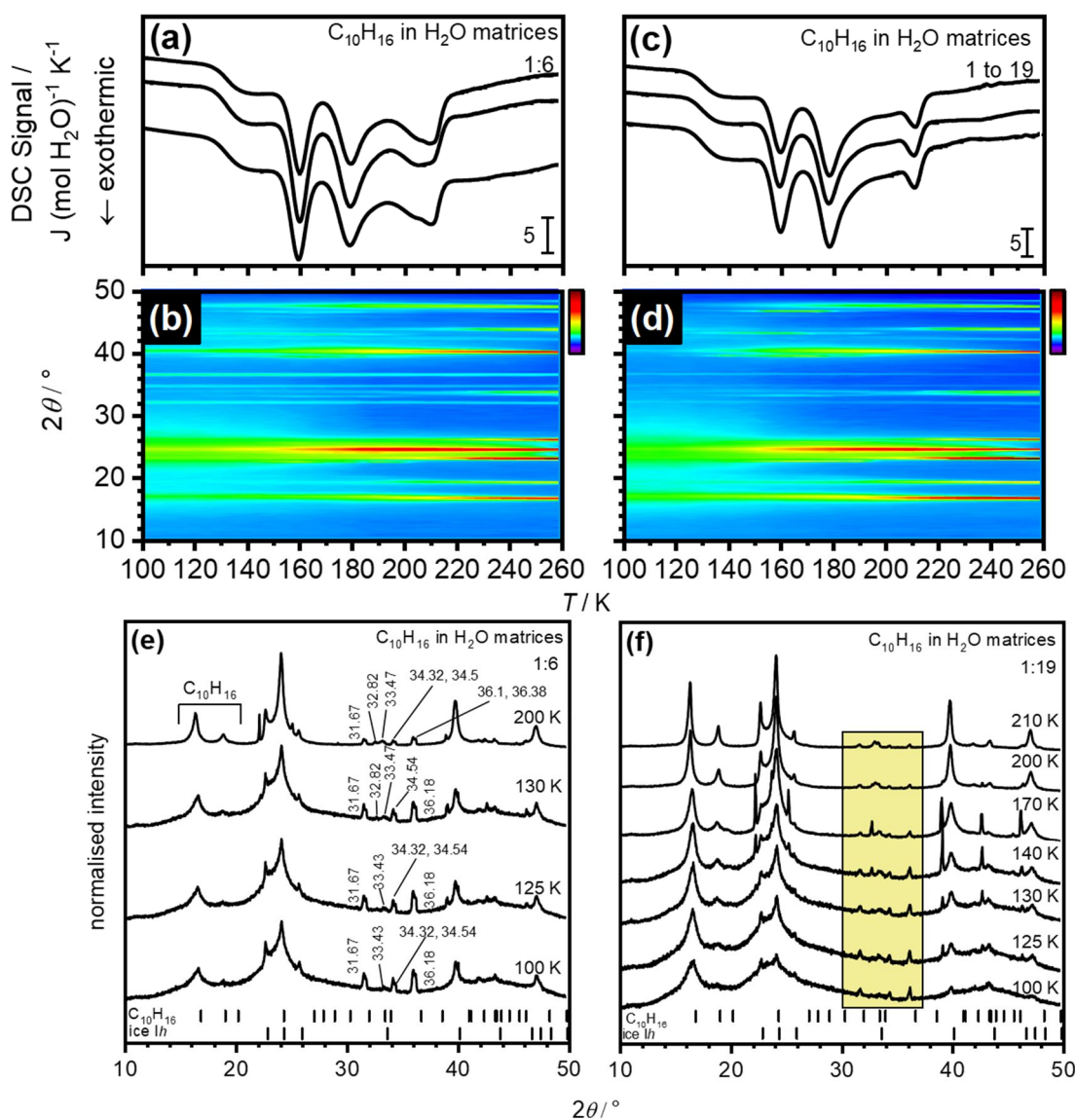


Figure 4.35. (a) and (c) DSC thermograms for a 1:6 and 1:19 mixture of C<sub>10</sub>H<sub>16</sub>/H<sub>2</sub>O, respectively, heated at a rate of 10 K min<sup>-1</sup>. These DSC scans were normalised per mole of H<sub>2</sub>O. (b)–(f) XRD patterns (Cu Kα, λ = 1.54 Å) of a mixture C<sub>10</sub>H<sub>16</sub>/H<sub>2</sub>O and molar ratios of 1:6 and 1:19, respectively shown by the contour plot of the patterns recorded upon heating from 100 K to 200 K in steps of 5 K and then 200 K to 260 K in steps of 10 K and selected patterns to show differences in Bragg features, respectively. Panel (e) has indicated Bragg positions on each diffraction pattern and panel (f) has been marked with a yellow shaded box to show where the Bragg features are found. The intensity from the diffraction data is shown on a square-root scale to emphasize the weaker features in the patterns. Tickmarks indicate the expected Bragg peaks for ice Ih and C<sub>10</sub>H<sub>16</sub>.

#### 4. Matrix-Isolated Adamantane in Amorphous Ice

Figure 4.35(a) and Figure 4.35(c) first show the DSC thermograms of the highest concentrated  $C_{10}H_{16}/H_2O$  mixtures, 1:6 and 1:19, respectively. Intriguingly, as described earlier, four discernible features in the DSC are observed. The thermograms in general are significantly distinct when compared to pure ASW (Chapter 2, Figure 2.14). The appearance of the calorimetric data does not show any differences in delayed exotherms, however, have much smaller associated areas for each feature. Both sets of thermograms indicate the annealing stage that occurs in the chamber at 125 K, a sharp exotherm is then observed for the well-known crystallisation of  $H_2O$  to ice *Isd* with an associated area of  $80 \pm 7 \text{ J mol}^{-1}$  and  $70 \pm 8 \text{ J mol}^{-1}$ , for Figure 4.35(a) and Figure 4.35(c), respectively. These areas are significantly smaller than that of pure ASW ( $1260 \pm 35 \text{ J mol}^{-1}$ ) and other molar ratios as listed previously. The addition of  $C_{10}H_{16}$  has significantly impacted the  $\Delta H$  associated with the crystallisation peak since the associated area here is approximately 16 times smaller than pure ASW.

Previously, for less concentrated samples, the third feature was observed at 175 K. The onset of the third sharp feature in Figure 4.35(a) and Figure 4.35(c) is observed at 169 K, 6 K less than previously seen. After 169 K for each set of thermograms, two features are seen simultaneously, one at 180 K and the last at 211 K. Once again, these two features can be assigned to coincide with the formation and decomposition of the clathrate hydrate, respectively. The feature at 211 K appears to be boarder, slightly distorted and stretched out more for the 1:6 sample when compared to the 1:19 sample. Both these features (180 K and 211 K) have similar areas, and they occur immediately after one another. The third feature is found at 210–212 K with an associated area of  $63 \pm 4 \text{ J mol}^{-1}$  and  $22.31 \pm 1 \text{ J mol}^{-1}$ , for the 1:6 and 1:19 molar ratios, respectively. This difference could be attributed to the significant difference in composition and a slow energy process taking place. Yet again, it is possible to assume a clathrate hydrate is formed but structural analysis from the diffraction data is needed. The question still remains as to what the exact nature of the features results from in the DSC, since Bragg peaks associated with only ice *Ih*,  $C_{10}H_{16}$ , and a few unassignable peaks can be seen in the XRD patterns at temperatures from 95 K to 260 K as depicted in Figure 4.35(b) and Figure 4.35(d).

The exotherms cannot simply result from only  $C_{10}H_{16}$  and ASW. Nevertheless, many abrupt features are seen after the crystallisation of  $H_2O$  to ice *Isd*, indicative of a highly complex mixture. Table 4.11 lists the summary of associated areas with the

#### 4. Matrix-Isolated Adamantane in Amorphous Ice

pronounced features in the thermograms as seen in Figure 4.35. Figure 4.35(b) and Figure 4.35(d) show the XRD patterns of the highly concentrated  $C_{10}H_{16}/H_2O$  mixtures. Despite the observations of a fully amorphous sample and  $C_{10}H_{16}$  intensifying upon heating as mentioned earlier, the XRD pattern already at 95 K for Figure 4.35(c) and Figure 4.35(d) display Bragg features which are consistent throughout the experiment until 270 K. The specific differences are shown in Figure 4.35(e) and Figure 4.35(f).

Despite the assignment of ASW, ice *Isd*, ice *Ih* and  $C_{10}H_{16}$  expelled out of the amorphous matrix, several other Bragg peaks are observed which are very similar to what has already been identified in earlier sections. Remarkably, Bragg features that do not disappear at any temperature are observed once again at  $2\theta = 31.6, 33.5$  (ice *Ih*),  $34.5$  and  $36.2^\circ$  for both ratios and do not cease to persist upon heating. It is safe to say that this case arises already from the beginning of heating and the system is undoubtedly extremely complex. For the 1:19 sample, the appearance of these Bragg features intensify after 125 K and the appearance of these features are generally less intense when compared to the 1:6 sample. The significant crystallographic Bragg feature identified here is observed at  $2\theta = 32.8^\circ$  and appears at 130 K, remaining until 260 K for the 1:6 sample and appears at 140 K for the 1:19 sample, again remaining until 260 K. However, in the latter molar ratio, this feature seems to appear with and coincide with the ice *Ih* peak at  $2\theta = 33.5^\circ$ . A full list of these Bragg features is defined in Table 4.12, where it is possible to see how they appear with temperature in comparison to each sample.

The peak of  $2\theta = 16.001^\circ$  originating from  $C_{10}H_{16}$  is already seen at 95 K, however only at 130 K, at a push, it can be stated the second  $C_{10}H_{16}$  peak is seen at  $2\theta = 19.771^\circ$ , which upon heating, shifts to lower  $d$ -spacing and is found at  $2\theta = 18.83^\circ$ . It is apparent from Figure 4.35, that the evolution of the concentrated sample with thermal annealing in diffraction, displays a faster appearance of Bragg peaks when compared to a 1:100 sample, where very much delayed  $C_{10}H_{16}$  peaks are seen. Unfortunately, Bragg peaks could not be assigned to any known clathrate hydrate and structural shifts could not be pinpointed since the XRD pattern features did not correlate well with the DSC thermogram features. The crystallisation of  $H_2O$  is not affected by the higher concentration of  $C_{10}H_{16}$  in the mixtures. However, it was still necessary to reach such high concentrations to additionally see if there was an effect on ASW.

## 4. Matrix-Isolated Adamantane in Amorphous Ice

The disparity between the diffraction data with respect to intensity presented in this section compared to the diluted samples could result from the sample having more crystalline domains.

*Table 4.11. Summary of the spread of enthalpies relating to pure ASW and codeposited samples from indicated molar ratios in Figure 4.35. Samples were deposited into the vacuum chamber via a pellet and annealed at 125 K. The DSC thermograms were recorded at 10 K min<sup>-1</sup> and at ambient pressure.*

Sample	Figure	$\Delta H / \text{J mol}^{-1}$		
		160 K	180 K	211 K
1:6	4.35(a)	80 $\pm$ 7	79 $\pm$ 8	63 $\pm$ 4
1:19	4.35(b)	70 $\pm$ 8	116 $\pm$ 6	22 $\pm$ 1
Pure ASW	-	1260 $\pm$ 35	-	-

*Table 4.12. Summary of the peculiar Bragg features with respect to the temperatures they appear in the XRD patterns in Figure 4.35(b), (d), (e) and (f). The Bragg peaks in parentheses are found in the XRD patterns as a double feature peak and the asterisk is marked since no extra features were observed at that temperature.*

$T / \text{K}$	$\text{C}_{10}\text{H}_{16}/\text{H}_2\text{O}$ , 1:6 molar ratio	$\text{C}_{10}\text{H}_{16}/\text{H}_2\text{O}$ , 1:19 molar ratio
95–125	31.67, (34.32 & 34.5), 36.18	31.8, 34.5, 36.32
130	31.67, 32.82, (33.47 & 34.5), 36.18	31.8, 34.5, 36.32
140–170	*	31.8, 32.89, 34.5, 36.32
200	31.6, 32.72, 33.34, (34.32 & 34.5), (36.18 & 36.38)	31.8, (32.8 & 33.19 & 33.49), 34.5, 36.32

### 4.5.12 Codeposition from a Round-Bottom Flask

Since each experiment carried out *via* the pellet method displayed results that could not identify the presence of the peculiar features in the DSC and XRD, it was decided that a different method to deposit the samples would be carried out. The spatial distribution of the sample on the deposition plate was found to be non-uniform and so, this next step would ensure that H<sub>2</sub>O and C<sub>10</sub>H<sub>16</sub> would be emitted from a single inlet tube, directly onto the plate to prevent any discrepancies. A uniform ratio would be expected for this approach and so, C<sub>10</sub>H<sub>16</sub> was deposited through a round-bottom flask and introduced into the vacuum chamber through the same inlet tube as used for the deposition of H<sub>2</sub>O. Both species mix together in the inlet tube and are deposited onto the plate through one location only. The XRD and DSC measurements for varying ratios are displayed in Figure 4.36 and Figure 4.37.



#### 4. Matrix-Isolated Adamantane in Amorphous Ice

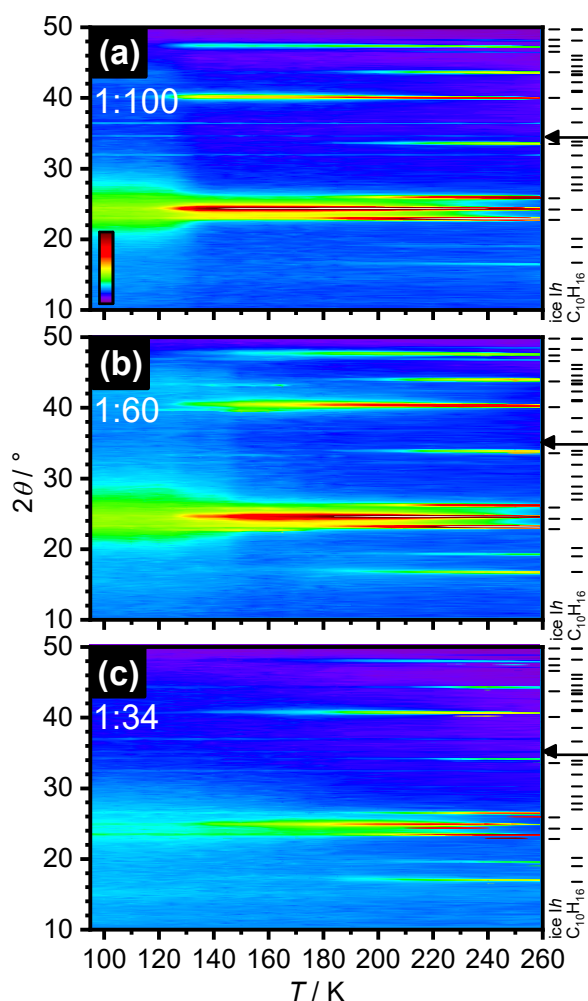


Figure 4.36. Contour plots of XRD patterns ( $\text{Cu K}\alpha$ ,  $\lambda = 1.54 \text{ \AA}$ ) recorded upon heating from 95 K to 260 K at ambient pressure for  $\text{C}_{10}\text{H}_{16}/\text{H}_2\text{O}$  deposited from a round-bottom flask with indicated molar ratios. The black arrows on the right-hand side of the contour plots highlight the position of  $2\theta = 34.5^\circ$ . The tickmarks on the side of the panels indicate the expected Bragg peak positions for ice Ih and  $\text{C}_{10}\text{H}_{16}$ .

With the exception of the crystallisation of  $\text{H}_2\text{O}$  and  $\text{C}_{10}\text{H}_{16}$  expelling out of the amorphous matrix upon thermal annealing, several peaks were observed with every ratio deposited onto the deposition plate.

The position of Bragg peaks occurring at different temperatures can be drawn for the 1:100 molar ratio of  $\text{C}_{10}\text{H}_{16}/\text{H}_2\text{O}$ , whereby, the expelling of  $\text{C}_{10}\text{H}_{16}$  out of the amorphous matrix is only seen slightly at a starting temperature of 200 K and further up to 260 K. However, what is interesting to note is, this is only one Bragg peak at  $2\theta = 16.001^\circ$ . The second peak, most frequently seen to intensify with this peak is not present as seen in Figure 4.36(a). A very small amount of  $\text{C}_{10}\text{H}_{16}$  is present in this sample, which is reasonably expected due to the highly  $\text{H}_2\text{O}$ -rich sample. In addition, already from the start of the temperature program at 95 K, Bragg peaks at  $2\theta = 31.9, 33.5$  (ice Ih),  $34.5$  and

#### 4. Matrix-Isolated Adamantane in Amorphous Ice

36.4° are present and grow until 125 K. After 130 K, the intensity of these peaks decreases significantly. As expected, at 210 K and  $2\theta = 33.5^\circ$ , ice *Ih* intensifies, and the peak sharpens until 260 K. The mysterious weak peak at  $2\theta = 34.5^\circ$  cannot be assigned to any known clathrate hydrate which is expected for a possible new clathrate hydrate. The main problem is that Bragg peaks are not systematic in any sense and the peaks are very weak. To complement the absence of the formation of a clathrate hydrate, in this case, the DSC thermogram [Figure 4.37(b)] only illustrates the crystallisation exotherm and no other exotherms are present. This conclusion is significantly different to when  $C_{10}H_{16}$  was deposited *via* a pellet as pellet experiments showed consistent DSC exotherms with corresponding unassignable Bragg peaks.

In Figure 4.36(b),  $C_{10}H_{16}$  is expelled out of the matrix after 190 K and not at 95 K for the 1:60 molar ratio of  $C_{10}H_{16}/H_2O$ , only a fully amorphous sample is seen at 95 K and thus, ASW transforms to ice *Isd* and ice *Ih* upon heating. No mysterious Bragg peaks in the region of  $2\theta = 31\text{--}36^\circ$  were displayed, however, the DSC thermogram for this ratio does not complement the absence of peaks in the diffraction data. The DSC thermogram [Figure 4.37(c)] illustrates the presumed formation of a clathrate hydrate and further, the decomposition of a clathrate hydrate. It can be speculated that perhaps there is preferred orientation within the system that may cause the absence of Bragg peaks which are seen in the calorimetry measurements. The long-range structure of the system may not be detected very well which causes the absence or presence of some peaks.

Similarly,  $C_{10}H_{16}$  is seen to grow out of the matrix after 190 K and not at 95 K for the  $C_{10}H_{16}$ -rich sample. This is significantly different compared to the samples that were prepared with a pellet. Essentially, depositing from a round-bottom flask delays the  $C_{10}H_{16}$  growing out of the matrix when compared to the samples prepared *via* a pellet. In Figure 4.36(c), from 115 K, several peaks appear. These are found at  $2\theta = 32.02$ , 34.64 and 36.42° and are not assigned to any known hydrate. During the thermal anneal, these Bragg peaks slightly shift towards lower  $2\theta$  angles. They remain throughout the experiment and do not intensify from 115 K to 260 K. At 200 K, the appearance of another peak at  $2\theta = \sim 33.7^\circ$  starts to grow which is characteristic of ice *Ih*. At 210 K, the appearance of a shoulder peak to the left-hand side of the Bragg peak at  $2\theta = 33.7^\circ$  is observed. This peak remains until 260 K. Such an observation could be attributed to the phase transition of  $C_{10}H_{16}$  where it transforms from tetragonal phase to the cubic phase after 208 K. Once again, as seen with the deposition of  $C_{10}H_{16}$  *via* a pellet, such peaks

#### 4. Matrix-Isolated Adamantane in Amorphous Ice

( $2\theta = 32.02, 34.64$  and  $36.42^\circ$ ) cannot be assigned to any known clathrate hydrate. However, the DSC thermogram in Figure 4.37(d) illustrates many features which are in line with the formation and decomposition of the clathrate hydrate after the transformation to ice *Isd*. For each DSC thermogram, all the features are extremely striking yet unfortunately, the corresponding XRD patterns do not display these features. The absence of the features in XRD that would corroborate with the DSC pronounced features can be attributed to the assumption that the clathrate hydrate may just arise in the chaos of the ASW to ice *Isd* transition. Nevertheless, this is just a speculation and yet the reason for the absence of these features in the XRD measurements remains unclear.

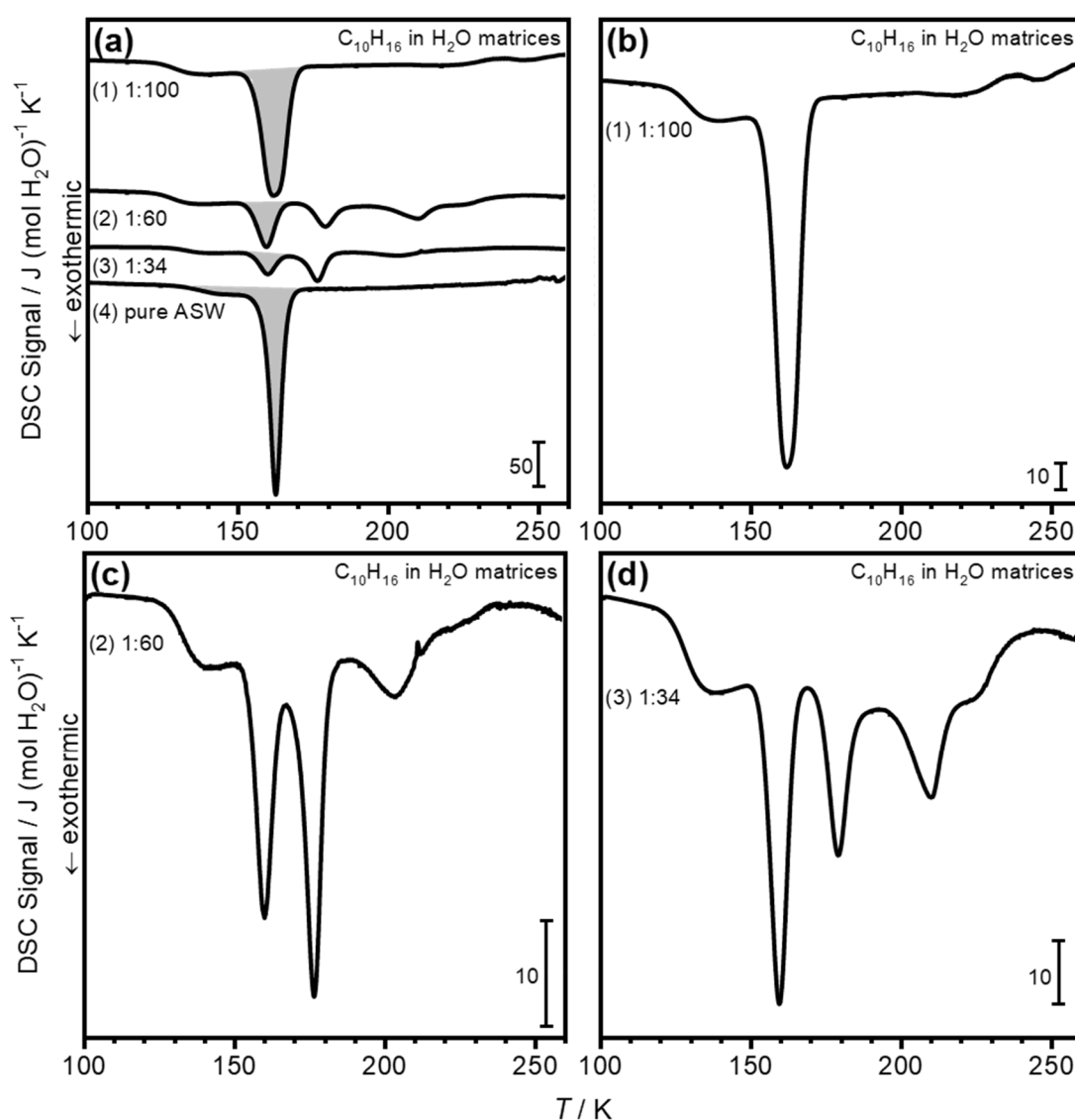


Figure 4.37. DSC thermograms for pure ASW and  $C_{10}H_{16}/H_2O$  molar ratios heated at a rate of  $10\text{ K min}^{-1}$ , where (a) comparison of pure ASW with all molar ratios and (b)–(d) single DSC thermograms from (a) given with indicated molar ratios and scale bars. The grey shaded areas in (a) depict the crystallisation of  $H_2O$  to ice *Isd*. These DSC scans were normalised per mole of  $H_2O$ .

## 4. Matrix-Isolated Adamantane in Amorphous Ice

The associated areas of the DSC exotherms are presented in Table 4.13. As expected, the H<sub>2</sub>O-rich sample displays a much larger crystallisation area due to less influence of the presence of C<sub>10</sub>H<sub>16</sub>. The first exotherm which plateaus after 125 K is the result of the annealing process within the chamber. What can be concluded for the XRD data is that the appearance of C<sub>10</sub>H<sub>16</sub> peaks is severely delayed and are not present from the beginning of the temperature program as seen when C<sub>10</sub>H<sub>16</sub> is deposited *via* a pellet.

*Table 4.13. Summary of the spread of enthalpies relating to pure ASW and codeposited samples from indicated molar ratios in Figure 4.37. Samples were deposited into the vacuum chamber via a round-bottom flask through the same inlet tube as H<sub>2</sub>O. The DSC thermograms were recorded at 10 K min<sup>-1</sup> and at ambient pressure.*

Sample	Scan in Figure 4.37	$\Delta H / \text{J mol}^{-1}$		
		160 K	175–179 K	212 K
1:100	1	1358±107	-	-
1:60	2	335±17	185±4	159±3
1:34	3	134±60	178±25	68±10
Pure ASW	4	1260±35	-	-

### 4.5.13 Vibrational Spectroscopy Characteristics of C<sub>10</sub>H<sub>16</sub>

‘Normal modes’ of vibration arise from the entire molecule absorbing light at their specific wavelengths. The peak frequency can provide us with structural information about the local environment. Normal modes with the same symmetry can be mixed to some extent, e.g., a C–C stretch in a hydrocarbon will have some C–H bending character, although it is still possible to determine the most dominant mode. Deuteration (D) of the molecule can be used to distinguish between modes as the vibrational frequencies are shifted towards lower wavenumbers. When O–D oscillators are introduced, coupling stretching transitions are blocked and isolated O–D oscillations are observed.<sup>79, 80</sup> As C<sub>10</sub>H<sub>16</sub> is a highly symmetric molecule with *T<sub>d</sub>* point group symmetry, C<sub>10</sub>H<sub>16</sub> is considered an ideal candidate for normal mode analysis. Raman spectroscopy gives the advantage of viewing the local structure of the binary mixture and in this case, many stretching regions can be observed.

C<sub>10</sub>H<sub>16</sub> consists of 26 atoms which result in  $3N-6 = 72$  degrees of vibrational freedom. The internal modes have been given by Bailey<sup>81</sup> and reproduced as given in upcoming Table 4.14. Since C<sub>10</sub>H<sub>16</sub> has a *T<sub>d</sub>* point group symmetry, 72 internal modes of vibration / normal modes are present which span the representation:<sup>82</sup>

$$\Gamma_{\text{int}} = 5 A_1 + A_2 + 6 E + 7 F_1 + 11 F_2$$

#### 4. Matrix-Isolated Adamantane in Amorphous Ice

Raman active modes are given by  $A_1$ ,  $E$  and  $F_2$  modes.<sup>82</sup> The  $A_2$  and  $F_1$  modes are forbidden vibrations in both IR and Raman spectra. Rao *et al.*<sup>82</sup> studied the high-pressure behaviour up to 26 GPa and ambient temperature of  $C_{10}H_{16}$  using Raman spectroscopy. Poor intensities from the 22 distinct modes in the Raman spectra are noted. Figure 4.38 shows the literature Raman bands of  $C_{10}H_{16}$ .

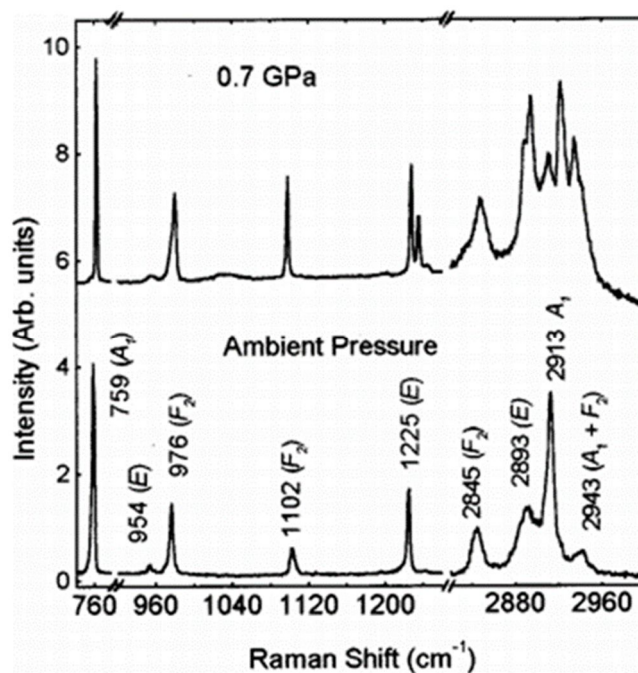


Figure 4.38. High-pressure Raman spectra of  $C_{10}H_{16}$  in its cubic phase and at ambient pressure and at 0.7 GPa corresponding to its tetragonal phase. The different modes have been displayed in brackets and given by R. Rao.<sup>82</sup> This figure has been reprinted from reference 82 with the permission of AIP Publishing.

As seen in Figure 4.38, the Raman bands display strong and medium intensities. The peak at  $759\text{ cm}^{-1}$  is assigned to the  $A_1$  mode and resembles the C–C symmetric stretching mode in the cubic phase. The bands assigned to the  $F_2$  modes are seen at  $976$  and  $1102\text{ cm}^{-1}$  which are indicative of the C–C stretch and C–H rock, whilst the band seen at  $1225\text{ cm}^{-1}$  can be attributed to HCC bending. The CH and  $CH_2$  groups of  $C_{10}H_{16}$  show bands which are due to the C–H stretching vibrations and appear in the Raman spectra from  $2800$ – $3000\text{ cm}^{-1}$ . The four main modes that appear within this region show a strong mode at  $2913\text{ cm}^{-1}$  which is due to  $C_{10}H_{16}$ 's methine group and also corresponds to an  $A_1$  species. The other three modes remaining show the C–H stretching arising from  $CH_2$  groups at  $2845$ ,  $2893$  and  $2943\text{ cm}^{-1}$ , respectively.<sup>82</sup> Other Raman bands that belong to the  $F_2$  and  $E$  species have been reported in the literature<sup>82</sup> and will not be discussed further.

#### 4. Matrix-Isolated Adamantane in Amorphous Ice

The orientationally disordered phase (high-temperature) of  $C_{10}H_{16}$  has a space group of  $Fm\bar{3}m$  and four molecules in the unit cell. In order to advance with the analysis of  $C_{10}H_{16}$  and its vibrational measurements, it is clever to assume that this phase is assembled from rigid molecules in octahedral format at sites of  $O_h$  symmetry. Therefore, this indicates that the molecular site symmetry will not be lower than the free molecule. No splitting of vibrational bands is expected and the selection rules should not change.<sup>82</sup>

In contrast, with respect to the low-temperature ordered phase with a space group of  $P\bar{4}2_1C$ , the factor group symmetry of  $D_{2d}$  is lower than the free molecule. Thus, selection rules will be stricter. In this phase, the normal modes can now be distributed amongst the  $D_{2d}$  symmetry species, so that, the forbidden  $A_2$  and  $F_1$  vibrations from  $T_d$  in the ordered phase are now Raman active.<sup>82</sup> In this ordered phase, the unit cell consists of two molecules in the crystal and thus, doublets may occur.

Raman spectroscopy was performed on the codeposited samples in this study.  $C_{10}H_{16}$  was deposited from a pellet in this section. The results from Raman spectroscopy demonstrate that mixing of the two species is achieved successfully which is of paramount importance for clathrate hydrate formation. In the case of bulk  $C_{10}H_{16}$  at room temperature (298 K), there are several spectral regions of interest which are depicted in Figure 4.39 and upcoming Table 4.15 defines the peak frequencies, above and below the phase transition.

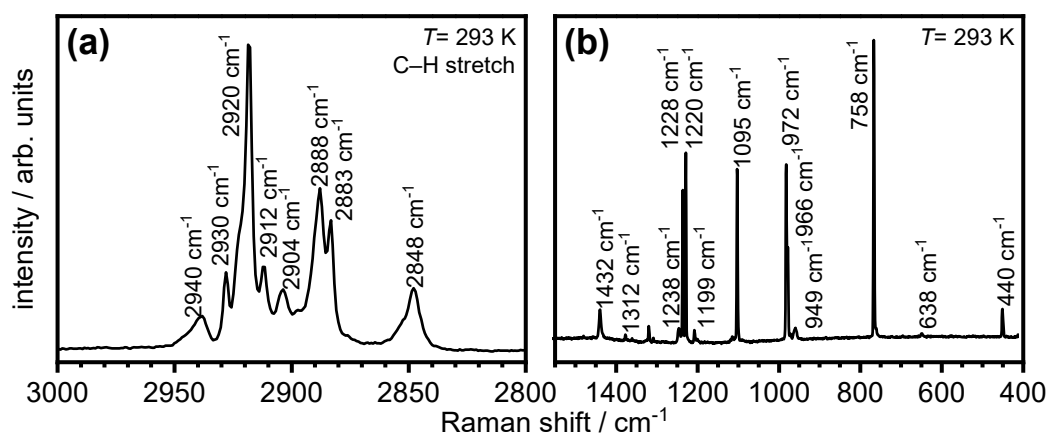


Figure 4.39. (a) Raman spectra of the C–H stretching region of pure  $C_{10}H_{16}$  at 293 K and (b) Raman spectra of the lower stretching region of  $C_{10}H_{16}$  above the phase transition, recorded at 293 K. Raman shifts were calibrated using the emissions of a neon lamp.

Several sharp features between the region of 2950–2840  $cm^{-1}$  [Figure 4.39(a)] and 700–1450  $cm^{-1}$  [Figure 4.39(b)] are illustrated. Jenkins *et al.*<sup>83</sup> reports that the phase transition

#### 4. Matrix-Isolated Adamantane in Amorphous Ice

from cubic to tetragonal at high and low temperature, respectively, is consistent with changes in the vibrational band through the transition. An interesting feature is the large width of the band given by the C–H stretching region at higher temperatures above the phase transition when compared to C<sub>10</sub>H<sub>16</sub> at lower temperatures and lower frequency modes. This feature may be due to the coupling of very high frequency modes with the lower frequency and disordered phase. The C–H stretching above the phase transition is depicted in Figure 4.39(a).

The low wavenumber region of the Raman spectrum from C<sub>10</sub>H<sub>16</sub> comprises five-strong Raman bands such that the intense features are, (i) CH<sub>2</sub> twist mode at 1220/1221 cm<sup>-1</sup>, (ii) breathing mode at 758/757 cm<sup>-1</sup>, (iii) CCC bend mode at 971/972 cm<sup>-1</sup>, (iv) CH<sub>2</sub> wag mode at 1097 cm<sup>-1</sup> and finally, (v) the scissor mode of CH<sub>2</sub> at 1435/1436 cm<sup>-1</sup>.<sup>83, 84</sup>

*Table 4.14. Peak frequencies of the Raman band assignments / cm<sup>-1</sup> of C<sub>10</sub>H<sub>16</sub> at 300 K and 75 K from the literature.<sup>83</sup>*

Assignment	300 K	75 K
CCC bend	400, 415, 445	398, 406, 442, 640
CC stretch	758	759
CH <sub>2</sub> rock		906
CC stretch	950	956
CCC bend	972	966, 975, 980
HCC bend	1098, 1221, 1313	1092, 1108, 1198, 1204, 1227, 1235, 1244, 1302, 1313, 1359, 1373
HCH bend	1436	1434, 1450
CH stretch	2948, 2984, 2916, 2942	2848, 2852, 2883, 2888, 2904, 2912, 2920, 2924, 2930, 2940

The Raman spectra of vapour deposited C<sub>10</sub>H<sub>16</sub>/H<sub>2</sub>O were collected in the intermolecular and intramolecular region and are depicted for a 1:34 and 1:100 molar ratio compared in Figure 4.40. C<sub>10</sub>H<sub>16</sub>'s high degree of symmetry enabled vibrational assignments to be drawn. The C–H stretching mode is split into four modes [Figure 4.40(a)] and these peak positions are in close agreement with literature values,<sup>81</sup> such that the C–H stretching mode of C<sub>10</sub>H<sub>16</sub> at 78 K in the concentrated sample is given by Raman modes at 2948, 2918, 2889 and 2850 cm<sup>-1</sup>. For the H<sub>2</sub>O-rich sample, less C<sub>10</sub>H<sub>16</sub> is present, and the C–H stretching modes are seen at 2948, 2923, 2893 and 2849 cm<sup>-1</sup>. The literature values for peak positions of C<sub>10</sub>H<sub>16</sub> for C–H stretching at 78 K are 2948, 2894 and 2850 cm<sup>-1</sup>. Comparing these peak positions to the experimentally obtained positions, the frequencies

#### 4. Matrix-Isolated Adamantane in Amorphous Ice

are not shifted much towards lower or higher wavenumbers despite the coexistence of both species.

The peak position at  $3080\text{ cm}^{-1}$  is due to ASW and is in line with previously reported Raman spectroscopic data for ASW. This feature is assigned to the symmetric stretching of all the  $\text{H}_2\text{O}$  molecules vibrating in phase with each other. The effect of introducing  $\text{C}_{10}\text{H}_{16}$  into amorphous ice is indicated by the well mixing of both species as seen in the Raman spectrum. ASW is only slightly affected by the introduction of the guest species in the sense that the main feature shifts towards higher wavenumbers. A slight shift towards higher wavenumbers with respect to the ASW feature is found when the concentration of  $\text{C}_{10}\text{H}_{16}$  is increased. The associated wavenumber of the ASW feature in the dilute sample is found to be  $3112\text{ cm}^{-1}$  and for the  $\text{C}_{10}\text{H}_{16}$ -rich sample, the associated wavenumber is found to be  $3117\text{ cm}^{-1}$ . A comparison of the high wavenumber spectra, the C–H stretch of the two mixed samples of 1:100 and 1:34 molar ratios ( $\text{C}_{10}\text{H}_{16}/\text{H}_2\text{O}$ ) are listed in Table 4.15.

It can be noted that in the vapour deposited mixtures, spectra are less resolved, meaning the peaks are less pronounced than compared to bulk  $\text{C}_{10}\text{H}_{16}$  recorded at room temperature. Due to difficulty in collecting vapour deposited  $\text{C}_{10}\text{H}_{16}$ , it was not possible to conduct Raman spectroscopy on this sample alone. When comparing both ratios with one another, in the intramolecular vibrational region, the measured C–H stretch is less intense and broader for the  $\text{H}_2\text{O}$ -rich sample than those shown in the  $\text{C}_{10}\text{H}_{16}$ -rich sample. The 1:34 sample is more prominent in intensity with the concentrated sample (1:34) when compared to the dilute 1:100 sample which is expected as more  $\text{C}_{10}\text{H}_{16}$  molecules are present in the concentrated sample. It must be stressed that the high wavenumber peaks show many different environments, as the amount of  $\text{C}_{10}\text{H}_{16}$  increases, the spectrum becomes sharper as the molecules cluster up.

The lower-frequency Raman spectra are presented in Figure 4.40(b) and were recorded at 78 K. The fully symmetric  $A_1$  C–C stretch is the breathing mode which is found at approximately  $756\text{ cm}^{-1}$ . The breathing mode peak position of the C–C stretch agrees with the peak position found in literature also of  $756\text{ cm}^{-1}$  at 78 K.<sup>81, 83</sup> The CCC stretch at approximately  $970\text{ cm}^{-1}$  is depicted in Figure 4.40(b) and also agrees well with the literature value of  $971\text{--}975\text{ cm}^{-1}$ .<sup>83, 85</sup> Raman modes at 1338, 1263, 1217 and  $1103\text{ cm}^{-1}$  in Figure 4.40(b) can be assigned to the HCC stretch at 78 K. A  $\text{CH}_2$  scissor mode



#### 4. Matrix-Isolated Adamantane in Amorphous Ice

is observed at  $1440\text{ cm}^{-1}$  which coincides with the literature value of  $1435\text{--}1436\text{ cm}^{-1}$  at room temperature and  $1434\text{ cm}^{-1}$  at  $75\text{ K}$ . In this case, the codeposited sample has been shifted to higher wavenumbers for the  $\text{CH}_2$  scissor mode. Raman modes at  $1700\text{ cm}^{-1}$  and  $1650\text{ cm}^{-1}$  have not been reported in the literature to the best of our knowledge. This may be due to a new phase of  $\text{C}_{10}\text{H}_{16}$ , a clathrate hydrate or simply because this is a complex mixture of both species. The Raman low wavenumber spectrum of the codeposited ordered  $\text{C}_{10}\text{H}_{16}$  phase shows features that are most relatable to the literature. It is important to note that the spectrum is very noisy due to external vibrations, cryostat movement and the nature of the sample itself. Thus, a lower S/N ratio is exhibited in the data presented here.

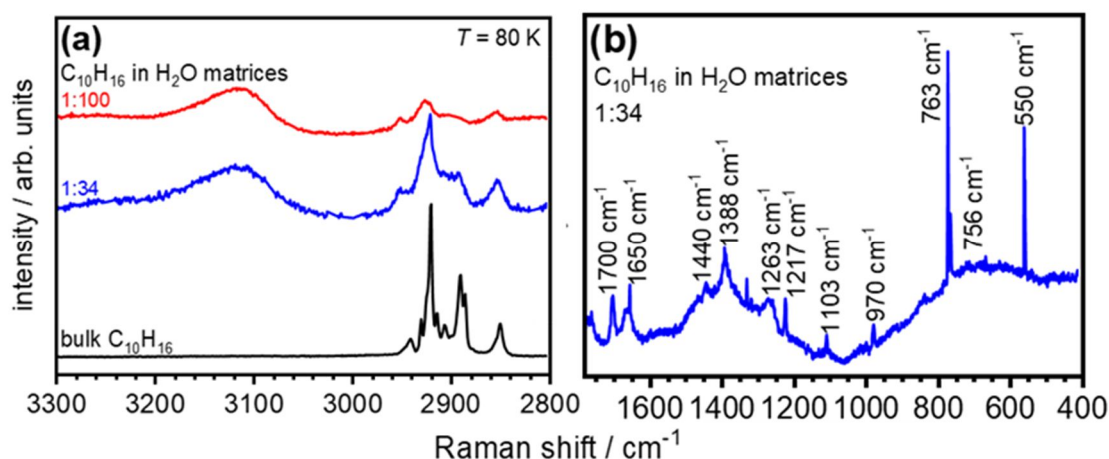


Figure 4.40. Raman spectra of (a)  $\text{C}_{10}\text{H}_{16}$  (black line, room temperature) and  $\text{C}_{10}\text{H}_{16}/\text{H}_2\text{O}$  with indicated molar ratios (1:100 (red) and 1:34 (blue) recorded at  $80\text{ K}$ ), showing many different environments. As the content of  $\text{C}_{10}\text{H}_{16}$  increases, the spectrum becomes sharper as molecules start to cluster up and (b) Raman spectrum of  $\text{C}_{10}\text{H}_{16}$ -rich sample in the lower wavenumber region. Cosmic ray peaks have been omitted for clarity. Raman shifts were calibrated using the emissions of a neon lamp.

Observing and comparing the room temperature,  $78\text{ K}$  data, and the literature frequencies with one another, there seems to be a reasonable correlation with the low wavenumber range between the peak positions in the spectra. However, there are more peaks present in the codeposited Raman spectrum. A probable explanation is the fact that as the complexity of the system is introduced, the Raman spectra shows increased discrepancies and more peaks become prominent.

Similarly, it was interesting to examine the effects of deuteration in the sample. Upon 100% deuteration of  $\text{H}_2\text{O}$ , the vibrational frequency of the ASW feature was shifted to lower frequencies as expected. No feature for ASW at  $3100\text{ cm}^{-1}$  was seen as expected

#### 4. Matrix-Isolated Adamantane in Amorphous Ice

and the O–D stretching was thus, observed at approximately  $2500\text{ cm}^{-1}$ . Figure 4.41(a) shows the coupled O–D region in the mixture. Introducing  $\text{D}_2\text{O}$  in the mixture did not pose any effect on the main C–H stretches in the sample as there was no exchange with the aliphatic hydrogen.

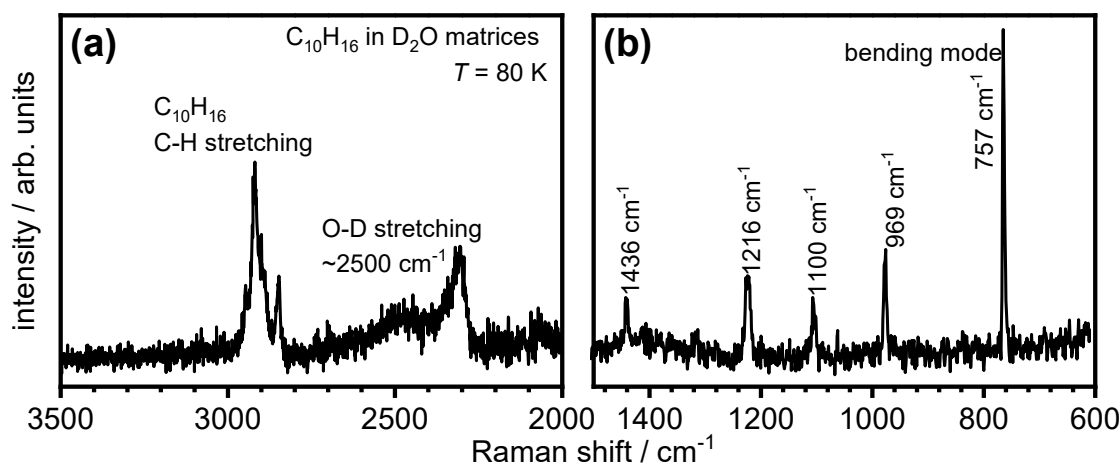


Figure 4.41. Raman spectra of  $\text{C}_{10}\text{H}_{16}$  in  $\text{D}_2\text{O}$  showing the (a) decoupled O–D stretch incorporated within the vapour deposited sample of a 1:100 molar ratio of  $\text{C}_{10}\text{H}_{16}/\text{D}_2\text{O}$  and (b) Raman spectra in the intramolecular low wavenumber region. Raman shifts were again calibrated using the emissions of a neon lamp.

Nevertheless, the existence and mixing of  $\text{H}_2\text{O}$  and  $\text{C}_{10}\text{H}_{16}$  in the samples is reported here, which is the ideal requirement for the formation of hydrates. To date, and to the best of our knowledge, this is the first time Raman spectra for an as-made vapour deposited sample of  $\text{C}_{10}\text{H}_{16}$  and  $\text{H}_2\text{O}/\text{D}_2\text{O}$  has been presented.

Table 4.15. Summary of the peak frequencies of the Raman band assignments /  $\text{cm}^{-1}$  of  $\text{C}_{10}\text{H}_{16}/\text{H}_2\text{O}$  at 78 K from this study. Note the assignment labelled ‘unknown’ is the new feature seen in the spectra.

Assignment	$\text{C}_{10}\text{H}_{16}/\text{H}_2\text{O}$ 78 K, 1:100	$\text{C}_{10}\text{H}_{16}/\text{H}_2\text{O}$ 78 K, 1:34	$\text{C}_{10}\text{H}_{16}/\text{D}_2\text{O}$ 78 K, 1:100
CC stretch	764	756, 763	757
CCC bend	974	970	969
HCC bend	1104, 1216, 1260, 1325, 1385	1103, 1217, 1263, 1388	1100, 1216
HCH bend	1441	1440	1436
unknown	1649, 1700, 1760	1650	-
CH stretch	2849, 2893, 2923, 2948	2850, 2889, 2918, 2948	2843, 2895, 2915, 2943

### 4.5.13.1 Raman Spectra upon Heating

Structural relaxation including the irreversible crystallisation of H<sub>2</sub>O from this complex system with C<sub>10</sub>H<sub>16</sub> guest species takes place during annealing below the order-disorder phase transition of C<sub>10</sub>H<sub>16</sub>. The thermal evolution of the Raman spectra of a 1:100 molar ratio of C<sub>10</sub>H<sub>16</sub>/H<sub>2</sub>O deposited at 82 K as the temperature was raised stepwise, from 78 K to 250 K, in the intramolecular region, is shown in Figure 4.42. As the sample was heated gradually in the cryostat to the temperatures required, the Raman spectra were recorded after immediate cooling back down to 78 K after each annealing step. Figure 4.42 does not display any appreciable intensity changes in the C<sub>10</sub>H<sub>16</sub> features with respect to temperature or recording time. A possible explanation of this observation may be the long lifetime of the phase of C<sub>10</sub>H<sub>16</sub>. The intensity of each spectrum has been normalised and calibrated with respect to the emissions of a neon lamp.

As the temperature of the sample is increased, the contributions of the C<sub>10</sub>H<sub>16</sub> Raman bands are seen to sharpen and intensify resolving into the modes that are described in the literature<sup>85</sup> and overlap with that seen in the Raman spectra of C<sub>10</sub>H<sub>16</sub> at room temperature. The temperature dependence of the phase transition (order-disorder) at low temperatures is accompanied by changes in the characteristic C–H stretching. These vibrations agree well with that reported in the Raman spectrum<sup>85</sup> of the tetragonal ordered phase, indicating thermal annealing, influencing the order. The C–H stretching modes are found at 2950, 2913, 2900, 2944, 2910 and 2849 cm<sup>-1</sup>. Note that these values are room temperature values. Before the phase transition at 200 K, the CH<sub>2</sub> methylene stretching at 2948 cm<sup>-1</sup> splits into two bands. A new shoulder at 2939 cm<sup>-1</sup> is observed, which is not present in other spectrums. The CH methine stretching at 2902 cm<sup>-1</sup> is also observed from 100 K and is very small in intensity. This feature can be seen towards the right-hand side of the C–H high frequency stretching mode at approximately 2916 cm<sup>-1</sup> (literature: 2912 cm<sup>-1</sup> <sup>86</sup>) which is observed as a shoulder and second component to the mode. This may be due to the appearance of two molecules in the unit cell of the crystal in its ordered phase which gives rise to the splitting.

The intensity of the bands of C<sub>10</sub>H<sub>16</sub> increase with temperature. The most significant increase is already seen at 100 K where the Raman mode splits and becomes more defined. A temperature-dependence on the band shapes of Raman intramolecular vibrations is a general characteristic trait of a samples relaxed nature due to ordering of the structure and this has also been found for other hydrocarbons.<sup>85</sup> Looking at the

#### 4. Matrix-Isolated Adamantane in Amorphous Ice

spectrum at 80 K compared to the other temperature spectra, the C–H stretching is substantially different as the Raman modes are broader and slightly weaker in intensity. This could possibly suggest the disorder in the as-made sample is at its maximum, however, as the temperature increases, the sample rapidly transforms to short-range order. A possible explanation is a highly porous sample due to the existence of ASW. As the sample is annealed in the cryostat, pores are already closed, but soon, C<sub>10</sub>H<sub>16</sub> guest species are expelled out of the amorphous matrix with a temperature increase. Structural relaxation of this sample progresses with the rearrangement of the H<sub>2</sub>O and C<sub>10</sub>H<sub>16</sub> molecules and by thermal motion. This type of behaviour is identified with other molecular systems which dominate with dispersive forces.<sup>85</sup> Nevertheless, C<sub>10</sub>H<sub>16</sub> exists in a different local environment in this study and a lower S/N ratio in the instrument is seen which cannot be prevented. Figure 4.42 illustrates how well-mixed these samples made in this study are, which relays back to one of the motivations for this chapter, the formation of clathrate hydrates.

The temperature program as shown in Figure 4.42 was also recorded to observe the spectral changes of the system due to ASW exhibiting structural relaxation and to exclude any effects of reversible thermal expansion. The changes upon thermal annealing of the sample from 80 K can be observed to 140 K where the transformation of ASW to ice *Isd* begins at approximately 140 K. Annealing the sample at 160 K leads to the irreversible crystallisation of H<sub>2</sub>O to ice *Isd* and upon further annealing after 160 K, all H<sub>2</sub>O evaporates as shown in Figure 4.42. The broad ASW peak sharpens in intensity as the temperature is increased and a shift in wavenumbers towards lower wavenumbers is demonstrated as the temperature increases. Upon thermal annealing from 80 K to 230 K, the frequency of the ASW feature changes from 3105 to 3086 cm<sup>-1</sup>.

Salzmann *et al.*<sup>58, 87</sup> have shown that structural relaxation upon annealing of low-density amorphous ice (LDA) and ASW compared to high-density amorphous ice (HDA) are in line with, (i) peak sharpening of the most intense feature in the  $\nu(\text{O–H})$  region, (ii) shifts to lower wavenumbers and (iii) intensity decrease in the shoulders of the most intense features to the high and low side of the wavenumbers. These same findings can be attributed to Figure 4.42 for the C<sub>10</sub>H<sub>16</sub>/H<sub>2</sub>O sample. The main feature that sharpens is interpreted as undergoing a structural order increase on an intermediate-range length scale. This is based on the knowledge that O–H oscillators in ice are capable of coupling with one another beyond the local environments of H<sub>2</sub>O.<sup>58</sup> Along with this theory, it is

#### 4. Matrix-Isolated Adamantane in Amorphous Ice

possible to propose that the shift in wavenumbers occurs due to the influence and presence of a second species within the matrix. Similarly, this shift in wavenumbers has been detected in Fourier Transform Infrared Spectroscopy (FTIR) and will be shown in upcoming Chapter 5.

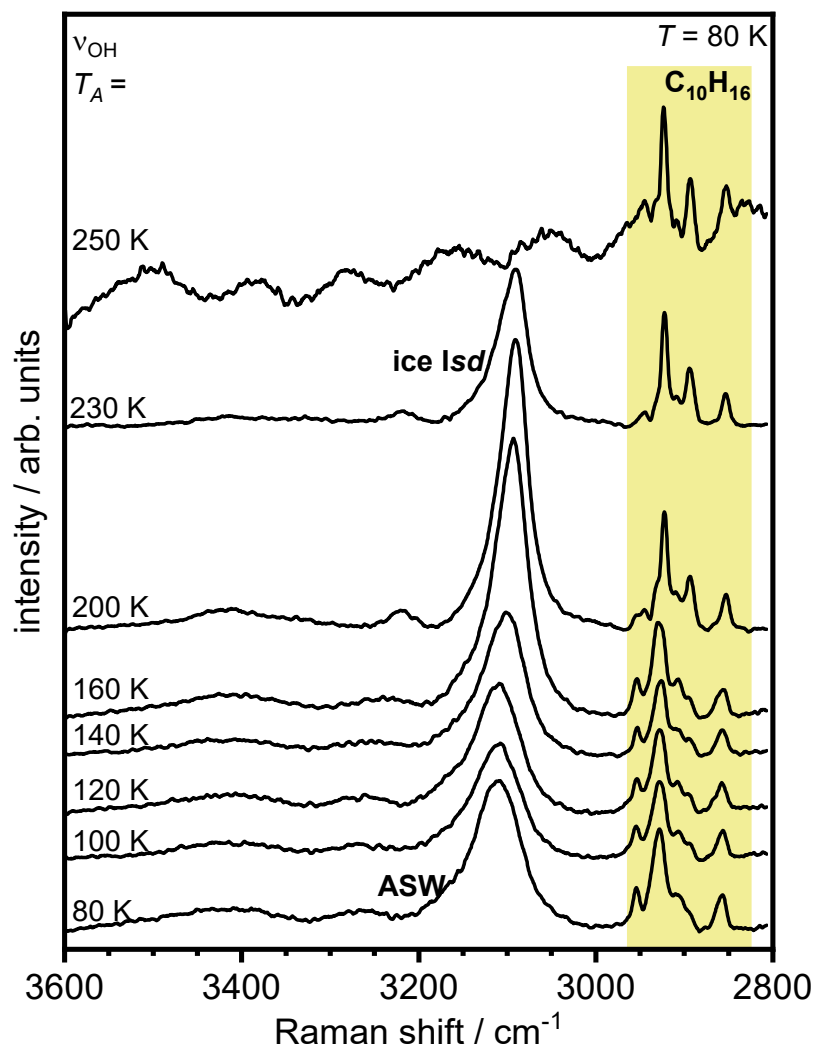


Figure 4.42. Raman spectra of  $C_{10}H_{16}/ASW$  at a 1:100 molar ratio in the coupled  $\nu(O-H)$  stretching region showing the irreversible phase transition of ASW to ice Isd upon thermal annealing. All Raman spectra have been recorded at 80 K after annealing at the temperatures as indicated in the figure, calibrated to a neon lamp, and shifted vertically for clarity.

##### 4.5.13.2 Spatial Distribution Across the Deposition Plate

It was proposed earlier that crystallising ASW, and hydrophobic molecules should yield clathrate hydrates. As mentioned earlier,  $C_{10}H_{16}$  as an ideal guest species should help to probe this formation. In addition to the spatially resolved XRD and DSC measurements, the entire inhomogeneous deposits were characterised with spatially solved Raman spectroscopy over a cross-section of the deposition plate to help characterise the complex

#### 4. Matrix-Isolated Adamantane in Amorphous Ice

mixture and solve the mysteries in XRD and DSC measurements with different levels of the  $C_{10}H_{16}$  hydrophobe.

For this step, to determine the different levels of composition across the plate, several small circular copper plates were attached to the large deposition plate, equidistant from each other. Thick layers of the samples were deposited onto these copper plates. Once deposition of three hours was complete, these copper plates were removed and stored in the  $LN_2$  dewar for analysis in Raman spectroscopy. The high wavenumber region of the Raman spectra of three different locations of the deposition plate; centre of the deposition plate, edge of deposition plate and midpoint of the radius of the deposition plate is shown in Figure 4.43.

The concentration of the species decreases further towards the outside of the plate than compared to the centre. This is represented by the relative intensities of the C–H stretching.

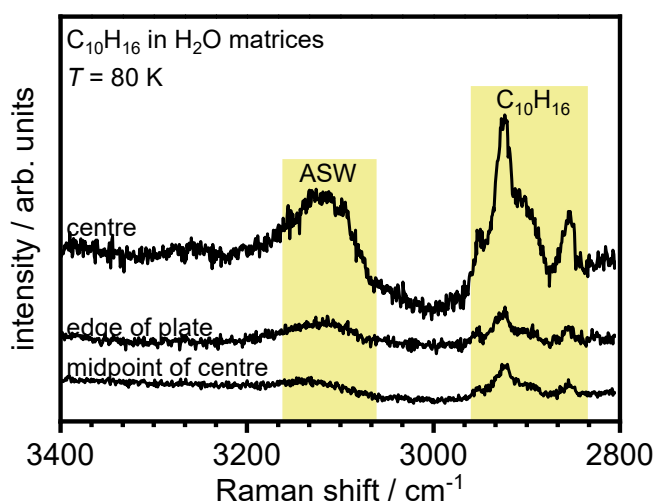


*Figure 4.43. Raman spectra of the high wavenumber region recorded from deposited layers of  $C_{10}H_{16}/H_2O$  at a 1:34 molar ratio at 78 K taken from the circular copper plates. All spectra have been calibrated with a neon emission lamp and have been moved vertically for visual clarity.*

The intensities in Figure 4.43 are also low due to the nature of collecting the sample, i.e., from a small copper surface. The removal of these copper plates from the deposition plate was difficult. Copper is a material that fluoresces in Raman spectroscopy. The fluorescence is more intense than the Raman scattering which means some features that may be observed in Raman spectroscopy may be hidden or significantly reduced in intensity. Intensive fluorescence emission from copper renders the acquisition of Raman

#### 4. Matrix-Isolated Adamantane in Amorphous Ice

spectra fairly difficult and in line with the poor S/N ratio obtained here. Nevertheless, it is still possible to see the  $C_{10}H_{16}$  and ASW features in Figure 4.43. The Raman spectra were recorded for copper alone at room temperature and demonstrated in Figure 4.44(a).

As established earlier with different uniformity over the deposition plate with DSC and XRD, it was necessary to find a material in which Raman spectroscopy could be carried out using various samples from varying locations on the deposition plate. Since copper fluoresces, the next material that would propose better measurements was aluminium. Aluminium as an alternative for depositing films was also recorded from 0 to  $3600\text{ cm}^{-1}$  wavenumbers at room temperature. It is evident that copper fluoresces much more than aluminium and so, from herein, samples were deposited onto three aluminium pieces equidistance from each other across the diameter of the deposition plate.

The most concentrated sample from various locations on the deposition plate was subject to thermal annealing in the Raman spectrometer from the temperature range of 78 K to 260 K. Samples were cooled back down after reaching the desired temperature to 78 K and a measurement was taken. The temperature program applied to the samples is provided in Figure 4.44 for the low wavenumber region only. The focus of this temperature program was the C–C stretch bending mode at literature values of  $758\text{ cm}^{-1}$  and  $759\text{ cm}^{-1}$  for 300 K and 75 K, respectively. Overall, no significant changes were observed when investigating the deposits at different locations for the high wavenumber region and so this data will not be shown.

#### 4. Matrix-Isolated Adamantane in Amorphous Ice

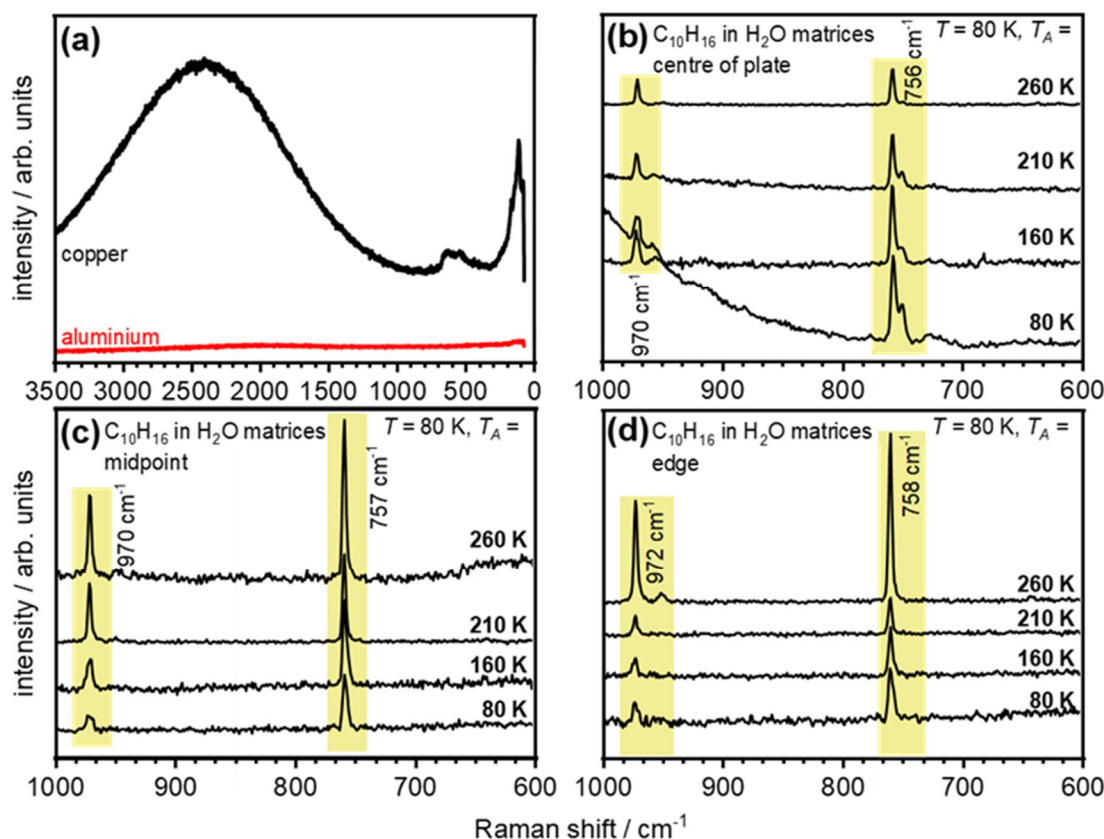


Figure 4.44. (a) Representative Raman spectra for copper (black line) and aluminium (red line) from 0  $\text{cm}^{-1}$  to 3600  $\text{cm}^{-1}$ . Raman spectra of a 1:100 molar ratio of  $\text{C}_{10}\text{H}_{16}/\text{H}_2\text{O}$  deposited onto small circular aluminium plates recorded at low wavenumbers where (b) deposit at the centre of the deposition plate, (c) deposit at the midpoint of radius of the deposition plate and (d) deposit at the edge of the deposition plate. All spectra have been normalised and calibrated against a neon emission lamp.

The totally symmetric C–C bending mode at the centre of the plate is seen at 756  $\text{cm}^{-1}$ , [Figure 4.44(b)] where most of the sample is located. This mode has been observed to split into two modes where the second mode is seen towards the right-hand side of the bending mode at 748  $\text{cm}^{-1}$ . Already at 80 K, there are two modes, and this 748  $\text{cm}^{-1}$  mode does not disappear regardless of the temperature change until after 210 K. It is interesting to note that this split in the bending mode has not been reported previously. The split is most prominent at 80 K and starts to decrease as the temperature increases, yet finally, disappears at 260 K when most of the  $\text{C}_{10}\text{H}_{16}$  evaporates. This feature can be proposed to be from the phase transition of  $\text{C}_{10}\text{H}_{16}$ . This band is always reported as a single band and not two bands in any of the phases.<sup>85</sup> It is very interesting to note that this split in the bending mode has been observed for the first time in this study. When comparing this feature to the edge and midpoint of the radius of the deposition plate, no splitting of the bending mode is identified at any case in temperature. As one moves away from the centre



#### 4. Matrix-Isolated Adamantane in Amorphous Ice

of the plate towards the edge, the bending mode shifts to higher wavenumbers from  $756\text{ cm}^{-1}$  to  $757\text{ cm}^{-1}$  and finally  $758\text{ cm}^{-1}$ . This splitting and also the shift may possibly be due to the difference in the non-uniformity and spatial composition differences across the deposition plate.

##### 4.5.13.3 Peak Ratios with Raman Spectroscopy

In light of the differences in the composition of the 1:100 and 1:34 molar ratios of  $\text{C}_{10}\text{H}_{16}/\text{H}_2\text{O}$ , the ratio of the low and high wavenumber peaks ( $\sim 757\text{ cm}^{-1}$  and  $\sim 2848\text{--}2940\text{ cm}^{-1}$ ) compared to the broad peak of ASW were investigated at each position on the deposition plate.

Specifically for the 1:100 molar ratio of  $\text{C}_{10}\text{H}_{16}/\text{H}_2\text{O}$ , Figure 4.45 depicts the peak area ratios of  $\text{C}_{10}\text{H}_{16}$  and  $\text{H}_2\text{O}$  for each position on the deposition plate.

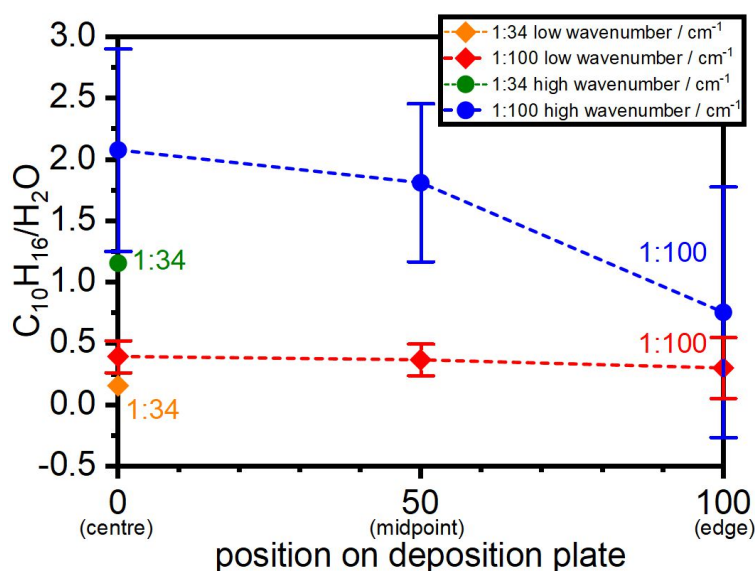


Figure 4.45. Influence of peak ratios,  $\text{C}_{10}\text{H}_{16}$  and  $\text{H}_2\text{O}$  with respect to the sample at different positions on the plate. The circle data points depict the ratios found for  $\text{C}_{10}\text{H}_{16}$  at high wavenumbers and the diamond data points depict the ratios found for  $\text{C}_{10}\text{H}_{16}$  at low wavenumbers ( $\sim 757\text{ cm}^{-1}$ ). Error bars are also depicted in the figure.

Generally, as a whole, it can be seen that the low wavenumber peak when compared to the high wavenumber peak ratios, have smaller associated areas regardless of their molar ratio, 1:34 or 1:100  $\text{C}_{10}\text{H}_{16}/\text{H}_2\text{O}$ . Even so, that for the 1:100 molar ratio, a smaller ratio in the low wavenumber peak is observed compared with that of the high wavenumber peaks. With respect to the sample at discernible positions of the deposition plate and referring to the 1:100 molar ratio of  $\text{C}_{10}\text{H}_{16}/\text{H}_2\text{O}$ , the centre of the plate shows a significant difference in the associated area compared to that of the edge of the deposition plate. As the sample

#### 4. Matrix-Isolated Adamantane in Amorphous Ice

moves away from the centre of the deposition plate, the ratio of  $C_{10}H_{16}/H_2O$  decreases, indicating that perhaps the sample is more concentrated at the centre of the deposition plate compared to the edge of the deposition plate. Although, when looking at the centre and midpoint of the deposition plate, the data points are within the upper error limit of the edge of the deposition plate. No significant changes regarding the low wavenumber peak with respect to the positions of the sample on the deposition plate has been detected. As can be seen in Figure 4.45, the 1:34 molar ratio of  $C_{10}H_{16}/H_2O$  does not show any data at the midpoint and centre of the deposition plate. This was due to experimental difficulties in collecting the spectra.

Once again, considering the Raman spectra as a whole, and as the XRD and DSC measurements have shown previously, the composition of the complex mixture across the eight-inch diameter deposition plate has now also been explored. From several sample preparation experiments; the effects of the composition, peak ratios, and the combination of both species in the matrix have been investigated.

### 4.6 Conclusions

It was successfully determined that the pores of ASW were open when the complex mixtures were not annealed within the vacuum chamber before removal. The formation of N<sub>2</sub> clathrate hydrates was reported and confirmed with a Rietveld refinement. Intriguingly, once the samples were annealed at 125 K in the vacuum chamber, the pores of ASW closed and the formation of N<sub>2</sub> clathrate hydrates was avoided.

After several methods of preparation and characterisation, many peculiar features were exhibited. Interestingly, the DSC exotherms suggest the formation and decomposition of clathrate hydrates, however, these were not consistent with the appearance of the unusual features in the XRD data. Obviously, if a sample contains more C<sub>10</sub>H<sub>16</sub>, it is easier from a kinetic point of view to form more regions of crystalline C<sub>10</sub>H<sub>16</sub> which explains the intense peaks found at low  $2\theta$  values. Equally, with the H<sub>2</sub>O-rich samples, the concentration of C<sub>10</sub>H<sub>16</sub> is low and not enough to form large aggregates that can be detected with diffraction at all times.

The theoretically proposed clathrate hydrate, however, mainly displayed features after the irreversible crystallisation of H<sub>2</sub>O to ice *Isd*. Unexpectedly, ice *Isd* was found to be the active material for forming the supposed clathrate hydrate in the DSC measurements. This finding is structurally distinct due to the number of additional peaks observed upon heating from what is already found in the literature with the formation of clathrate hydrates. This in-depth analysis using different methods of depositing and several other factors is indicative of an extremely complex structure. Nevertheless, both species have been found to be well-mixed and confirmed with many characterisation techniques in this study.

Depending on the composition of the complex mixture, the nature of the result observed varies, such that observed Bragg peaks could not be assigned to any known clathrate hydrate. The thermal annealing and heating of the matrix gives rise to many open-ended questions and has provided tantalising exposure to what could be achieved with respect to the hydration of hydrophobic species.

In the case of the H<sub>2</sub>O-rich sample, the complex changes that occur in the XRD patterns upon heating (Figure 4.24) are apparent from 95 K and are also present up to 270 K. The same finding is observed for samples deposited through the same inlet tube as H<sub>2</sub>O. Despite a complex system and the combination of both species, the crystallisation

#### 4. Matrix-Isolated Adamantane in Amorphous Ice

of H<sub>2</sub>O is not severely affected. C<sub>10</sub>H<sub>16</sub> is observed to expel out of the amorphous matrix upon heating. Unfortunately, even after heating the sample in the vacuum chamber to yield clathrate hydrates at different temperatures, proved unsuccessful.

Spatially resolved Raman scattering investigations were also undertaken to elucidate the completely inhomogeneous deposits upon heating. For the first time, the experimental Raman spectra for embedded C<sub>10</sub>H<sub>16</sub> species in vapour deposited amorphous ice has been explored. The spectra have been assigned in good agreement with comparison to the literature.<sup>85, 86</sup> Complementing all the DSC and XRD data recorded in this study, the crystallisation of H<sub>2</sub>O to ice *Isd* is identified with minimal changes in all Raman spectra, despite the existence of two species. The temperature evolution of the Raman spectra as shown in Figure 4.42 illustrates the changes that occur before and after the phase transition of C<sub>10</sub>H<sub>16</sub>. Regarding the distribution across the plate and in particular, the centre of the deposition plate, the Raman mode indicated a split in the symmetrical C–C breathing mode. This may indicate two different molecular environments in the sample which have not been reported before.

To complement the conclusions drawn from this in-depth study on the hydrophobe C<sub>10</sub>H<sub>16</sub>, efforts should be made to appreciate how tremendously complex this system is to each and every method of preparation and analysis. In the case of all samples, both H<sub>2</sub>O and C<sub>10</sub>H<sub>16</sub> are well observed and well-mixed. The literature fails to illustrate any interaction of C<sub>10</sub>H<sub>16</sub> in H<sub>2</sub>O deposited in this way, except for a study on the expected sH hydrate<sup>47</sup> by other methods which may have been useful at the time of its publication, however, fail to provide the actual structural nature of the hydrate.

A shortcoming of this thesis is present, caused by the lack of assignment of the peculiar Bragg peaks that emerge and also exist from the beginning of the temperature program of embedded C<sub>10</sub>H<sub>16</sub> in amorphous ice. Peaks were subject to indexing and should be indexed more thoroughly and in-depth, however, they are unlikely to be assigned, due to disparity with one another and stronger peaks are needed. An understanding of what is occurring upon thermal annealing of this complex system may help to assist the appreciation of the elements involved with the hydration of hydrophobic species. Thus, such a system could potentially be used in industrial applications. The mixtures as prepared in this study remain poorly understood. It is envisaged that

#### 4. Matrix-Isolated Adamantane in Amorphous Ice

computational calculations may be able to introduce invaluable insights into this system and the processes taking place upon heating after the transition to ice *Isd*.

Given how versatile H<sub>2</sub>O is, and in light of the search for new clathrate hydrates, an entirely open-ended question in this area is whether H<sub>2</sub>O could act as a ‘helper’ molecule to allow itself to fill gaps where the H<sub>2</sub>O cages hydrate hydrophobic molecules to achieve space-filling structures. Drawing conclusions from this study, it would be wise to say that a new clathrate hydrate may have been formed or that a new phase of C<sub>10</sub>H<sub>16</sub> has been observed. However, the preparation route and experimental conditions may need to be altered for the optimal clathrate hydrate formation alongside accurate indexing of peaks.

The next step would now be to characterise the 1:100 C<sub>10</sub>H<sub>16</sub>/H<sub>2</sub>O sample since very interesting results were obtained and preparing this sample worked well. Without these experiments carried out in this particular study, the 1:100 ratio would not have been known to give such interesting results. The aim now is to delve deeper into the study of the structure of H<sub>2</sub>O in the hydration shell using the C<sub>10</sub>H<sub>16</sub> as a ‘nanoprobe’.

Regarding the concentration of C<sub>10</sub>H<sub>16</sub>, it is assumed that for a 1:100 molar ratio, each C<sub>10</sub>H<sub>16</sub> will contain more than two hydration layers. Yet, this ‘nanoprobe’ still contributes 9% of the total hydrogen content of the sample, which means that C<sub>10</sub>H<sub>16</sub> still represents a meaningful contribution to the total structure factor. Thus, the next chapter employs the carbon species as a ‘nanoprobe’ within the amorphous ice to learn about H<sub>2</sub>O properties. The total structure factors of the porous as-made material are required for accurate structural refinement using Empirical Potential Structure Refinement (EPSR)<sup>88</sup>,<sup>89</sup> method with the isotopic substitution technique (Chapter 5).

## 4.7 References

1. R. S. Smith, R. A. May and B. D. Kay, *J. Phys. Chem. B*, 2016, **120**, 1979-1987.
2. G. Natesco, A. Bar-Nun and T. Owen, *Icarus*, 2003, **162**, 183-189.
3. R. S. Smith, N. G. Petrik, G. A. Kimmel and B. D. Kay, *Acc. Chem. Res.*, 2012, **45**, 33-42.
4. S. K. Talewar, S. O. Halukeerthi, R. Riedlaicher, J. J. Shephard, A. E. Clout, A. Rosu-Finsen, G. R. Williams, A. Langhoff, D. Johannsmann and C. G. Salzmann, *J. Chem. Phys.*, 2019, **151**, 134505.
5. Z. Guennoun, C. Aupetit and J. Mascetti, *Phys. Chem. Chem. Phys.*, 2011, **13**, 7340-7347.
6. Z. Guennoun, C. Aupetit and J. Mascetti, *J. Phys. Chem. A*, 2011, **115**, 1844-1852.
7. J. Bouwman, A. L. Mattioda, H. Linnartz and L. J. Allamandola, *Astron. Astrophys.*, 2011, **525**, A93.
8. A. M. Cook, A. Ricca, A. L. Mattioda, J. Bouwman, J. Roser, H. Linnartz, J. Bregman and L. J. Allamandola, *Astrophys. J.*, 2015, **799**, 14.
9. A. L. F. de Barros, A. L. Mattioda, A. Ricca, G. A. Cruz-Diaz and L. J. Allamandola, *Astrophys. J.*, 2017, **848**, 112.
10. E. Michoulier, C. Toubin, A. Simon, J. Mascetti, C. Aupetit and J. A. Noble, *J. Phys. Chem. C*, 2020, **124**, 2994-3001.
11. T. Salter, J. Stubbing, L. Brigham and W. Brown, *Front. Astron. Space Sci.*, 2021, **8**, 644227.
12. A. Courty, M. Mons, I. Dimicoli, F. Piuzzi, M.-P. Gaigeot, V. Brenner, P. de Pujo and P. Millié, *J. Phys. Chem. A*, 1998, **102**, 6590-6600.
13. R. Ruiterkamp, Z. Peeters, M. H. Moore, R. L. Hudson and P. Ehrenfreund, *Astron. Astrophys.*, 2005, **440**, 391-402.
14. M. Fisher and J. P. Devlin, *J. Phys. Chem. A*, 1995, **99**, 11584-11590.
15. A. Lignell and M. S. Gudipati, *J Phys Chem A*, 2015, **119**, 2607-2613.
16. D. T. Bowron and J. L. Finney, *J. Phys. Chem. B*, 2007, **111**, 9838-9852.
17. D. T. Bowron, A. K. Soper and J. L. Finney, *J. Chem. Phys.*, 2001, **114**, 6203-6219.
18. M.-L. Tan, J. R. Cendagorta and T. Ichiye, *J. Am. Chem. Soc.*, 2013, **135**, 4918-4921.
19. A. Patzer, M. Schütz, T. Möller and O. Dopfer, *Angew. Chem. Int. Ed.*, 2012, **124**, 5009-5013.
20. G. A. Mansoori, *Adv. Chem. Phys.*, 2007, **136**, 207-258.
21. P. Negrier, M. Barrio, M. Romanini, J. L. Tamarit, D. Mondieig, A. I. Krivchikov, L. Kepinski, A. Jezowski and D. Szweczyk, *Cryst. Growth Des.*, 2014, **14**, 2626-2632.
22. G. C. McIntosh, M. Yoon, S. Berber and D. Tománek, *Phys. Rev. B*, 2004, **70**, 045401.
23. Y. Wang, E. Kioupakis, X. Lu, D. Wegner, R. Yamachika, J. E. Dahl, R. M. K. Carlson, S. G. Louie and M. F. Crommie, *Nat. Mater.*, 2008, **7**, 38-42.
24. J. E. Dahl, S. G. Liu and R. M. K. Carlson, *Science*, 2003, **299**, 96.
25. K.-W. Yeung, Y. Dong, L. Chen, C.-Y. Tang, W.-C. Law and G. C.-P. Tsui, *Nanotechnol. Rev.*, 2020, **9**, 650-669.
26. E. O. R. Beake, M. G. Tucker, M. T. Dove and A. E. Phillips, *Chem. Phys. Chem.*, 2017, **18**, 459-464.
27. A. Štimac, M. Šekutor, K. Mlinarić-Majerski, L. Frkanec and R. Frkanec, *Molecules*, 2017, **22**, 297.

#### 4. Matrix-Isolated Adamantane in Amorphous Ice

28. H. Schwertfeger, A. A. Fokin and P. R. Schreiner, *Angew. Chem. Int. Ed.*, 2008, **47**, 1022-1036.
29. Y. C. Chan, K. K. H. Choy, A. H. C. Chan, K. M. Ng, S. Liu, S. F. Sciamanna, J. E. Dahl and R. M. K. Carlson, *J. Chem. Eng. Data*, 2008, **53**, 1767-1771.
30. C. G. Windsor, D. H. Saunderson, J. N. Sherwood, D. Taylor and G. S. Pawley, *J. Phys. C: Solid State Phys.*, 1978, **11**, 1741-1759.
31. W. Nowacki, *Helv. Chim. Acta.*, 1945, **28**, 1233-1242.
32. C. E. Nordman and D. L. Schmitkons, *Acta. Cryst.*, 1965, **18**, 764-767.
33. S.-S. Chang and E. F. Westrum Jr, *J. Phys. Chem.*, 1960, **64**, 1547-1551.
34. A. B. Bazyleva, A. V. Blokhin, G. J. Kabo, M. B. Charapennikau, V. N. Emel'yanenko, S. P. Verevkin and V. Diky, *J. Phys. Chem. B*, 2011, **115**, 10064-10072.
35. V. Vijayakumar, A. B. Garg, B. K. Godwal and S. K. Sikka, *Chem. Phys. Lett.*, 2000, **330**, 275-280.
36. T. Clark, T. M. O. Knox, H. Mackle and M. A. McKerverey, *J. Chem. Soc., Faraday Trans.*, 1977, **73**, 1224-1231.
37. R. M. Paroli, N. T. Kawai, I. S. Butler and D. F. R. Gilson, *Can. J. Chem.*, 1988, **66**, 1973-1978.
38. P. Negrier, M. Barrio, J. L. Tamarit and D. Mondieig, *J. Phys. Chem. B*, 2014, **118**, 9595-9603.
39. B. B. Hassine, P. Negrier, M. Barrio, D. Mondieig, S. Massip and J. L. Tamarit, *Cryst. Growth Des.*, 2015, **15**, 4149-4155.
40. J. Reiser, E. McGregor, J. Jones, R. Enick and G. Holder, *Fluid Phase Equilib.*, 1996, **117**, 160-167.
41. C. W. Pistorius and H. Snyman, *Z. Phys. Chem. (NF)*, 1964, **43**, 278.
42. P. J. van Ekeren, A. C. G. van Genderen and G. J. K. van den Berg, *Thermochim. Acta.*, 2006, **446**, 33-35.
43. X. Ma, B. Wigington and D. Bouchard, *Langmuir*, 2010, **26**, 11886-11893.
44. A. Omont and H. Bettinger, *Astron. Astrophys.*, 2021, **650**, A193.
45. J. A. Ripmeester, S. T. John, C. I. Ratcliffe and B. M. Powell, *Nature*, 1987, **325**, 135-136.
46. J. A. Ripmeester and C. I. Ratcliffe, *J. Phys. Chem.*, 1990, **94**, 8773-8776.
47. J. P. Lederhos, A. P. Mehta, G. B. Nyberg, K. J. Warn and E. D. Sloan, *AIChE J.*, 1992, **38**, 1045-1048.
48. J. A. Ripmeester, C. I. Ratcliffe, D. D. Klug and J. S. Tse, *Ann. N. Y. Acad. Sci.*, 1994, **715**, 161-176.
49. G. A. Jeffrey, *Inclusion Compounds*, Academic Press, New York, 1984.
50. V. Kosyakov, *J. Struct. Chem.*, 1995, **36**, 803-808.
51. A. Sum, C. Koh and E. Sloan, *Ind. Eng. Chem. Res.*, 2009, **48**, 7457-7465.
52. W. Blokzijl and J. B. F. N. Engberts, *Angew. Chem., Int. Ed. Engl.*, 1993, **32**, 1545-1579.
53. E. Mayer and A. Hallbrucker, *J. Chem. Soc., Chem. Commun.*, 1989, **12**, 749-751.
54. D. Johannsmann, *Phys. Chem. Chem. Phys.*, 2008, **10**, 4516-4534.
55. I. Mokbel, K. Růžicka, V. r. Majer, V. Růžicka, M. Ribeiro, J. Jose and M. Zábranský, *Fluid Phase Equilib.*, 2000, **169**, 191-207.
56. T. Loerting, M. Bauer, I. Kohl, K. Watschinger, K. Winkel and E. Mayer, *J. Phys. Chem. B*, 2011, **115**, 14167-14175.
57. J. J. Shephard, PhD thesis, Durham University, 2014.
58. J. J. Shephard, J. S. O. Evans and C. G. Salzmann, *J. Phys. Chem. Lett.*, 2013, **4**, 3672-3676.

#### 4. Matrix-Isolated Adamantane in Amorphous Ice

59. A. Hallbrucker and E. Mayer, *J. Chem. Soc., Faraday Trans.*, 1990, **86**, 3785.
60. A. Hallbrucker and E. Mayer, *Icarus*, 1991, **90**, 176-180.
61. A. C. Larson, R. B. Dreele and B. Toby, "General Structure Analysis System (GSAS)", Los Alamos National Laboratory Report LAUR 86-748 2000.
62. C. Lobban, PhD thesis, University College London, 1998.
63. A. D. Fortes, *Acta. Cryst.*, 2018, **74**, 196-216.
64. B. H. Toby, *J. Appl. Crystallogr.*, 2001, **34**, 210-213.
65. E. F. Burton and W. F. Oliver, *Nature*, 1935, **135**, 505-506.
66. L. G. Dowell and A. P. Rinfret, *Nature*, 1960, **188**, 1144-1148.
67. A. Hallbrucker, E. Mayer and G. P. Johari, *J. Phys. Chem.*, 1989, **93**, 4986-4990.
68. J. A. Ghormley, *J. Chem. Phys.*, 1968, **48**, 503-508.
69. D. MacFarlane and C. Angell, *J. Phys. Chem.*, 1984, **88**, 759-762.
70. M. A. Floriano, Y. P. Handa, D. D. Klug and E. Whalley, *J. Chem. Phys.*, 1989, **91**, 7187-7192.
71. A. Hallbrucker and E. Mayer, *J. Phys. Chem.*, 1987, **91**, 503-505.
72. G. P. Johari, G. Fleissner, A. Hallbrucker and E. Mayer, *J. Phys. Chem.*, 1994, **98**, 4719-4725.
73. W. F. Kuhs, C. Sippel, A. Falenty and T. C. Hansen, *Proc. Natl. Acad. Sci. U. S. A.*, 2012, **109**, 21259-21264.
74. Y. Jin, M. Kida and J. Nagao, *J. Phys. Chem. C*, 2013, **117**, 23469-23475.
75. R. S. Smith, T. Zubkov, Z. Dohnálek and B. D. Kay, *J. Phys. Chem. B*, 2009, **113**, 4000-4007.
76. G. A. Kimmel, K. P. Stevenson, Z. Dohnálek, R. S. Smith and B. D. Kay, *J. Chem. Phys.*, 2001, **114**, 5284-5294.
77. K. P. Stevenson, G. A. Kimmel, Z. Dohnalek, R. S. Smith and B. D. Kay, *Science*, 1999, **283**, 1505-1507.
78. Z. Dohnálek, G. A. Kimmel, P. Ayotte, R. S. Smith and B. D. Kay, *J. Chem. Phys.*, 2003, **118**, 364-372.
79. T. H. Carr, J. J. Shephard and C. G. Salzmann, *J. Phys. Chem. Lett.*, 2014, **5**, 2469-2473.
80. B. Minceva-Sukarova, W. F. Sherman and G. R. Wilkinson, *Spectrochim. Acta. A*, 1985, **41**, 315-318.
81. R. T. Bailey, *Spectrochim. Acta.*, 27A, 1971, **27**, 1447-1453.
82. R. Rao, T. Sakuntala, S. K. Deb, A. P. Roy, V. Vijaykumar, B. K. Godwal and S. K. Sikka, *J. Chem. Phys.*, 2000, **112**, 6739-6744.
83. T. E. Jenkins and J. Lewis, *Spectrochim. Acta. Part A*, 1980, **36**, 259-264.
84. J. Filik, J. N. Harvey, N. L. Allan, P. W. May, J. E. P. Dahl, S. Liu and R. M. K. Carlson, *Spectrochim. Acta. Part A*, 2006, **64**, 681-692.
85. L. Bistričić, G. Baranović and S. Ilijić, *Spectrochim. Acta., Part A*, 2005, **61**, 1537-1546.
86. J. O. Jensen, *Spectrochim. Acta. A*, 2004, **60**, 1895-1905.
87. J. J. Shephard, S. Klotz, M. Vickers and C. G. Salzmann, *J. Chem. Phys.*, 2016, **144**, 204502.
88. A. K. Soper, *Chem. Phys.*, 1996, **202**, 295-306.
89. A. K. Soper, *Phys. Rev. B*, 2005, **72**, 104204.



## 5 Total Neutron Scattering of Amorphous Solid Water with Embedded Adamantane

### 5.1 Introduction

This chapter focuses on the use of neutron diffraction and the isotopic substitution technique to investigate the local structure of vapour deposited amorphous solid water (ASW) from the perspective of finely dispersed adamantane ( $C_{10}H_{16}$ ) ‘nanoprobes’. Laboratory experiments render the preparation of carbonaceous species of low volatilities with amorphous ice difficult, and so, very little is documented about the dynamics and structures of such unusual mixtures. For the first time, the sintering of the amorphous ice matrix, as well as the precursors for the formation of clathrate hydrates from the viewpoint of the carbon guest species, is studied. Experimental studies were carried out on the Pulsed Neutron and Muon Source synchrotron, ISIS,<sup>1</sup> (Rutherford Appleton Laboratory of the Science and Technology Facilities Council, on the Harwell Science and Innovation Campus in Oxfordshire, United Kingdom) on the ‘The Near and InterMediate Range Order Diffractometer’ (NIMROD) situated in Target Station 2 (TS2). A large  $Q$  (magnitude of the momentum transfer vector) range on NIMROD has been utilised for simultaneously studying the atomic and mesoscale ASW structure upon heating. The low- $Q$  range data highlights pore morphology which may provide unprecedented insights into the long-debated glass transition of ASW.<sup>2-9</sup>

The diffraction data are fitted with the Empirical Potential Structure Refinement (EPSR) method<sup>10, 11</sup> in order to obtain information about the local structure of ASW. This amorphous ice-‘nanoprobe’ matrix has been discussed extensively with in-house characterisation techniques in Chapter 4. This chapter employs the fundamental background of diffraction, the method of total scattering and the theory of computational modelling used for structural reconstruction of neutron diffraction data performed using the EPSR method as described extensively in Chapter 2. It is important to note, this chapter aims to deliver a comprehensive report of the results obtained, additionally, providing relevant information regarding the techniques used throughout this chapter. A more detailed account on computational modelling tools can be found elsewhere.<sup>12, 13</sup>

### 5.2 Aims

To understand hydrophobic hydration in terms of structure and cage formation exhibited by amorphous solid water (ASW) followed from the viewpoint of the carbon guest species,  $C_{10}H_{16}$ . The structural analysis is carried out with the EPSR method and EPSR tools<sup>10, 11</sup> (described later) and the ANGULA software.<sup>14-17</sup>

### 5.3 Experimental Details

#### 5.3.1 Materials

Heavy water, i.e., deuterated water ( $D_2O$ , 99.9% D) was purchased from Sigma Aldrich. Prior to using  $H_2O$ ,  $HDO$  and  $D_2O$  in sample preparation, several freeze-pump-thaw cycles were carried out to ensure containments were eliminated. The mixture of  $HDO$  was prepared at the Department of Chemistry, UCL, using 50 mol% mixtures of  $H_2O$  and  $D_2O$ . Protiated and deuterated  $C_{10}H_{16}$  were used as received from Sigma Aldrich with purities of  $\geq 99\%$  H and 98 atom% D, respectively, and used with no further purification.

#### 5.3.2 Binary Mixtures

A total of seven isotopically substituted mixtures of  $C_{10}H_{16}$  dispersed in ASW were prepared from  $H_2O$ ,  $D_2O$  and a 50/50 mixture of  $H_2O$  and  $D_2O$  to form  $HDO$ . The structural purity of these isotopic samples was verified with a mass spectrometer (MS) and Raman spectroscopy prior to codeposition with  $C_{10}H_{16}$ . The samples specifically prepared were:

- (i)  $C_{10}H_{16}/H_2O$
- (ii)  $C_{10}H_{16}/D_2O$
- (iii)  $C_{10}H_{16}/HDO$
- (iv)  $C_{10}D_{16}/H_2O$
- (v)  $C_{10}D_{16}/D_2O$
- (vi)  $C_{10}D_{16}/HDO$
- (vii)  $C_{10}D_{16}/D_2O$  (concentrated)

where (i)–(vi) are of composition 1:100 and (vii) is a composition of 1:34  $C_{10}D_{16}$  to  $D_2O$  molecules.

This section aims to provide a guided tour for the compositional preparation of the samples and further, the diffraction data measurements which were undertaken at the

## 5. Total Neutron Scattering of Amorphous Solid Water with Embedded Adamantane

Pulsed Neutron and Muon Source synchrotron, ISIS, on the NIMROD beamline. Samples at ISIS were subject to pressure and temperature by characterising at 80 K (as-made) with further heating to 140 K ( $T_A = 140$  K,  $T = 80$  K) and 230 K, achieving sintering and structural relaxation of the sample.<sup>18</sup>

### 5.3.3 Calibrating the Deposition Rate of $C_{10}D_{16}$

The preparation of pellets is described in Chapter 4 of this thesis. By means of using a quartz-crystal microbalance (QCM) with precise adjustment, monitoring and control, the ratio of  $H_2O$  to  $C_{10}H_{16}$  molecules was obtained. The QCM was used for calibrating the deposition rate of  $C_{10}D_{16}$  and the typical deposition process as carried out for calibrating the deposition rate of  $C_{10}H_{16}$  in Chapter 4 was implemented.

The deposition rates of  $C_{10}D_{16}$  as a function of the temperature of the evaporation source have been depicted in Figure 5.1. This figure includes one set of calibration data of a five-tonne pellet of  $C_{10}H_{16}$  highlighted in a dashed black line to show the difference in deposition rates with differing species. For  $C_{10}D_{16}$ , two sets of calibration data were carried out with five-tonne pellets (triangle data points), and it was concluded that they displayed highly dissimilar deposition rates which were non-uniform when compared to one another. Further to this anomaly, it was decided that the preparation of a pellet of  $C_{10}D_{16}$  should require more force. Thus, an applied force of eight tonnes to prepare the pellet was then implemented and used to calibrate the deposition rate of  $C_{10}H_{16}$ . From Figure 5.1, it is possible to conclude that the QCM response shows that deposition rate after 275 K was unreliable and fairly unstable. Nevertheless, the eight-tonne pellet for temperatures up to 275 K did coincide with one set of data for a five-tonne pellet. Due to the highly expensive nature and limited amounts of the  $C_{10}D_{16}$  available to use in the laboratory, an eight-tonne pellet was used for each experiment that comprises  $C_{10}D_{16}$  and amorphous ice. It was further calculated and described in the next section that for a ratio of 1:100  $C_{10}H_{16}$  to  $H_2O$  molecules, deposition rates above 275 K were not needed.

## 5. Total Neutron Scattering of Amorphous Solid Water with Embedded Adamantane

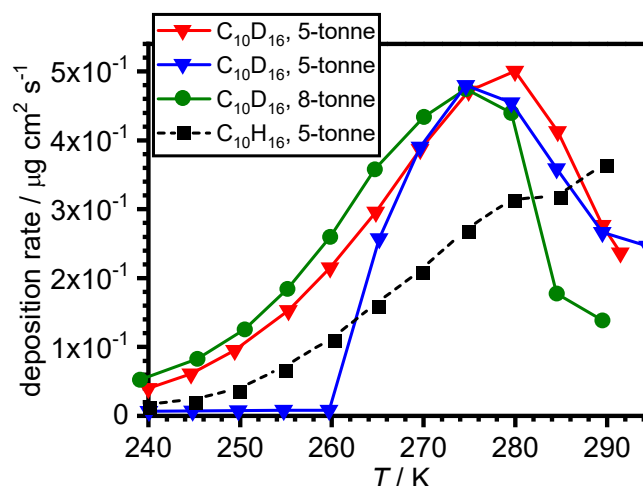


Figure 5.1. Calibration data for  $C_{10}D_{16}$  showing the relationship of deposition rate as a function of temperature where the black dashed line is a repeat of one set of calibration data of pure  $C_{10}H_{16}$  used for visual purposes, illustrating how both species differ in deposition rates and the need for calibrating these deposition rates. The red and blue lines with triangles for data points are of five-tonne pellets of  $C_{10}D_{16}$  showing the difference in deposition rates and the green line is the calibration of the deposition rate of an eight-tonne pellet of  $C_{10}D_{16}$ .

### 5.3.4 Molar Ratios of $C_{10}D_{16}$ and $H_2O$

Regarding the concentration of  $C_{10}H_{16}$  and  $C_{10}D_{16}$ , a 1:100 molar ratio of  $C_{10}H_{16}$  to  $H_2O$  was prepared. For this ratio, two layers of hydration are expected. Therefore, it was already decided that a 1:100 ratio was to be prepared for these mixtures to enable the precise determination of structure factors required for accurate structural refinements using the EPSR method in combination with the isotopic substitution technique. This ratio would ensure the behaviour of hydrophobic hydration from the viewpoint of the carbon guest species is explored, but also, grasp the behaviour of bulk  $H_2O$ .

The deposition rate for  $H_2O$  ( $0.0363 \mu\text{mol cm}^{-2} \text{s}^{-1}$ ) was employed as calculated in Chapter 4 and the calibration data displayed in Figure 5.1 was used to determine a molar ratio of  $H_2O/C_{10}D_{16}$  with a  $C_{10}D_{16}$  molar mass of  $152.3326 \text{ g mol}^{-1}$ . The mass deposition rates of  $C_{10}D_{16}$  at different evaporation source temperatures were divided by the molar mass of  $C_{10}D_{16}$  to obtain molar deposition rates as shown in Table 5.1.

## 5. Total Neutron Scattering of Amorphous Solid Water with Embedded Adamantane

*Table 5.1. C<sub>10</sub>D<sub>16</sub> deposition rate, molar deposition rate and H<sub>2</sub>O/C<sub>10</sub>D<sub>16</sub> molar ratios for a specific temperature of the evaporation source calculated with a H<sub>2</sub>O deposition rate of 0.0363  $\mu\text{mol cm}^{-2} \text{s}^{-1}$ .*

$T / \text{K}$	C <sub>10</sub> D <sub>16</sub> deposition rate / $\mu\text{g cm}^{-2} \text{s}^{-1}$	C <sub>10</sub> D <sub>16</sub> molar deposition rate / $\mu\text{mol cm}^{-2} \text{s}^{-1}$	Approximate H <sub>2</sub> O/C <sub>10</sub> D <sub>16</sub> molar ratio
245	0.07750	$5.09 \times 10^{-4}$	100:1
290	0.13368	$8.78 \times 10^{-4}$	34:1

To realise a molar ratio of 1:100, C<sub>10</sub>D<sub>16</sub>/H<sub>2</sub>O, the deposition rate corresponding to this evaporation source temperature was 245 K and no further deposition rates were used for the main bulk of the work presented in this chapter, unless stated otherwise.

### 5.3.5 Preparation of the Deposition Plate

A copper deposition plate (diameter = 20.3 cm) was designed with a slit that perfectly allows sample cells/cans, specifically those used at ISIS (details provided later) to fit into and thus, the opening for this slit is completely flush with the plate and samples can easily be scraped into the slit. Prior to carrying out experiments, the plate was washed with H<sub>2</sub>O and sandpaper (aluminium oxide, 80  $\mu\text{m}$  grit) was used to remove a copper oxide layer and roughen the surface of the deposition plate to ensure that the deposit sticks to the plate. Ethanol was used to further clean the plate and compressed gas was used to eliminate any sandpaper left in the holes/slits on the plate.

### 5.3.6 Sample Container for NIMROD

Null scattering, i.e., coherent scattering is zero, titanium-zirconium (Ti<sub>0.68</sub>Zr<sub>0.32</sub>, 68% titanium and 32% zirconium) flat plate geometry sample cans (Figure 5.2) were employed for the neutron scattering measurements. Two different sample can sizes were used with internal dimensions of  $3.8 \times 3.8 \times 2.0 \text{ mm}^3$  (2.88  $\text{cm}^3$ ) and  $3.8 \times 3.8 \times 1.0 \text{ mm}^3$  (1.44  $\text{cm}^3$ ), both with a wall thickness of 1.1 mm.<sup>19</sup> These alloy cells are inert which make them ideal to use as sample containers. Samples were transferred into these cells under liquid nitrogen (LN<sub>2</sub>) temperature (77 K) and specific details for the sample can are shown below in Figure 5.2.

## 5. Total Neutron Scattering of Amorphous Solid Water with Embedded Adamantane

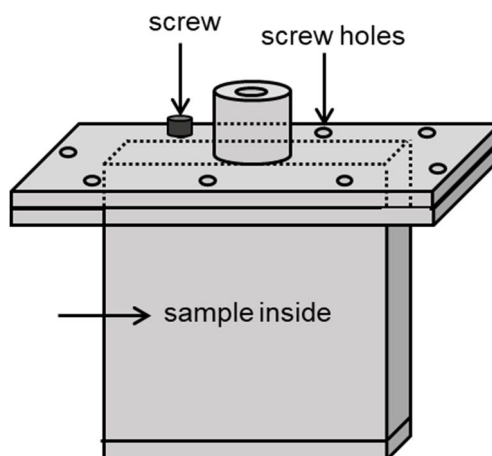


Figure 5.2. Schematic illustration of the flat plate  $Ti_{0.68}Zr_{0.32}$  alloy sample can used for the NIMROD experiments.

Prior to cryogenic deposition experiments, sample cans were also thoroughly cleaned with  $H_2O$ , ethanol solvent, and further dried in an oven to prevent the capture of moisture. Once dried for over eight hours and ready for sample insertion, they were removed from the oven and compressed air was applied to the surfaces of the cans to remove any excess dust.

### 5.3.7 Cryogenic Deposition Experiments

The vapour deposits were prepared with the apparatus in Chapter 2, Figure 2.5 using the same procedures as mentioned in previous chapters. To reiterate, the deposition experiments were carried out with baffled flow using an iron mesh covering the  $H_2O$ -inlet tube. Prior to evacuating the chamber, a pellet of one gram of  $C_{10}H_{16}$  or  $C_{10}D_{16}$  was cooled down in ambient conditions to 240 K to prevent sublimation of the material. Once this temperature was achieved, the base pressure of the chamber prior to depositing both species achieved was approximately  $8 \times 10^{-6}$  mbar and 82 K for a base temperature of the deposition plate. At the start of deposition, the Peltier element is slowly set to the specific temperature by altering the voltage that produces a 1:100 molar ratio of  $C_{10}D_{16}$  to  $H_2O$ . Once the desired temperature was achieved, at this point and at the same time, the pressure for one of:  $H_2O/D_2O/HDO$  was slowly increased to  $1 \times 10^{-1}$  mbar leaking in the vapour *via* the graduated needle valves connected to the liquid reservoir. The deposition time used in this case was four hours to allow enough sample to be deposited onto the deposition plate for sample removal and transfer into the sample can, accounting for any sample loss during the transfer process.

## 5. Total Neutron Scattering of Amorphous Solid Water with Embedded Adamantane

After a four-hour deposition, the pressure inside the chamber was reduced back to base pressure/high-vacuum ( $8 \times 10^{-6}$  mbar) and thus, the sample was removed. Gram scale amounts of sample were deposited where approximately  $\sim 3.5$  g of H<sub>2</sub>O entered the vacuum chamber. Specific detail for sample removal has been provided in Chapter 2. Once the sample was removed under LN<sub>2</sub> conditions, the deposit was scraped into the slit of the plate which consisted of a pre-cooled (77 K) ISIS specific sample cell (Ti<sub>0.68</sub>Zr<sub>0.32</sub>), completely flush with the deposition plate.

The granular deposit was immensely compacted with a slim spatula into the Ti<sub>0.68</sub>Zr<sub>0.32</sub> sample can. D<sub>2</sub>O samples were compacted into the 2 mm cans while the H<sub>2</sub>O and HDO samples were compacted into the 1 mm cans. Once the sample was filled to the top of the can, a fine-cut slim sheet of tissue paper, slightly smaller than the area of the sample can, was placed on top of the can to prevent sample loss. The lid of the can was pre-cooled (77 K) and screwed on with four screws equally spaced across the area of the lid. In total, seven samples were prepared successfully at the Department of Chemistry, UCL and transported to ISIS in a LN<sub>2</sub> storage dewar ready for neutron diffraction data collection.

### 5.3.8 Fourier Transform Infrared Spectroscopy (FTIR)

For transmission Fourier Transform Infrared Spectrometry (FTIR) measurements, ASW samples were prepared with 5 w% D<sub>2</sub>O as an isotopic impurity (5 w% D<sub>2</sub>O + 95 w% H<sub>2</sub>O). Samples were codeposited as thin films onto calcium fluoride (CaF<sub>2</sub>) windows (UQG Optics, WCF-152 CaF<sub>2</sub> Window – Mono, thickness = 2 mm, and diameter = 15 mm). Pure ASW, pure C<sub>10</sub>H<sub>16</sub>, H<sub>2</sub>O-rich (1:100, C<sub>10</sub>H<sub>16</sub>/H<sub>2</sub>O) and C<sub>10</sub>H<sub>16</sub>-rich (1:34, C<sub>10</sub>H<sub>16</sub>/H<sub>2</sub>O) samples were deposited for 2.5 minutes with a H<sub>2</sub>O-inlet pressure of  $1 \times 10^{-1}$  mbar. The process for depositing sample onto windows suitable for the FTIR has been described in Chapter 2. However, to reiterate, these windows are placed firmly inside a circular copper ring, separated by a Teflon ring, and attached to the deposition plate with three screws. Before any sample measurements were taken, a background scan with only the empty cryostat at 78 K was recorded. This was to ensure the best alignment was achieved for sample characterisation. These samples were recorded at 78 K, then heated to 140 K, and cooled back down to 78 K to record a spectrum. Further to this, the sample was further heated to 230 K from 78 K to desorb H<sub>2</sub>O and a spectrum was recorded after cooling back down to 78 K.

## **5.4 ISIS Experiments on NIMROD**

### **5.4.1 Details of Experiments at ISIS**

Prior to inserting the samples into the beam, several normalisation data were collected for appropriate corrections as described in Chapter 2, section 2.6.3. Corrections to the raw measured data are input into the Gudrun*N* software.<sup>20, 21</sup> Background measurements are crucial when refining and correcting raw data. The scattering data from the sample is subtracted from all the below-mentioned measurements to ensure only the sample is analysed. Such measurements are as follows:

- (i) empty instrument (candlestick –  $30 \times 30$  beam)
- (ii) empty vanadium candlestick
- (iii) empty closed cycle refrigerator (CCR)
- (iv) empty sample container
- (v) sample with container

The raw data can be normalised to a standard, vanadium, in Gudrun*N*. The empty instrument and vanadium candlestick were measured in the neutron beam for one hour each. The scattering from the vanadium is effectively almost incoherent and is used for the instrument calibration and normalisation as its differential cross section (DCS) can accurately be determined. The empty  $\text{Ti}_{0.68}\text{Zr}_{0.32}$  cans corresponding to each of the samples were measured once neutrons had been collected for the sample as the  $\text{Ti}_{0.68}\text{Zr}_{0.32}$  flat-plate cans were filled and packed at UCL, and empty cans could not be measured beforehand. The CCR measurement can also be used for normalisation purposes. For NIMROD, the temperature is significantly different compared to ambient and so, a CCR which decreases in temperature was required for the experiments. If the pressure is more than ambient, then the thickness and material of the sample container become extremely crucial when analysing the diffraction data.

The mounting and containment of the sample are highly vital for structure factor measurements to be employed in EPSR analysis since the diffractometer is sensitive to positioning. All sample and calibration instruments handling alongside the loading procedures were performed under cryogenic conditions. The  $\text{Ti}_{0.68}\text{Zr}_{0.32}$  sample can was mounted into the end of the vanadium candlestick holder using M8 screw threads and



## 5. Total Neutron Scattering of Amorphous Solid Water with Embedded Adamantane

immediately transferred into the helium cryostat at 77 K in an organised manner. Any LN<sub>2</sub> that was transferred with samples were pumped out of the sample volume.

All samples were characterised at a base temperature of 80 K. After collecting 150  $\mu$ A of TOF scattering with the neutron current held for four hours, the samples were heated to 140 K in 5 K steps collecting 15  $\mu$ A at each temperature to achieve sintering and structural relaxation of the sample.<sup>22</sup> The samples were then cooled back down to 80 K and another set of data was recorded for four hours and 160  $\mu$ A were collected for these annealed samples. Success from annealing was measured down to very low- $Q$  intensity (characteristic of the NIMROD instrument). Neutron scattering was recorded continuously for all samples. In addition to the heating program run on all the samples, the D<sub>2</sub>O samples in the 2 mm Ti<sub>0.68</sub>Zr<sub>0.32</sub> cans were heated gradually to 230 K from 80 K while collecting high-quality diffraction data to follow on from the processes as shown in the ISIS proposal found in the appendix (Appendix 2). In brief, heating to 230 K should, in turn, show the crystallisation of H<sub>2</sub>O and perhaps show the formation/decomposition of clathrate hydrates.<sup>23-25</sup> Post-collecting neutron scattering data for each measurement, the samples and empty components were left inside the instrument before removal for approximately one hour, to prevent any exposure to remaining radiation.

The main software employed for data acquisition, temperature control and other functions were run on the Sample Environment Control Interface (SECI) software. Measurements carried out at the NIMROD instrument effectively reduces the influence of ‘inelastic perturbations’ by means of employing detectors, covering low scattering angles. Inelastic perturbation affects the background scattering levels of the data and it is possible to subtract these perturbations specific to NIMROD using the GudrunV software package.<sup>20</sup>

This software allows for the reduction of inelastic perturbations arising from light atoms, corrections, and conversions to suitable data formats of, \*.dat, \*.txt and \*.mint01 files for further analysis with the EPSR method. For the procedure of estimating the amount of perturbation, the scattered intensity is ‘binned’ as a function of the wavelength of the neutrons. A general perturbation is achieved and then refined by iterating and subtracting estimates of the inelasticity features. The corrections for inelasticity are comprehensively described by Soper.<sup>21</sup>

### 5.5 Results and Discussion

Due to the complex nature of ASW arising from its microporosity, the precise experimental details of cryogenic physical vapour deposition can have distinct effects on the morphologies of the ASW deposits.<sup>26</sup> During deposition of the material, defects and voids are created in the amorphous ice mixture. Sintering of ASW has recently been followed by neutron diffraction and the low- $Q$  diffraction intensity has been analysed.<sup>5, 9, 27</sup> Upon heating in a vacuum, pore collapse in the matrix is observed in the 120–140 K range as also shown in previous studies.<sup>26</sup> However, if these pores are filled with gases before the collapse, then the formation of clathrate hydrates can be observed upon heating. Thus, it was important to collect diffraction data before pore collapse (as-made, 80 K) and after pore collapse (after annealing at 140 K).

#### 5.5.1 Merged Differential Cross Section (DCS) Data

In order to investigate the temperature dependence of the pore collapse and sintering of this complex binary mixture, scattering data of the D<sub>2</sub>O matrices with protiated and deuterated C<sub>10</sub>H<sub>16</sub> in H<sub>2</sub>O matrices of 1:100 molar ratio were monitored from 80 K through to 230 K. The temperature program applied to C<sub>10</sub>H<sub>16</sub>/D<sub>2</sub>O and C<sub>10</sub>D<sub>16</sub>/D<sub>2</sub>O is as follows:-

1. Samples were characterised at 80 K for four hours, collecting a total of 160  $\mu$ A.
2. Samples were annealed from 90 K to 140 K for 90 minutes, collecting a total of 60  $\mu$ A, achieving sintering and structural relaxation.
3. Further to this, samples were cooled back down to 80 K and a total of 160  $\mu$ A were collected for four hours.
4. Samples were heated back to 140 K for a long-annealing process for three hours, collecting 120  $\mu$ A.
5. After the long annealing at 140 K, samples were heated once again from 150 K to 230 K for 135 minutes, collecting 90  $\mu$ A.

A schematic diagram of what is expected to happen upon these annealing steps is provided in Figure 5.3.

## 5. Total Neutron Scattering of Amorphous Solid Water with Embedded Adamantane

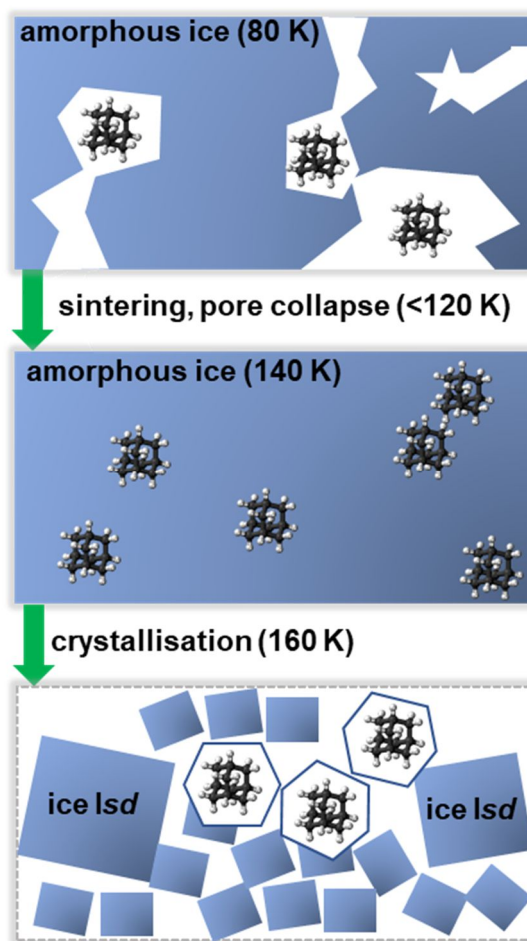


Figure 5.3. Schematic illustration of the processes expected to occur within the matrix of amorphous ice and C<sub>10</sub>H<sub>16</sub>.

The merged DCS collected over 16 hours at the time and temperature intervals mentioned above are shown in Figure 5.4(a)–(c) and as a contour plot in (d) for C<sub>10</sub>H<sub>16</sub> in D<sub>2</sub>O and in a similar format in Figure 5.5 for C<sub>10</sub>D<sub>16</sub> in D<sub>2</sub>O matrices.

## 5. Total Neutron Scattering of Amorphous Solid Water with Embedded Adamantane

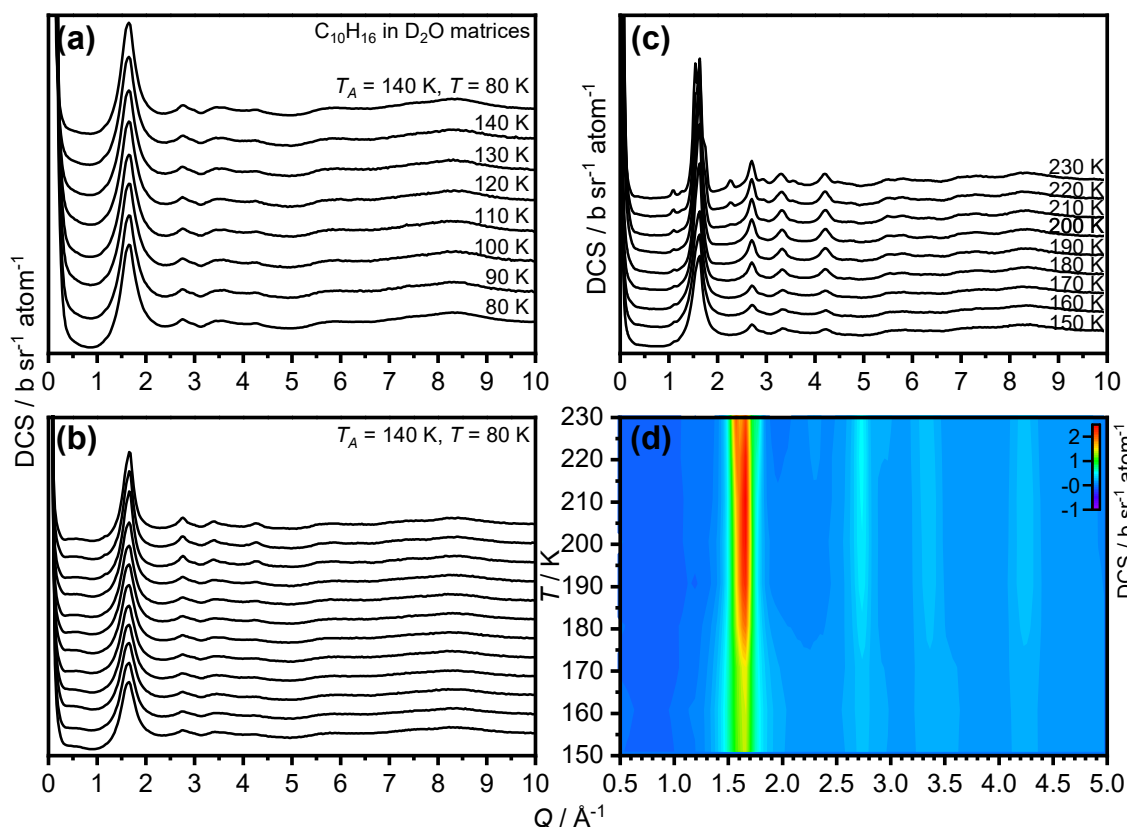


Figure 5.4. (a)–(c) Neutron diffraction DCS data of C<sub>10</sub>H<sub>16</sub> in D<sub>2</sub>O matrices at a 1:100 molar ratio accumulated over 16 hours heated from 80–230 K, where the data have been offset vertically for clarity and (d) contour plot illustrating the temperature variation in the DCS on linear DCS scales between 0 and 5.0 b sr<sup>-1</sup> atom<sup>-1</sup>.

In Figure 5.4,  $Q$  is shown on a linear scale to show the diffraction data after it has been corrected for multiple scattering, attenuation, and inelastic perturbations. Prior to crystallisation, two pronounced features can be observed in the DCS data. At approximately 120 K, the intensity in  $Q$  starts to decrease and the intensity of the sharp peak at 1.65 Å<sup>-1</sup> increases. During the annealing stage at 140 K in Figure 5.4(b), the low- $Q$  intensity does not change much and Bragg reflections at 1.65, 2.75, 3.37 and 4.35 Å<sup>-1</sup> start to emerge which are characteristic of ice I. The increase and decrease in the scattering length density and low- $Q$  intensity, respectively, indicate the collapse of pores of ASW at 120 K until 160 K. The peak at 1.65 Å<sup>-1</sup> is seen to increase in intensity during this same annealing stage which is rather peculiar. This observation may be due to compaction, where the exertion of temperature makes the sample denser. On the other hand, the influence of ordering of ASW due to structural relaxation of the sample after the orientational glass transition at 136 K is why this occurs. Significant low- $Q$  intensity >150 K, indicates that these samples are unrelaxed until they approach crystallisation.

## 5. Total Neutron Scattering of Amorphous Solid Water with Embedded Adamantane

From the perspective of the  $C_{10}H_{16}$  nanoprobe, the pore collapse should lead to increased levels of hydration where the coordination number (CN) of hydrated  $C_{10}H_{16}$  increases. Around 160 K, ASW crystallises irreversibly to give stacking disordered ice (ice *Isd*), and this is reflected in the sharpening and intensifying of the peak centred at  $1.65 \text{ \AA}^{-1}$ . After crystallisation, this peak shows a shoulder broadening towards the right-hand side of the peak at 220 K and finally a split at 230 K.

After the samples were heated to 140 K, achieving sintering and structural relaxation, another set of data were collected for the samples as shown in Figure 5.4(c), where from 140 K, the sample was thermally heated to 230 K. Throughout the entire temperature profile, the Bragg peak at  $2.75 \text{ \AA}^{-1}$  grows immensely with heating and similarly to the left-hand side of this peak, at  $3.89$  and  $4.28 \text{ \AA}^{-1}$ , a similar trend upon heating is observed. At a push, it can be stated that at 150 K, a small shoulder at  $1.15 \text{ \AA}^{-1}$  starts to grow from the main peak centred at  $1.65 \text{ \AA}^{-1}$  and once a temperature of 220 K is approached, a second shoulder between the shoulder at  $1.15 \text{ \AA}^{-1}$  and  $1.65 \text{ \AA}^{-1}$  is also observed at  $1.31 \text{ \AA}^{-1}$ . The second shoulder coincides with the growth of three other shoulders towards the right-hand side of the main peak ( $1.65 \text{ \AA}^{-1}$ ) at  $2.33$ ,  $3.04$  and  $3.60 \text{ \AA}^{-1}$ . All three shoulders intensify and sharpen as 230 K is approached. The sample becomes more relaxed and since  $C_{10}H_{16}$  is matrix-isolated, it simply gets pushed out of the matrix. The explanation for these peaks may be due to the growth of a clathrate hydrate or a new phase of  $C_{10}H_{16}$ . Without the structural analysis from ESPR, it is not possible to confirm the existence of a clathrate hydrate.

As in Figure 5.4, the full temperature profile for the  $C_{10}H_{16}/D_2O$  was described in four panels, Figure 5.5 illustrates the same profile for a fully deuterated sample:  $C_{10}D_{16}/D_2O$  at a 1:100 molar ratio. As described above, the same peculiar features before the characteristic ice I peak at  $1.65 \text{ \AA}^{-1}$  appears at  $1.14 \text{ \AA}^{-1}$  from 150 K through to 230 K and a small shoulder observed at  $1.29 \text{ \AA}^{-1}$  at 210 K appears; both these features grow in intensity until 230 K. After the ice I peak, at 210 K, a small shoulder appears at  $2.32$ ,  $3.01$  and  $3.37 \text{ \AA}^{-1}$  which remain until 230 K. To the best of our knowledge, these shoulders as described for Figure 5.4 and Figure 5.5 have not been seen before in the literature. They may be due to the fact that there are two species in the matrix where  $C_{10}H_{16}$  is finely dispersed in the complex system.

## 5. Total Neutron Scattering of Amorphous Solid Water with Embedded Adamantane

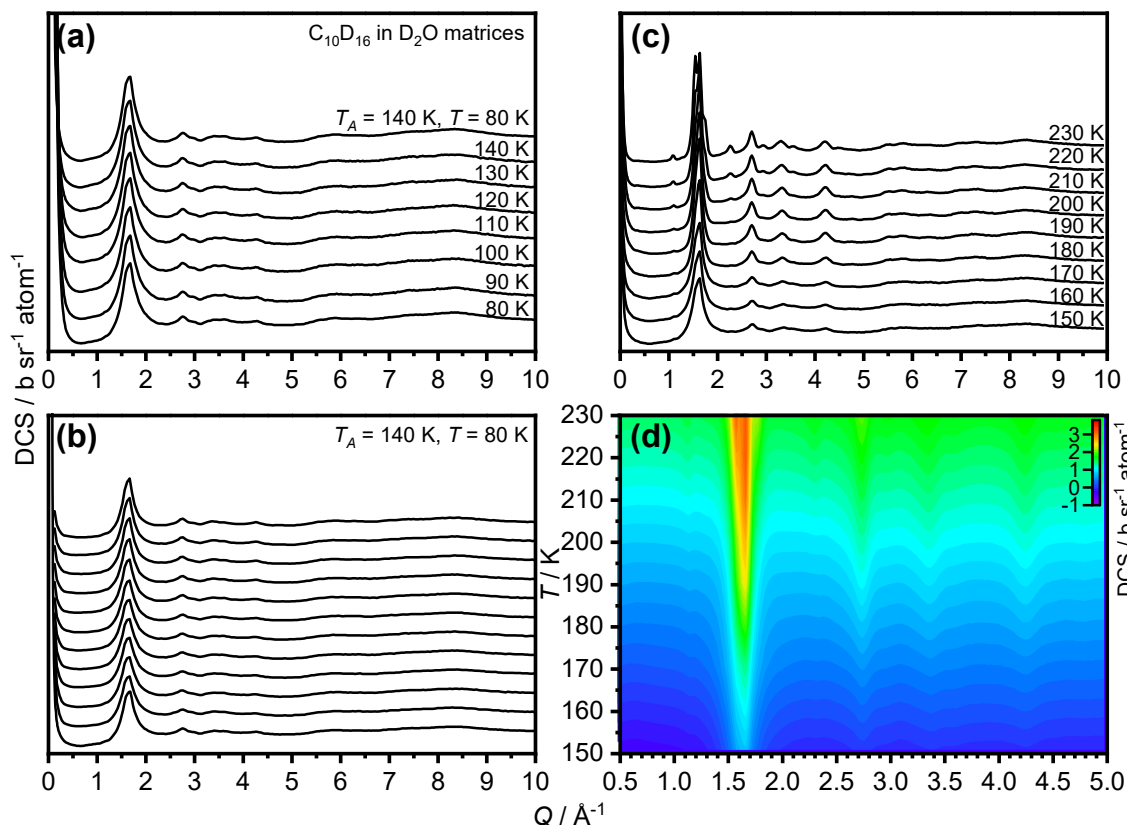


Figure 5.5. (a)–(c) Neutron diffraction DCS data of  $C_{10}D_{16}$  in  $D_2O$  matrices at a 1:100 molar ratio accumulated over 16 hours heated from 80–230 K, where the data have been offset vertically for clarity and (d) contour plot illustrating the temperature variation in the DCS on linear DCS scales between 0 and 5.0  $b \text{ sr}^{-1} \text{ atom}^{-1}$ .

### 5.5.2 Small Angle Scattering Data (SANS)

The full range of total scattered intensities of  $C_{10}H_{16}$  in a  $D_2O$  matrix from 80–230 K are depicted in Figure 5.6 and Figure 5.8 in the  $Q$  range from 0.01–20  $\text{\AA}^{-1}$ . For further discussion, the  $Q$ -range can be seen or viewed as two parts:- shown on a log10 scale, below and above 1  $\text{\AA}^{-1}$  in Figure 5.7 and Figure 5.9. These figures are divided into broad parts such that the parameters defining the complex matrix can be divided into three regions: (i) data before 140 K, where no significant changes occur, (ii) long annealed data at 140 K, to achieve sintering and structural relaxation of the sample and (iii) data for 150 K and beyond, where hydrate formation would be expected and where crystallisation of  $H_2O$  is detected.

Considering the SANS signal and conferring to the heterogeneous nature of the ASW matrix, the low  $Q$ -range displays high intensity. This slope and shape of the SANS data shows where  $Q < 1 \text{ \AA}^{-1}$  enables the observations of the properties of water-ice on the

## 5. Total Neutron Scattering of Amorphous Solid Water with Embedded Adamantane

mesoscale. One of the main features in the SANS data is the large shoulder at low  $Q$  from approximately  $0\text{--}0.1\text{ \AA}^{-1}$ . This shoulder is present for all scattered data. At higher temperatures, this shoulder is not present as such, indicating the highly porous nature of ASW at  $T < 120\text{ K}$ . Starting at  $80\text{ K}$  to approximately  $140\text{ K}$ , a ‘kink’ in the shoulder is observed at  $0.05\text{ \AA}^{-1}$ . During the annealing stages at  $140\text{ K}$ , this shoulder decreases in intensity, showing the effects of annealing and a decrease in the coherent scattering. However, after the long annealing stage at  $140\text{ K}$ , at higher temperatures, the shoulder deviates and shows an increase in the ‘hump’ or ‘kink’ starting around  $200\text{ K}$  ( $0.05\text{ \AA}^{-1}$ ). From  $200\text{--}230\text{ K}$ , this large shoulder is seen to increase after having been suppressed to lower  $Q$  during relaxation at  $140\text{ K}$ . The shoulder in the scattered data from all temperatures does not significantly shift to different  $Q$  values which is indicative that pores do not shrink or grow. The flattening of the scattered intensity between  $0.1$  and  $1\text{ \AA}^{-1}$  is seen from  $80$  to  $180\text{ K}$  and indicates pore collapse has occurred.

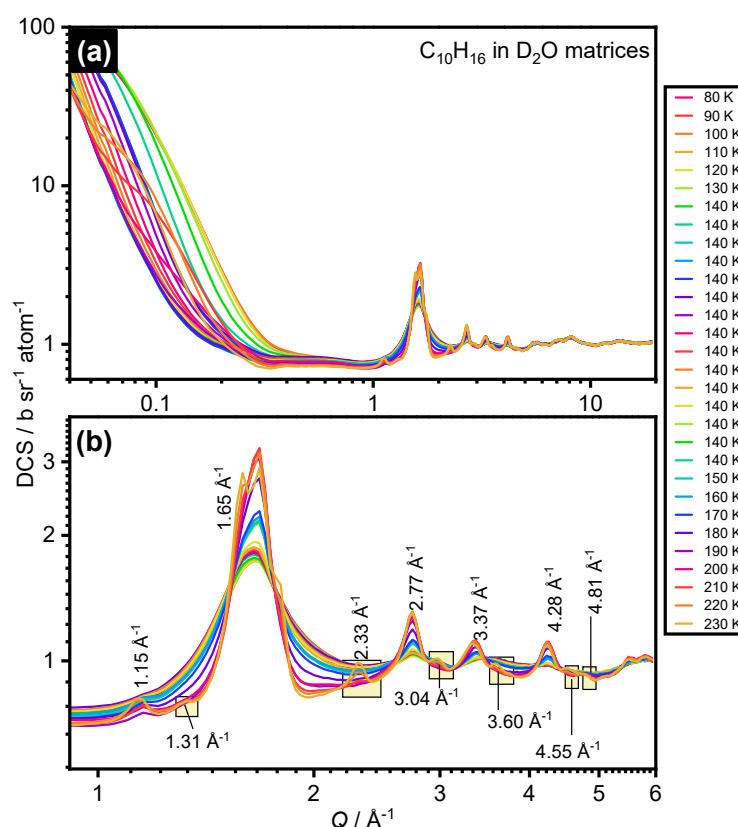


Figure 5.6. NIMROD neutron scattering data covering the mesoscale and molecular scale scattering cross-sections defining the temperature evolution of  $\text{C}_{10}\text{H}_{16}$  in  $\text{D}_2\text{O}$  molar ratio of 1:100 matrices between  $80\text{--}230\text{ K}$ , where (a) measured data from  $Q$ -values of  $0.04$  to  $20\text{ \AA}^{-1}$  and (b) measured from (a) with  $Q$ -values of  $0.9$  to  $6\text{ \AA}^{-1}$ . Highlighted features in yellow boxes denote the appearance of new Bragg features. Spectra are shown as a function of temperature.

## 5. Total Neutron Scattering of Amorphous Solid Water with Embedded Adamantane

Overall, the main peaks already at 80 K which intensify upon heating are seen at 1.65, 2.77, 3.42 and 4.28  $\text{\AA}^{-1}$ . For the data recorded above 140 K, sharp Bragg peaks start to form in this region of  $Q$  values from 1–10  $\text{\AA}^{-1}$ . Particularly at 150 K, the appearance of a peak at 1.15  $\text{\AA}^{-1}$  is observed to intensify and sharpen as the temperature increases up to 230 K. At approximately 1.65  $\text{\AA}^{-1}$  seen in all patterns from 80 K to 230 K, this peak indicates the presence of ice I and is extremely pronounced until 230 K where at this temperature, the Bragg peak splits. The strong peak signal in the scattered data in the intermediate  $Q$ -range implies and provides clear evidence for the transition from an amorphous as-made (80 K) sample, crystallising to ice *Isd* and further to hexagonal ice (ice *Ih*) above the crystallisation temperature of H<sub>2</sub>O at  $T > 140$  K. At 200 K, as already mentioned, but repeated here for clarity, a series of new Bragg peaks appear and grow in intensity upon heating. They are seen at 1.31, 2.33, 3.04, 3.60, 4.55 and 4.81  $\text{\AA}^{-1}$  (as highlighted in Figure 5.6) and to the best of our knowledge, have not been reported in the literature before. This is undoubtedly due to the presence of two species in the matrix.

Below 140 K, as expected, no sign of crystallisation is detected as reflected in the broadness of the main ice I peak. It is possible to conclude that the flattening of the SANS data below  $T = 140$  K is not due to crystallisation but ASW morphology inferring pore collapse, and regardless of any changes in the as-made (80 K) sample data, the intermolecular bonding remains amorphous below 140 K. The isothermal hold at 140 K for three hours started to display the narrowing of the peak at 1.65  $\text{\AA}^{-1}$  and the appearance of new Bragg peaks.



## 5. Total Neutron Scattering of Amorphous Solid Water with Embedded Adamantane

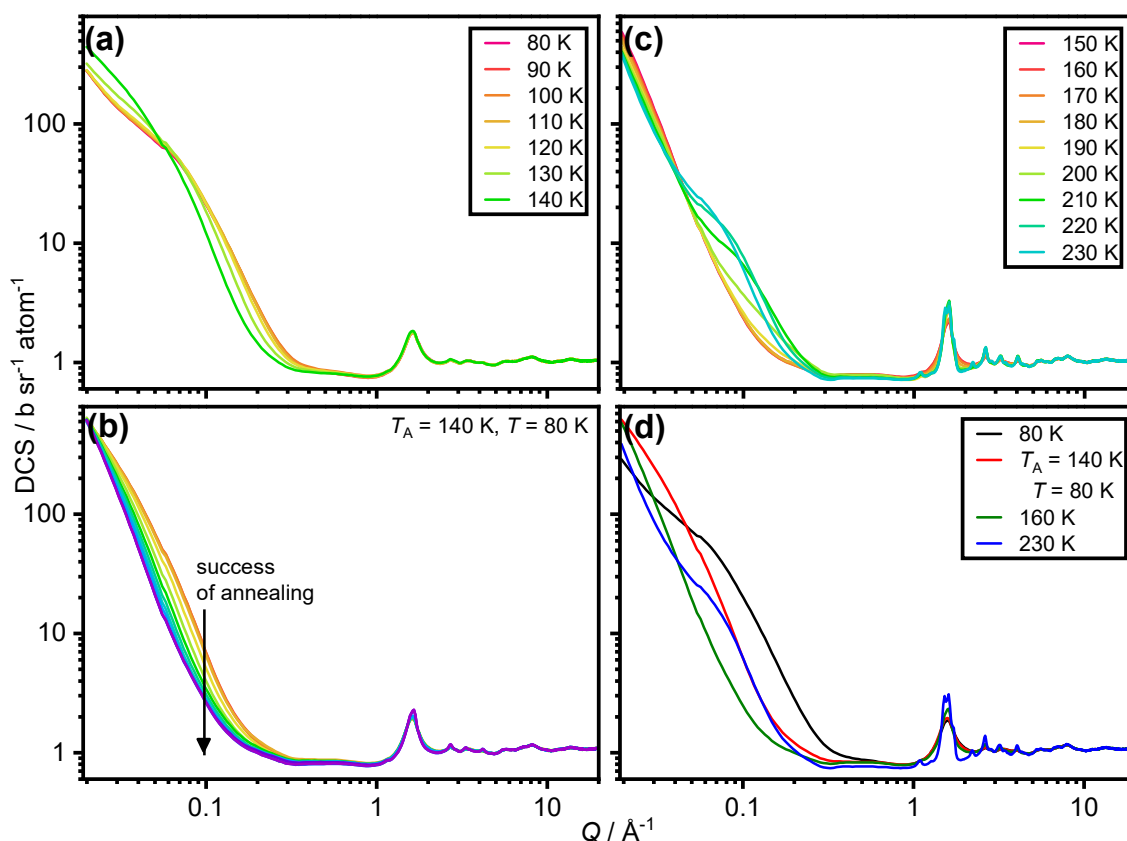


Figure 5.7. NIMROD neutron scattering spectra ( $C_{10}H_{16}/D_2O$  at a 1:100 molar ratio), covering the mesoscale and molecular scale scattering cross-sections showing the scattering signal DCS ( $b\ sr^{-1}\ atom^{-1}$ ) as a function of the momentum transfer,  $Q$ , which is thus, inversely proportional to the length scale. Sequential plots, (a), (b) and (c) show the temperature evolution in several steps between 80 and 230 K, from a  $Q$  range of 0.01–20  $\text{\AA}^{-1}$  where (a) 80–140 K, (b) isothermal pause at 140 K for three hours, (c) heating from 150–230 K and (d) specific temperatures from (a)–(c) to show the differences upon heating.

The merged DCS levels are shown as overlapping diffraction patterns and are displayed in Figure 5.8(a), and more clearly in Figure 5.9(a). These figure show  $Q$ -values on a log10 scale to highlight changes occurring at low  $Q$  and prior to crystallisation in Figure 5.9(a) and Figure 5.9(b).

A decrease in the shoulder of the fully deuterated sample from 80 K to 140 K can be seen. The merged DCS level decreases at 0.1  $\text{\AA}^{-1}$  at 80 K, indicating that the high scattering intensity for the pure as-made sample at 80 K is due to increased scattering levels of hydrogen. At 120 K, a more pronounced decrease in the DCS level is experienced. With the increase in temperature, after 140 K, the DCS level and intensity at  $Q < 0.3\ \text{\AA}^{-1}$  begins to decrease further and the intensity of the ice I peak at 1.65  $\text{\AA}^{-1}$  sharpens and intensifies. At 160 K, the low- $Q$  intensity does not experience much change

## 5. Total Neutron Scattering of Amorphous Solid Water with Embedded Adamantane

and Bragg reflections associated with ice I appear at 2.73, 3.36 and 4.35  $\text{\AA}^{-1}$ . The Bragg peak at  $\sim 3.3 \text{ \AA}^{-1}$  may indicate a higher density phase of vapour deposited ice and could be attributed to evidence for the polymorphism in ASW.<sup>28</sup> The decrease in the low- $Q$  intensity complements the increase in the homogeneity of the scattering length density and thus, suggest the pores within ASW already collapse during the annealing stage after 120 K. Until a temperature of 160 K, the pores of ASW are not completely eliminated. It must be noted that during 120 K to 160 K, the peak centred at 1.65  $\text{\AA}^{-1}$  still increases in intensity. At a push, it can be stated that this increase is due to a density increase from compaction of the sample or the influence of relaxation of ASW during the long annealing stage at 140 K prior to the crystallisation of H<sub>2</sub>O to ice *Isd*.

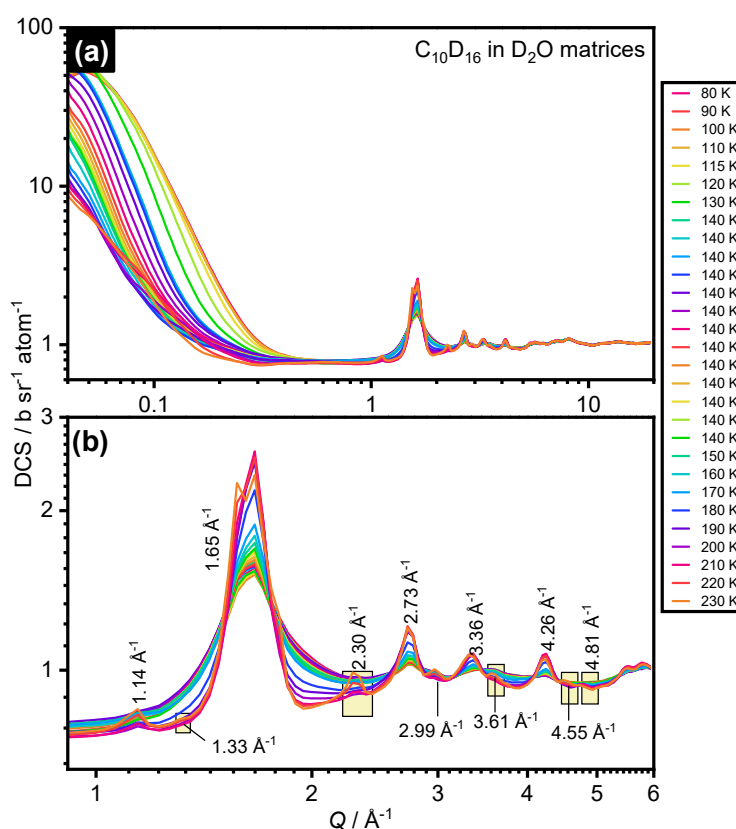


Figure 5.8. NIMROD neutron scattering data covering the mesoscale and molecular scale scattering cross-sections defining the temperature evolution of  $C_{10}D_{16}$  in  $D_2O$  molar ratio of 1:100 matrices between 80–230 K, where (a) measured data from  $Q$ -values of 0.04 to 20  $\text{\AA}^{-1}$  and (b) measured from (a) with  $Q$ -values of 0.9 to 6  $\text{\AA}^{-1}$ . Highlighted features in yellow boxes denote the appearance of new Bragg features. Spectra are shown as a function of temperature.

A separated temperature profile of Figure 5.8(a) is provided in Figure 5.9, where changes in the DCS level and scattering intensity are seen more clearly. As the intensity decreases at low  $Q$  during the long annealing stage at 140 K, the rate of sintering could be suggested

## 5. Total Neutron Scattering of Amorphous Solid Water with Embedded Adamantane

to be highly dependent on temperature and suggest that the porosity of ASW is significantly reduced. It could also be proposed that a specific temperature is required to close a pore with considerations of its size. The crystallisation of the matrix occurs immediately after relaxation and sintering, suggesting that the structure and dynamics of ASW is closely related. Very small pores would be classed as structural defects, and if they closed upon heating, then bulk relaxation which is required for crystallisation should occur when a pore size would approach close to zero. It is important to note, this is just speculation from the data presented in this work.

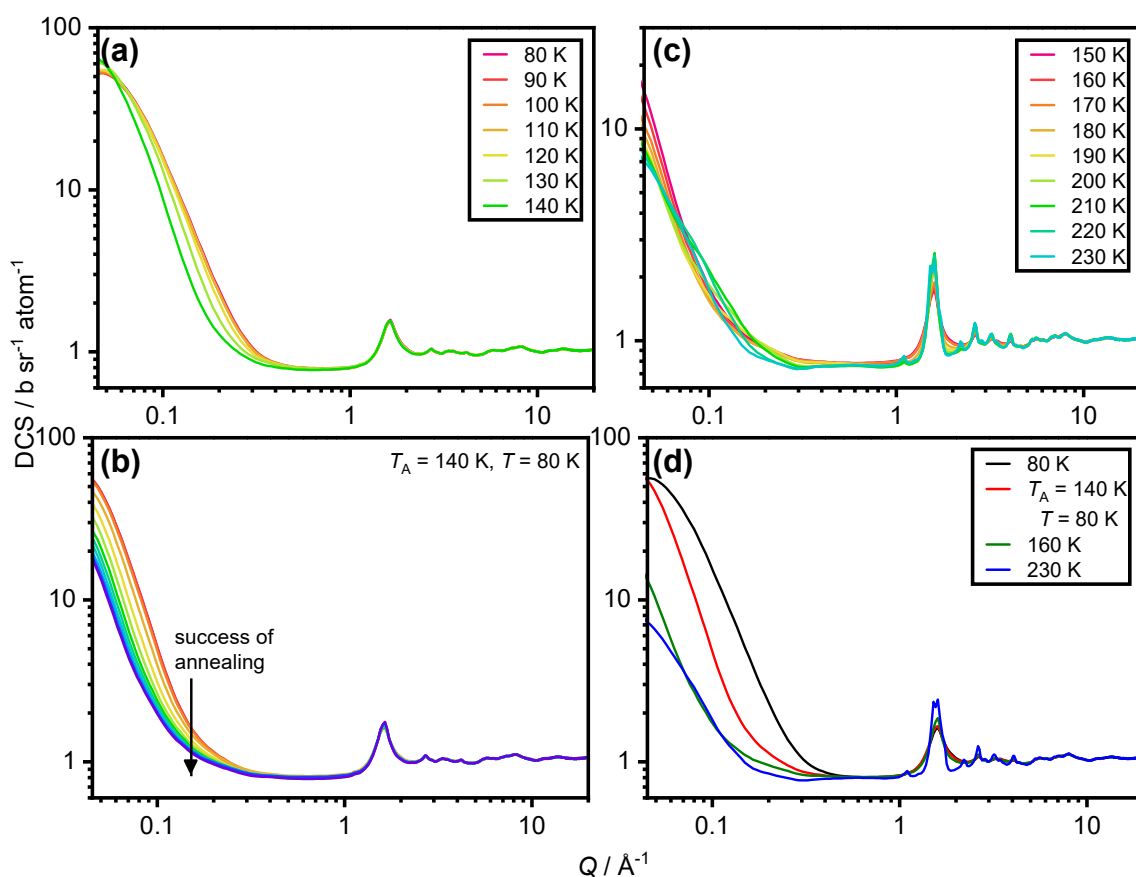


Figure 5.9. NIMROD neutron scattering spectra ( $C_{10}D_{16}/D_2O$  at a 1:100 molar ratio), covering the mesoscale and molecular scale scattering cross-sections showing the scattering signal DCS ( $b\ sr^{-1}\ atom^{-1}$ ) as a function of the momentum transfer,  $Q$ , which is thus, inversely proportional to the length scale. Sequential plots, (a), (b) and (c) show the temperature evolution in several steps between 80 and 230 K, from a  $Q$  range of 0.01–20  $\text{\AA}^{-1}$  where (a) 80–140 K, (b) isothermal pause at 140 K for three hours, (c) heating from 150–230 K and (d) specific temperatures from (a)–(c) to show the differences upon heating.

To conclude the results from  $H_2O$ -rich samples with embedded  $C_{10}H_{16}$ , SANS data has been analysed for  $C_{10}H_{16}$  and  $C_{10}D_{16}$  in  $D_2O$  matrices. Overall, for both samples,  $C_{10}H_{16}$  in  $D_2O$  and  $C_{10}D_{16}$  in  $D_2O$  show that the sample is unrelaxed until crystallisation due to

## 5. Total Neutron Scattering of Amorphous Solid Water with Embedded Adamantane

low- $Q$  intensity at  $T > 150$  K and sintering has been observed. The observations of new Bragg peaks have been identified and are proposed to arise from the mixture of both species. The EPSR method would now be needed to confirm how H<sub>2</sub>O hydrates the hydrophobic species and to confirm whether these Bragg peaks arise from a possible new type of clathrate hydrate. The observations are based upon samples as-made at 80 K, whereas temperatures reaching as low as 10–60 K in astrophysical environments are indicative of the formation of ASW. The structural evolution for pores, the collapse of pores and behaviour of H<sub>2</sub>O deposited at lower temperatures will thus, be a subject of future studies. However, it must be appreciated that this is the first time C<sub>10</sub>H<sub>16</sub> has been finely dispersed in a matrix of H<sub>2</sub>O.

In addition to obtaining neutron diffraction data for the 1:100 H<sub>2</sub>O-rich samples, a sample of high concentration, 1:34 C<sub>10</sub>H<sub>16</sub>-rich sample, was also subjected to the same temperature measurements as previously described. Figure 5.10 and Figure 5.11 display the corrected SANS diffraction data.

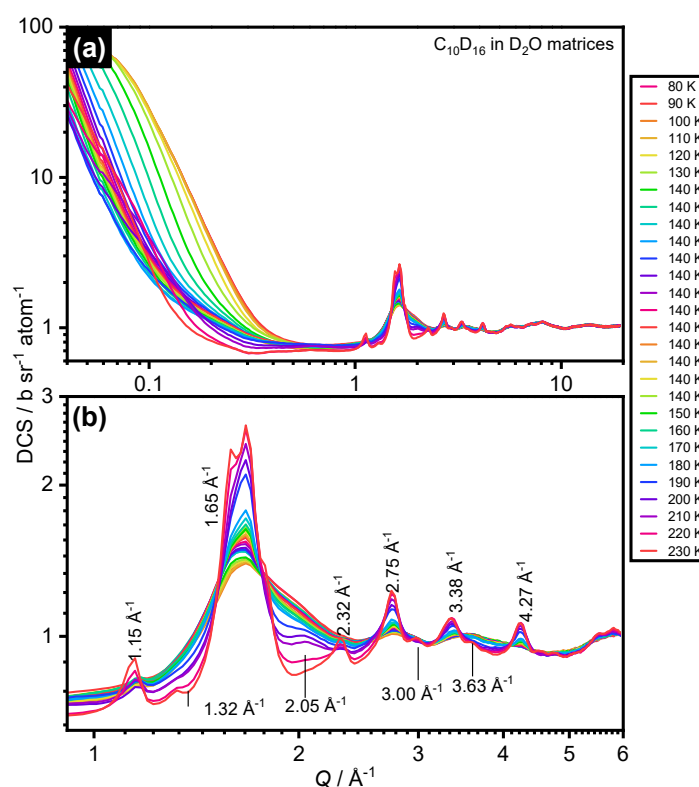


Figure 5.10. NIMROD neutron scattering data covering the mesoscale and molecular scale scattering cross-sections defining the temperature evolution of C<sub>10</sub>D<sub>16</sub> in D<sub>2</sub>O molar ratio of 1:34 matrices between 80–230 K, where (a) measured data from  $Q$ -values of 0.04 to 20 Å<sup>-1</sup> and (b) measured data from (a) with  $Q$ -values of 0.9 to 6 Å<sup>-1</sup>. Spectra are shown as a function of temperature.

## 5. Total Neutron Scattering of Amorphous Solid Water with Embedded Adamantane

As seen previously for the 1:100 isotopically mixed samples, similar trends and Bragg peaks are observed for the  $C_{10}D_{16}$ -rich sample. A summary of Bragg peaks is provided and listed in Table 5.2 for all samples from neutron diffraction patterns. Intriguingly, from 190–210 K, a small Bragg peak to the right-hand side of the main ice I peak emerges. This Bragg peak can be found at  $2.05 \text{ \AA}^{-1}$  after crystallisation and it could be proposed that due to the significantly higher concentration of  $C_{10}H_{16}$  in the sample when compared to the  $H_2O$ -rich samples, a clathrate hydrate may be forming. This peak does not appear after 210 K. Unexpectedly and once again, as seen in Chapter 4, from the XRD patterns, ice *Isd* is the active material for making a new clathrate hydrate. However, one can only assume this is the case. Nevertheless, it could also be stated that a new phase of  $C_{10}H_{16}$  is seen but not all Bragg peaks are detected. Figure 5.11 displays the breakdown of the temperature measurements carried out on the  $C_{10}H_{16}$ -rich sample.

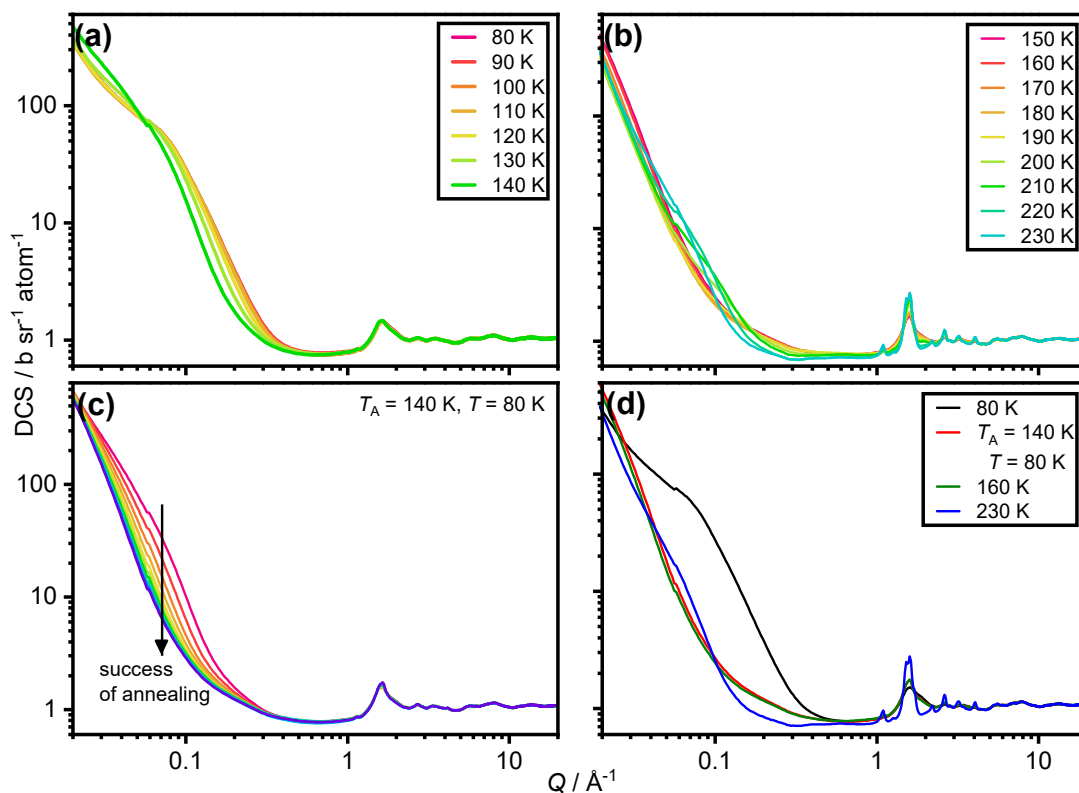


Figure 5.11. NIMROD neutron scattering spectra ( $C_{10}D_{16}/D_2O$  at a 1:34 molar ratio), covering the mesoscale and molecular scale scattering cross-sections showing the scattering signal DCS ( $b \text{ sr}^{-1} \text{ atom}^{-1}$ ) as a function of the momentum transfer,  $Q$ , which is thus, inversely proportional to the length scale. Sequential plots, (a), (b) and (c) show the temperature evolution in several steps between 80 and 230 K, from a  $Q$  range of 0.01–20  $\text{\AA}^{-1}$  where (a) 80–140 K, (b) isothermal pause at 140 K for three hours, (c) heating from 150–230 K and (d) specific temperatures from (a)–(c) to show the differences upon heating.

## 5. Total Neutron Scattering of Amorphous Solid Water with Embedded Adamantane

Table 5.2. Summary of the SANS data with listed Bragg peaks characteristic of ice I and new identified peaks.

Sample	Figure	Ice I Bragg peaks / $\text{\AA}^{-1}$	New Bragg peaks / $\text{\AA}^{-1}$
$\text{C}_{10}\text{H}_{16}/\text{D}_2\text{O}$ 1:100	5.6 5.7	1.65, 2.33, 2.75, 3.37, 4.28	1.15, 1.31, 3.04, 3.60
$\text{C}_{10}\text{D}_{16}/\text{D}_2\text{O}$ 1:100	5.8 5.9	1.65, 2.33, 2.73, 3.36, 4.35	1.15, 1.31, 3.04, 3.60, 4.55, 4.81
$\text{C}_{10}\text{D}_{16}/\text{D}_2\text{O}$ 1:34	5.10 5.11	1.65, 2.32, 2.75, 3.38, 4.27	1.15, 1.32, 2.05, 3.00, 3.63

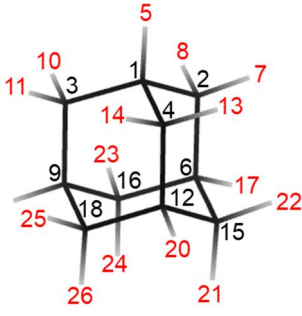
### 5.6 Details of Structural Reconstruction by the EPSR Method

For structural reconstruction, a standard Monte Carlo (MC) simulation was carried out with the EPSR software<sup>10, 11</sup> and used to fit the experimental data bringing the simulation to equilibrium, to obtain full structural models of the matrices. In order to create a structural model representing the structure of such a complex/binary mixture over large enough distances to be thermodynamically accurate, a cubic box of dimension 64.673828  $\text{\AA}$  was employed and filled with 8000  $\text{H}_2\text{O}$  molecules and 80  $\text{C}_{10}\text{H}_{16}$  molecules giving an atomic number density of 0.09641  $\text{\AA}^{-3}$  atoms, consistent with the experimental density of ASW at 80 K (as-made) and after annealing at 140 K. This sized box was large enough to minimise the dependence on PBC and allowed for structurally representative clustering of  $\text{C}_{10}\text{H}_{16}$  to form within the simulation box. It must be stressed that clustering is allowed to occur, however, does not occur in a reproducible fashion.

The following labels were assigned to atomic sites on the  $\text{C}_{10}\text{H}_{16}$  molecules and  $\text{H}_2\text{O}$  molecules: (i)  $\text{C}_{10}\text{H}_{16}$ : C1, H1, C2, H2 for carbon atoms of methine nature (CH) and the corresponding hydrogen atom and for carbon atoms of methyldene nature ( $\text{CH}_2$ ) with the corresponding hydrogen atoms, respectively, (ii)  $\text{H}_2\text{O}$ : O and  $\text{H}_w$  for the oxygen atom and two hydrogen atoms, respectively. The average bond angles, lengths of  $\text{C}_{10}\text{H}_{16}$ , the 12–6 Lennard Jones (LJ) parameters and partial charges were taken from OPLS-AA (Optimized Potentials for Liquid Simulations of all atoms) force field<sup>29</sup> used to seed the process for the EPSR model. These parameters are summarised in Table 5.3.<sup>30</sup> The assumed O–H and H–H intramolecular distances are 0.976 and 1.55  $\text{\AA}$ , respectively.

## 5. Total Neutron Scattering of Amorphous Solid Water with Embedded Adamantane

Table 5.3. Atom nomenclature for all the labelled atoms in the EPSR models where red atom labels are hydrogen and black atom labels are carbon, LJ depths ( $\epsilon$ ), core diameter ( $\sigma$ ), atomic mass ( $M$ ) and Coulomb charge parameters ( $q$ ) employed for the reference potentials that further seed the EPSR model as presented in this study. The second half of the table denotes the bond lengths and angles for the atoms in  $C_{10}H_{16}$ .

Molecule & atom numbering	atom type	$\epsilon / \text{kJ mol}^{-1}$	$\sigma / \text{\AA}$	mass ( $M / \text{amu}$ )	charge ( $q / e$ )
	C1	0.276144	3.5	12.0110	-0.06000
	C2	0.276144	3.5	12.0110	-0.12000
	H1	0.125520	2.5	2.0000	0.06000
	H2	0.125520	2.5	2.0000	0.06000
	O1	0.65	3.1	15.999	-0.8476
	H <sub>w</sub>	0.00	0.00	2.0000	0.4238
	bond	angle	-	bond	bond length
	C2 C1 C2	109.81320	-	C1-C2	1.53503
	C2 C1 H1	109.11520	-	C1-H1	1.03972
	C1 C2 C1	108.78149	-	C2-H2	1.08424
	C1 C2 H2	108.88074	-	-	-
	H2 C2 H2	112.42291	-	-	-

The process of EPSR was initiated by equilibration based on the set of reference potentials as provided in Table 5.3, the atomic density of system, geometry and chemical stoichiometry.<sup>19</sup> Once the model had reached equilibration, structure factors were calculated and compared with the data. The model in a first instance will not reproduce the data sufficiently well and thus, the interatomic site-site potential can be simultaneously iterated to refine and drive the simulated data towards an agreement with the experimental data. This is achieved *via* introducing and switching on the so-called empirical potentials as explained in Chapter 2, section 2.6.4. This allows for electronic and molecular information to be built into the EPSR refinement process. Once an agreement with the simulated and experimental data was observed, the potential was thus, adequately refined, and the simulation was run for many hours to proceed without further perturbation of the potentials. Once the system finished equilibrating, approximately 20,000 model iterations for data acquisition were accumulated for both sets of data run at 80 K (as-made) and after annealing at 140 K to obtain structural information from the models by obtaining the best possible fits to the data. A wealth and ensemble of average structural information were accumulated over many configurations.

## 5. Total Neutron Scattering of Amorphous Solid Water with Embedded Adamantane

The angle-dependent correlation functions shown later in this thesis in Figure 5.20 and Figure 5.21 have been obtained by fitting generalized spherical harmonic functions<sup>31, 32</sup> to the partial structure factors using the auxiliary routine in EPSR termed, SHARM and SDF. The Clebsch-Gordon coefficients were used for the spherical harmonic functions and are such that:  $l_1 = 1, 2, 3, 4$ ,  $l_2 = 1, 2, 3, 4$ ,  $m_1 = 0$  and  $n_2 = 0$ . The input parameters used to produce the plot in Figure 5.18 with *plot2D* and *plot3D* programmes are listed in Table 5.4.

Table 5.4. Input parameters for the plotting programmes used to visualize the angle-dependent correlation functions.

	$g(r, \alpha)$	$g(r, \alpha)$	$g(r, \theta, \phi)$
Figure	Figure 5.23	Figure 5.18	Figure 5.18
plotting programme	<i>plot2d (OCF)</i>	<i>plot2d (SDF)</i>	<i>plot3djmol (SDF)</i>
$l_1, l_2$	1 1	1 0	1 0 1
$n_1, n_2$	1 1	1 0	1 0
$m$	1	0	0
$n_{vary}$	4	1	1
$ph\_th\_ch$ ( $\theta, \phi$ )	X Y 0 0 where, X = 70, 80, 90° Y = 63, 1, 30°	0 0 0 0	0 0 0

The values of  $l_1$  and  $n_1$  enable the control of the direction of theta ( $\theta$ ) and phi ( $\phi$ ) of the H<sub>2</sub>O molecule (second molecule) relative to the axes that is defined for C<sub>10</sub>H<sub>16</sub>. The axes are defined here from the centre of mass (COM) of C<sub>10</sub>H<sub>16</sub> to the oxygen atom of H<sub>2</sub>O. If these were given the value of 0, then it would mean the corresponding coordinate would be averaged. If no axes on the molecule were defined, no orientation correlation functions (OCF), or two-dimensional spatial density functions (SDF) would be present.

Fixing the values of  $l_1$ ,  $l_2$ ,  $n_1$ ,  $n_2$  and  $m_2$  allows the user to control the particular distribution functions. The orientation of H<sub>2</sub>O is controlled by the values of  $l_2$ ,  $n_2$  and  $m$ . For the specific two-dimensional SDFs (upcoming Figure 5.29),  $l_2$ ,  $n_2$  and  $m = 0$  as in this case, averaging over the second molecule is needed. For the three-dimensional SDF plots (upcoming Figure 5.29),  $n_{vary}$  is 1 as the variation in theta\_1 and phi\_1 is needed to calculate the angular coordination. The surfra level depends on the data. A standard value of 15%, is where most molecules are possibly shown.



## 5. Total Neutron Scattering of Amorphous Solid Water with Embedded Adamantane

The coordinates after every fifth iteration were saved and so the extraction of heavily detailed structural information *via* the construction of three-dimensional models constrained by different data sets was obtained. In addition, the ANGULA software<sup>14</sup> was used to extract the COM pair correlation functions of  $g_{\text{COM-O}}(r)$ ,  $g_{\text{COM-H}}(r)$ , positional maps, and OCFs. The  $t_{ij}(r)$  functions (as defined in Chapter 2) were also separated into contributions from a number of closet neighbours.

### 5.6.1 Data Fitting

Once the box of atoms is created, the simulation is transferred onto the EPSR program in order to see the starting configuration and how it fits with the diffraction data. To do this, a \*.wts file is created which directly tells EPSR how to compare the distribution of the simulated data with the experimental diffraction data. The neutron weights file, \*.nwts, defines chemical symbols and allows the conversion to scattering lengths. Hydrogen can exchange with other hydrogen atoms and so the weight files of each sample were treated differently in EPSR. Each weight file needs to assign an isotope type to each atom and the current weight file would have no reference to H2. Thus, these were assigned with correct atomic compositions. Table 5.5 displays the samples and their abundance which were required for the EPSR model.

During the data fitting initially, the correction of raw data was carried out with GudrunN as mentioned in Chapter 2, section 2.6.3 differently for each sample. For example, the D<sub>2</sub>O samples were assumed to be slightly contaminated with H<sub>2</sub>O. This may be due to the experimental procedure where the sample is exposed to atmospheric moisture for a few seconds and some mixing with H<sub>2</sub>O may occur. The pure D<sub>2</sub>O sample would be the most susceptible to this kind of unavoidable error as the incoherent cross-section of light hydrogen is much higher than deuterium. This indicates that a small amount of hydrogen in the sample would make a large difference to the levels.

After several attempts of simulating data in EPSR using the data that had been corrected in GudrunN, in particular, the \*.wts file did not agree well with the EPSR model and thus, it was revealed that minuscule amounts of hydrogen impurities were identified in the D<sub>2</sub>O samples. This may have been due to some LN<sub>2</sub> in the pores of ASW. Thus, the atomic composition of the D<sub>2</sub>O samples were iterated with 2, 5, 7 and 10% H<sub>2</sub>O impurity in GudrunN. The resulting data for 5% hydrogen impurity in the D<sub>2</sub>O samples gave the best fit to the structure factors,  $F(Q)$ , in EPSR.

## 5. Total Neutron Scattering of Amorphous Solid Water with Embedded Adamantane

Table 5.5. The neutron weight files with assigned weights for each isotope, where the exchange = 1 if this atom exchanges with other atoms and 0 otherwise. The abundance is the list of mass numbers and abundances where 0 is assigned for a natural isotope.

sample	atom	exchange	abundance
C <sub>10</sub> H <sub>16</sub> /H <sub>2</sub> O	H1	0	0 1
	H2	0	0 1
	H <sub>w</sub>	0	0 1
C <sub>10</sub> H <sub>16</sub> /D <sub>2</sub> O	H1	0	0 1
	H2	0	0 1
	H <sub>w</sub>	0	2 0.95 0 0.05
C <sub>10</sub> H <sub>16</sub> /HDO	H1	0	0 1
	H2	0	0 1
	H <sub>w</sub>	0	0 0.5 0 0.5
C <sub>10</sub> D <sub>16</sub> /H <sub>2</sub> O	H1	0	2 1
	H2	0	2 1
	H <sub>w</sub>	0	0 1
C <sub>10</sub> D <sub>16</sub> /D <sub>2</sub> O	H1	0	2 1
	H2	0	2 1
	H <sub>w</sub>	0	2 0.95 0 0.05
C <sub>10</sub> D <sub>16</sub> /HDO	H1	0	2 1
	H2	0	2 1
	H <sub>w</sub>	0	2 0.5 0 0.5

While the first estimates of the structure from the simulation were gathered, the energy and the pressure of the model were simultaneously monitored. They should be negative and positive, respectively. The pressure became negative on switching on the empirical potential which caused voids to form in the simulation box, giving rise to additional small-angle scattering. This is due to the ice samples containing pores which is characteristic of ASW. Upon switching on the empirical potential, the energy was positive and thus, it was required to decrease further. However, as the energy was not stable, the simulation indicated an intramolecular MC ‘shake’ occurred (i.e., moves atoms within a molecule, through MC moves). This results in higher energy due to changed intermolecular separations. These movements should be small, resulting in a small energy change. At this point, it was important to plot the simulation box to ensure no H<sub>2</sub>O molecules were trapped inside the C<sub>10</sub>H<sub>16</sub>, and if so, the box had to be re-randomised. During the structural reconstruction and data fitting, this problem was encountered in a few attempts (two/three times) and so, the simulation box had to be re-randomised.

## 5. Total Neutron Scattering of Amorphous Solid Water with Embedded Adamantane

### 5.6.2 Total Structure Factors ( $F(Q)$ )

Using the EPSR method approach,<sup>10, 11</sup> three-dimensional structural models of C<sub>10</sub>H<sub>16</sub> in H<sub>2</sub>O matrices have been achieved for measurements collected as-made and after annealing at 140 K which are in agreement with the experimentally obtained neutron diffraction data as shown in Figure 5.12. Six  $F(Q)$ s with different hydrogen contrasts are available from the experiments carried out in this study and the  $F(Q)$  data is shown up to 20 Å. As several isotopically substituted mixtures were prepared and measured, fitting the diffraction data significantly increased the reliability of the structure refinement process. The differences between the diffraction datasets at each temperature as shown in Figure 5.12 are caused by the different neutron scattering properties of <sup>1</sup>H (−3.74 fm) and D (+6.67 fm).

Small differences can be seen in the experimental and EPSR-derived model of C<sub>10</sub>H<sub>16</sub> in H<sub>2</sub>O matrices located at low- $Q$  values where there is an increase in the intensity with an increase in scattering contrast. These discrepancies are caused by inelastic scattering caused by hydrogen. In addition, this observation indicates the presence of local concentration fluctuations of C<sub>10</sub>H<sub>16</sub> in H<sub>2</sub>O matrices.

The most noticeable improvements to the fits were observed in the 1 to 4 Å<sup>−1</sup>  $Q$ -range which is highly sensitive to intermolecular correlations. It can be concluded that the potential parameters taken from the OPLS-AA force field<sup>29</sup> produced a reasonable starting structure. However, the descriptive power of the empirical potentials was required to obtain the best possible fits to the experimental data.

EPSR converged the measured and simulated diffraction data by optimizing the so-called empirical potentials in an iterative process until a good fit was achieved. This was vital for obtaining accurate intermolecular structural information. These empirical potentials are defined between every intermolecular atom pair of the complex system as mentioned earlier. To illustrate how the empirical potentials affect the data, the fits of two as-made samples before switching on the empirical potentials have been displayed in Figure 5.13. This indicates the highly advantageous role that EPSR plays in driving the model towards a good agreement with the experimental data.

## 5. Total Neutron Scattering of Amorphous Solid Water with Embedded Adamantane

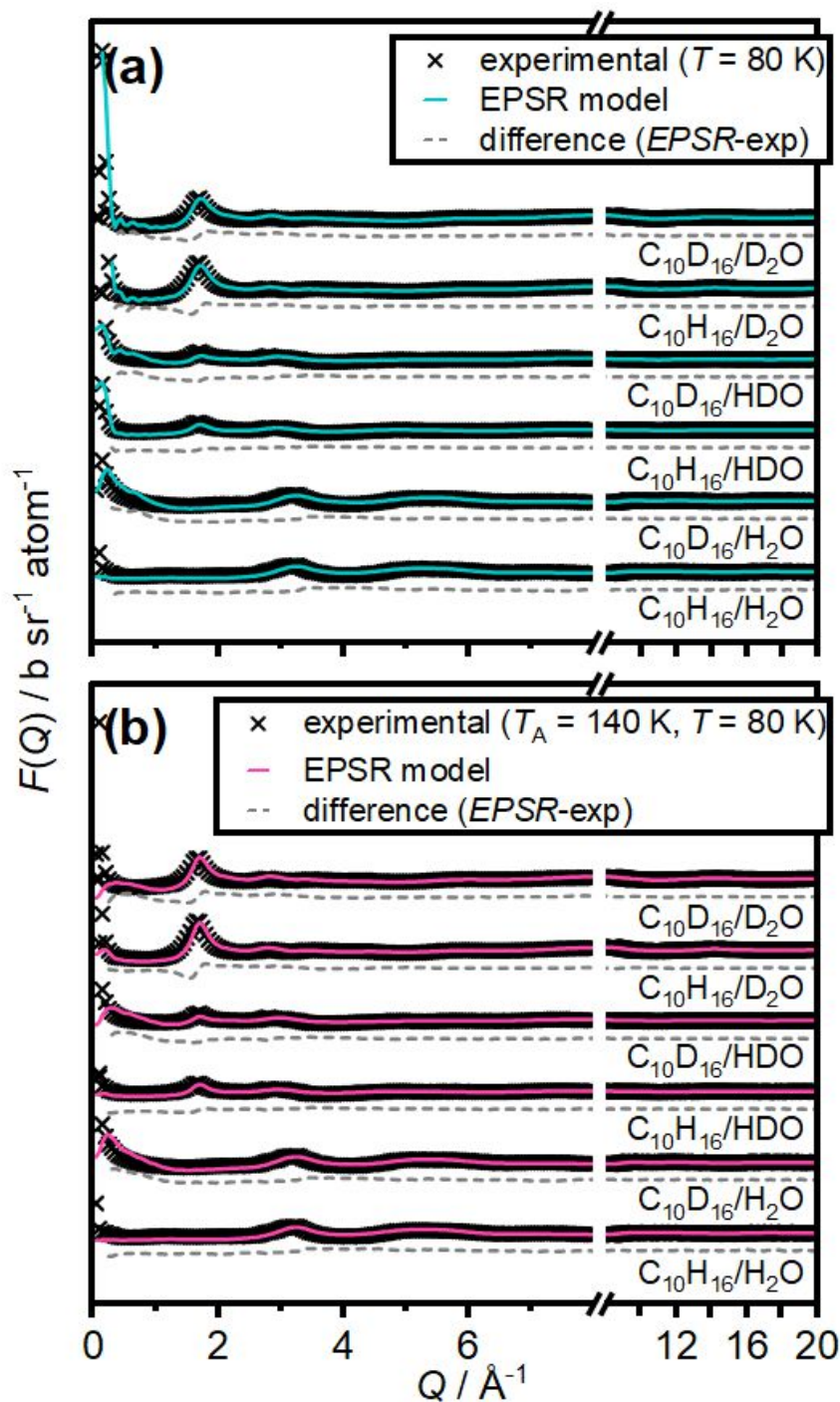


Figure 5.12. Experimental (black crosses) and calculated neutron diffraction data at (a) 80 K (as-made, solid blue lines) and (b) after annealing at 140 K (solid pink lines) from EPSR-derived total structure factors,  $F(Q)$  for a series of isotopically different  $\text{C}_{10}\text{H}_{16}$  and  $\text{H}_2\text{O}$  substituted samples including H/D = 50/50 in reciprocal space. The grey dashed lines are the subsequent differences between the experimental and EPSR models and have been shifted vertically for clarity. The diffraction data in (a) and (b) are offset vertically in order of increasing scattering length density contrast.

## 5. Total Neutron Scattering of Amorphous Solid Water with Embedded Adamantane

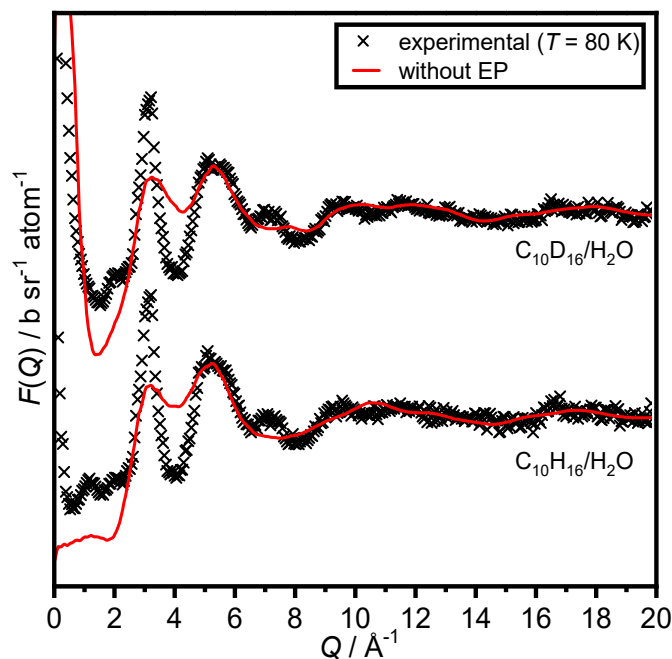


Figure 5.13. Experimentally measured diffraction data (black crosses) and the simulated EPSR-derived total structure factors,  $F(Q)$ , indicated samples without the empirical potentials at (a) 80 K (as-made sample). The use of the empirical potential clearly shows the part in which EPSR plays in driving the simulation towards a good agreement with the data.

## 5. Total Neutron Scattering of Amorphous Solid Water with Embedded Adamantane

### 5.6.3 Pair Distribution Functions (PDFs)

The specific interactions which exist between neighbouring molecules govern the local structure of liquids. In the case of the binary mixture here, a similar approach can be employed. Atoms of neighbouring molecules have attractive interactions which can be revealed by sharp, intense features in the isotropic intermolecular pair correlation functions defined as,  $g_{ij}(r)$ .

From a structural model of C<sub>10</sub>H<sub>16</sub> within the amorphous ice, 21 radially averaged pair correlations functions,  $g_{ij}(r)$ , can be obtained:  $g_{Hw-Hw}(r)$ ,  $g_{O1-Hw}(r)$ ,  $g_{O1-O1}(r)$ ,  $g_{H2-Hw}(r)$ ,  $g_{H2-O1}(r)$ ,  $g_{H2-H2}(r)$ ,  $g_{H1-Hw}(r)$ ,  $g_{H1-O1}(r)$ ,  $g_{H1-H2}(r)$ ,  $g_{H1-H1}(r)$ ,  $g_{C2-Hw}(r)$ ,  $g_{C2-O1}(r)$ ,  $g_{C2-H2}(r)$ ,  $g_{C2-H1}(r)$ ,  $g_{C2-C2}(r)$ ,  $g_{C1-Hw}(r)$ ,  $g_{C1-O1}(r)$ ,  $g_{C1-H2}(r)$ ,  $g_{C1-H1}(r)$ ,  $g_{C2-C1}(r)$ ,  $g_{C1-C1}(r)$ , from the EPSR model. These are related to the corresponding partial structure factors,  $S_{ij}(Q)$ , by Fourier sine transform<sup>12</sup> as described in Chapter 2, section 2.5.9.6. Figure 5.14 displays an entire comparison of these  $g_{ij}(r)$  from both EPSR models (as-made at 80 K and after annealing at 140 K) of C<sub>10</sub>H<sub>16</sub> in H<sub>2</sub>O matrices together with corresponding differences between both temperatures. Table 5.6 provides the distance ranges in Å and the CN,  $N_{ij}(r)$  of species  $j$  from species  $i$  at a distance  $r$ , calculated by the equation as follows:

$$N_{ij}(r) = \int_0^r g_{ij}(r) \rho_j \cdot 4\pi r^2 dr \quad \text{Equation 5.1}$$

These functions reflect the probability of finding atoms of type  $j$ , as a function of the distance,  $r$ , from an  $i$ -type atom. The local maximum determines the most likely interaction distance in this type of function.

## 5. Total Neutron Scattering of Amorphous Solid Water with Embedded Adamantane

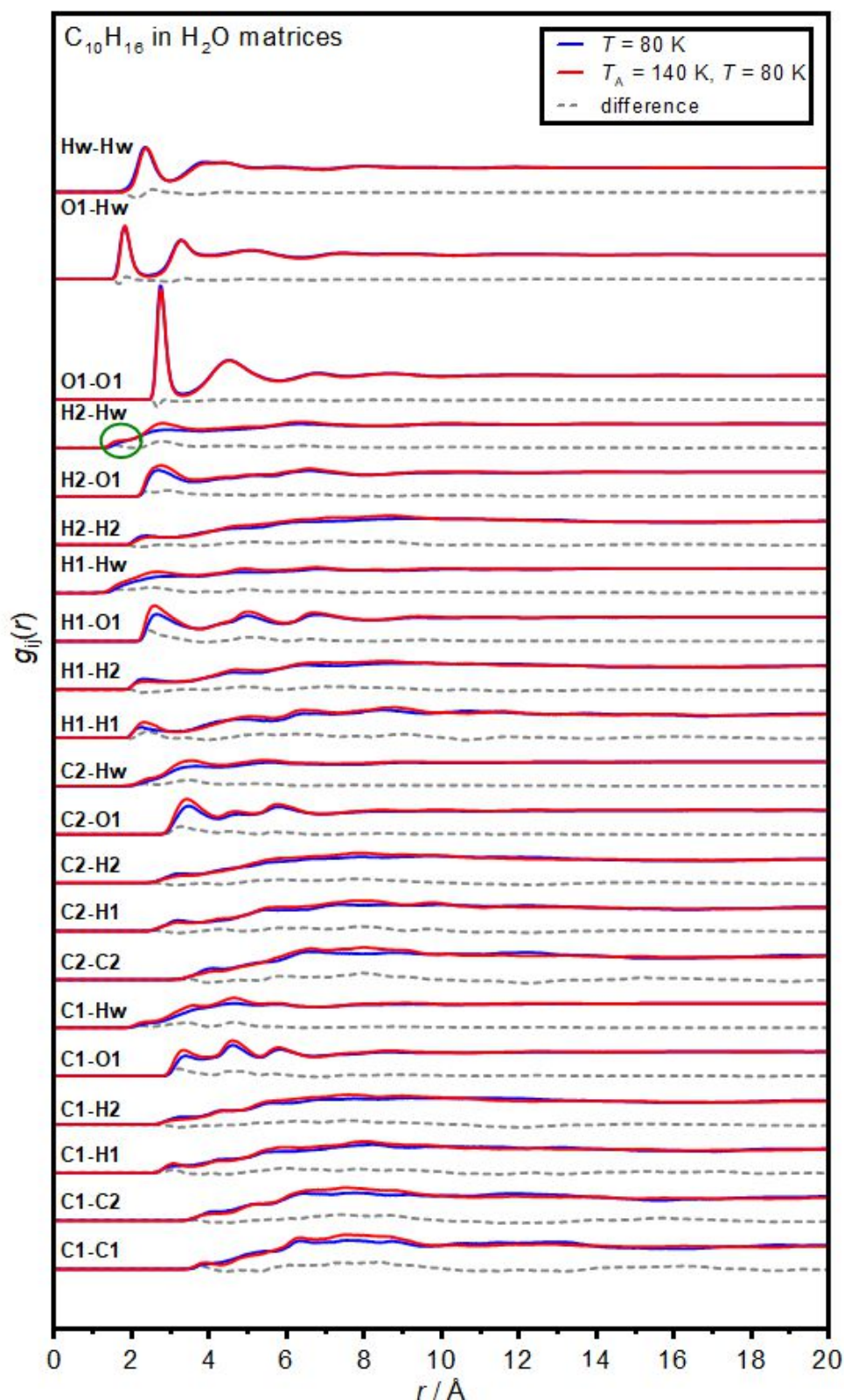


Figure 5.14. EPSR-derived intermolecular PDFs of every  $g_{ij}(r)$  for data recorded at 80 K (as-made, blue lines) and after annealing at 140 K (red lines). The grey dashed lines are the differences between the two temperatures and the data have been shifted vertically for clarity. The green circle highlighted on the  $g_{ij}(r)$  of H2-Hw will be described later with the ANGULA software.

## 5. Total Neutron Scattering of Amorphous Solid Water with Embedded Adamantane

The oscillations in the  $g_{ij}(r)$  of H1–H<sub>w</sub> with maxima at ~2.64, 4.89, 6.79 and 10.02 Å, indicate positional ordering reaching out into at least the third coordination shell. Similarly, the oscillations in the  $g_{ij}(r)$  of H2–H<sub>w</sub>, display peak maxima at 2.78, 6.38, 10.18 and 14.01 Å, indicating positional ordering reaching to again, at least the third coordination shell. A shoulder bump at 1.62 Å as indicated by the green circle in Figure 5.14 is more highly pronounced for the after annealed at 140 K data in the  $g_{ij}(r)$  of H2–H<sub>w</sub>, indicating an O–H bond of the H<sub>2</sub>O pointing towards the C<sub>10</sub>H<sub>16</sub>. A wealth of structural information can be gathered from here and more detail with the ANUGLA analysis is provided later.

The broader oscillations in the  $g_{ij}(r)$  for C1–H<sub>w</sub> and C2–H<sub>w</sub> have slightly more pronounced features for the annealed samples and thus, indicate a more ordered hydration sphere. Peaks at low  $r$  in the  $g_{ij}(r)$  for C1–H<sub>w</sub> and C2–H<sub>w</sub> are quite similar, suggesting there are several interactions involving the carbon atoms which are also important in the mixture reaching out to the third coordination shell. The atom pair, C1–H<sub>w</sub> displays four weak peaks when compared to C2–H<sub>w</sub> showing only three weak, broad peaks. The oscillations in the  $g_{ij}(r)$  for C1–O and C2–O atom pairs indicate more stronger and defined peaks with maxima at ~3.41, 4.61, 5.77, 8.46, 9.96 and 12.38 Å, showing positional ordering which reaches past the third coordination shell. A large, broad peak is seen for both atom pairs, H1–O and H2–O which once again, reach out far into the third coordination shell. Nevertheless, most  $g_{ij}(r)$  atom pairs show three well-defined coordination shells which are localised at different distances. Table 5.6 aims to identify the maximum and minimum of the PDFs for every  $g_{ij}(r)$ . In general, compared to the as-made (80 K) data for  $g_{ij}(r)$ , most of the peak maxima in the annealed at 140 K data are more defined, suggesting that after annealing the matrix at 140 K, more structural order is present in the hydration sphere.



## 5. Total Neutron Scattering of Amorphous Solid Water with Embedded Adamantane

*Table 5.6. Minimum and maximum PDFs for a few  $g_{ij}(r)$  from Figure 5.14 in the first coordination shell.*

correlation, $g_{ij}(r)$	$r_{\min} / \text{\AA}$	$r_{\max} / \text{\AA}$
C1–O1	2.83	4.01
C2–O1	2.82	4.17
H1–H1	1.81	3.15
H1–H2	1.79	3.30
H1–O1	2.11	3.79
H1–H <sub>w</sub>	1.14	3.67
H2–H2	1.83	3.01
H2–O1	2.09	3.56
H2–H <sub>w</sub>	1.19	-

Additionally, Figure 5.15(a) compares the results for the pair correlation function for H<sub>2</sub>O in the binary system for:  $g_{\text{OO}}(r)$ ,  $g_{\text{Hw-Hw}}(r)$  and  $g_{\text{O1-Hw}}(r)$  atom pairs of H<sub>2</sub>O around C<sub>10</sub>H<sub>16</sub> and also the interaction of C<sub>10</sub>H<sub>16</sub> [Figure 5.15(b)] with each other using the EPSR method. There is close agreement between both the as-made (80 K) and after annealing at 140 K temperature data sets.

## 5. Total Neutron Scattering of Amorphous Solid Water with Embedded Adamantane

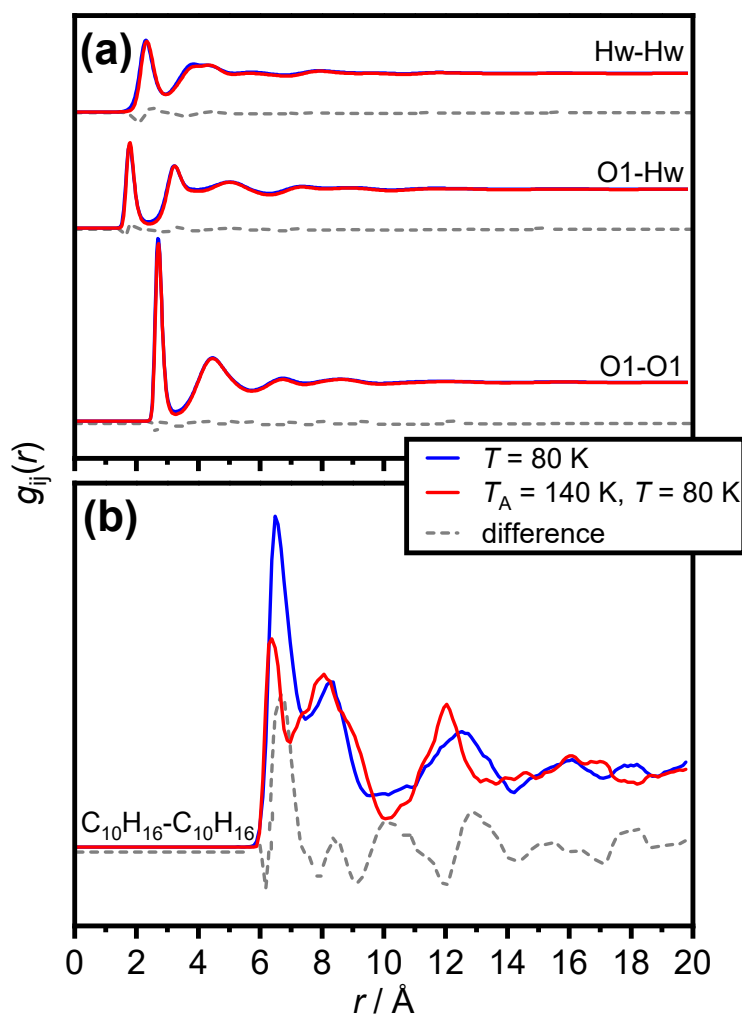


Figure 5.15. EPSR-derived three intermolecular PDFs for (a)  $H_2O$ ,  $g_{O1-O1}(r)$ ,  $g_{O1-Hw}(r)$  and  $g_{Hw-Hw}(r)$ , from bottom to top, respectively and (b)  $C_{10}H_{16}$  with  $C_{10}H_{16}$ . The continuous blue and red lines show the difference between the as-made at 80 K and after annealing at 140 K data, respectively. The dashed grey lines represent the difference in the temperature data sets and the data has been shifted vertically for clarity.

Looking at the  $g_{ij}(r)$  between  $C_{10}H_{16}$  and  $H_2O$  and comparing the  $g_{ij}(r)$  of  $H_2O$  as provided in Figure 5.15, the  $g_{ij}(r)$  interaction is much more sharply defined at low distances,  $r$ , for  $H_2O$  only than those of  $C_{10}H_{16}$ – $H_2O$  pairs in Figure 5.14. This is perhaps unsurprising given the polarity of  $H_2O$  and its strong tendency to form hydrogen bonds. The  $g_{ij}(r)$  of the  $C_{10}H_{16}$  COM–COM is shown in Figure 5.15(b). The  $g_{ij}(r)$  for  $C_{10}H_{16}$ – $C_{10}H_{16}$  is of a highly unreliable nature as it is dilute in the binary mixture. The  $C_{10}H_{16}$ – $C_{10}H_{16}$  interaction is clearly much less reliable in comparison to the  $C_{10}H_{16}$ – $H_2O$  and  $H_2O$ – $H_2O$  atom pairs. However, what can be stated is that fine dispersion or mixing of  $C_{10}H_{16}$  in  $H_2O$  has been successfully achieved. A summary for the  $g_{ij}(r)$  of the interactions between  $H_2O$  molecules and lastly,  $C_{10}H_{16}$ – $C_{10}H_{16}$  are provided below in Table 5.7.

## 5. Total Neutron Scattering of Amorphous Solid Water with Embedded Adamantane

Table 5.7. Minimum and maximum PDFs of  $H_2O-H_2O$  and  $C_{10}H_{16}-C_{10}H_{16}$   $g_{ij}(r)$  atom pairs from Figure 5.15 in the first coordination shell.

correlation, $g_{ij}(r)$	$r_{\min} / \text{\AA}$	$r_{\max} / \text{\AA}$
O1–O1	2.44	3.31
O1–H <sub>w</sub>	1.45	2.46
H <sub>w</sub> –H <sub>w</sub>	1.51	2.98
C <sub>10</sub> H <sub>16</sub> –C <sub>10</sub> H <sub>16</sub>	5.94	7.56 (80 K, as-made)
		6.99 ( $T_A = 140$ K, $T = 80$ K)

### 5.6.4 Centre of Mass (COM) Pair Distribution Functions (PDFs)

The COM of  $C_{10}H_{16}$  and the correlation with an oxygen atom on the  $H_2O$  molecule was set up using the SHARM routine in EPSR (Figure 5.16). The COM of  $C_{10}H_{16}$  to the hydrogen atom of  $H_2O$  is shown later which was produced using the ANGULA software.

Both the as-made (80 K) and annealed samples (140 K) show similar trends. Three distinct coordination shells can be pinpointed. For both temperature sets of data, the shell maxima occur at 4.64, 7.51 and 8.83 Å. The second and third peaks are smaller and slightly broader in shape indicating that they are less structured. Comparing both as-made (80 K) and after annealing at 140 K data, more structural order is seen with 140 K data coinciding with the sharper more intense peak maxima. Interestingly, even with three clearly defined coordination shells, there is some structure beyond the third coordination shell. The spatial correlation only starts to decay very slowly for both the as-made at 80 K and after annealing at 140 K measurements beyond 20 Å, concurrently with the absence of low- $Q$  measurements and simultaneously with the  $F(Q)$  as shown in Figure 5.16. To conclude, hydration is more complete after annealing.

The CN can be calculated from the integration of the  $g_{ij}(r)$ , however, solving integration limits remains a challenge, and the CN can be difficult to determine. The CN was calculated by converting  $g_{ij}(r)$  to  $t_{ij}(r)$  according to  $t_{ij}(r) = 4\pi r^2 \rho g_{ij}(r)$  and the area under the curve gives the CN. The CN for the as-made (80 K) sample was determined as 16 and for the after annealed at 140 K sample, the CN was determined as 21.

## 5. Total Neutron Scattering of Amorphous Solid Water with Embedded Adamantane

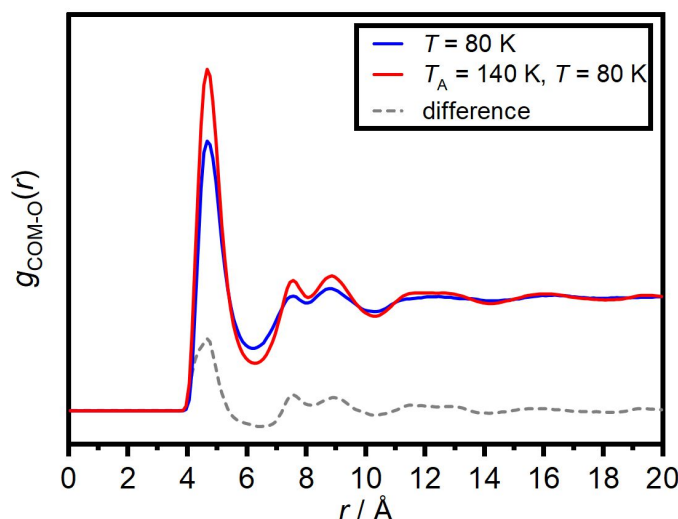


Figure 5.16. EPSR-derived intermolecular PDFs of the COM–O interaction,  $g_{\text{COM-O}}(r)$  for data recorded as-made (80 K, blue line) and after annealing at 140 K (red line). The grey dashed line is the difference between the two temperatures and the difference has been shifted vertically for clarity.

Despite the difference in temperature, the intrinsic intermolecular structure is not disrupted. Since PDFs reflect the number density of the surrounding species, in this case, the H<sub>2</sub>O molecules, the second minimum of each peak can be used to define the next coordination shell of the system.

### 5.6.5 Additional Simulations

After the two simulation boxes were produced with sensible fits and structural data could be extracted, two additional simulation boxes were generated with identical LJ parameters, weights, and empirical potentials etc., for both as-made (80 K) and after annealing at 140 K diffraction data. This was to compare the  $g_{ij}(r)$  atom pairs from the additional simulation with the simulated data that has already been presented here to ensure that the initial mixing of the atoms did not change the  $g_{ij}(r)$  atom pairs. The comparison of the data used throughout this chapter (run 1) is compared with the secondary simulation boxes (run 2) for the  $g_{ij}(r)$  of atoms pairs for H<sub>2</sub>O interactions, C<sub>10</sub>H<sub>16</sub> interactions and finally, the H<sub>2</sub>O and C<sub>10</sub>H<sub>16</sub> interaction. These atom pairs were obtained by the SHARM routine. As can be seen from Figure 5.17, no significant changes are seen with the  $g_{ij}(r)$  atom pairs. However, to reiterate, the improvements to the fit of the diffraction data, once the empirical potentials were switched on, were accompanied by a highly complex  $g_{ij}(r)$  of the COM–COM of C<sub>10</sub>H<sub>16</sub>, implying that the COM–COM interaction of C<sub>10</sub>H<sub>16</sub> mixing as already known from run 1, was not reproduced well by

## 5. Total Neutron Scattering of Amorphous Solid Water with Embedded Adamantane

the starting potentials and is very unreliable, giving rise to a spurious structure regardless of the temperature.

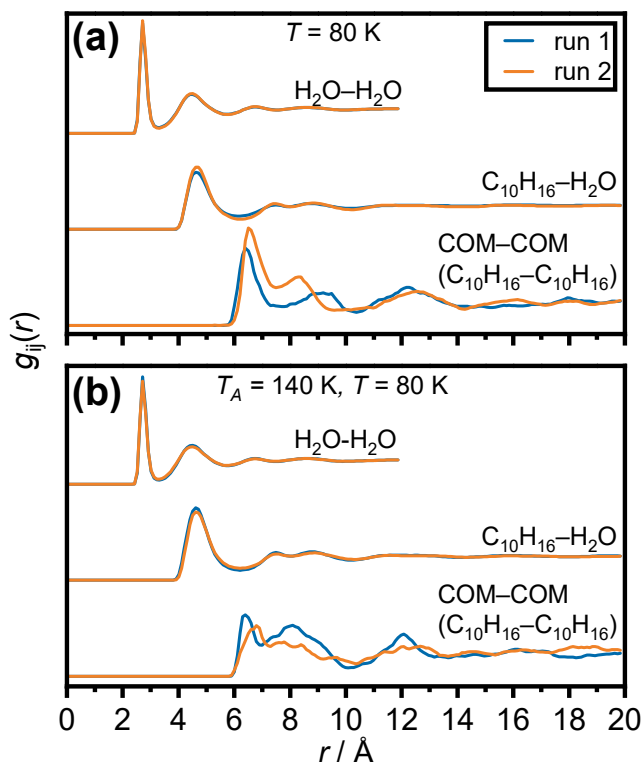


Figure 5.17. EPSR-derived intermolecular PDFs of the  $g_{ij}(r)$  for data recorded at (a) 80 K (as-made) and (b) after annealing at 140 K, where run 1 is illustrated by blue lines and run 2 for the confirmation of valid run 1 results, is displayed as orange lines.

### 5.6.6 Structural Ordering

The PDFs only provide a one-dimensional picture of the structure. Accordingly, SDFs can be used to aid such visualisation and the spatial arrangement of H<sub>2</sub>O molecules around C<sub>10</sub>H<sub>16</sub> within the first coordination shell is presented herein. To investigate the local structure of the C<sub>10</sub>H<sub>16</sub>/H<sub>2</sub>O matrix and short-range order of these molecules in more detail, angle-dependent intermolecular pair correlation functions were obtained from both the EPSR method and ANGULA analysis. Therefore, two degrees of freedom have to be analysed separately:

- (i) those concerning the relative positions of the molecules.
- (ii) those concerning their relative orientations.

Each angle that has been used in this study for the analysis of relative positions and orientations of the molecules has been depicted in Figure 5.18(a). Beyond looking at the

## 5. Total Neutron Scattering of Amorphous Solid Water with Embedded Adamantane

$g_{ij}(r)$ , the spherical harmonics are inspected, highlighting pronounced structural differences within the matrix.

The EPSR method allows the fitting of data by carrying out simulations on the data sets and EPSR tools such as the SHARM, *plot2d* and *plot3d* routine, allow the mapping of the structure around every molecule in the simulation box and averages the spatial and relative orientation of the remaining molecules around them. For this analysis, to describe the positional ordering of the system, the carbon atom of C<sub>10</sub>H<sub>16</sub> reference molecule was placed at the origin of a coordinate system and the hydrogen atom was placed in line with the  $z_1$  axis, where the  $x_1z_1$  plane comprises a C–H bond. Lastly, the  $y$ -axis is the cross product of the  $z_1$  axis and  $x_1$ -axis, as shown in Figure 5.18(a). The second molecule, H<sub>2</sub>O, as seen in Figure 5.18(a), is defined by a set of spherical coordinates at a distance,  $r$ , with the polar and azimuthal angles,  $\theta_{\text{COM}}$  and  $\phi_{\text{COM}}$  respectively, with respect to the reference molecule. The probability of finding the second molecule with respect to the reference molecule is defined by the  $g_{\text{COM-O}}(r, \theta, \phi)$  correlation function. Both  $\theta$  and  $\phi$  angles will be discussed as the angular position relative to the COM of C<sub>10</sub>H<sub>16</sub> to stress the fact that the relative distance between the COM of C<sub>10</sub>H<sub>16</sub> to the oxygen atoms are at a fixed position when the molecular neighbours are discussed individually.

### 5.6.7 Spatial Density Functions (SDFs) from EPSR

The SHARM routine in EPSR was used to calculate the spherical harmonic coefficients for the SDFs and OCFs. The way in which SHARM was set up within the EPSR shell will briefly be described here.

For the SDFs as shown in this section, a total of 12 SHARM coefficients for  $l_1$  values were used to map out the distribution of the H<sub>2</sub>O molecules with respect to C<sub>10</sub>H<sub>16</sub> at the origin to ensure the orientation of H<sub>2</sub>O molecules is captured which was of paramount importance. A total of four SHARM coefficients were used for  $l_2$  values. The use of more SHARM coefficients replicated the six-fold symmetry looking down on a C1–H bond. A three-fold symmetry was set up for the C<sub>10</sub>H<sub>16</sub> molecule irrespective of the symmetry of other parts of the molecule as they have not been included in the calculation. Since the second molecule is H<sub>2</sub>O, the orientation of the second molecule was intended to be plotted, and so, a two-fold symmetry was implemented into the EPSR shell.

## 5. Total Neutron Scattering of Amorphous Solid Water with Embedded Adamantane

The central atoms of  $C_{10}H_{16}$  were set up as C1–C2 and the first axis definition of  $C_{10}H_{16}$  specified, was the  $z$ -axis, assumed to run from the COM of  $C_{10}H_{16}$  to the midpoint of a C–H bond. In setting up a second axis, a set of atoms cannot be assigned which lie along the specified axis and so, a vector is drawn from the COM of  $C_{10}H_{16}$  to specified atoms and thus, the second axis definition for the central  $C_{10}H_{16}$  molecule was set up as a  $x_1$  axis, which is assumed to lie in the plane defined by this vector and the first  $z$ -axis.

The first axis definition for the  $H_2O$  molecule was set up so that  $z$  was the axis going through the midpoint between atoms two and three, i.e., the two hydrogen atoms, so it is aligned with the molecule's dipole moment. The second axis definition was defined with atom two on the  $H_2O$  molecule and is setup so that it lies in the  $z$ - $y$  plane of the molecule. The  $y$  axis here is set to be orthogonal to the  $z_1$  axis.<sup>33</sup> It is important to note when setting up SHARM, the molecule must have at least one plane of mirror symmetry and this must at least coincide with the  $z$ - $x$  plane. If a plane did not exist in a real molecule, the results would be misleading and would not work.<sup>33</sup> The current version of the EPSR method, EPSR26,<sup>33</sup> is able to deal with chiral molecules.

The EPSR routine *plot2d* was used to take a slice from the three-dimensional (shown in upcoming Figure 5.18) SDFs using the commands as provided in Table 5.4. A two-dimensional slice through the three-dimensional SDFs for  $C_{10}H_{16}$  in  $H_2O$ , showing the distribution of a  $H_2O$  molecule around the first coordination shell around the  $C_{10}H_{16}$  reference molecule is presented in Figure 5.18(b) and Figure 5.18(d) for the as-made (80 K) and after annealing at 140 K models, respectively. The most likely position of the oxygen atoms can be seen from this  $g_{COM-O}(r, \theta)$  function. This function is averaged over  $\phi$  and thus, only depends on the radial COM to oxygen atom distance and  $\theta$ . The two-dimensional density projection clearly shows the strong preference for  $H_2O$  molecules in the  $z_1$  direction between a C–H bond.

The central  $C_{10}H_{16}$  molecule is shown as a small white dot at the origin of the coordinate system. The advantage of a slice through an SDF is the increased intensity information from this contour plot, however, the three-dimensional aspect is lost. The orientation of the  $H_2O$  molecules with respect to the COM of  $C_{10}H_{16}$  as seen in Figure 5.18(b) and Figure 5.18(d), indicates that the density of the  $H_2O$  molecule as a function of  $r$ , is very strong in the first coordination shell. The correlations in the first coordination after annealing at 140 K are stronger than in the as-made sample at 80 K. The most intense

## 5. Total Neutron Scattering of Amorphous Solid Water with Embedded Adamantane

features of the slice through the two-dimensional SDF show the  $\theta = 70, 80$  and  $90^\circ$  which indicate areas of high probability of finding a  $\text{H}_2\text{O}$  molecule in the first coordination shell. This two-dimensional SDF is not averaged over  $\varphi$  as only a slice through the three-dimensional SDF was desired.

Three-dimensional structural information is presented by so-called SDFs which make use of fractional isosurface levels (FSL) and highlight specific volumes of where the most likely positions of oxygen atoms are expected. Figure 5.18(c) and Figure 5.18(e) show the nearest neighbour COM–O SDF plotted using *plot3djmol* which highlights the volume where the COM–O pair correlation function takes the highest values.<sup>32, 34</sup> As the precise variations in  $g_{ij}(r)$  are difficult to show in three-dimension, the distribution of the spatial arrangements is presented via lobes using FSLs. Lobes are formed in three dimensions which contain a specified fraction of atoms. Different variations in the view of the isosurface levels are displayed for lucidity. The shaded lobes can be considered to be the maxima in peaks in the  $g_{ij}(r)$ . The most probable regions with an occupancy level of 0.45 in the first coordination shell, up to 6.5 Å, are shown in Figure 5.18(c) and Figure 5.18(e).

The distribution of  $\text{H}_2\text{O}$  molecules around  $\text{C}_{10}\text{H}_{16}$  can be observed with a continuous network structure circumscribing the  $\text{C}_{10}\text{H}_{16}$  molecule by encapsulation, indicating the presence of five- and six-membered rings encircling the entire molecule. These cages can be seen as somewhat distorted and there is a preference for these cages to arrange around  $\text{C}_{10}\text{H}_{16}$  so that there are six, five-membered rings for every  $\text{CH}_2$  group on  $\text{C}_{10}\text{H}_{16}$  and four, six-membered rings for every CH group in  $\text{C}_{10}\text{H}_{16}$ . To the best of our knowledge, this type of  $5^66^4$  polyhedron has not yet been identified (refer to Chapter 1, Figure 1.11 of this thesis for known clathrate hydrate types). Nevertheless, from the analysis in EPSR, the arrangement of oxygen atoms can be seen with more clarity with the ANGULA analysis. With the symmetry of the cage, the three types of oxygen atoms become more apparent as can be seen with EPSR. This would suggest that there is more than one type of arrangement for the oxygen atoms. The oxygen atoms find themselves arrange in a specific order and three different types of oxygen atoms exist based on the ANGULA analysis which is described in the upcoming analysis.



## 5. Total Neutron Scattering of Amorphous Solid Water with Embedded Adamantane

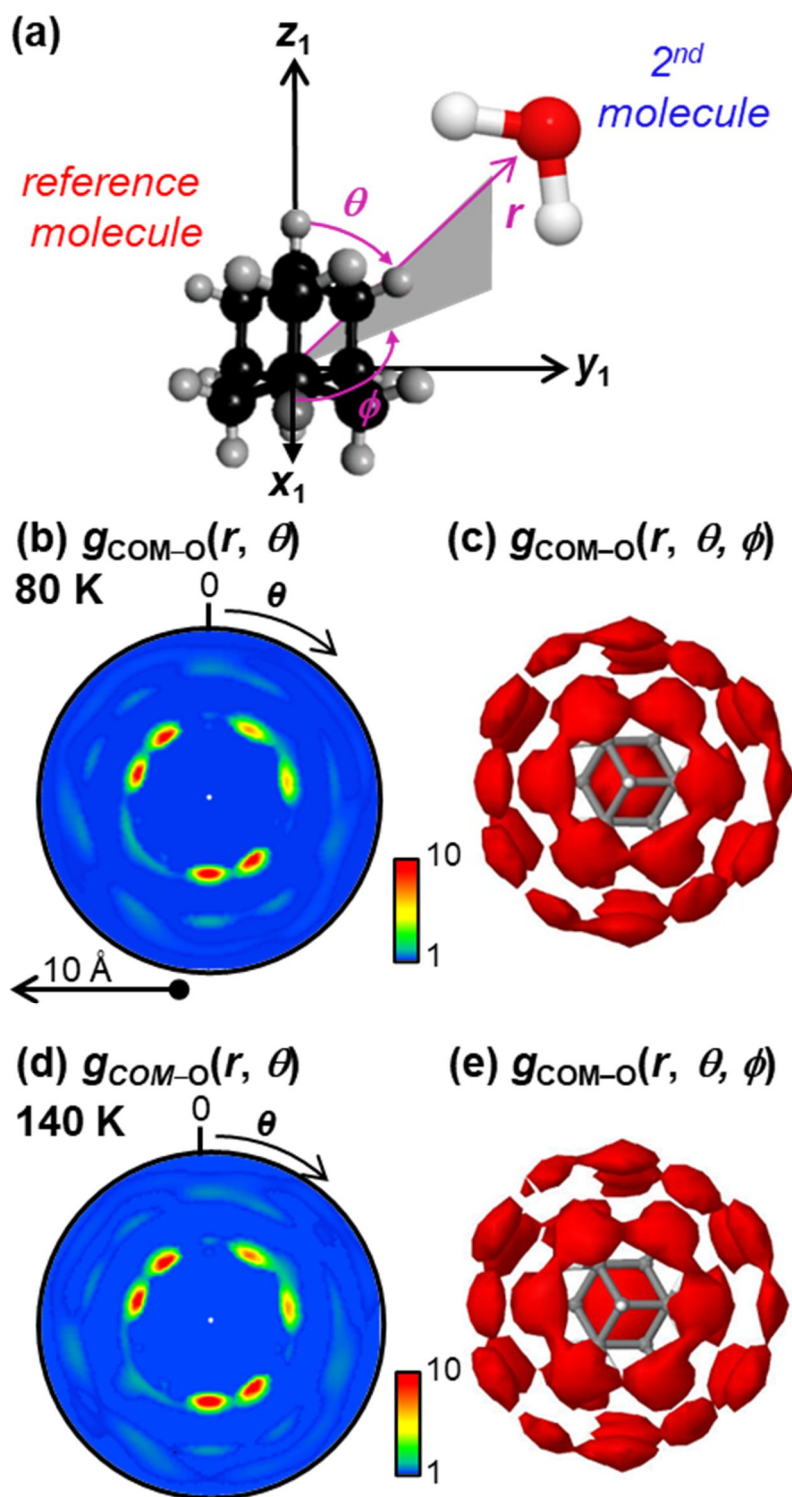


Figure 5.18. (a) Schematic illustration showing the fixed orientation of the reference molecule,  $\text{C}_{10}\text{H}_{16}$ , and the spherical coordinates that define the positions of atoms of a second molecule,  $\text{H}_2\text{O}$ , in the coordination shell. (b, d) Contour plots of  $g_{\text{COM-O}}(r, \theta)$  for 80 K (as-made) and after annealing at 140 K, respectively from the result of running SDF on EPSR simulations of the system. Both (c) and (d) illustrates the result of running SDF on the EPSR simulations for the as-made at 80 K and after annealed at 140 K matrices and thus, plotting the results via plot3djmol. Both SDFs are plotted with FSLs of 0.45.

## 5. Total Neutron Scattering of Amorphous Solid Water with Embedded Adamantane

In an effort to explicitly illustrate the structure of this complex mixture within the first intermolecular shell, variations in the FSLs of 0.15, 0.30, 0.50 and 0.70 have been used to depict the cages around  $C_{10}H_{16}$ . This approach has been shown to prevent any problems arising due to curtailing the data at specifically chosen FSL levels.

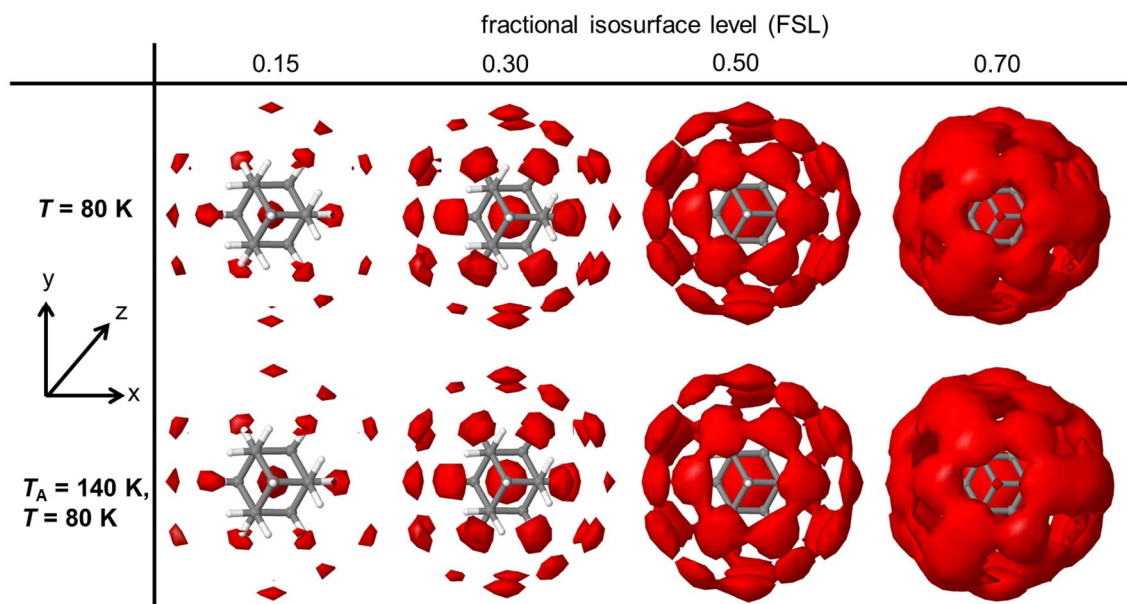


Figure 5.19. Three-dimensional SDFs with FSL of 0.15, 0.30, 0.50 and 0.70 for as-made (80 K) and after annealing at 140 K EPSR models. The SDFs shown here are for the interaction of the COM of  $C_{10}H_{16}$  and  $H_2O$ .

A noticeable feature within these plots are the similar lobe shapes for both temperature data sets, as-made at 80 K and after annealing at 140 K. Extending the understanding of these three-dimensional functions in terms of molecular arrangements within the coordination shells can be summarised from the PDFs. The spatial distribution of  $H_2O$  molecules has a dominating influence already in the first coordination shell. Most oriented molecules are correlated with CH locations and a cage can be seen to form around the  $C_{10}H_{16}$ . With increasing the FSL level, the shaded red lobes in these plots show a general trend of increasing volume. Increasing the FSL levels and greater volume contained in the lobes reflects the shape and the distribution of the positions of the  $H_2O$  molecules compared to the COM. Comparing both temperature sets of data, with increasing temperature, the cage type structure becomes slightly more structured. At 80 K (as-made), the structure is only slightly less disordered, with slightly less spatial homogeneity in the first coordination shell. In addition to the general cage structure as shown with these SDF plots, the positions of the  $H_2O$  molecules with respect to their most

## 5. Total Neutron Scattering of Amorphous Solid Water with Embedded Adamantane

likely positions about the reference molecule reveal the nature of this specific cage type structure. This arrangement is analysed and discussed in more depth with analysis by the ANGULA software<sup>14</sup> in section 5.7.

### 5.6.8 Orientational Correlation Functions (OCFs) from EPSR

OCFs provide detailed information on the relative orientation of the second molecule and how it is distributed as a function of  $r$  for a given set of Euler angles as described earlier ( $\theta_2, \varphi_2, \chi_2$ ). Molecules are known to rotate about their COM and therefore, the centre of the coordinates are placed at the COM of the  $C_{10}H_{16}$  reference molecule with the alignment of the C–H bonds with the  $z_1$  axis.<sup>35</sup> The dipole moment of  $H_2O$  is defined with angle  $\alpha$ , with respect to the dipole moment of the  $C_{10}H_{16}$  reference molecule as shown in upcoming Figure 5.23. The OCFs shown here indicate the changes observed for different arrangements of oxygen atoms as will be shown in the next section with the ANGULA analysis and a more in-depth explanation.

## **5.7 ANGULA Analysis**

### **5.7.1 Centre of Mass (COM) Pair Distribution Functions (PDFs)**

The first step when analysing the relative positions of the molecules in this binary mixture is to calculate the number of molecules that can be found within the first neighbour shell. Both the SHARM routine (EPSR tool) and the ANGULA software allow the extraction of the PDF from the COM of C<sub>10</sub>H<sub>16</sub> to the H<sub>2</sub>O molecule. The nature of the COM of C<sub>10</sub>H<sub>16</sub> and the interaction with oxygen or hydrogen of H<sub>2</sub>O is closely examined in Figure 5.20(a) and Figure 5.20(b), respectively, which show the pair correlation function of the COM to the oxygen and hydrogen of the H<sub>2</sub>O molecules,  $g_{\text{COM-O}}(r)$  and  $g_{\text{COM-H}}(r)$ , respectively. Concurrently, the contributions of oxygen molecules from the closet H<sub>2</sub>O molecules calculated from the simulations for both sets of temperature data is shown in Figure 5.20. The contribution is proportional to the probability of finding a H<sub>2</sub>O molecule at a certain distance from the C<sub>10</sub>H<sub>16</sub> reference molecule.

Both temperature sets of data, as-made (80 K) and after annealing at 140 K show similar trends with one another. Several distinct intermolecular coordination shells can be recognised. The shortest COM of C<sub>10</sub>H<sub>16</sub>–O  $g_{ij}(r)$  distance is 3.92 Å. The maximum peak in the C<sub>10</sub>H<sub>16</sub>–O  $g_{ij}(r)$  is 4.71 Å which indicates that the interaction distance in the COM of C<sub>10</sub>H<sub>16</sub> to the oxygen atom of H<sub>2</sub>O is significantly long. The shortest distance on the other hand is 2.96 Å and a maximum peak for the C<sub>10</sub>H<sub>16</sub>–H  $g_{ij}(r)$  is 4.59 Å, representing a shorter interaction distance when compared to the  $g_{ij}(r)$  of C<sub>10</sub>H<sub>16</sub>–O. The first neighbour shell is well-defined as the number of molecules comprised within the first peak as seen in the  $g_{ij}(r)$ . As mentioned earlier, the molecular CN can be calculated from the integration of the  $g_{ij}(r)$ , however, solving integration limits remains a challenge, and thus, the CN is difficult to determine. As mentioned earlier, the  $t_{ij}(r)$  correlation function is calculated from  $g_{ij}(r)$  according to  $t_{ij}(r) = 4\pi r^2 \rho g_{ij}(r)$  which means that the area under  $t_{ij}(r)$  equates to the CN. A brief summary of the peaks from Figure 5.20 is provided in Table 5.8 below. After ~12 Å, the peaks in both  $g_{ij}(r)$  become less structured as the peaks appear to broaden out and show spatial correlation decay beyond this distance.

## 5. Total Neutron Scattering of Amorphous Solid Water with Embedded Adamantane

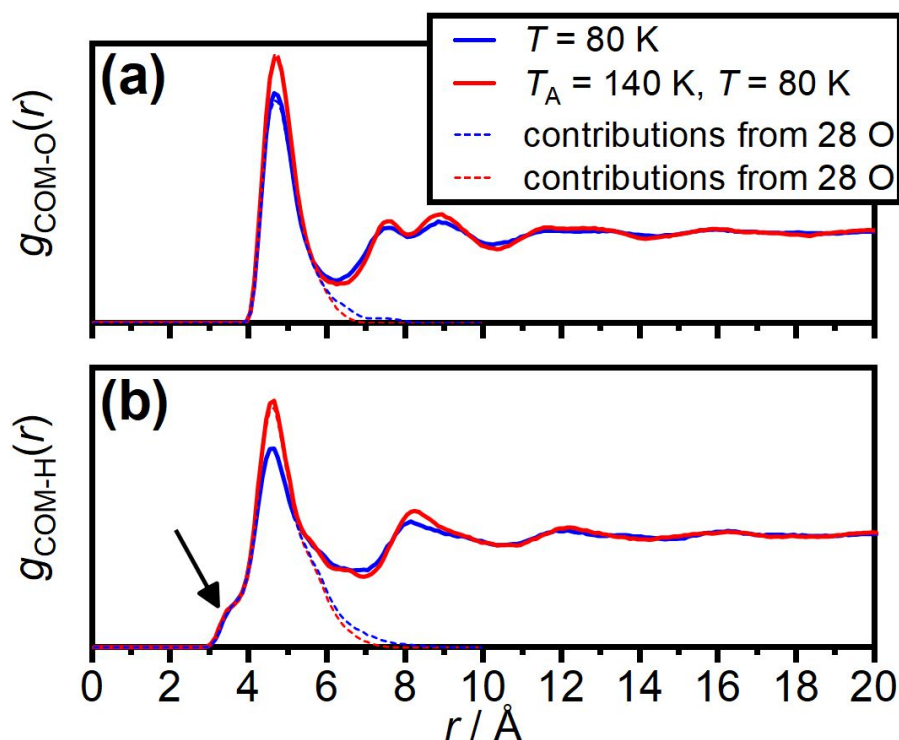


Figure 5.20. The pair correlation functions for the COM of  $\text{C}_{10}\text{H}_{16}$  (a)  $g_{ij}(r)$  of COM–O and (b)  $g_{ij}(r)$  of COM–H at 80 K (as-made sample, solid red lines) and after annealing at 140 K (solid blue lines) obtained from the ANGULA analysis.<sup>14</sup> The  $g_{ij}(r)$  shown here as the dotted lines are the contributions from 28 oxygen molecules that reproduce the first peak in the  $g_{ij}(r)$ . The black arrow indicates the presence of an O–H bond pointing towards the COM of  $\text{C}_{10}\text{H}_{16}$ .

Figure 5.20 is quite remarkable in the sense that the first coordination shell shows the contribution of exactly 28 oxygen molecules. Amazingly, these oxygen atoms are found to perfectly fit and reproduce the entire  $g_{ij}(r)$  for the first molecular coordination shell for both the COM–O and COM–H. This shows that the first coordination shell is already very ordered for the as-made sample at 80 K. In this present case, contrary to what would be commonly expected, such as disorder, this data along with supporting evidence with the EPSR three-dimensional SDFs coincides with a new, incredibly well-structured hydrate cage with 28 oxygen atoms existing for this complex system. This hydrate cage is exclusively interpreted by the contribution from the 28 oxygen atoms in relation to the first peak in the  $g_{ij}(r)$  for both data sets. The first hydration shell is very highly structured for both as-made (80 K) and after annealing at 140 K and resolved with respect to the  $g_{ij}(r)$ . Table 5.8 provides a summary of the correlation and their respective minimum and maximum PDF for the three coordination shells.

## 5. Total Neutron Scattering of Amorphous Solid Water with Embedded Adamantane

Table 5.8. Minimum and maximum PDF of the COM of  $C_{10}H_{16}$  to oxygen and hydrogen atom pairs from Figure 5.20 for the coordination shells.

correlation, $g_{ij}(r)$	Coordination shell	$r_{\min} / \text{\AA}$	$r_{\max} / \text{\AA}$
COM–O	1	3.92	6.28
	2	6.28	8.10
	3	8.10	10.36
COM–H	1	2.92	6.98
	2	6.98	10.60

As indicated in Figure 5.20(b), by the black arrow, a significant shoulder is seen in the  $g_{ij}(r)$  for the COM–H for the first coordination shell. This is evidence that the closest  $H_2O$  molecules have O–H bonds pointing towards the COM of  $C_{10}H_{16}$ . These closest O–H bonds are then not hydrogen-bonded to the COM of  $C_{10}H_{16}$ , which is very fascinating and distinct compared to known clathrate hydrates. Overall, it is interesting that a non-polar molecule such as  $C_{10}H_{16}$  shows quite strong orientation correlations in its hydration shell. The question to consider now may be that is there any spatial distributions of  $H_2O$  molecules with the O–H pointing towards the  $C_{10}H_{16}$  i.e., do most of the oriented  $H_2O$  molecules correlate with the C–H locations or are the most probable locations based on the SDF? ANGULA analysis in the upcoming section will confirm this.

### 5.7.2 Oxygen Positional Ordering in the First Hydration Shell

The ANGULA software allows the user to look at specific conditions of the spatial positions and relative orientation of molecules. The fundamental differences between the EPSR method/tools and the ANGULA software are that Soper<sup>10, 11</sup> uses spherical harmonics and for the ANGULA software, Pardo<sup>14-17</sup> essentially analyses the real space structure. The ANGULA software identifies angles that define the structure of disordered phases from files generated by EPSR or molecular dynamics (MD) with atomic positions. The relative position and orientation of two molecules can be calculated as the distance is added, fixing the positions of molecules.<sup>14</sup>

Bivariate probability distribution graphs plotting the spherical coordinates of the dipole  $[\cos(\theta_{\text{pos}}), \phi_{\text{pos}}]$  of the defined coordinate system shows the angular position of the COM of  $C_{10}H_{16}$  to the first neighbouring oxygen atom and displays the areas of the highest probability of a molecular position of oxygen. Figure 5.21(a) is a repeat of Figure 2.38, Chapter 2, showing the way in which molecules in this system are defined.

## 5. Total Neutron Scattering of Amorphous Solid Water with Embedded Adamantane

Since it was established from the  $g_{ij}(r)$  that 28 oxygen atoms exist in the first coordination shell relative to the COM of  $C_{10}H_{16}$ , the most likely positions of the 28 oxygen atoms are displayed in Figure 5.21(b) and Figure 5.21(c) for the as-made (80 K) and after annealing at 140 K data, respectively. Several local maxima originating from three distinct dispositions are seen in this bivariate positional probability distribution map. Without any analysis, it is possible to see the local maxima arranged into cages of five- and six-membered rings. This reflects and complements the three-dimensional SDFs as found from the analysis with EPSR.

It is now essential to determine how the oxygen atoms are arranged around the COM of  $C_{10}H_{16}$  and the vectors as described earlier. In Figure 5.21(b), it has been recognised that there are three different types of oxygen atoms located in three different positions around the  $C_{10}H_{16}$  in the first coordination shell. The most probable types of oxygen atoms that exist are located in the entire positional region of  $-1 < (\cos\theta)_{\text{pos}} < 1$ . From this point onwards, the  $H_2O$  molecules with oxygen atoms are labelled, 'A', 'B' and 'C'. The oxygen atoms labelled 'A' are found in the equatorial region at  $\cos(\theta_{\text{pos}}) = 0$  and 'A' atoms are also found in the northern hemisphere and southern hemisphere of this bivariate map,  $0.7 < \cos(\theta_{\text{pos}}) < 0.8$  and  $-0.7 < \cos(\theta_{\text{pos}}) < -0.8$ , respectively. For the  $H_2O$  molecules with oxygen atom of type, 'B', the positional arrangement can also be seen at  $0.4 < \cos(\theta_{\text{pos}}) < 0.6$ ,  $0.1 < \cos(\theta_{\text{pos}}) < 0.3$  and  $0.7 < \cos(\theta_{\text{pos}}) < 0.9$ . The oxygen atoms labelled 'C' are found at  $0.2 < \cos(\theta_{\text{pos}}) < 0.4$ . There are 12  $H_2O$  molecules with 'A' oxygen atoms, 12 'B' oxygen atoms and 4 'C' oxygen atoms, totalling 28 oxygen atoms. Upcoming Figure 5.22 explains the detail of the number of oxygen atoms for each type.

What is quite remarkable and unexpected is that the oxygen atoms are seen in the same location already at 80 K (as-made) and after annealing at 140 K. There is no dramatic effect or changes from annealing the matrices, however, annealing the sample minimizes the energy and so the structure is slightly more ordered. Since more structural order is present after annealing at 140 K, it could be stated that more hydration is achieved, and the coordination shells become more defined after annealing. Once again, it is also evident from this type of probability map that connecting the  $H_2O$  molecules with 'A', 'B' and 'C' oxygen atoms form a cage structure of five- and six-membered rings in line with the 28 oxygen atoms found for  $g_{ij}(r)$  of the COM–O and COM–H and also in line with the SDF structures as plotted with EPSR.



## 5. Total Neutron Scattering of Amorphous Solid Water with Embedded Adamantane

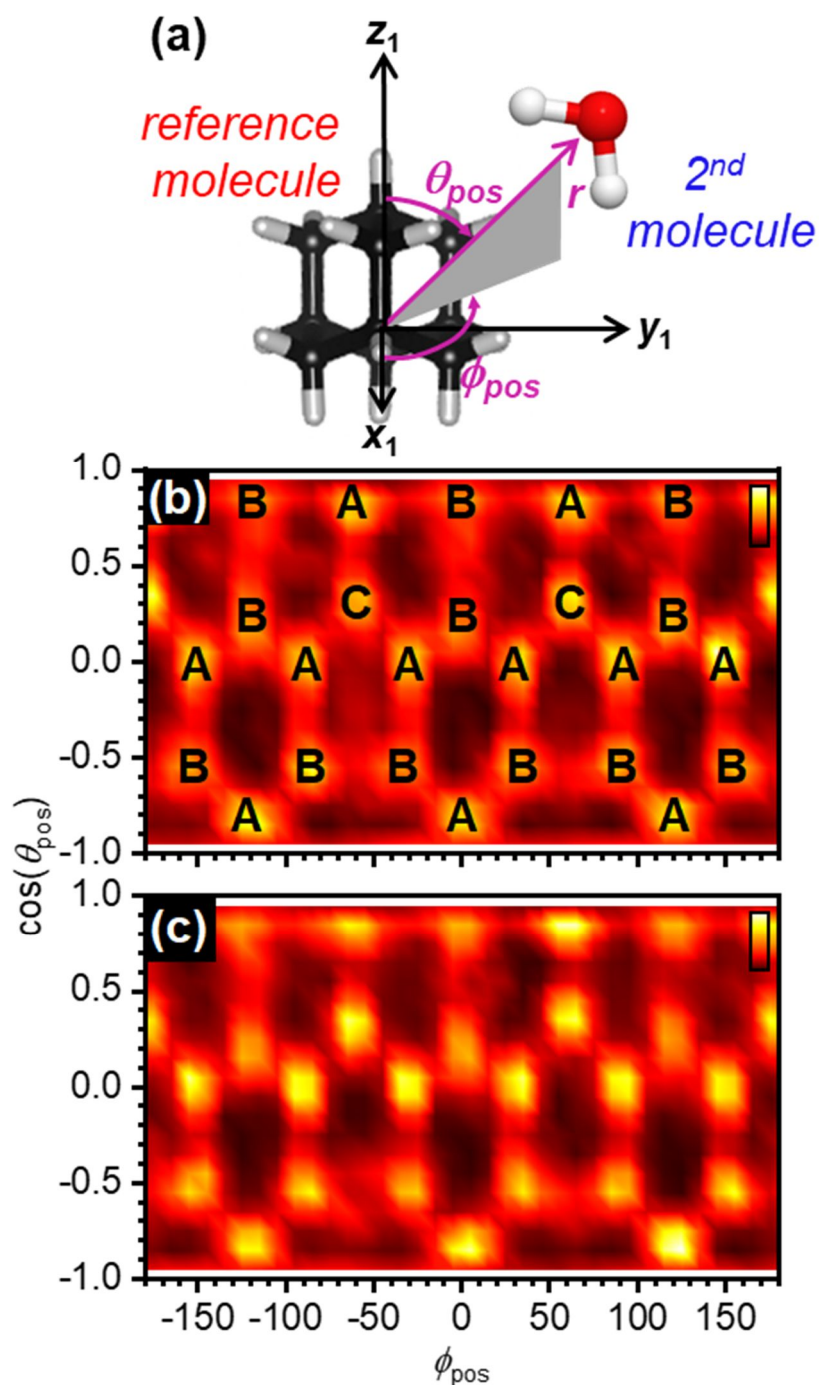


Figure 5.21. (a) Schematic illustration of a well-defined coordinate system, the fixed orientation of the COM of  $C_{10}H_{16}$  surrounded by spherical coordinates  $(\theta_{pos}, \phi_{pos})$ , that define the positions of the atoms of the second molecule,  $H_2O$  in the coordination shell, (b) and (c) the two-dimensional bivariate positional probability distribution displaying the spherical coordinates of the positions of the first nearest neighbours showing the areas of highest probability of a molecular position of oxygen, where (b) is the as-made 80 K data and (c) after annealing at 140 K data. Labels in panel (b) are given as 'A', 'B' and 'C' to denote the positions of the  $H_2O$  molecules with different oxygen atom orientation around  $C_{10}H_{16}$ . The contour plot serves as a guide to delimitate regions of maxima and minima arising from the data.



## 5. Total Neutron Scattering of Amorphous Solid Water with Embedded Adamantane

This type of analysis has been extended so that for the sake of completeness, the result for the probability functions up to the first eight H<sub>2</sub>O molecules for both sets of temperature data can be found at the end of this section which depicts the same results as indicated for the first nearest neighbour.

Having established there are H<sub>2</sub>O molecules with three types of positions of the oxygen atom around the C<sub>10</sub>H<sub>16</sub> in the first coordination shell, located in the equatorial region and the northern/southern hemisphere of these bivariate distribution maps, there are a total of 28 defined oxygen atoms. It must be noted that one type of H<sub>2</sub>O molecule may be more ordered than the other and so, the arrangement of oxygens around the C<sub>10</sub>H<sub>16</sub> is not random, such that, H<sub>2</sub>O molecules with four oxygen atoms (labelled 'C') lie in front of each 'cyclohexane' ring, there are 12 oxygen atoms (labelled 'B') where two each lie at the sides of each CH<sub>2</sub> group and another 12 oxygen atoms (labelled 'A') where three are situated around every CH of C<sub>10</sub>H<sub>16</sub>. Figure 5.22(a), Figure 5.22(b), and Figure 5.22(c) define the way in which each oxygen atom is positioned around a central C<sub>10</sub>H<sub>16</sub> molecule.

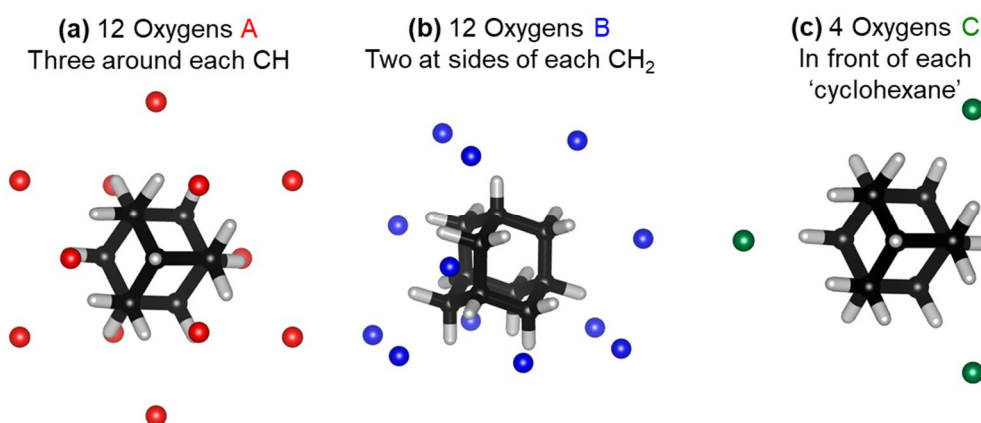


*Figure 5.22. Schematic illustration of the three types of oxygen atoms of the H<sub>2</sub>O molecules orientated around C<sub>10</sub>H<sub>16</sub> making up a cage framework where (a), (b) and (c) are denoted in red, blue, and green oxygen atoms and represent 'A', 'B' and 'C' oxygen atoms, respectively. Hydrogen atoms have been omitted for visual clarity.*

Due to the interactions of C<sub>10</sub>H<sub>16</sub> and H<sub>2</sub>O and referring back to the bivariate positional maps, a distorted cage conformation is adopted by the system such as that shown in Figure 5.23. Figure 5.23 illustrates the encapsulation of one C<sub>10</sub>H<sub>16</sub> molecule within a defined hydrate cage with various coloured oxygen atoms representing the differences in positional ordering around C<sub>10</sub>H<sub>16</sub>. The oxygen atoms connect the newly identified cage structure as indicated previously in Figure 5.21(b) and Figure 5.21(c).

## 5. Total Neutron Scattering of Amorphous Solid Water with Embedded Adamantane

### 5.7.3 Orientational Correlation Functions (OCFs): SHARM and ANGULA

In addition to Figure 5.23, the two-dimensional contour plots in these figures show the OCFs from the EPSR method,  $g_{\text{COM-O}}(r, \theta)$ , where the oxygen atoms are located at  $\theta$  angles of 70, 80 and 90°. The  $\varphi$  values are given by 63, 1 and 30°. The  $\theta$  values of 70, 80 and 90° were taken from the positions of the different oxygen atoms from the ANGULA positional map in Figure 5.21(b) and Figure 5.21(c). H<sub>2</sub>O molecules with oxygen atoms of type ‘A’ were found at  $\cos(\theta_{\text{pos}}) = -0.015$  and so,  $\theta = 90.89^\circ$ . Similarly, the same process was carried out for H<sub>2</sub>O molecules with oxygen atoms of types ‘B’ and ‘C’ due to areas of the highest density which provide the probability of finding oxygen atoms in the first coordination relative to the COM of C<sub>10</sub>H<sub>16</sub>.

In relation to the OCFs, orientational correlations are weakly present in the first and second coordination shell. It is also important to note that the orientational correlations of the H<sub>2</sub>O molecules around C<sub>10</sub>H<sub>16</sub> are less pronounced in the as-made 80 K models compared to those in the after annealed at 140 K models as indicated by weaker maxima in the OCFs [Figure 5.23(e)]. The angle,  $\alpha$ , reflects the dipole alignment with respect to the  $z_1$  axis for a given  $\theta$  and  $\varphi$ . The power of the EPSR method outputting OCFs is that once the spherical harmonics have been calculated and refined, the OCF can be calculated for an arbitrary number of  $\theta$  values and the distances between the molecules is not limited. The SHARM routine allows the user to build in molecular symmetry naturally into the OCFs by choosing suitable  $l$  and  $m$  values.<sup>36</sup>

## 5. Total Neutron Scattering of Amorphous Solid Water with Embedded Adamantane

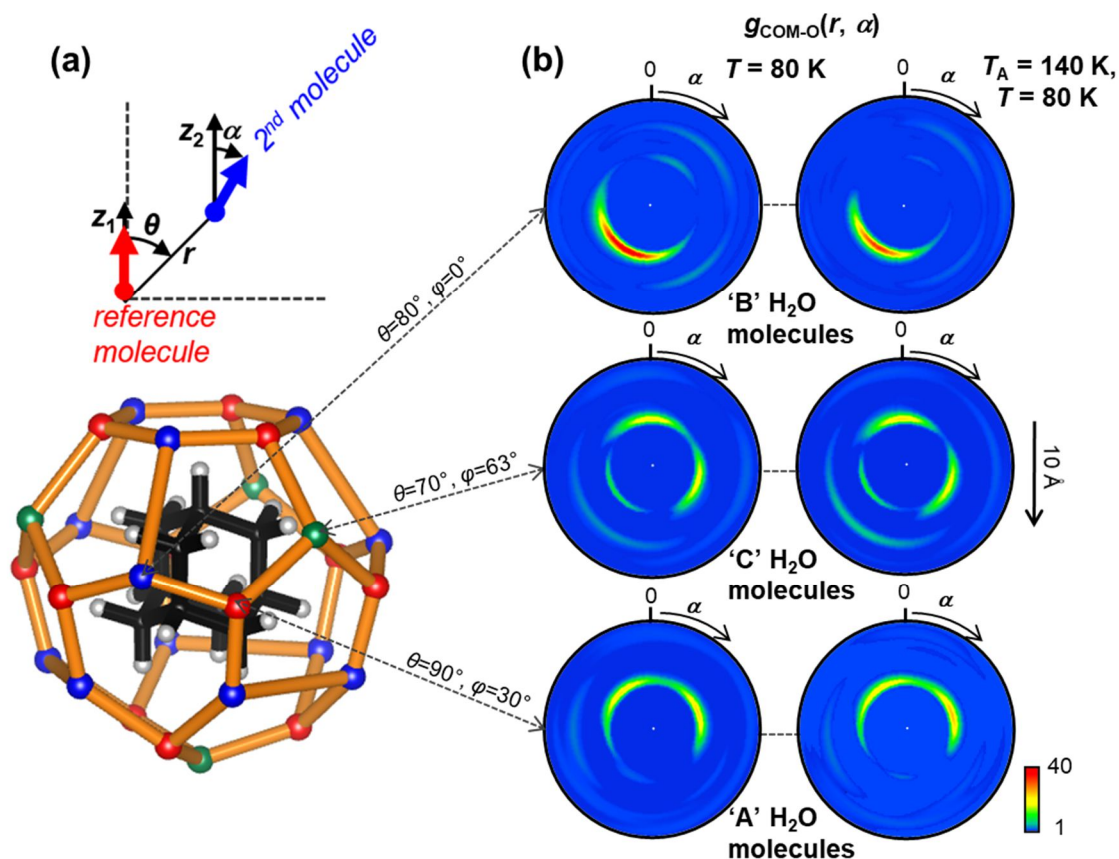


Figure 5.23. (a) Structure of newly identified cage type,  $5^6 6^4$ . The bonds connecting the network of oxygen atoms are depicted with orange lines. Note:  $5^6 6^4$  means that the cage is made up of six-pentagonal and four-hexagonal membered rings. Carbon atoms in the guest  $C_{10}H_{16}$  species are depicted in black colour and the hydrogens of  $C_{10}H_{16}$  are shown in grey. Hydrogen atoms from the cage have been omitted for clarity and (b) OCF contour plots of  $g_{COM-O}(r, \alpha)$  at 80 K (as-made sample, left-hand side) and after annealing at 140 K sample (right-hand side) for specified values of  $\theta$  and  $\phi$ . The relative orientation of the dipole moment of the second molecule is defined by the angle  $\alpha$  and  $r$  is the separation from the COM of  $C_{10}H_{16}$ .

It is evident that in the initial measurements and after sintering of the matrix, this unexpected structure surrounding  $C_{10}H_{16}$  consists of layers of distorted cages of six-pentagonal faces for every  $CH_2$  group on  $C_{10}H_{16}$  and four-hexagonal faces for every  $CH$  group in  $C_{10}H_{16}$ . Interestingly, looking at the five-membered ring territory, they are found next to one another. With the evidence of 28 oxygen atoms surrounding  $C_{10}H_{16}$  from the  $g_{ij}(r)$  and from Figure 5.23(a) and Figure 5.23(b), this new cage type, with no isolated pentagons is labelled according to polyhedra nomenclature for one cage type as,  $5^6 6^4$ . From observing the bivariate two-dimensional density maps in Figure 5.21(b) and Figure 5.21(c) for the COM of  $C_{10}H_{16}$  to the oxygen atom of  $H_2O$ , the location of these five- and

## 5. Total Neutron Scattering of Amorphous Solid Water with Embedded Adamantane

six-membered rings or cages are identified which serve to define a new polyhedron, not reported in the literature.<sup>37, 38</sup>

Even at 80 K for the as-made sample, it is perhaps not expected that a clathrate hydrate cage will form. This  $5^66^4$  cage has a significant impact on the structure of the matrix and could provide a possible explanation for several experimental observations regarding hydrophobic hydration. In general, it is difficult to make clathrate hydrates and this cage structure identified here does not identify with or occur in any tabulation of known or hypothetical structures in the literature and is remarkably, in fact, not space-filling. Clathrate hydrates that are space-filling are those described in Chapter 1 of this thesis; cubic structure I (CS-I), cubic structure II (CS-II) and the hexagonal structure, sH. This new finding suggests that the limit of where a guest species can form a hydrate has been exceeded. It is known that  $C_{10}H_{16}$  is a larger molecule when compared to standard clathrate hydrate guest species.  $H_2O$  molecules would be expected to respond to the voids and dips in the structure already at 80 K (as-made) which have not been detected previously due to the highly porous nature of the sample. Due to this unusual, distorted cage structure, it has thus, proved difficult to produce a clathrate hydrate. With this carefully mixed complex matrix of  $C_{10}H_{16}$  and ASW, preferred orientation of  $H_2O$  molecules is observed.

A new cage structure with  $C_{10}H_{16}$  embedded into the amorphous ice matrix is identified and it is proposed that the new polyhedron structure should be recognised with the abbreviation,  $5^66^4$ . As mentioned in the previous chapter, the ‘barrel cage’ with cage types,  $5^{12}6^8$  is the largest cage observed so far in clathrate hydrates. Guest molecules with van der Waals diameters of 8.6 Å fit into this structure.<sup>39</sup> Figure 5.24 compares the ‘barrel’ cage and the new polyhedron as discovered in this thesis, the  $5^66^4$  cage type. A number of hypothetical clathrate hydrate structures have been postulated ( $4^35^96^{27}3$  or  $4^35^{12}6^{18}3$ ),<sup>40, 41</sup> yet a complete picture of all the probable networks, specifically larger cages, is a difficult topological problem and many of these topologies have not yet been uncovered.<sup>40</sup> The pursuit for large-caged clathrate hydrates is timely due to the current attention towards open framework materials and their use in energy-related applications,<sup>42</sup> space research and relevance in the context of hydrophobic hydration.<sup>43</sup>

## 5. Total Neutron Scattering of Amorphous Solid Water with Embedded Adamantane

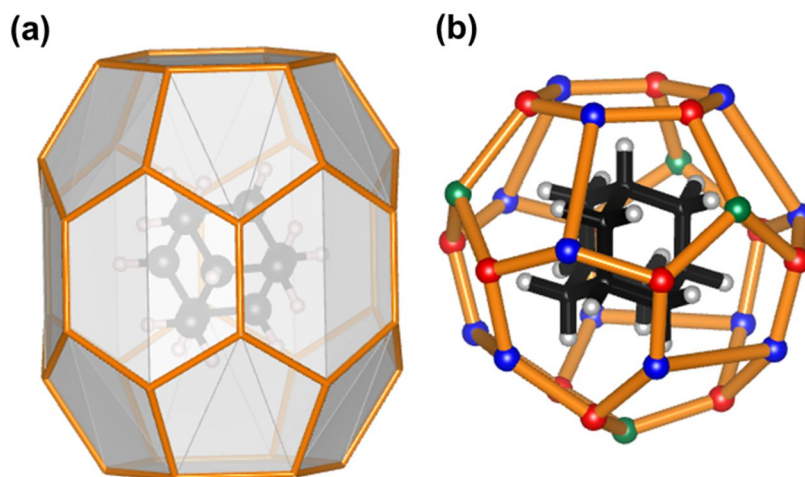


Figure 5.24. (a) Largest cage observed in clathrate hydrates so far, named the barrel' cage,  $5^{12}6^8$  with  $C_{10}H_{16}$  situated inside the cage and (b) newly defined polyhedron cage,  $5^66^4$  as determined from this study. Both cages have been created in the Vesta software and both (a) and (b) are drawn to scale.

Furthermore, the positional ordering of the first eight H<sub>2</sub>O molecules in the first hydration shell of the system has been defined using bivariate probability distribution maps of both sets of temperature data. The first eight H<sub>2</sub>O molecules that are positioned around the COM of C<sub>10</sub>H<sub>16</sub> have been illustrated in Figure 5.25 and Figure 5.26 for as-made (80 K) and after annealed at 140 K data, respectively. It must be noted that the H<sub>2</sub>O molecules with 'C' type oxygen atoms are first, followed by the H<sub>2</sub>O molecules with 'A' type oxygen atoms and finally H<sub>2</sub>O molecules with 'B' type oxygen atoms.

## 5. Total Neutron Scattering of Amorphous Solid Water with Embedded Adamantane

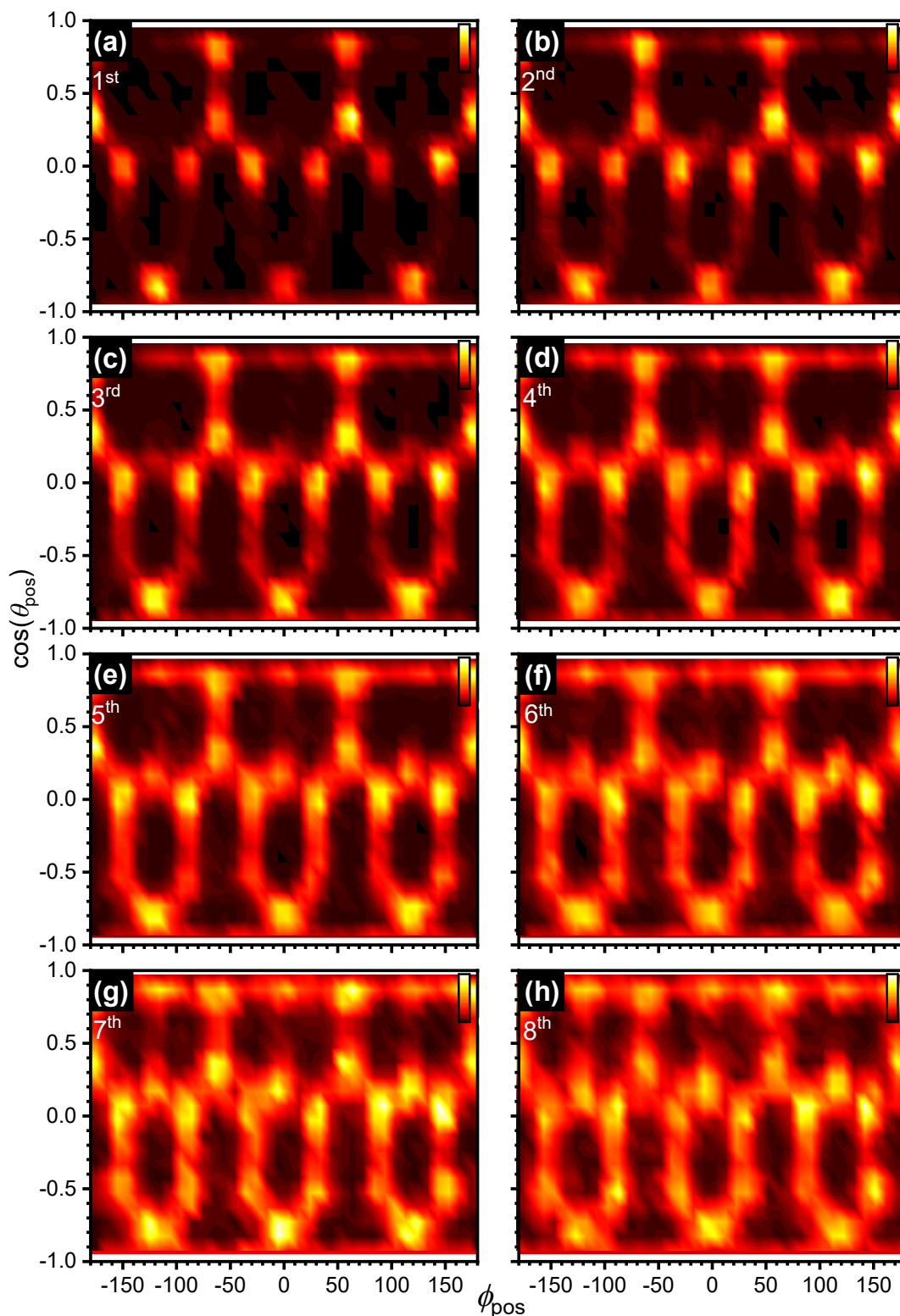


Figure 5.25. Bivariate probability distribution maps for the as-made (80 K) measurements of the positional ordering of the first eight  $\text{H}_2\text{O}$  molecules around  $\text{C}_{10}\text{H}_{16}$ , where (a)–(h) have been indicated on the figure corresponding to the  $\text{H}_2\text{O}$  molecule positions around the COM of  $\text{C}_{10}\text{H}_{16}$ . The contour plots serve as a guide to delimitate regions of maxima and minima arising from the data.



## 5. Total Neutron Scattering of Amorphous Solid Water with Embedded Adamantane

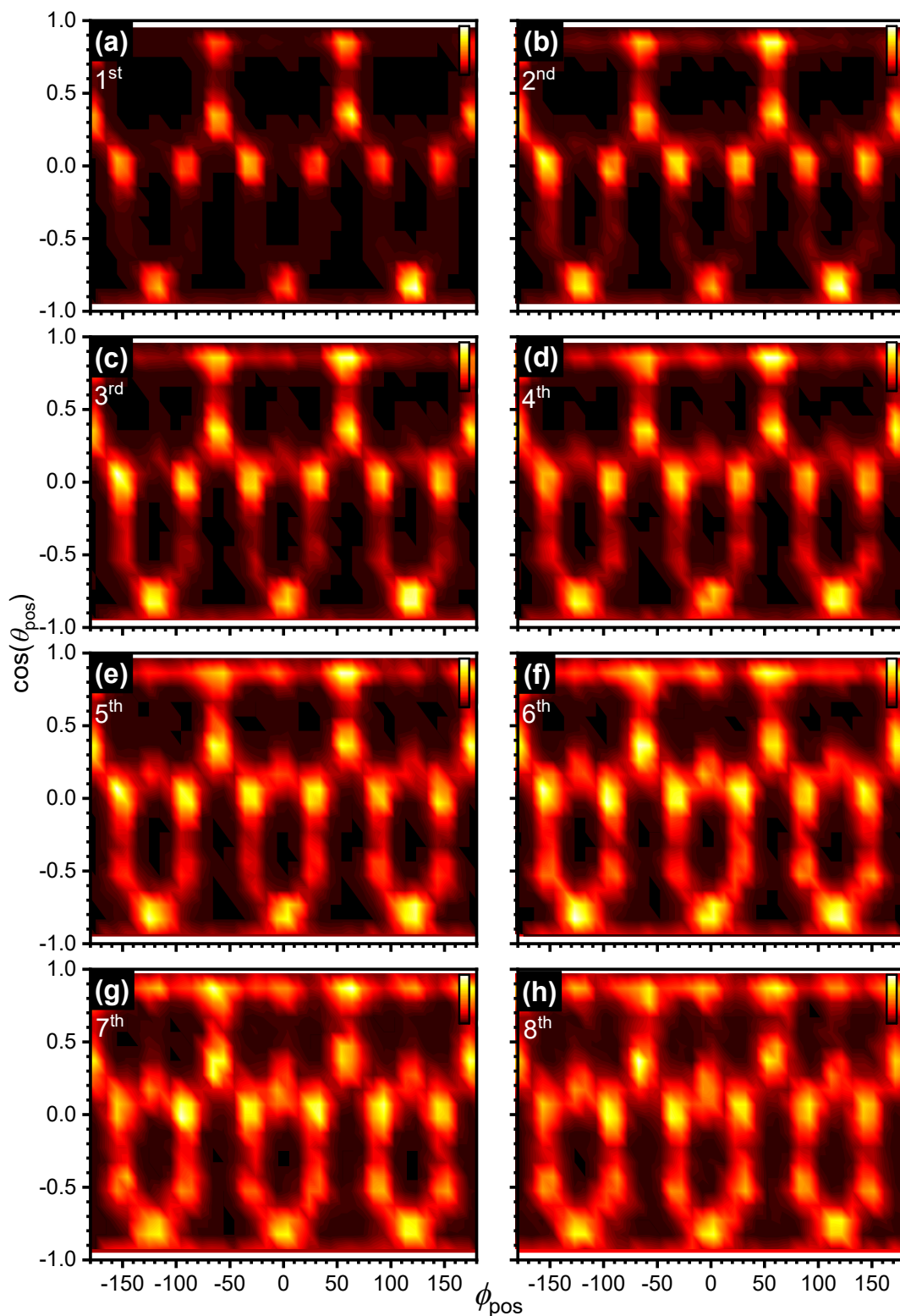


Figure 5.26. Bivariate probability distribution maps for the after annealed at 140 K measurements of the positional ordering of the first eight  $\text{H}_2\text{O}$  molecules around  $\text{C}_{10}\text{H}_{16}$ , where (a)–(h) have been indicated on the figure corresponding to the  $\text{H}_2\text{O}$  molecule positions around the COM of  $\text{C}_{10}\text{H}_{16}$ . The contour plots serve as a guide to delimitate regions of maxima and minima arising from the data.

## 5. Total Neutron Scattering of Amorphous Solid Water with Embedded Adamantane

In addition to recognising that there are 28 oxygen atoms surrounding  $C_{10}H_{16}$ , it was necessary to prove that they are no defects in the system which may alter the 28-molecule cage. Thus, bivariate positional maps of  $C_{10}H_{16}$  with 27 and 29  $H_2O$  molecules were investigated and are shown in Figure 5.27 for both samples, as-made (80 K) and after annealing at 140 K.

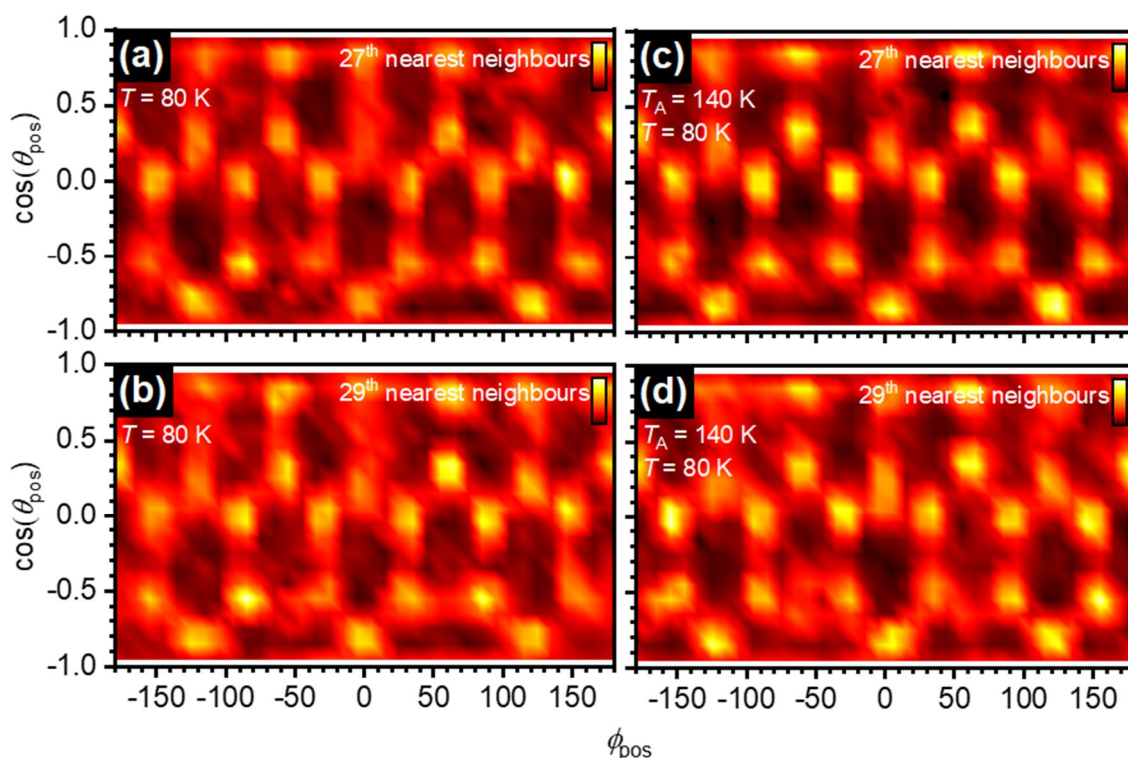


Figure 5.27. Bivariate positional maps  $[\cos(\theta_{pos}), \phi_{pos}]$  where column 1 [(a) and (b)] is generated from the as-made samples at 80 K and column 2 corresponds to after annealed samples at 140 K [(c) and (d)], where (a) and (c) are the 27<sup>th</sup> nearest neighbours and (b) and (d) are the 29<sup>th</sup> nearest neighbours.

The analysis of  $C_{10}H_{16}$  molecules with 27 and 29  $H_2O$  molecules was found to show the same type of cage, however, with point defects. Figure 5.27 clearly defines how the 27 and 29 nearest neighbour  $H_2O$  molecules are very similar to the positional map for 28 nearest neighbours (Figure 5.21), or at least, it is probable to say that the defects are statistical and not in a given direction, i.e., the positional arrangements do not appear in new spots on the map. It is still very evident that the new cage structure exists in the  $5^66^4$  arrangement.



### 5.7.4 Hydrogen Positional Ordering in the First Hydration Shell

To investigate how well-defined the cage structure is, the positional distribution map for the hydrogen atoms were also investigated. Figure 5.28 depicts a bivariate map for the COM of  $C_{10}H_{16}$  to the hydrogen atoms of  $H_2O$  molecules in the shoulder peak (bump) and finally the first coordination shell which was plotted with limits of 3.9 and 6.9 Å and correspond to the  $r_{\min}$  and  $r_{\max}$  of the first  $g_{ij}(r)$  peak for the COM to oxygen, as seen earlier in Figure 5.20. This was to ensure a direct comparison of the probability distribution maps for COM–O and COM–H could be made and to confirm whether the cages appear at the same distances. Additionally, this analysis was carried out to investigate if there is hydrogen bonding between the oxygens within the new cage type. It was necessary to exclude the hydrogens pointing towards the COM of  $C_{10}H_{16}$  here as well. In this case, mapping the hydrogen atom positions at the same distance as the oxygen atoms in the first coordination shell enabled the hydrogen-bonded network to be visualised. The hydrogen-bonded network is seen between the oxygen atom positions forming the cage type network as can be seen in Figure 5.28.

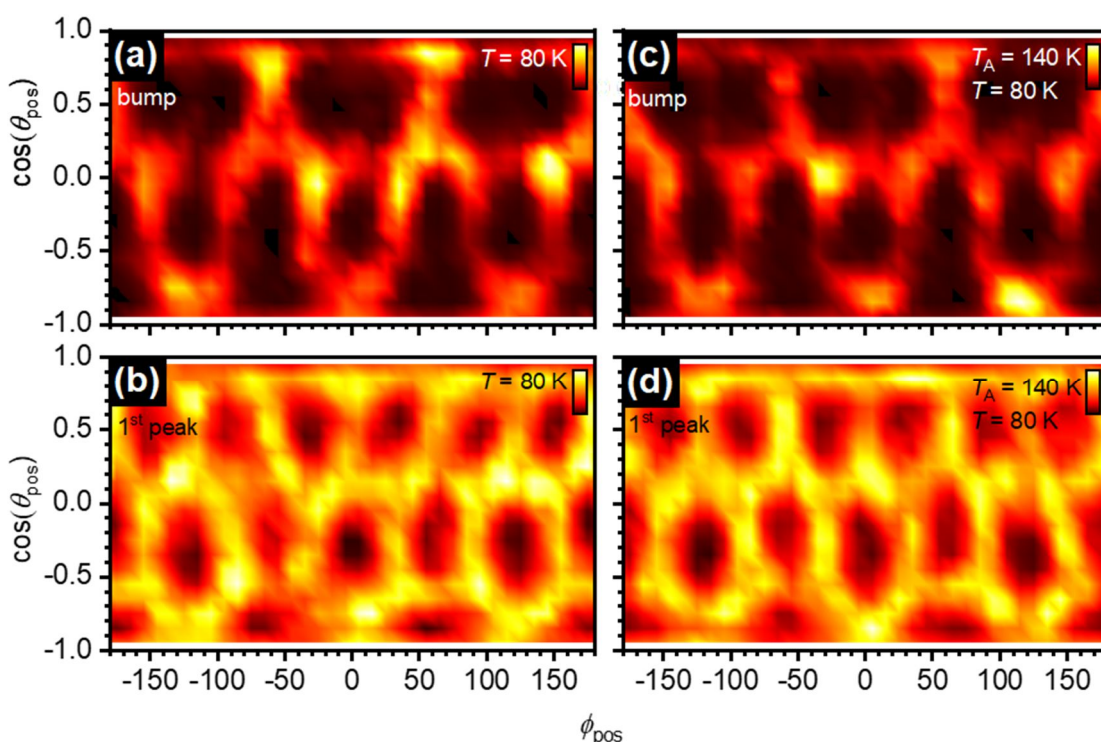


Figure 5.28. Bivariate positional maps  $[\cos(\theta_{pos}), \phi_{pos}]$  of the hydrogen positioning of the shoulder peak/bump [(a) and (c), as-made and after annealing at 140 K, respectively] before the first  $g_{ij}(r)$  peak [(b) and (d), as-made and after annealing at 140 K, respectively] taken from the limits of the COM–O  $g_{ij}(r)$  first peak.

## 5. Total Neutron Scattering of Amorphous Solid Water with Embedded Adamantane

Interestingly, after several types of analysis, there is a plethora of evidence to suggest the presence of a new hydrogen-bonded cage surrounding  $C_{10}H_{16}$  for both temperature sets of data obtained from the neutron diffraction experiments, the EPSR method and the ANGULA software.

### 5.7.5 Orientational Ordering in the First Hydration Shell

Since the positional arrangement of the oxygen atoms and hydrogen atoms were determined, the orientational correlations of the  $H_2O$  molecules were now examined with the ANUGLA software. The preferred molecular arrangement of the  $H_2O$  molecules around  $C_{10}H_{16}$  in the first coordination shell have been determined by two characteristic angles,  $(\theta_{\text{dip}})$  and  $(\alpha_{\text{OH}})$ . Both these angles have a reference vector where one points outwards from the  $C_{10}H_{16}$  molecules. Specifically, one vector links the COM of  $C_{10}H_{16}$  with the oxygen atom of  $H_2O$  as can be seen in Figure 5.29(a) by the dashed black line. The vectors determining the orientation of  $H_2O$  are such that:

1.  $\cos(\theta_{\text{dip}})$  is the angle between the reference vector and the dipole moment of  $H_2O$ .
2.  $\cos(\alpha_{\text{OH}})$  is the angle between the reference vector and that linking the O–H bond of the  $H_2O$  molecules.

It must be noted that both vectors are of paramount importance and must be used to characterize the orientation of the  $H_2O$  molecules, since fixing one of the two vectors would allow a rotation about the fixed vector. Figure 5.29(b) and Figure 5.29(c) provides  $g_{ij}(\theta)$  for the first coordination shell with respect to the angles as defined in Figure 5.29(a).

## 5. Total Neutron Scattering of Amorphous Solid Water with Embedded Adamantane

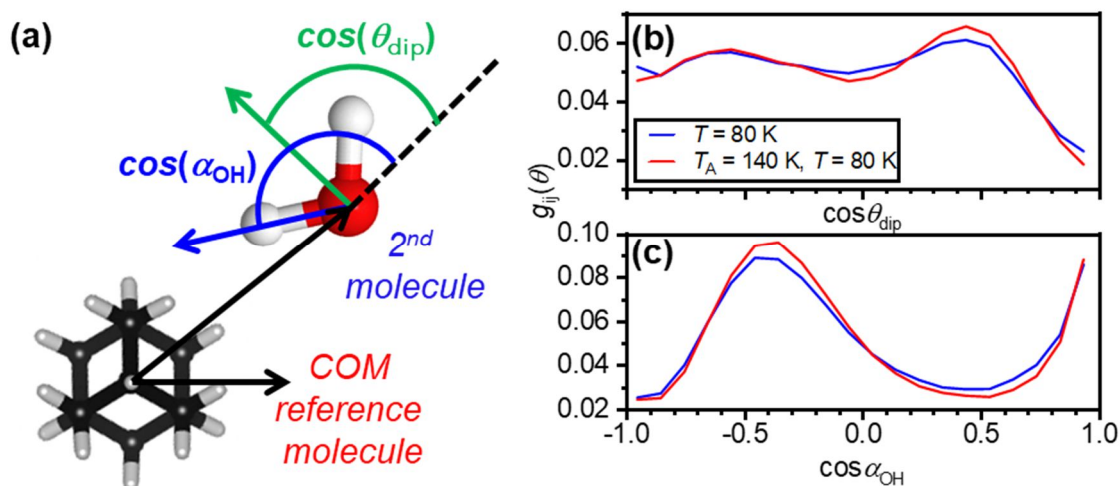


Figure 5.29. (a) Schematic illustration of the definition of axes used to calculate the OCFs, (b) and (c) a slice of the EPSR simulation box from the ANGULA software showing the interactions of  $H_2O$  molecules with the COM of  $C_{10}H_{16}$  according to dipole moment and OH angles as displayed in (a) for the first coordination shell.

Generally, looking at both the  $\cos(\theta_{dip})$  and  $\cos(\alpha_{OH})$  interactions with the  $H_2O$  molecules with respect to  $g_{ij}(\theta)$ , both the as-made (80 K) and after annealing at 140 K samples follow the same trend. There are no significant differences between the temperate data sets for both Figure 5.29(b) and Figure 5.29(c). Figure 5.29(b) depicts a broad peak approximately  $\cos(\theta_{dip}) = -0.5$  and a larger peak at  $\cos(\theta_{dip}) = 0.5$ . These peaks can be observed in a bivariate plot as described and shown in Figure 5.30 below. Maxima spots observed at these two peaks are depicted in the corresponding and upcoming bivariate plots, Figure 5.30(a), and Figure 5.30(c). Similarly, as seen in Figure 5.30(c) for the interactions with the  $H_2O$  molecules of  $\cos(\alpha_{OH})$  with respect to  $g_{ij}(\theta)$ , a significantly large peak is seen at approximately  $\cos(\alpha_{OH}) = -0.6$  and also observed as a maxima spot in the following figure described hereafter, Figure 5.30(b) and Figure 5.30(d). The dip in Figure 5.29(c) after  $\cos(\alpha_{OH}) = -0.4$  shows intensity may be lost as one would approach higher distances and thus, the bivariate distribution functions as a function of  $r$  were investigated to confirm this peculiar finding hereafter. Note: Figure 5.29(b) and Figure 5.29(c) correspond to Figure 5.30 as described below.

A bivariate plot of the probability distribution function of  $\cos(\theta_{dip})$  and  $\cos(\alpha_{OH})$  as a function of the radial distance,  $r$ , is illustrated in Figure 5.30 for the as-made (80 K) and after annealing at 140 K analysis, respectively. Generally, the data is more prominent in

## 5. Total Neutron Scattering of Amorphous Solid Water with Embedded Adamantane

the 140 K measurements due to more structural ordering for both  $\cos(\theta_{\text{dip}})$  and  $\cos(\alpha_{\text{OH}})$ . Figure 5.30(a) and Figure 5.30(c) have been marked with white arrows to show where the high maxima spots are found, which correspond to the positional map as shown in Figure 5.21(a) and Figure 5.21(b) for both  $\cos(\theta_{\text{dip}}) = 60$  and  $\cos(\theta_{\text{dip}}) = -60$ . This position relates the H<sub>2</sub>O molecules to the northern and southern hemisphere of the bivariate probability distribution map. Similarly, the equatorial positions of the molecules in the positional map in Figure 5.21(a) and Figure 5.21(b) correspond to the H<sub>2</sub>O molecules that lie in the  $\cos(\alpha_{\text{OH}})$  plane at  $\cos(\alpha_{\text{OH}}) = \sim 0.45$  and  $r = \sim 4.5$  Å indicated by the white arrows and high maxima.

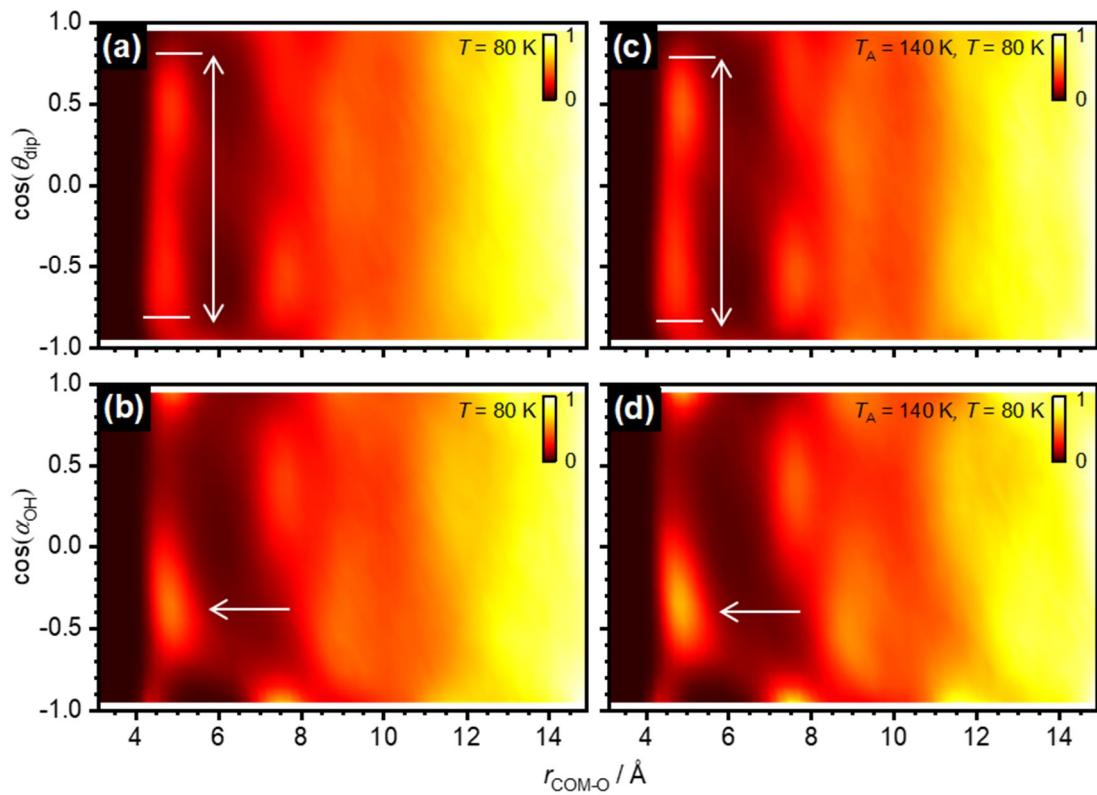


Figure 5.30. Contour plots for the characteristic angles as defined in the main text and shown earlier [Figure 5.29(a)],  $\cos(\theta_{\text{dip}})$  and  $\cos(\alpha_{\text{OH}})$  as a function of  $r$  for the (a), (b) as-made sample at 80 K and (c), (d) annealed at 140 K data. The contour plot serves as a guide to delimitate regions of maxima and minima arising from the data. In this case, the maxima spots are indicated by white arrows.

Despite more structural order in the after annealed samples at 140 K, overall, there is much more structure for the  $\cos(\alpha_{\text{OH}})$  when compared to  $\cos(\theta_{\text{dip}})$ . In any case, there is a peak at low  $r$ , for  $r = 4.5$  Å as mentioned earlier in Figure 5.30(b) and Figure 5.30(d) and regarding these two plots, there is a large gap after  $r = 4.5$  Å until a second peak arises at

## 5. Total Neutron Scattering of Amorphous Solid Water with Embedded Adamantane

high  $r$ , where  $r = 8 \text{ \AA}$ . After this distance, the peaks appear to be more smeared out and more dilute. At this point, a small dip is also seen at  $r = 11.5 \text{ \AA}$ . Thus, where the positions of peaks are found, the intensity is missing as one approaches higher  $r$  which is rather peculiar. The sequence of events as one increases in  $r$ , is as follows: peak, large gap, peak, gap and finally a shadow of another peak where a tiny dip is seen and thus, the features become entirely dilute and strong features cease to be seen. It is probable to say that as the sequence of events progresses, the sample becomes more dilute. This contour plot is rather informative as the distribution of angles is depicted and if the average of this plot was taken, the peaks would be much more smeared out than already displayed.

Schematics diagrams of how the first nearest  $\text{H}_2\text{O}$  molecules are oriented with respect to the COM of  $\text{C}_{10}\text{H}_{16}$  have been illustrated in Figure 5.31 according to the angles defined in Figure 5.29(a). Note that, the  $\text{H}_2\text{O}$  molecule configurations: (i), (ii), (iii) and (iv) will be referred to hereon and will be used as a standard when discussing the OCFs. The way in which one can describe and discuss differences with respect to orientation, keeping in mind the way in which the axes are defined in Figure 5.29(a), is such that:

1. Configuration (i): dipole moment of  $\text{H}_2\text{O}$  points inwards to the COM of  $\text{C}_{10}\text{H}_{16}$ .
2. Configuration (ii): dipole moment of  $\text{H}_2\text{O}$  points inwards to the COM of  $\text{C}_{10}\text{H}_{16}$ .
3. Configuration (iii): dipole moment of  $\text{H}_2\text{O}$  points directly towards the COM of  $\text{C}_{10}\text{H}_{16}$ .
4. Configuration (iv): dipole moment of  $\text{H}_2\text{O}$  points away from the COM of  $\text{C}_{10}\text{H}_{16}$ .

## 5. Total Neutron Scattering of Amorphous Solid Water with Embedded Adamantane

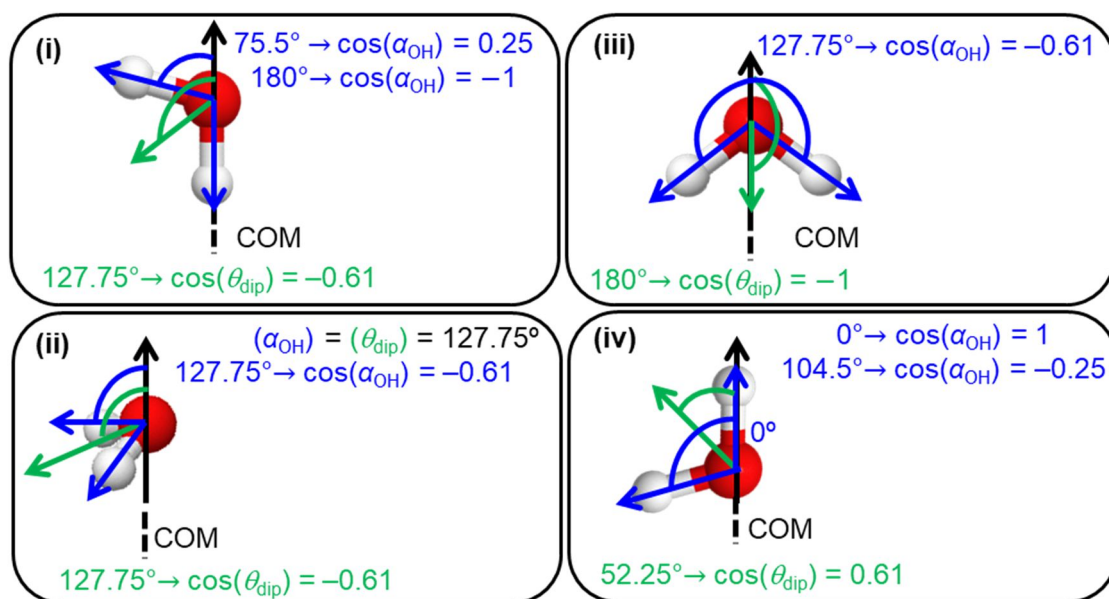


Figure 5.31. Schematic diagram of possible H<sub>2</sub>O configurations that can be found with respect to the COM of C<sub>10</sub>H<sub>16</sub>. The arrows are colour coordinated with Figure 5.29(a) where the blue arrows show the  $\cos(\alpha_{OH})$  angles and green arrows show the dipole moments,  $\cos(\theta_{dip})$ . The black solid arrow shows the COM of C<sub>10</sub>H<sub>16</sub> with a black dashed line showing the reference vector from the COM of C<sub>10</sub>H<sub>16</sub>.

The dipole moments in Figure 5.31(i) and Figure 5.31(ii) point in the same direction, however, it is not possible to distinguish between both cases as one cannot specify where the hydrogen atoms are, as they are equivalent. The hydrogen atoms could be in many different locations for a given orientation of the dipole moment. Also in Figure 5.31(ii), the  $\cos(\theta_{dip})$  and  $\cos(\alpha_{OH})$  are the same angle, such that the angle is  $(\theta_{dip}) = 127.75^\circ$  and thus,  $\cos(\theta_{dip})$  or  $\cos(\alpha_{OH})$  is  $-0.61$ . On the other hand, since the dipole moment is different in cases, (iii) and (iv), O–H is defined. For instance, with the latter, when the dipole moment points in such a fashion that since the O–H bond is along the axis, the O–H bond can be defined. Also, for example, with (iv), the dipole moment points away and rotates about the axis and so,  $\cos(\alpha_{OH})$  stays the same. There are two  $(\alpha_{OH})$  angles at  $0^\circ$  and  $104.5^\circ$ , equating to  $\cos(\alpha_{OH}) = 1$  and  $-0.25$ , respectively. The dipole angle,  $(\theta_{dip})$  is  $52.25^\circ$  and will be found in the OCF at  $\cos(\theta_{dip}) = 0.61$ . With the configurations on the right-hand side of Figure 5.31, it is possible to have  $\cos(\alpha_{OH})$ , however, with the two configurations on the left-hand side, only a range for  $\cos(\alpha_{OH})$  can be presented. Additionally, in Figure 5.31(iii), two spots in the OCF should be found for this configuration since the angles of  $(\alpha_{OH}) = 127.75^\circ$  will be found at  $\cos(\alpha_{OH}) = -0.61$ .

## 5. Total Neutron Scattering of Amorphous Solid Water with Embedded Adamantane

A typical OCF plot has been depicted in Figure 5.32 with illustrations at the foot of the figure showing how the configurations of the H<sub>2</sub>O molecules are oriented. One can always refer back to Figure 5.31 for details of  $\cos(\alpha_{\text{OH}})$  and  $\cos(\theta_{\text{dip}})$ . This bivariate probability plot for this orientation of H<sub>2</sub>O of the first nearest neighbour is depicted here as the maxima regions are seen clearly and also depicted to demonstrate the analysis that is carried out for the three different oxygen atoms and their orientations. At longer distances, the orientational contribution becomes structureless and asymptotically will tend to zero as the system becomes more disordered. This bivariate type of contour plot is much more convenient to clearly illustrate how the H<sub>2</sub>O molecules are oriented in specific conditions when compared to a simple average as in EPSR, which would, in fact, cancel molecules out pointing in opposite directions. Two orientations of the dipole can be identified for the closest H<sub>2</sub>O molecules to the COM of C<sub>10</sub>H<sub>16</sub> in the first coordination shell.

1. Configuration (i): the maxima spot at  $\cos(\theta_{\text{dip}}) = -0.61$  indicates a high probability that the dipole moment of H<sub>2</sub>O point towards the COM of C<sub>10</sub>H<sub>16</sub>, i.e.,  $(\theta_{\text{dip}}) = 127.75^\circ$ . This angle is compatible with an O–H vector pointing towards the COM of C<sub>10</sub>H<sub>16</sub> or a rotation about this direction. Also, the corresponding spot is found at  $\cos(\alpha_{\text{OH}}) = 1$  and  $\cos(\alpha_{\text{OH}}) = 0.25$ . At  $\cos(\alpha_{\text{OH}}) = 0.25$ , a high probability that the dipole moment points slightly towards the COM of C<sub>10</sub>H<sub>16</sub> is seen at approximately  $(\theta_{\text{dip}}) = 75.5^\circ$ .
2. Configuration (ii): another maxima spot also is seen at  $\cos(\theta_{\text{dip}}) = -0.61$ , implying that the dipole moment of H<sub>2</sub>O and the O–H bond is found to point towards C<sub>10</sub>H<sub>16</sub> at  $(\theta_{\text{dip}}) = 127.75^\circ$ . The corresponding  $\cos(\alpha_{\text{OH}}) = -0.4$ .
3. Configuration (iii): the O–H bond is seen to point towards the COM of C<sub>10</sub>H<sub>16</sub> and the dipole moment is in line with the COM. Maxima spots on the contour plot are seen at  $\cos(\theta_{\text{dip}}) = -1$  and thus,  $\cos(\alpha_{\text{OH}}) = -0.61$ .
4. Configuration (iv): two areas of high probability also arise due to a H<sub>2</sub>O molecule at  $\cos(\theta_{\text{dip}}) = 0.61$ , showing orientation at  $(\theta_{\text{dip}}) = 52.25^\circ$ . The dipole moment is seen to point away from the COM and the O–H vector points upwards and towards the COM of C<sub>10</sub>H<sub>16</sub>, found at maxima spots of  $\cos(\alpha_{\text{OH}}) = 1$  or  $-0.25$ .



## 5. Total Neutron Scattering of Amorphous Solid Water with Embedded Adamantane

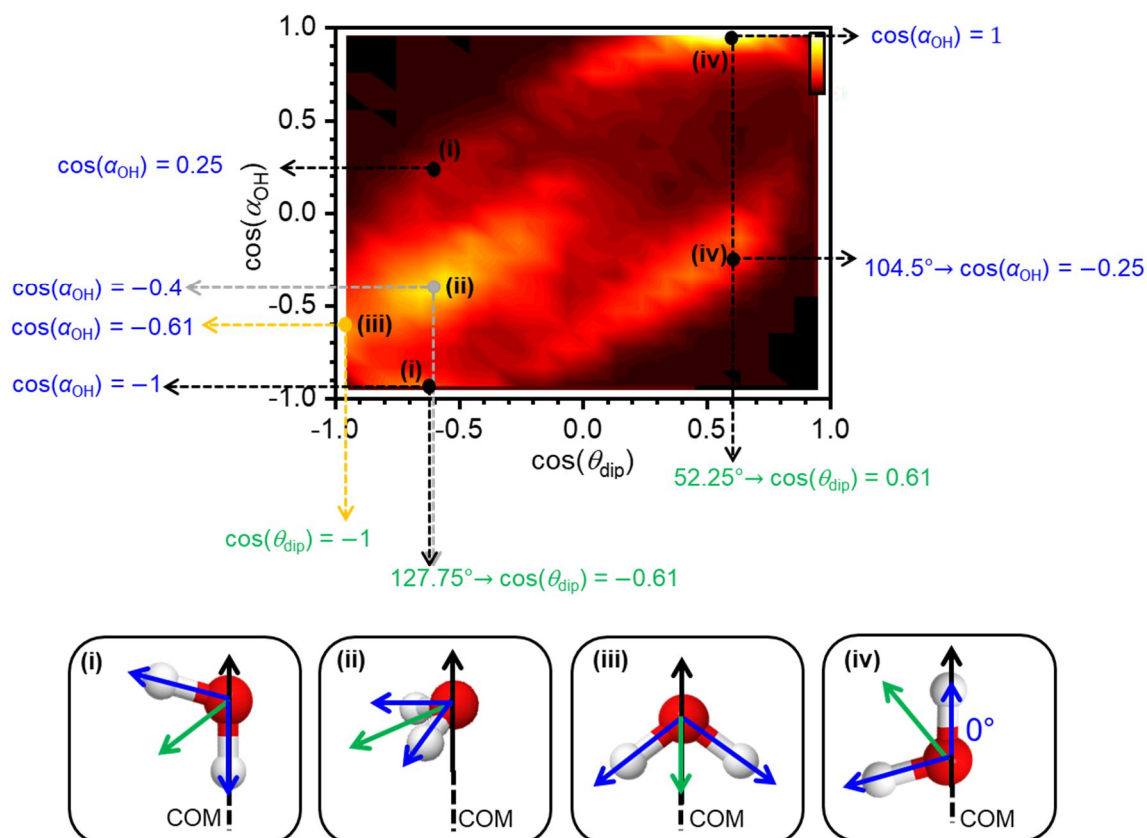


Figure 5.32. Orientation of the nearest  $\text{H}_2\text{O}$  molecule surrounding the COM of  $\text{C}_{10}\text{H}_{16}$ , and corresponding orientations of the  $\text{H}_2\text{O}$  molecules are denoted (i), (ii), (iii) and (iv) calculated from the schematic illustration in Figure 5.29(a) and are replicas of the schematics shown in Figure 5.31. The contour plot serves as a guide to delimitate regions of maxima and minima arising from the data.

Orientational ordering is dependent upon which  $\text{H}_2\text{O}$  molecules one views. Figure 5.33 separates the OCFs for each oxygen atom type and the same analysis as mentioned above, is applied. Figure 5.33 specifically defines and illustrates the orientation of the three types of oxygen atoms for both the as-made (80 K) samples and the annealed samples (140 K). To analyse the orientational correlations of the  $\text{H}_2\text{O}$  molecules with three types of oxygen atoms,  $\cos(\alpha_{\text{OH}})$  and  $\cos(\theta_{\text{dip}})$  were investigated as analysed in Figure 5.32. Although only the result for one atom of each type in the first nearest neighbour is shown, the other spots of the different atom types contain the same information due to the highly symmetric nature of  $\text{C}_{10}\text{H}_{16}$ . For example, molecules at  $(\theta_{\text{dip}}) = 50^\circ$  have the same orientation as those in  $(\theta_{\text{dip}}) = 130^\circ$ .

Towards the bottom of Figure 5.33 is a reference key, representing the orientations of the  $\text{H}_2\text{O}$  molecules [(i), (ii), (iii) and (iv)] as shown in Figure 5.31 and Figure 5.32. In



## 5. Total Neutron Scattering of Amorphous Solid Water with Embedded Adamantane

general, the orientation correlations for the H<sub>2</sub>O molecules with 'B' oxygen atoms show very clear maxima and minima spots for as-made (80 K) measurements when compared to the maxima and minima of H<sub>2</sub>O molecules with 'A' and 'C' oxygen atoms. With respect to the H<sub>2</sub>O molecules with 'B' oxygen atoms, the orientations are strong and there are three different ways in which the H<sub>2</sub>O molecules are oriented around the COM of C<sub>10</sub>H<sub>16</sub>, referring to the reference key at the foot of the figure and as shown in Figure 5.33. Configuration (iv) is seen at two maxima spots:  $\cos(\theta_{\text{dip}}) = 0.61$  and  $\cos(\alpha_{\text{OH}}) = 1$  and  $-0.25$ . This configuration refers to the H<sub>2</sub>O dipole moment pointing away from the COM of C<sub>10</sub>H<sub>16</sub>. The dipole moment in configuration (ii) is found to point towards the COM of C<sub>10</sub>H<sub>16</sub> at  $\cos(\theta_{\text{dip}}) = -0.61$  and  $\cos(\alpha_{\text{OH}}) = -0.4$ . The third type of H<sub>2</sub>O configuration seen for the H<sub>2</sub>O molecules with 'B' type oxygen atoms is where the dipole moment points directly towards the COM of C<sub>10</sub>H<sub>16</sub> (iii), found at  $\cos(\theta_{\text{dip}}) = -1$  and  $\cos(\alpha_{\text{OH}}) = -0.61$ . Thus, the  $(\theta_{\text{dip}}) = 180^\circ$  and  $(\alpha_{\text{OH}}) = 127.75^\circ$ .

In comparison to the H<sub>2</sub>O molecules with 'B' oxygen atoms, for the H<sub>2</sub>O molecules with 'A' oxygen atoms, three maxima spots are observed, insinuating that the dipole moment points away and towards the COM of C<sub>10</sub>H<sub>16</sub>: configurations (iv) and (i), respectively, and the O–H bond points away and towards the COM of C<sub>10</sub>H<sub>16</sub>: configurations (iv) and (i), respectively. The H<sub>2</sub>O molecules with 'A' oxygen atoms share two maxima spots at  $(\alpha_{\text{OH}}) = 75.7^\circ$  where  $\cos(\alpha_{\text{OH}}) = 0.25$  and a second maxima spot at  $(\theta_{\text{dip}}) = 127.75^\circ$ , where  $\cos(\theta_{\text{dip}})$  is found at  $-0.61$ , configuration (i). Assessing the H<sub>2</sub>O molecules with both 'A' and 'B' oxygen atoms, the new maxima in H<sub>2</sub>O molecules with 'A' oxygen atoms not seen in the H<sub>2</sub>O molecules with 'B' oxygen atoms, is visible at  $(\theta_{\text{dip}}) = 127.75^\circ$  and  $\cos(\theta_{\text{dip}}) = -0.61$ , labelled configuration (i). Very weak minima are seen for the H<sub>2</sub>O molecule dipole moments and O–H bonds pointing towards the COM for the H<sub>2</sub>O molecules with 'A' arrangement of oxygen atoms when compared to the H<sub>2</sub>O molecules with 'B' oxygen atoms; configuration (ii). It could be speculated that this configuration (ii) is not present in Figure 5.33(a). In general, the H<sub>2</sub>O molecules with 'A' oxygen atoms have less orientation correlations of H<sub>2</sub>O molecules when compared to the H<sub>2</sub>O molecules with 'B' oxygen atoms and thus, H<sub>2</sub>O molecules with 'B' oxygen atoms depict stronger orientation correlations.

## **5. Total Neutron Scattering of Amorphous Solid Water with Embedded Adamantane**

Moving onto the H<sub>2</sub>O molecules with 'C' type oxygen atoms, all four configurations defined in Figure 5.32 are observed. The first nearest neighbour H<sub>2</sub>O molecule dipole moment with strong maxima is found to point inwards and towards – configuration (i) and (ii), directly pointing towards (iii) and outwards (iv), to the COM of C<sub>10</sub>H<sub>16</sub>. The H<sub>2</sub>O molecules with 'C' oxygen atom types have nearly as strong orientation correlations as do the H<sub>2</sub>O molecules with 'B' oxygen atoms, yet, with the addition of the maxima spot of configuration (i) as found for the H<sub>2</sub>O molecules with 'A' type oxygen atoms and absent for the H<sub>2</sub>O molecules with 'B' oxygen atoms.

## 5. Total Neutron Scattering of Amorphous Solid Water with Embedded Adamantane

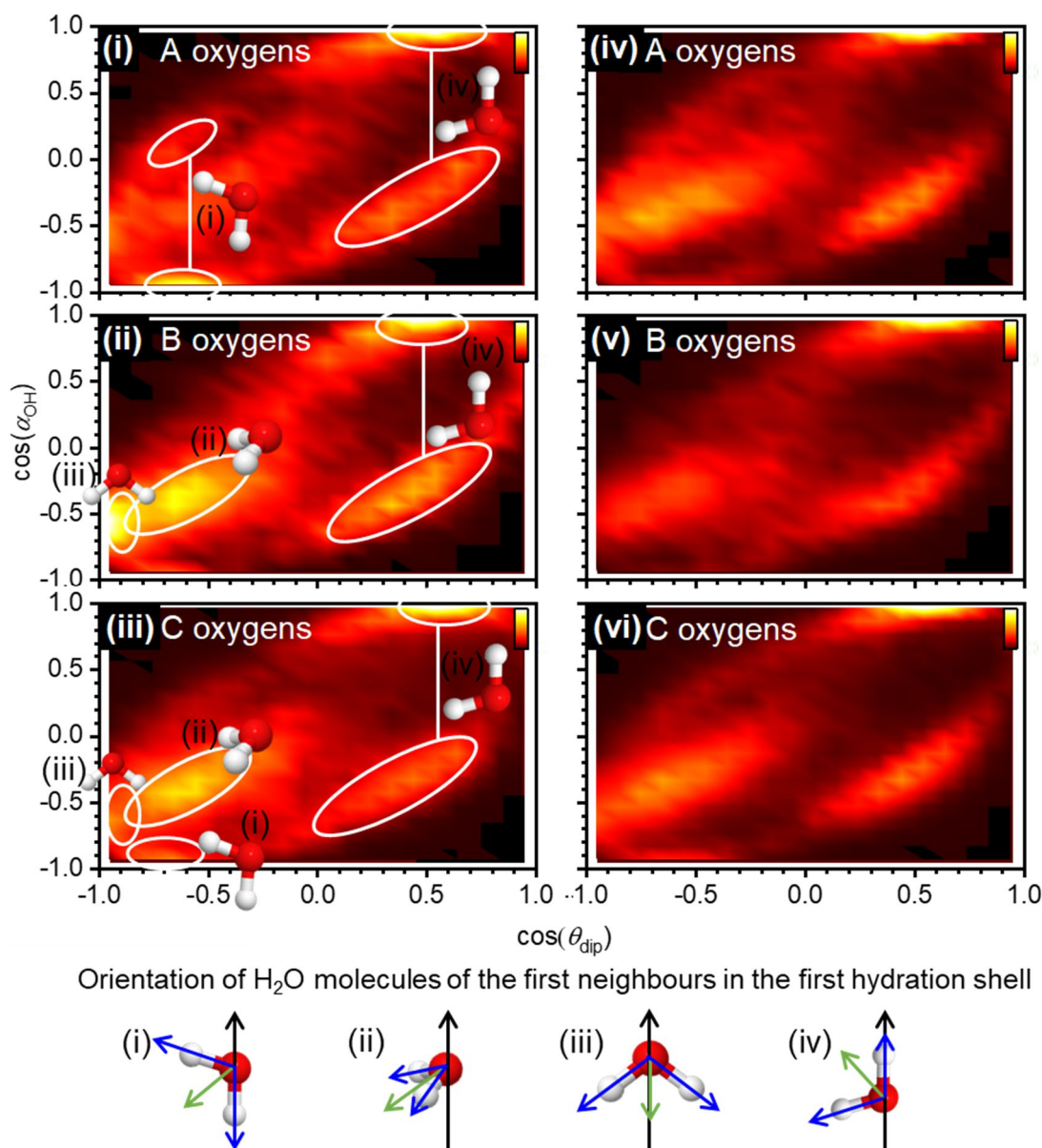


Figure 5.33. Bivariate probability distribution maps showing the orientation of the three types of oxygen atoms in H<sub>2</sub>O surrounding C<sub>10</sub>H<sub>16</sub> plotted as a function of  $\cos(\theta_{\text{dip}})$  and  $\cos(\alpha_{\text{OH}})$  where (i)–(iii) as-made (80 K) data and (iv)–(vi) after annealing at 140 K data. The contour plots serve as a guide to delimitate regions of maxima and minima arising from the data. At the foot of the figure beneath the contour plots, is a key to the configurations as depicted in Figure 5.31, so one can refer to when looking at the orientations of H<sub>2</sub>O for the first nearest neighbours in the OCF contour plots.

For the sake of completeness, the results of the orientational correlations for the system up to the eighth H<sub>2</sub>O molecule as a function of  $\cos(\theta_{\text{dip}})$  and  $\cos(\alpha_{\text{OH}})$  for both sets of temperature data (as-made at 80 K and after annealing at 140 K) are shown in upcoming Figure 5.35 and Figure 5.36, respectively at the end of this section.

## 5. Total Neutron Scattering of Amorphous Solid Water with Embedded Adamantane

To further investigate which molecular arrangements cause the features of the distorted cages, a schematic and bivariate probability distribution function for positional ordering and orientational ordering of the first closest H<sub>2</sub>O molecule at 140 K were replotted as previously shown in Figure 5.26(a) and Figure 5.33(iv), for Figure 5.34. Since there are no significant changes with the as-made (80 K) and after annealing at 140 K samples, in this case, with after annealed samples at 140 K, more ordered structure data was employed.

Figure 5.34(a) indicates a schematic of the H<sub>2</sub>O molecules with oxygen atoms with labels 'A' and 'C' from the cage structure present in the first coordination shell. The H<sub>2</sub>O molecules with oxygen atoms of type 'B' are not present in the first H<sub>2</sub>O molecule around the C<sub>10</sub>H<sub>16</sub>, and this is supportively relayed in the bivariate probability distribution function as shown in Figure 5.34(b). Figure 5.34(c) represents the OCF for the position of the first H<sub>2</sub>O molecule only, rather than the entire molecular distribution in the first coordination shell as in Figure 5.21(b) and Figure 5.21(c).

Concerning the relative orientational correlation of H<sub>2</sub>O around the COM of C<sub>10</sub>H<sub>16</sub> in the after annealed data (140 K), remarkably, the position of the closest O–H bond in the first coordination shell is found to point towards the six-membered ring of the COM of C<sub>10</sub>H<sub>16</sub>. This correlation is reflected in the  $g_{ij}(r)$  of H<sub>2</sub>–H<sub>w</sub> atom pair as a shoulder on the first coordination shell peak as indicated with a black arrow in Figure 5.20(b). The closest H<sub>2</sub>O molecules have O–H bonds pointing towards the COM of C<sub>10</sub>H<sub>16</sub> along the line through the centre of the six-membered rings of C<sub>10</sub>H<sub>16</sub>. Thus, they are far away from the CH/CH<sub>2</sub> groups as possible. The orientations of the H<sub>2</sub>O molecules with different oxygen atom arrangements can be referred back to Figure 5.32.

Unexpectedly, the closest O–H bonds are then not hydrogen-bonded to anything which is very interesting and different compared to what is expected of clathrate hydrates. Clathrate hydrates consist of a network of hydrogen-bonded H<sub>2</sub>O molecules. It is therefore proposed that C<sub>10</sub>H<sub>16</sub> provides a nice pocket for the O–H bond to situate itself in and one can speculate that this type of interaction is a 'multipolar' interaction between the closest H<sub>2</sub>O molecules and C<sub>10</sub>H<sub>16</sub>. Overall, it is very interesting that a non-polar molecule such as C<sub>10</sub>H<sub>16</sub> shows quite strong orientational correlations in its first hydration shell. It is inferred that this is a relatively unusual type of arrangement and thus, the complex binary mixture is said to be extremely geometry influenced.

## 5. Total Neutron Scattering of Amorphous Solid Water with Embedded Adamantane

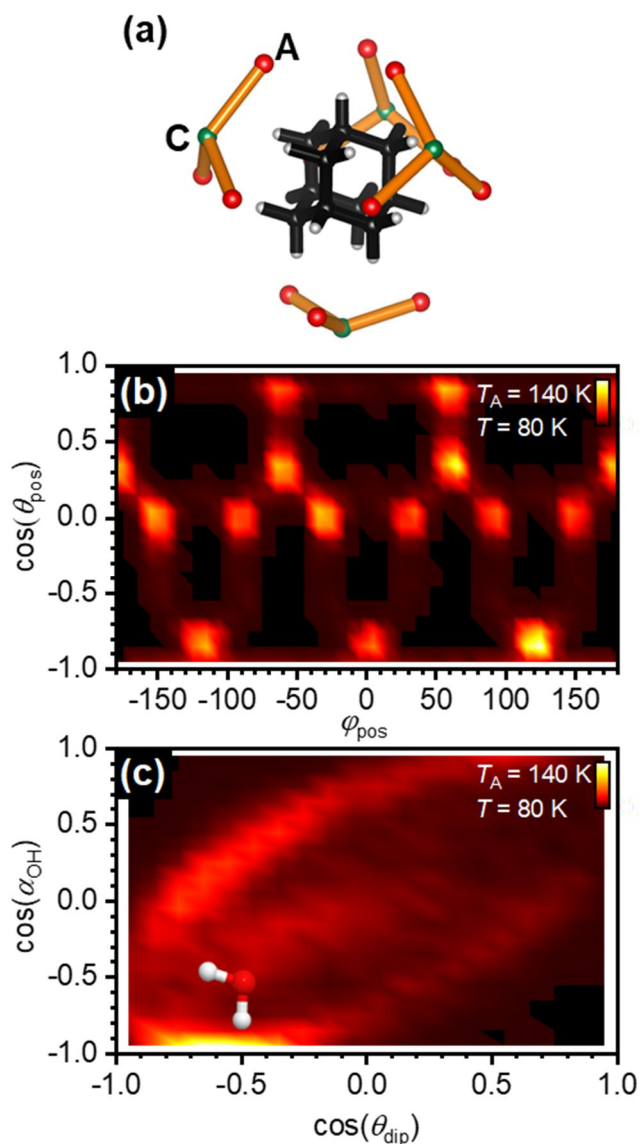


Figure 5.34. (a) Schematic illustration of the  $\text{H}_2\text{O}$  molecules with oxygen atoms of type 'A' and type 'C' around  $\text{C}_{10}\text{H}_{16}$ , (b) bivariate probability distribution map showing the positions of the oxygen atoms around  $\text{C}_{10}\text{H}_{16}$  and (c) bivariate probability distribution map showing how exactly the  $\text{H}_2\text{O}$  molecules are positioned around  $\text{C}_{10}\text{H}_{16}$  for the first nearest oxygen atom neighbour. The contour plots serve as a guide to delimitate regions of maxima and minima arising from the data.

In addition, bivariate probability distribution maps from both sets of temperature data showing up to eight nearest  $\text{H}_2\text{O}$  molecules are illustrated around the COM of  $\text{C}_{10}\text{H}_{16}$  and how they are oriented in upcoming Figure 5.35 and Figure 5.36. The OCF for the second  $\text{H}_2\text{O}$  molecule is very similar to the first  $\text{H}_2\text{O}$  molecule, where the O–H bond points towards the COM of  $\text{C}_{10}\text{H}_{16}$ . For the third and fourth  $\text{H}_2\text{O}$  molecules, the O–H bonds are more disordered.  $\text{H}_2\text{O}$  molecules thus, undergo orientational ordering and depending on which  $\text{H}_2\text{O}$  one views, different orientation will be observed. An increase in the OCFs

## 5. Total Neutron Scattering of Amorphous Solid Water with Embedded Adamantane

after heating is observed whereby, stronger correlations in the first coordination shell and weaker correlations in the second hydration shell are identified.

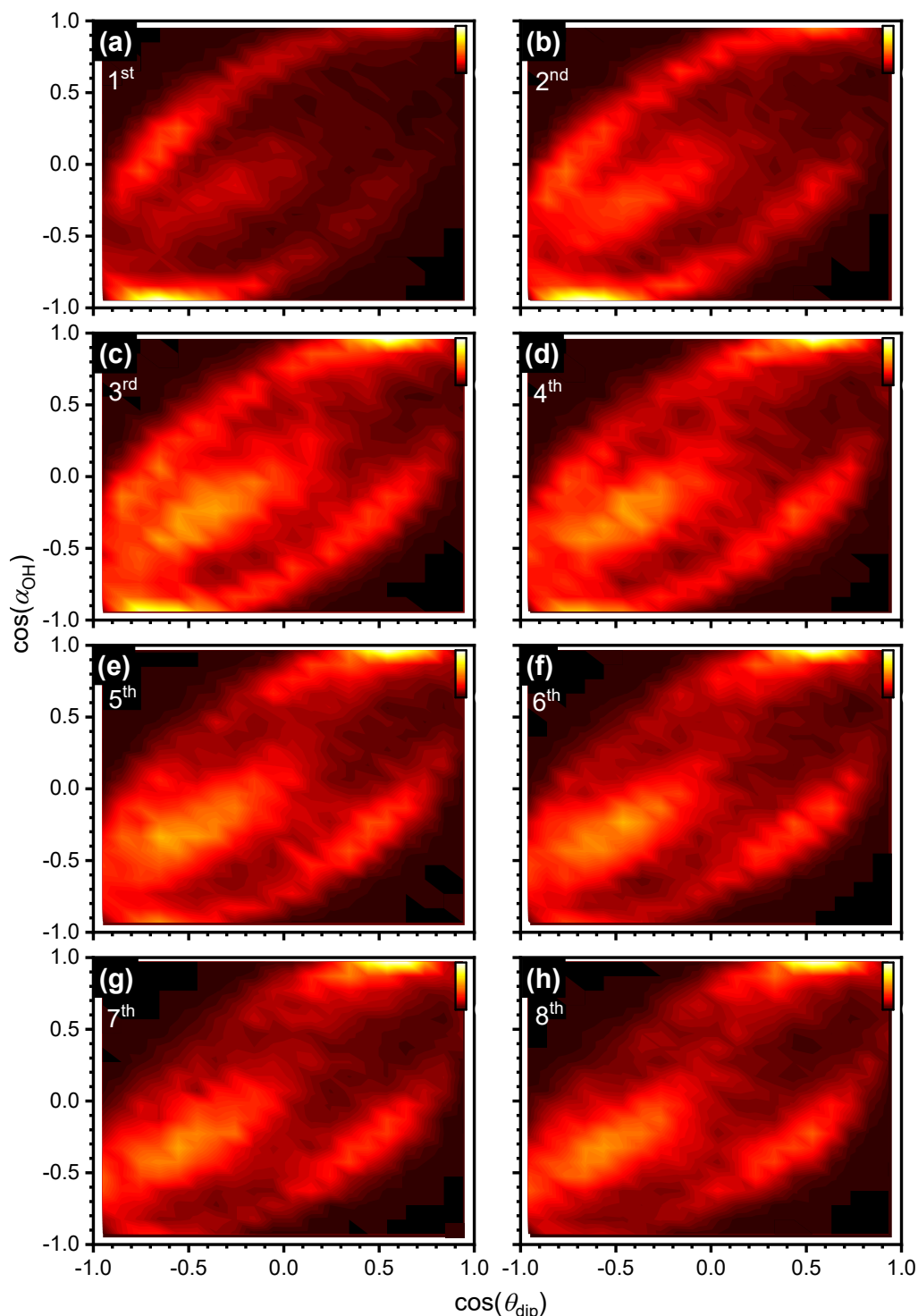


Figure 5.35. Bivariate distribution maps for the as-made (80 K) measurements showing how the first eight  $\text{H}_2\text{O}$  molecules are oriented around the COM of  $\text{C}_{10}\text{H}_{16}$  plotted as a function of the radial distance,  $r$ , where (a)–(h) have been indicated on the figure corresponding to the  $\text{H}_2\text{O}$  molecule orientations around the COM of  $\text{C}_{10}\text{H}_{16}$ . The contour plots serve as a guide to delimitate regions of maxima and minima arising from the data.

## 5. Total Neutron Scattering of Amorphous Solid Water with Embedded Adamantane

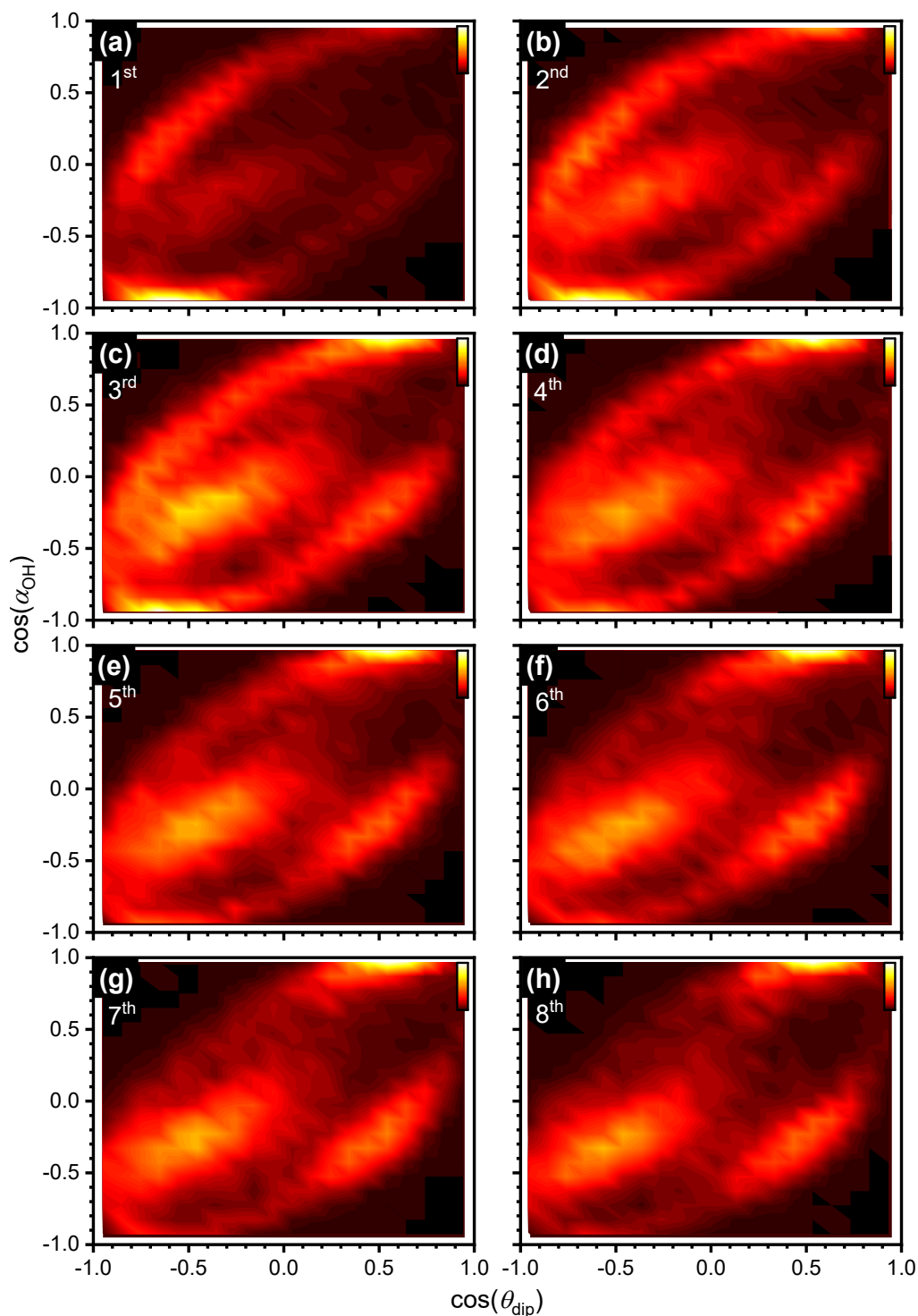


Figure 5.36. Bivariate distribution maps for the after annealed at 140 K measurements showing how the first eight H<sub>2</sub>O molecules are oriented around the COM of C<sub>10</sub>H<sub>16</sub> plotted as a function of the radial distance,  $r$ , where (a)–(h) have been indicated on the figure corresponding to the H<sub>2</sub>O molecule orientations around the COM of C<sub>10</sub>H<sub>16</sub>. The contour plots serve as a guide to delimitate regions of maxima and minima arising from the data.

### 5.8 Fourier Transform Infrared Spectroscopy (FTIR)

The H<sub>2</sub>O and D<sub>2</sub>O vibrational modes are well established in the literature for vapour deposited amorphous ice.<sup>28</sup> The spectra for H<sub>2</sub>O above 3050 cm<sup>-1</sup> and D<sub>2</sub>O above 2300 cm<sup>-1</sup> are fairly broad and featureless for both crystalline and amorphous ice.<sup>28</sup> The clarification of these spectra has proved difficult and the origin of the modes lacked a detailed understanding. Insightful interpretation of these modes arose from Whalleys<sup>44</sup> comparison of high-pressure ice VIII (ordered) and ice VII (disordered). These were compared with IR spectra from cubic ice (ice Ic), both ordered and disordered and concluded that even ice Ih and ice Ic were indistinguishable.<sup>44</sup> In this section, the stretching mode at the highest wavenumbers is investigated and it is possible to infer some information from the gas phase. However, additionally, at low wavenumbers, librations and hindered translations are present. The libration of ice Ic has been calculated by del Rosso *et al.*<sup>45</sup> and found to be different from ice Ih. This difference is only subtle yet quite significant and this work will not be discussed here (this content is a preprint and has not yet been peer-reviewed).

In the work presented in this chapter, a dilute solution of D<sub>2</sub>O (5 w%) in H<sub>2</sub>O (95 w%) was vapour deposited with C<sub>10</sub>H<sub>16</sub> for a 1:100 molar ratio at 82 K and FTIR was carried out to investigate the local structure of the deposits at temperatures of 78 K and after annealing at 140 K. The FTIR spectra as presented in Figure 5.37 illustrates measurements recorded immediately after the transfer of the sample into the cryostat [Figure 5.37(a) and (b)] and annealed to 140 K where the measurement was taken once the sample was re-cooled back down to 78 K [Figure 5.37(c) and (d)] for spectral recognition. Samples were recorded at 78 K and after annealing to 140 K following the data set as collected in neutron diffraction and presented earlier. This approach enables the spectral changes to occur well before crystallisation of the sample and the structural relaxation and sintering of the sample caused by thermal annealing can be observed, respectively.

It is possible to ‘switch off’ the coupling of the stretching modes of ice by introducing deuterium which serves to act as an isotopic impurity, thus, measuring the decoupled vibrations,  $\mu(\text{O}-\text{D})^2$ ,<sup>46, 47</sup> caused by the disparity in the substantial frequency of O–H and O–D.<sup>47</sup> The low concentration of O–D oscillators blocks the coupling stretching transitions<sup>2</sup> and so, isolated O–D oscillations are observed.<sup>46, 47</sup> The isolated



## 5. Total Neutron Scattering of Amorphous Solid Water with Embedded Adamantane

decoupled vibrations allows one to see spectral changes from localised regions of the ice.<sup>2</sup> The spectroscopic information observed in IR spectroscopy and Raman spectroscopy are identical due to identical spectroscopic selection rules of  $\mu(\text{O-D})$ .<sup>2</sup> To achieve a high S/N ratio spectra of the decoupled O-D mode, the FTIR of the codeposited samples of  $\text{C}_{10}\text{H}_{16}$  and ice containing 5 w%  $\text{D}_2\text{O}$  + 95 w%  $\text{H}_2\text{O}$  were investigated. The reported FTIR spectrum of the codeposited samples contains three main components such that they are:  $\text{H}_2\text{O}$ , HDO (since  $\text{D}_2\text{O}$  is dilute, virtually no  $\text{D}_2\text{O}$  left) and also  $\text{C}_{10}\text{H}_{16}$ . Peak fitting in OriginPro 2018 software allowed changes in width and position of the isolated O-D stretching to be followed.

A subtraction for a linear baseline for each data set between  $2300\text{--}2550\text{ cm}^{-1}$  and  $2800\text{--}2950\text{ cm}^{-1}$  was carried out and normalised to the intensity of the most intense peak. As mentioned above, due to the 5 w%  $\text{D}_2\text{O}$  in the samples, such a low concentration and the large frequency mismatch between the O-D and O-H oscillators allows the observation of decoupled  $\mu(\text{O-D})$  vibrations.<sup>2, 48</sup> The  $\mu(\text{O-D})$  vibration shows very little intra- or intermolecular coupling and so, the width and position of the  $\mu(\text{O-D})$  absorption indicate the strength of the O-D bonds and the range of the hydrogen bonding environment. The structural relaxation of ASW is caused by the increase in hydrogen bonding and so, studying the  $\mu(\text{O-D})$  absorption is an ideal route by means of investigating the processes that occur upon heating.

At 80 K, the FTIR spectra show the decoupled O-D oscillator with an absorbance peak centred at  $2440\text{ cm}^{-1}$  for all samples and are attributed to the 5 w%  $\text{D}_2\text{O}$  in the sample. For comparative purposes, as mentioned earlier, the area under each curve as shown in the spectra have been normalized. The O-H absorbance peaks for pure ASW has been seen at  $3242\text{ cm}^{-1}$  as shown in Chapter 2, Figure 2.16. This section only focuses on the decoupled O-D oscillator.

Focussing on only the  $\mu(\text{O-D})$  mode, as the concentration of  $\text{C}_{10}\text{H}_{16}$  increases, the absorbance peak at  $2440\text{ cm}^{-1}$  shifts to higher wavenumbers, indicating that introducing a guest species,  $\text{C}_{10}\text{H}_{16}$ , leads to a weakening of the hydrogen bonds and stronger O-H bonds. The arrow in Figure 5.37 is drawn to show the shift of the O-D absorbance band. Figure 5.38 displays a summary of the shifts in wavenumbers for Figure 5.37 at the end of this section. This shift in the O-D stretching towards higher wavenumbers with respect

## 5. Total Neutron Scattering of Amorphous Solid Water with Embedded Adamantane

to increasing  $C_{10}H_{16}$  content is consistent with the  $H_2O$  molecules where an O–H bond is seen to point towards the COM of  $C_{10}H_{16}$ .

The FTIR spectra clearly show evidence for the mixing of both species. The stretching for  $C_{10}H_{16}$  was not seen to shift in position with respect to the content of  $C_{10}H_{16}$  and/or with temperature.

Overall, the results from the FTIR measurements support a model of hydrophobic hydration whereby the  $H_2O$  molecules in the first coordination shell are not fully hydrogen-bonded to the  $C_{10}H_{16}$ , reflecting how the cage structure is also not hydrogen-bonded to the COM of  $C_{10}H_{16}$ .

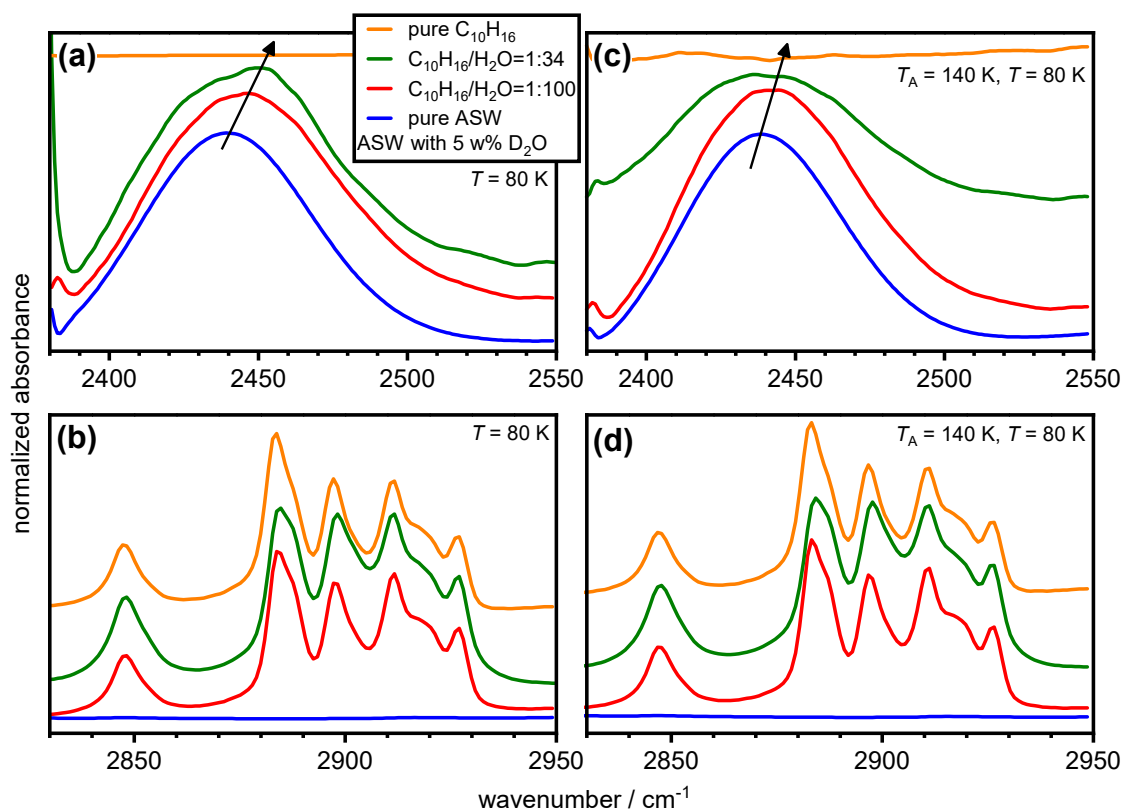


Figure 5.37. FTIR absorbance spectra of (a) and (c)  $\mu(O-D)$  vibrations in four different samples: (1) pure ASW with 5 w%  $D_2O$ ,  $C_{10}H_{16}/H_2O$  (1:100 and 1:34 molar ratio) with 5 w%  $D_2O$  and finally pure  $C_{10}H_{16}$  as indicated in the text box in panel (a). The deposition time was 2.5 minutes with a  $H_2O$  inlet pressure of  $1 \times 10^{-1}$  mbar. Data is presented for an as-made sample (80 K), (a) and (b), and an after annealed sample at 140 K in, (c) and (d). Both (b) and (d) show the spectral regions of  $C_{10}H_{16}$  for the as-made (80 K) and after annealed sample at 140 K, respectively. Each sample has been subtracted for a linear baseline and normalised with respect to the highest intensity peak.

## 5. Total Neutron Scattering of Amorphous Solid Water with Embedded Adamantane

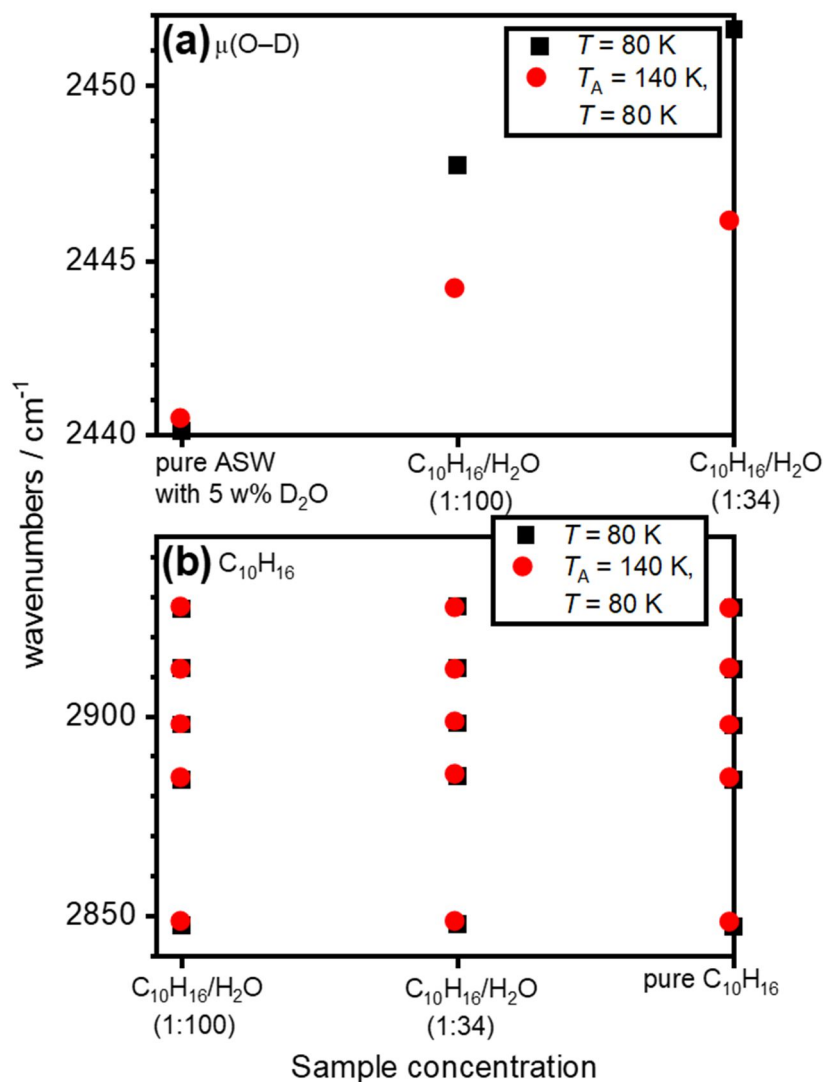


Figure 5.38. Summary of the frequency shift measurements from the various sample concentrations: (1) pure ASW with 5 w%  $\text{D}_2\text{O}$ ,  $\text{C}_{10}\text{H}_{16}/\text{H}_2\text{O}$  (1:100 and 1:34 molar ratio) with 5 w%  $\text{D}_2\text{O}$  and finally pure  $\text{C}_{10}\text{H}_{16}$  as indicated in the panels where (a)  $\mu(\text{O-D})$  vibrations and (b)  $\text{C}_{10}\text{H}_{16}$  stretching modes.

## **5.9 Discussion of Hydrophobic Hydration**

Understanding the behaviour of H<sub>2</sub>O near surfaces requires the understanding of the H<sub>2</sub>O-vapour interface.<sup>49</sup> The most influential relevance is veered towards the interface of H<sub>2</sub>O and hydrophobic species since no hydrogen bonds are formed at the hydrophobic surface.<sup>49</sup> The basis of the hydrophobic effect<sup>50</sup> comes about from the changes in the solvation of molecules with hydrophobic nature upon association. Such an effect is responsible for a number of processes such as protein folding, surfactant aggregation and compartmentalisation processes.<sup>50</sup>

The main aim of this study was to address the structure of H<sub>2</sub>O in the hydration shells of the hydrophobe, C<sub>10</sub>H<sub>16</sub>. The innovative approach as presented in this work has opened up new spyholes into studying the structure of H<sub>2</sub>O in the hydration shells of other hydrophobes. Previous experimental studies were strictly limited to amphiphilic molecules<sup>51-53</sup> due to the low solubility of hydrophobic species in H<sub>2</sub>O. For instance, the solubility of C<sub>60</sub> fullerene in liquid H<sub>2</sub>O is estimated to be  $1 \times 10^{-9} \text{ mol L}^{-1}$ , rendering the structural study of hydration shells practically, impossible.<sup>54</sup> The mixing of both H<sub>2</sub>O and the hydrophobe in this work, prohibits this obstacle as successful mixing is achieved through the codeposition from the vapour phase. Structural insights are highly important here with respect to hydrophobic hydration and data is discussed in a wider context of the poorly understood, hydrophobic effect.<sup>50</sup>

Since probing H<sub>2</sub>O around dissociated hydrophobic molecules has proved experimentally difficult due to their low solubility, the current insight arises from only theoretical and computational studies.<sup>55, 56</sup> The ‘iceberg’ model hydration shell was coined,<sup>57</sup> based upon partial molar volumes of alcohols in H<sub>2</sub>O and along these lines, it was proposed that H<sub>2</sub>O forms pentagonal rings around the hydration shell of hydrophobic species. However, there have been many controversies that have challenged this structural view both from a diffraction experiment<sup>58</sup> and the computational side.<sup>59</sup> The arguments that have been brought forward suggest that the ‘iceberg’ around hydrophobes should be perceived from the perspective of slow dynamics, whereby there is simulation<sup>60</sup> and experimental evidence.<sup>61</sup> Slower dynamics have demonstrated to lead to more ordered structures, more than what is implied by the ‘iceberg’ model.<sup>57</sup>

The structural arrangement of H<sub>2</sub>O molecules hydrating hydrophobic species undergo immense changes as a function of the size and shape of the hydrophobe. Extreme

## 5. Total Neutron Scattering of Amorphous Solid Water with Embedded Adamantane

examples include unusual ‘square ice’, found to be sandwiched between two graphene sheets<sup>62, 63</sup> (described later) and clathrate hydrates. In this study, C<sub>10</sub>H<sub>16</sub> was successfully hydrated and to compare this successful hydration to a similar analogue to C<sub>10</sub>H<sub>16</sub> would be difficult considering there is a lack of experimental evidence. Experimental findings have not yet been conducted in the exciting cross-over regime from small to large hydrophobic species. The orientational ordering of H<sub>2</sub>O at the graphene interface, CH<sub>4</sub> confined in H<sub>2</sub>O and computational studies for carbon interfaces is discussed in this section as a comparison to the complex system in the work presented in this thesis.

The hydrophobic effect has been investigated for graphite-like surfaces computationally.<sup>64</sup> In this case, the behaviour of contained H<sub>2</sub>O and potential de-wetting effects have been determined from two parallel H<sub>2</sub>O confining surfaces, marking the hydrophobic interaction.<sup>64-68</sup> The hydrogen bond network of H<sub>2</sub>O is disrupted in hydrophobic-like surfaces as H<sub>2</sub>O molecules in close proximity to the surface lack hydrogen bonds that face towards the surface. This has similarly been reciprocated for an extended homogenous flat graphene sheet.<sup>69</sup> The lack of, and insignificant attractive interactions of the H<sub>2</sub>O molecules with the surface, would be expected to suffer in a direction that can be compensated by a propensity of improving the hydrogen bond interactions with nearest neighbours in other directions.<sup>68</sup> This improvement would imply molecules in the first hydration shell would be better structured than the bulk due to the lowering of their local densities, indicting quite interesting dynamical effects.<sup>69</sup>

Alarcón *et al.*<sup>68</sup> studied the structure and orientation of H<sub>2</sub>O molecules using MD at model hydrophobic surfaces. The main focus was the geometry role of H<sub>2</sub>O hydration at graphene, carbon nanotubes and fullerene surfaces, taking into account different radii and investigating the outer and convex surface.<sup>68</sup> To this end, the first hydration layer of H<sub>2</sub>O in proximity to the surface of graphene and nanotubes was found to be much more structured than the bulk. The orientation of the O–H bonds was found to be parallel to the hydrophobic surface, pointing towards the bulk.<sup>68</sup> The first H<sub>2</sub>O hydration layers were identified as well oriented in relation to the surface, with a clear tendency for the arrangement to veer towards that consistent with ice *Ih* structuring.<sup>68</sup> This ice-like structure defines the first two to three H<sub>2</sub>O layers and follows the *c* axis of the ice *Ih* basal plane but is oppositely found for the water-air interface. This structure is rapidly lost as one moves out of the surface to the bulk structure. As the radii of the nanotubes decreases,

## 5. Total Neutron Scattering of Amorphous Solid Water with Embedded Adamantane

i.e., the curvature of the surfaces increases, H<sub>2</sub>O molecules lose structure and orientation. When dealing with an extended surface, the monotonic loss of the local structure for proximal H<sub>2</sub>O molecules shows a smooth decrease. However, the structure and orientation are lost quickly when the surface becomes partially or completely non-extended due to the stringent constraints imposed by the surface.<sup>68</sup>

Overall, it has been established by computational studies that the local structure index implies that H<sub>2</sub>O molecules in close proximity to the graphene layer are substantially more structured than the bulk.<sup>68, 69</sup> This effect is lost and fades beyond 8–10 Å and is independent of temperature.<sup>69</sup> As a consequence of improved interactions with the first nearest neighbours, the structured H<sub>2</sub>O molecules present slow dynamics when compared to the bulk.<sup>69</sup> The slowing down of H<sub>2</sub>O molecules insinuates a glassy behaviour and could, in turn, be relevant for understanding the glass transition of confined H<sub>2</sub>O.<sup>69</sup>

In addition, MD studies have been carried out on H<sub>2</sub>O locked between two sheets of graphene, signifying a prototypical example of hydrophobic confinement.<sup>62</sup> One possible phase, ‘square ice’ was observed with nanoconfined H<sub>2</sub>O at room temperature. This phase has a high packing density (1.5 times greater than common ice) and a symmetry that is different from the tetrahedral geometry of the hydrogen bonding in H<sub>2</sub>O. There are also several other phases and Figure 5.39 depicts the phase diagram for monolayer H<sub>2</sub>O with respect to confinement width and pressure.<sup>63</sup> The structure is still strictly tetragonal due to the qualitative difference between inter- and intralayer bonding.<sup>62</sup> The simulations have indicated that square ice assembles in the bilayer and trilayer crystallites, and should be present within hydrophobic nanochannels under ambient conditions.<sup>62</sup> There are major gaps in the understanding of the structure of low-dimensional ice at room temperature. Confined two-dimensional ice has been reported as a function of pressure.<sup>63</sup> The square phase was found to be stable up to ~2 GPa and agrees well with the observation of ‘square ice’ that is confined within two graphene sheets. Low-dimensional ice existence has been suggested to help explain fast H<sub>2</sub>O permeation through carbon nanotubes, graphene membranes and generally hydrophobic nanocapillaries. Square ice helps support this idea.<sup>62, 63</sup>

## 5. Total Neutron Scattering of Amorphous Solid Water with Embedded Adamantane

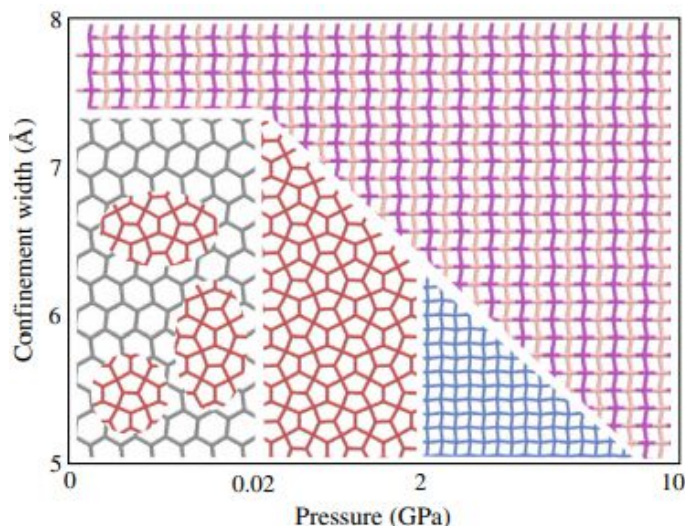


Figure 5.39. Phase diagram of monolayer ice with respect to confinement width and pressure. This figure has been reprinted from reference 63.

To conclude here, phases transitions of the monolayer ice phases have been studied. Hexagonal and pentagonal Cairo-tiled structures have been predicted and as mentioned, when the pressure is increased to 2 GPa, the so-called ‘square ice’ phase is observed. A comprehensive account of these phases is described elsewhere<sup>63</sup> and a complete picture of two-dimensional water is yet desirable.

The orientation of the embedded hydrophobe, methane ( $\text{CH}_4$ ) with respect to  $\text{H}_2\text{O}$  was investigated by Bove *et al.*<sup>70</sup> The rotation of the embedded  $\text{CH}_4$  molecules is often discussed in filled ices. To compare,  $\text{CH}_4$  molecules under rotational motion have been enclosed in metal-organic frameworks,<sup>71</sup> though,  $\text{CH}_4$ – $\text{CH}_4$  distances are larger than studied for the  $\text{CH}_4$  hydrate (MH-III) by Bove *et al.*<sup>70</sup> Hence, a clear evolution of the system where  $\text{CH}_4$  molecules have relatively free rotational motion to hindered  $\text{CH}_4$  molecules in a tightly locked cage were understood by studying the orientation for pressure between 3 and 45 GPa by MD simulations.<sup>70</sup> At 20 GPa, the gradual orientational ordering of the  $\text{CH}_4$  guest molecules displays a complete locking-in, which occurs with a distortion of guest molecules progressively.

The orientational probability density function [ $P_{\text{CH}}(\theta, \varphi)$ ] of the  $\text{CH}_4$  molecules enclosed within the  $\text{H}_2\text{O}$  frame at different pressures was investigated. Figure 5.40(a) illustrates the probability distribution of the CH polar angles  $P_{\text{CH}}(\theta, \varphi)$  and Figure 5.40(b) gives the configurations of the  $\text{CH}_4$  molecules. For simplicity, the pressure of 25.3 GPa [Figure 5.40(iv)] displays four very well-defined peaks which result from the presence of

## 5. Total Neutron Scattering of Amorphous Solid Water with Embedded Adamantane

four CH bonds, indicative of an ordered structure. CH<sub>4</sub> guest molecules are distributed as defined in Figure 5.40(ii). At low pressures [Figure 5.40(i)], the orientational disorder is seen with broad peaks and two peaks at  $\varphi = 30$  and  $150^\circ$  are seen to become broader at  $\theta = 90^\circ$ . The configuration corresponding to this change is the onset of the A/B dynamical disorder. With the intermediate pressures of 6.9 and 16.4 GPa, angle  $\varphi$  does not change, while  $\theta$  broadens significantly. These changes are attributed to disorder in the configurations of A<sup>+</sup>, A<sup>−</sup> and also B<sup>+</sup>, B<sup>−</sup> in Figure 5.40(b). As pressure increases,  $P_{\text{CH}}(\theta, \varphi)$  implies an increase in anisotropy, illustrating a pressure-induced orientational lock-in exhibited by the guest CH<sub>4</sub> molecule. Firstly at 5 GPa, and secondly at  $\sim 20$  GPa, where A/B motions disappear and the  $\pm$  orientations are locked in, respectively. Compared to pure CH<sub>4</sub>,<sup>72</sup> it has been debated<sup>73, 74</sup> that CH<sub>4</sub> orientational ordering may occur at 20 GPa in MH-III. Bove *et al.*<sup>70</sup> provides direct evidence for the orientational ordering and determined that it is not as straightforward as initially thought.<sup>70</sup>

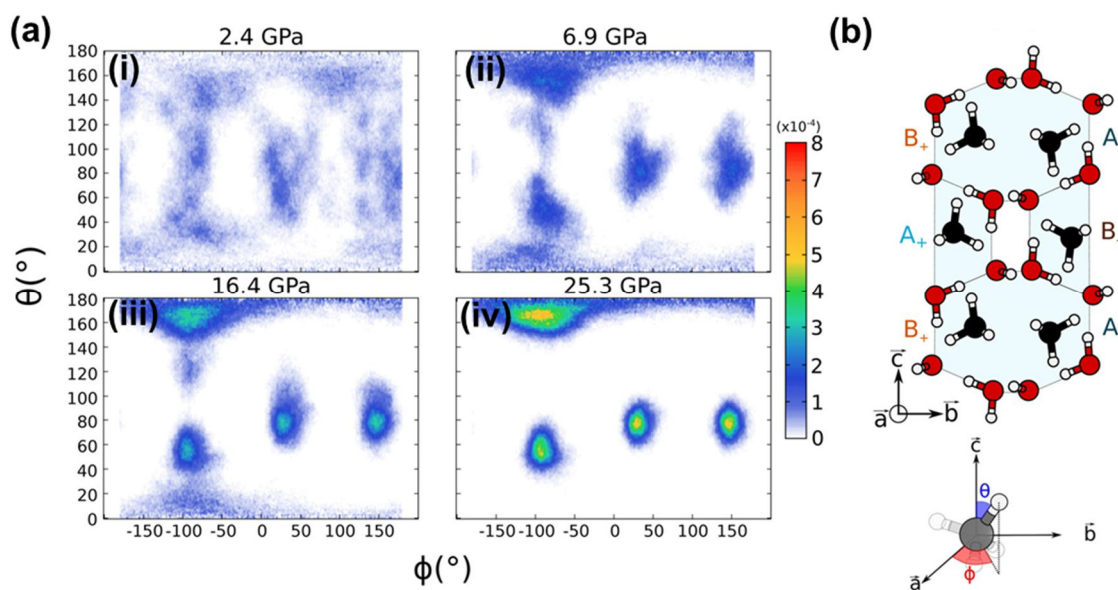


Figure 5.40. (a) Orientational probability distributions of the CH polar angles,  $P_{\text{CH}}(\theta, \varphi)$  at pressures computed at (i)–(iv), 2.4, 6.9, 16.4 and 25.3 GPa, respectively for one molecule given in the B<sup>−</sup> configuration and (b) possible CH<sub>4</sub> configurations given as A/B $\pm$ . The stacking along the a axis is given by A/B $\pm$ , stacking along the b axis is given by A<sup>+</sup>/B<sup>−</sup> or A<sup>−</sup>/B<sup>−</sup> and the stacking along the c axis is given by A<sup>+</sup>/B<sup>+</sup> (or A<sup>−</sup>/B<sup>−</sup>). This figure has been reprinted and adapted from reference 70 with the permission from ACS Publications.

As mentioned previously, amphiphiles molecules have been studied experimentally to a greater extent than hydrophobic molecules. The hydrophobic interaction is thought to increase with temperature. Yet the detailed nature remains unknown for the



## 5. Total Neutron Scattering of Amorphous Solid Water with Embedded Adamantane

intermolecular interactions. As expected, solute molecules are observed to cluster throughout the increasing content of the non-polar to non-polar headgroups and interactions change with an increase in temperature.<sup>51</sup> The OCFs of H<sub>2</sub>O around amphiphiles such as *tert*-butanol have been studied.<sup>51, 52</sup> The most dominant orientation of the capping molecule shows its *z* axis which is oriented at 90°, termed a T-like orientation towards the central molecule. This type of orientation is unexpected since earlier studies showed an ‘in-line’ configuration with two O–CC vectors.<sup>51</sup> With respect to 0.06 mole fraction of *tert*-butanol, the orientation ordering between the alcohol molecules is diverse and about three to four molecules are found as the average cluster size. Molecules in the clusters will interact *via* non-polar and non-polar group interactions.<sup>51</sup> With the solute-to-solute interactions, no significant hydrogen bonding of the alcohol to alcohol between neighbouring solutes was found.<sup>51</sup> The solute molecules were seen to cluster when the contact between the non-polar headgroups was increased and similarly, as the temperature increased, the detailed geometry of the interactions increased.<sup>51</sup> The disassembly of the clusters with a temperature increase was not found to mirror those found in the low-temperature system.<sup>51</sup> The overall temperature-dependence is anticipated to be that of an expected hydrophobically driven system, however, the distinct temperature dependencies is complex, indicating that it is misleading to think amphiphiles aggregate in terms of hydrophobic hydration.<sup>51</sup>

In a second study, for tertiary butanol-water mixtures, a substantial perturbation to the structural correlations in the intermediate range in solvent H<sub>2</sub>O has been observed.<sup>52</sup> Tertiary butanol was studied to explore hydrophobic hydration since the hydroxyl group is hydrophilic and provides polar character, while the alkyl group on the molecule is typically thought to exhibit structural perturbations to the surrounding solvent.<sup>52</sup>

The perturbation is conceptually linked to an increase in local density of the solvent molecules; however, this is only evident in the second hydration shell of H<sub>2</sub>O–H<sub>2</sub>O correlations and after.<sup>52</sup> The H<sub>2</sub>O–H<sub>2</sub>O first neighbour correlations were found to be the same as pure H<sub>2</sub>O.<sup>52</sup> This finding suggests that a large amphiphilic molecule perturbs the solvent structure and contradicts previous experimental findings of little solvent perturbation by large solutes or hydrophobic molecules.<sup>75, 76</sup> These previous studies raised concerns governing the standard Frank and Evans<sup>57</sup> coined ‘iceberg’ model and the structural origin of the hydrophobic interaction. The H<sub>2</sub>O molecules that hydrated the

## 5. Total Neutron Scattering of Amorphous Solid Water with Embedded Adamantane

non-polar regimes of *tert*-butanol, adopted a tangential orientation to the non-polar surface which is the classical expected orientation. The molecules in close proximity to the hydrophilic hydroxyl group adopted hydrogen bonding configurations.

With an insight of these results carried out by Finney *et al.*,<sup>52</sup> it would appear structurally insufficient on the grounds of modelling or understanding the earlier dominant view that hydrophobic processes are dominated by near-neighbour hydration perturbations. There is no meaningful perturbation from the structure of the first hydration shell of a non-polar group which was found in H<sub>2</sub>O. A tightening and compression of the structure of H<sub>2</sub>O is seen in H<sub>2</sub>O's second neighbour distance.<sup>52</sup>

In addition, the H<sub>2</sub>O structure and solute distribution was studied for tetramethylammonium chloride at room temperature. It was indicated that the hydrogen–hydrogen PDF for H<sub>2</sub>O did not change significantly with respect to concentration when compared to that of pure H<sub>2</sub>O. Thus, implying that the structure of H<sub>2</sub>O did not increase in the long-distance range or nearest-neighbour compared to pure H<sub>2</sub>O.<sup>76</sup>

In light of the discussion here, mainly graphene and CH<sub>4</sub> have been investigated in the literature using computational methods and have been discussed here since C<sub>10</sub>H<sub>16</sub> is larger than CH<sub>4</sub> yet smaller than graphene which is an infinitely larger molecule. Amphiphilic molecules have been studied experimentally and hydrophobic molecules have been studied more computationally. It has been exceedingly difficult to experimentally prepare and further analyse the hydration of H<sub>2</sub>O with hydrophobic species since it is known from computational studies that the implications these types of systems bring about, have implications beyond H<sub>2</sub>O interfacial phenomena. For the first time, the hydration of C<sub>10</sub>H<sub>16</sub> has been successfully achieved in this thesis, exhibiting a wealth of structural information.

### **5.10 Conclusions**

Overall, as demonstrated for the first time in this study, the hydrophobic hydration of  $C_{10}H_{16}$  in  $H_2O$  matrices has successfully been achieved. The positional and orientational ordering of  $H_2O$  molecules around hydrophobic  $C_{10}H_{16}$  in amorphous ice has been presented and the work presented in this chapter has provided new insights into the structure of this complex matrix. Using neutron diffraction and the isotopic substitution technique, the local structure of vapour deposited ASW from the local perspective of codeposited  $C_{10}H_{16}$  ‘nanoprobes’ has been investigated. For the first time, the sintering of the amorphous ice matrix, as well as the precursors for the formation of hydrates from the viewpoint of the carbon guest species, has been explored.

The first structural models of the  $C_{10}H_{16}/H_2O$  system that are consistent with their experimental diffraction data have been produced using the EPSR method in order to obtain information about the local structure and correct the pair interaction potentials with comparison to the diffraction data. The ANGULA software has also been employed to confirm and expand upon the results obtained in EPSR. Both structural models show strong orientation correlations and spatially defined intermolecular contacts as defined by both the EPSR and ANGULA software. Measurements were carried out at two distinct temperatures: as-made at 80 K and after annealing at 140 K. Data was analysed to the levels of intermolecular OCFs in combination with spherical harmonic coefficient analysis. Generally, the outcomes revealed a subtle temperature dependence of the complex system, however, this structural perturbation suggested more order in the structure at higher temperatures. Additionally, more hydrophobic hydration is induced, and the local density is enhanced in the structure at higher temperatures.

The well-mixed matrix of both species is fundamentally very distinct and has excitingly shown the formation of a new polyhedron cage where  $H_2O$  surrounds the  $C_{10}H_{16}$  guest species with five- and six-membered rings for every CH and  $CH_2$  group, respectively. Interestingly, the emerging picture here is the tendency for the system to adopt this  $5^66^4$  structure in both the as-made (80 K) and after annealing at 140 K data, where the matrix undergoes more pronounced changes in its local environment upon heating.

A total of 28  $H_2O$  molecules builds up the entire framework of the structure and three different types of oxygen atom arrangements around the cage have been identified

## 5. Total Neutron Scattering of Amorphous Solid Water with Embedded Adamantane

with the ANGULA analysis. Bivariate probability density maps have shown to locate these different oxygen atoms and have been labelled in the main text. Remarkably, this special positional ordering constitutes a new finding, whereby, the O–H bonds of the closest H<sub>2</sub>O molecules are found to point towards the COM of C<sub>10</sub>H<sub>16</sub>. The closest H<sub>2</sub>O molecules are then not hydrogen-bonded to the COM of C<sub>10</sub>H<sub>16</sub> or to one another and thus, a multipolar interaction has been postulated. This result is quite unexpected, and it is interesting that a non-polar molecule such as C<sub>10</sub>H<sub>16</sub> demonstrates quite strong orientation correlations already in its first hydration shell. Since experimental studies were hitherto, carried out on amphiphilic molecules and very limited for hydrophobic species, this study provides a significant step forward, linking the network of H<sub>2</sub>O molecules with the newly defined polyhedron, successfully achieving the hydration of hydrophobic species, C<sub>10</sub>H<sub>16</sub>.

In addition, the spectroscopic signature has been captured for the O–D oscillations and have identified that increasing the content of C<sub>10</sub>H<sub>16</sub> in the matrix shifts the frequency of this vibration to higher wavenumbers, indicative of the weakening of hydrogen bonds and stronger O–H bonds. No changes with respect to C<sub>10</sub>H<sub>16</sub> peaks have been detected with the FTIR measurements.

Ultimately, this work has further demonstrated the importance of studying H<sub>2</sub>O with guest species and highlights the potency of such matrices with guest species in facilitating researchers to examine hydration of hydrophobic species in the search for new polyhedra with distinct geometries. The study of hydrophobic hydration of hydrophobic moieties has begun to be appreciated as a ripe area of research since it has been very difficult to achieve hydration of hydrophobic species experimentally. Matrices as those produced here can be optimised and fine-tuned to their performances in a variety of applications since C<sub>10</sub>H<sub>16</sub> is a diamondoid. Diamondoids are the building blocks of nanotechnology which can be used in polymer science and chemical synthesis.<sup>77</sup>

## 5.11 References

1. J. W. G. Thomason, *Nucl. Instrum. Methods Phys. Res., Sect. A*, 2019, **917**, 61-67.
2. J. J. Shephard, J. S. O. Evans and C. G. Salzmann, *J. Phys. Chem. Lett.*, 2013, **4**, 3672-3676.
3. M. Fisher and J. P. Devlin, *J. Phys. Chem. A*, 1995, **99**, 11584-11590.
4. J. J. Shephard and C. G. Salzmann, *J. Phys. Chem. Lett.*, 2016, **7**, 2281-2285.
5. C. R. Hill, C. Mitterdorfer, T. G. Youngs, D. T. Bowron, H. J. Fraser and T. Loerting, *Phys. Rev. Lett.*, 2016, **116**, 215501.
6. J. Swenson, *Phys. Chem. Chem. Phys.*, 2018, **20**, 30095-30103.
7. F. Perakis, K. Amann-Winkel, F. Lehmkuhler, M. Sprung, D. Mariedahl, J. A. Sellberg, H. Pathak, A. Spah, F. Cavalca, D. Schlesinger, A. Ricci, A. Jain, B. Massani, F. Aubree, C. J. Benmore, T. Loerting, G. Grubel, L. G. M. Pettersson and A. Nilsson, *Proc. Natl. Acad. Sci. U. S. A.*, 2017, **114**, 8193-8198.
8. Y. Xu, N. G. Petrik, R. S. Smith, B. D. Kay and G. A. Kimmel, *Proc. Natl. Acad. Sci. U. S. A.*, 2016, **113**, 14921-14925.
9. C. R. Kwang-Hua, *Physica A*, 2019, **519**, 18-21.
10. A. K. Soper, *Chem. Phys.*, 1996, **202**, 295-306.
11. A. K. Soper, *Phys. Rev. B*, 2005, **72**, 104204.
12. D. S. Sivia, *Elementary Scattering Theory For X-ray and Neutron Users*, OUP Oxford, 2011.
13. M. P. Allen and D. J. Tildesley, *Computer Simulation of Liquids*, OUP Oxford, 2 edn., 2017.
14. L. C. Pardo, ANGULA Software Download, <https://gcm.upc.edu/en/members/luis-carlos/angula/ANGULA>, (accessed 5th January, 2021).
15. L. C. Pardo, A. Henao and A. Vispa, *J. Non-Cryst. Solids*, 2015, **407**, 220-227.
16. L. C. Pardo, A. Henao, S. Busch, E. Guàrdia and J. L. Tamarit, *Phys. Chem. Chem. Phys.*, 2014, **16**, 24479-24483.
17. A. J. Johnston, S. Busch, L. C. Pardo, S. K. Callear, P. C. Biggin and S. E. McLain, *Phys. Chem. Chem. Phys.*, 2016, **18**, 991-999.
18. J. J. Shephard, S. Klotz, M. Vickers and C. G. Salzmann, *J. Chem. Phys.*, 2016, **144**, 204502.
19. D. T. Bowron, J. L. Finney, A. Hallbrucker, I. Kohl, T. Loerting, E. Mayer and A. K. Soper, *J. Chem. Phys.*, 2006, **125**, 194502.
20. A. K. Soper, *GudrunN and GudrunX: Programs for correcting raw neutron and x-ray total scattering data to differential cross section*, Science & Technology Facilities Council, Swindon, UK, 2011.
21. A. K. Soper, *Mol. Phys.*, 2009, **107**, 1667-1684.
22. A. Hallbrucker, E. Mayer and G. P. Johari, *J. Phys. Chem.*, 1989, **93**, 4986-4990.
23. A. Hallbrucker and E. Mayer, *J. Chem. Soc., Faraday Trans.*, 1990, **86**, 3785.
24. E. Mayer and A. Hallbrucker, *J. Chem. Soc., Chem. Commun.*, 1989, **12**, 749-751.
25. A. Hallbrucker and E. Mayer, *Icarus*, 1991, **90**, 176-180.
26. S. K. Talewar, S. O. Halukeerthi, R. Riedlaicher, J. J. Shephard, A. E. Clout, A. Rosu-Finsen, G. R. Williams, A. Langhoff, D. Johannsmann and C. G. Salzmann, *J. Chem. Phys.*, 2019, **151**, 134505.
27. C. Mitterdorfer, M. Bauer, T. G. Youngs, D. T. Bowron, C. R. Hill, H. J. Fraser, J. L. Finney and T. Loerting, *Phys. Chem. Chem. Phys.*, 2014, **16**, 16013-16020.

## 5. Total Neutron Scattering of Amorphous Solid Water with Embedded Adamantane

28. C. A. Tulk, D. D. Klug, R. Branderhorst, P. Sharpe and J. A. Ripmeester, *J. Chem. Phys.*, 1998, **109**, 8478-8484.
29. W. L. Jorgensen, D. S. Maxwell and J. Tirado-Rives, *J. Am. Chem. Soc.*, 1996, **118**, 11225-11236.
30. J. Chang and S. I. Sandler, *J. Chem. Phys.*, 2004, **121**, 7474-7483.
31. S. J. Billinge and M. Thorpe, *Local Structure from Diffraction*, Springer Science & Business Media, Plenum, New York, 1998.
32. C. Gray and K. Gubbins, *Theory of Molecular Fluids: Fundamentals*, Clarendon Press, Oxford, 1984.
33. A. K. Soper, Empirical Potential Structure Refinement EPSRshell User Manual Version 26, (accessed 16th March, 2020).
34. I. M. Svishchev and P. G. Kusalik, *J. Chem. Phys.*, 1993, **99**, 3049-3058.
35. J. J. Shephard, A. K. Soper, S. K. Callear, S. Imberti, J. S. O. Evans and C. G. Salzmann, *Chem. Commun.*, 2015, **51**, 4770-4773.
36. A. K. Soper, C. Andreani and M. Nardone, *Phys. Rev. E*, 1993, **47**, 2598-2605.
37. B. A. Buffett, *Annu. Rev. Earth Planet Sci.*, 2000, **28**, 477-507.
38. J. S. Loveday and R. J. Nelmes, *Phys. Chem. Chem. Phys.*, 2008, **10**, 937-950.
39. J. A. Ripmeester, S. T. John, C. I. Ratcliffe and B. M. Powell, *Nature*, 1987, **325**, 135-136.
40. G. A. Jeffrey, *Inclusion Compounds*, Academic Press, New York, 1984.
41. V. Kosyakov, *J. Struct. Chem.*, 1995, **36**, 803-808.
42. A. Sum, C. Koh and E. Sloan, *Ind. Eng. Chem. Res.*, 2009, **48**, 7457-7465.
43. A.-H. Delsemme and P. Swings, *Annales d'Astrophysique*, 1952, **15**, 1-6.
44. E. Whalley, *Can. J. Chem.*, 1977, **55**, 3429-3441.
45. L. Rosso, M. Celli, D. Colognesi, S. Rudic, N. English and L. Ulivi, 2021, chemrxiv.14769987.v14769981.
46. T. H. Carr, J. J. Shephard and C. G. Salzmann, *J. Phys. Chem. Lett.*, 2014, **5**, 2469-2473.
47. B. Minceva-Sukarova, W. F. Sherman and G. R. Wilkinson, *Spectrochim. Acta. A*, 1985, **41**, 315-318.
48. W. Hage, A. Hallbrucker, E. Mayer and G. P. Johari, *J. Chem. Phys.*, 1994, **100**, 2743-2747.
49. J. R. Cendagorta and T. Ichiye, *J. Phys. Chem. B*, 2015, **119**, 9114-9122.
50. W. Blokzijl and J. B. F. N. Engberts, *Angew. Chem., Int. Ed. Engl.*, 1993, **32**, 1545-1579.
51. D. T. Bowron and J. L. Finney, *J. Phys. Chem. B*, 2007, **111**, 9838-9852.
52. D. T. Bowron, A. K. Soper and J. L. Finney, *J. Chem. Phys.*, 2001, **114**, 6203-6219.
53. M.-L. Tan, J. R. Cendagorta and T. Ichiye, *J. Am. Chem. Soc.*, 2013, **135**, 4918-4921.
54. X. Ma, B. Wigington and D. Bouchard, *Langmuir*, 2010, **26**, 11886-11893.
55. D. Chandler, *Nature*, 2005, **437**, 640-647.
56. H. S. Ashbaugh and L. R. Pratt, *Rev. Mod. Phys.*, 2006, **78**, 159.
57. H. S. Frank and M. W. Evans, *J. Chem. Phys.*, 1945, **13**, 507-532.
58. P. Buchanan, N. Aldiwan, A. K. Soper, J. L. Creek and C. A. Koh, *Chem. Phys. Lett.*, 2005, **415**, 89-93.
59. T. Head-Gordon, *Proc. Natl. Acad. Sci. U. S. A.*, 1995, **92**, 8308-8312.
60. S. Matysiak, P. G. Debenedetti and P. J. Rossky, *J. Phys. Chem. B*, 2011, **115**, 14859-14865.

## 5. Total Neutron Scattering of Amorphous Solid Water with Embedded Adamantane

61. N. Galamba, *J. Phys. Chem. B*, 2013, **117**, 2153-2159.
62. G. Algara-Siller, O. Lehtinen, F. C. Wang, R. R. Nair, U. Kaiser, H. A. Wu, A. K. Geim and I. V. Grigorieva, *Nature*, 2015, **519**, 443-445.
63. J. Chen, G. Schusteritsch, C. J. Pickard, C. G. Salzmann and A. Michaelides, *Phys. Rev. Lett.*, 2016, **116**, 025501.
64. N. Choudhury and B. M. Pettitt, *J. Phys. Chem. B*, 2005, **109**, 6422-6429.
65. D. M. Huang and D. Chandler, *Proc. Natl. Acad. Sci. U. S. A.*, 2000, **97**, 8324.
66. X. Huang, C. J. Margulis and B. J. Berne, *Proc. Natl. Acad. Sci. U. S. A.*, 2003, **100**, 11953-11958.
67. N. Giovambattista, C. F. Lopez, P. J. Rossky and P. G. Debenedetti, *Proc. Natl. Acad. Sci. U. S. A.*, 2008, **105**, 2274-2279.
68. L. M. Alarcón, D. C. Malaspina, E. P. Schulz, M. A. Frechero and G. A. Appignanesi, *Chem. Phys.*, 2011, **388**, 47-56.
69. D. C. Malaspina, E. P. Schulz, L. M. Alarcón, M. A. Frechero and G. A. Appignanesi, *Eur. Phys. J. E*, 2010, **32**, 35-42.
70. S. Schaack, U. Ranieri, P. Depondt, R. Gaal, W. F. Kuhs, A. Falenty, P. Gillet, F. Finocchi and L. E. Bove, *J. Phys. Chem. C*, 2018, **122**, 11159-11166.
71. M. Savage, I. da Silva, M. Johnson, J. H. Carter, R. Newby, M. Suyetin, E. Besley, P. Manuel, S. Rudić, A. N. Fitch, C. Murray, W. I. F. David, S. Yang and M. Schröder, *J. Am. Chem. Soc.*, 2016, **138**, 9119-9127.
72. R. Bini and G. Pratesi, *Phys. Rev. B*, 1997, **55**, 14800.
73. S.-I. Machida, H. Hirai, T. Kawamura, Y. Yamamoto and T. Yagi, *Phys. Chem. Minerals*, 2007, **34**, 31-35.
74. D. Klug, J. Tse, Z. Liu and R. J. Hemley, *J. Chem. Phys.*, 2006, **125**, 154509.
75. A. Soper and J. Finney, *Phys. Rev. Lett.*, 1993, **71**, 4346.
76. J. Turner, A. Soper and J. Finney, *Mole. Phys.*, 1992, **77**, 411-429.
77. A. Patzer, M. Schütz, T. Möller and O. Dopfer, *Angew. Chem. Int. Ed.*, 2012, **124**, 5009-5013.

## 6 Final Conclusions and Outlook

This thesis aims to examine the behaviour of water ( $\text{H}_2\text{O}$ ) by introducing several guest species into an amorphous ice matrix. This includes for the first time, a guest species that is a solid at room temperature. These highly complex mixtures have been successfully characterised and exhibit remarkable and unprecedented insights towards understanding the bulk properties of  $\text{H}_2\text{O}$ .

The abundance of amorphous solid water (ASW) across the universe has rendered it a prototypical and representative material for exploring physical vapour deposition processes. Intricately detailed and with a multifaceted nature, ASW has a strong tendency to form highly porous structures.<sup>1</sup> The combination of ASWs structural heterogeneity beyond length scales and the dynamic behaviour of  $\text{H}_2\text{O}$  molecules, is underpinned in this study.

Initially, gaseous ‘nanoprobes’ were incorporated into ASW matrices to detect the gas-trapping environments in the macroscopic films of ASW.<sup>2</sup> ASW films of thickness 25–100  $\mu\text{m}$  were codeposited with minuscule amounts of argon (Ar), methane ( $\text{CH}_4$ ), carbon dioxide ( $\text{CO}_2$ ) and helium. These complex films were subject to heating in the 95–185 K temperature range. Interestingly, three discernible desorption processes have been observed which are ascribed to: (1) desorption of argon out of cracks in ASW which are removed upon heating above 100 K, (2) argon is released from collapsed internal voids at  $\sim 125$  K and finally, (3) fully matrix-isolated argon is liberated as it is induced by the crystallisation of ASW to ice *Isd* at  $\sim 155$  K. The collapse of pores in ASW during desorption process (2) arises due to the fundamental orientational glass transition of ASW/low-density amorphous ice (LDA).<sup>3,4</sup> Since nanoscale  $\text{Ar}@ASW$ <sup>5,6</sup> mixtures have demonstrated desorption process (3), the first two desorption processes in this study are assigned to the macroscopic dimensions of the thick ASW films prepared in this study. Argon was established as the ideal material to incorporate into vapour deposited ice as a result of its small and inert nature. However, to confirm the origin of the new desorption features and local environments,  $\text{CH}_4$ ,  $\text{CO}_2$ , and helium were employed as additional ‘nanoprobes’. In the case for  $\text{CH}_4@ASW$ , the three discernible desorption processes were observed which means  $\text{CH}_4$  can also be trapped in three different environments as illustrated in Chapter 3. When compared to  $\text{Ar}@ASW$ , for desorption features (2) and (3), a shift towards higher temperatures can be observed for the  $\text{CH}_4$  nanoprobes. The



analysis as provided in Table 3.1 and Figure 3.23 (Chapter 3) quantitatively shows the stronger van der Waals interaction in ASW with CH<sub>4</sub>. The concentration of CH<sub>4</sub> in ASW was found to be 10 times greater when compared to the concentration of argon in ASW.<sup>2</sup> Conversely, helium was found to be quite mobile and thus, was not able to be trapped in the ASW matrix at 95 K. The low volatility of CO<sub>2</sub> compared to the other nanoprobe,<sup>7</sup> meant that the first desorption feature was not clearly observed. It was speculated that due to a simple delay at high temperature, desorption process (1) overlapped with process (2). In the literature, it has been demonstrated that for ASW mixtures CO<sub>2</sub>-rich, CO<sub>2</sub> is mobile in the mixture and can lead to segregation of CO<sub>2</sub><sup>8</sup> or low-temperature desorption features.<sup>9, 10</sup> It is likely that these effects may pose an influence to the temperature-programmed desorption (TPD) as shown in Figure 3.15(d), Chapter 3. Overall, it is evident that ASW morphology is influenced by a film thickness increase (Figure 3.19, Chapter 3), owing to a highly complex ASW film. Thinner films do not show the same desorption behaviour as thick macroscopic films prepared in this study.<sup>2</sup> ASW's ability to trap gaseous species arises from its complex nature and it is considered as an important material for a range of cosmological processes.<sup>11</sup> The emerging picture of the new desorption features will be the emphasis of future studies.

To further delve into the assignments of these desorption features, the morphology of ASW was investigated. The flow of H<sub>2</sub>O-vapour in line with the deposition plate was baffled with an iron mesh resulting in a reduced desorption feature of process (1) and a substantially increased amount of matrix-isolated argon gas.

In line with the complex nature of ASW, the product of crystallisation, stacking disordered ice (ice *Isd*) from this study, has proved to be distinct from the literature.<sup>12-16</sup> Different fractions of stacking events and second-order memory effects were exhibited. Upon heating ASW, the cubicity from 160–190 K was observed and seen to decrease, tending towards a more hexagonal nature as expected. The precise details of stacking disorder present in ice *Isd* have proved to affect its chemical and physical properties.<sup>17-19</sup> Future studies to determine how, and if, the underlying structural differences present in ASW alter the stacking disorder in ice *Isd*, will need to be investigated. In addition, the complicated changes occurring upon heating these films around crystallisation, as monitored by the quartz-crystal microbalance (QCM), will need to be explored further.

## 6. Final Conclusions and Outlook

Studying the behaviour of ASW from the viewpoint of these gaseous ‘nanoprobes’ and in particular, argon, has provided a truly significant standpoint from which to assess the complex, multifaceted nature of ASW. Overall, it can be concluded that quantitative insights into gas trapping environments were achieved and the crystallisation phenomena of ASW was independent of the trapped gaseous species. The gaseous species did, however, when compared with one another, display highly dissimilar desorption features, attributed to their properties.

Since the vast majority of investigations on ASW mixtures have been conducted and focussed on ‘gas-laden’ amorphous ices,<sup>2, 20-22</sup> the guest species, adamantane ( $C_{10}H_{16}$ ), with low volatility was prepared by codeposition with amorphous ice, since very little is known about the structure and dynamics of  $H_2O$  in such unusual mixtures. With precise control over the deposition rates,  $C_{10}H_{16}$  ‘nanoprobe’ was finely dispersed and embedded within the amorphous ice matrix. In the first instance, codeposited samples were heated from 95–270 K in an in-house X-ray diffractometer and were not annealed in the vacuum chamber at 125 K, resulting in the formation of the nitrogen clathrate hydrate of cubic structure II, CS-II (Chapter 4). The presence of this clathrate hydrate was caused by the removal of the sample under liquid nitrogen ( $LN_2$ ) conditions, thus, entering the open pores of ASW.

Hereafter, the pores of ASW were always closed by annealing the sample in the vacuum chamber at 125 K before removal. Extremely valuable insights have been gained from the matrices across a wide composition range ( $C_{10}H_{16}/H_2O$  with ratios of 1:100–1:6). The addition of  $C_{10}H_{16}$  in vapour deposited amorphous ice has allowed the detection of several peculiar features in both calorimetry and diffraction for both the  $H_2O$ -rich sample, compared to that of the  $C_{10}H_{16}$ -rich samples. These features could not easily be assigned to any known type of clathrate hydrates. Based upon nuclear magnetic resonance (NMR) and X-ray diffraction (XRD) measurements in the literature,<sup>23</sup> the sH clathrate hydrate has been found to form with guest species,  $C_{10}H_{16}$ .<sup>24</sup> However, a definitive crystal structure is yet to be determined. Several methods of deposition were carried out in order to yield this hydrate and characterise the structure *via* XRD. Intriguingly, the different matrices prepared, consisted of sharp features which related to neither ice nor  $C_{10}H_{16}$  itself. Unexpectedly, in some cases, clathrate hydrate formation was seen to proceed from the ASW/ice *Isd* transition. During this transition, one goes from an amorphous to a crystalline solid, thus, a lot of changes occur and in this ‘chaos’, a clathrate hydrate forms.

However, provided that these features were actually from a clathrate hydrate, samples were then equally prepared several times and surprisingly, consistent results were not observed. Different types of methods with respect to how the samples were deposited into the vacuum chamber was implemented. The spatial distribution and uniformity across the deposition plate was considered. After several efforts aiming to yield the clathrate hydrate through different preparation methods, many features present in the differential scanning calorimetry (DSC) data were difficult to assign in the XRD data. It could be suggested that the samples show preferred orientation or simply, the absence of Bragg peaks in the XRD as seen in the DSC measurements could be speculated to the fact that the proposed clathrate hydrate Bragg peaks were produced from the ‘chaos’ of the ASW to ice *Isd* transition. It is unclear as to why there are differences in the calorimetric and diffraction data seeing as the sample is from the same experiment.

In the 1:100 and 1:34 molar ratio samples of  $C_{10}H_{16}/H_2O$ , clathrate hydrate-like characteristics and pronounced features were observed from the exotherms in calorimetry. In any case of using different deposition methods, the crystallisation properties of ASW were not affected by the introduction of the hydrophobe. However, it was concluded that the emergence of these mysterious features in the matrices is the undoubted result of a highly complex matrix. Nevertheless, this is maximally exciting since it was established that the hydrophobe does affect the behaviour of  $H_2O$ . Overall, the matrices proved to be undoubtedly more complex and difficult to understand than first appreciated, caused by the elusive behaviour of both the  $H_2O$ -rich and  $C_{10}H_{16}$ -rich samples. Given the different methods in depositing  $C_{10}H_{16}$  during these investigations, hopefully in the near future, clathrate hydrates will be achieved. Efforts need to be directed towards bridging the gap between the experimental set-up and obtaining the correct composition. With the latter, a wider range of compositions may be explored and with the former, generally higher pressures and lower temperatures need to be achieved to potentially form a clathrate hydrate. *In situ* clathrate hydrate formation under ultra-high vacuum and cryogenic conditions has not been explored experimentally, however, it is proposed that they may grow epitaxially at low pressure by annealing gas-water mixtures or by performing on other clathrate hydrates.<sup>25</sup>

Thus, to build upon the conclusions drawn in this chapter, future work should investigate preparing clathrate hydrates with even lower pressures which can potentially be first, determined by computational methods and secondly, ascertained with more advanced experimental set-ups.

The final chapter in this thesis aimed to demonstrate and elucidate the structure of H<sub>2</sub>O in hydration shells of C<sub>10</sub>H<sub>16</sub>. Since discovering that some unassignable peaks in the XRD (Chapter 4) arise from the formation of a clathrate hydrate, it became necessary to further characterise C<sub>10</sub>H<sub>16</sub>/H<sub>2</sub>O in detail on the Near InterMediate Range Order Diffractometer (NIMROD) at ISIS.<sup>26</sup> Such measurements enable the study of the matrices with a view on their astrophysical relevance, but also, in using C<sub>10</sub>H<sub>16</sub> as a ‘nanoprobe’, it was possible to address a range of fundamental questions regarding the structure and dynamics of the ASW matrix.

It was believed that the H<sub>2</sub>O-rich sample of 1:100 C<sub>10</sub>H<sub>16</sub> to H<sub>2</sub>O molar ratio would provide the best results in neutron diffraction. In this case, C<sub>10</sub>H<sub>16</sub> is an ideal material to incorporate into the amorphous ice as a result of its highly symmetric nature and non-polar properties. Initially, more than two hydration layers were expected for C<sub>10</sub>H<sub>16</sub> and even with this dilute composition, C<sub>10</sub>H<sub>16</sub> represented a meaningful contribution to the total structure factor.

Empirical Potential Structure Refinement (EPSR)<sup>27-29</sup> models are now available for as-made (80 K) and after annealed at 140 K C<sub>10</sub>H<sub>16</sub>/H<sub>2</sub>O matrices. Despite extreme similarities, the annealed samples show stronger correlations and more structural order with respect to C<sub>10</sub>H<sub>16</sub> and H<sub>2</sub>O molecules, which results from structural relaxation and sintering of the sample. There is a strong tendency for the closest H<sub>2</sub>O molecules to point towards the centre of mass (COM) of C<sub>10</sub>H<sub>16</sub>. Remarkably, these H<sub>2</sub>O molecules have been realised to arrange themselves in a special type of arrangement, forming a new polyhedron cage with notation, 5<sup>6</sup>6<sup>4</sup>, around C<sub>10</sub>H<sub>16</sub>. Intriguingly, there are 28 well-structured H<sub>2</sub>O molecules in the first coordination shell, and only the closest O–H bonds are then not hydrogen-bonded to the COM of C<sub>10</sub>H<sub>16</sub> or to one another, which is the oppositely marked case for all other clathrate hydrates. Indeed, this type of arrangement has not been identified before and thus, a multipolar interaction is suggested. It is interesting that a non-polar molecule such as C<sub>10</sub>H<sub>16</sub> shows quite strong orientation correlations in its hydration shell already at 80 K. Extraordinarily, three different positional arrangements of the H<sub>2</sub>O molecules have been identified and labelled in Chapter 5. These oxygen atoms are those building up the framework of the five- and six-membered rings in line with 28 oxygen atoms. Four oxygen atoms (labelled ‘C’) lie in front of each ‘cyclohexane’ ring, there are 12 oxygen atoms (labelled ‘B’), where two each lie at the sides of each CH<sub>2</sub> group and another 12 oxygen atoms (labelled ‘A’), where three are situated around every CH of C<sub>10</sub>H<sub>16</sub>. This cage is very well-defined already at

80 K and ANGULA<sup>30, 31</sup> analysis was also carried out to show that C<sub>10</sub>H<sub>16</sub> molecules with 27 and 29 H<sub>2</sub>O molecules in fact, show the same type of cage, however, with point defects. The divergence from a fully amorphous sample at H<sub>2</sub>O-rich concentrations has put into question the nature of the new cage which is so well-defined already at 80 K.

Studying the structure and dynamics of amorphous ice from the viewpoint of the carbon guest species has proved to be a truly remarkable perspective from which to assess the search for newly defined geometries and the search for larger-caged polyhedra. The new cage characterised by neutron diffraction and confirmed with structural analysis with the EPSR method and the ANGULA software has been unheard of, up until now, in this study. This cage can be prepared in a reproducible manner under strict deposition conditions and molar composition. The large number of H<sub>2</sub>O molecules surrounding C<sub>10</sub>H<sub>16</sub> has provided evidence for the successful mixing and hydration of the matrix and hydrophobic species, respectively.

The addition of C<sub>10</sub>H<sub>16</sub> to amorphous ice has allowed us to detect the uncharted regime of small hydrophobes in ASW, facilitated by vapour deposition of both species. In any case, a clathrate hydrate was not prepared since the H<sub>2</sub>O molecules were not hydrogen-bonded to anything and thus, it would be probable to suggest that the anomalous and peculiar features that could not be assigned in Chapter 4, were due to this new cage type with preferred orientation.

Molecular-level insights into the structure and dynamics of interfacial H<sub>2</sub>O were discussed in the context of the H<sub>2</sub>O-carbon interface. Overall, it can be concluded that C<sub>10</sub>H<sub>16</sub> was an ideal nanoprobe to incorporate within the amorphous ice matrix as it heavily influenced hydrophobic hydration, namely where: (i) a newly defined polyhedron with distorted cages was identified, where the H<sub>2</sub>O molecules building the framework of the cage did not experience any hydrogen bonding in the manner that ice does, and (ii) remarkably, the closest H<sub>2</sub>O molecules were found to point towards the COM of C<sub>10</sub>H<sub>16</sub>.

As a whole, and considering the research carried out over the course of this thesis, several invaluable insights have been acquired which are likely to have prolonged implications towards the understanding of H<sub>2</sub>O. Particularly that, where the results obtained from the last chapters with the C<sub>10</sub>H<sub>16</sub> ‘nanoprobe’ should help build strong contributions towards the ongoing search for new polyhedra and hydration of hydrophobic species, providing a highly templating impact towards the hydrophobic effect.<sup>32</sup>

## 6. Final Conclusions and Outlook

This thesis has drawn many conclusions, and to build upon them, the use of larger hydrophobes would be beneficial in order to determine the crossover from small to large hydrophobes. In a similar fashion to the research carried out with the ESPR method and the ANGULA software for  $C_{10}H_{16}$  in  $H_2O$ , these larger hydrophobes may be used to help understand the behaviour and peculiar anomalies of  $H_2O$  in low-temperature and low-pressure environments. Upon changing the size and shape of new non-polar species, complementary information explaining the preferential formation of new polyhedra will be unveiled. It would be very interesting to gather an appreciation for the positions of the  $H_2O$  molecules when the hydrophobe is anything other than  $C_{10}H_{16}$ , finely incorporated into the amorphous ice matrix. For instance, it would be beneficial to obtain pair distribution functions (PDFs) and spatial density functions (SDFs) of a large gallery of hydrophobic species to discover which open framework architectures are possible with larger guest species.

Furthermore, this truly multidisciplinary project has opened up new spyholes to critical processes occurring at the water-carbon interface. It would be interesting to see if computational techniques have the capabilities to probe larger hydrophobes in water-ice cages to identify which structures are predicted. A technique sensitive to the composition of matrices as produced here could possibly be implemented and further optimised in a computer model, isolating new polyhedra cages.

## 6.1 References

1. E. Mayer and R. Pletzer, *J. Phys. Colloq.*, 1987, **48**, C1-581-C581-586.
2. S. K. Talewar, S. O. Halukeerthi, R. Riedlaicher, J. J. Shephard, A. E. Clout, A. Rosu-Finsen, G. R. Williams, A. Langhoff, D. Johannsmann and C. G. Salzmann, *J. Chem. Phys.*, 2019, **151**, 134505.
3. M. Fisher and J. P. Devlin, *J. Phys. Chem. A*, 1995, **99**, 11584-11590.
4. J. J. Shephard and C. G. Salzmann, *J. Phys. Chem. Lett.*, 2016, **7**, 2281-2285.
5. P. Ayotte, R. S. Smith, K. P. Stevenson, Z. Dohnálek, G. A. Kimmel and B. D. Kay, *J. Geophys. Res. Planets*, 2001, **106**, 33387-33392.
6. A. Bar-Nun, G. Notesco and T. Owen, *Icarus*, 2007, **190**, 655-659.
7. M. P. Collings, M. A. Anderson, R. Chen, J. W. Dever, S. Viti, D. A. Williams and M. R. S. McCoustra, *Mon. Not. R. Astron. Soc.*, 2004, **354**, 1133-1140.
8. K. Isokoski, J. B. Bossa, T. Triemstra and H. Linnartz, *Phys. Chem. Chem. Phys.*, 2014, **16**, 3456-3465.
9. J. L. Edridge, K. Freimann, D. J. Burke and W. A. Brown, *Philos. Trans. R. Soc., A*, 2013, **371**, 20110578.
10. J. He, S. M. Emtiaz, A. Boogert and G. Vidali, *Astrophys. J.*, 2018, **869**, 41.
11. S. Kwok, *Physics and Chemistry of the Interstellar Medium*, University Science Books, Sausalito, USA, 2007.
12. W. F. Kuhs, C. Sippel, A. Falenty and T. C. Hansen, *Proc. Natl. Acad. Sci. U. S. A.*, 2012, **109**, 21259-21264.
13. T. L. Malkin, B. J. Murray, C. G. Salzmann, V. Molinero, S. J. Pickering and T. F. Whale, *Phys. Chem. Chem. Phys.*, 2015, **17**, 60-76.
14. T. C. Hansen, M. M. Koza and W. F. Kuhs, *J. Phys.: Condens. Matter*, 2008, **20**, 285104.
15. T. L. Malkin, B. J. Murray, A. V. Brukhno, J. Anwar and C. G. Salzmann, *Proc. Natl. Acad. Sci. U. S. A.*, 2012, **109**, 1041-1045.
16. C. G. Salzmann, B. J. Murray and J. J. Shephard, *Diamond Relat. Mater.*, 2015, **59**, 69-72.
17. J. E. Shilling, M. A. Tolbert, O. B. Toon, E. J. Jensen, B. J. Murray and A. K. Bertram, *Geophys. Res. Lett.*, 2006, **33**, L17801.
18. B. J. Murray, C. G. Salzmann, A. J. Heymsfield, S. Dobbie, R. R. Neely and C. J. Cox, *Bull. Am. Meteorol. Soc.*, 2015, **96**, 1519-1531.
19. T. H. Carr, J. J. Shephard and C. G. Salzmann, *J. Phys. Chem. Lett.*, 2014, **5**, 2469-2473.
20. R. S. Smith, R. A. May and B. D. Kay, *J. Phys. Chem. B*, 2016, **120**, 1979-1987.
21. G. Notesco, A. Bar-Nun and T. Owen, *Icarus*, 2003, **162**, 183-189.
22. R. S. Smith, N. G. Petrik, G. A. Kimmel and B. D. Kay, *Acc. Chem. Res.*, 2012, **45**, 33-42.
23. J. A. Ripmeester, S. T. John, C. I. Ratcliffe and B. M. Powell, *Nature*, 1987, **325**, 135-136.
24. J. P. Lederhos, A. P. Mehta, G. B. Nyberg, K. J. Warn and E. D. Sloan, *AIChE J.*, 1992, **38**, 1045-1048.
25. W. L. Mao, H. K. Mao, A. F. Goncharov, V. V. Struzhkin, Q. Guo, J. Hu, J. Shu, R. J. Hemley, M. Somayazulu and Y. Zhao, *Science*, 2002, **297**, 2247-2249.
26. D. T. Bowron, A. K. Soper, K. Jones, S. Ansell, S. Birch, J. Norris, L. Perrott, D. Riedel, N. J. Rhodes, S. R. Wakefield, A. Botti, M. A. Ricci, F. Grazzi and M. Zoppi, *Rev. Sci. Instrum.*, 2010, **81**, 033905.

27. A. K. Soper, Empirical Potential Structure Refinement EPSRshell User Manual Version 26, (accessed 16th March, 2020).
28. A. K. Soper, *Phys. Rev. B*, 2005, **72**, 104204.
29. A. K. Soper, *Chem. Phys.*, 1996, **202**, 295-306.
30. L. C. Pardo, ANGULA Software Download,  
<https://gcm.upc.edu/en/members/luis-carlos/angula/ANGULA>, (accessed  
accessed 5th January, 2021).
31. L. C. Pardo, A. Henao and A. Vispa, *J. Non-Cryst. Solids*, 2015, **407**, 220-227.
32. W. Blokzijl and J. B. F. N. Engberts, *Angew. Chem., Int. Ed. Engl.*, 1993, **32**,  
1545-1579.



## Appendix

### Appendix 1. Formation of Nitrogen (N<sub>2</sub>) Clathrate Hydrates

The additional differential scanning calorimetry (DSC) and X-ray diffraction (XRD) patterns shown below relate to Chapter 4, section 4.5.1.

Figure 1 displays once again, several features significantly different from a DSC thermogram of pure amorphous solid water (ASW) illustrating the complexity of this system. Feature (i) can be described as the crystallisation from ASW to stacking disordered ice (ice *Isd*), (ii) the formation of the N<sub>2</sub> cubic structure II (CS-II) clathrate hydrate and (iii) the decomposition of the clathrate hydrate. The latter two steps are seen in the corresponding XRD patterns as displayed in Figure 1(b), whereby the formation of the clathrate hydrate occurs after the transition to ice *Isd*, forming at approximately 190–200 K and further decomposing after 220 K. External hexagonal ice (ice *Ih*) impurities and sample holder peaks have been denoted with asterisks or shown with other tickmarks.

The General Structure Analysis System (GSAS)<sup>1,2</sup> software was used to confirm the presence of the N<sub>2</sub> CS-II clathrate hydrate. The diffraction pattern of the 1:37 molar ratio of C<sub>10</sub>H<sub>16</sub> in H<sub>2</sub>O matrices at 210 K with the Rietveld refinement is shown in Figure 2. The Rietveld refinement indicates the presences of ice *Ih*, adamantane (C<sub>10</sub>H<sub>16</sub>) and the CS-II clathrate hydrate. This is the first time this mixture has been prepared and analysed to the best of our knowledge.

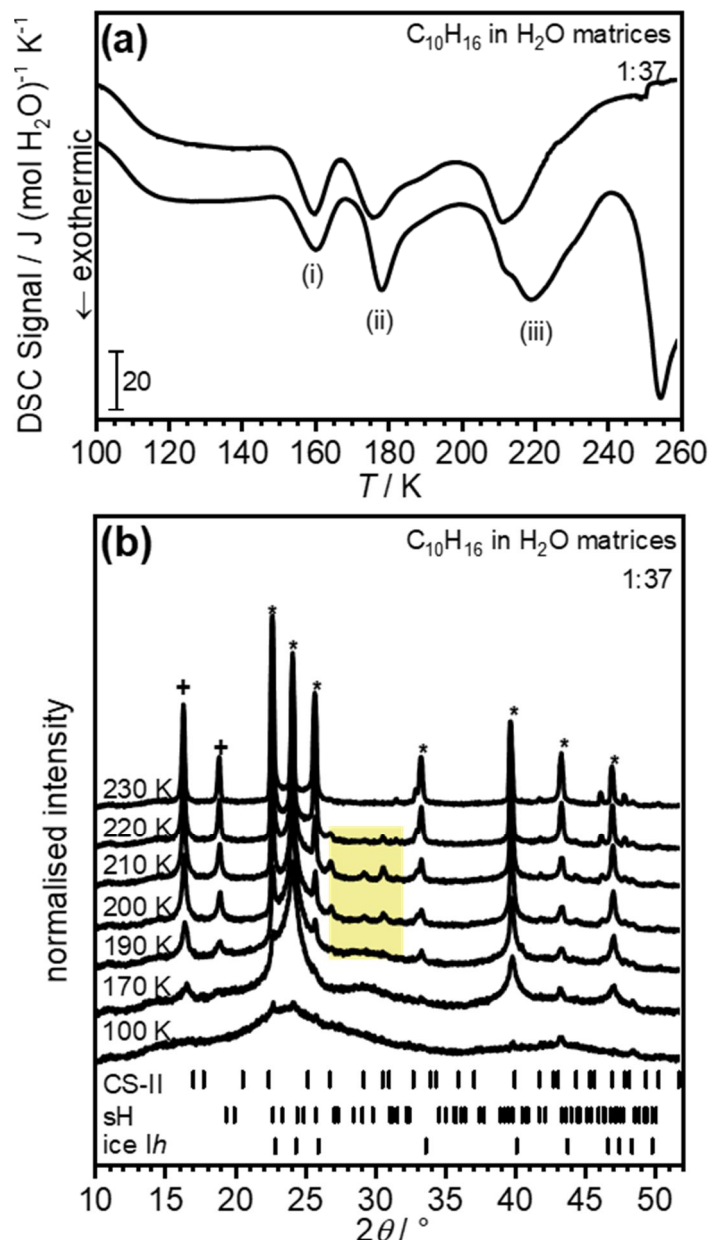


Figure 1. (a) DSC thermograms of unannealed C<sub>10</sub>H<sub>16</sub>/H<sub>2</sub>O prepared at a molar ratio of 1:37 and heated at 10 K min<sup>-1</sup> where, (i) crystallisation of ASW to ice Isd, (ii) formation of the N<sub>2</sub> clathrate hydrate and (iii) decomposition of the clathrate hydrate. The DSC signals are normalised with respect to per mole of H<sub>2</sub>O. (b) XRD patterns (Cu Kα, λ = 1.54 Å) at several temperatures of a 1:37 C<sub>10</sub>H<sub>16</sub>/H<sub>2</sub>O mixture. The tickmarks indicate the positions of the expected Bragg peaks for ice Ih, sH hydrate and CS-II hydrate. The yellow-shaded area shows the Bragg peaks of the expected CS-II hydrate. The plus '+' sign shows the two main C<sub>10</sub>H<sub>16</sub> peaks aggregating out of the mixture and the asterisks, '\*' show the ice Ih Bragg peaks. Some minor contaminates may arise due to sample transfer in a humid environment or external ice Ih on the sample holder.

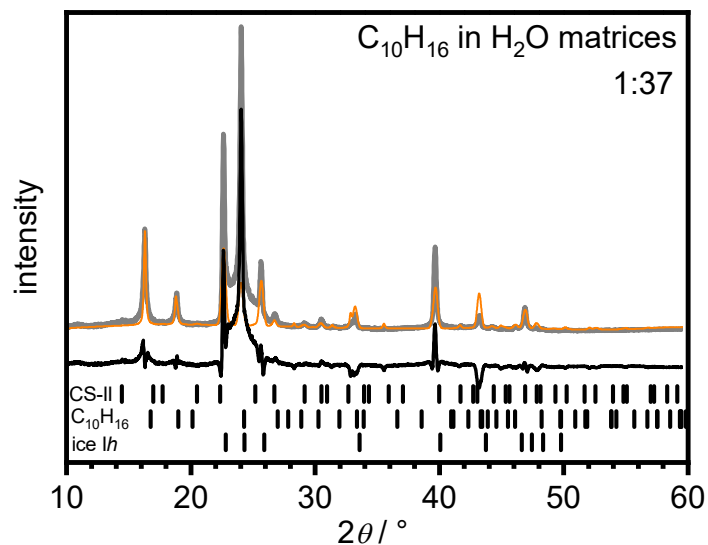


Figure 2. XRD pattern (Cu K $\alpha$ ,  $\lambda = 1.54 \text{ \AA}$ ) of a 1:37 molar ratio of C<sub>10</sub>H<sub>16</sub>/H<sub>2</sub>O matrices at 210 K. The experimental data is displayed as a thick grey line and the thinner orange line displays the Rietveld fit from GSAS. The thin black line indicates the differences between the experimental and fitted data. This figure includes tickmarks, indicating the expected positions of Bragg peaks of ice Ih, C<sub>10</sub>H<sub>16</sub> and the CS-II clathrate hydrate.

## References

1. A. C. Larson, R. B. Dreele and B. Toby, "General Structure Analysis System (GSAS)", Los Alamos National Laboratory Report LAUR 86-748 2000.
2. B. H. Toby, *J. Appl. Crystallogr.*, 2001, **34**, 210-213.

### **Appendix 2.** The Near and InterMediate Range Order Diffractometer (NIMROD) Proposal Submitted 17<sup>th</sup> October 2018

The experiments conducted on the NIMROD beamline were from proposal number RB 1910462.

#### Sample record:

Instrument: NIMROD, 6 days

Special Requirements: Helium Cryostat

Container:  $\text{Ti}_{0.68}\text{Zr}_{0.32}$  flat plate

Temperature Range: 80–200 K

**Adamantane in amorphous ice: A nanoprobe for detecting sintering, glass-transition, and clathrate hydrate formation**



